NASA Contractor Report 3049

Experimental Investigation of a 0.15-Scale Model of an Underfuselage Normal-Shock Inlet

P. C. Leamer and I. G. Kennon

CONTRACT NAS3-21139
OCTOBER 1978

NASA

NASA Contractor Report 3049

Experimental Investigation of a 0.15-Scale Model of an Underfuselage Normal-Shock Inlet

P. C. Leamer and I. G. Kennon
General Dynamics
Fort Worth, Texas

Prepared for
Lewis Research Center
under Contract NAS3-21139

National Aeronautics
and Space Administration

**Scientific and Technical
Information Office**

1978

FOREWORD

This report represents a modification of an existing General Dynamics Fort Worth Division Report MR-P-362, Data Analysis Report for YF-16 0.15-Scale Inlet Conducted at NASA/Lewis, by P. C. Leamer. The requirements of NASA Policy Directive NPD 2220.4 regarding the use of SI Units have been waived in accordance with the provisions of paragraph 5d of that Directive by the Director of Lewis Research Center.

TABLE OF CONTENTS

TABLE OF CONTENTS (continued)

SUMMARY

A 0.15-scale model of an underfuselage engine inlet designed for a single-engine fighter airplane was tested in the NASA Lewis Research Center's 8- by 6-ft wind tunnel. The inlet is a kidney-shaped, fixed-geometry, normal-shock configuration displaced from the fuselage to prevent ingestion of fuselage boundary layer. A short splitter plate extends forward of the top surface of the inlet to isolate the inlet shock from the fuselage boundary layer.

The purpose of the test was to obtain the performance of a baseline inlet and the effects of several configuration variations. These variations were splitter-plate length and included angle, fuselage boundary-layer-diverter height, cowl sidewall cutback, splitter-plate boundary-layer bleed, and vortex generators in the inlet duct. The effects on inlet performance of an airplane nose boom, of struts in the boundary-layer diverter channel, and of throat rakes in the inlet were also determined. Inlet data were obtained as a function of angle of attack, angle of sideslip, and simulated engine airflow in the 0.6 to 2.0 Mach number range.

The model was instrumented primarily to obtain the airflow, pressure recovery, steady-state and instantaneous total pressure distortion, and turbulence levels at the engine face. Additional instrumentation was provided to determine the properties of the inlet flow field upstream of the inlet, at the inlet throat, within the inlet duct, and in the fuselage boundary-layer diverter channel.

The test results demonstrated the following:

1. The performance characteristics of the baseline inlet configuration are good. The turbulence levels are generally low, and the model data indicate that the full-scale pressure recoveries are adequate for the mission and maneuver requirements of the airplane.

2. The inlet flow remains stable (no buzz) for all conditions within the flight and maneuver envelope of the aircraft.

3. The flow-field measurements ahead of and at the splitter-plate leading edge confirm that the diverter stand-off distance and the outboard divergence between the upper plate and the fuselage are adequate to prevent low-energy air from entering the inlet.

4. No throat-plane flow separation was detected at Mach 1.6 for the baseline inlet, but some did occur at Mach 2.0 at the outboard rake stations.

5. The slotted-ramp, trimmed-splitter-plate with cutback-cowl, and the 13^{o}-non-porous-ramp configurations did not eliminate the high-Mach-number throat-plane flow separation. However, the 13^{o}-porous-ramp-bleed inlet offered some potential for eliminating this separation.

6. Vortex generators provided no real improvement in engine-face pressure distribution, and generally caused a decrease in pressure recovery and an increase in turbulence levels.

7. The nose boom and the diverter struts had no effect on inlet performance.

8. The throat rakes had a small effect on inlet pressure recovery at some of the subsonic test conditions. These rakes were removed for all of the performance testing.

INTRODUCTION

The inlet described in this report was designed for a single-engine, lightweight, low-cost, multi-role tactical fighter airplane. The airplane's primary mission is air superiority in the subsonic-to-Mach 1.6 speed range, with a dash capability to Mach 2.0. The inlet for such an aircraft must maintain high pressure recovery (engine thrust) and low pressure distortion (freedom from engine stall) during maneuvers at high angle of attack. To aid in selecting the inlet type for this application, analytical trade studies were made which compared the weight and performance of the following inlet types:

- Variable ramp ($M_{design} = 2.2$)
- Fixed ramp or spike with bypass ($M_{design} = 2.0$)
- Normal-shock inlet

It was concluded from these trade studies that a fixed-geometry, normal-shock inlet configuration, located in the protective flow field of the airplane forebody, would meet the mission requirements with minimum cost and weight.

In this report, the results of the third of a series of development tests to define the design and performance of the inlet are presented. The first two tests, using the same basic 0.15-scale inlet model and reported in References 1 and 2, established that a kidney-shaped inlet conforming to the rounded bottom of the fuselage was the best overall design. Other inlet designs tested were a D-shaped normal-shock inlet, a wedge-ramp inlet, and a precompression-bump inlet. In addition to inlet type and shape, other configuration variables that were tested included forebody shape, boundary-layer diverter design, and cowl-lip bluntness.

The third test, conducted at the NASA Lewis Research Center in 1972, thoroughly documented the performance of the then-currently selected inlet as a baseline configuration, and tested small variations in inlet configuration that had resulted from airplane/inlet design interactions or that had the potential for improving inlet performance.

In addition to inlet performance, the characteristics of the flow field upstream of the inlet and at the inlet throat were measured.

The inlet model was tested in the NASA Lewis Research Center's 8- by 6-ft Wind Tunnel over the Mach number range 0.6 to 2.0 at angles of attack from -10° to 40° at subsonic speeds and from -5° to 20° at supersonic speeds. Angle-of-sideslip effects were obtained to 15° subsonically and to 10° supersonically. Model airflow simulated the complete range of engine airflow and determined the stability limits of the inlet.

This report contains a description of the model and its instrumentation and the results of the test that are related to steady-state inlet performance and flow-field characteristics. The high-response pressure-distribution data related to inlet/engine compatibility are not included in this report but are available in Reference 3. Although these tests were part of the development of a particular inlet type for a specific aircraft and mission, the results are pertinent to inlets of the same type and integration characteristics regardless of the application.

SYMBOLS

B.L.	Buttock line, inches
℄	Centerline
CW	Clockwise
DELTA P	$(P_{T_{max}} - P_{T_{min}})$
DX1	Fan distortion index, defined as $Ka2/Ka2)_{Limit}$
F.S.	Fuselage station, inches
Ka2	Pressure distortion factor for engine fan based on the 40 steady-state total-pressure probes at the compressor face (See Appendix B)
$Ka2)_{Limit}$	Instantaneous screening limit of fan pressure distortion factor as defined by Pratt and Whitney Aircraft (See Appendix B)
L.E.	Leading edge
M	Mach number
P	Static pressure
P_T	Total pressure
$P_{T_{Max}}$	Maximum total pressure at each test condition from the 40 steady-state compressor-face probes
$P_{T_{Min}}$	Minimum total pressure at each test condition from the 40 steady-state compressor-face probes
P_{T_O}	Freestream total pressure
P_{TRMS}	Root-mean-square average of high-response total pressure

SYMBOLS (Cont'd)

$\overline{P}_{TRMS}$	The average of the P_{TRMS} values, calculated by analog computer, from 20 selected high-response pressure probes at the compressor face (selected probes are denoted in this report as the shaded ones in Figure 18)
P_{T2}	Total pressure at compressor face
$\overline{P}_{T2}$	Average compressor-face total pressure
T_{T2}	Total temperature of airflow at compressor face, ^{o}R
W	Airflow, lbm/sec
W.L.	Waterline
WC2	Engine corrected airflow, $W\sqrt{\theta_2}/\delta_2$, lbm/sec
Y	Distance from surfaces, inches
α (or ALPHA)	Angle of attack, degrees, measured between waterline plane and freestream direction. Positive α is nose up.
β (or BETA)	Angle of sideslip, degrees, measured between buttock-line plane and freestream direction. Positive β is nose left.
δ_2	Relative pressure at compressor face $= \overline{P}_{T2}$, psia/14.696
θ_2	Relative temperature at compressor face $= T_{T2}$, $^{o}R/518.7$

APPARATUS AND PROCEDURE

Test Facility

The model was tested in the NASA Lewis Research Center's 8- by 6-Foot Supersonic Wind Tunnel at Cleveland, Ohio. This wind tunnel is a continuous-operation closed- or open-circuit wind tunnel with a maximum Mach number of 2.1 and a lower Mach number limit determined by model blockage or shock reflection. During this test the tunnel was operated as a closed-circuit tunnel and the minimum Mach number was 0.6.

The tunnel is driven by an electrically powered compressor supplying a maximum of 2×10^6 cu ft of air per minute to a flexible-wall nozzle which can be varied to control test-section Mach number. The test section, 39 ft long by 8 ft high by 6 ft wide, has a supersonic section and a perforated transonic section. Following the test section, the air enters a cooler and a drier to complete the closed air circuit. Additional information on the operating characteristics, model support system, and data systems for this tunnel is provided in Reference 4.

Model Description

The composite forebody/inlet model is shown installed in the NASA/Lewis 8- by 6-Foot Wind Tunnel in Figure 1. The model is a 0.15-scale simulation of true airplane geometry from the nose boom to fuselage station (F.S.) 250 (full scale) on the upper surface and to F.S. 262.5 on the lower surface. External contours of this portion of the airplane forebody and inlet are shown in Figure 2. Internal inlet lines, shown in Figure 3, are simulated to the engine face. The internal area distribution of the relatively long S-shaped duct is given in Figure 4.

The general arrangement of the model is shown in Figure 5. The model consists of a support beam, fuselage forebody, inlet cowl, fuselage-boundary-layer diverter, secondary-air inlets, subsonic duct, primary-airflow metering system, pitch and yaw mechanism, and tunnel sting adapter. Pitch

and yaw mechanisms, not shown in Figure 5, were required to extend the pitch and yaw range of the 8- by 6-Foot Wind-Tunnel support strut to the 40^{o} pitch and 15^{o} yaw angles required for testing this inlet/forebody model.

Three different inlet cowl designs were tested on the model. Two of these cowls were modified to provide a total of five different inlet configurations. These configurations are described below:

(1) C13 — This baseline configuration, which simulates the YF-16 inlet, has an upper splitter-plate extension of 10 inches and a solid (non-porous) ramp with a 5^{o} inclination to the flow. The splitter-plate standoff distance from the fuselage is 3.65 inches at the leading edge. Full-scale inlet capture area is 826.7 square inches with a throat area of 713 square inches. This inlet is shown in Figure 6.

(2) C13A — Configuration C13A is cowl C13 with a slotted ramp for boundary-layer bleed. The bleed air is discharged into the diverter channel through exits as shown in Figure 6.

(3) C15 — C15 is identical to the baseline configuration (C13) except for the 13^{o} porous ramp. This inlet configuration is shown in Figure 7.

(4) C15A — Configuration C15A is cowl C15 without the porous ramp bleed. Refer to Figure 7.

(5) C14 — Configuration C14 has cut-back cowl sides, a trimmed splitter plate which extends forward 8 inches, and a slightly smaller inlet capture area (819 sq. in.). This inlet is depicted in Figure 8.

Each of these inlet cowls incorporated a thin, inclined, vertical tension strut to reduce cowl deformation under bursting pressure loads. This strut is visible in the inlet shown in Figure 1.

To ensure that a turbulent boundary layer would exist on the splitter plate, thus simulating full-scale inlet operation, a strip of grit 0.15 in. wide and 0.004 in. thick (actual dimensions, model scale) was placed on the underside of the splitter plate 0.25 in. from the leading edge.

The forebody boundary layer was diverted from the inlet by a reflex-curve diverter, shown in Figure 9. Secondary air inlets terminate the diverter at its outboard edges. The model permitted testing a range of diverter heights; heights of 3.30 inches and 3.65 inches (full scale) were tested.

From the inlet cowl, the subsonic duct extends to the simulated engine face, where the pressure recovery of the inlet is measured. Just downstream of the engine face is a calibrated flow-metering system having a remotely positioned conical plug that varies the flow exit area. These parts are shown in Figure 5.

Instrumentation

The model was instrumented to obtain steady-state and high-response pressures in the external flow field, on the forebody, within the inlet, and in the flow-metering system. The high-response data system is not discussed in this report but is described in Reference 3. The Lewis Research Center scanivalves and data system were used to acquire and record all steady-state pressures.

Model instrumentation is illustrated in Figures 10 through 18. All station numbers and dimensions shown in these figures are full-scale. The principal stations for instrumentation on the model are shown in Figure 10. The locations of static-pressure taps on the forebody and the boundary-layer diverter are shown in Figure 11. Three 7-tube rakes at F.S. 155, shown in Figure 12, were employed

to evaluate flow properties of the fuselage boundary layer forward of the inlet.

Measurements of the flow characteristics at the leading edge of the top of the cowl (the splitter plate separating the inlet airflow from the fuselage boundary layer) were made by the rakes shown in Figure 13. A special "splitter-plate-only" configuration, which simulated the extension of the upper cowl plate without the cowl enclosure, was utilized for these flow-field surveys. A photograph of the splitter plate and its instrumentation installed on the model forebody is presented in Figure 14.

Throat total-pressure and cowl static-pressure tap locations are shown in Figure 15. The throat rakes and other flow-field instrumentation were removed before inlet engine-face performance was measured. A photograph of the throat rake instrumentation is presented in Figure 16. The locations of the duct-wall static-pressure taps are shown in Figure 17.

Inlet total-pressure recovery was obtained from eight 5-tube rakes at the simulated engine-face station, as shown in Figure 18. The probes were positioned in centers of equal area. High-response pressures were obtained from probes and Kulite transducers located as shown in Figure 18. This high-response data was used in inlet/engine compatibility studies (not included in this report) and in the measurement of the turbulence levels of the inlet flow. The solid symbols (squares) shown in Figure 18 designate the probes used to obtain the average value of the turbulence parameter, $\overline{P}_{T_{RMS}}/\overline{P}_{T_2}$.

Static-pressure taps at the flow-plug exit measured the pressure at that point for use in determining the rate of airflow through the inlet.

Test Conditions

The inlet model was tested over the following range of test conditions:

Mach No.:	0.6, 0.9, 1.2, 1.38, 1.58, 1.78, and 1.96

Reynolds No.:	3.8×10^6 per ft at M = 0.6 to 5.0×10^6 per ft at high supersonic speeds
Angle of Attack:	-10° to 40°, subsonic -5° to 20°, supersonic
Angle of Sideslip:	0° to 15°, subsonic 0° to 10°, supersonic
Airflow:	Varied with Mach number to span the engine airflow range from below minimum hot-day idle airflow to approximately 10 percent greater than maximum engine airflow

The complete as-run test program is given in Appendix A.

Reynolds Number Effects on Boundary-Layer-Diverter Height

Proper scaling of the required boundary-layer-diverter height from 0.15-scale testing to full-scale flight conditions necessitates consideration of the Reynolds numbers for the two conditions. At full-scale flight conditions and Mach 2.0, 50,000 ft of altitude, the calculated Reynolds number and flat-plate boundary-layer thickness at the splitter plate leading edge are 27.1×10^6 and 2.62 inches, respectively (based on an effective length of 11.5 ft). For the wind-tunnel test conditions at Mach 2.0 (Reynolds No. per ft = 5.0×10^6), the corresponding full-scale calculated boundary-layer thickness is 2.97 inches. Thus, the boundary layer is relatively thicker on the model than on the airplane by about 13 percent. From previous tests, it was established that a diverter height about 25 percent greater than the calculated flatplate boundary-layer height is desirable for the flow field associated with this configuration and its operating envelope. Diverter heights of 3.30 and 3.65 inches (full scale) were tested.

DISCUSSION OF RESULTS

The data obtained during this test were used primarily to select the best inlet configuration from the several that were tested and to define the performance and distortion levels of that inlet as a function of Mach number, angle of attack and sideslip, and engine airflow. Measurements in the flow field ahead of the inlet and at the inlet allowed determination of the characteristics of the boundary layer ahead of and over the splitter-plate leading edge. The extent of flow separation at the inlet throat caused by interaction of the normal shock with the splitter-plate boundary layer was obtained from throat-rake instrumentation. The potential of several ramp and splitter-plate modifications in reducing flow separation at the throat was investigated. The effects of minor configuration variables such as the airplane nose boom and duct vortex generators were also determined.

The test results are presented in the following order:

1. Performance of the selected inlet configuration (C13) for the most important operating conditions.

2. Detailed performance for the selected configuration as affected by Mach number, angle of attack and sideslip, and airflow.

3. Pressure distribution of the airflow at the engine face for the selected configuration.

4. Characteristics of the flow at various points upstream of and within the inlet.

5. Effects of boundary-layer diverter height on the inlet flow field and inlet performance.

6. Effects of configuration variables on inlet performance.

Selected Inlet Configuration

The baseline inlet configuration, designated C13, was selected as the preferred inlet. This inlet is shown in Figure 6. It has a 10-inch-long splitter plate of minimal thickness (5^{o} included angle). No internal throat boundary-layer bleed is employed. Fuselage boundary layer is diverted by means of a 3.65-inch-high (full scale) wedge-type diverter.

The performance of this inlet is presented below, first in summary form at the principal operating conditions, and then in detailed form for all the flight and operating conditions that were tested. The data shown is that obtained from the model without correction for scale effects. The nose boom was mounted on the forebody.

Summary of Performance for the Selected Configuration

Pressure recovery of the C13 inlet at rated engine corrected airflow (WC2), 1^{o} angle of attack (α), and zero sideslip (β) is shown versus Mach number in Figure 19. For comparison, the pressure recovery computed from theoretical normal-shock losses and subsonic duct losses of Reference 5 is also presented. As would be expected for this inlet type, agreement between experimental and computed pressure recoveries is good. At an angle of attack of 1^{o}, the local Mach number at the inlet is only about 0.005 less than freestream Mach number.

The effect of airflow on inlet pressure recovery at $\alpha = 1^{o}$ and β = zero is shown in Figure 20 for the various test Mach numbers. The computed subsonic duct loss that was used with the shock loss to obtain the computed pressure recovery in Figure 19 is also shown in Figure 20.

The effect of angle of attack on pressure recovery at rated airflow is shown in Figure 21 for the test Mach numbers. Note that the precompression effect of the airplane forebody at positive angles of attack causes a significant improvement in pressure recovery at supersonic speeds and causes a corresponding decrement at negative angles of attack.

A comparison of the range of α and β covered in the model test and the required range for inlet/engine compatibility during aircraft maneuvering is presented in Figure 22 for subsonic and supersonic flight speeds. The range of test conditions meets or exceeds these maneuverability requirements. Except for a few extreme conditions, the test range also exceeds the predicted range of α and β for maximum-g rolling pullouts, as shown by the shaded areas in Figure 22.

In Figures 23 through 29, the effects of α and β on pressure recovery, distortion, and root-mean-square turbulence are shown for rated airflow at each of the test Mach numbers. Distortion of the flow at the simulated engine face is given in terms of the conventional parameter $\Delta P/\bar{P}_{T_2} = (P_{T_{MAX}} - P_{T_{MIN}})/\bar{P}_{T_2}$ and the fan distortion index DX1. DX1 is the ratio of the fan pressure distortion factor to the limiting distortion factor for inlet/engine compatibility defined by the engine manufacturer. The term "Series II" that is applied to DX1 in the plotted curves refers to the particular correlation of engine stall margin with engine-face pressure distribution for the Pratt and Whitney Aircraft F100 engine that was in effect at the time of this test. If DX1 approaches 1.0, further study of the instantaneous distortion levels obtained from high-response transducers is warranted to determine potential conditions of inlet/engine incompatibility.

The turbulence of the flow at the engine face station is presented as $P_{T_{RMS}}/\bar{P}_{T_2}$ which is the average of the root-mean-square of the pressure fluctuations, measured on 20 high-response pressure probes, divided by the average engine-face total pressure. The turbulence parameter and the distortion parameter DX1 are combined in the process of predicting inlet/engine compatibility. This process is not discussed in this report but is presented in Reference 3.

The data in Figures 23 through 29 show that, subsonically, the performance characteristics of the inlet are essentially constant for angles of attack up to about 30° but degrade at $\alpha = 40^{\circ}$. With the exception of pressure recovery, the performance parameters are also fairly insensitive to angle-of-attack variations at supersonic speeds. Supersonically the pressure recovery levels vary significantly

with angle of attack, showing a favorable increase with increasing angle of attack.

The inlet buzz limits were determined by throttling the airflow until the normal shock forward of the inlet became unstable and produced a high level of turbulence and distortion. The airflows at which buzz was encountered in the C13 are shown in Figure 30 as a function of Mach number, angle of attack, and angle of sideslip. The airflows at which buzz occurs are well below the minimum engine airflows for realistic operating conditions.

Detailed Performance for the Selected Configuration

One of the major objectives of the test was to completely map the performance of the selected inlet configuration for all conditions within the flight and maneuver envelope of the aircraft. Data were obtained at Mach numbers from 0.6 to 1.96 for angles of attack from -10° to 40° subsonically and -5° to 20° supersonically. The angle-of-attack sweeps were coupled with sideslip excursions to 15° subsonically and to 10° supersonically.

A complete set of inlet performance parameters for the selected inlet configuration (C13) is contained in Figures 31 through 69. The parameters, presented as a function of engine airflow, include the engine-face average pressure recovery, root-mean-square turbulence levels, fan distortion index, and maximum-minus-minimum pressure differential data. Each page of plots represents data taken at a constant Mach number and angle of attack.

Airflow variations affect each of the performance parameters differently. Pressure recovery varies slightly with airflow in the low transonic Mach number range, but is insensitive to airflow at speeds equal to or greater than approximately Mach 1.6. For angles of attack up to 30°, the engine-face turbulence levels do not vary significantly with airflow at any of the test Mach numbers. The maximum-minus-minimum pressure differential, while fairly insensitive to α variations, does vary directly with airflow.

The test data reflect a degradation in inlet performance with sideslip. The degradation becomes significant for angles of sideslip in excess of 5° and occurs at low angles

of attack. The degradation generally increases with airflow and decreases with increasing angle of attack.

Engine-Face Circumferential Pressure Distribution

The engine-face steady-state instrumentation consisted of 40 total-pressure probes located on eight equally spaced rakes in five rings of equal area. Circumferential distribution plots of the individual probe pressures around each of the five rings are presented in Figures 70 through 80 for Configuration C13. Representative data are shown for Mach numbers of 0.9, 1.58, and 1.97. These figures show the effect of sideslip at constant Mach number/angle-of-attack conditions. All data are for rated engine airflow.

The distributions in these figures show that, for zero sideslip, regions of low-energy air are present near the duct walls at all angles of attack. The low-pressure regions are most prominent near the top and bottom of the duct and increase in severity at the higher angles of attack.

Flow-Field Characteristics

Flow-field total pressures were measured forward of the inlet at F.S. 155, at the splitter-plate leading edge (F.S. 160), on the splitter plate forward of the inlet lip at F.S. 165.5, and at the inlet throat (F.S. 175). Static pressures were measured on the fuselage forward of the inlet, on the diverter, and on the internal surface of the inlet cowl and duct. These data are discussed below.

Fuselage Boundary-Layer Characteristics

Fuselage boundary-layer-thickness measurements were made 5 inches ahead of the inlet top-plate leading edge (F.S. 155) on the splitter-plate-only configuration (refer to Figures 13 and 14). The fuselage rake instrumentation illustrated in Figure 12, was used to obtain data on the model centerline (B.L. 0.0) and at 8.0 and 15.67 inches from the centerline (full scale) on the right-hand side of the model. Surveys at Mach 0.9 encompassed an angle-of-attack range from -9^{o} to 6^{o} with sideslip excursions from $+5^{o}$ to -15^{o}. Supersonically, data were obtained at Mach

1.57 and 1.96 at angles of attack of -5°, 1°, and 6° with sideslip angles extending from +5° to -10°. These attitudes were found, from previous tests, to be the most critical in terms of boundary-layer thickness for the airplane maneuver envelope. All data were taken with the nose boom mounted on the model forebody. Since the flow-field rakes were located on the right-hand side of the model, most of the tests to obtain sideslip effects were made at negative β (nose right) which produced the least favorable flow field.

The fuselage-rake data are presented in Figures 81 through 90 in the form of sideslip sweeps at constant Mach number and angle of attack. These results show that a maximum boundary-layer thickness of about 3.8 inches (full scale) occurs at the B.L. 0.0 rake and a maximum thickness of about 4.0 inches occurs at the B.L. 8.0 and B.L. 15.67 rakes. These maximum thicknesses occur at Mach 0.9 and 1.96 in the -9° to +1° angle-of-attack range. The thickness was reduced markedly at 6° of angle of attack. Usually, increasing the angle of sideslip caused the boundary layer to become thicker.

The standoff distances of the splitter plate from the fuselage at B.L. 0.0, 8.0, and 15.67 are 3.65, 4.1, and 5.4 inches, respectively. These standoff distances are greater than the boundary-layer thickness except at Mach 0.9, α = -5°, where thickness is about 3.8 inches. For four of the 46 test conditions, a flow disturbance appears to fall across one of the rakes, resulting in a low pitot pressure recovery in this area, but the diverter is not designed to exclude these isolated disturbances. For the vast majority of flight conditions, the diverter height tested is adequate to exclude the low-energy fuselage boundary layer from the inlet.

Flow Field Over the Splitter Plate

The flow-field characteristics at the splitter-plate leading edge (F.S. 160) and on the plate at F.S. 165.5 were measured with the splitter-plate rake instrumentation illustrated in Figure 13. These data were obtained over the same range of test conditions that were encompassed during the fuselage boundary layer surveys at F.S. 155. The model diverter height for this sequence of readings was set at 3.65 inches (full scale) to simulate the flow field conditions for an airplane geometric diverter height of 3.3 inches. The relationship of model and full-scale boundary-

layer thickness was discussed in the APPARATUS and PROCEDURE section. The nose boom was on the model for these tests.

The primary objectives of these flow-field measurements were to (1) determine the extent, if any, of low-energy boundary layer air spillage over the splitter-plate leading edge; and (2) to detect any leading-edge-induced flow separation on the splitter-plate ramp surface.

The total-pressure profiles measured at Stations 160 and 165.5 are presented in Figures 91 through 102 in the form of angle-of-sideslip sweeps at constant Mach/angle-of-attack conditions. Inspection of these data indicates that the diverter height of 3.65 inches at the inlet centerline is adequate to prevent ingestion of low-energy air for the vast majority of the test conditions. All of the pressure profiles, both at the leading edge of the lip and 5.5 inches aft of the lip on the inner surface, are relatively flat except for those at Mach 0.88/ $\alpha = -9^{o}$, where the ingestion of some low-energy air is indicated. These low-energy profiles occur at large sideslip angles on the rakes at B.L.s 0.0 and 8.5 and at low sideslip angles on the rake at B.L. 17.0. These profiles reflect the conditions at which low pressures were measured on the fuselage boundary-layer rakes at F.S. 155.

With the exception of the Mach 0.88, $\alpha = -9^{o}$, $\beta = 0^{o}$ condition, the pressure profiles measured by the rakes on the splitter plate 5.5 inches aft of the leading edge do not reveal any leading-edge-induced flow separation. The profiles are relatively flat for all three test Mach numbers and generally reflect the presence of high-energy air on the ramp surface for all combinations of α and β tested.

Flow-Field Characteristics at the Throat Plane

A portion of the test was devoted to establishing the characteristics of the flow at the throat plane (F.S. 175) for the baseline inlet configuration (C13). The total-pressure rakes shown in Figures 15 and 16 were used to obtain the throat flow-field data for a range of α / β combinations at Mach numbers of approximately 0.9, 1.6, and 2.0. Data were taken for diverter heights of 3.65 and 3.3 inches, with and without the nose boom. The data, presented in Figures 103 through 122, are restricted to data for the 3.65-

inch diverter height with the nose boom mounted to the model forebody. The data at Mach 0.9 and 1.6 are for rated airflow. The data at Mach 2.0 reflect the effects of airflow.

Subsonically, the Mach 0.9 results presented in Figures 103 through 106 show no areas of low pressure at the throat except for a small area on the sidewall rake (on the lee side of the inlet sidewall) during sideslip. The pressure profiles at $\alpha = 20^{o}$ are all very good. Data taken at $\alpha = 40^{o}$ with the 3.3-inch diverter (not included in the figures) indicate a small area of low pressure on the inlet cowl (lower) lip. This low-pressure area is interpreted as a region of flow separation on the lip, but it is not severe. Supersonically, the only flow separation noted in the throat-plane data for zero sideslip and rated airflow occurs at Mach 1.96. The data in Figure 112 show that separated flow does exist near the splitter-plate surface at an angle of attack of -5^{o}. The flow separation occurs at the outboard stations and not on the centerline. These regions of low-energy air diminish in extent with an increase in angle of attack, and completely disappear somewhere in the range of $1^{o}\ \alpha$ to $6^{o}\ \alpha$.

The data in Figures 107 through 115 show that sideslip has a detrimental effect on the throat-plane flow field at Mach 1.57, $\alpha = -5^{o}$ and at Mach 1.96 in the -5^{o} to $6^{o}\ \alpha$ range. For these conditions, regions of low-energy air are induced near the splitter-plate surface and the side of the cowl by the cross flow. For all other combinations of Mach number and angle of attack at rated airflow, the profiles reflect that high-quality flow is present throughout the throat plane, even with 10^{o} of sideslip.

The effects of airflow variation on throat-pressure profiles are presented in Figures 115 through 122 for Mach 1.96, the condition at which the most severe levels of flow separation (low-pressure regions) were observed. The airflow was varied from about 107 percent of maximum rated airflow to less than hot day idle airflow. These data show that the degree of flow separation at the throat plane diminishes as the airflow is reduced. The flow separation at $\alpha = -5^{o}$ and $\beta = 0^{o}$ completely disappears at an airflow approximately 20 percent below rated airflow. Although separation occurred, the gentle curvature and expansion of the diffuser allowed reattachment, and good performance was obtained at the engine face.

Overall, the trends in the throat-pressure-profile data, shown herein as a function of airflow and angles of attack and sideslip, support the conclusion that throat-plane flow separation is induced by interaction of the normal shock with the boundary layer on the splitter-plate ramp surface. An increase in angle of attack, for example, or a decrease in airflow results in a reduction in the amount of separation. Either of these has the effect of positioning the shock in a more forward location on the ramp surface where the boundary layer is thinner. Interaction of the normal shock with the thinner boundary layer would result in the trends observed in the test data.

Fuselage/Diverter Static-Pressure Profiles

Fuselage and diverter static-pressure data from the instrumentation illustrated in Figure 11 were recorded during the test primarily to indicate the location of shock waves in these areas. The effects of engine-airflow variations on these static pressure at various angles of attack at zero sideslip for nominal Mach numbers of 0.9, 1.2, 1.4, 1.6, 1.8, and 2.0 are shown in Figures 123 through 145. Inlet Configuration C13 was mounted on the model. Other pertinent configuration details are noted on the figures. The dashed lines that appear in the figures at F.S. 167 and 225 represent the beginning and ending of the diverter. The leading edge of the splitter plate occurs at F.S. 160. The blank sections appearing in the diverter-pressure profiles at F.S. 170 and 200 correspond to erroneous pressure data, which was deleted from the magnetic tape used to generate these plots.

The fuselage static pressures ahead of and at the splitter-plate leading edge reflect the behavior of the normal shock as a function of Mach number, angle of attack, and engine airflow. The profile data presented for Mach 1.21 and 1.39 indicate that, in this Mach-number range, the normal shock is resting on the fuselage surface or near the plate leading edge for all combinations of angle of attack and engine airflow. For Mach numbers in the range of 1.6 to 2.0 the normal shock appears to stay on the plate at low angles of attack, and only approaches the leading edge at reduced airflows. At the high angles of attack in this Mach number range, however, the profiles indicate the shock does spill over onto the fuselage surface for airflows approximately

rated and below. Even though the normal shock appears to spill off the splitter plate at a number of conditions, the plate standoff distance is apparently adequate to prevent ingestion of low-energy air in quantities sufficient to adversely affect inlet performance.

In general, the static-pressure profiles reveal that the splitter plate does not have an adverse effect on the approaching flow field. Those profiles near the plate leading edge which are not influenced by the impingement of the normal shock on the plate appear uniform and flat. This indicates that the flow characteristics into the diverter channel are good and that an adequate amount of flow-channel divergence exists.

Cowl and Duct Static-Pressure Profiles

Cowl and duct static pressures for the baseline inlet (C13) were measured by means of the instrumentation illustrated in Figures 15 and 17. Pressures were measured from the splitter-plate leading edge and cowl lip to the simulated engine face on the top and bottom surfaces of the duct. Also, pressures were measured on the right- and left-hand cowl walls from F.S. 175 to F.S. 200. Details of the configuration are noted on the data plot figures.

The cowl and duct static-pressure data are presented in Figures 146 through 175 as airflow sweeps at constant angle of attack, zero sideslip, and constant Mach number. Data are shown for nominal Mach numbers of 0.6, 0.9, 1.2, 1.4, 1.6, 1.8, and 2.0. The discontinuity in the upper internal-surface-pressure profiles at F.S. 167.5 and 200 is caused by faulty pressure readings at these locations.

The pressure distributions appearing in the figures exhibit trends that are typical for a normal-shock inlet. At the subsonic Mach numbers, at high airflows, and at $\alpha = 40^{\circ}$, there is evidence of a slight flow separation around the inlet lip. The pressure profiles on the upper surface (splitter plate) do not indicate any large pressure rises typical of strong shocks at Mach numbers less than 1.6. These rather sharp pressure rises appear at Mach 1.6, 1.8, and 2.0 for high-airflow, low-angle-of-attack test conditions. At $\alpha = 20^{\circ}$ and at airflows less than rated airflow, there is no strong pressure rise on the splitter plate.

At most of the test conditions, a large part of the pressure rise in the inlet airflow is developed forward of the splitter-plate leading edge.

Effect of Diverter Height on Inlet Flow Field and Performance

Most of the testing was done with the boundary-layer-diverter height set at 3.65 inches (full-scale). As explained previously, this diverter standoff distance was required at the test Reynolds numbers to properly simulate the full-scale flow field with a 3.3-inch diverter on the airplane at a reference flight condition. During the throat-plane flow-field investigation on the baseline inlet configuration, a limited amount of data was obtained with the diverter height set at 3.3 inches.

Figures 176 through 187 present throat-pressure profiles and engine-face summary data obtained at the two different diverter standoff distances. Comparisons are shown for angles of attack of -5°, 1°, and 6°, where a diverter-height effect is most likely to occur, for zero sideslip, and for Mach numbers of 1.57 and 1.96. The comparisons show that a decrease in diverter height from 3.65 to 3.3 inches has no effect on the internal flow-field data recorded at Mach 1.57, and only a minor effect at Mach 1.96. These results reinforce the fuselage-rake and splitter-plate-rake data discussed previously, which show that the thickness of the boundary layer at the centerline of the inlet is 3.3 inches or less at these Mach numbers.

Effects of Configuration Variables

The data discussed in the previous sections are for the baseline C13 inlet configuration with the nose boom installed on the model forebody. Several modifications to the baseline inlet and variations to the model configuration were tested to determine their effects on inlet performance. The changes consisted of the removal of the nose boom; the substitution of various cowl and splitter-plate geometries (a slotted-ramp splitter plate, a 13°-ramp splitter plate,

a 13°-porous-ramp splitter plate, and a trimmed splitter plate with cutback cowl); and the addition of diverter support struts and duct vortex generators. The effect of the presence of throat rakes on inlet performance was also determined. The results of testing these configuration variations are discussed in the following subsections.

Effects of the Nose Boom on Inlet Flow Field and Performance

The supersonic flow-field data from a previous test showed that a thickening of the boundary layer occurred on the fuselage centerline at zero sideslip and low angles of attack. The thickening effect did not exist off the centerline at zero sideslip, and disappeared on the centerline with sideslip. It was suspected that the nose boom was producing this effect.

In order that this suspicion could be confirmed or disproved, tests with and without the nose boom installed were conducted. Comparison plots showing the results of these tests are presented in Figures 188 through 205. The data comparisons are for zero sideslip and angles of attack of -5°, 1°, and 6°. Flow-field comparisons for the fuselage rakes and the splitter-plate rakes are shown for Mach 1.56 and 1.96. Comparisons of the data measured at the inlet throat plane and at the engine face are presented for Mach 1.96 only.

The results clearly indicate that the nose boom has an effect on the centerline flow-field characteristics at zero sideslip in the -5° to 1° α range, but has essentially no effect at 6°. The fuselage-rake data recorded at F.S. 155 (Figures 188 through 193) show a significant thickening of the boundary layer at -5° α due to the presence of the nose boom and a lesser thickening at 1° α . These data, however, indicate that the diverter height is adequate to skim off the additional low-energy air on the centerline caused by the nose boom.

Figures 200 through 205 contain comparisons of the Mach 1.96 data recorded at the throat plane and at the engine face. The throat profiles show a favorable nose-boom effect on the centerline of the upper-plate surface at -5° α , but show no effect at the higher angles of attack. The engine-face data comparisons, however, indicate that even though a

nose-boom effect is present at the forward end of the inlet, it is completely attenuated by the long duct and cannot be detected at the engine face.

Effect of Slotted-Ramp Splitter-Plate

The throat-rake data for inlet Configuration C13 showed that low-pressure regions existed near the surface of the sides of the splitter plate, particularly at Mach 1.96, at low angles of attack and for conditions of sideslip. These low-pressure regions were attributed to flow separation caused by interaction of the inlet shock with the splitter-plate boundary layer. To reduce this interaction, Configuration C13A was designed to bleed off the splitter-plate boundary layer into the diverter channel through two transverse slots, as shown in Figure 6.

The effects of the slotted ramp on the flow-field conditions at the throat plane and engine face are presented in Figures 206 through 217. Comparisons of slotted-ramp test data with that obtained on the baseline inlet configuration are shown at Mach numbers of 1.57 and 1.96 for angles of attack of -5^{o}, 1^{o}, and 6^{o}.

The configuration comparison plots show that the slotted ramp does not offer any potential in reducing this flow separation, apparently due to insufficient removal of boundary layer through the slots. Figures 209 and 210 in particular show that flow separation is still present on the slotted ramp at Mach 1.96 and low angles of attack. The engine-face data comparisons indicate that both the baseline and slotted-ramp configurations exhibit about the same performance level.

Effect of the 13^{o}-Ramp Splitter Plate

An inlet with a 13^{o}-ramp-included-angle splitter plate, designated Configuration C15A, was evaluated during the test as a possible method of reducing the throat-plane flow separation which characterizes the normal-shock type inlet at high freestream Mach numbers. This configuration is illustrated in Figure 7. The baseline inlet splitter plate (Figure 6) has a ramp included-angle of 5^{o}. The larger ramp angle reduces the Mach number of the flow along the splitter

plate and thereby reduces the pressure rise across the normal shock.

The results of the evaluation of this configuration are presented in Figures 218 through 229. In these figures, the throat-pressure profiles and engine-face performance data of Configuration C15A are compared with those of the baseline Configuration C13. The comparisons are presented at Mach 1.57 and 1.96 for angles of attack of -5°, 1°, and 6°.

The throat-pressure profile comparisons at Mach 1.57 show that there is little difference in the pressure profiles for the two configurations. At Mach 1.96, however, the 13° splitter-plate significantly reduces the degree of flow separation at the throat at $\alpha = 1^{\circ}$. At $\alpha = -5^{\circ}$ very little improvement is shown in the throat pressure profile for the higher ramp angle.

The engine-face data show that the 13° ramp results in a slightly higher pressure recovery for both Mach 1.57 and Mach 1.96. At Mach 1.96, however, the distortion of the engine-face pressure is significantly greater for the C15A configuration.

Effect of 13°-Porous-Ramp Splitter Plate

Inlet Configuration C15, shown in Figure 7, has the 13°-ramp splitter plate of Configuration C15A plus boundary-layer removal holes in the ramp surface. Details of the porous-ramp bleed arrangement are shown in Figure 7.

Of the techniques evaluated during the test, this configuration offered the most potential for reducing the high-Mach-number throat-plane flow separation. As a result, it was selected as the backup inlet configuration for the YF-16 aircraft and underwent a limited amount of performance mapping across the entire test Mach number range. Upon completion of the performance-mapping task, the porous-surface area was extended 2 inches (full scale) aft to evaluate the effect of increasing the ramp bleed.

Figures 230 through 241 contain comparisons of test data for the two porous-ramp bleed configurations (basic C15 and C15 with increased bleed) with that obtained on the baseline inlet. Figures 233 and 234 show that the basic

amount of porous-ramp bleed (C15) completely eliminates the throat-plane flow separation at 1^{o} α and reduces it at -5^{o} α. The increased-bleed configuration does not provide any further improvement. Figures 236 through 241 show that, in terms of pressure recovery and turbulence levels, the C15 configuration also exhibits the best engine-face performance. The maximum-minus-minimum pressure differentials, however, are higher than those of the baseline inlet.

Effect of Trimmed Splitter Plate

As a part of the effort to reduce the flow separation along the splitter plate at high Mach numbers, an inlet having a revised splitter-plate and cowl contour was tested. This configuration, designated Configuration C14 (called the "trimmed splitter-plate" configuration), is shown in Figure 8. The principal differences between the C13 and C14 inlets are that the C14 inlet has a splitter plate that is 2 inches shorter and has a rounded, rather than a straight, leading edge in the plan view. The cowl sidewalls of the C14 inlets are cut back at their intersection with the splitter plate. It was hoped that the buildup of boundary layer on the plate surface at the outboard stations (where the throat separation is the most evident) would be alleviated due to the shorter plate length and/or a bleeding off of the boundary layer through the corners between the upper plate edges and the cowl sides. A thinner boundary layer on the plate surface, in turn, would reduce the extent of throat-plane flow separation due to normal-shock/boundary-layer interaction.

The test results for the trimmed-splitter-plate configuration are presented in Figures 242 through 253, which contain comparisons of the C14 throat-plane and engine-face data to that for the baseline inlet. The comparisons are for Mach numbers of 1.57 and 1.96 and angles of attack of -5^{o}, 1^{o}, and 6^{o} at zero sideslip. In general, the data indicate that the trimmed-plate configuration offers no real potential for eliminating the high-Mach-number throat-plane flow separation. The engine-face comparisons, however, show that it does have a slightly lower turbulence level when compared to the baseline inlet.

Effect of Diverter Struts

During the final design phase of the inlet structure, it was anticipated that small struts might be required in the diverter channel for structural integrity of the upper plate extension. A single biconvex airfoil-shaped strut 2 in. long by 0.25 in. thick (full scale) was located on each side of the inlet at B.L. 11.0 and F.S. 167, 7 in. aft of the splitter-plate leading edge. These struts were tested on the model to determine if their presence would have any detrimental effect on inlet performance.

The results are presented in Figures 254 through 259. These figures contain comparisons of diverter static pressure and engine-face performance data as obtained on the baseline inlet with and without the diverter struts installed. The comparisons are for zero sideslip and 1^{o} α at Mach numbers of 0.9, 1.58, and 1.97. They confirm that the diverter channel flow and inlet engine-face performance characteristics are not adversely affected by the presence of the struts.

Effect of Vortex Generators

A series of runs was made during the test with vortex generators installed around the circumference of the subsonic duct at F.S. 300. The vortex generators consisted of nine pairs of 7-percent-thick half-circular-arc airfoil sections having 3-inch chords and 1.5-inch span heights (full scale). The pairs of vortex generators were equally spaced about 12 inches apart around the duct. The effect of the vortex generators on the inlet engine-face performance characteristics is presented in Figures 260 through 276. Data comparisons are shown at different combinations of sideslip and angle of attack at Mach numbers of 0.9, 1.56, and 1.96.

The results indicate that the presence of the vortex generators generally causes a slight reduction in the subsonic pressure recovery, an increase in the turbulence levels, and a reduction in the maximum-minus-minimum pressure differentials. The effect is less pronounced with sideslip, and also appears to diminish with increasing freestream Mach number. Overall, these results show that the vortex generators offer no real potential for improving the engine-face flow field.

Effect of Throat Rakes on Inlet Performance

Engine-face performance data shown previously in this report were obtained with the throat rakes removed unless specified otherwise. A small amount of data was taken with the rakes in place to determine the effect of these rakes on inlet performance of the C13 Configuration.

Comparisons of engine-face performance data obtained on the baseline inlet configuration with and without the throat-rake instrumentation installed are presented in Figures 277 through 284 as a function of corrected airflow. The comparisons are shown for zero sideslip and representative angles of attack at Mach numbers of 0.9, 1.58, and 1.97. These data show that the throat-rake instrumentation has an effect on the subsonic data but has no significant effect on the supersonic data. The primary effect subsonically is a decrease in pressure recovery. The amount of reduction at rated airflow is approximately 0.5 percent at $-9^{o}\alpha$ and about 1.0 percent at $20^{o}\alpha$.

CONCLUSIONS

The results of the test of a 0.15-scale underfuselage, fixed-geometry, normal-shock inlet show that the baseline inlet, with minimal splitter-plate ramp angle and without boundary-layer bleed, provides good performance to Mach 2.0. Performance at high angle of attack is especially good. The inlet stability and the pressure recovery, pressure uniformity, and turbulence levels at the engine face are satisfactory for most conditions within the flight maneuver envelope for the aircraft for which the inlet was designed.

Conclusions concerning the specific configuration items tested are as follows:

1. No throat-plane flow separation was detected at Mach 1.6 for the baseline inlet configuration, but some did occur at the outboard rake stations at Mach 2.0.

2. The slotted-ramp, trimmed-plate, and 13°-solid-ramp configurations were not effective in eliminating the throat-plane-flow separation observed at Mach 2.0 for the baseline inlet.

3. The 13° porous-ramp bleed configuration offered some potential for eliminating the high-Mach-number throat-plane flow separation. Consequently, it was selected as the backup inlet configuration for the YF-16 aircraft and underwent a limited amount of performance mapping.

4. The flow-field measurements ahead of and at the splitter-plate leading edge confirmed that the 3.65-inch diverter standoff distance is adequate to prevent low-energy air from entering the inlet.

5. The flow-field surveys near the plate leading edge also confirmed that the amount of outboard divergence between the upper plate and fuselage is adequate.

6. The vortex generators offered no real improvement in the engine-face pressure distribution, and in general caused a decrease in pressure recovery and an increase in the turbulence levels.

7. The nose boom caused a slight thickening of the boundary layer on the fuselage centerline at zero sideslip and low angles of attack. The effect of the nose boom, however, was completely attenuated by the long subsonic duct and was not detectable at the engine face.

8. The proposed diverter struts had no adverse effect on inlet performance at the engine face.

9. The throat rakes had a small effect on inlet pressure recovery at some of the subsonic test conditions. Therefore, these rakes were removed for the performance tests.

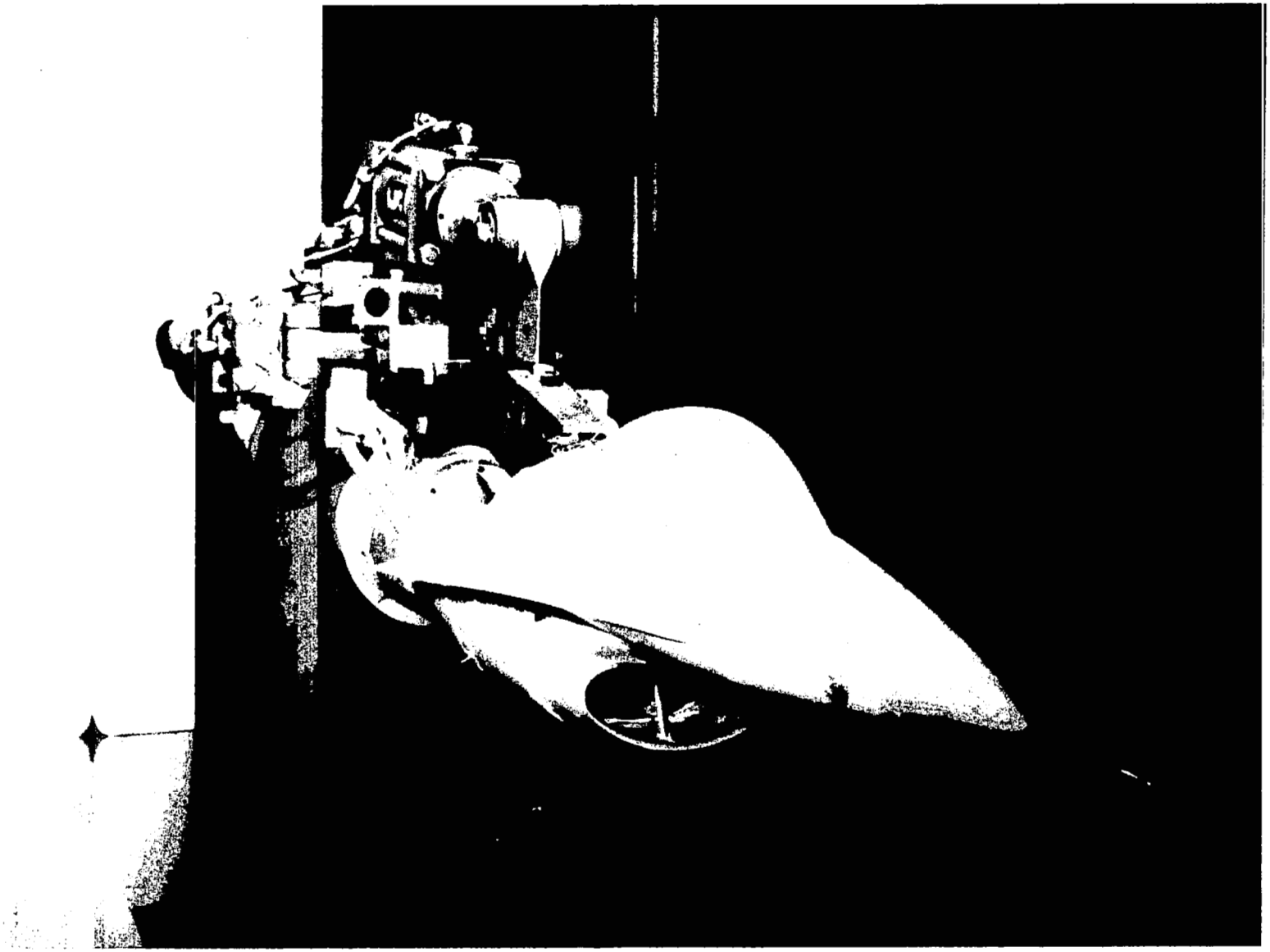

Figure 1 Model Installed in NASA Lewis Research Center 8- x 6-Ft Transonic Test Section

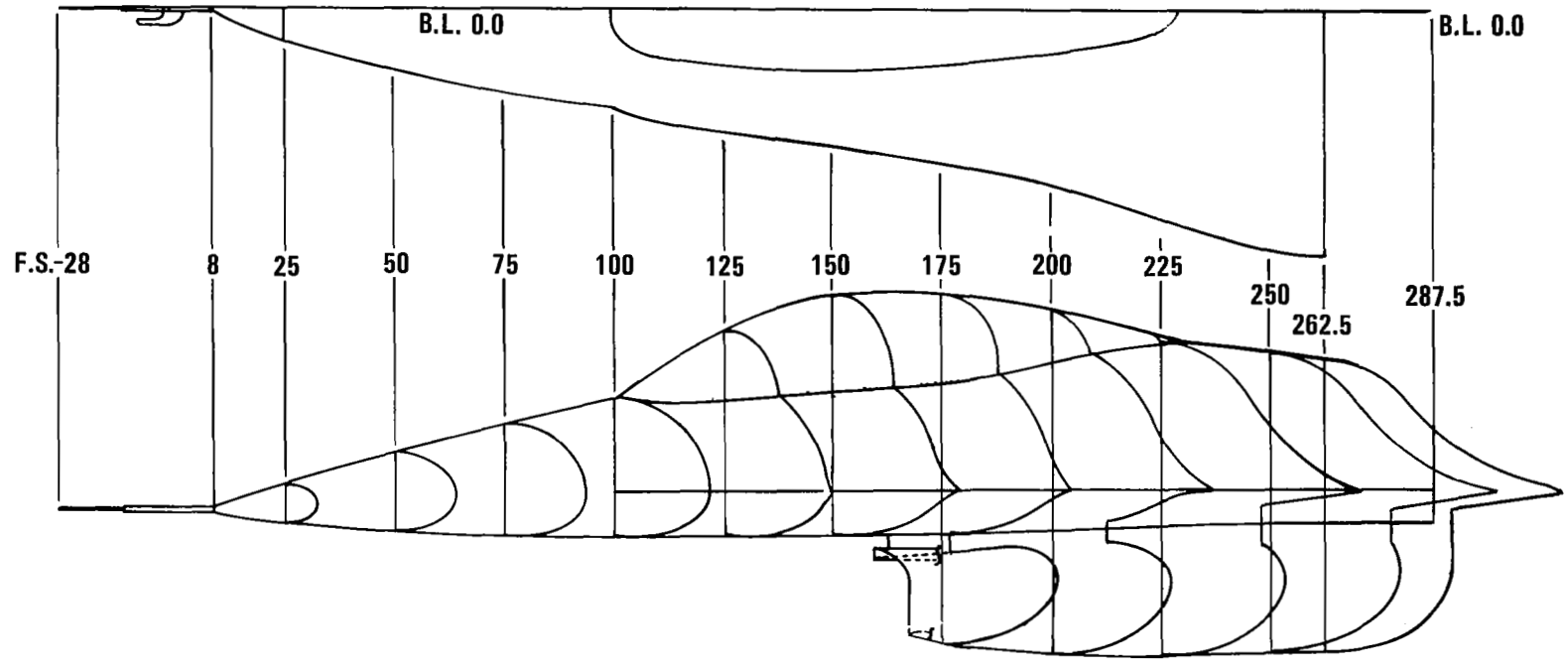

Figure 2 Forebody and Inlet External Lines

Inlet Lip Ellipse Ordinates				
Line	a	b	c	d
1	.60	2.40	1.20	4.80
2	.60	2.40	1.20	4.80
3	.60	2.40	1.18	4.72
4	.60	2.40	1.15	4.60
5	.60	2.40	1.09	4.36
6	.60	2.40	1.00	4.00
7	.60	2.40	.87	3.48
8	.60	2.40	.75	3.00
9	.58	2.32	.64	2.56
10	.56	2.24	.56	2.24
11	.51	2.04	.51	2.04
12	.47	1.88	.47	1.88
13	.45	1.80	.45	1.80
14	.44	1.76	.44	1.76
15	.43	1.72	.43	1.72
16	.42	1.68	.42	1.68
17	.39	1.56	.39	1.56
18	.36	1.44	.36	1.44
19	.31	1.24	.31	1.24
20	.26	1.04	.26	1.04
21	.20	.80	.20	.80
22	.13	.52	.13	.52
23	.06	.24	.06	.24
24	.06	.24	.06	.24
25	.06	.24	.06	.24

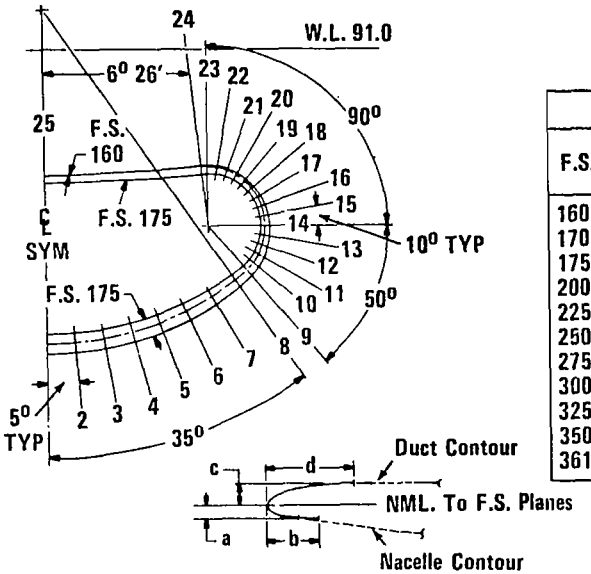

Duct Internal Coordinates			
F.S.	W.L. @ B.L. 0.0		Max Half-Breadth
	Upper	Lower	
160	76.95	–	–
170	76.08	57.42	25.14
175	75.86	58.62	24.70
200	77.54	59.13	24.70
225	82.61	62.64	24.70
250	89.16	67.48	23.87
275	96.32	71.62	21.90
300	102.46	73.85	19.74
325	106.55	74.02	18.16
350	108.35	73.62	17.42
361.55	108.40	73.60	17.40

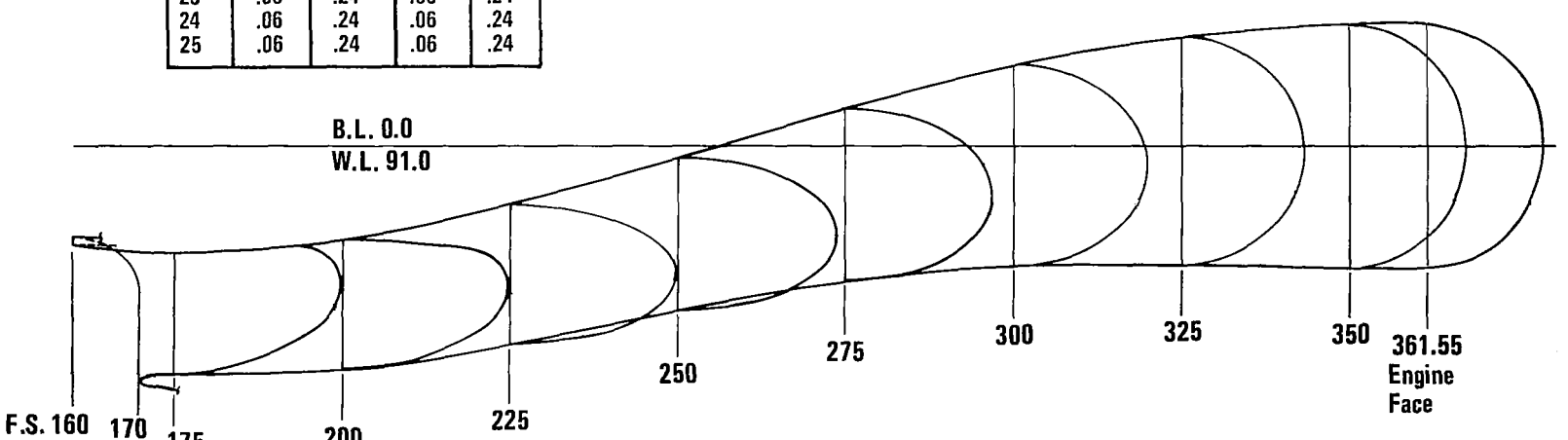

Figure 3 Inlet Internal Lines

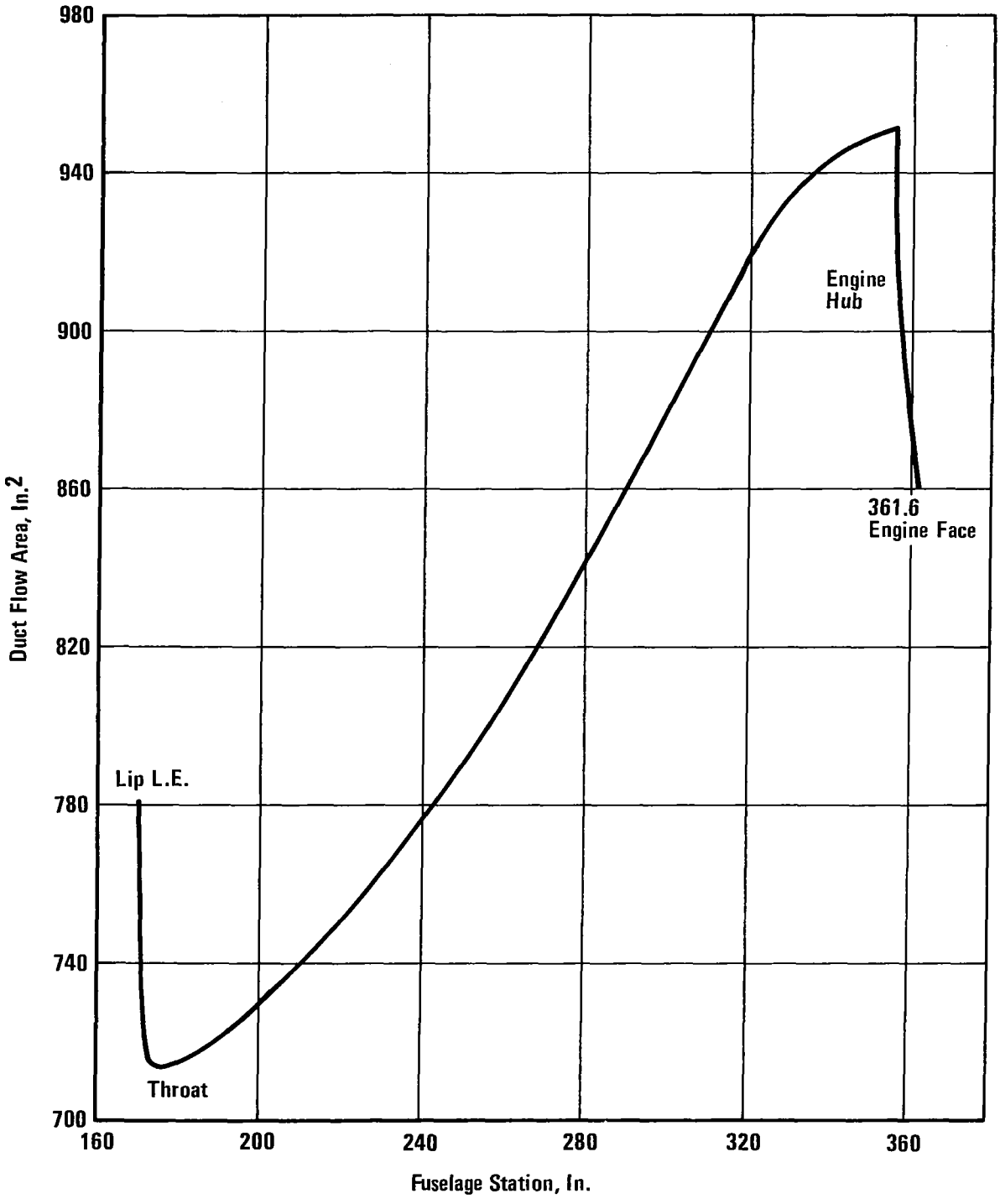

Figure 4 Inlet Diffuser Area Distribution

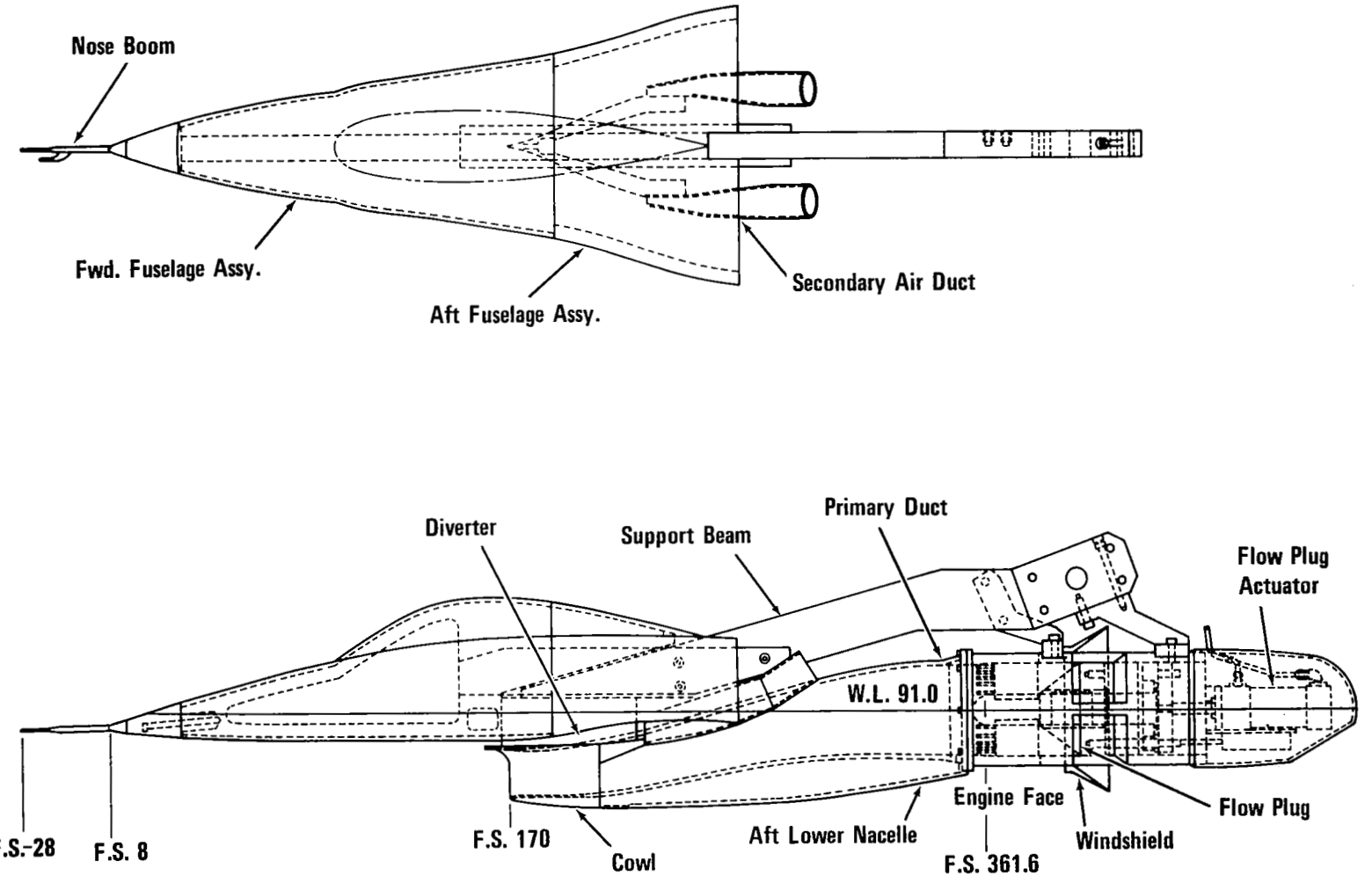

Figure 5 Model General Arrangement

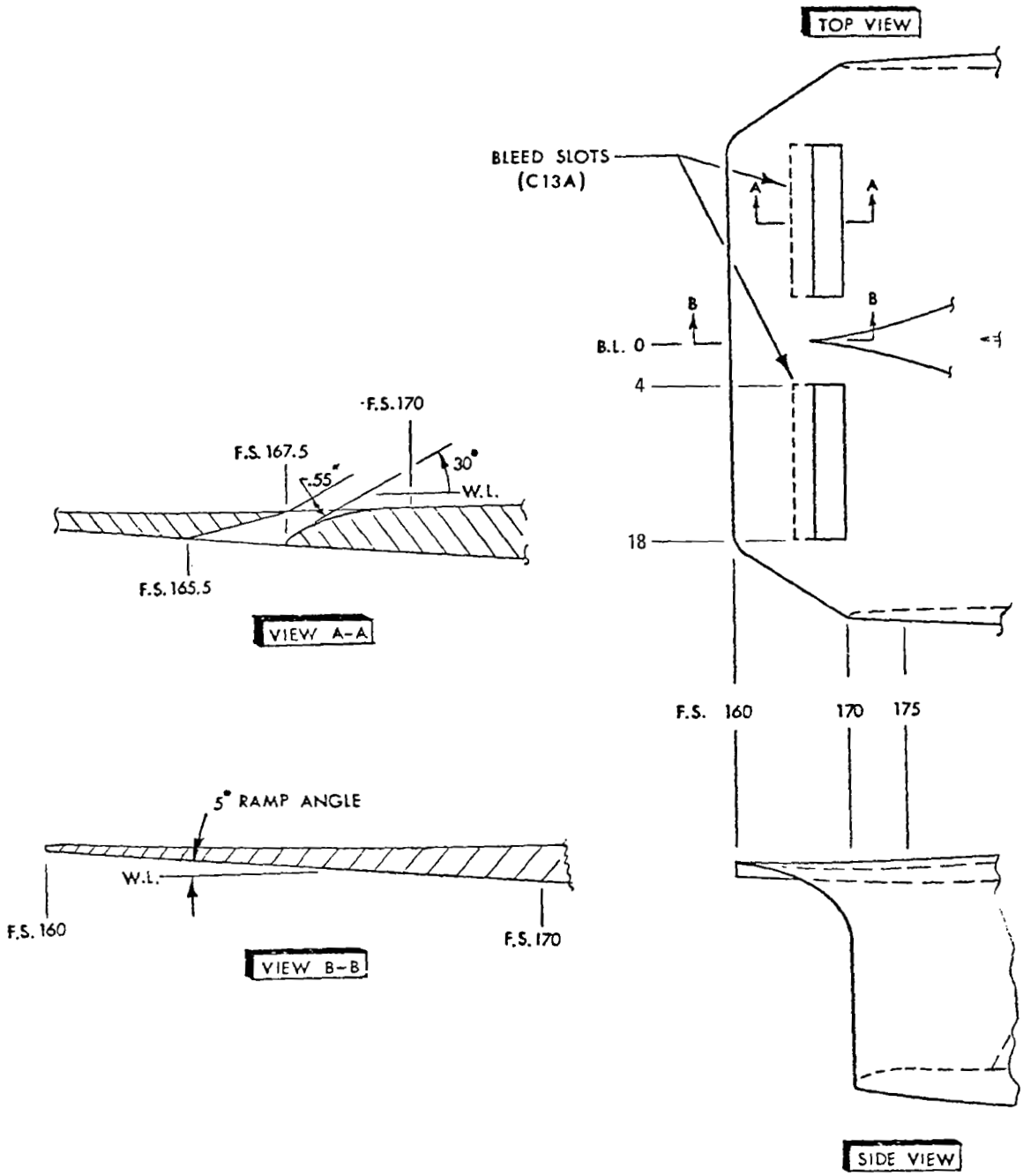

Figure 6 C13 Baseline Inlet Configuration; C13A Baseline Configuration + Bleed Slots

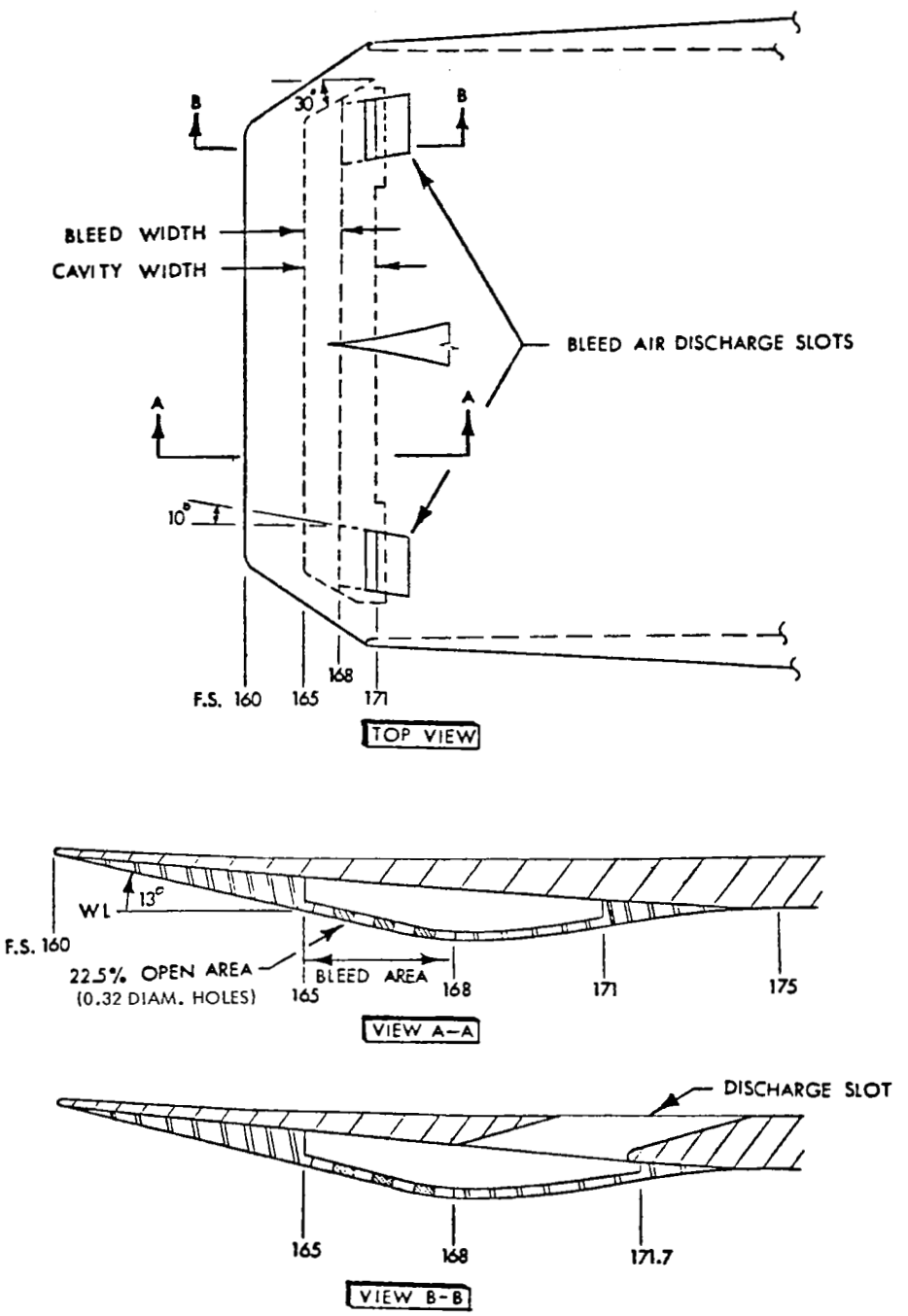

Note: C15A = C15 Without Bleed

Figure 7 C15 Inlet Configuration (13° Ramp With Porous Bleed)

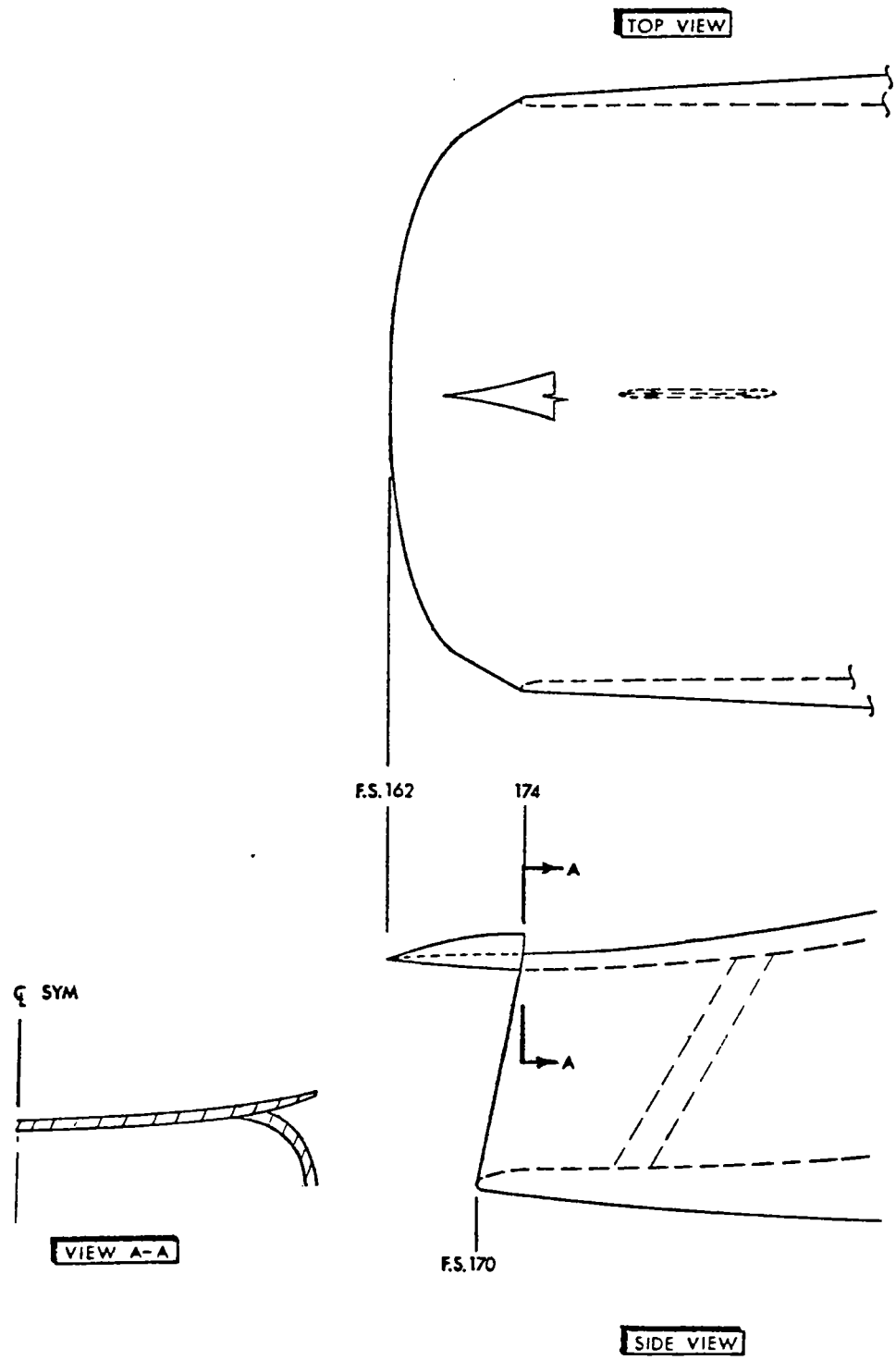

Figure 8 C14 Inlet Configuration (Trimmed Splitter Plate)

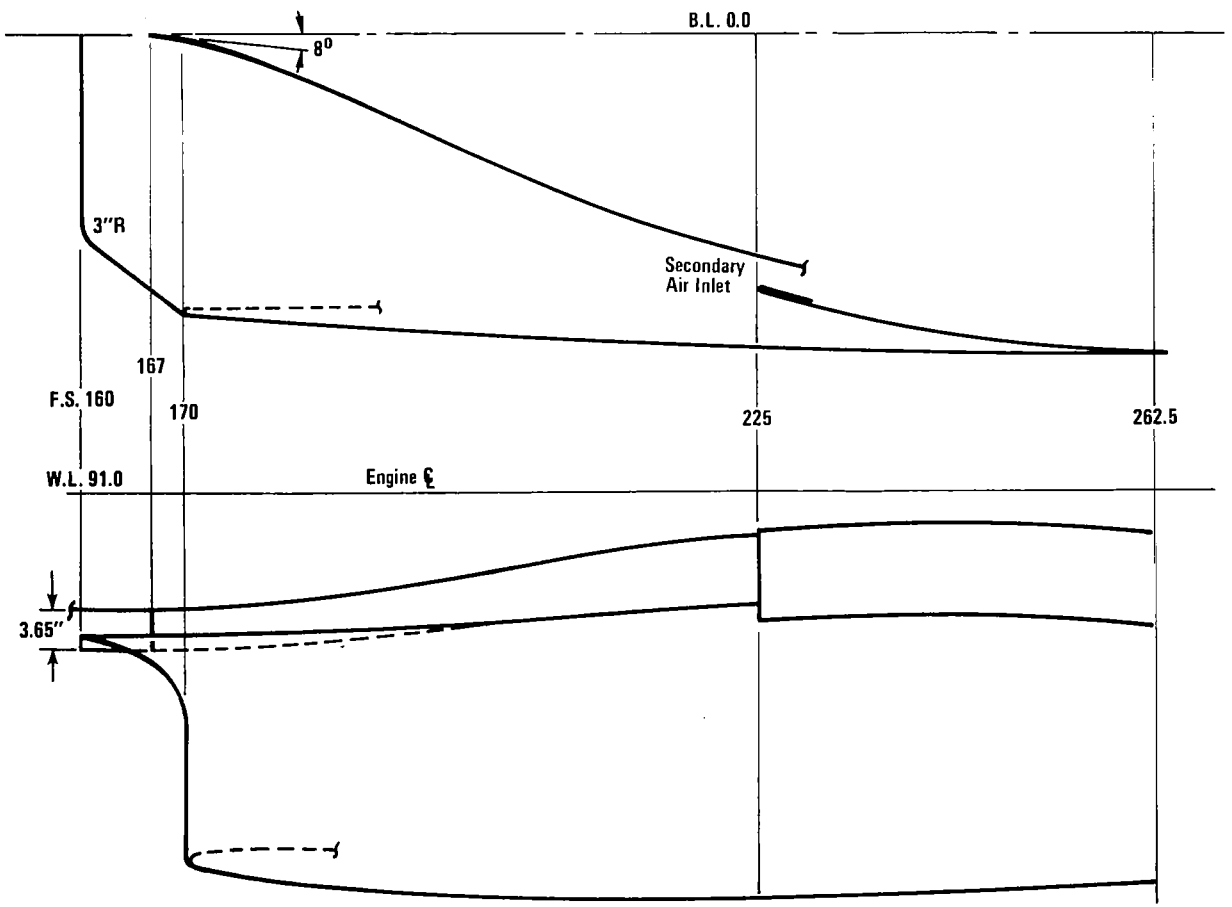

DIVERTER COORDINATES

F.S.	Height, In.	Half-Breadth, In.
167	3.65	0
170	3.80	0.53
180	4.18	2.80
190	4.39	5.87
200	4.59	9.42
210	4.92	13.08
220	5.24	16.58
225	5.35	18.25
225	7.02	20.63
230	7.05	22.37
240	7.20	25.25
250	7.69	27.30
262.5	9.65	28.92

Figure 9 Boundary-Layer Diverter Lines

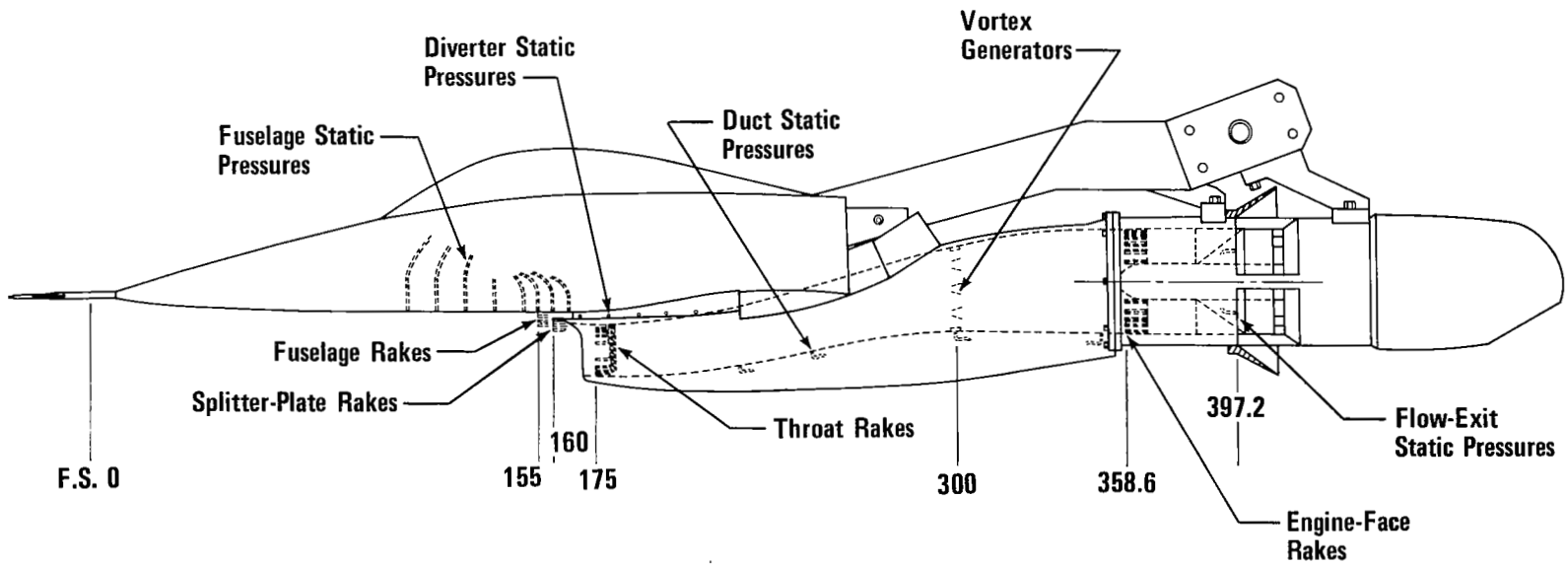

Figure 10 Inlet Model Assembly, Showing Principal Instrumentation Stations

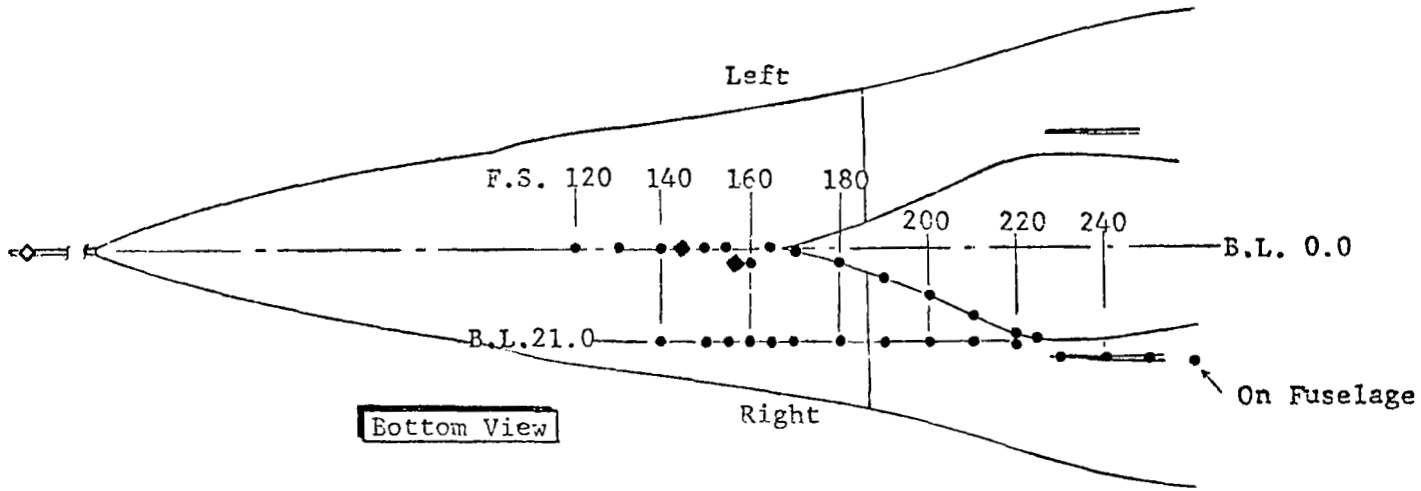

Figure 11 Fuselage and Diverter Instrumentation

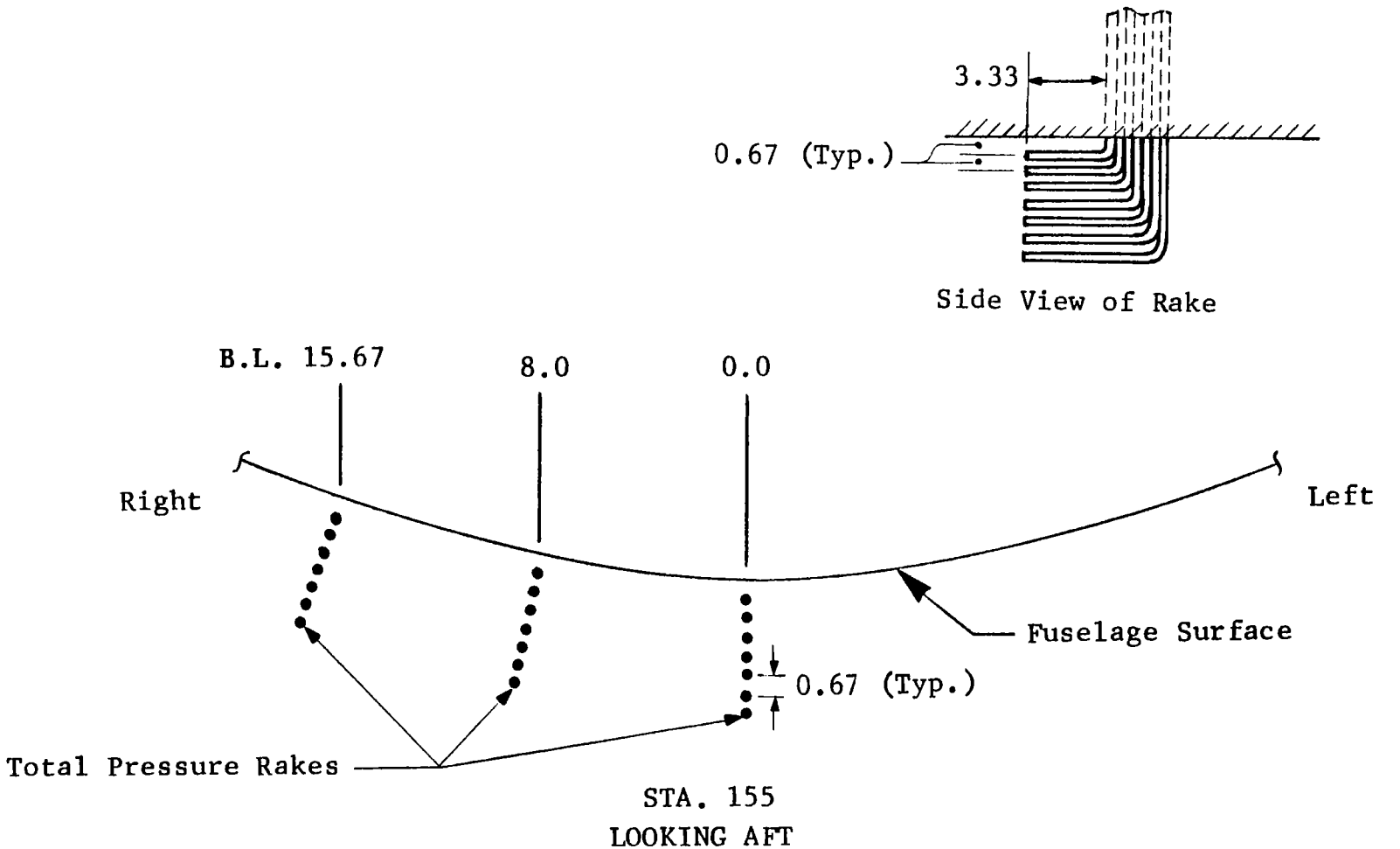

Figure 12 Fuselage Rake Instrumentation

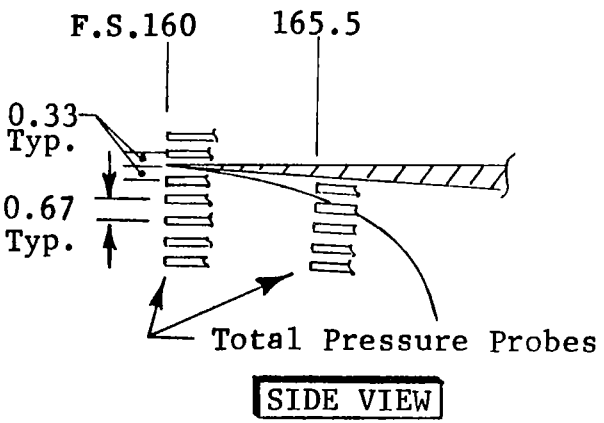

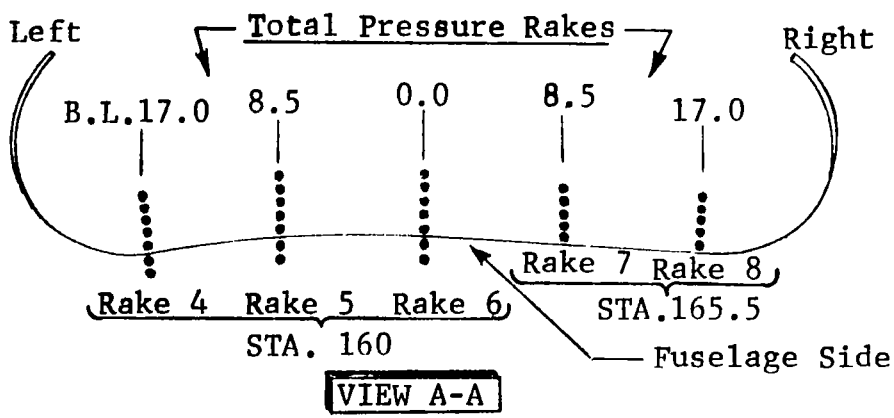

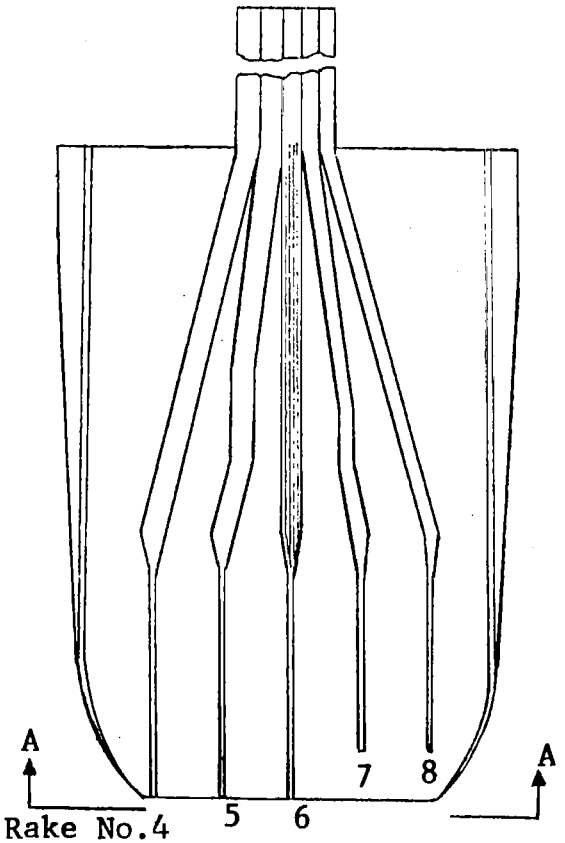

Figure 13 Splitter-Plate Rake Instrumentation

Figure 14 Splitter-Plate-Only Configuration, Showing Fuselage Rakes and Splitter-Plate Rakes

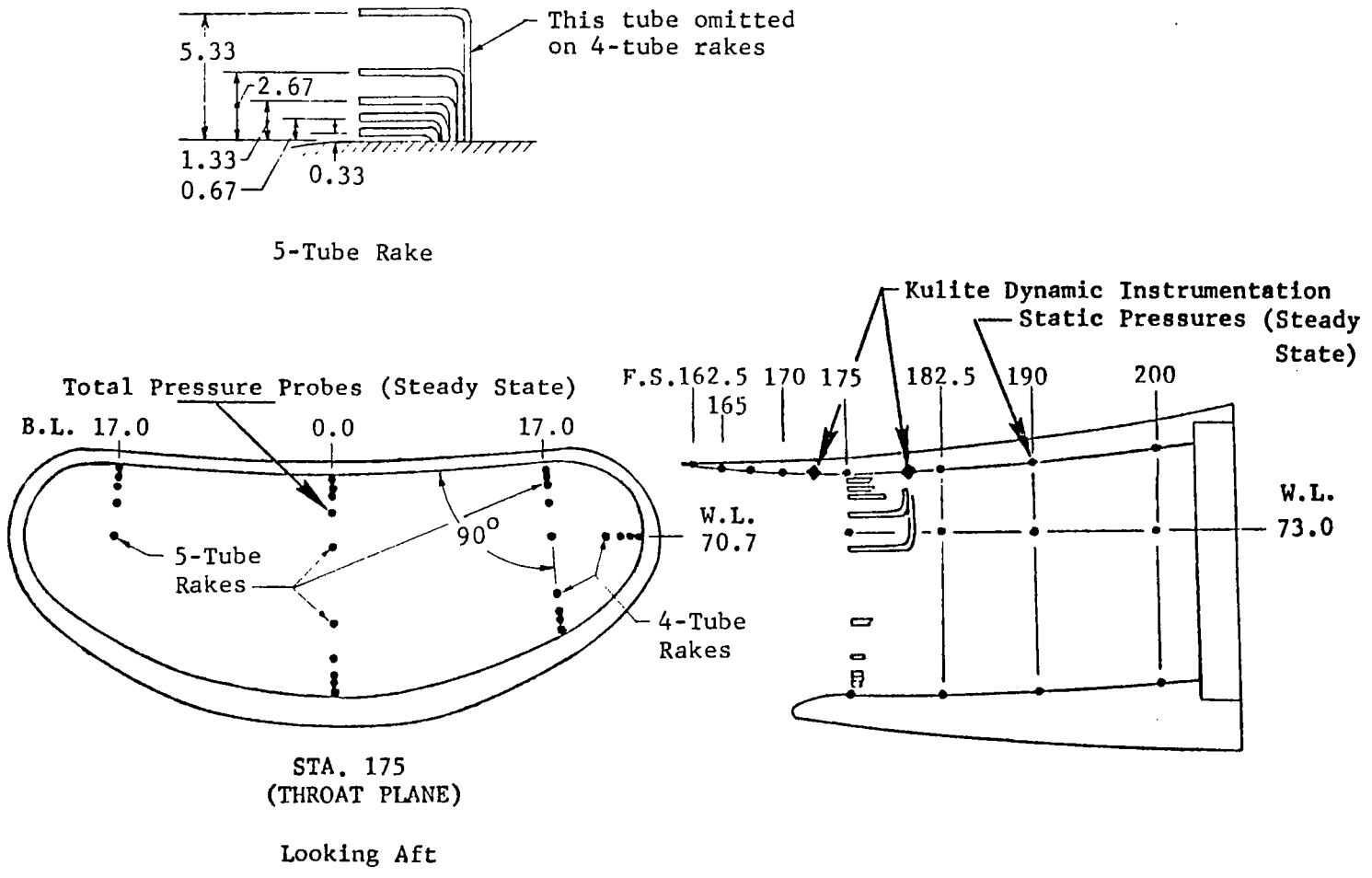

Figure 15 Throat Total- and Cowl Static-Pressure Instrumentation

Figure 16 Photograph Showing Throat Rake Instrumentation and Duct Strut

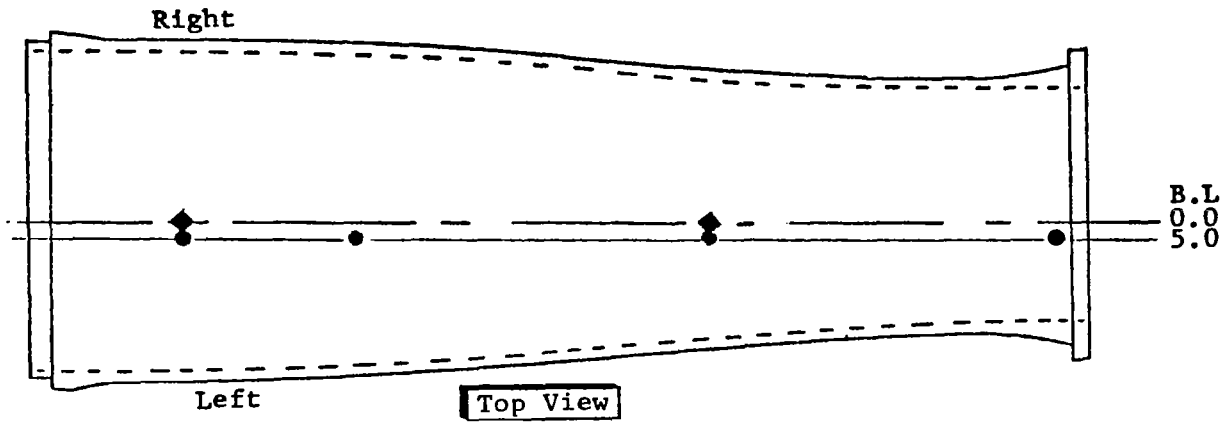

● High-Response Static Pressure Taps

● Steady-State Static Pressure Taps

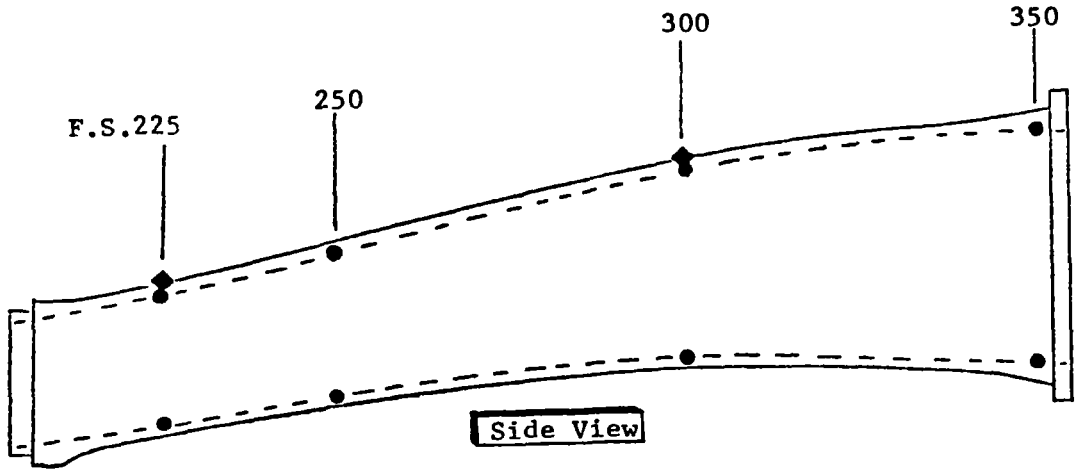

Figure 17 Duct Static-Pressure Instrumentation

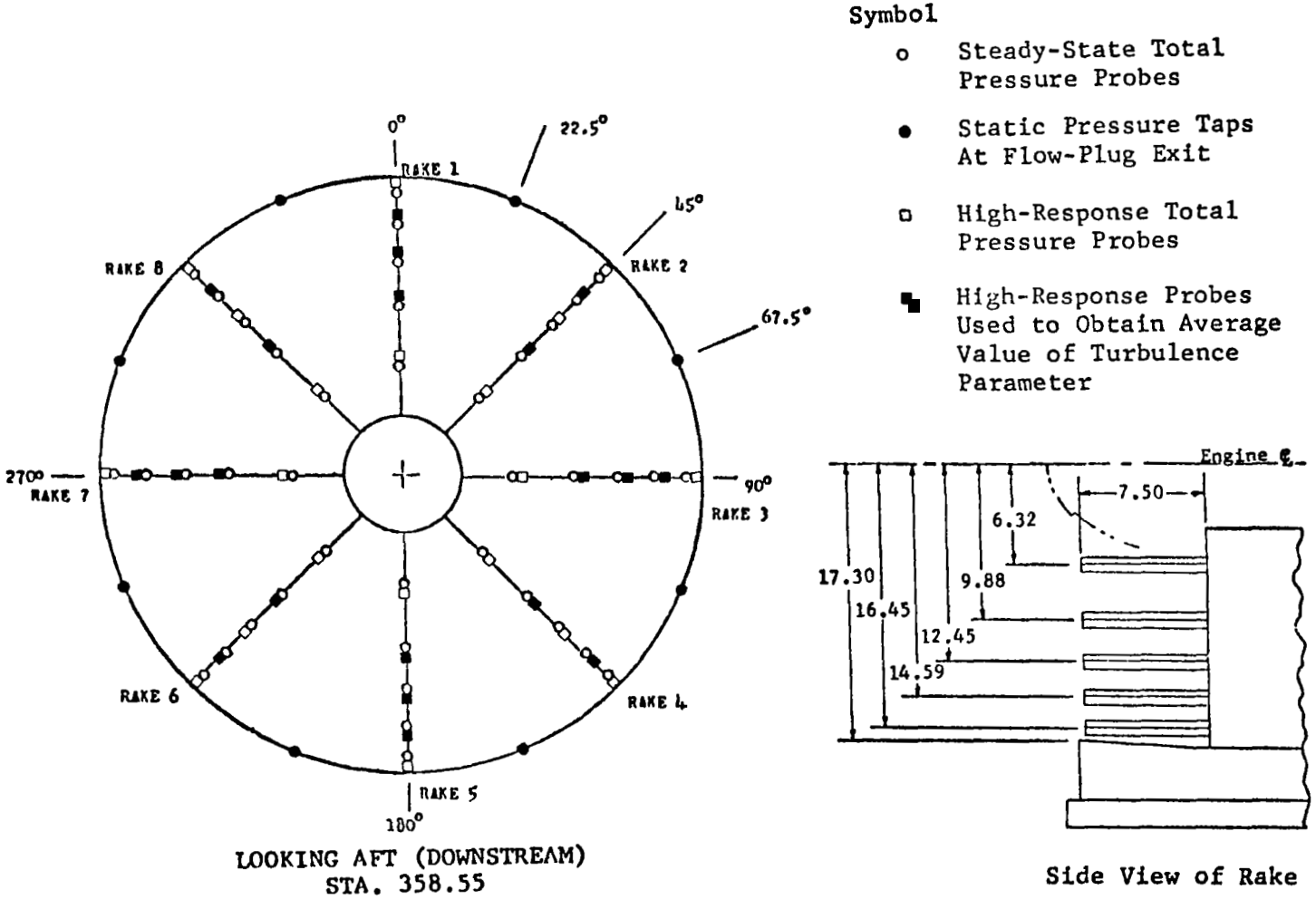

Figure 18 Engine-Face Pressure Instrumentation

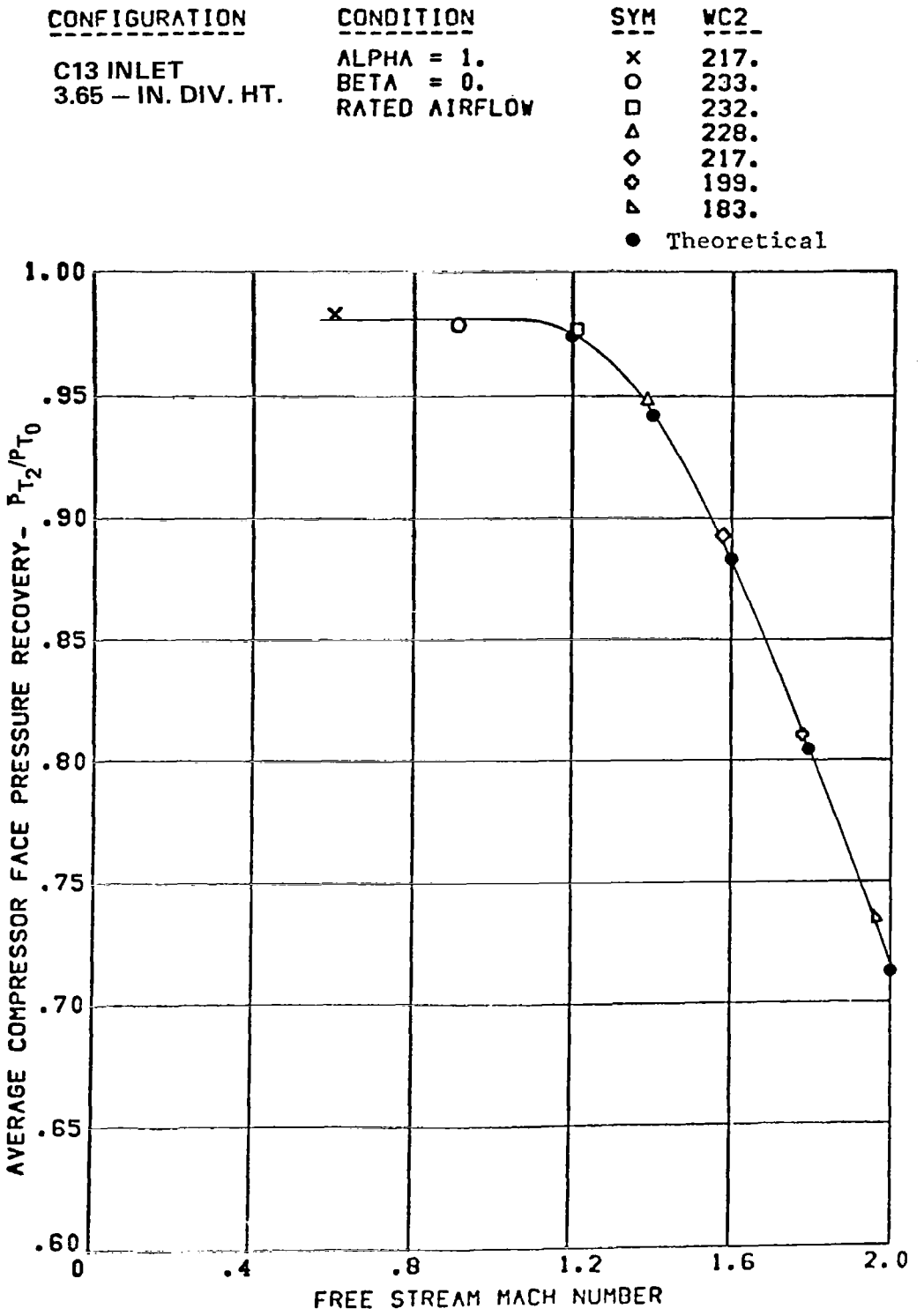

Figure 19 Inlet Pressure Recovery for Selected Configuration at Rated Airflow

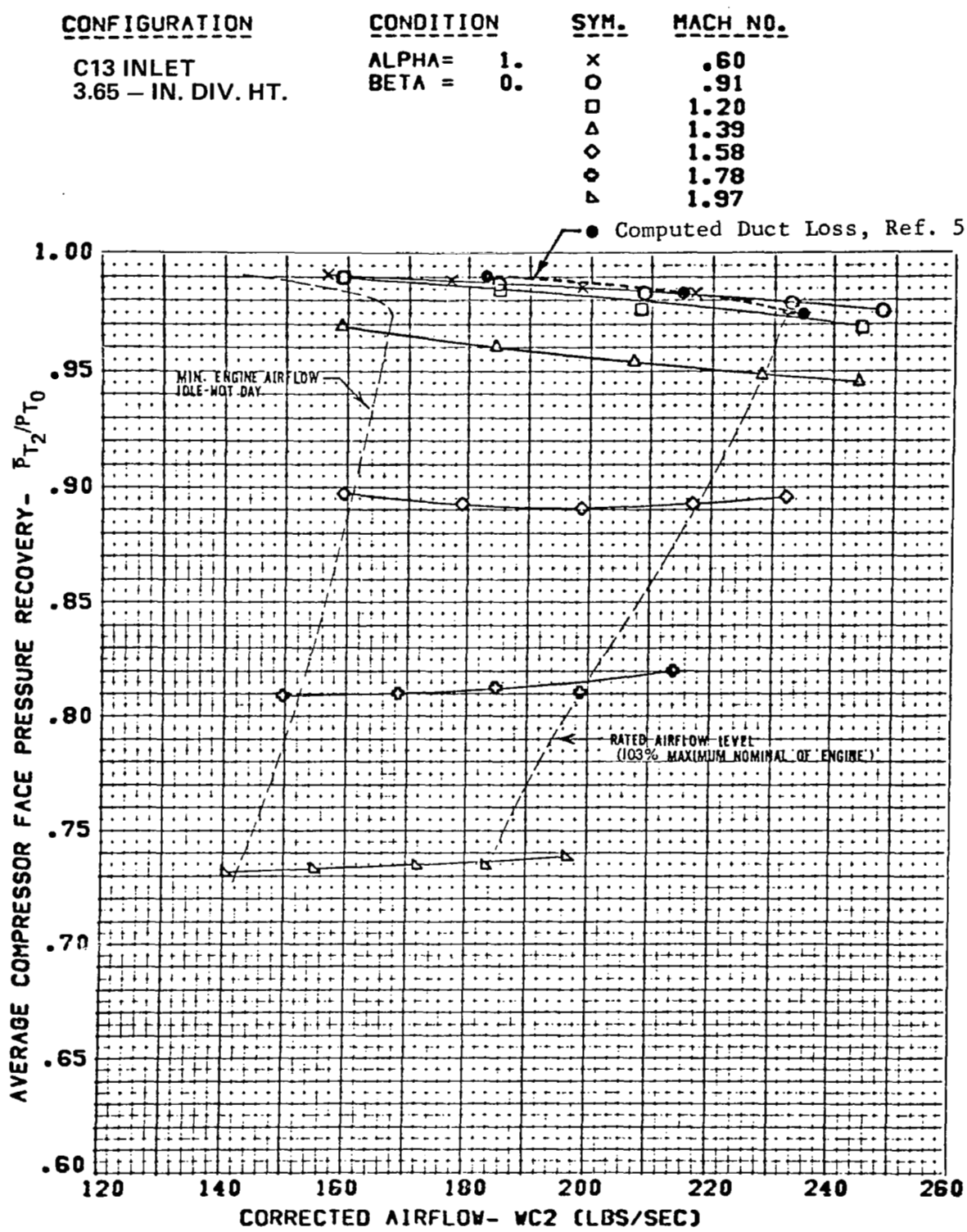

Figure 20 Inlet Pressure Recovery for Selected Configuration; Effect of Airflow

CONFIGURATION	CONDITION	SYM	MACH
C13 INLET 3.65 – IN. DIV. HT.	BETA = 0. RATED AIRFLOW	× ○ □ △ ◇ ⬦ ▵	.60 .90 1.21 1.36 1.58 1.78 1.96

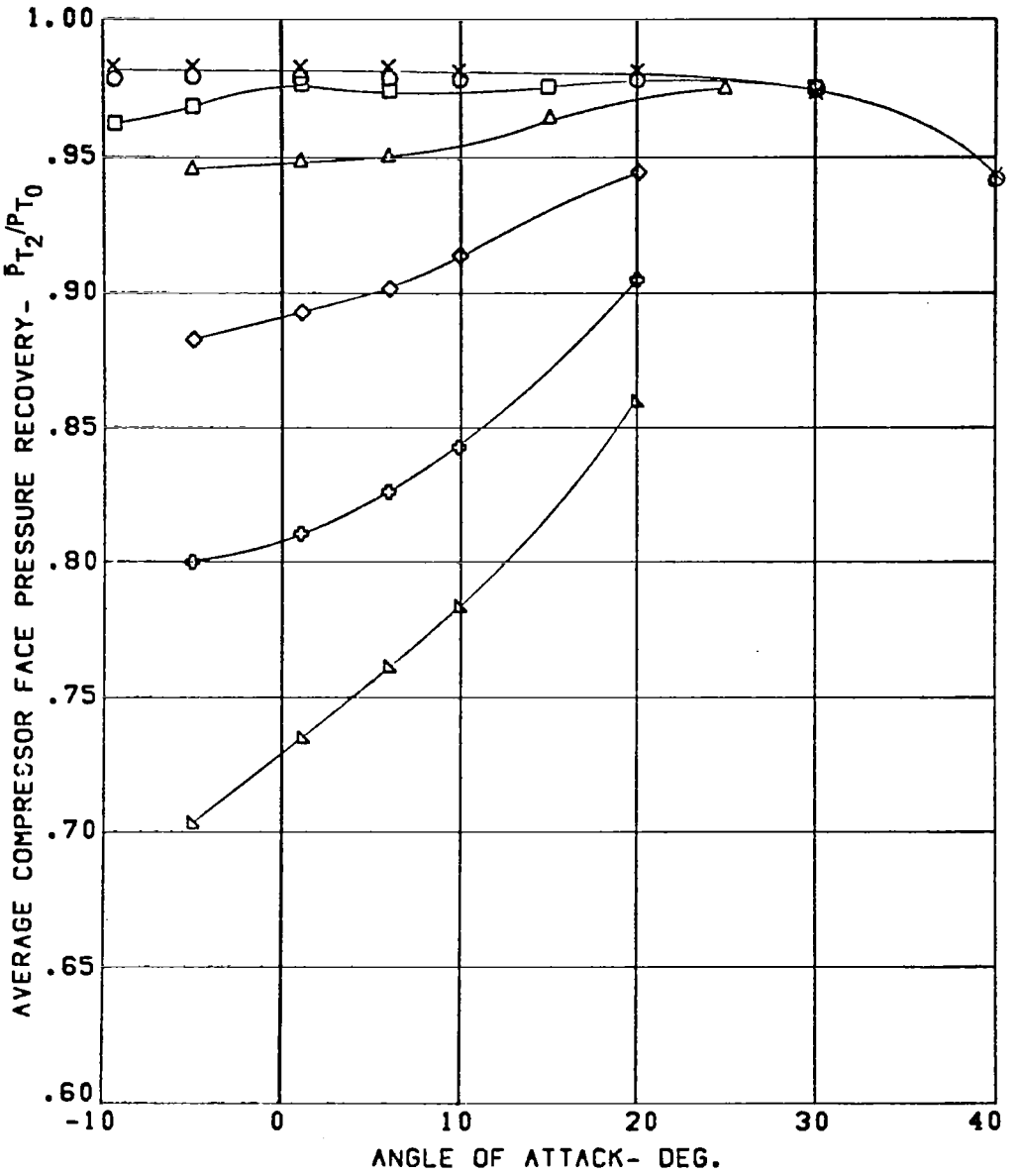

Figure 21 Effect of Angle of Attack on Pressure Recovery of Selected Inlet at Rated Airflow

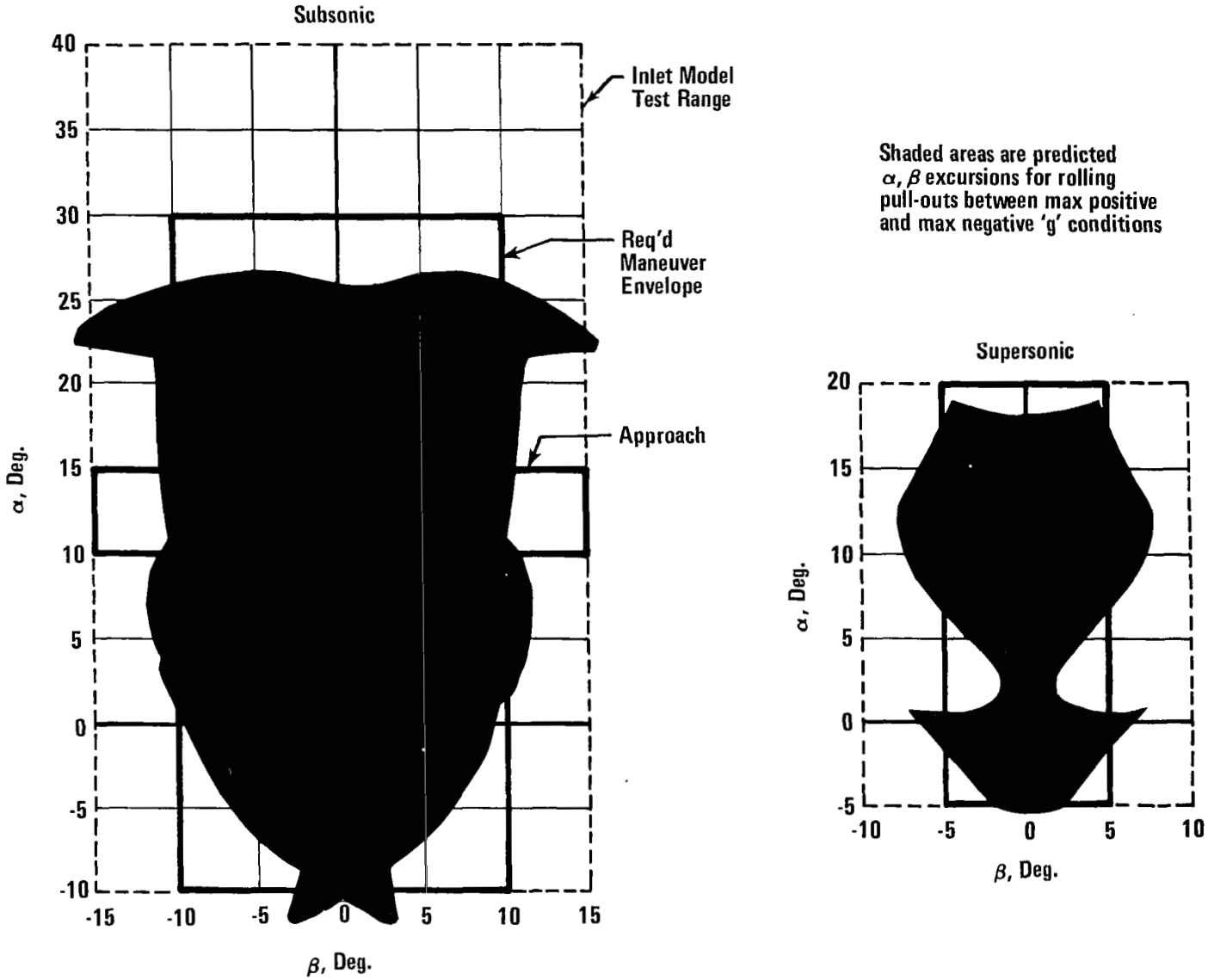

Figure 22 YF-16 Maneuver Envelope and Inlet Model Test α, β Range

CONFIGURATION	CONDITION	SYM	BETA (DEG.)
C13 INLET 3.65 – IN. DIV. HT.	MACH= .60 WC2 = 211.	□ △ ◇ ▷	0. -5. -10. -15.

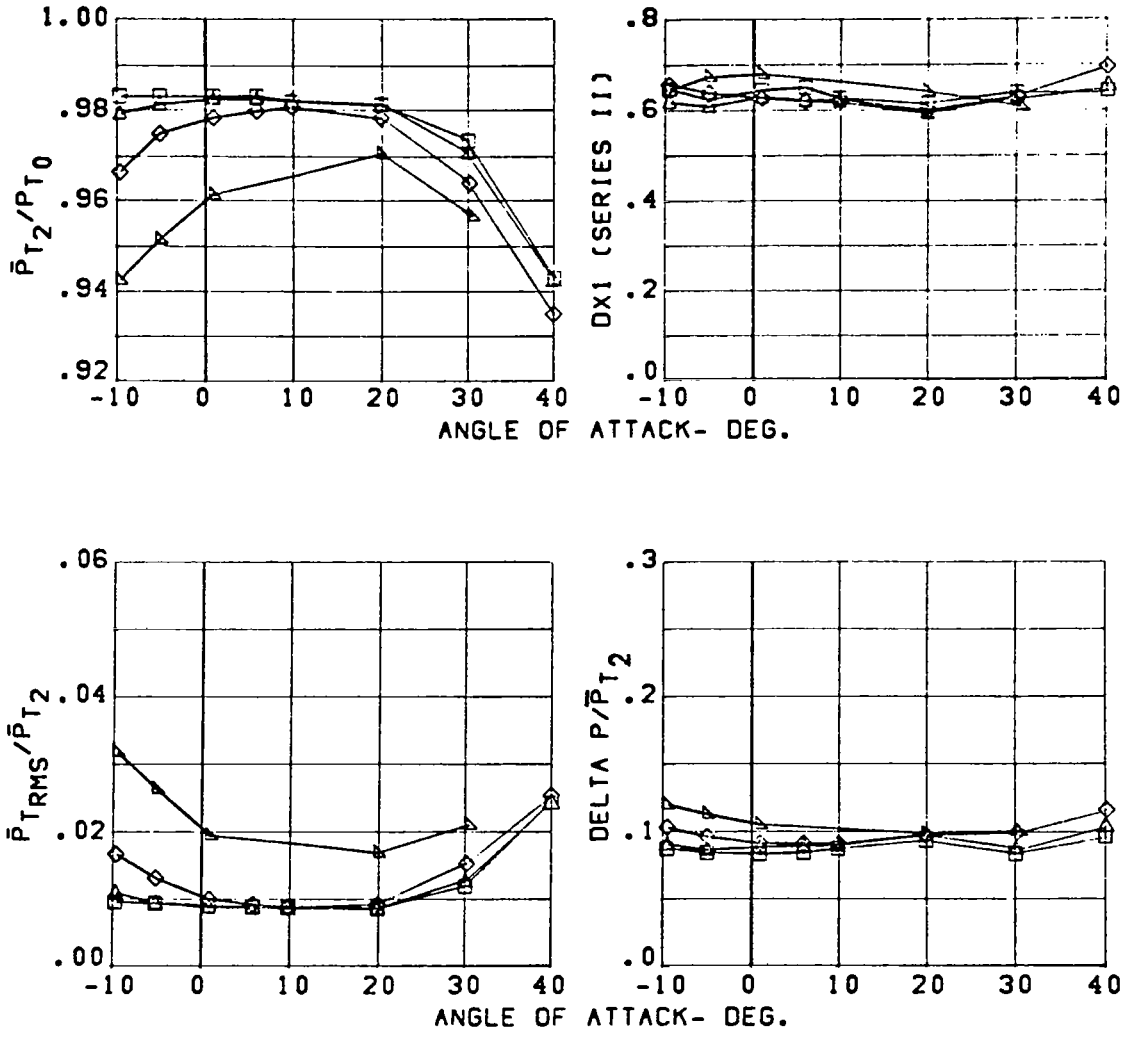

Figure 23 Effect of Angle of Attack and Sideslip on Pressure Recovery, Turbulence, and Distortion at Engine Face at Rated Airflow; Mach 0.60

CONFIGURATION	CONDITION	SYM	BETA (DEG.)
C13 INLET 3.65 – IN. DIV. HT.	MACH= .90 WC2 = 229.	□ △ ◇	0. -5. -10.

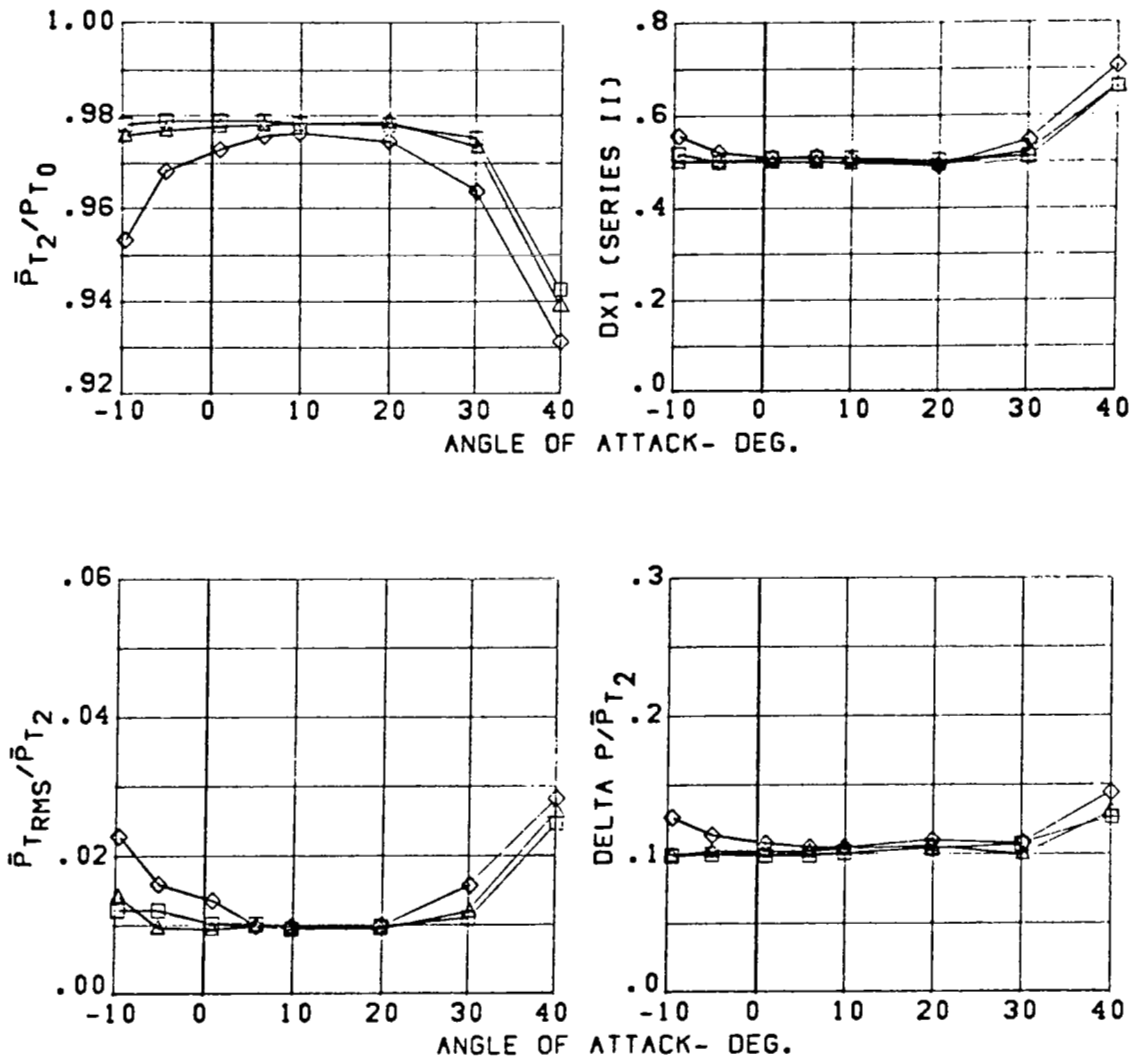

Figure 24 Effect of Angle of Attack and Sideslip on Pressure Recovery, Turbulence, and Distortion at Engine Face at Rated Airflow; Mach 0.90

CONFIGURATION	CONDITION	SYM	BETA (DEG.)
C13 INLET 3.65 – IN. DIV. HT.	MACH= 1.21 WC2 = 232.	□ △ ◇	0. -5. -10.

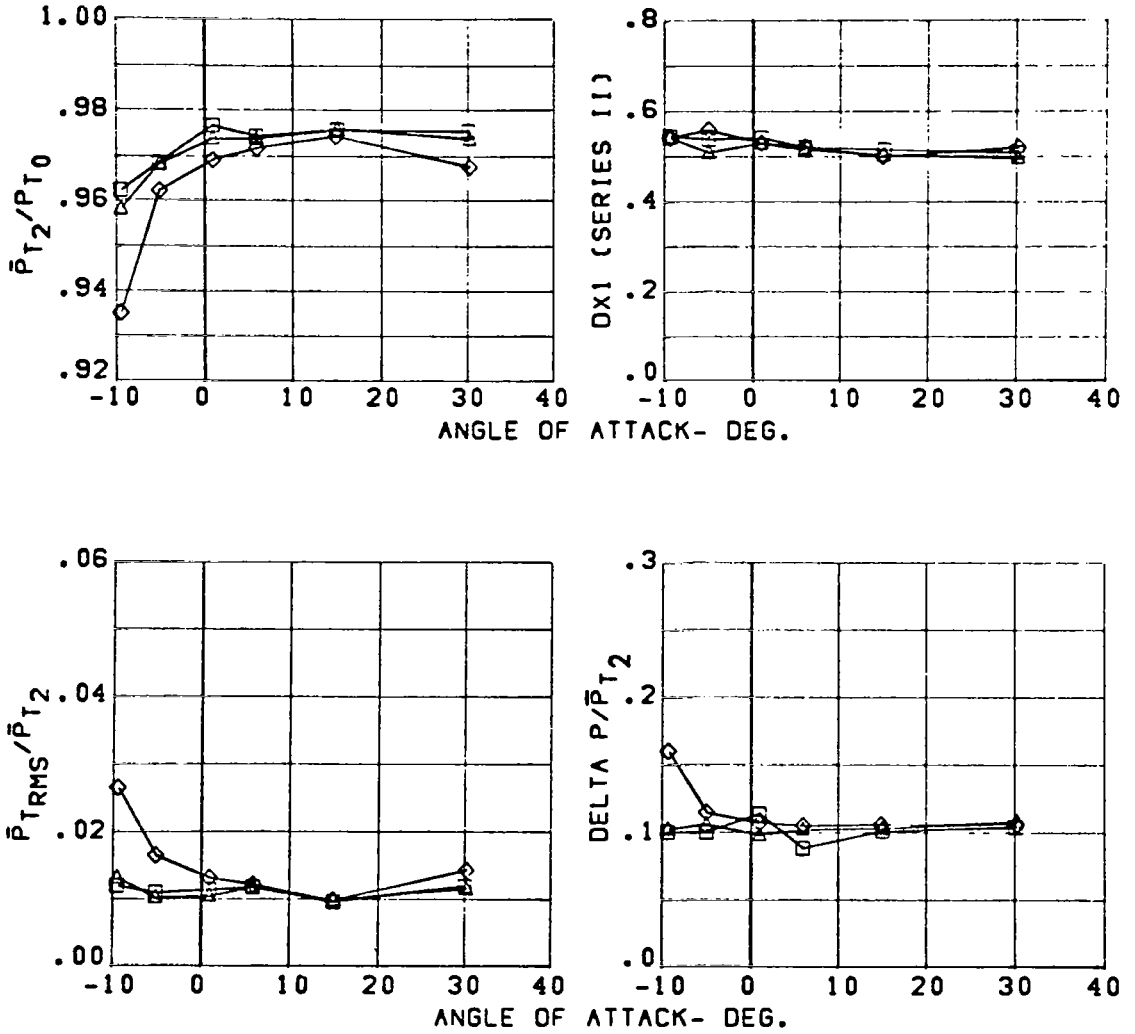

Figure 25 Effect of Angle of Attack and Sideslip on Pressure Recovery, Turbulence, and Distortion at Engine Face at Rated Airflow; Mach 1.21

CONFIGURATION	CONDITION	SYM	BETA (DEG.)
C13 INLET 3.65 – IN. DIV. HT.	MACH= 1.36 WC2 = 228.	□ △ ◇	0. -5. -10.

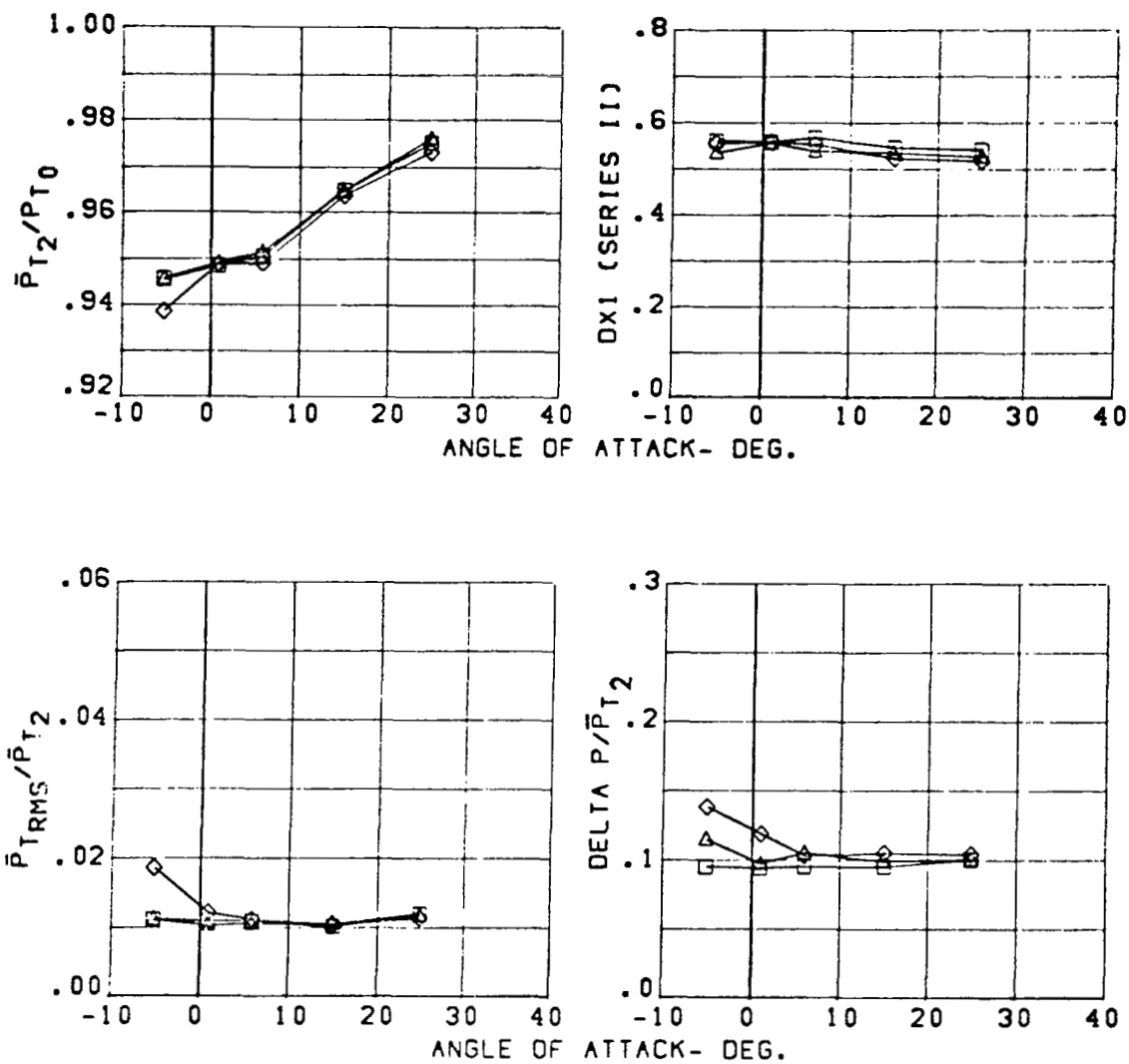

Figure 26 Effect of Angle of Attack and Sideslip on Pressure Recovery, Turbulence, and Distortion at Engine Face at Rated Airflow; Mach 1.36

CONFIGURATION	CONDITION	SYM	BETA (DEG.)
C13 INLET 3.65 – IN. DIV. HT.	MACH= 1.58 WC2 = 218.	□ △ ◇	0. -5. -10.

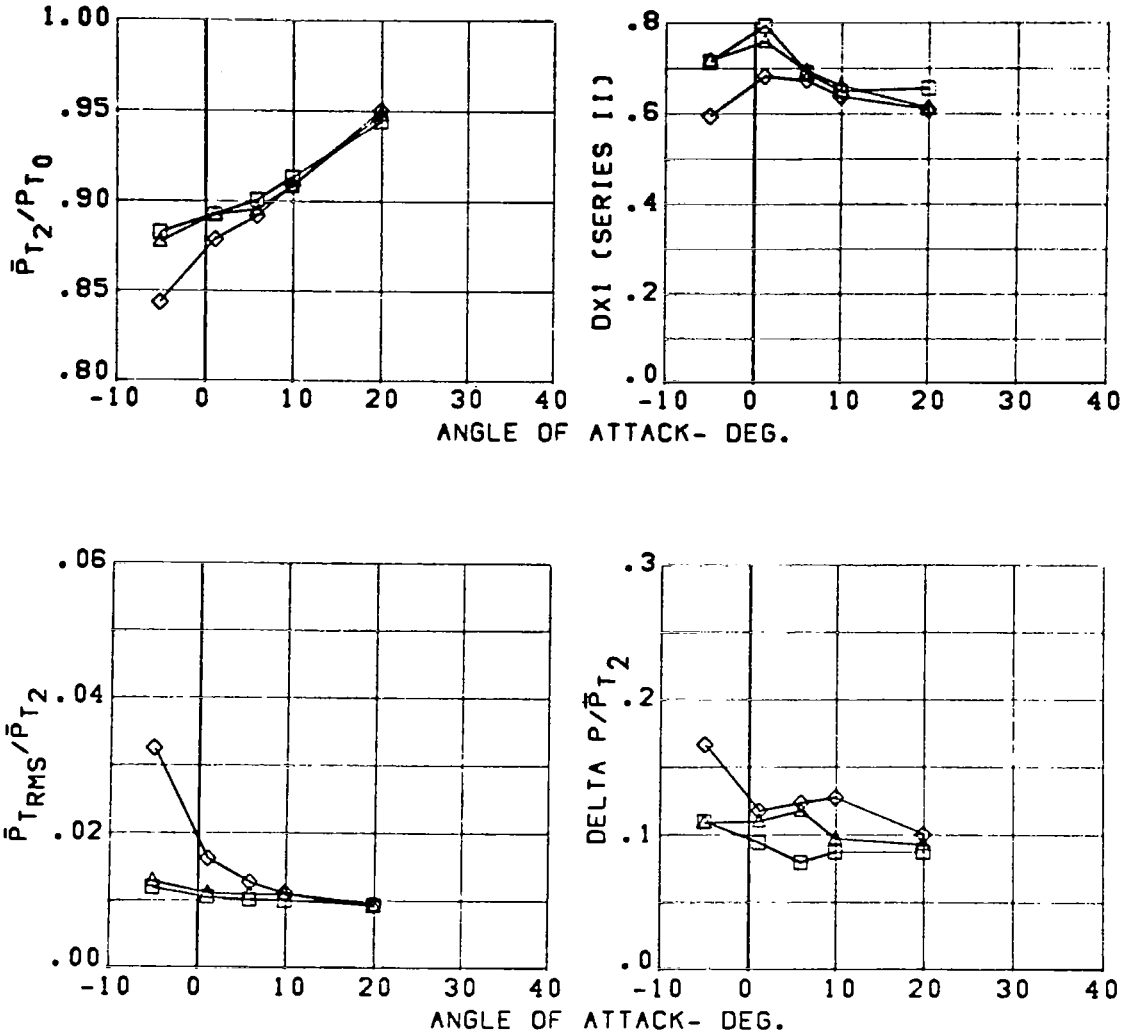

Figure 27 Effect of Angle of Attack and Sideslip on Pressure Recovery, Turbulence, and Distortion at Engine Face at Rated Airflow; Mach 1.58

CONFIGURATION	CONDITION	SYM	BETA (DEG.)
C13 INLET 3.65 – IN. DIV. HT.	MACH= 1.78 WC2 = 200.	□ △ ◇	0. -5. -10.

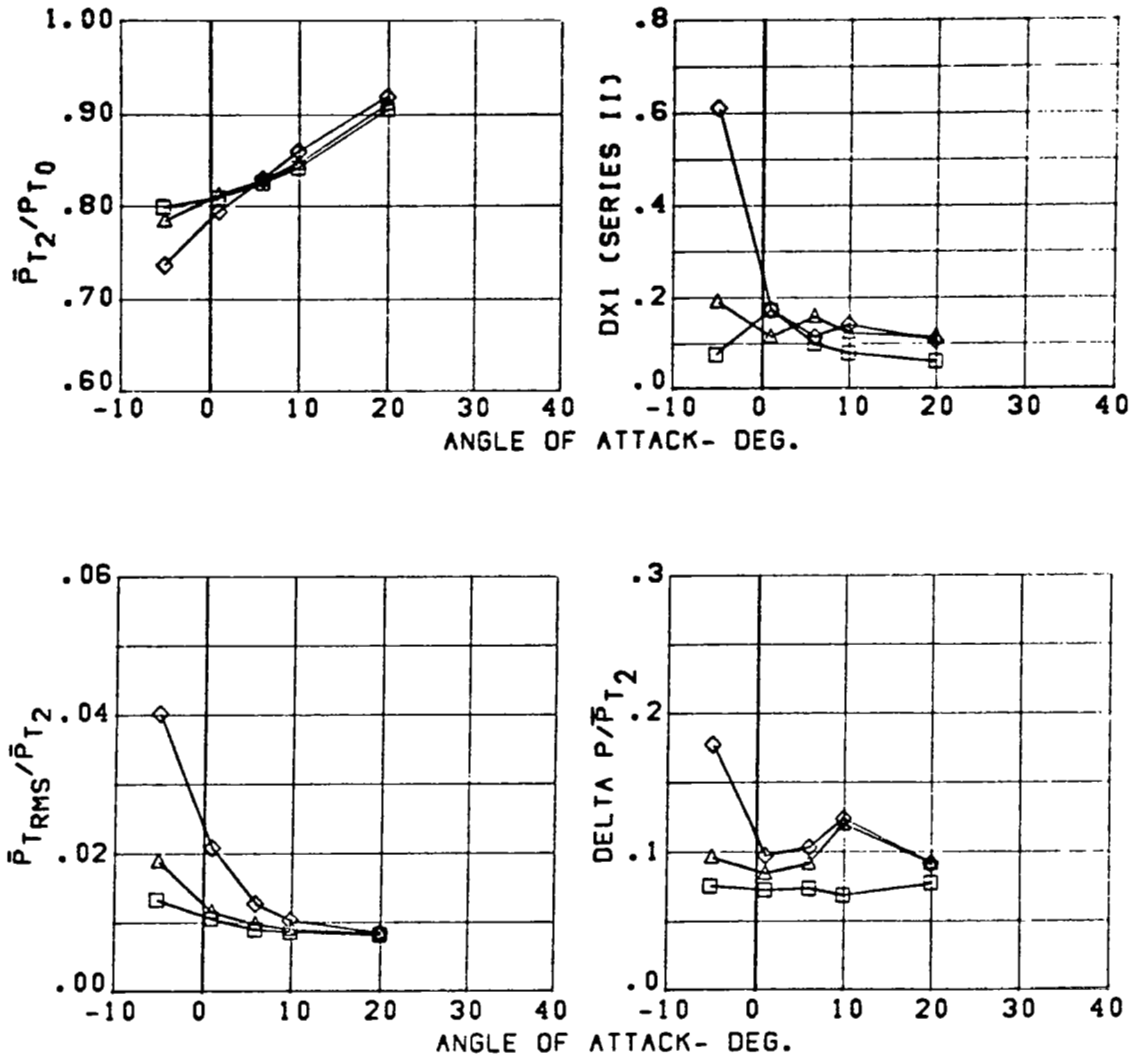

Figure 28 Effect of Angle of Attack and Sideslip on Pressure Recovery, Turbulence, and Distortion at Engine Face at Rated Airflow; Mach 1.78

CONFIGURATION	CONDITION	SYM	BETA (DEG.)
C13 INLET 3.65 – IN. DIV. HT.	MACH= 1.96 WC2 = 184.	□ △ ◇	0. -5. -10.

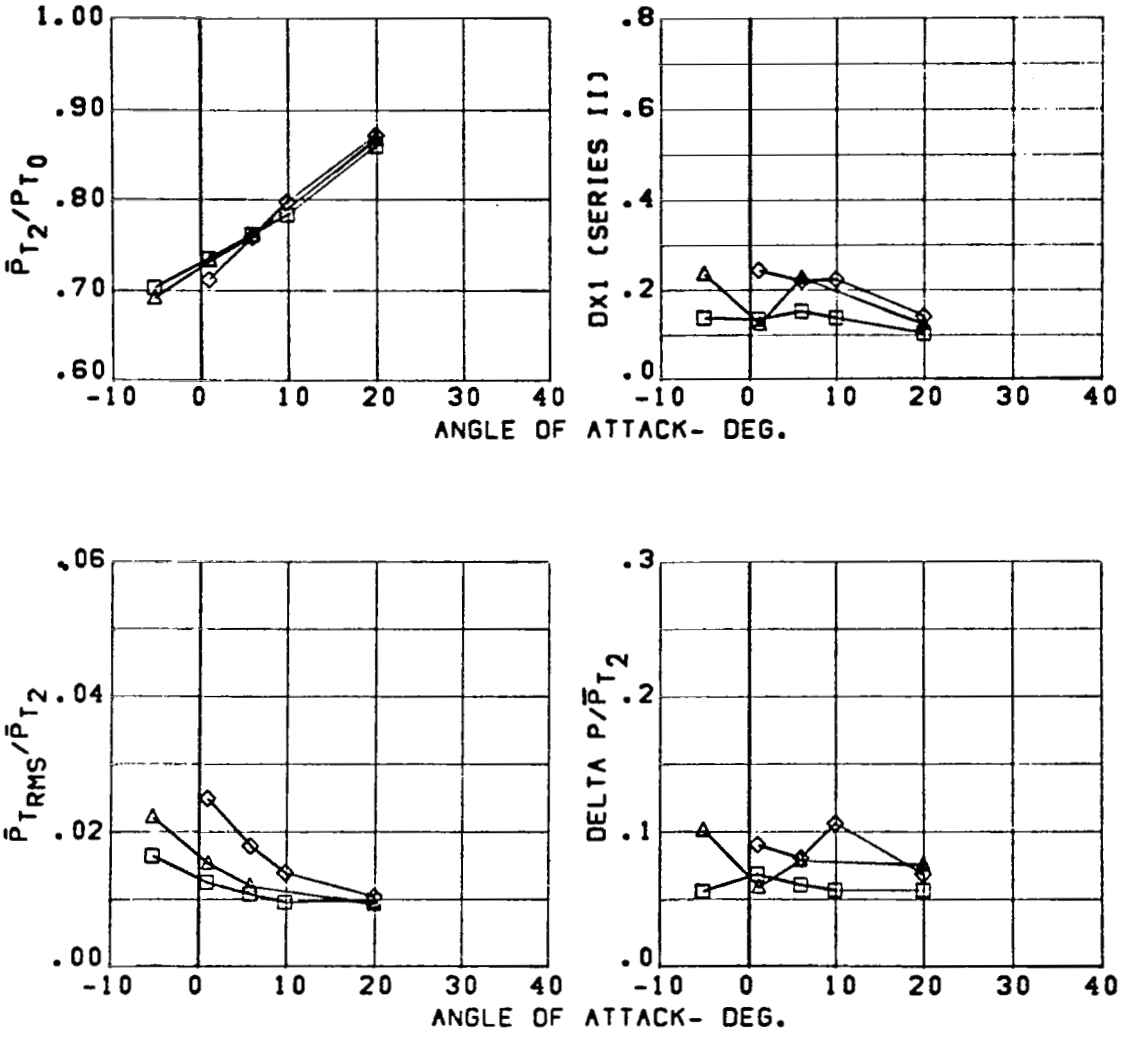

Figure 29 Effect of Angle of Attack and Sideslip on Pressure Recovery, Turbulence, and Distortion at Engine Face at Rated Airflow; Mach 1.96

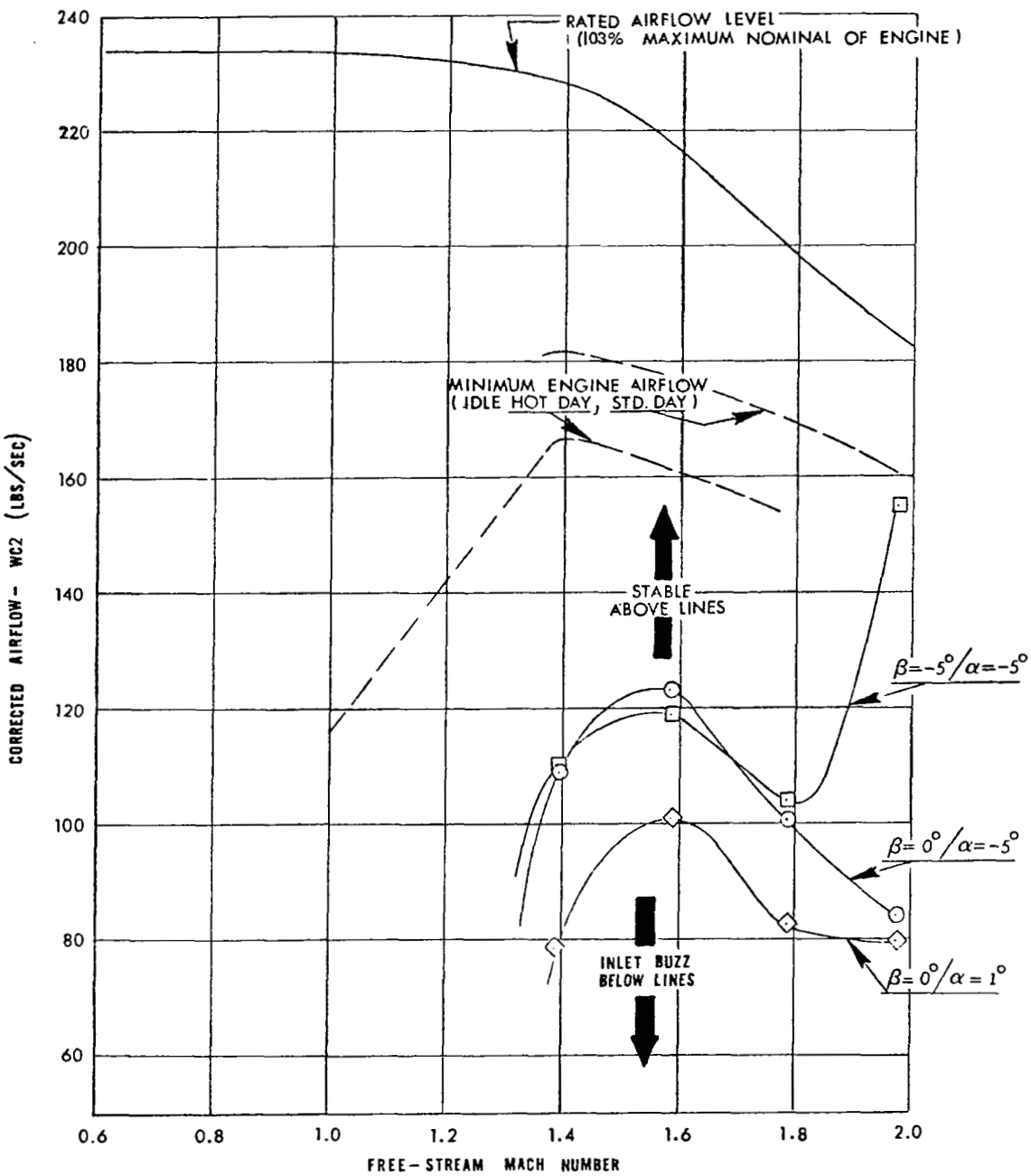

Figure 30 Inlet Stability (Buzz) Limits, Configuration C13

CONFIGURATION	CONDITION	SYM.	BETA (DEG)
C13	MACH = .61	□	0.
3.65 IN. DIV. HT.	ALPHA= -9.	△	-5.
THROAT RAKES OUT		◇	-10.
		▷	-15.

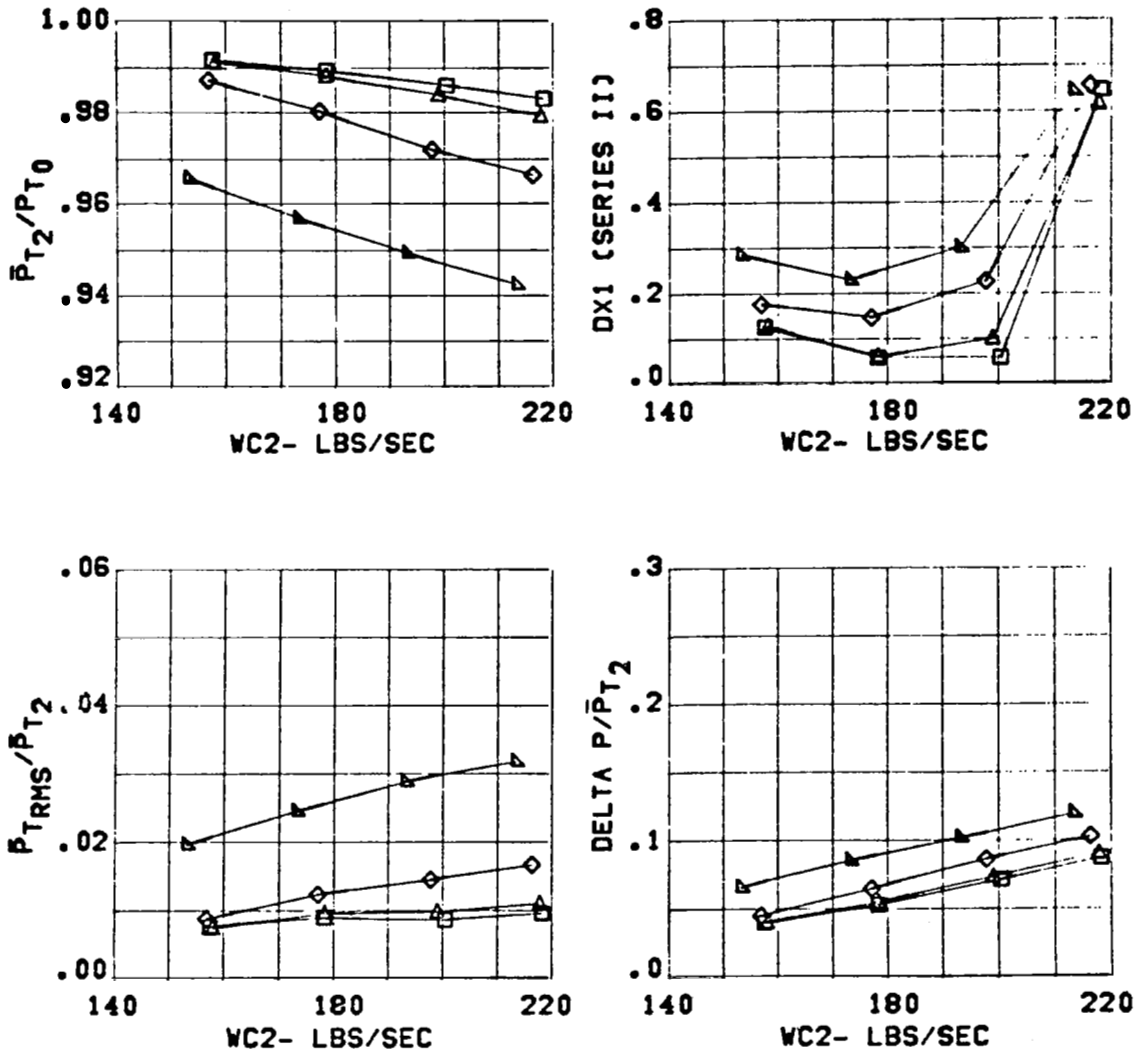

Figure 31 Inlet Performance for Configuration C13

CONFIGURATION	CONDITION	SYM.	BETA (DEG)
C13	MACH = .60	□	0.
3.65 IN. DIV. HT.	ALPHA= -5.	△	-5.
THROAT RAKES OUT		◇	-10.
		▷	-15.

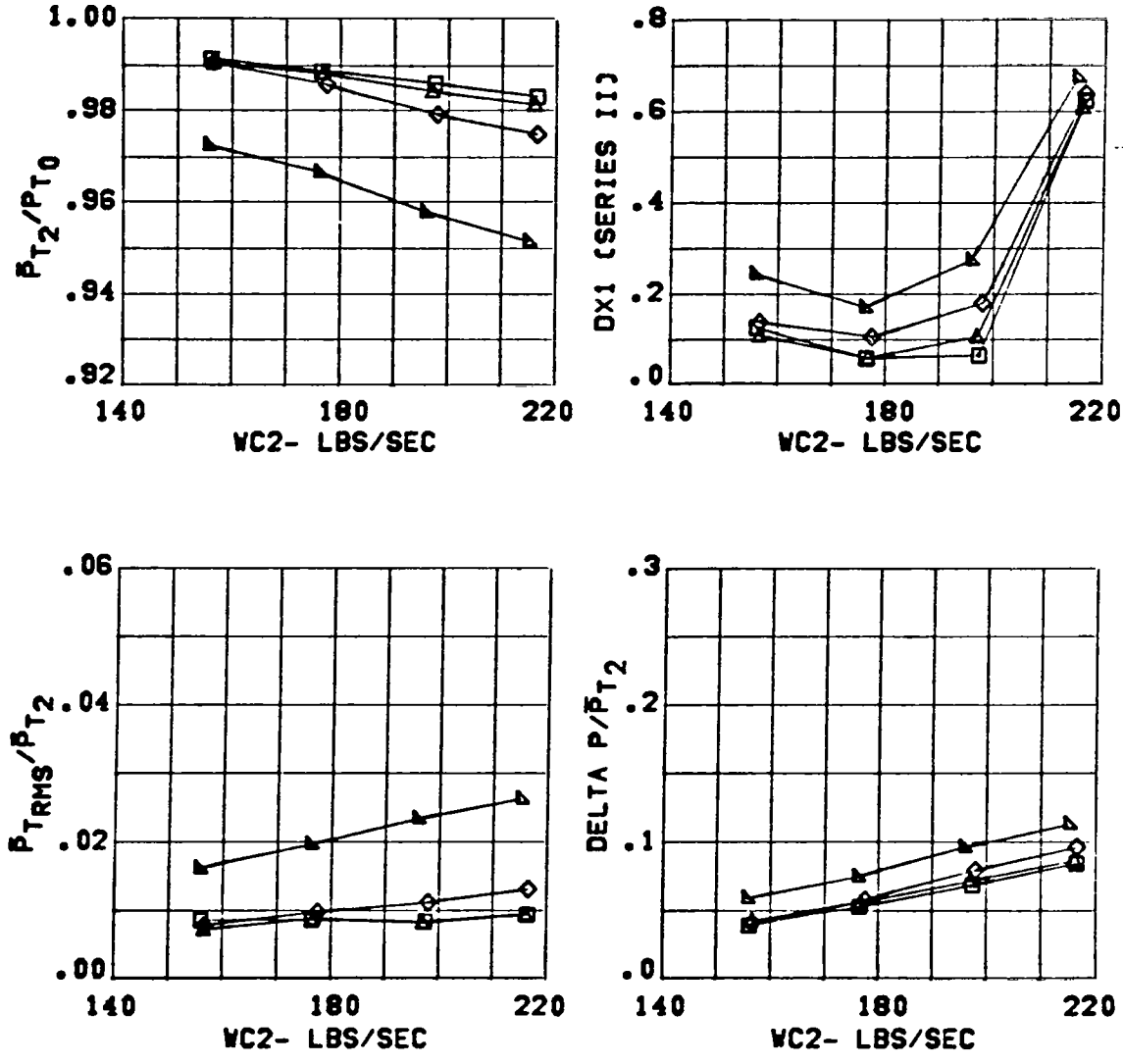

Figure 32 Inlet Performance for Configuration C13

CONFIGURATION	CONDITION	SYM.	BETA (DEG)
C13	MACH = .60	□	0.
3.65 IN. DIV. HT.	ALPHA= 1.	△	-5.
THROAT RAKES OUT		◇	-10.
		▷	-15.

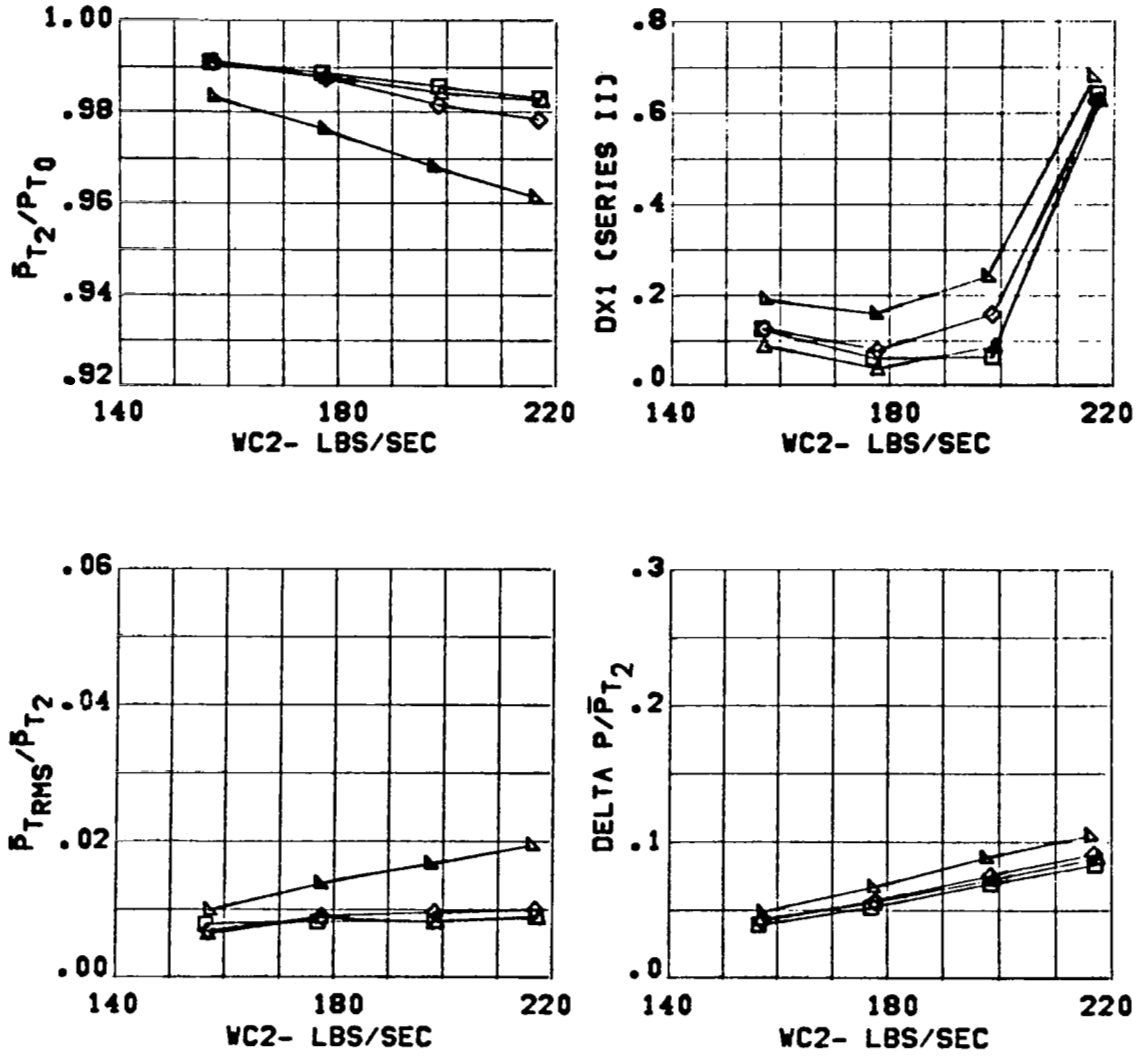

Figure 33 Inlet Performance for Configuration C13

CONFIGURATION	CONDITION	SYM.	BETA (DEG)
C13	MACH = .60	□	0.
3.65 IN. DIV. HT.	ALPHA= 6.	△	-5.
THROAT RAKES OUT		◇	-10.

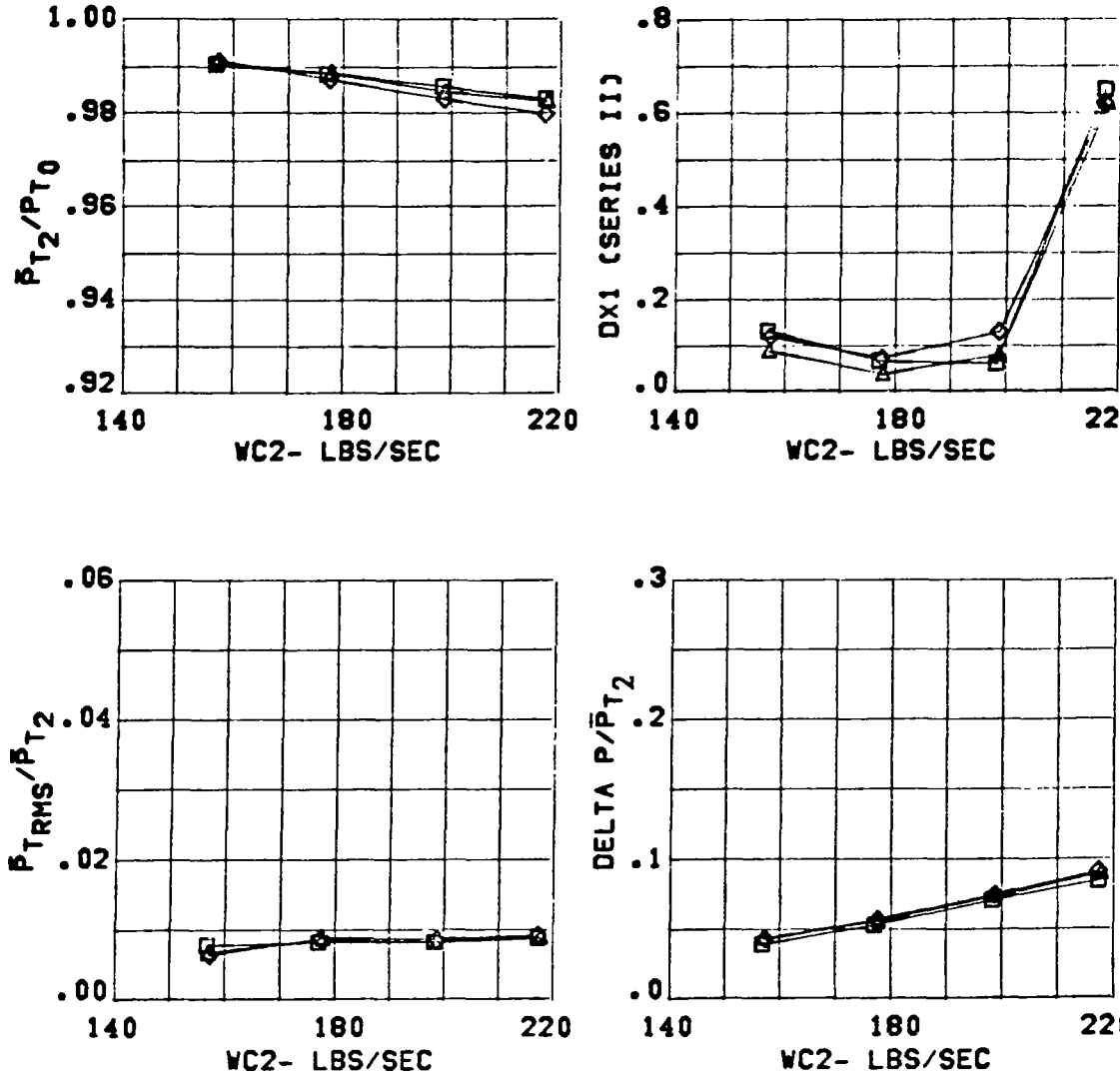

Figure 34 Inlet Performance for Configuration C13

CONFIGURATION	CONDITION	SYM.	BETA (DEG)
C13	MACH = .60	□	0.
3.65 IN. DIV. HT.	ALPHA= 10.	△	-5.
THROAT RAKES OUT		◇	-10.

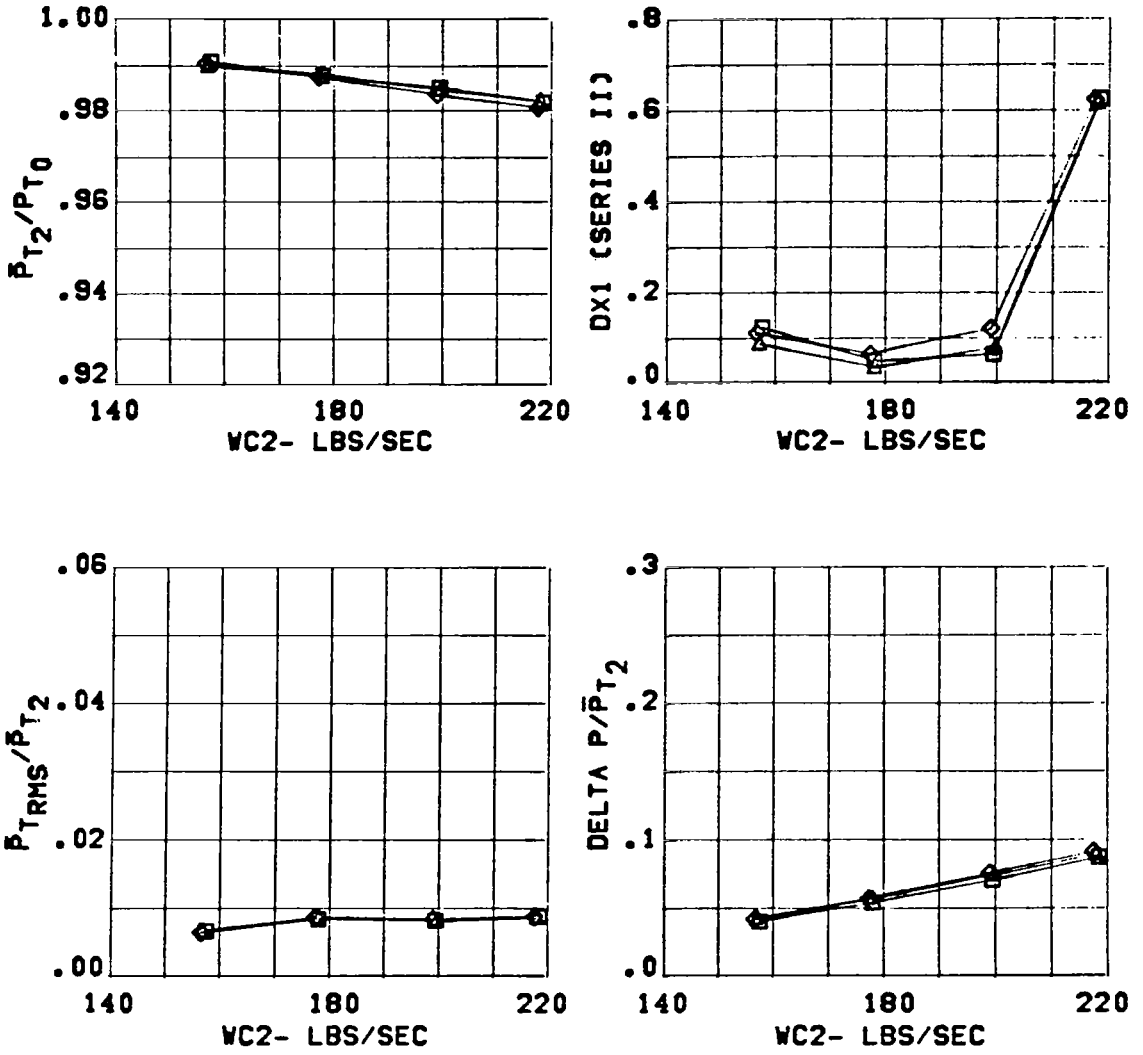

Figure 35 Inlet Performance for Configuration C13

CONFIGURATION	CONDITION	SYM.	BETA (DEG)
C13	MACH = .60	□	0.
3.65 IN. DIV. HT.	ALPHA= 20.	△	-5.
THROAT RAKES OUT		◇	-10.
		▷	-15.

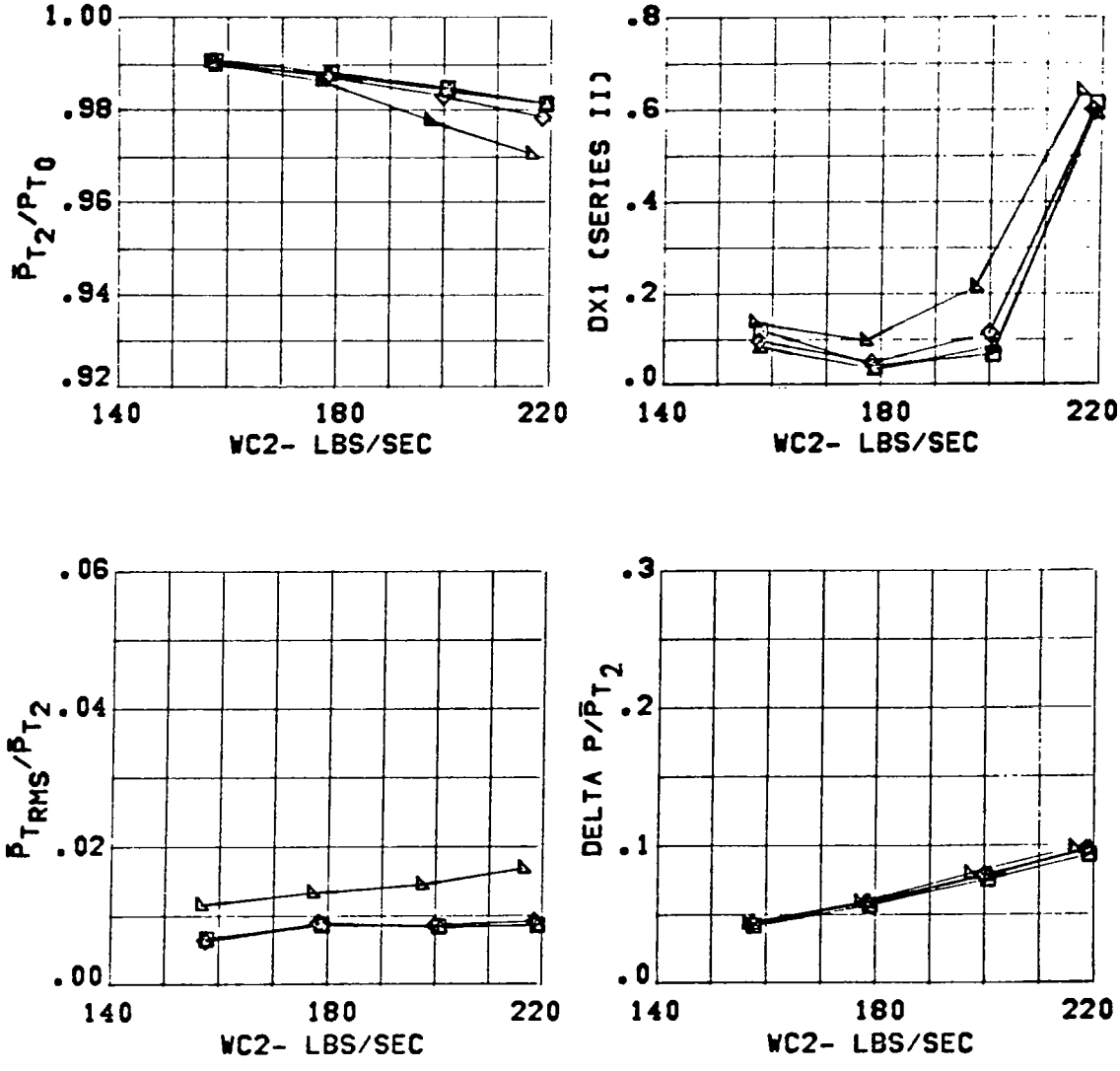

Figure 36 Inlet Performance for Configuration C13

CONFIGURATION	CONDITION	SYM.	BETA (DEG)
C13 3.65 IN. DIV. HT. THROAT RAKES OUT	MACH = .60 ALPHA= 30.	□ △ ◇ ▷	-1. -5. -10. -15.

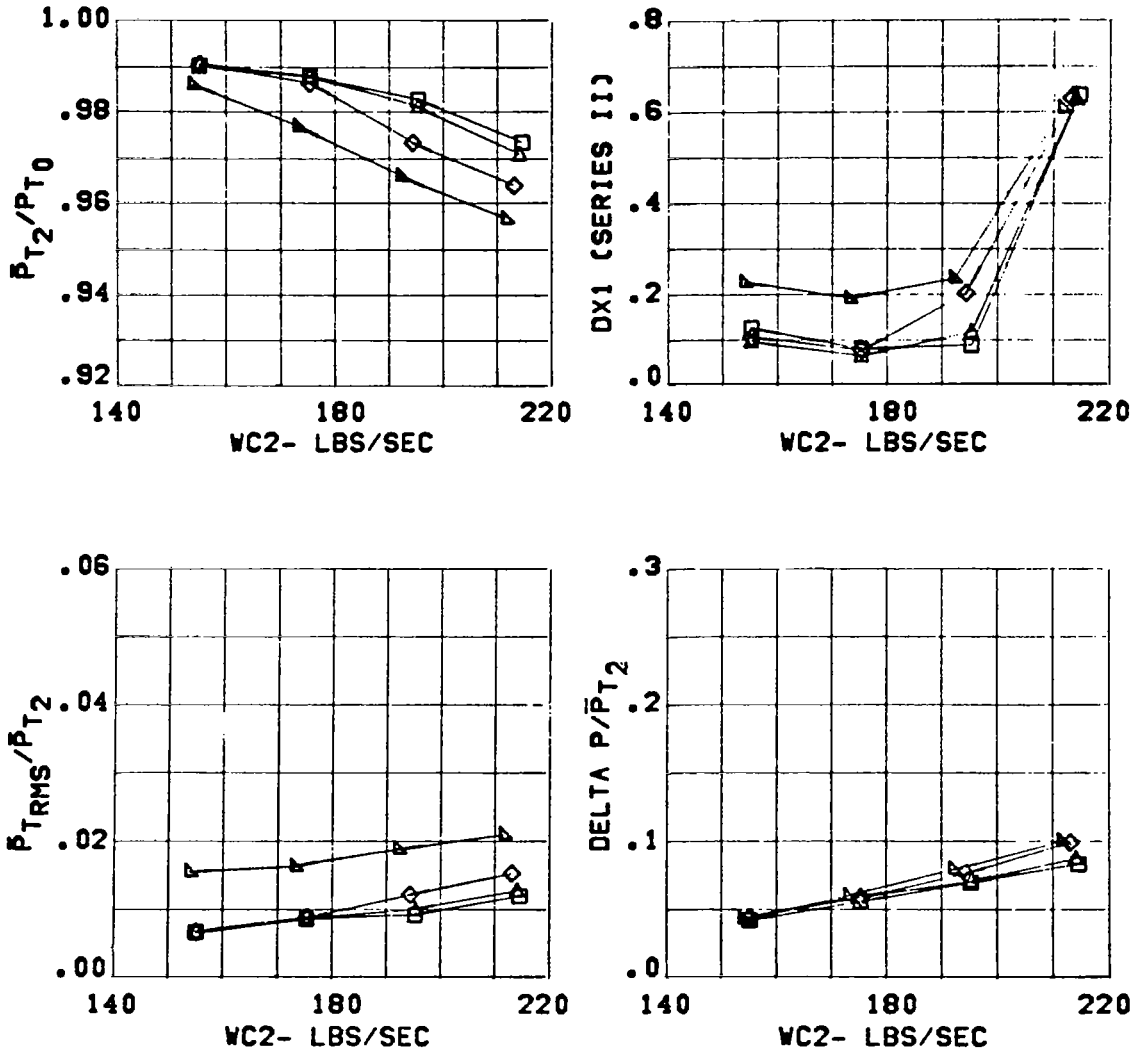

Figure 37 Inlet Performance for Configuration C13

CONFIGURATION	CONDITION	SYM.	BETA (DEG)
C13	MACH = .59	□	-0.
3.65 IN. DIV. HT.	ALPHA= 40.	△	-5.
THROAT RAKES OUT		◇	-10.

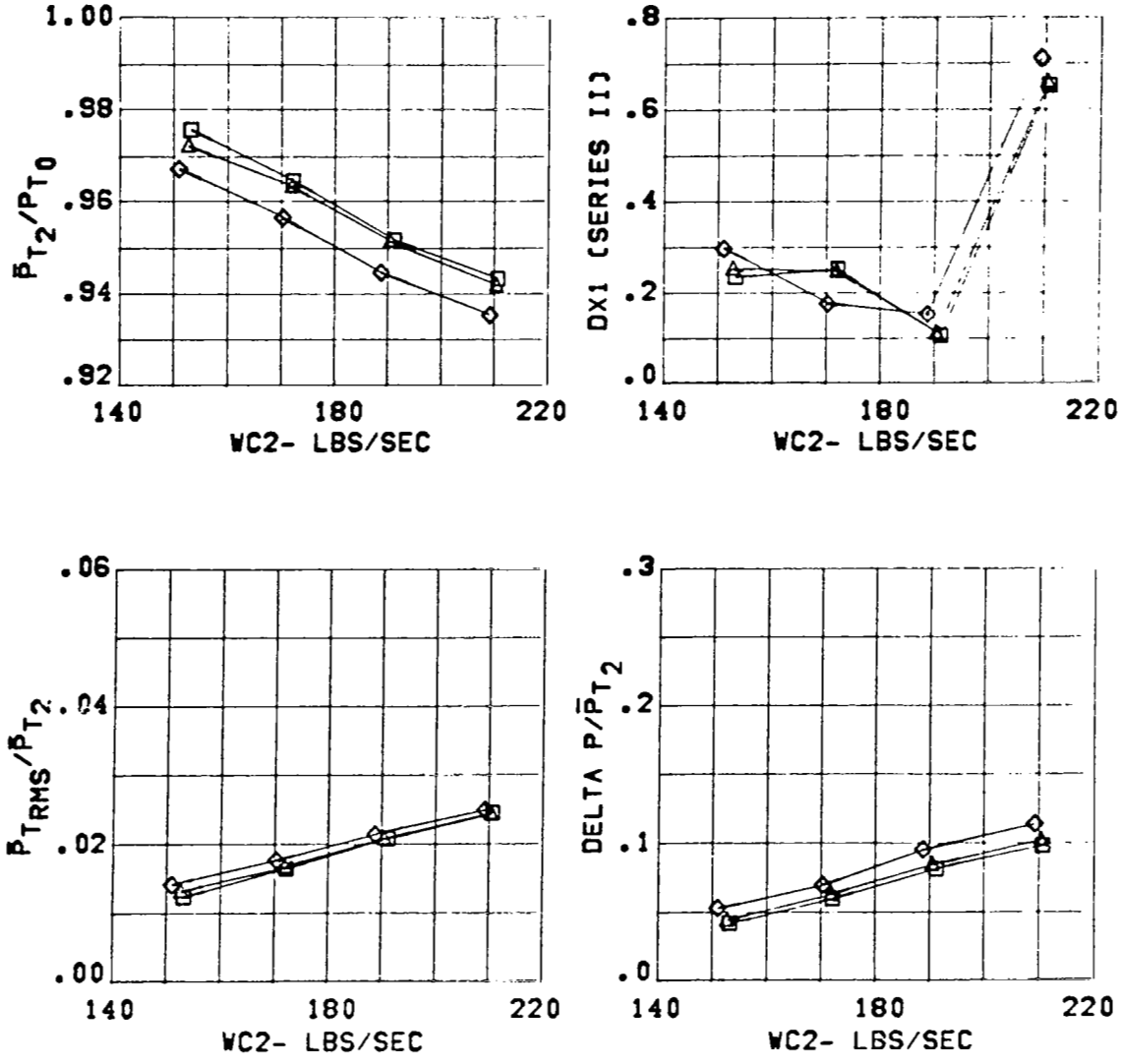

Figure 38 Inlet Performance for Configuration C13

CONFIGURATION	CONDITION	SYM.	BETA (DEG)
C13	MACH = .90	□	0.
3.65 IN. DIV. HT.	ALPHA= -9.	△	-5.
THROAT RAKES OUT		◇	-10.

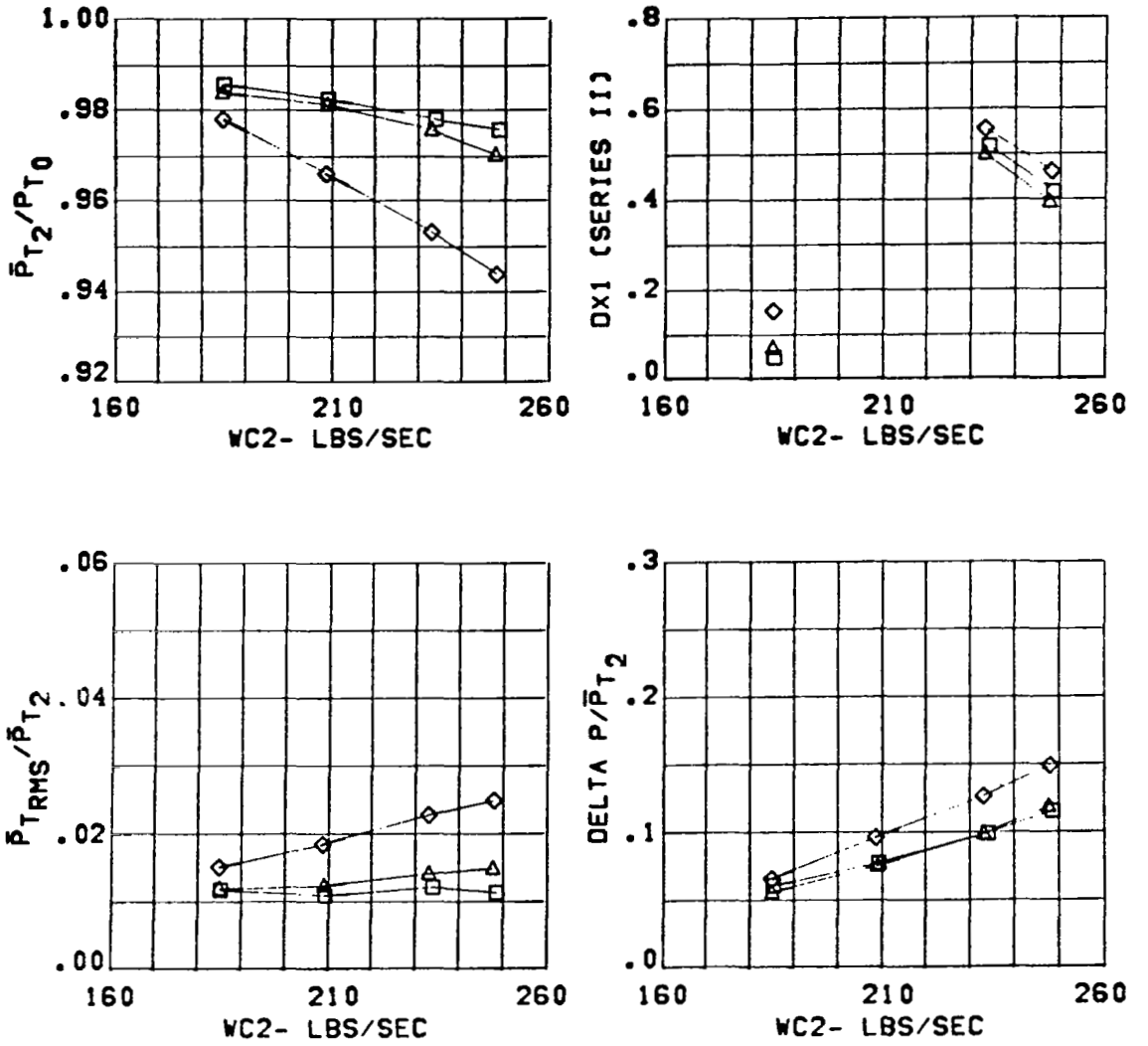

Figure 39 Inlet Performance for Configuration C13

CONFIGURATION	CONDITION	SYM.	BETA (DEG)
C13	MACH = .91	□	0.
3.65 IN. DIV. HT.	ALPHA= -5.	△	-5.
THROAT RAKES OUT		◇	-10.

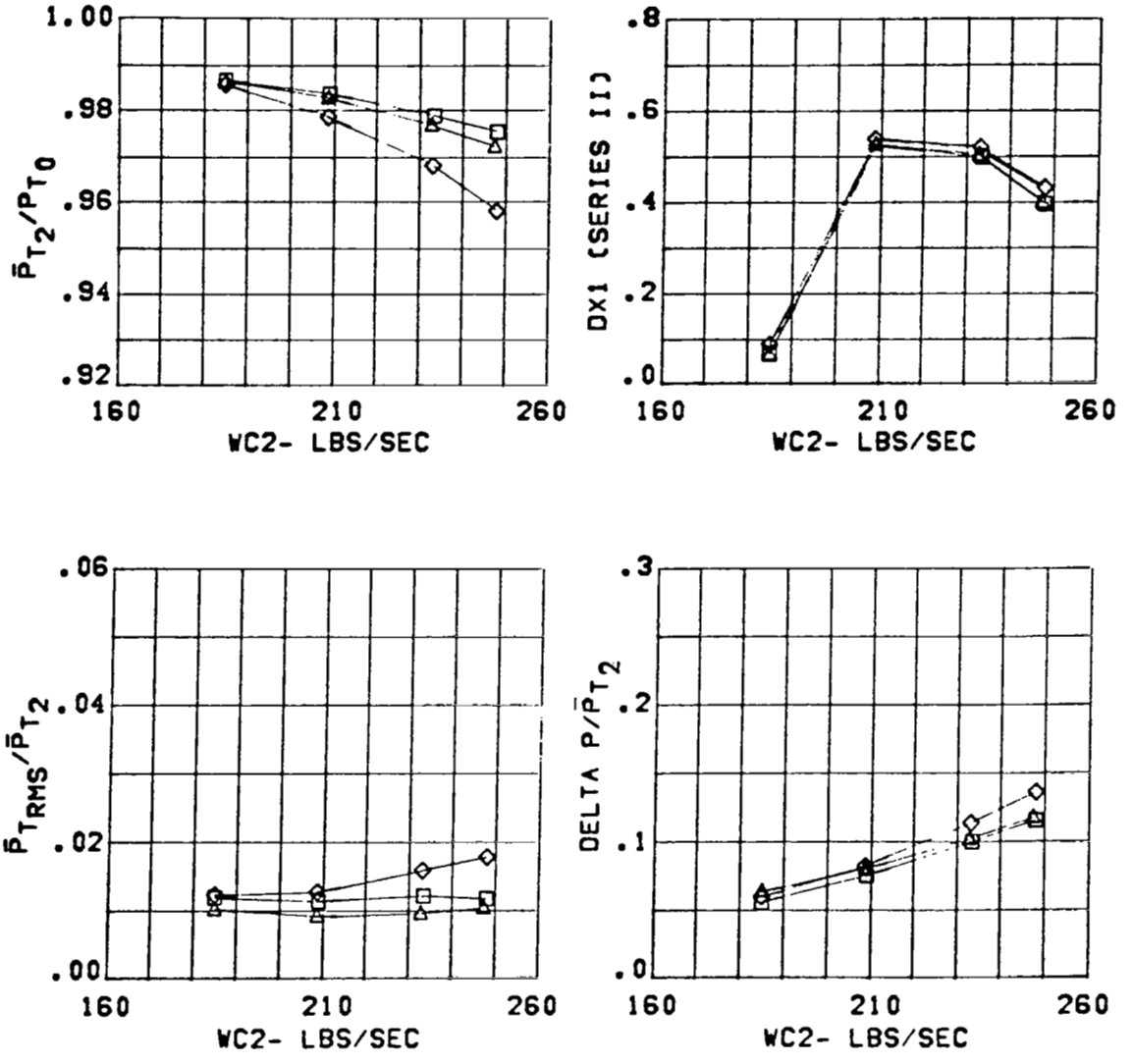

Figure 40 Inlet Performance for Configuration C13

CONFIGURATION	CONDITION	SYM.	BETA (DEG)
C13	MACH = .91	□	0.
3.65 IN. DIV. HT.	ALPHA= 1.	△	-5.
THROAT RAKES OUT		◇	-10.

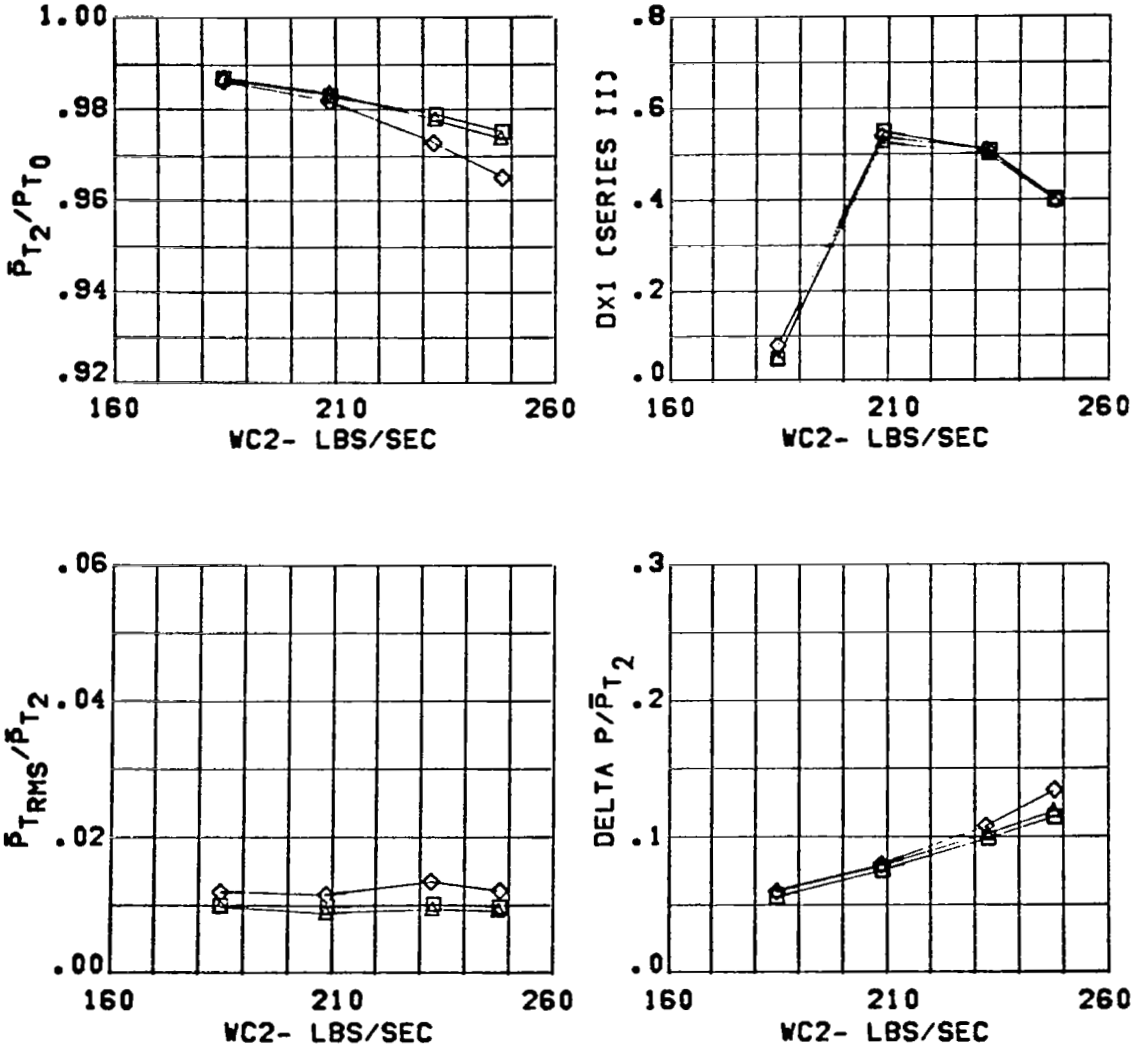

Figure 41 Inlet Performance for Configuration C13

CONFIGURATION	CONDITION	SYM.	BETA (DEG)
C13	MACH = .91	□	0.
3.65 IN. DIV. HT.	ALPHA= 6.	△	-5.
THROAT RAKES OUT		◇	-10.

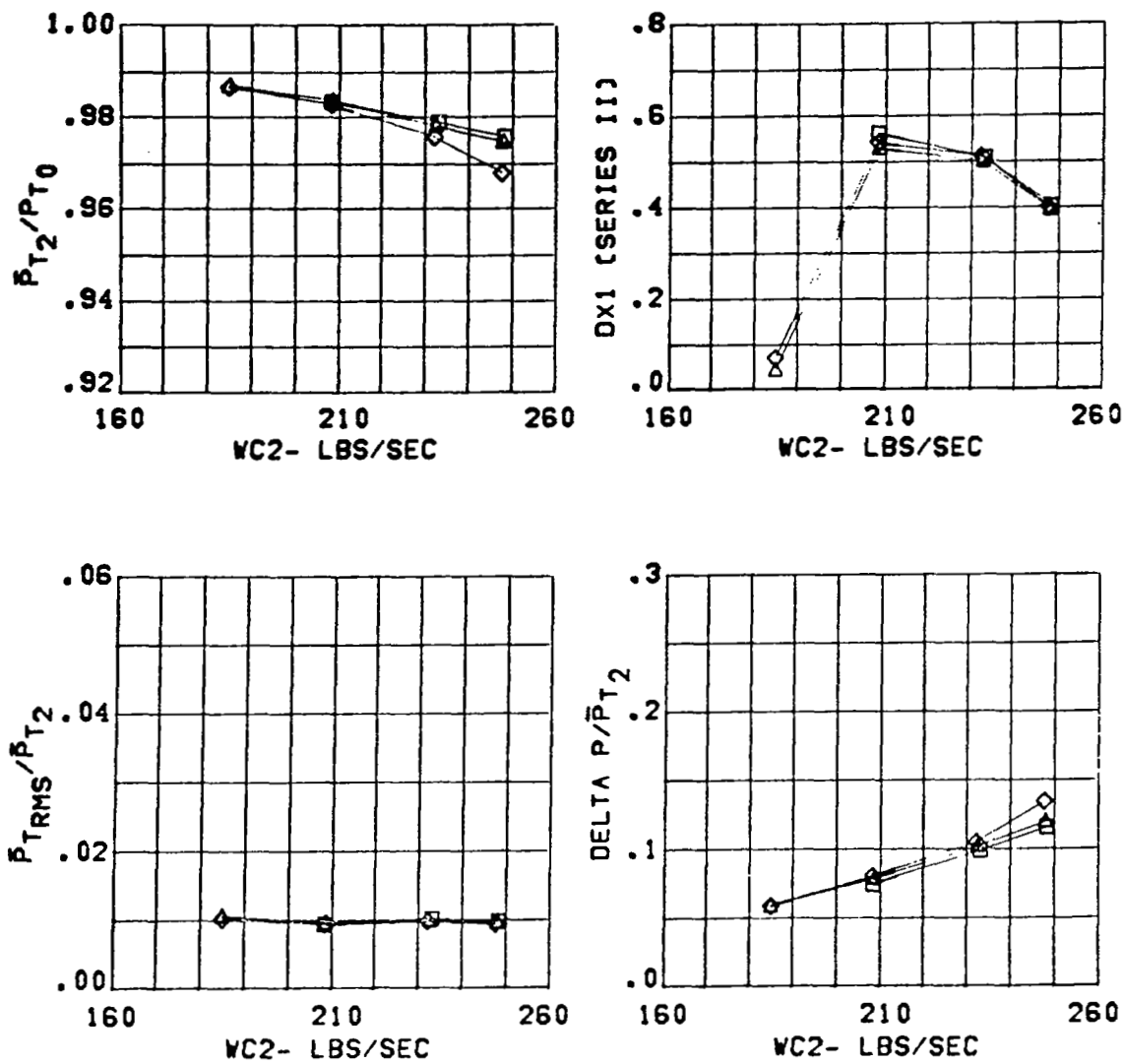

Figure 42 Inlet Performance for Configuration C13

CONFIGURATION	CONDITION	SYM.	BETA (DEG)
C13	MACH = .91	□	-0.
3.65 IN. DIV. HT.	ALPHA= 10.	△	-5.
THROAT RAKES OUT		◇	-10.

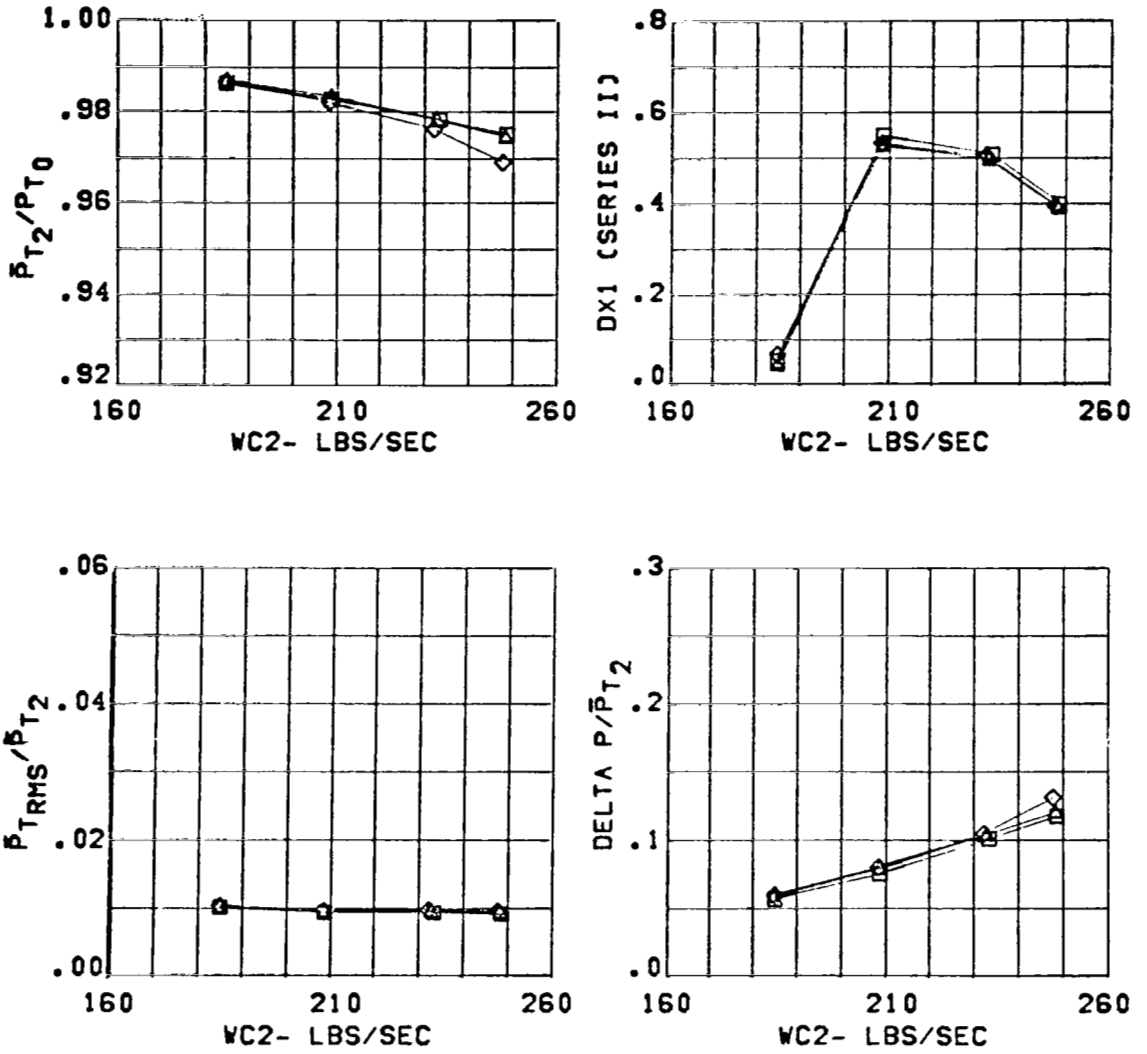

Figure 43 Inlet Performance for Configuration C13

CONFIGURATION	CONDITION	SYM.	BETA (DEG)
C13	MACH = .89	□	0.
3.65 IN. DIV. HT.	ALPHA= 20.	△	-5.
THROAT RAKES OUT		◇	-10.

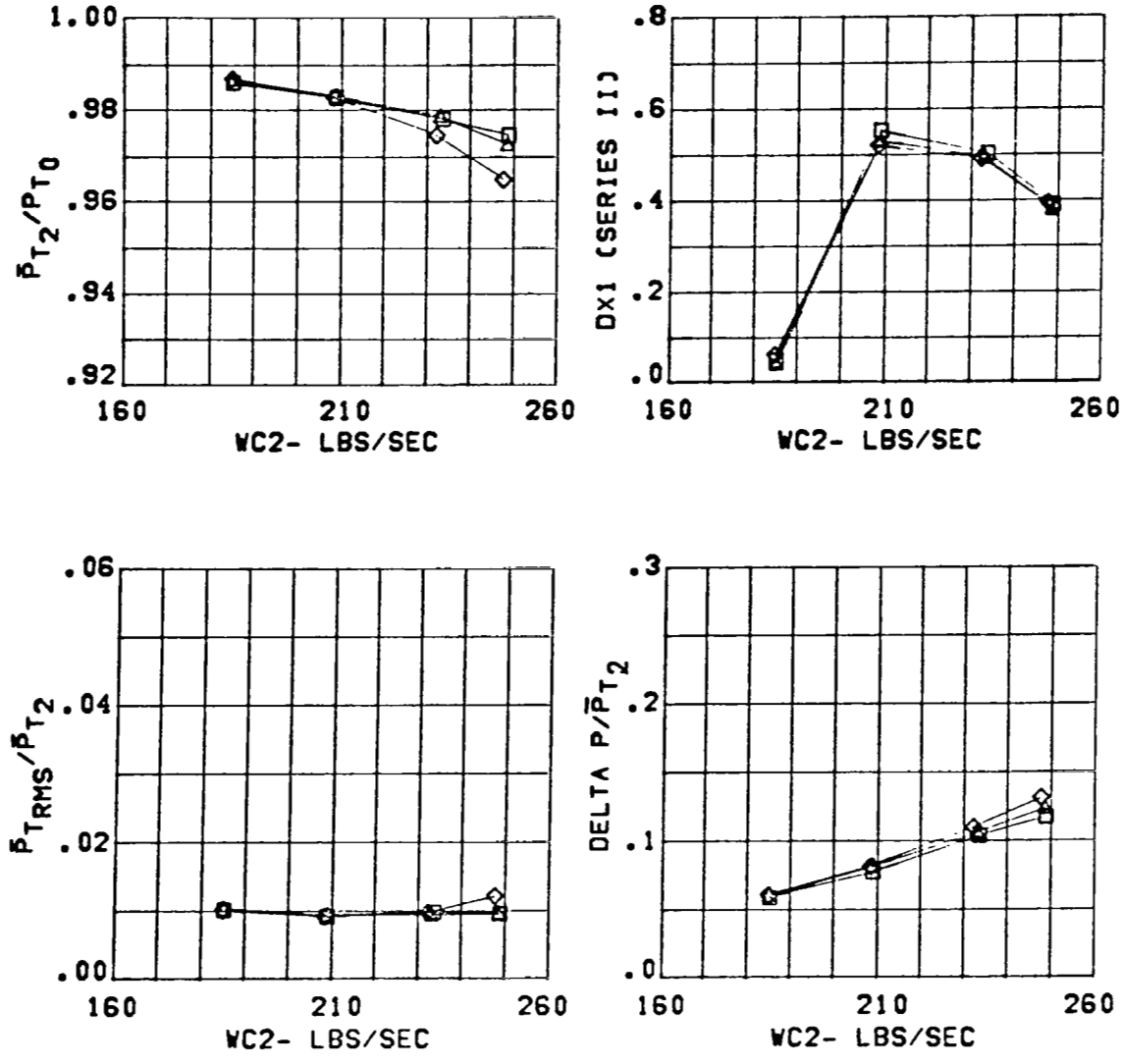

Figure 44 Inlet Performance for Configuration C13

CONFIGURATION	CONDITION	SYM.	BETA (DEG)
C13	MACH = .90	□	-1.
3.65 IN. DIV. HT.	ALPHA= 30.	△	-5.
THROAT RAKES OUT		◇	-10.

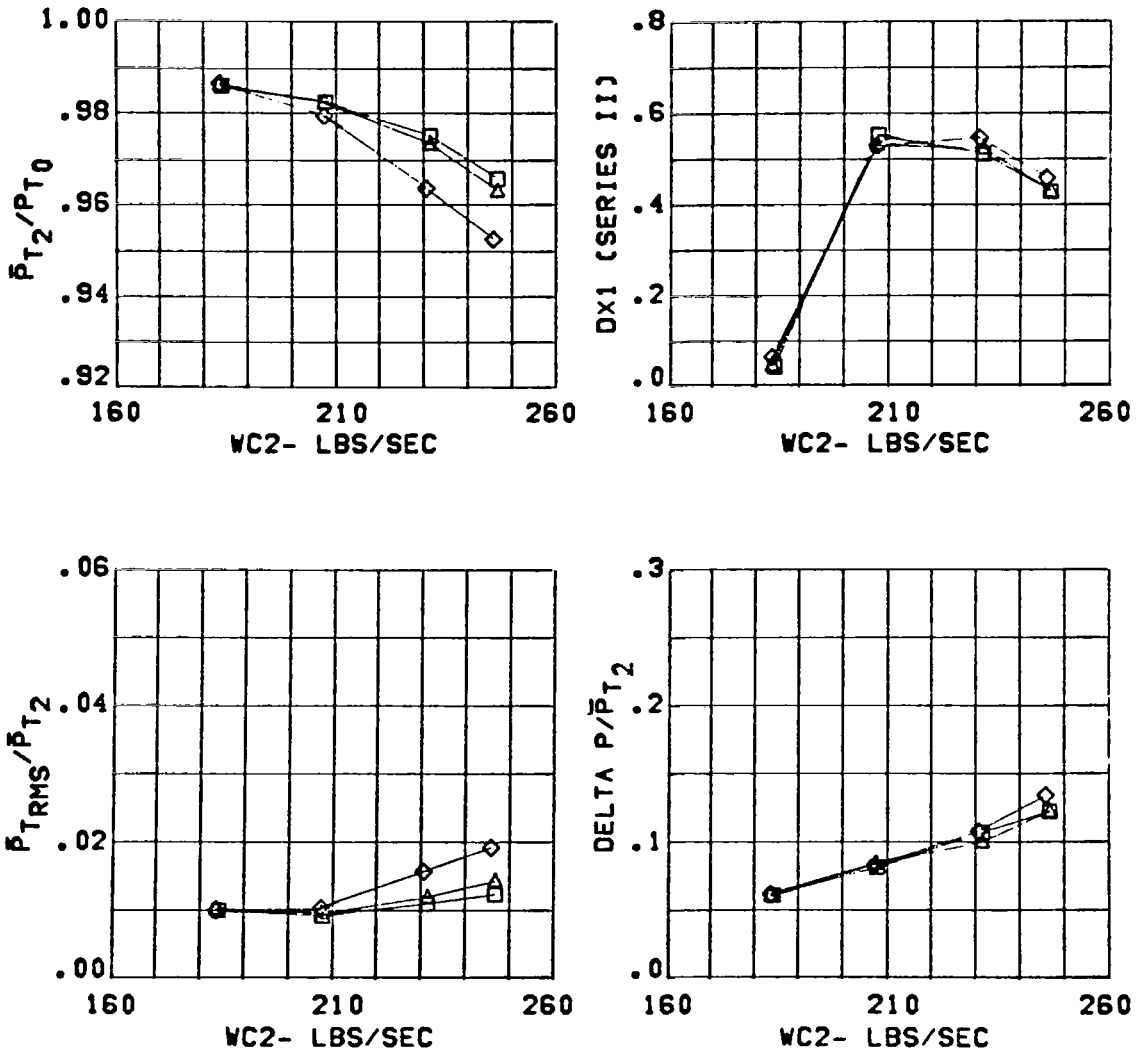

Figure 45 Inlet Performance for Configuration C13

CONFIGURATION	CONDITION	SYM.	BETA (DEG)
C13	MACH = .90	□	0.
3.65 IN. DIV. HT.	ALPHA= 40.	△	-5.
THROAT RAKES OUT		◇	-10.

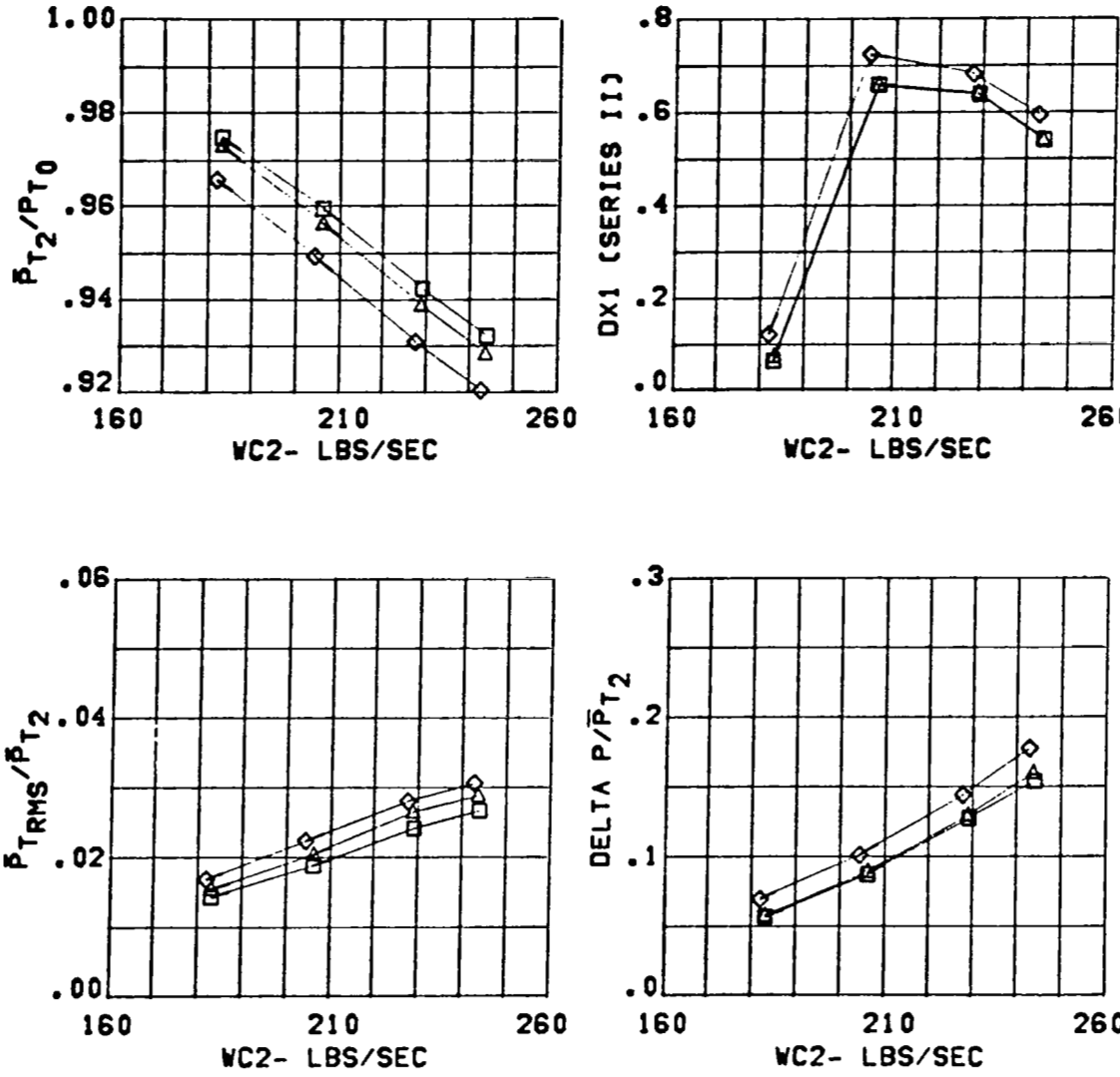

Figure 46 Inlet Performance for Configuration C13

CONFIGURATION	CONDITION	SYM.	BETA (DEG)
C13	MACH = 1.21	□	0.
3.65 IN. DIV. HT.	ALPHA= -9.	△	-5.
THROAT RAKES OUT		◇	-10.

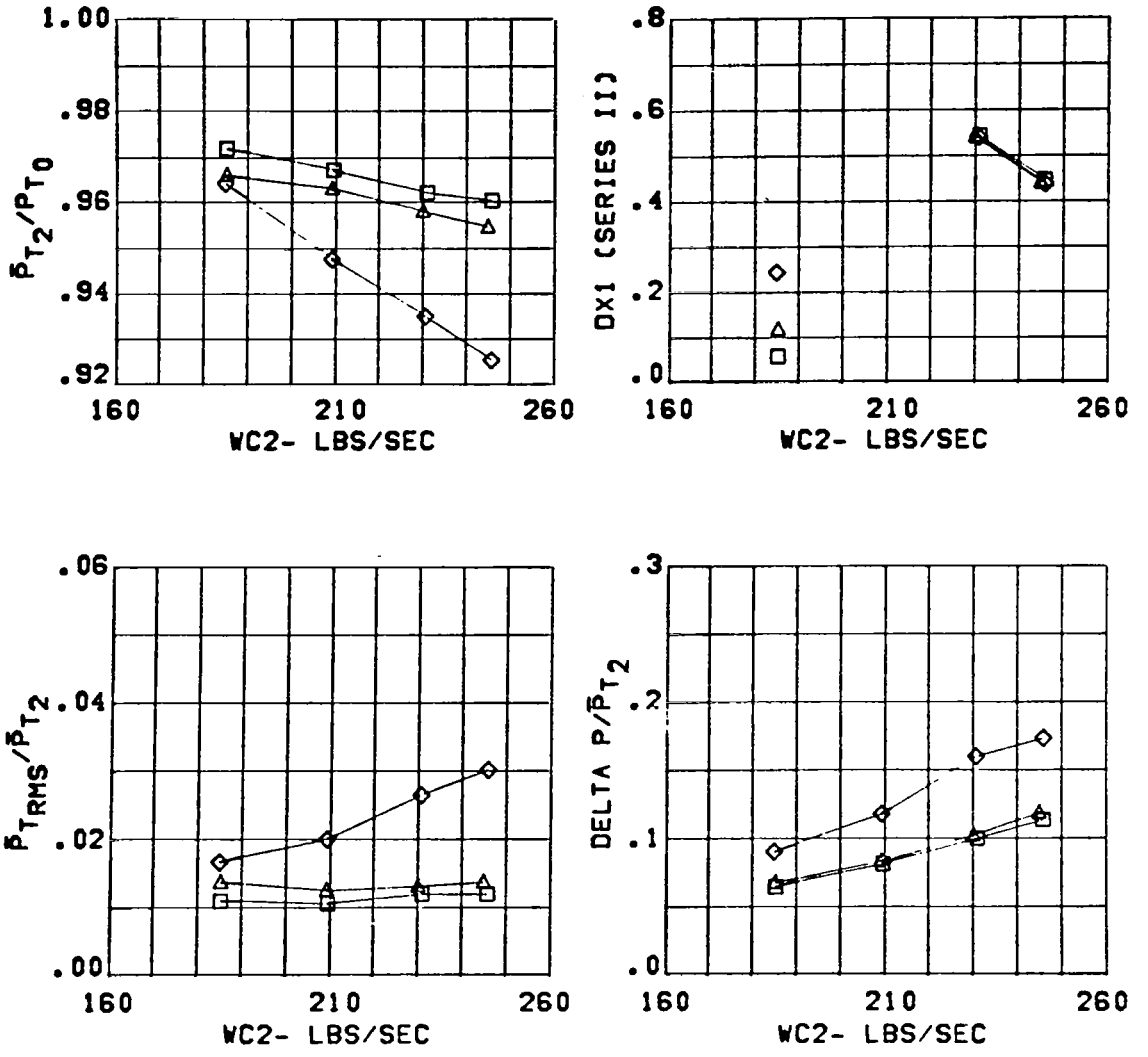

Figure 47 Inlet Performance for Configuration C13

CONFIGURATION	CONDITION	SYM.	BETA (DEG)
C13 3.65 IN. DIV. HT. THROAT RAKES OUT	MACH = 1.21 ALPHA= -5.	□ △ ◇	0. -5. -10.

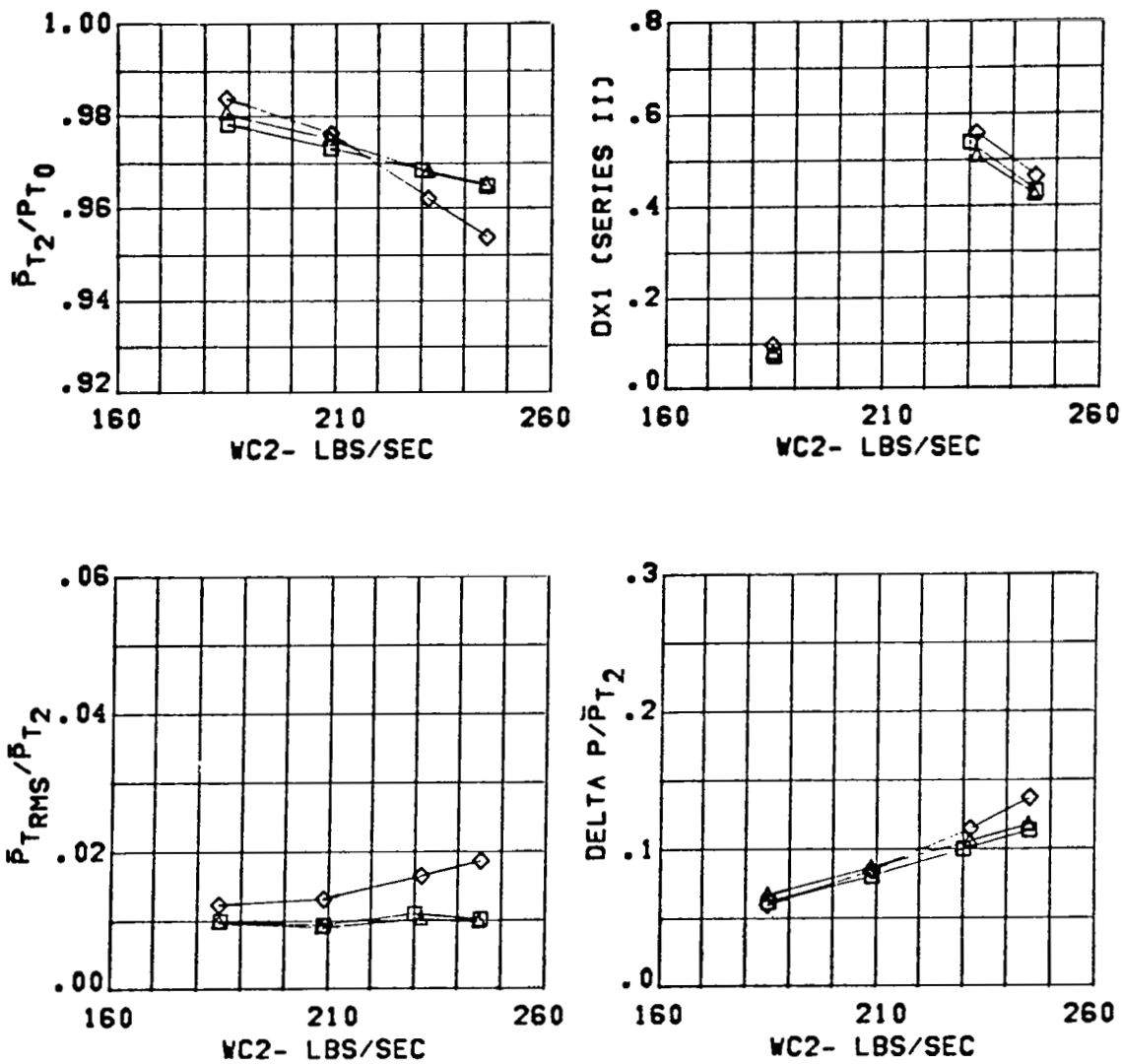

Figure 48 Inlet Performance for Configuration C13

CONFIGURATION	CONDITION	SYM.	BETA (DEG)
C13	MACH = 1.20	□	0.
3.65 IN. DIV. HT.	ALPHA= 1.	△	-5.
THROAT RAKES OUT		◇	-10.

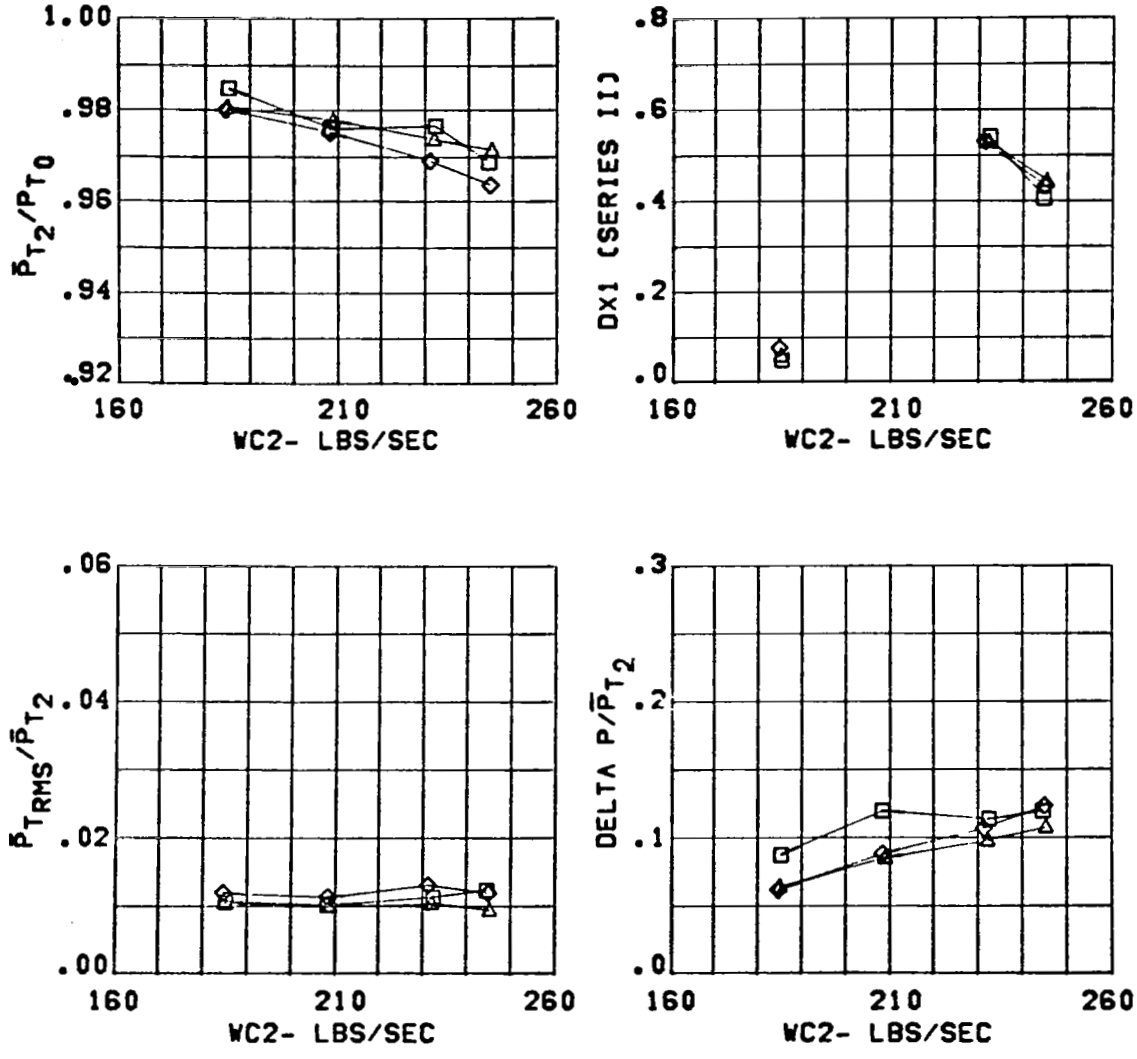

Figure 49 Inlet Performance for Configuration C13

CONFIGURATION	CONDITION	SYM.	BETA (DEG)
C13	MACH = 1.21	□	0.
3.65 IN. DIV. HT.	ALPHA= 6.	△	-5.
THROAT RAKES OUT		◇	-10.

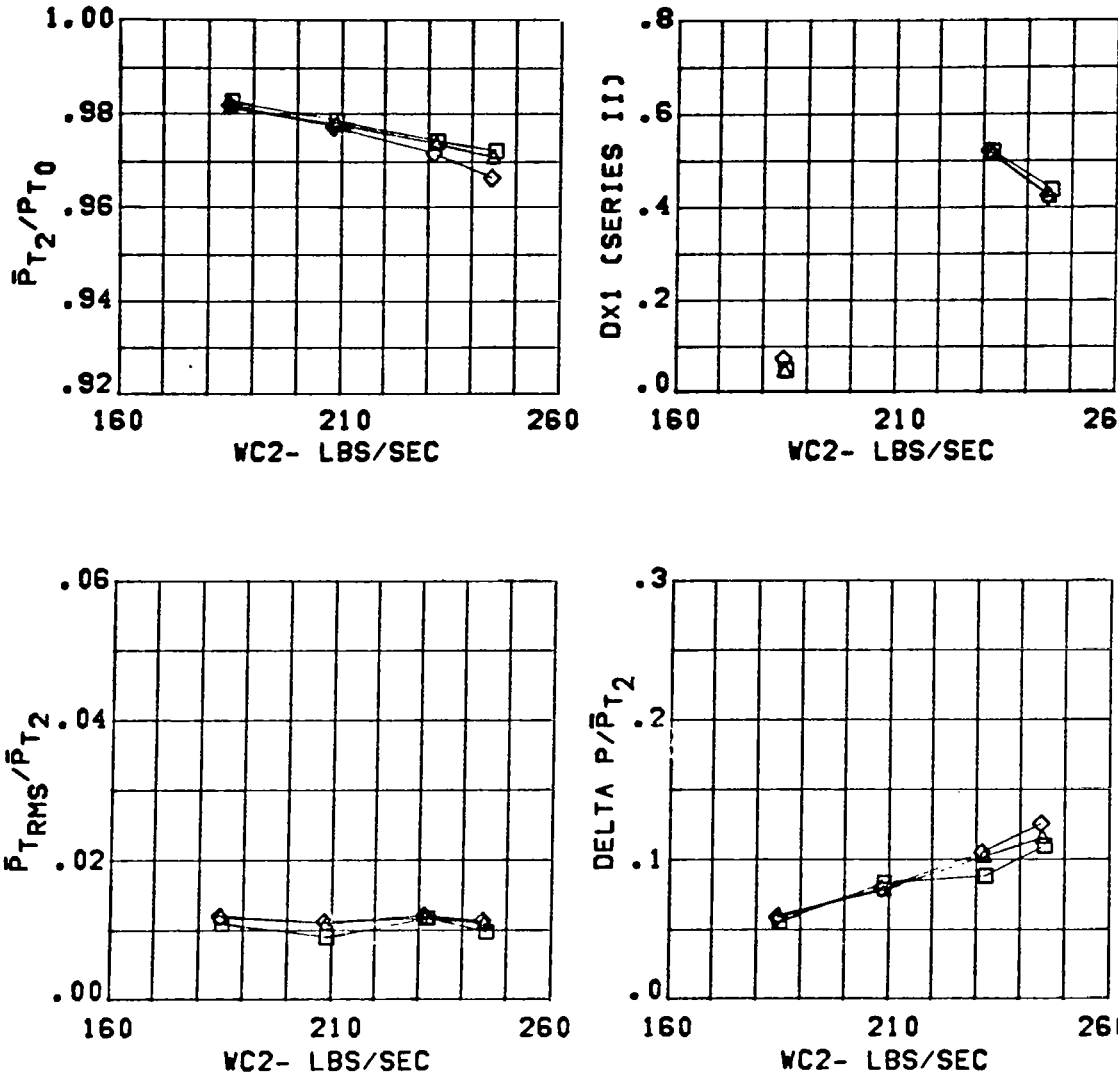

Figure 50 Inlet Performance for Configuration C13

CONFIGURATION	CONDITION	SYM.	BETA (DEG)
C13	MACH = 1.21	□	0.
3.65 IN. DIV. HT.	ALPHA= 15.	△	-5.
THROAT RAKES OUT		◇	-10.

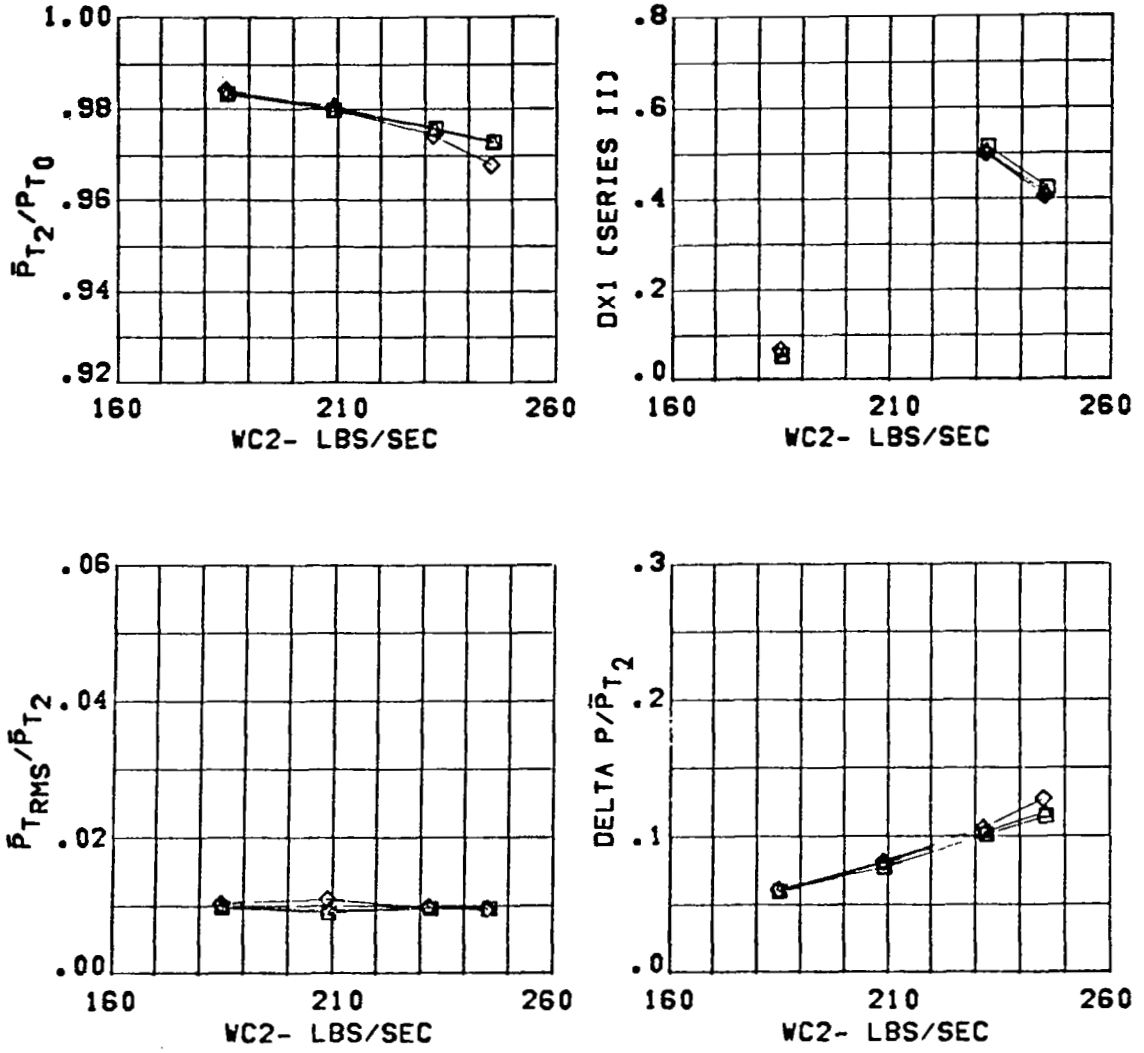

Figure 51 Inlet Performance for Configuration C13

CONFIGURATION	CONDITION	SYM.	BETA (DEG)
C13	MACH = 1.21	□	0.
3.65 IN. DIV. HT.	ALPHA= 30.	△	-5.
THROAT RAKES OUT		◇	-10.

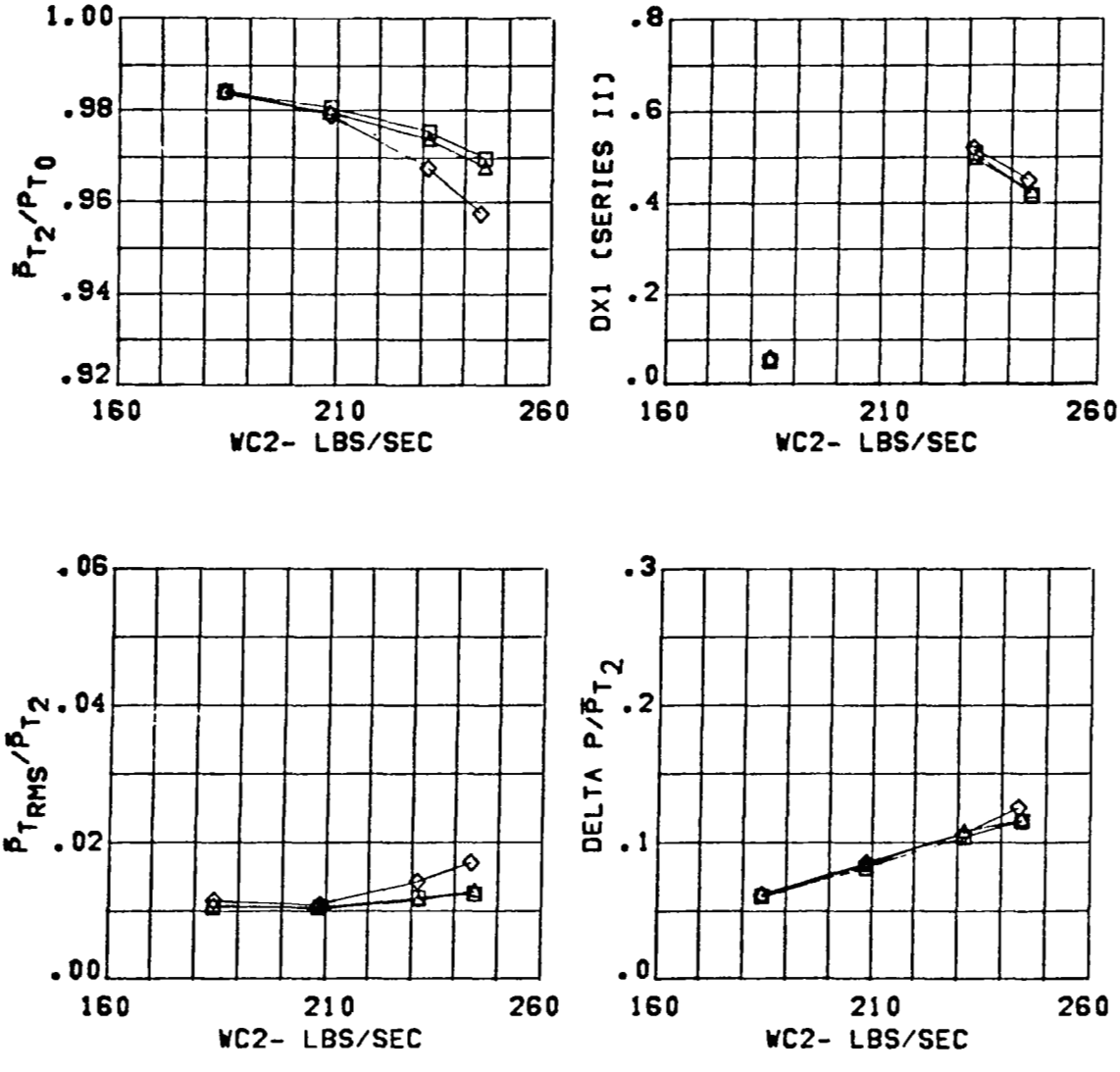

Figure 52 Inlet Performance for Configuration C13

CONFIGURATION	CONDITION	SYM.	BETA (DEG)
C13	MACH = 1.36	□	0.
3.65 IN. DIV. HT.	ALPHA= -5.	△	-5.
THROAT RAKES OUT		◇	-10.

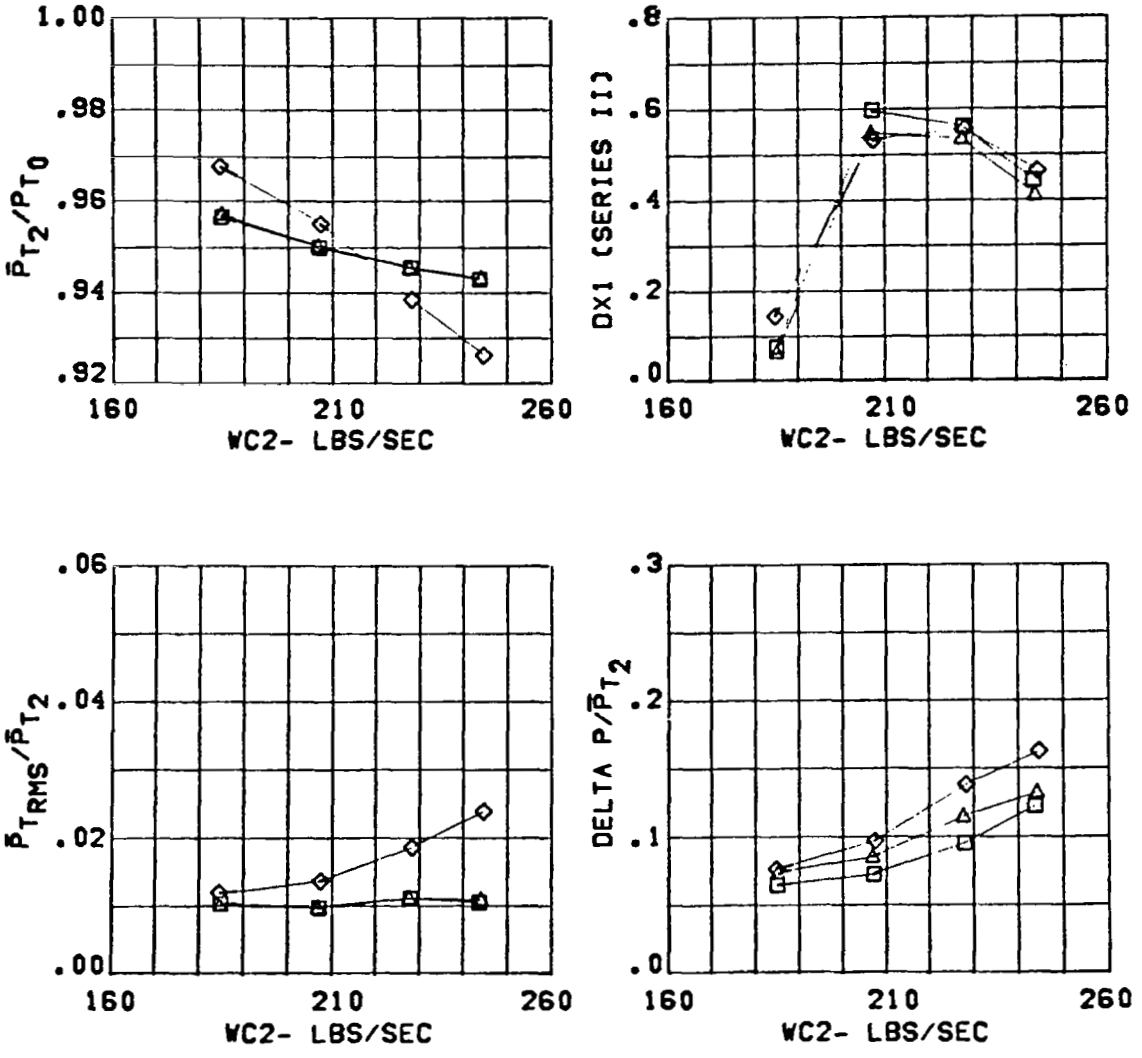

Figure 53 Inlet Performance for Configuration C13

CONFIGURATION	CONDITION	SYM.	BETA (DEG)
C13	MACH = 1.39	□	0.
3.65 IN. DIV. HT.	ALPHA= 1.	△	-5.
THROAT RAKES OUT		◇	-10.

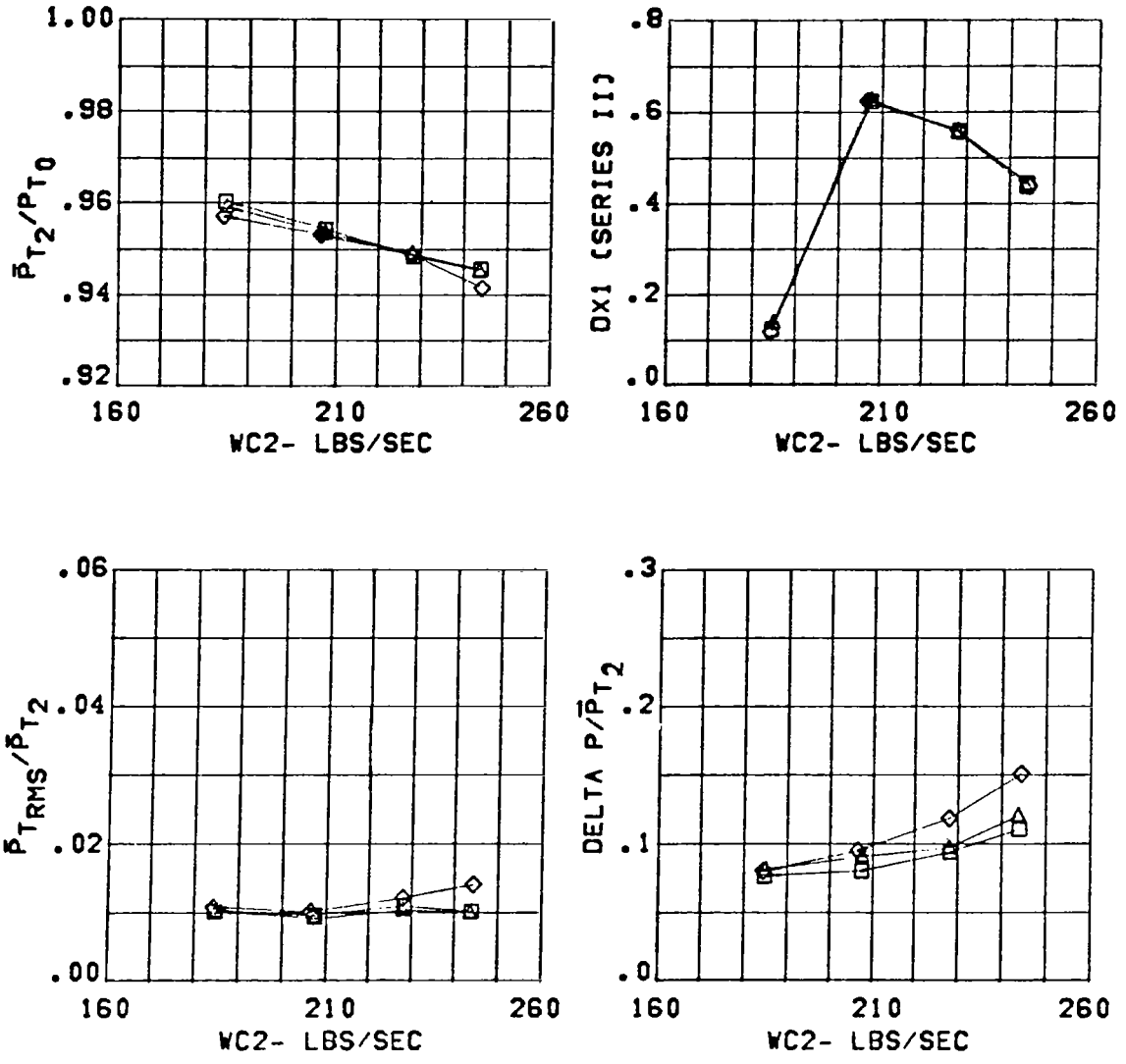

Figure 54 Inlet Performance for Configuration C13

CONFIGURATION	CONDITION	SYM.	BETA (DEG)
C13	MACH = 1.39	□	0.
3.65 IN. DIV. HT.	ALPHA= 6.	△	-5.
THROAT RAKES OUT		◇	-10.

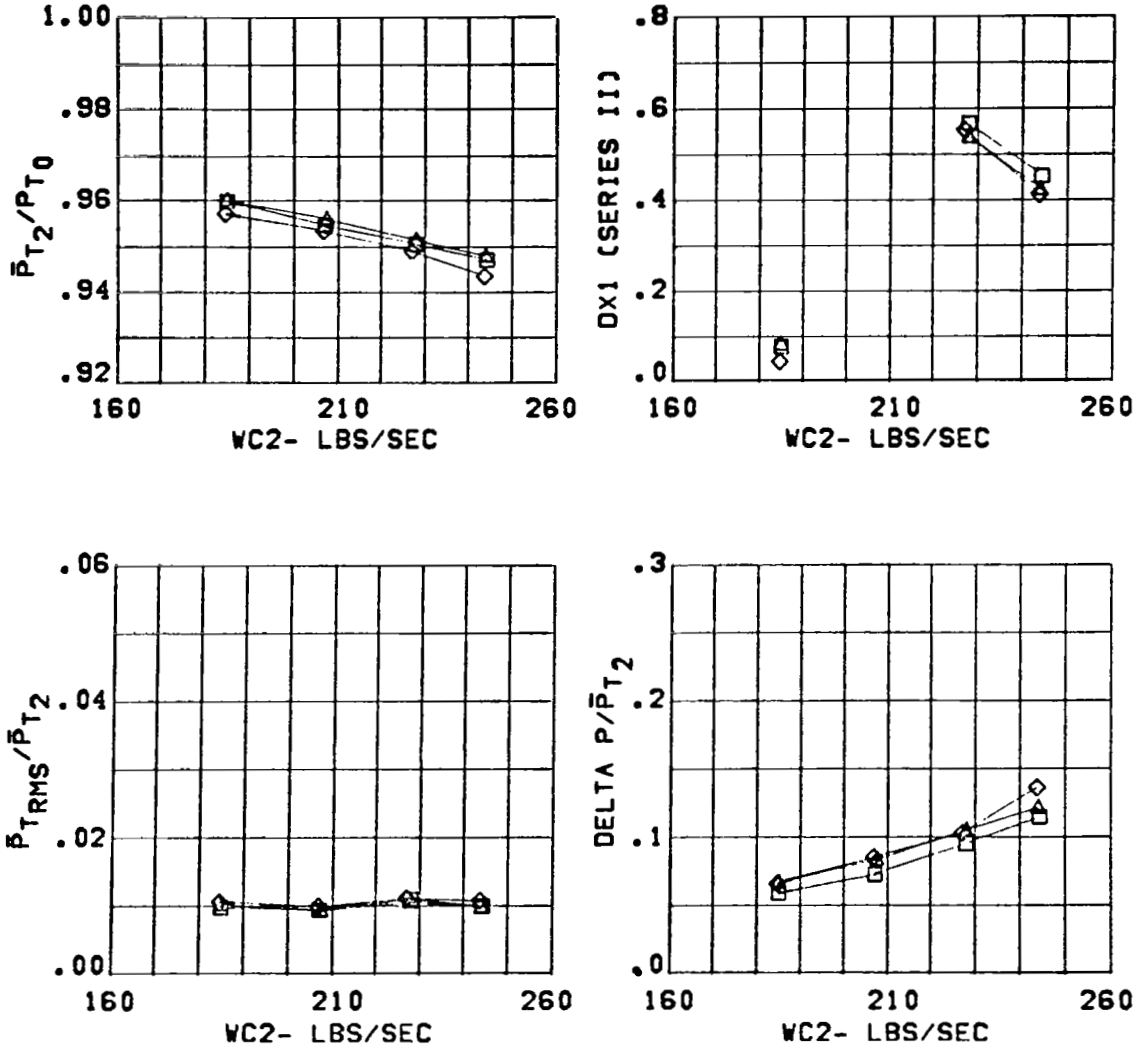

Figure 55 Inlet Performance for Configuration C13

CONFIGURATION	CONDITION	SYM.	BETA (DEG)
C13	MACH = 1.38	□	0.
3.65 IN. DIV. HT.	ALPHA= 15.	△	-5.
THROAT RAKES OUT		◇	-10.

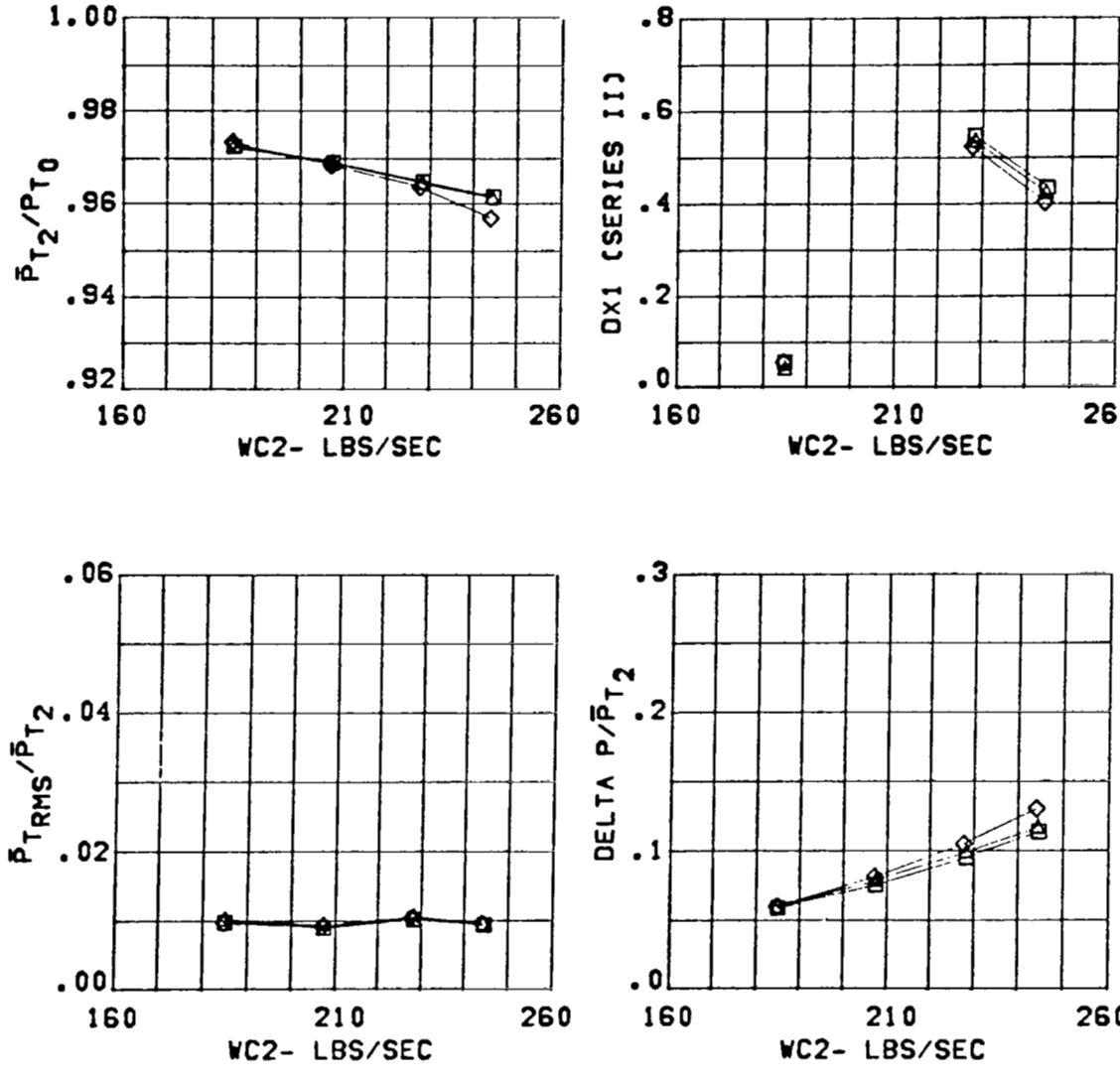

Figure 56 Inlet Performance for Configuration C13

CONFIGURATION	CONDITION	SYM.	BETA (DEG)
C13	MACH = 1.36	□	0.
3.65 IN. DIV. HT.	ALPHA= 25.	△	-5.
THROAT RAKES OUT		◇	-10.

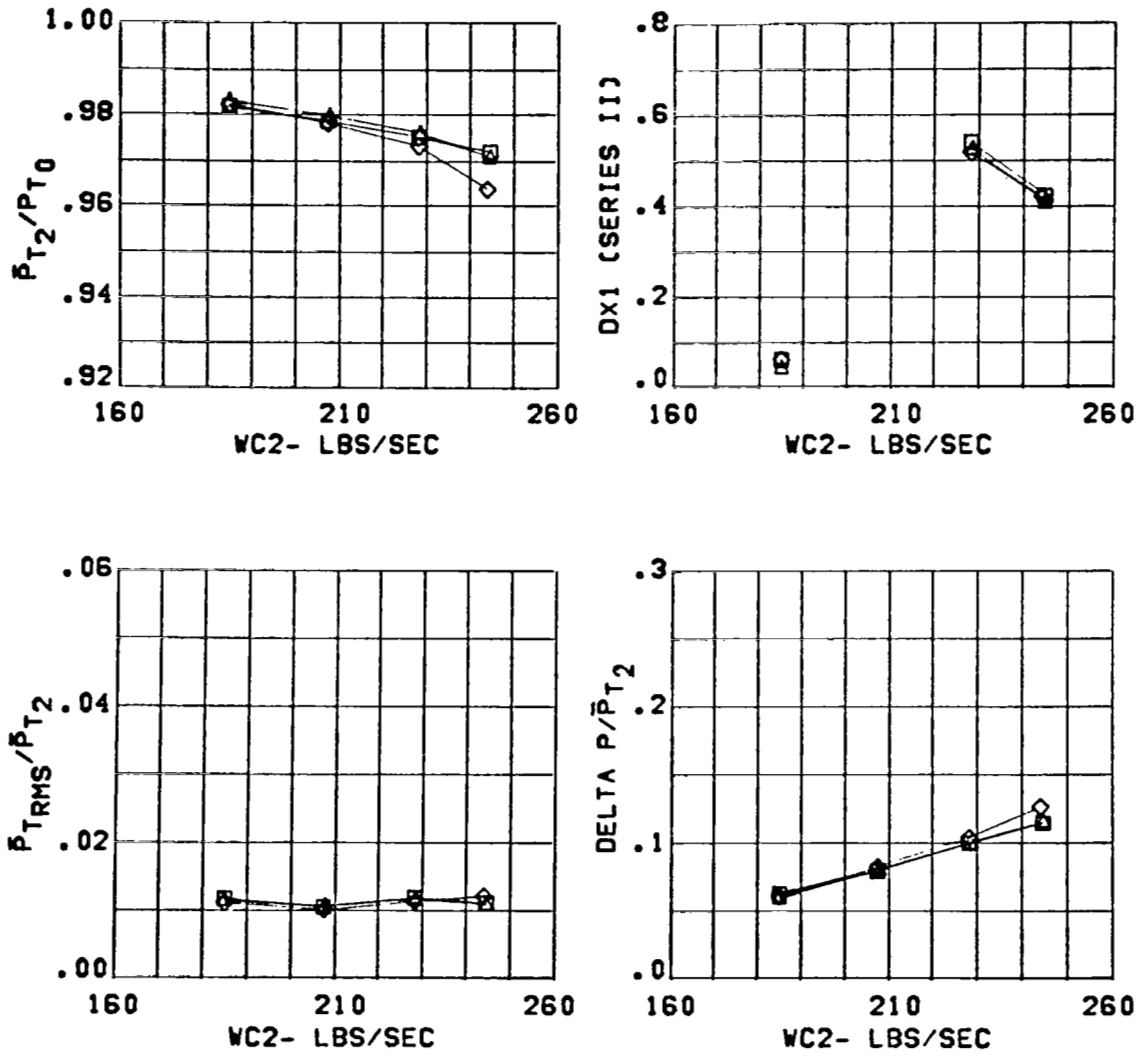

Figure 57 Inlet Performance for Configuration C13

CONFIGURATION	CONDITION	SYM.	BETA (DEG)
C13	MACH = 1.58	□	0.
3.65 IN. DIV. HT.	ALPHA= -5.	△	-5.
THROAT RAKES OUT		◇	-10.

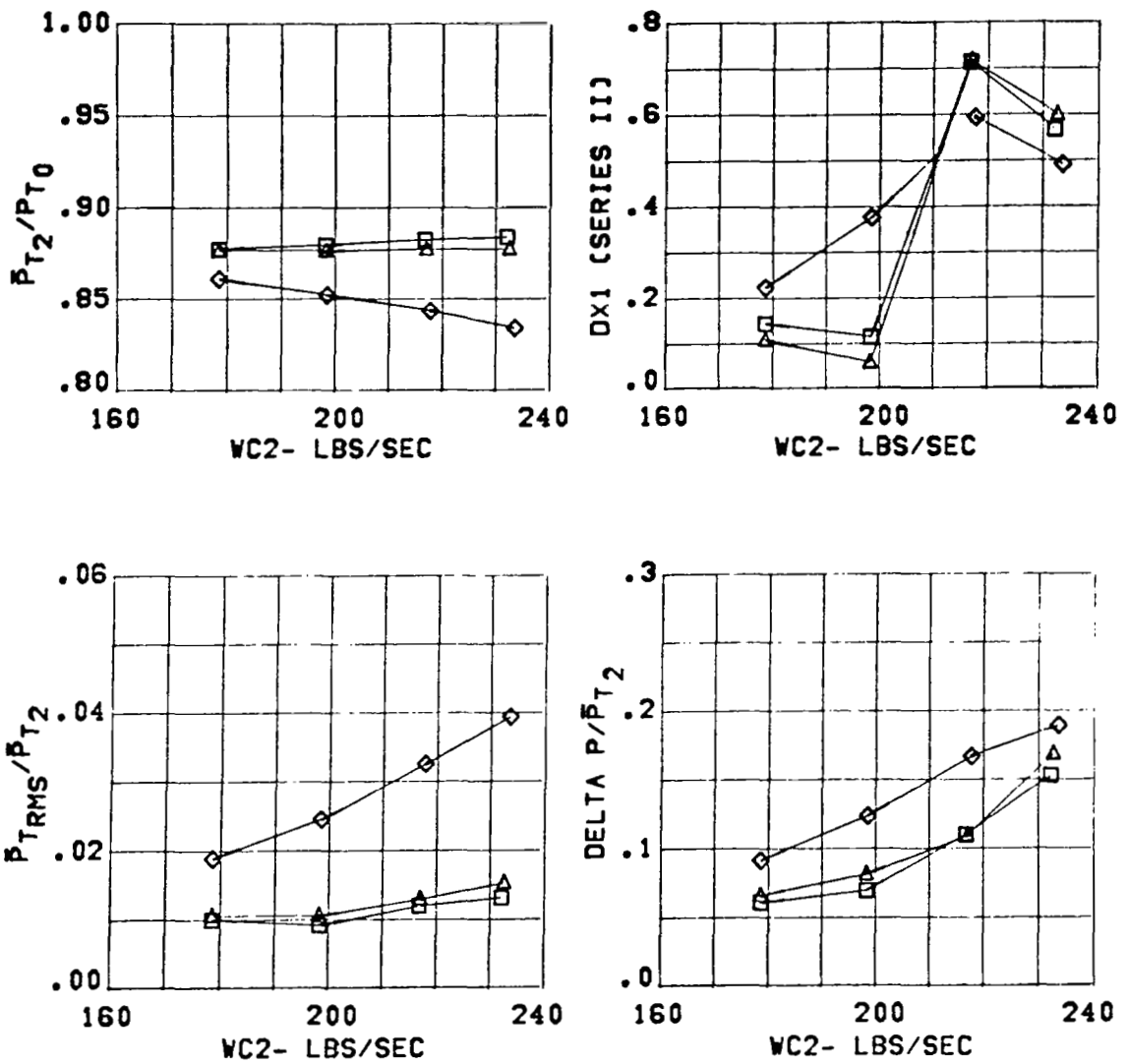

Figure 58 Inlet Performance for Configuration C13

CONFIGURATION	CONDITION	SYM.	BETA (DEG)
C13	MACH = 1.58	□	0.
3.65 IN. DIV. HT.	ALPHA= 1.	△	-5.
THROAT RAKES OUT		◇	-10.

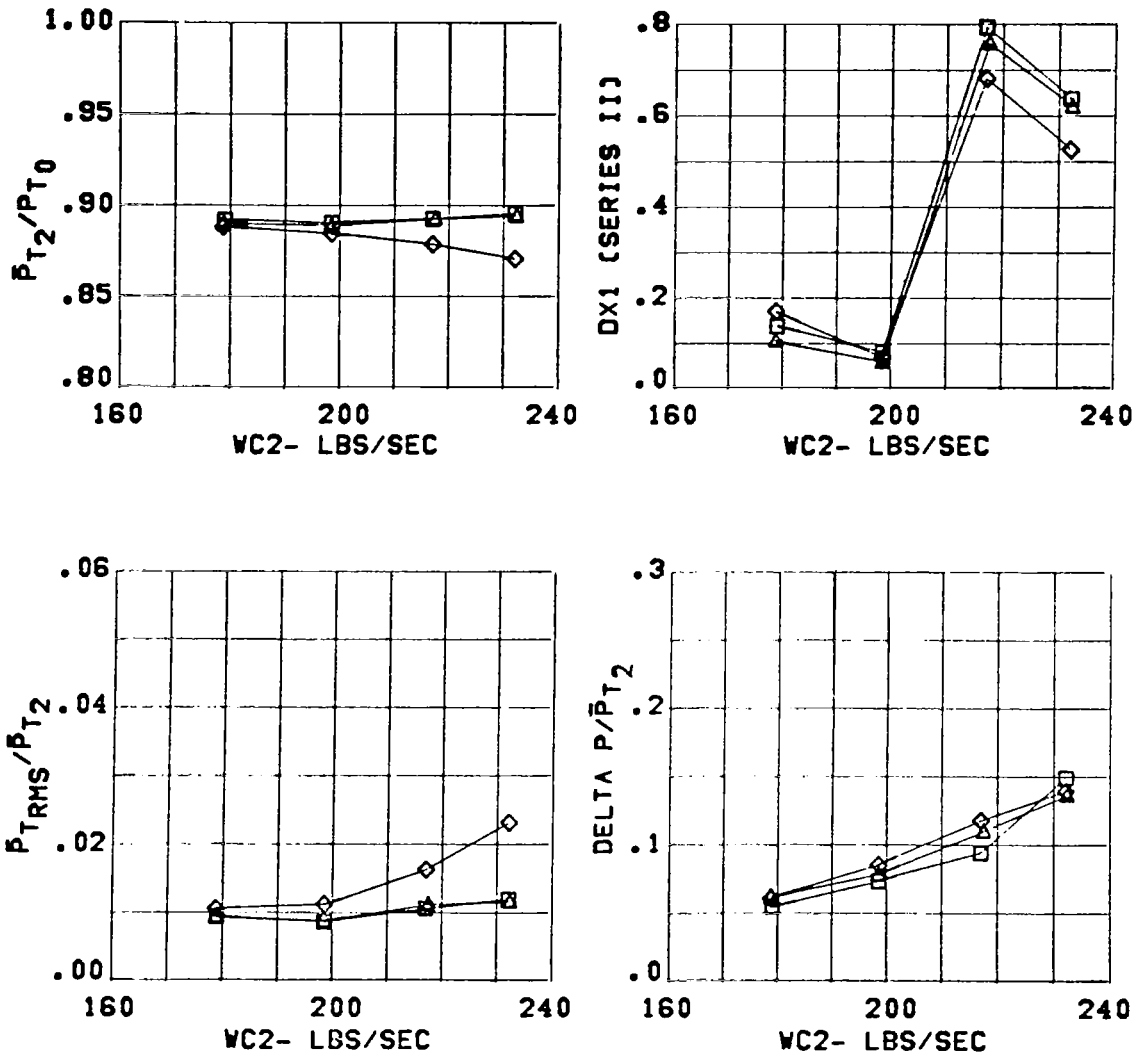

Figure 59 Inlet Performance for Configuration C13

CONFIGURATION	CONDITION	SYM.	BETA (DEG)
C13	MACH = 1.58	□	0.
3.65 IN. DIV. HT.	ALPHA= 6.	△	-5.
THROAT RAKES OUT		◇	-10.

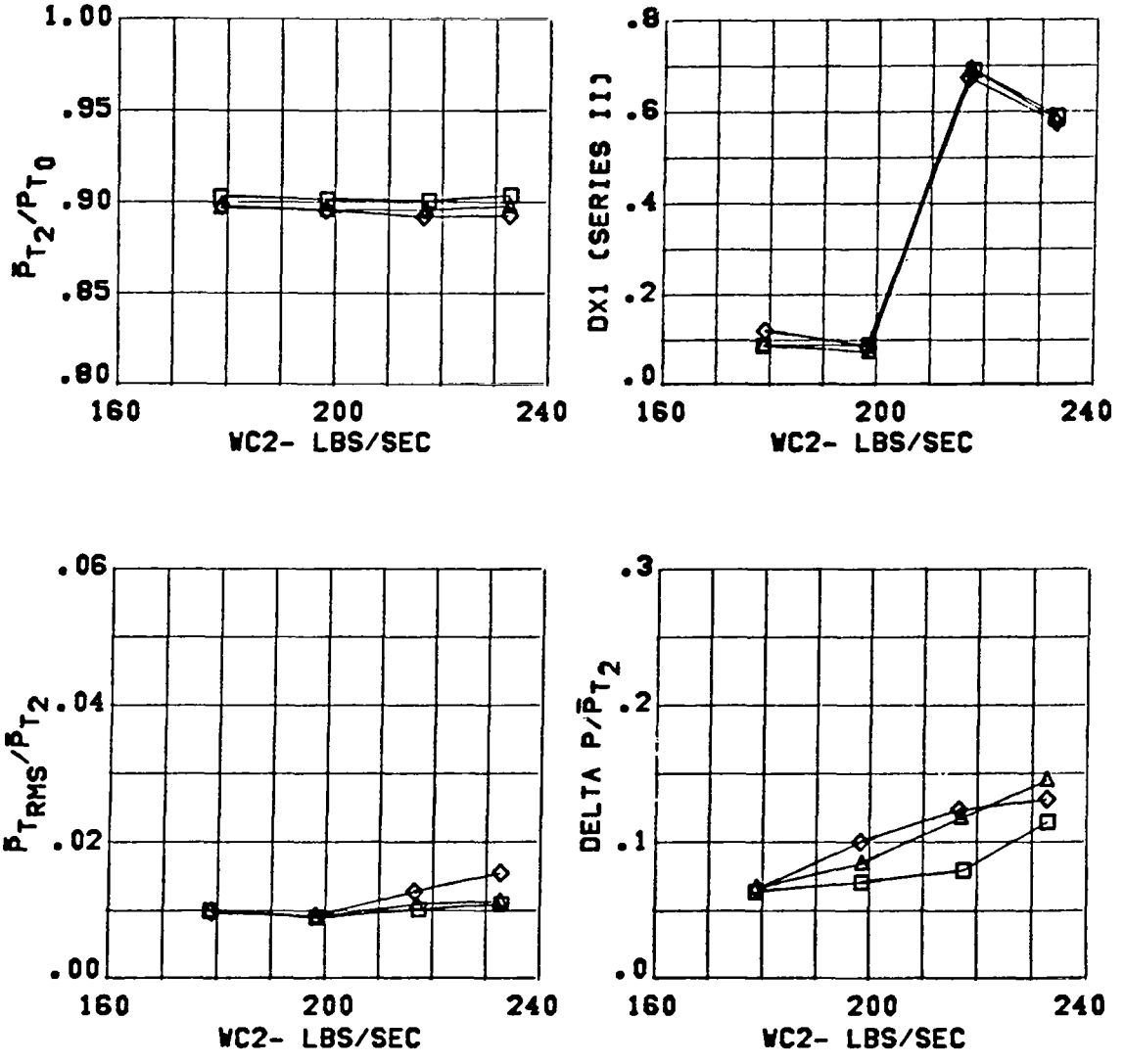

Figure 60 Inlet Performance for Configuration C13

CONFIGURATION	CONDITION	SYM.	BETA (DEG)
C13	MACH = 1.58	□	0.
3.65 IN. DIV. HT.	ALPHA= 20.	△	-5.
THROAT RAKES OUT		◇	-10.

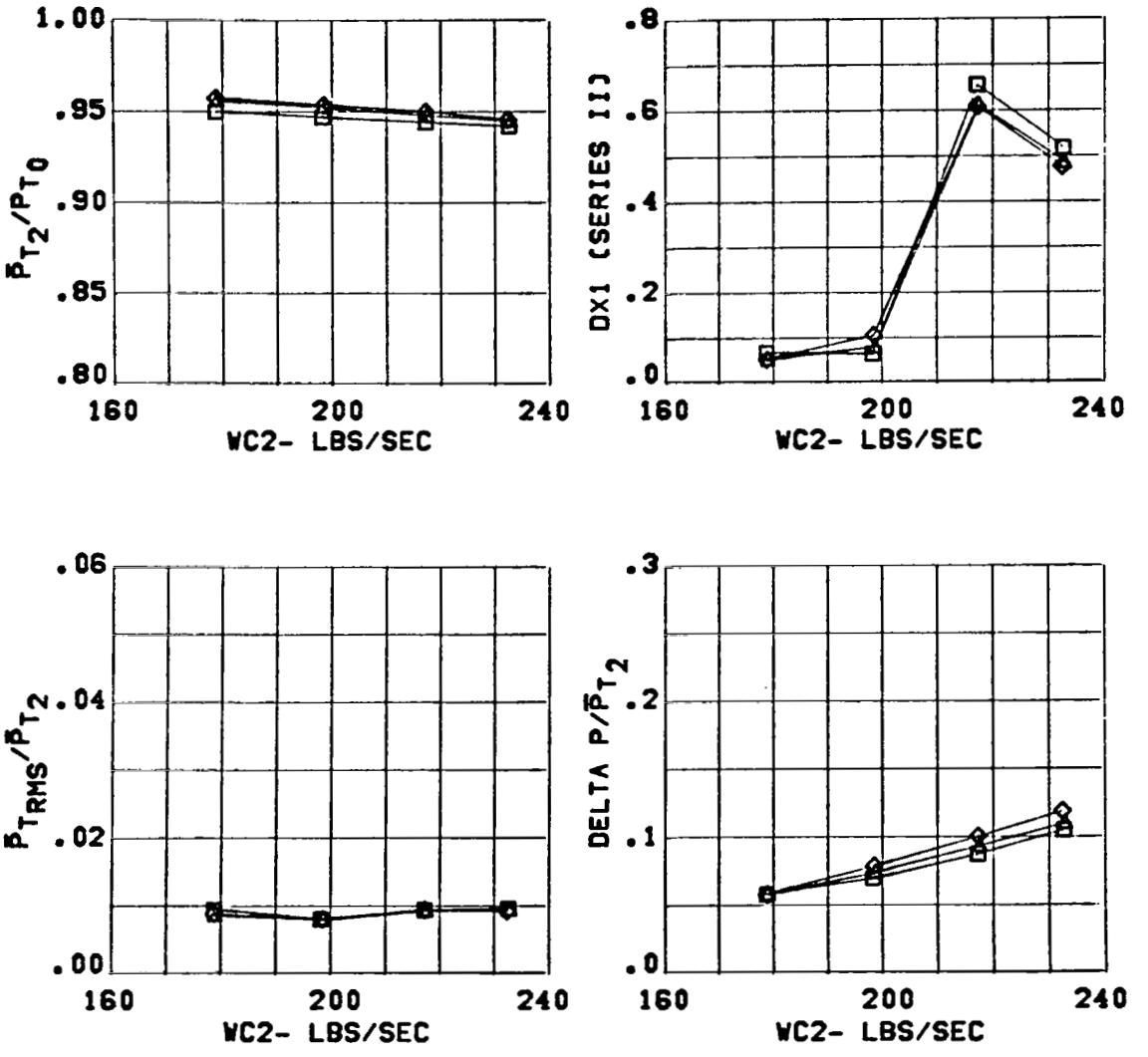

Figure 61 Inlet Performance for Configuration C13

CONFIGURATION	CONDITION	SYM.	BETA (DEG)
C13	MACH = 1.78	□	0.
3.65 IN. DIV. HT.	ALPHA= -5.	△	-5.
THROAT RAKES OUT		◇	-10.

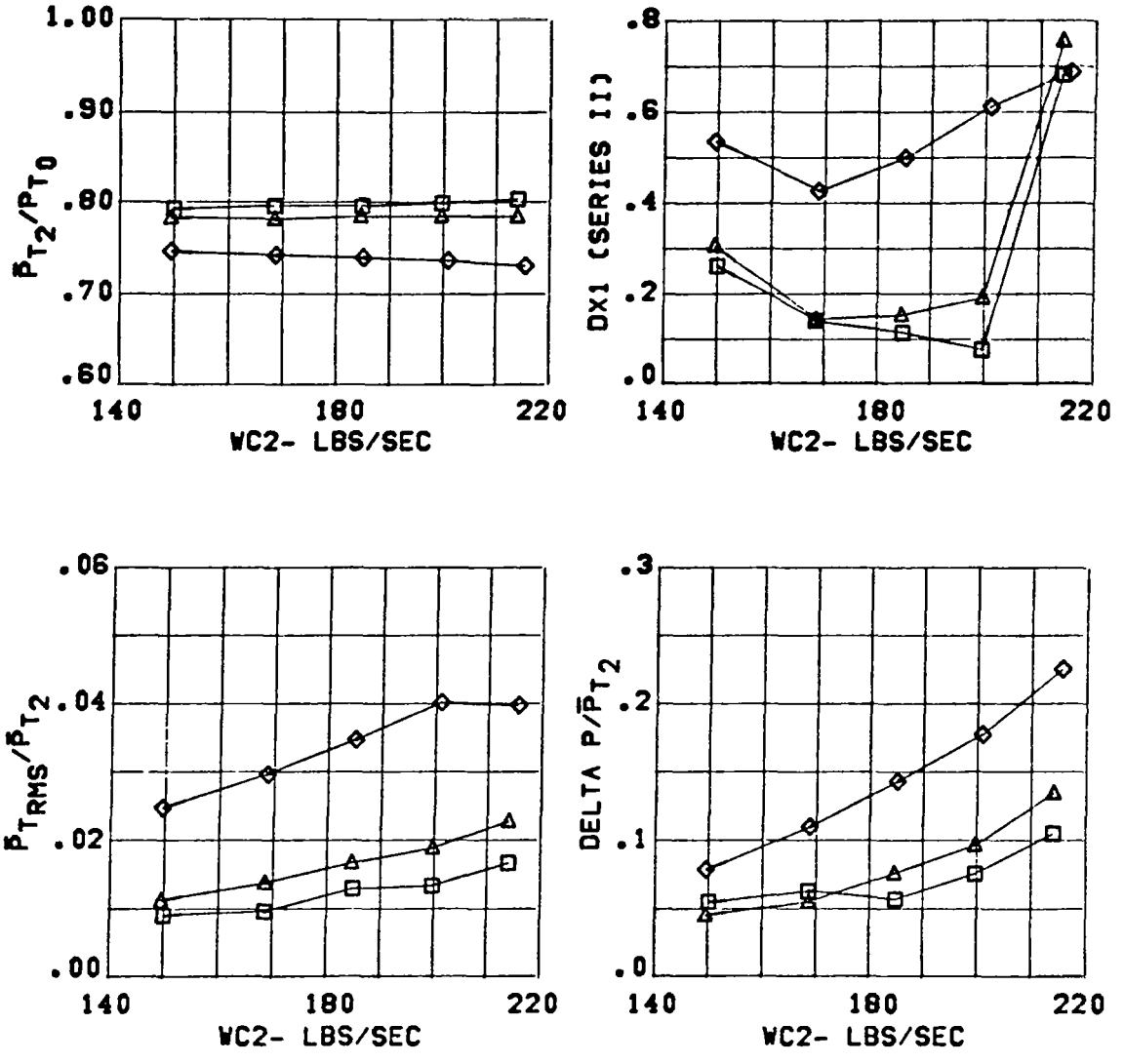

Figure 62 Inlet Performance for Configuration C13

CONFIGURATION	CONDITION	SYM.	BETA (DEG)
C13	MACH = 1.78	□	0.
3.65 IN. DIV. HT.	ALPHA= 1.	△	-5.
THROAT RAKES OUT		◇	-10.

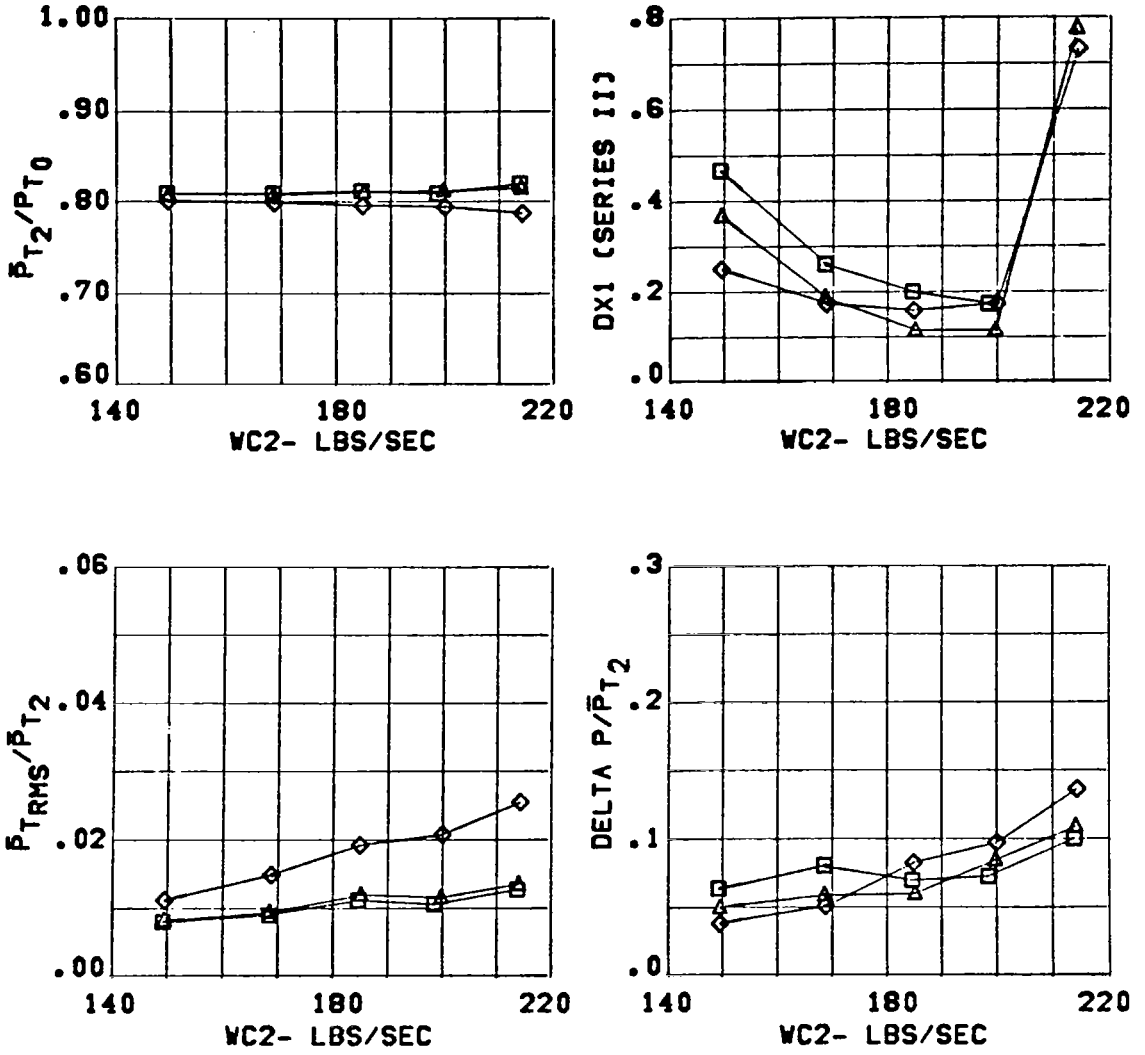

Figure 63 Inlet Performance for Configuration C13

CONFIGURATION	CONDITION	SYM.	BETA (DEG)
C13	MACH = 1.78	□	0.
3.65 IN. DIV. HT.	ALPHA= 6.	△	-5.
THROAT RAKES OUT		◇	-10.

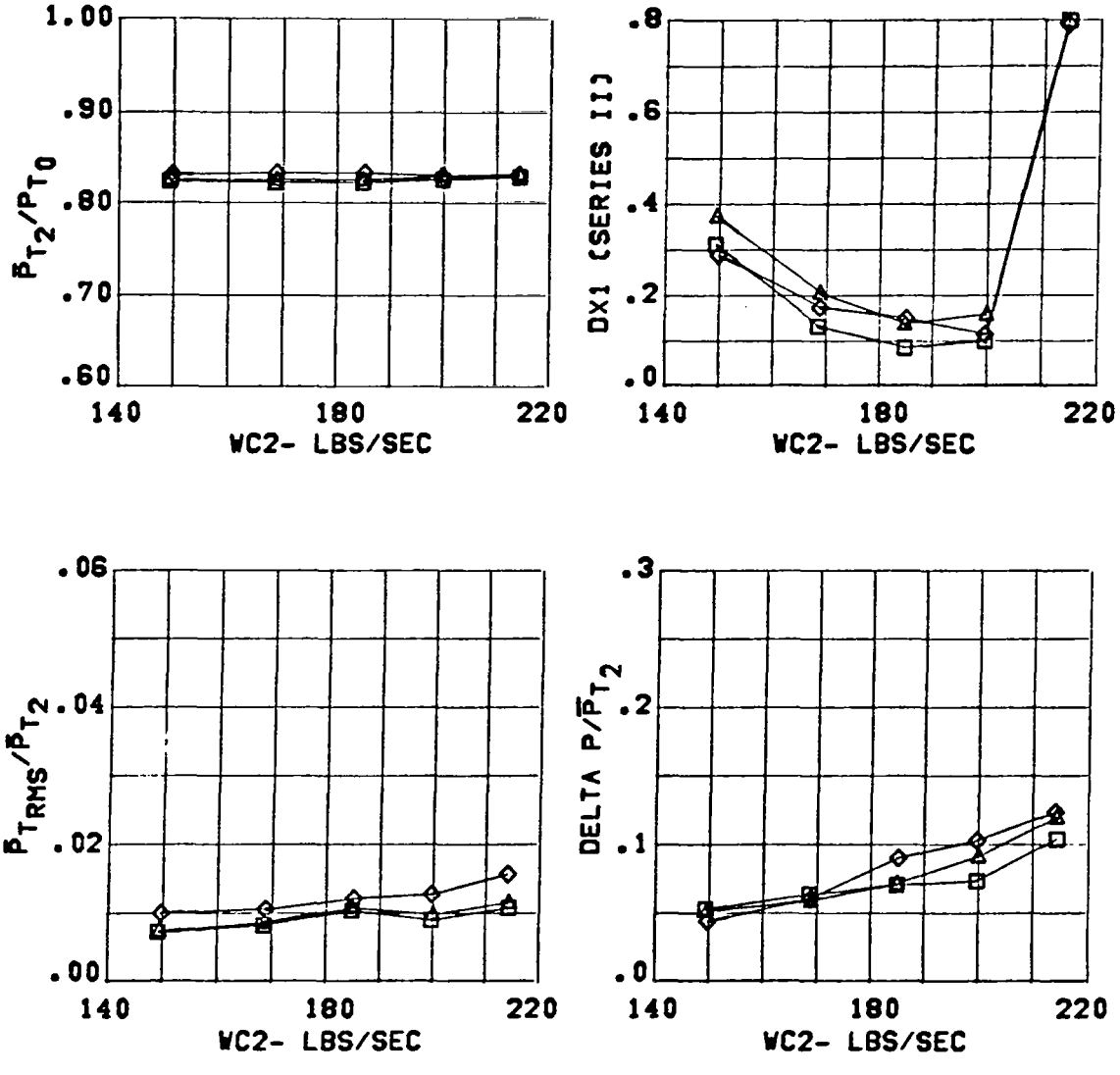

Figure 64 Inlet Performance for Configuration C13

CONFIGURATION	CONDITION	SYM.	BETA (DEG)
C13	MACH = 1.78	□	0.
3.65 IN. DIV. HT.	ALPHA= 20.	△	-5.
THROAT RAKES OUT		◇	-10.

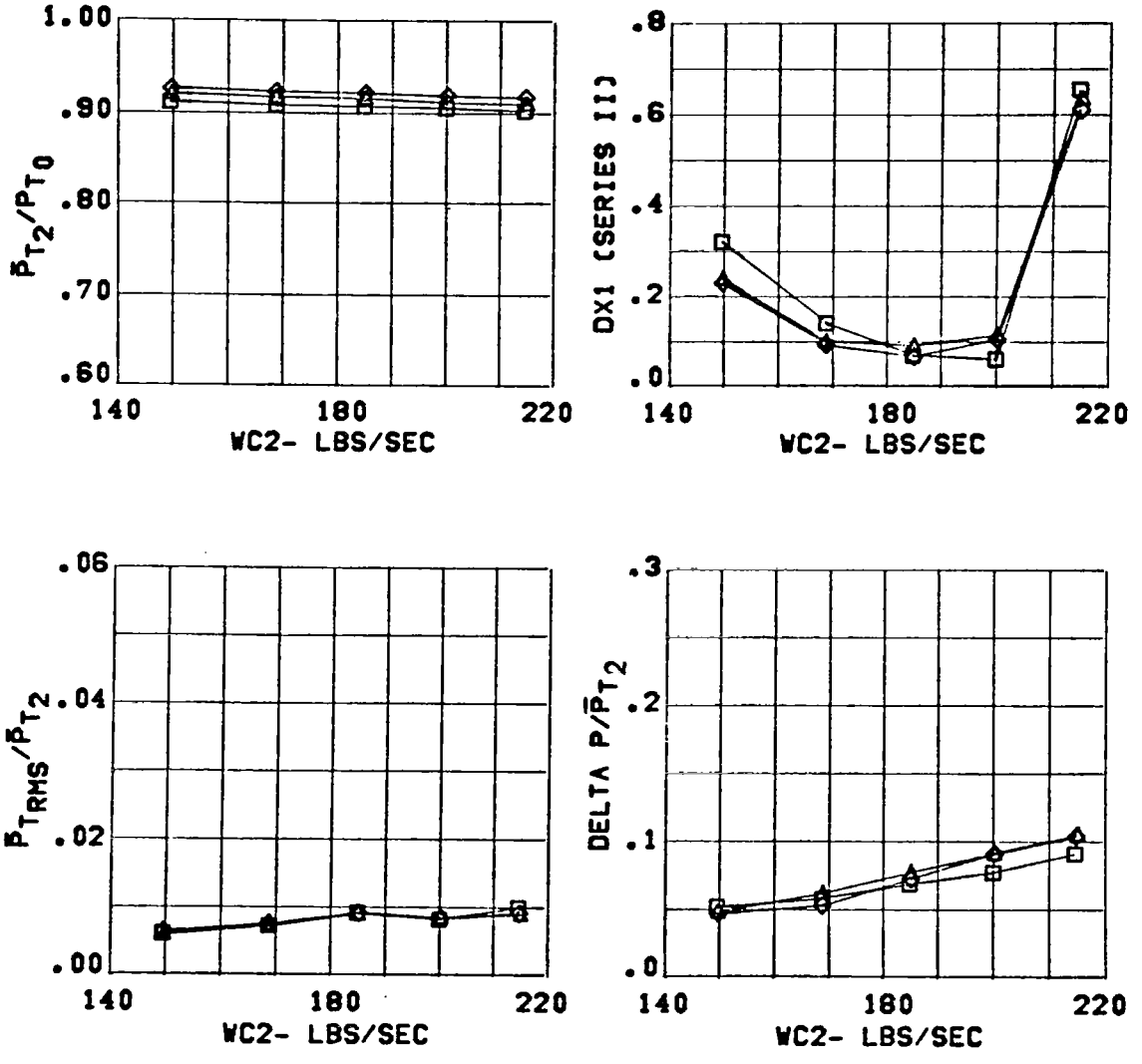

Figure 65 Inlet Performance for Configuration C13

CONFIGURATION	CONDITION	SYM.	BETA (DEG)
C13	MACH = 1.97	□	0.
3.65 IN. DIV. HT.	ALPHA= -5.	△	-5.
THROAT RAKES OUT		◇	-10.

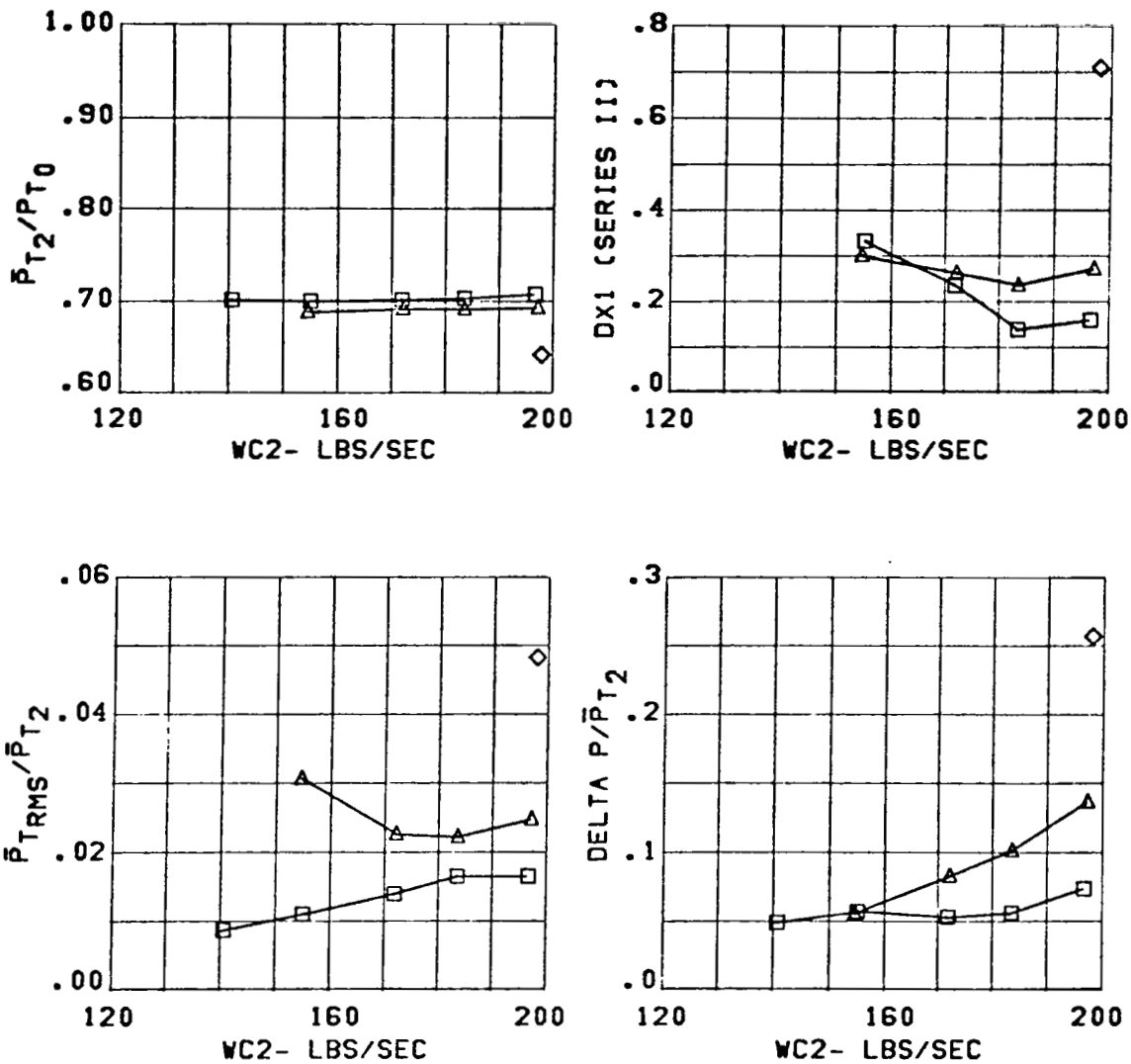

Figure 66 Inlet Performance for Configuration C13

CONFIGURATION	CONDITION	SYM.	BETA (DEG)
C13	MACH = 1.97	□	0.
3.65 IN. DIV. HT.	ALPHA= 1.	△	-5.
THROAT RAKES OUT		◇	-10.

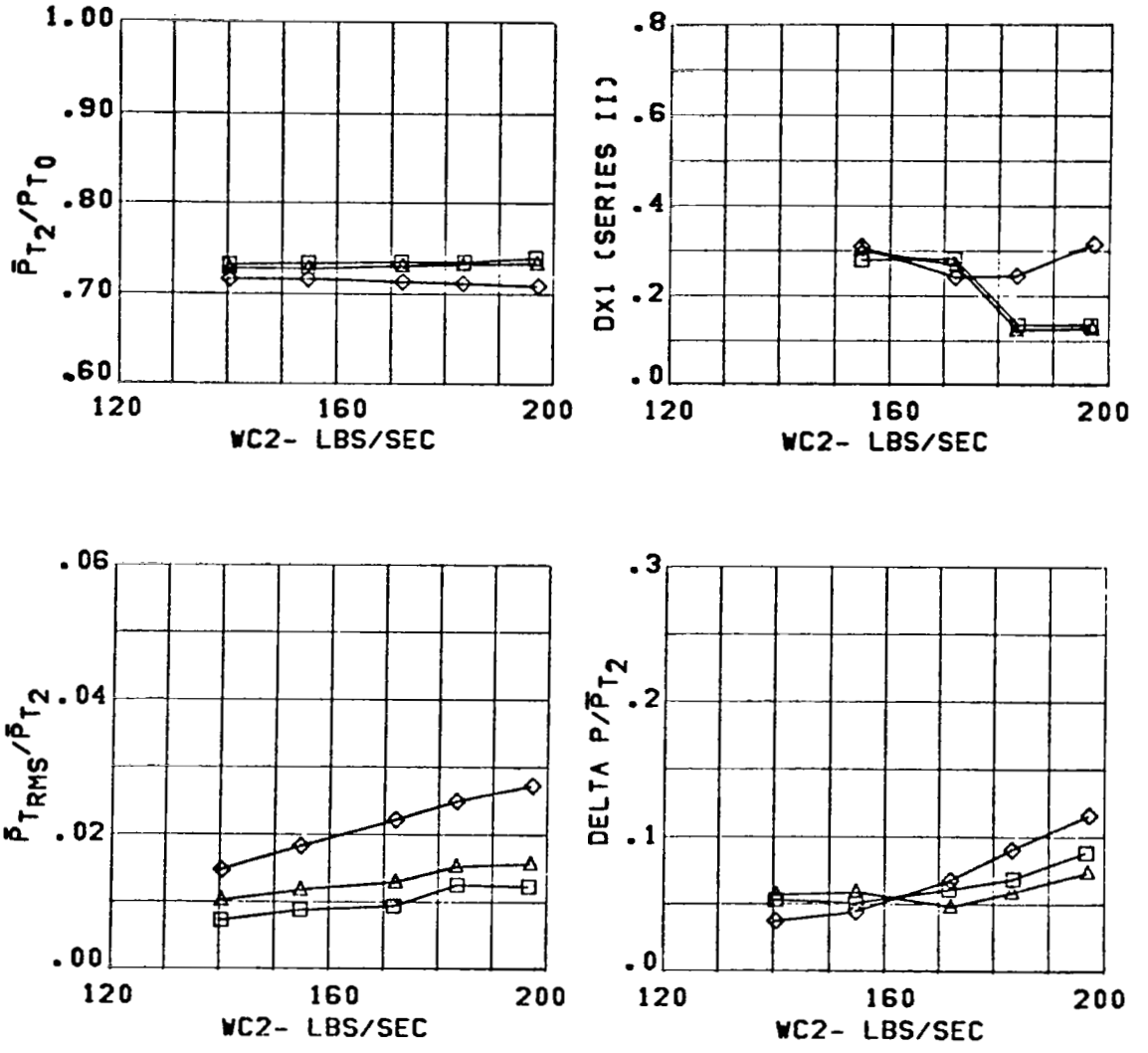

Figure 67 Inlet Performance for Configuration C13

CONFIGURATION	CONDITION	SYM.	BETA (DEG)
C13	MACH = 1.97	□	0.
3.65 IN. DIV. HT.	ALPHA= 6.	△	-5.
THROAT RAKES OUT		◇	-10.

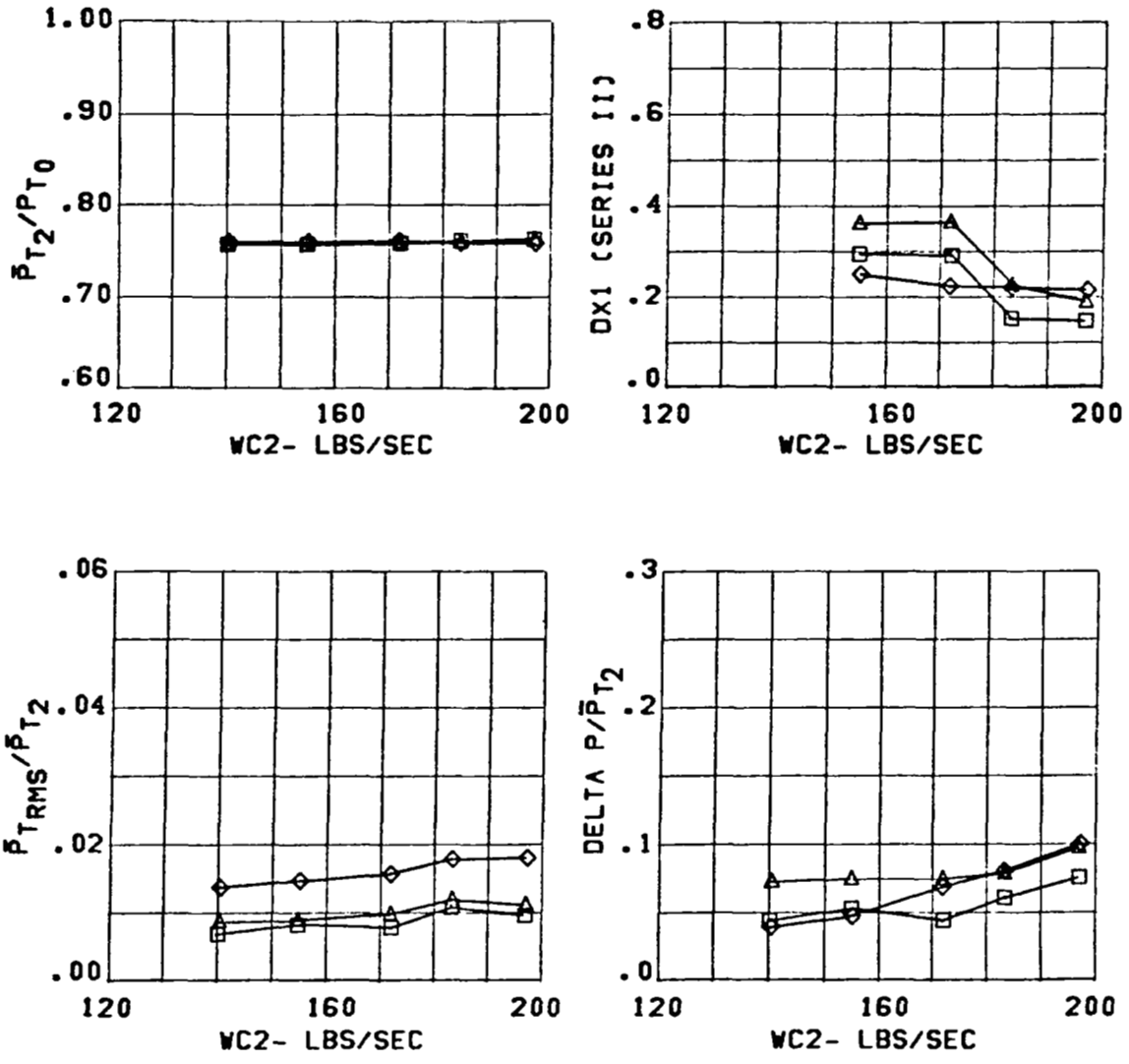

Figure 68 Inlet Performance for Configuration C13

CONFIGURATION	CONDITION	SYM.	BETA (DEG)
C13	MACH = 1.96	□	0.
3.65 IN. DIV. HT.	ALPHA= 20.	△	-5.
THROAT RAKES OUT		◇	-10.

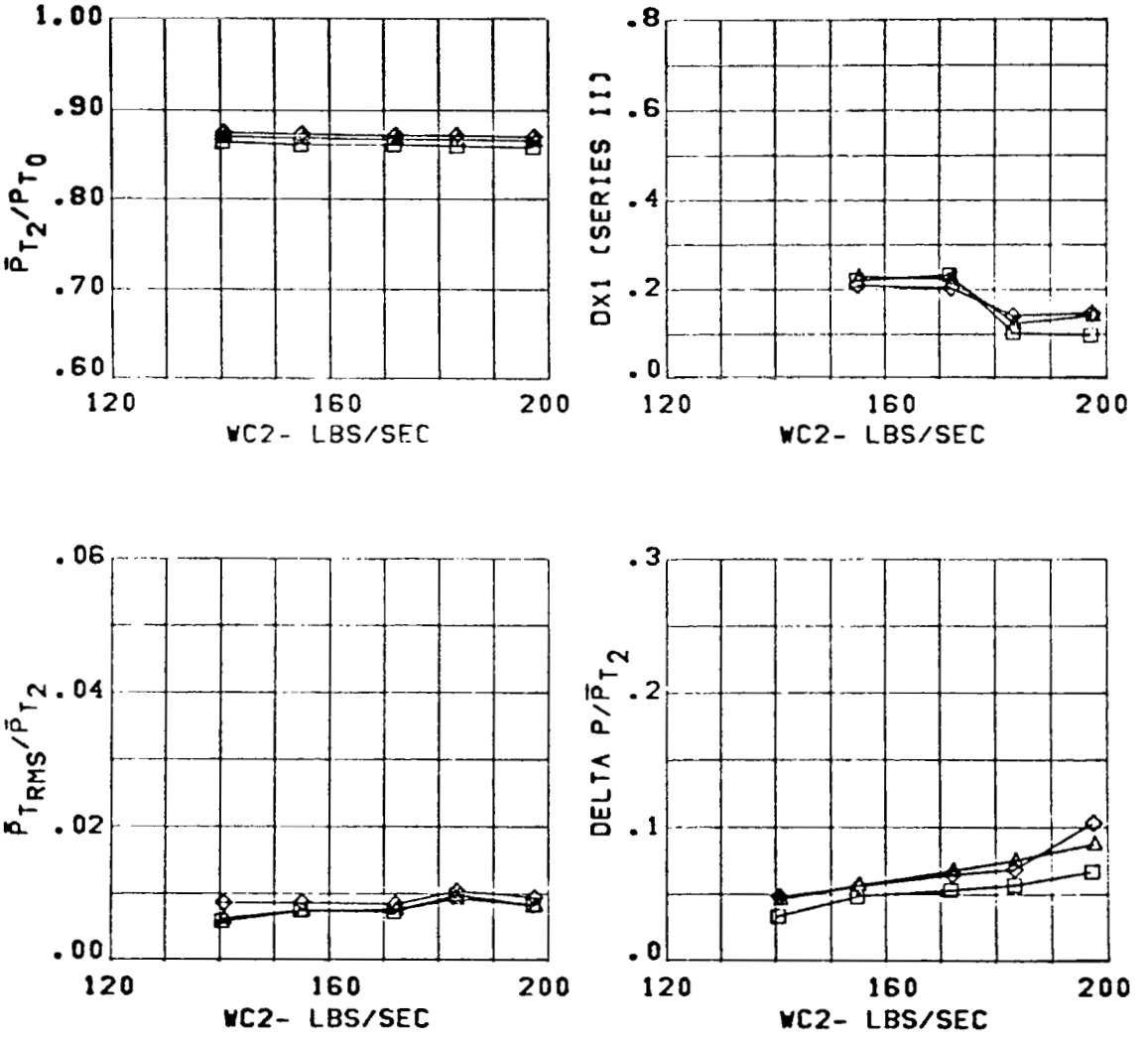

Figure 69 Inlet Performance for Configuration C13

CONFIGURATION	CONDITION	SYM	BETA	$\bar{PT2/PT0}$
C13	MACH = .91	□	0.	.978
3.65 IN. DIV.	ALPHA= -9.	△	-5.	.976
V.G.S OUT	WC2 = 233.	◇	-10.	.953

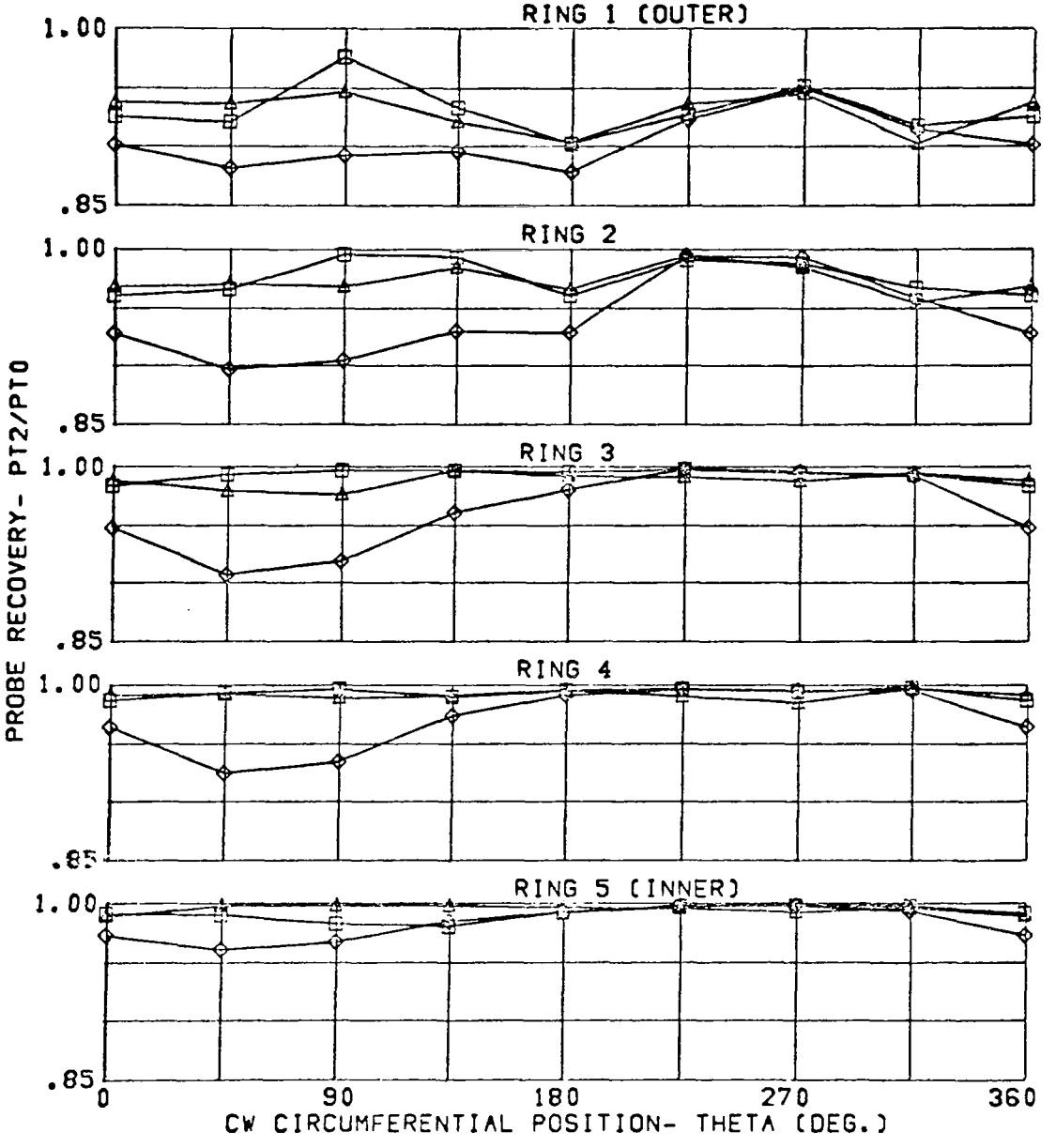

Figure 70 Circumferential Pressure Distribution at Engine Face for Inlet Configuration C13

CONFIGURATION	CONDITION	SYM	BETA	$\overline{PT2/PT0}$
C13	MACH = .91	□	0.	.979
3.65 IN. DIV.	ALPHA= 1.	△	-5.	.978
V.G.S OUT	WC2 = 233.	◇	-10.	.973

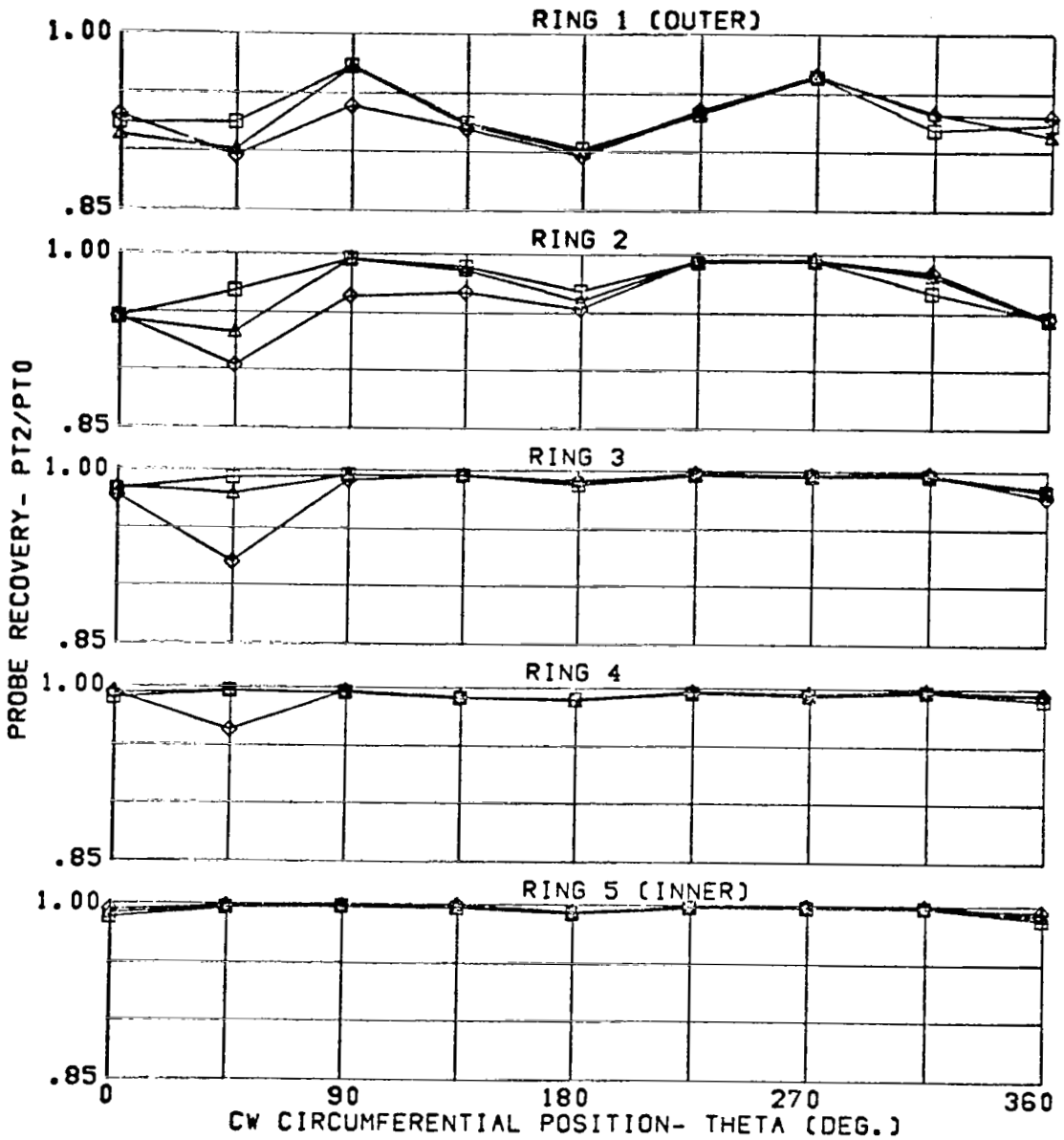

Figure 71 Circumferential Pressure Distribution at Engine Face for Inlet Configuration C13

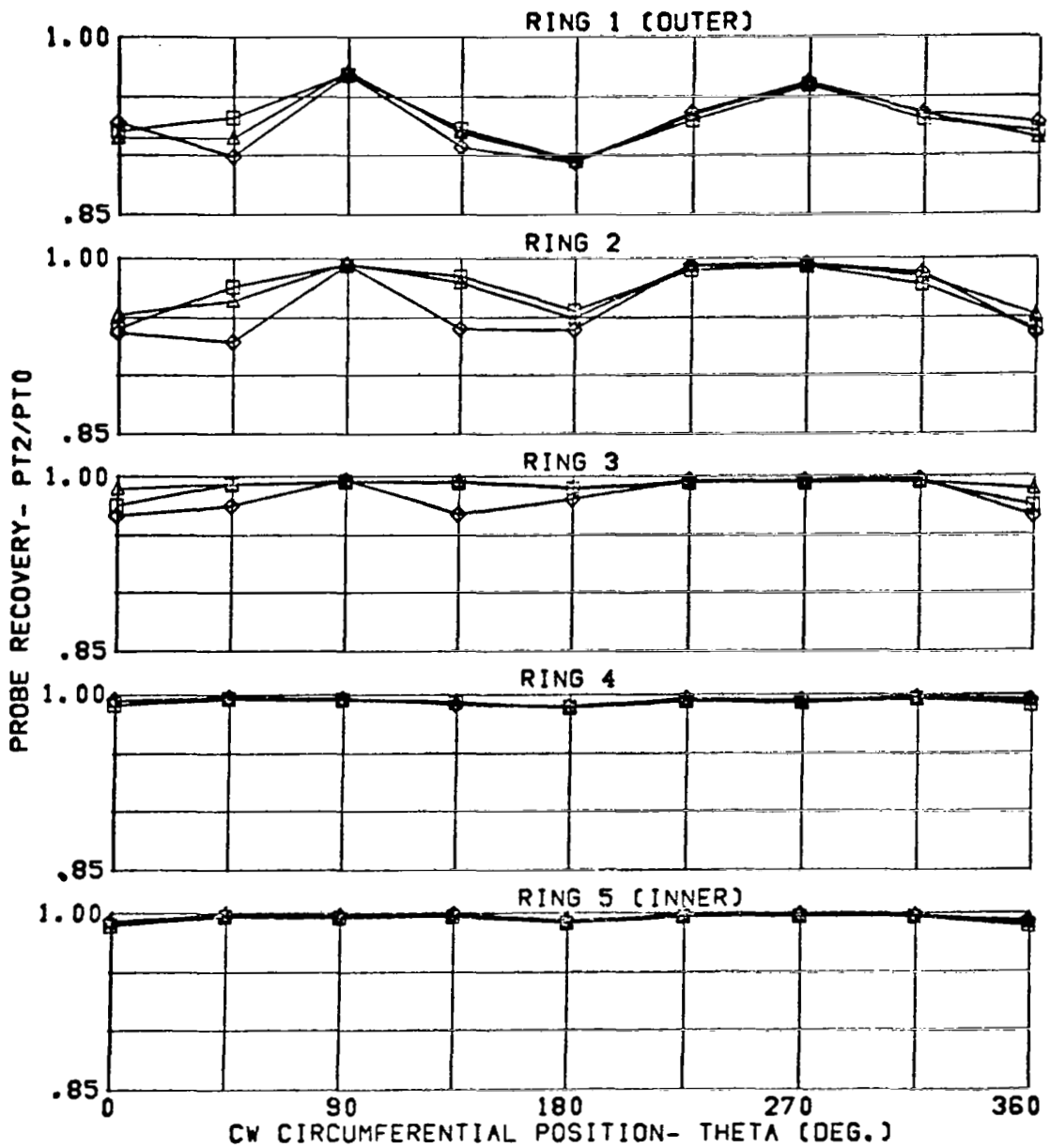

Figure 72 Circumferential Pressure Distribution at Engine Face for Inlet Configuration C13

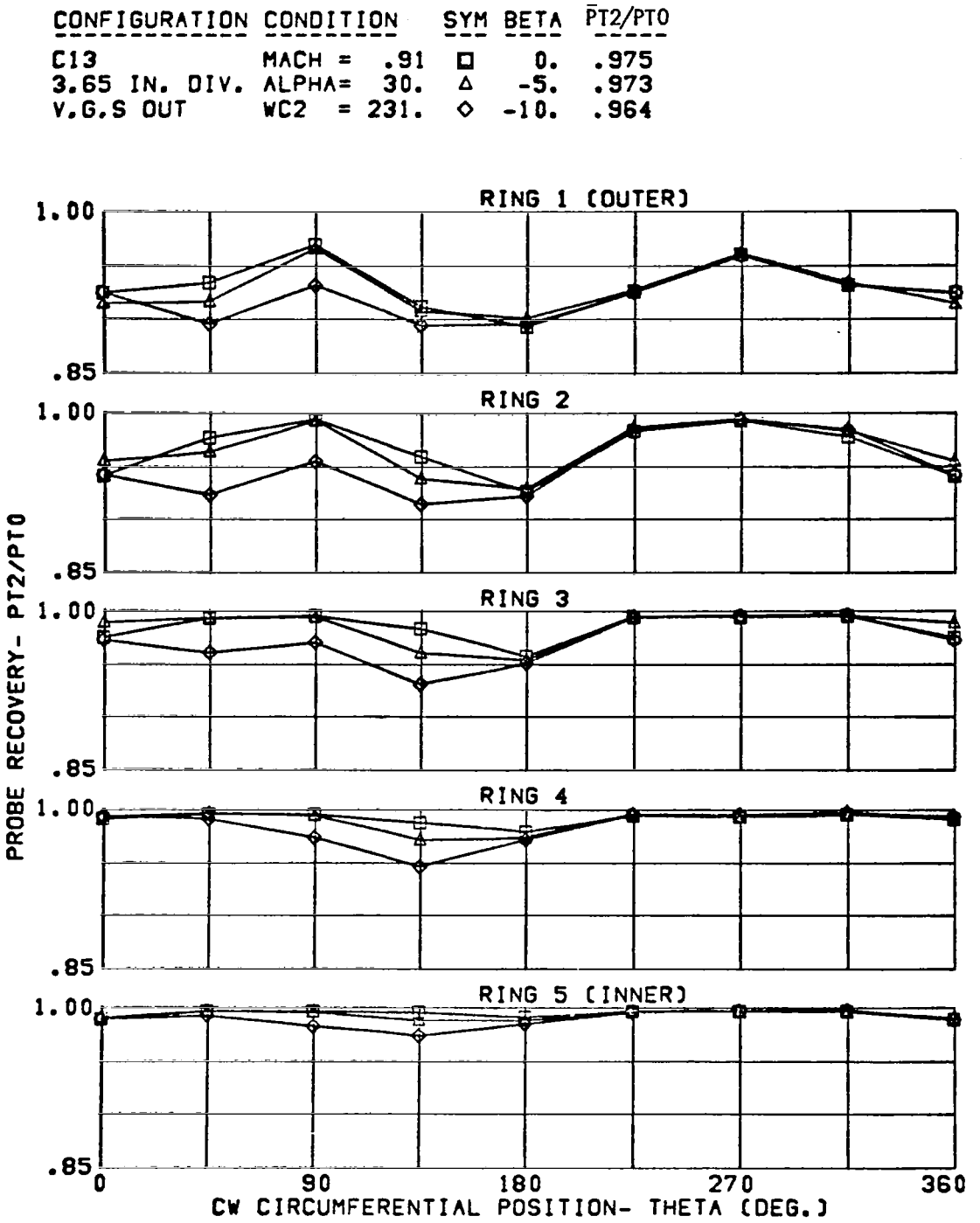

Figure 73 Circumferential Pressure Distribution at Engine Face for Inlet Configuration C13

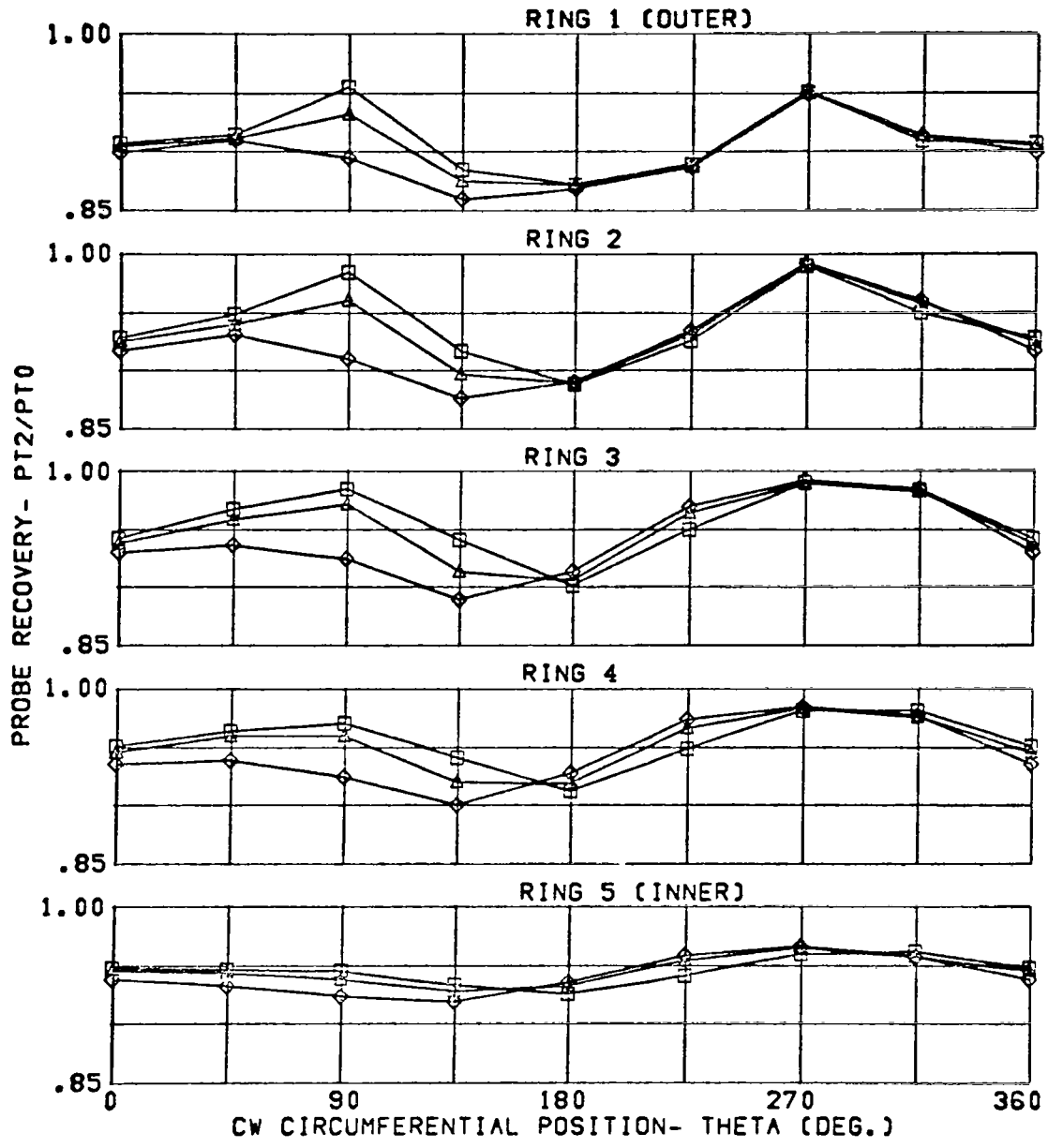

Figure 74 Circumferential Pressure Distribution at Engine Face for Inlet Configuration C13

CONFIGURATION	CONDITION	SYM	BETA	$\bar{PT2/PT0}$
C13	MACH = 1.58	□	0.	.882
3.65 IN. DIV.	ALPHA= -5.	△	-5.	.878
V.G.S OUT	WC2 = 218.	◇	-10.	.844

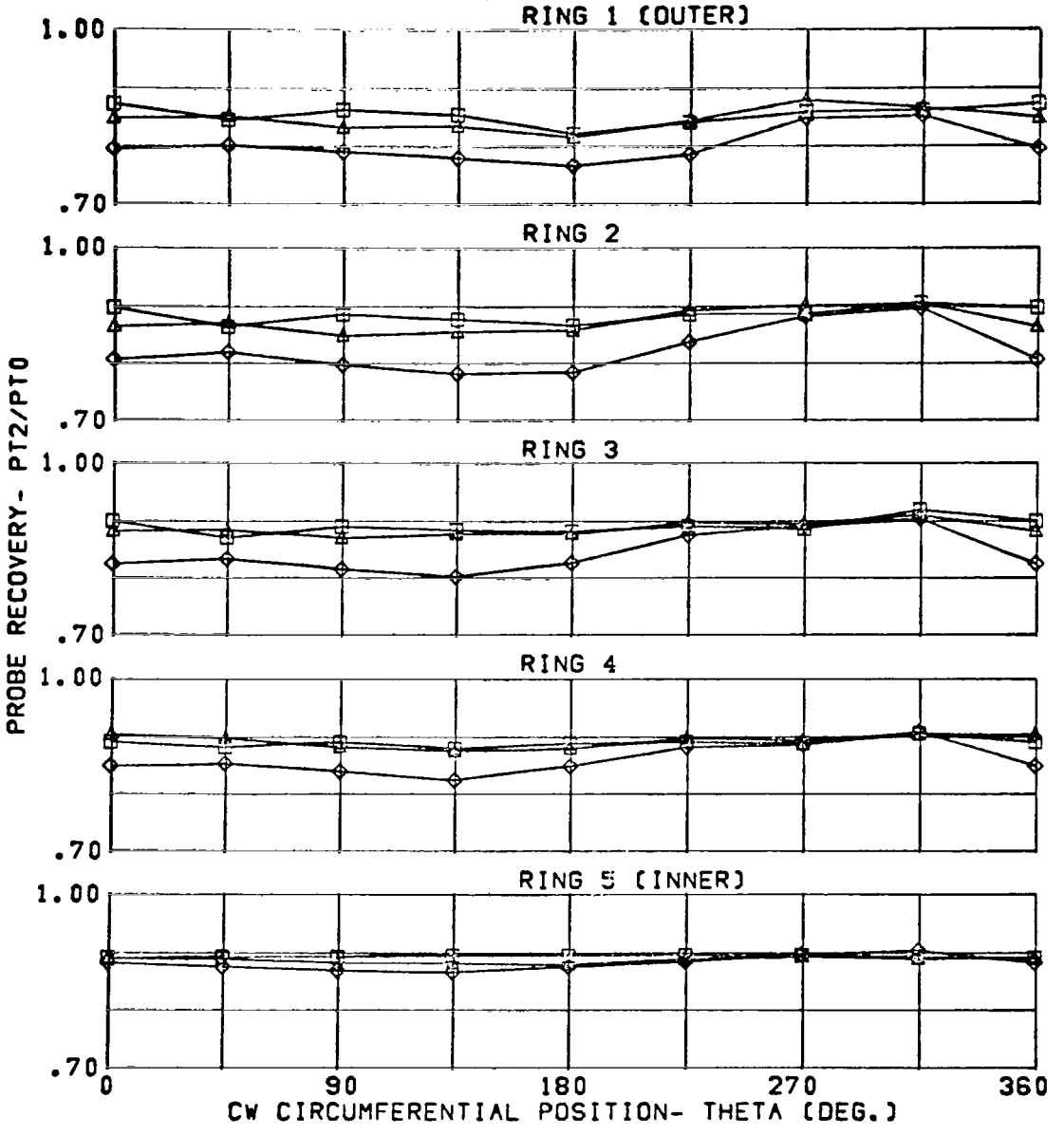

Figure 75 Circumferential Pressure Distribution at Engine Face for Inlet Configuration C13

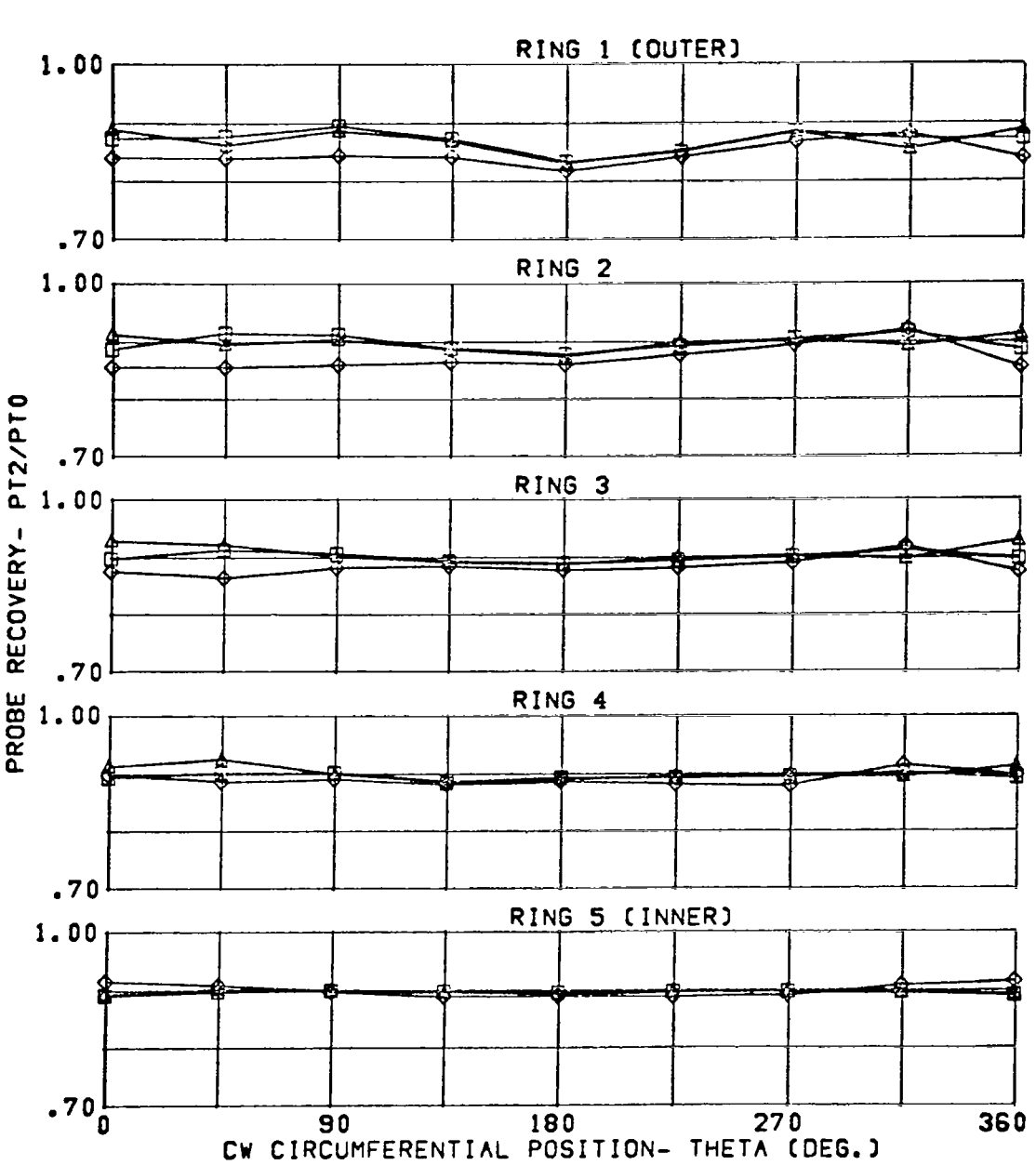

Figure 76 Circumferential Pressure Distribution at Engine Face for Inlet Configuration C13

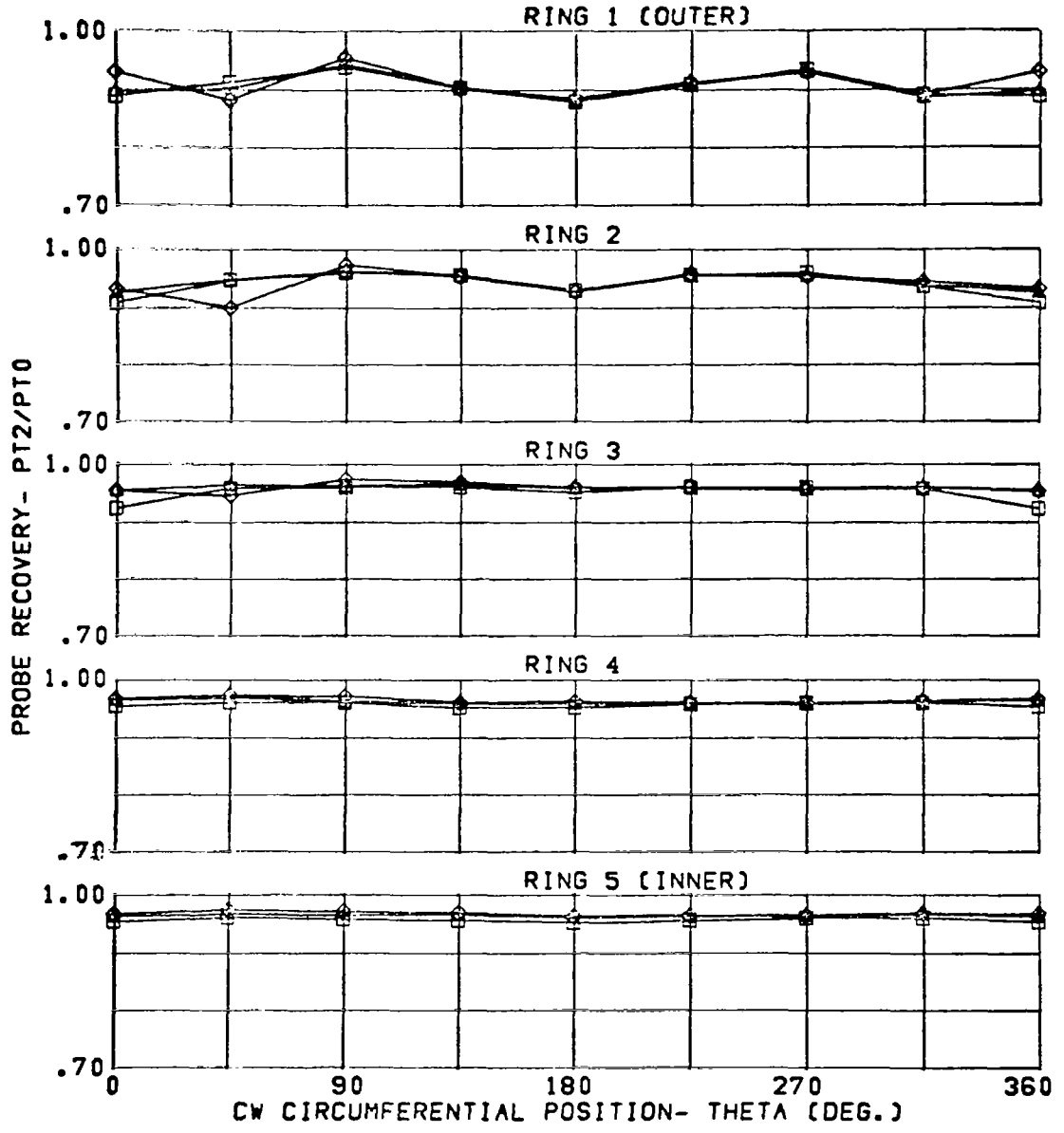

Figure 77 Circumferential Pressure Distribution at Engine Face for Inlet Configuration C13

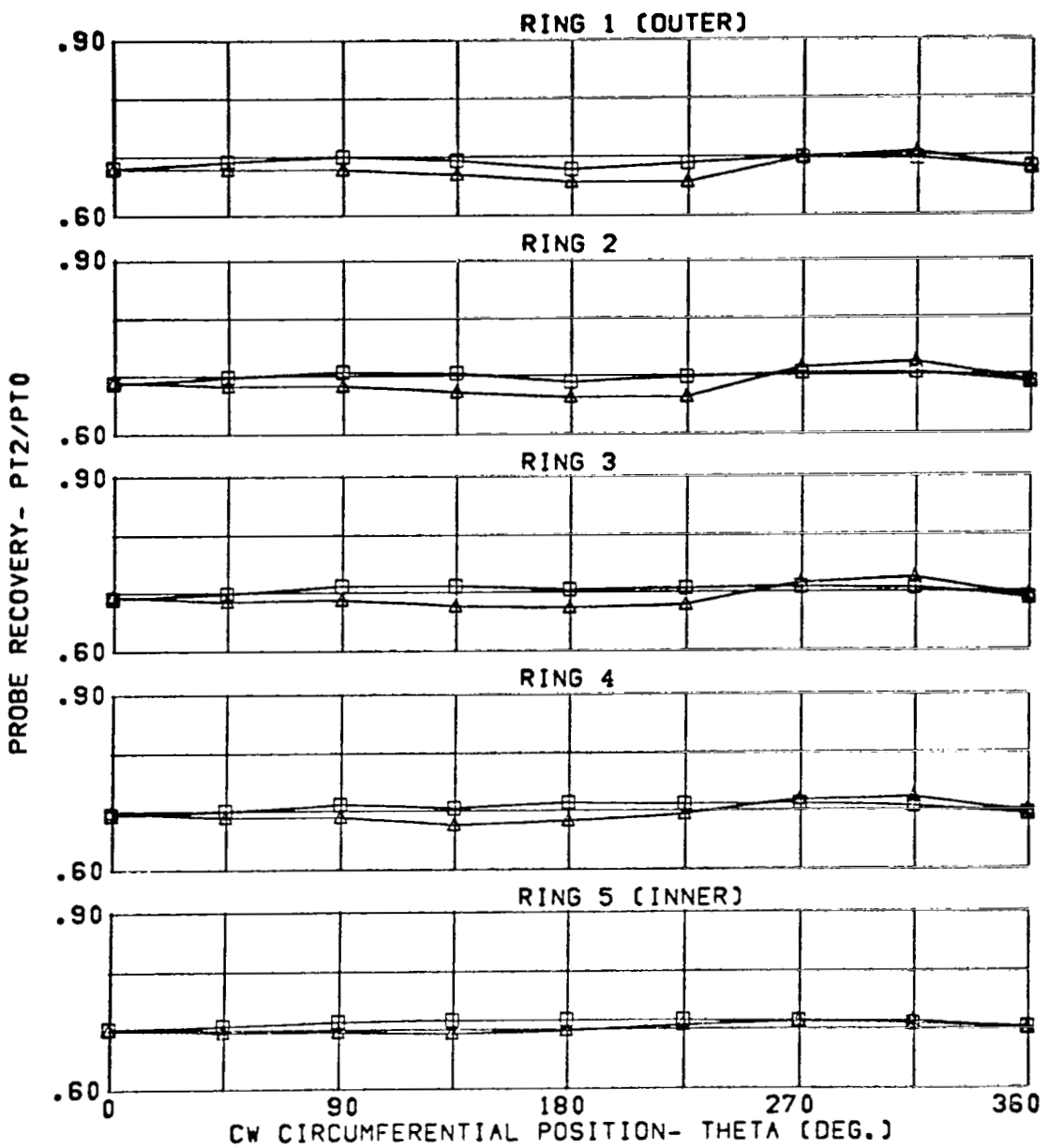

Figure 78 Circumferential Pressure Distribution at Engine Face for Inlet Configuration C13

CONFIGURATION	CONDITION	SYM	BETA	$\bar{PT2}/PT0$
C13	MACH = 1.97	□	0.	.734
3.65 IN. DIV.	ALPHA= 1.	△	-5.	.731
V.G.S OUT	WC2 = 183.	◇	-10.	.711

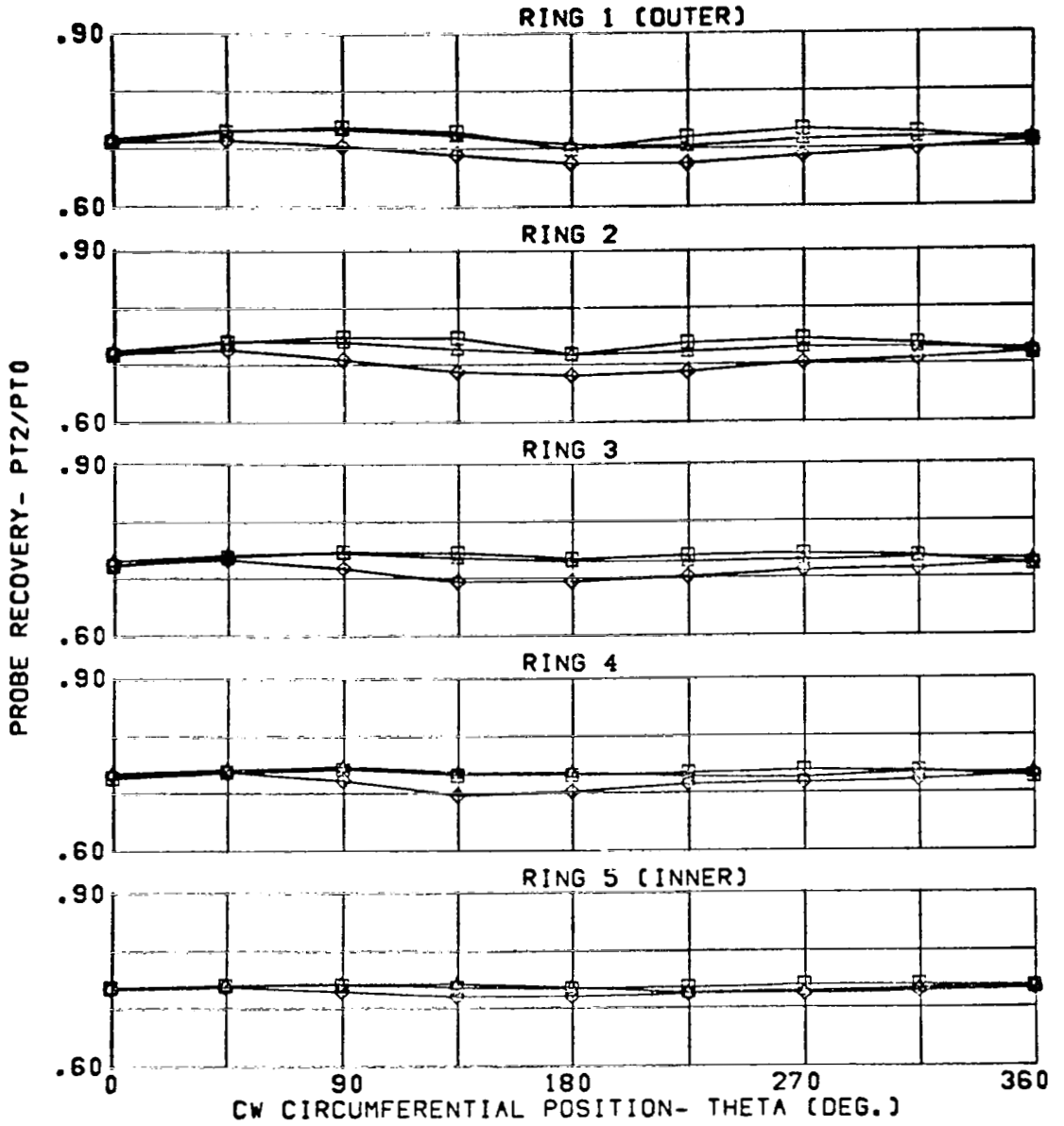

Figure 79 Circumferential Pressure Distribution at Engine Face for Inlet Configuration C13

CONFIGURATION	CONDITION	SYM	BETA	$\bar{PT2}/PT0$
C13	MACH = 1.96	□	0.	.859
3.65 IN. DIV.	ALPHA= 20.	△	-5.	.866
V.G.S OUT	WC2 = 183.	◇	-10.	.871

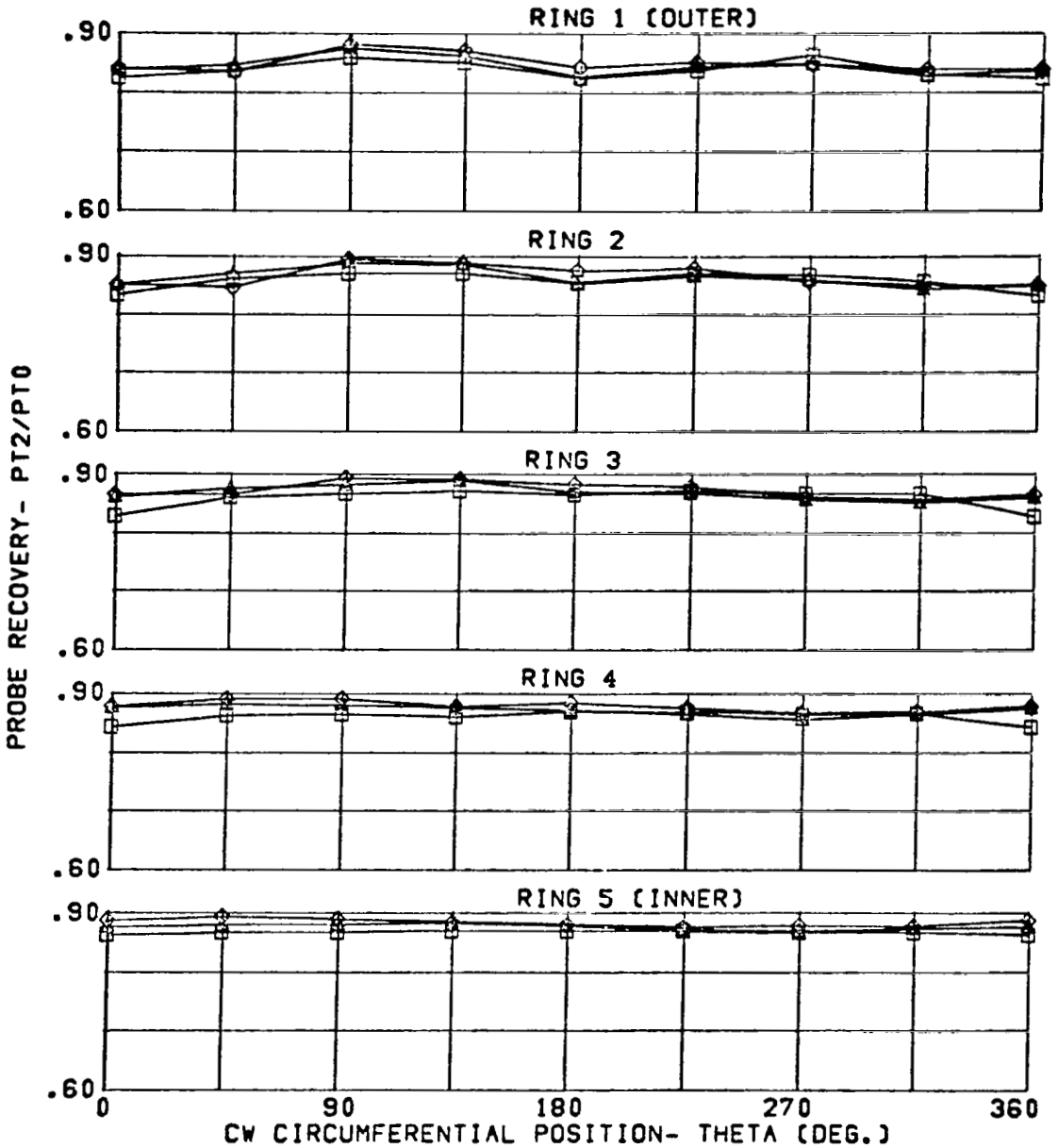

Figure 80 Circumferential Pressure Distribution at Engine Face for Inlet Configuration C13

CONFIGURATION	CONDITION	SYM.	BETA (DEG)
SPLITTER ONLY	MACH = .89	○	4.
3.65 IN. DIV. HT.	ALPHA= -9.	□	-0.
NOSE BOOM ON		△	-5.
		◇	-10.
		▷	-15.

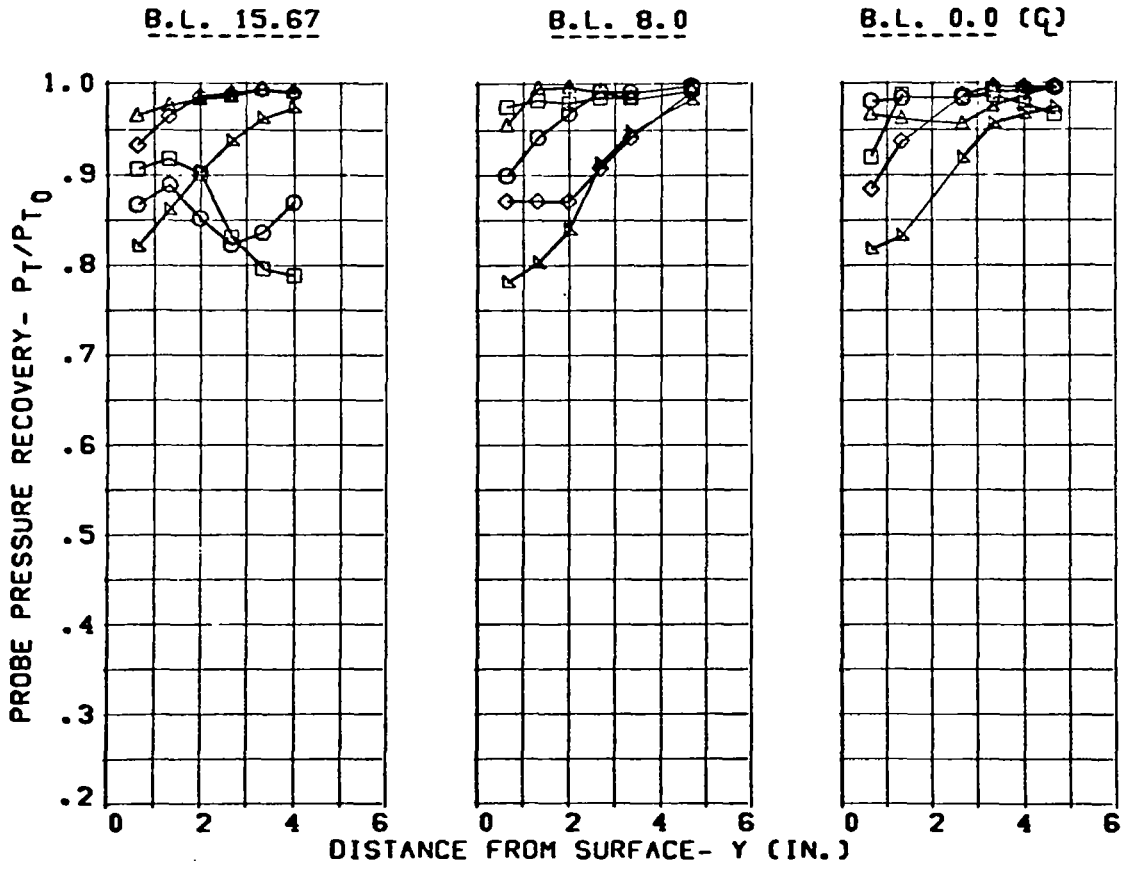

Figure 81 Fuselage Boundary Layer Total-Pressure Profiles, F.S. 155

CONFIGURATION	CONDITION	SYM.	BETA (DEG)
SPLITTER ONLY	MACH = .90	○	5.
3.65 IN. DIV. HT.	ALPHA= -5.	□	-0.
NOSE BOOM ON		△	-5.
		◇	-10.
		▷	-15.

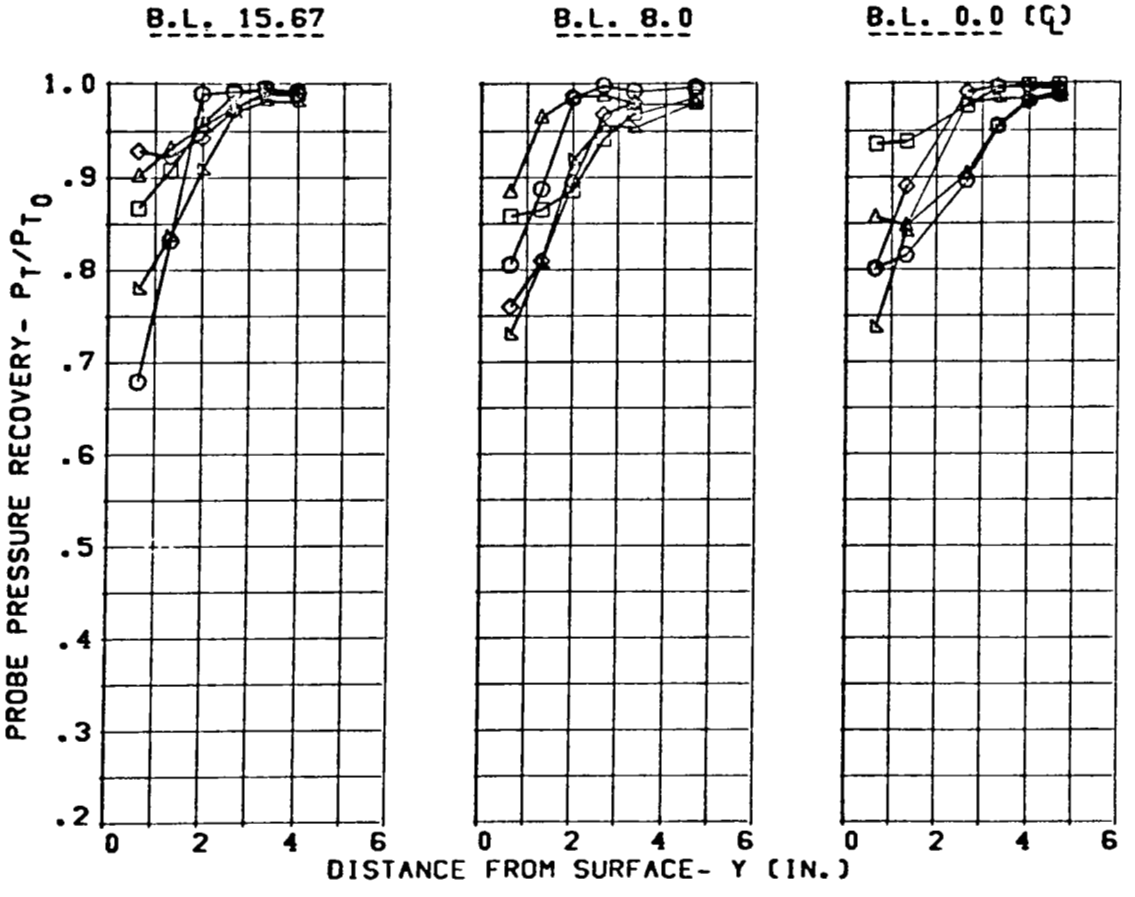

Figure 82 Fuselage Boundary Layer Total-Pressure Profiles, F.S. 155

CONFIGURATION	CONDITION	SYM.	BETA (DEG)
SPLITTER ONLY	MACH = .90	○	4.
3.65 IN. DIV. HT.	ALPHA= 1.	□	-0.
NOSE BOOM ON		△	-5.
		◇	-10.
		▷	-15.

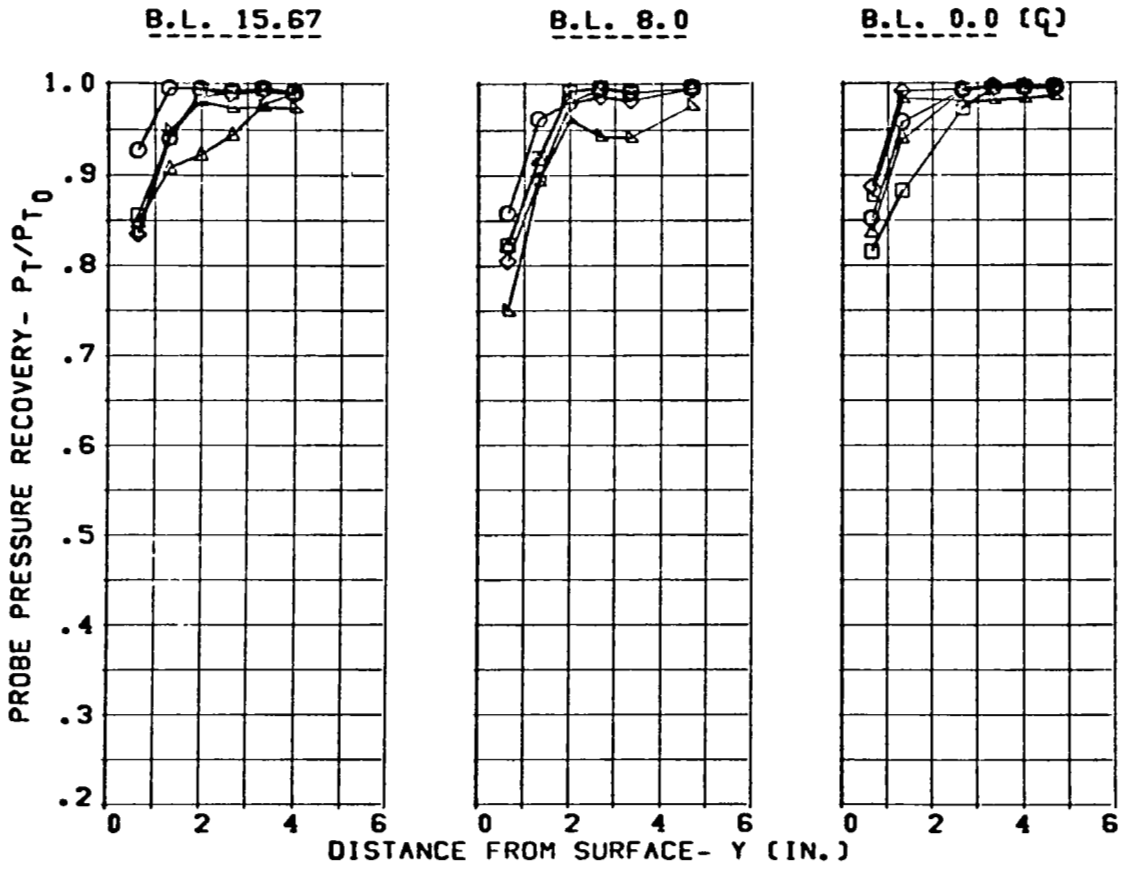

Figure 83 Fuselage Boundary Layer Total-Pressure Profiles, F.S. 155

CONFIGURATION	CONDITION	SYM.	BETA (DEG)
SPLITTER ONLY	MACH = .91	○	5.
3.65 IN. DIV. HT.	ALPHA= 6.	□	-0.
NOSE BOOM ON		△	-5.
		◇	-10.
		▷	-15.

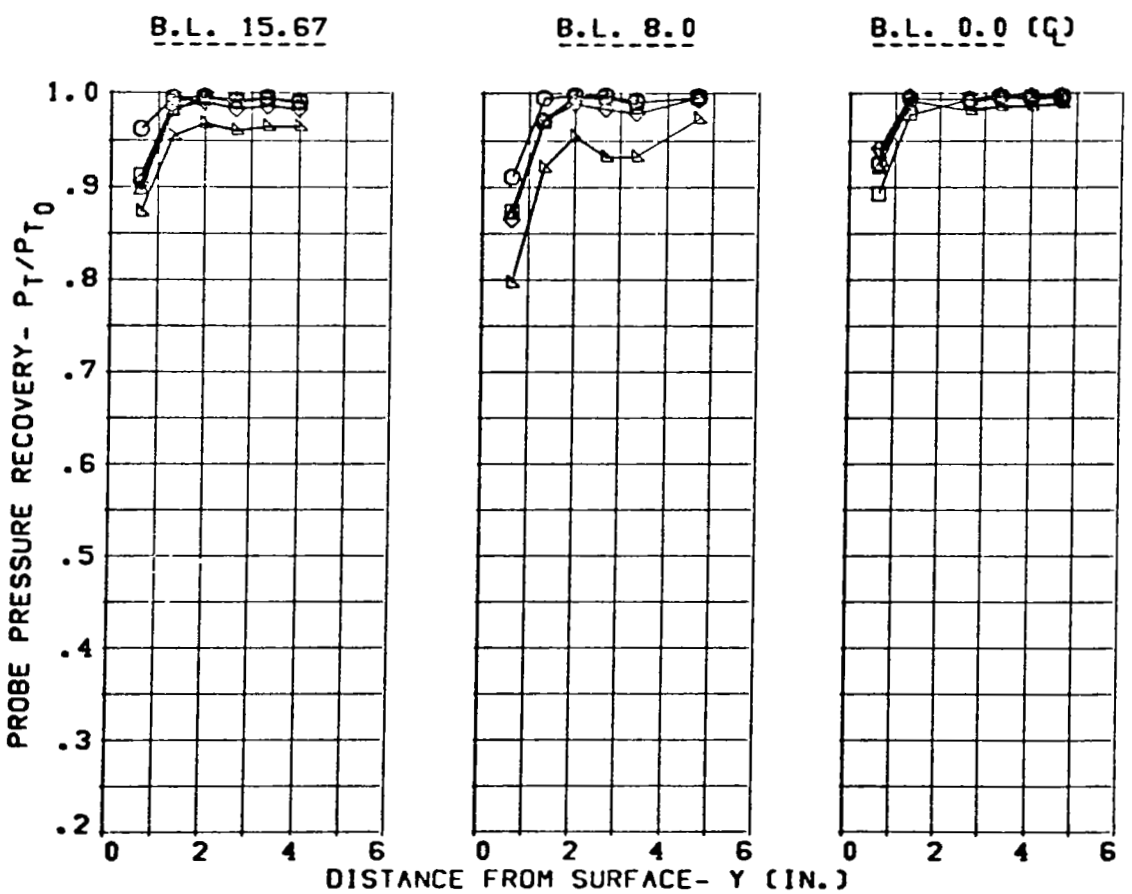

Figure 3.1-22

Figure 84 Fuselage Boundary Layer Total-Pressure Profiles, F.S. 155

CONFIGURATION	CONDITION	SYM.	BETA (DEG)
SPLITTER ONLY	MACH = 1.57	○	5.
3.65 IN. DIV. HT.	ALPHA= -5.	□	0.
NOSE BOOM ON		△	-5.
		◇	-10.

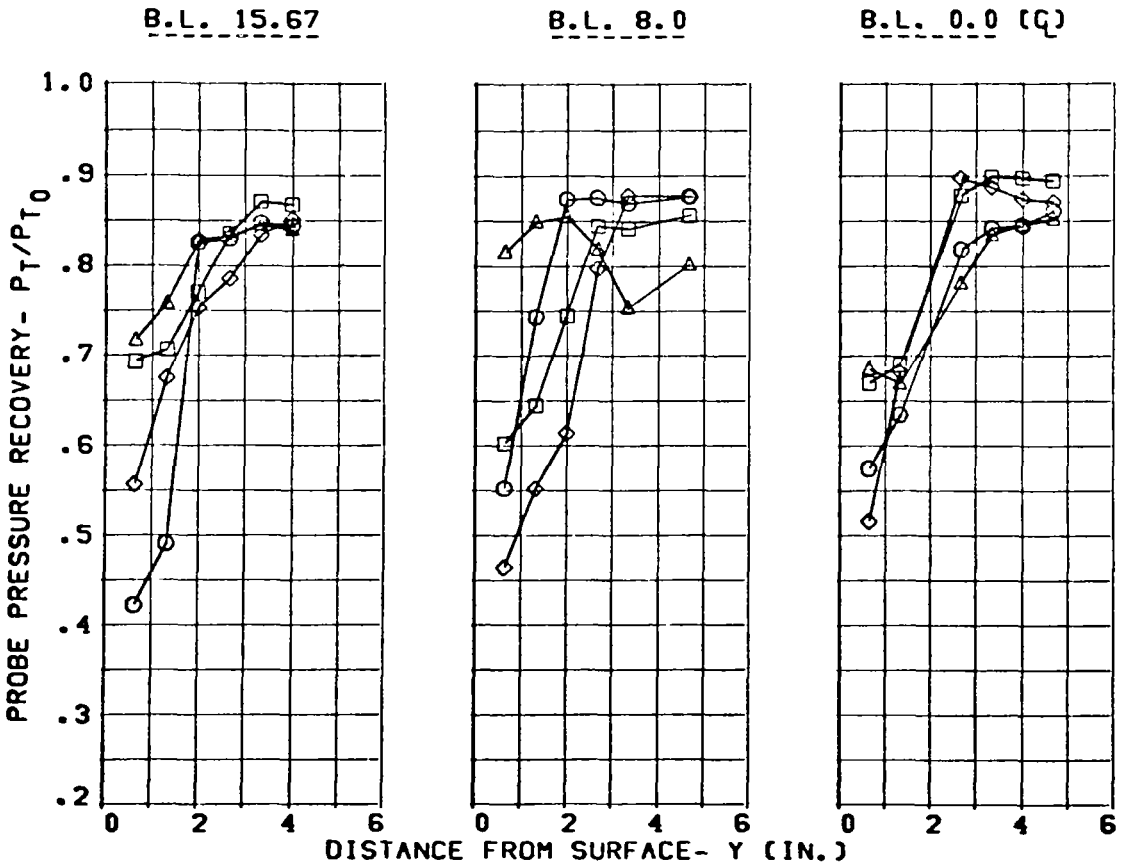

Figure 85 Fuselage Boundary Layer Total-Pressure Profiles, F.S. 155

CONFIGURATION	CONDITION	SYM.	BETA (DEG)
SPLITTER ONLY 3.65 IN. DIV. HT. NOSE BOOM ON	MACH = 1.57 ALPHA= 1.	○ ◇ □ △ ◇	5. 2. -0. -5. -10.

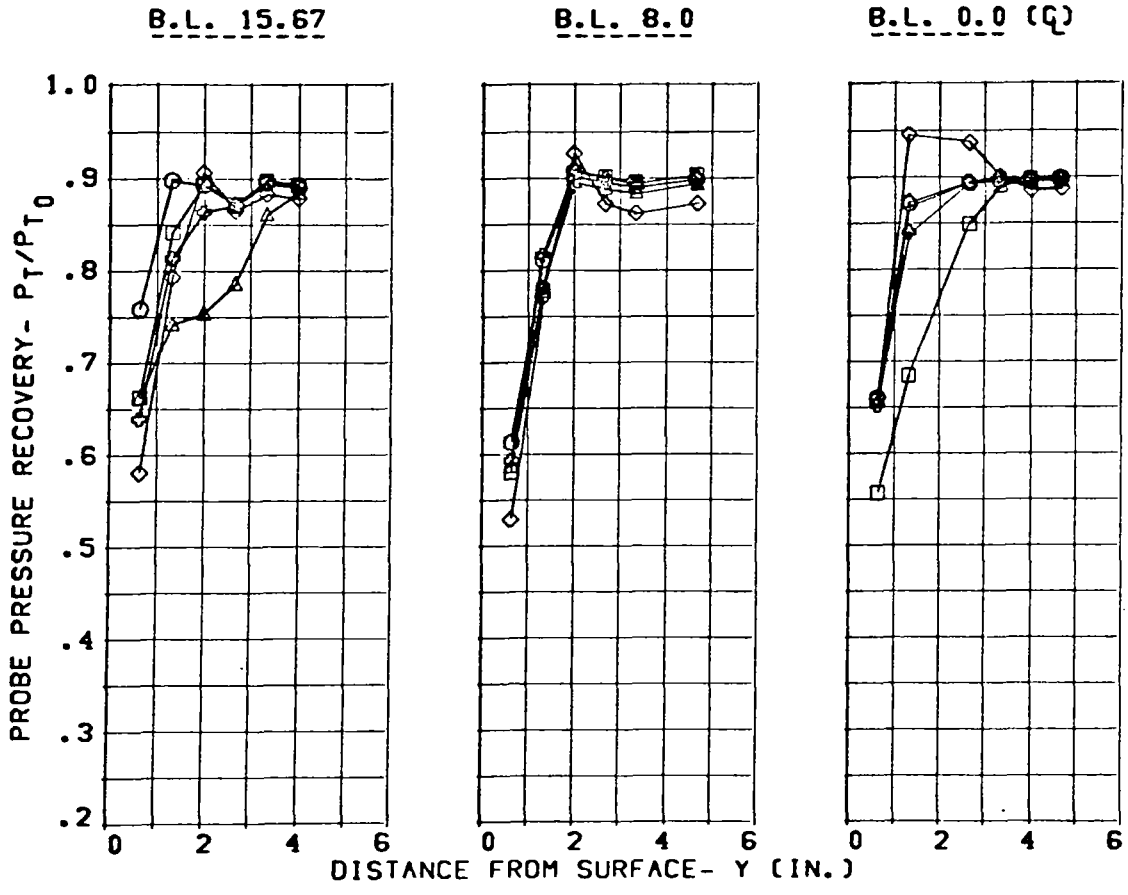

Figure 86 Fuselage Boundary Layer Total-Pressure Profiles, F.S. 155

CONFIGURATION	CONDITION	SYM.	BETA (DEG)
SPLITTER ONLY 3.65 IN. DIV. HT. NOSE BOOM ON	MACH = 1.57 ALPHA= 6.	○ □ △ ◇	5. -0. -5. -10.

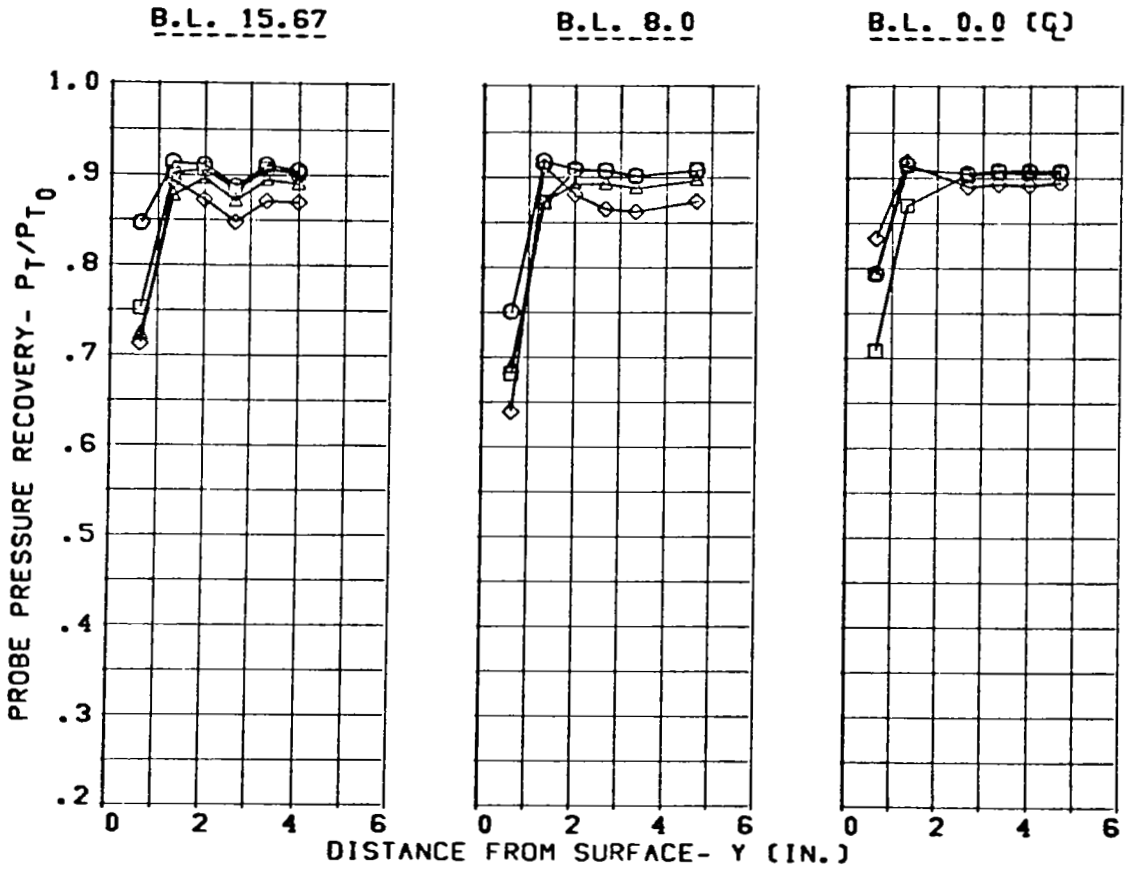

Figure 87 Fuselage Boundary Layer Total-Pressure Profiles, F.S. 155

CONFIGURATION	CONDITION	SYM.	BETA (DEG)
SPLITTER ONLY	MACH = 1.96	○	5.
3.65 IN. DIV. HT.	ALPHA= -5.	□	0.
NOSE BOOM ON		△	-5.
		◇	-10.

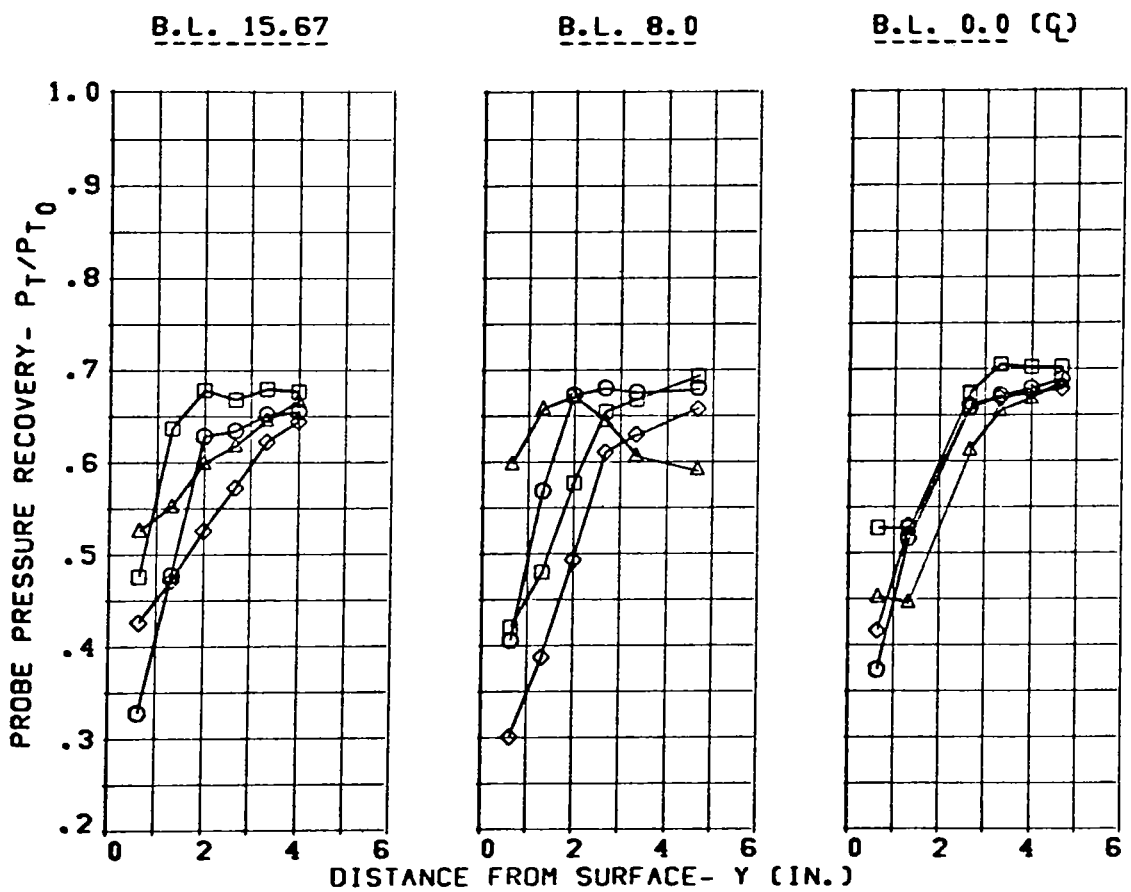

Figure 88 Fuselage Boundary Layer Total-Pressure Profiles, F.S. 155

CONFIGURATION	CONDITION	SYM.	BETA (DEG)
SPLITTER ONLY	MACH = 1.96	○	5.
3.65 IN. DIV. HT.	ALPHA= 1.	◇	2.
NOSE BOOM ON		□	0.
		△	-5.
		◇	-10.

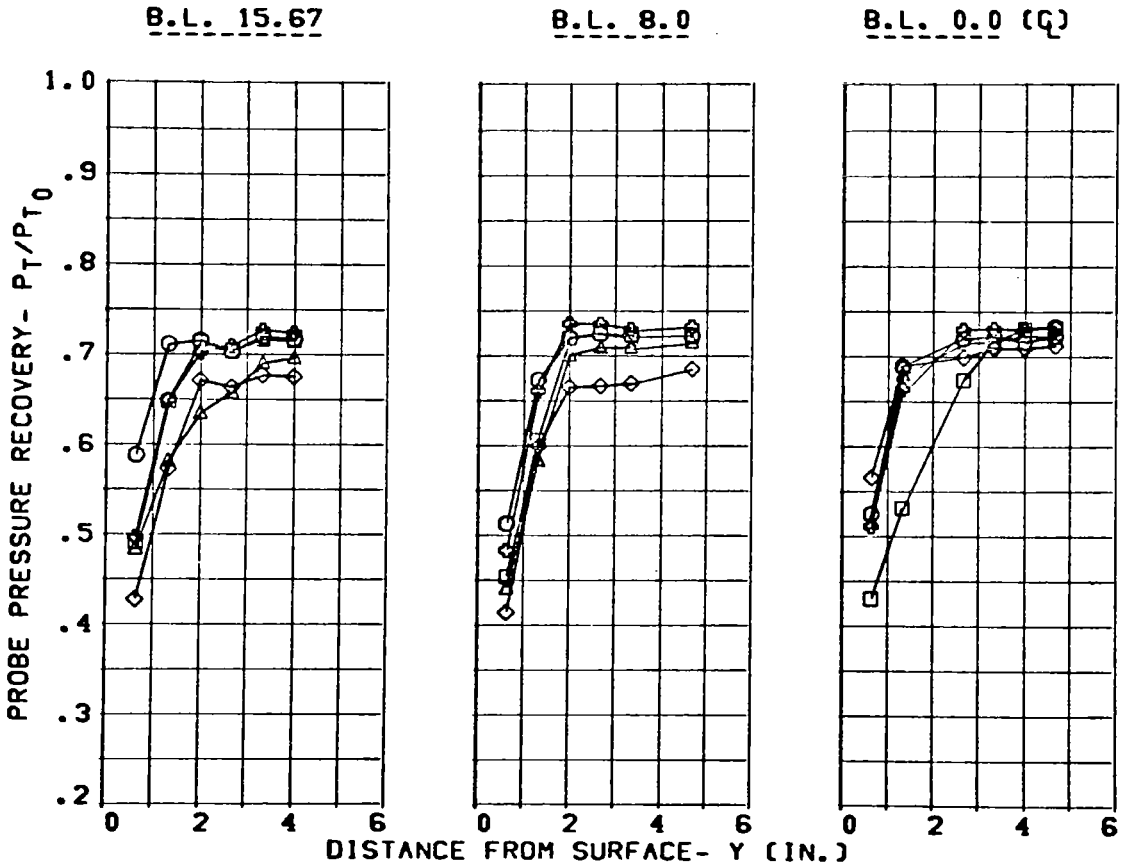

Figure 89 Fuselage Boundary Layer Total-Pressure Profiles, F.S. 155

CONFIGURATION	CONDITION	SYM.	BETA (DEG)
SPLITTER ONLY	MACH = 1.96	○	5.
3.65 IN. DIV. HT.	ALPHA= 6.	□	0.
NOSE BOOM ON		△	-5.
		◇	-10.

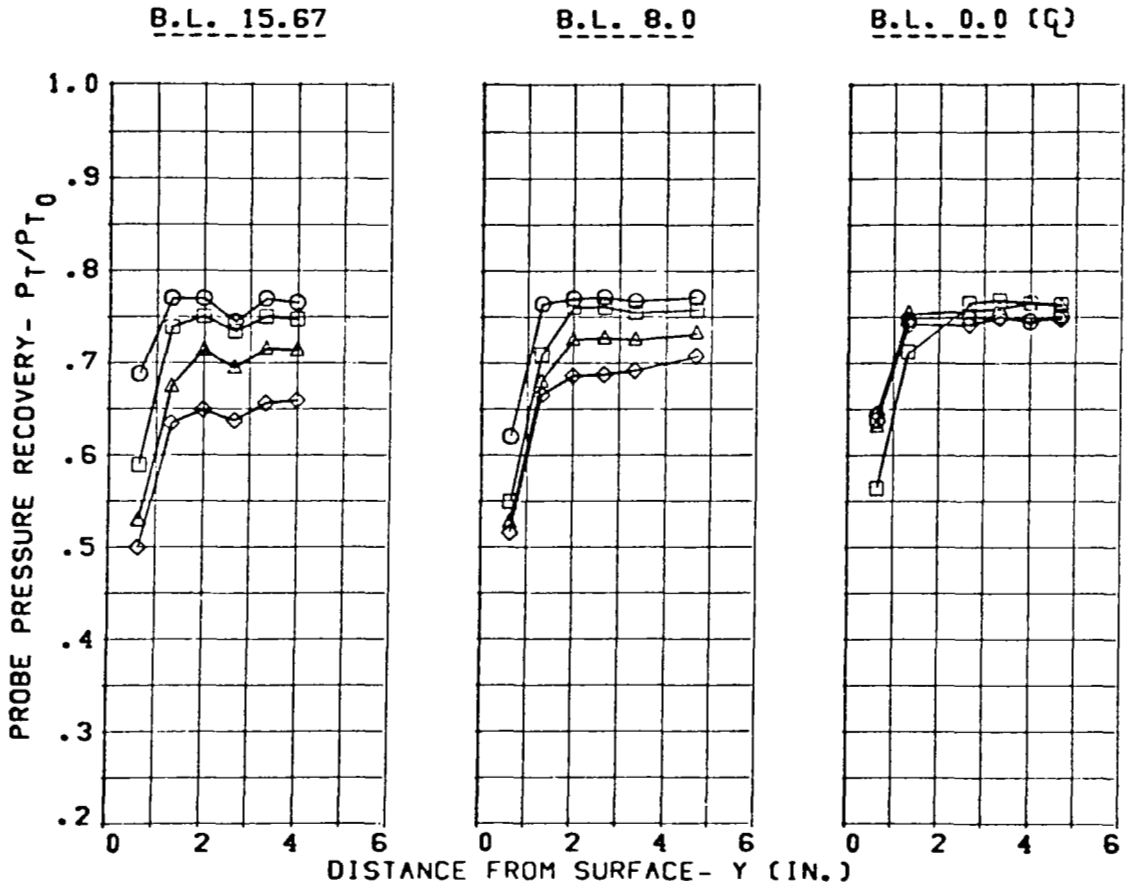

Figure 90 Fuselage Boundary Layer Total-Pressure Profiles, F.S. 155

CONFIGURATION	CONDITION	SYM.	BETA (DEG)
SPLITTER ONLY	MACH = .88	○	5.
3.65 IN. DIV. HT.	ALPHA= -9.	□	0.
NOSE BOOM ON		△	-5.
FUS. RAKES OFF		◇	-10.
		▷	-15.

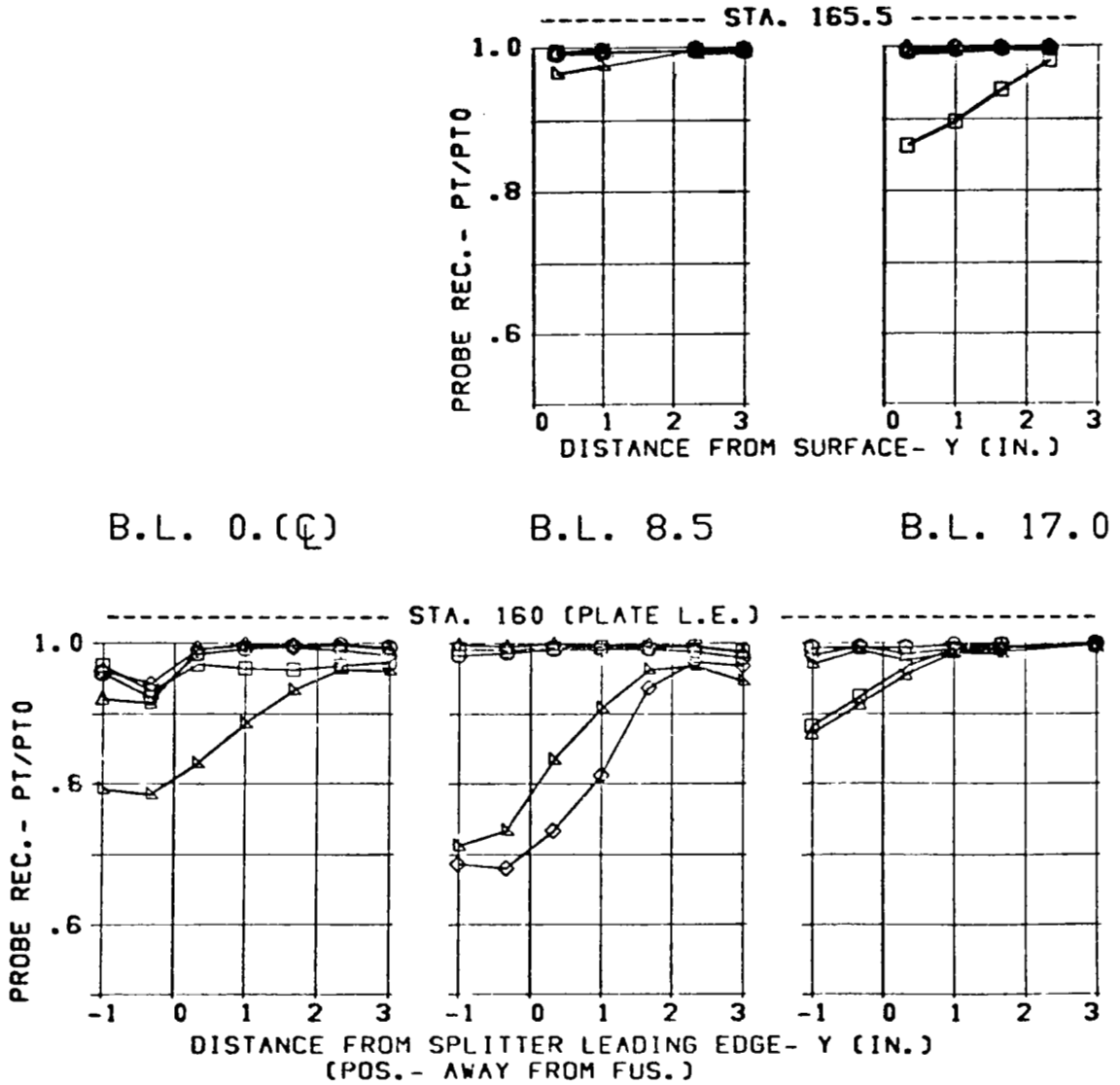

Figure 91 Splitter-Plate Boundary Layer Total Pressure Profiles

CONFIGURATION	CONDITION	SYM.	BETA (DEG)
SPLITTER ONLY	MACH = .88	○	5.
3.65 IN. DIV. HT.	ALPHA= -5.	□	-0.
NOSE BOOM ON		△	-5.
FUS. RAKES OFF		◇	-10.
		▷	-15.

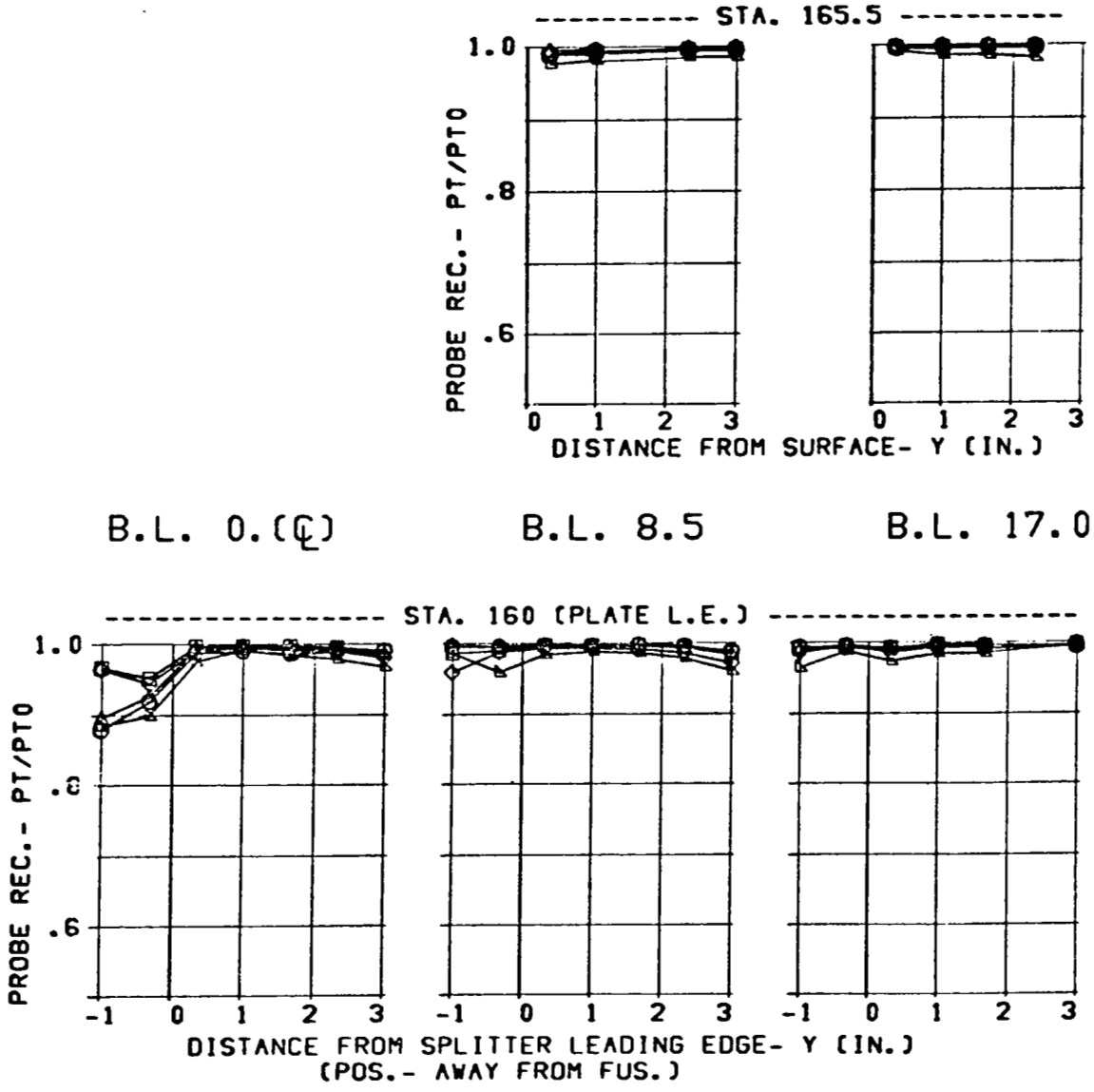

Figure 92 Splitter-Plate Boundary Layer Total Pressure Profiles

CONFIGURATION	CONDITION	SYM.	BETA (DEG)
SPLITTER ONLY	MACH = .85	O	5.
3.65 IN. DIV. HT.	ALPHA= 1.	□	0.
NOSE BOOM ON		△	-5.
FUS. RAKES OFF		◇	-10.
		▷	-15.

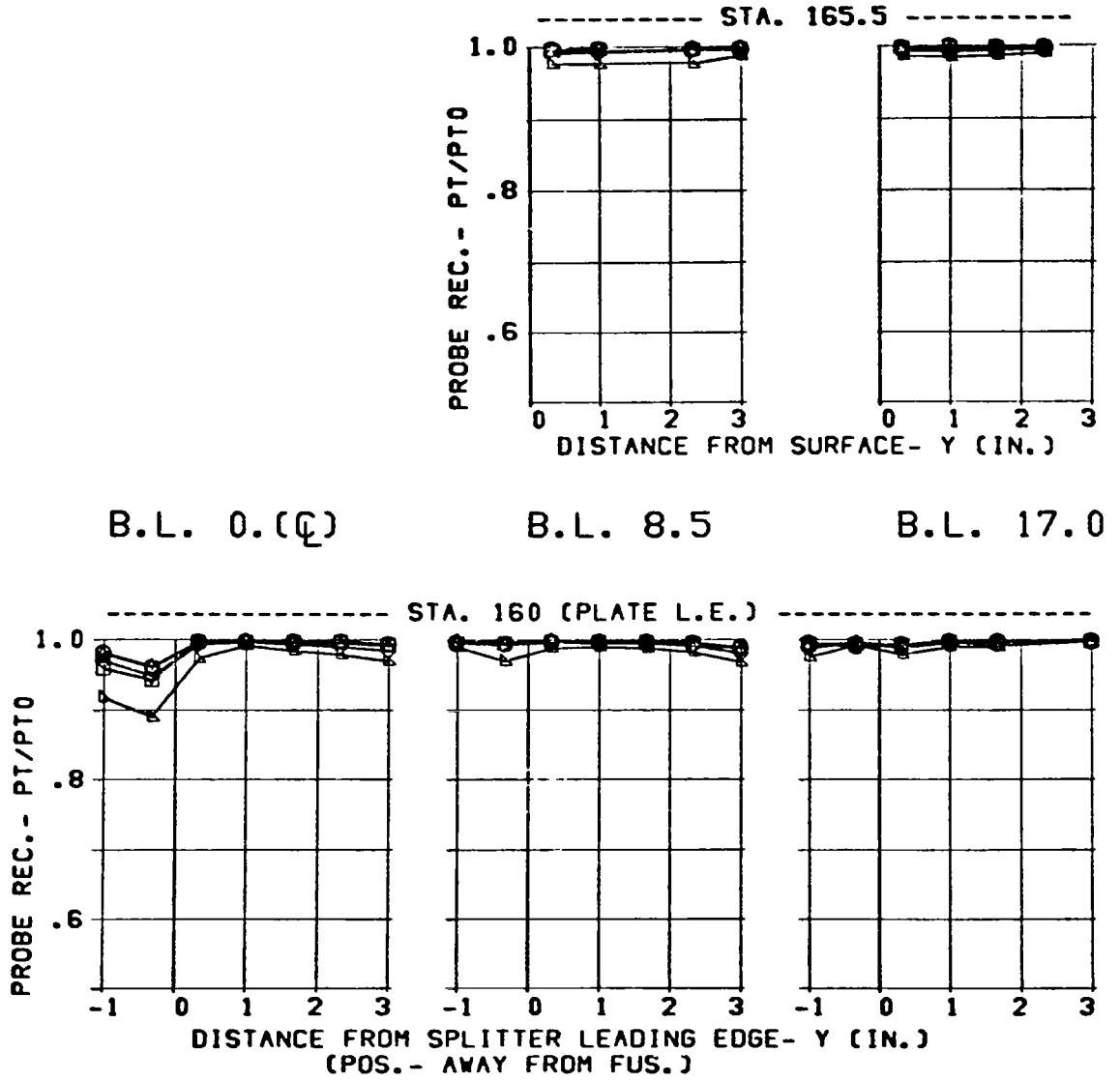

Figure 93 Splitter-Plate Boundary Layer Total Pressure Profiles

CONFIGURATION	CONDITION	SYM.	BETA (DEG)
SPLITTER ONLY	MACH = .89	○	5.
3.65 IN. DIV. HT.	ALPHA= 6.	□	0.
NOSE BOOM ON		△	-5.
FUS. RAKES OFF		◇	-10.
		▷	-15.

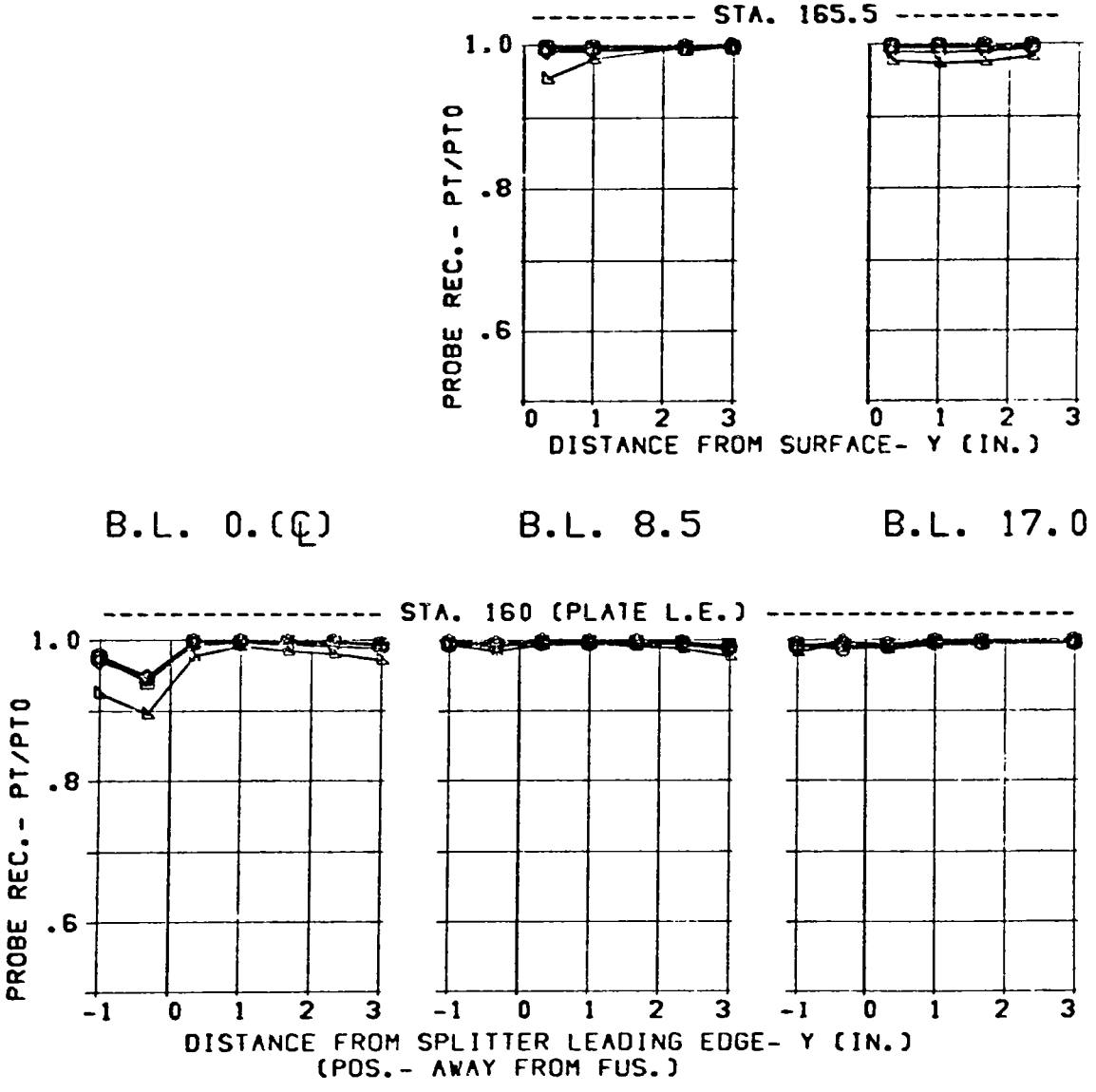

Figure 94 Splitter-Plate Boundary Layer Total Pressure Profiles

CONFIGURATION	CONDITION	SYM.	BETA (DEG)
SPLITTER ONLY	MACH = 1.57	O	4.
3.65 IN. DIV. HT.	ALPHA= -5.	□	0.
NOSE BOOM ON		△	-5.
FUS. RAKES OFF		◇	-10.

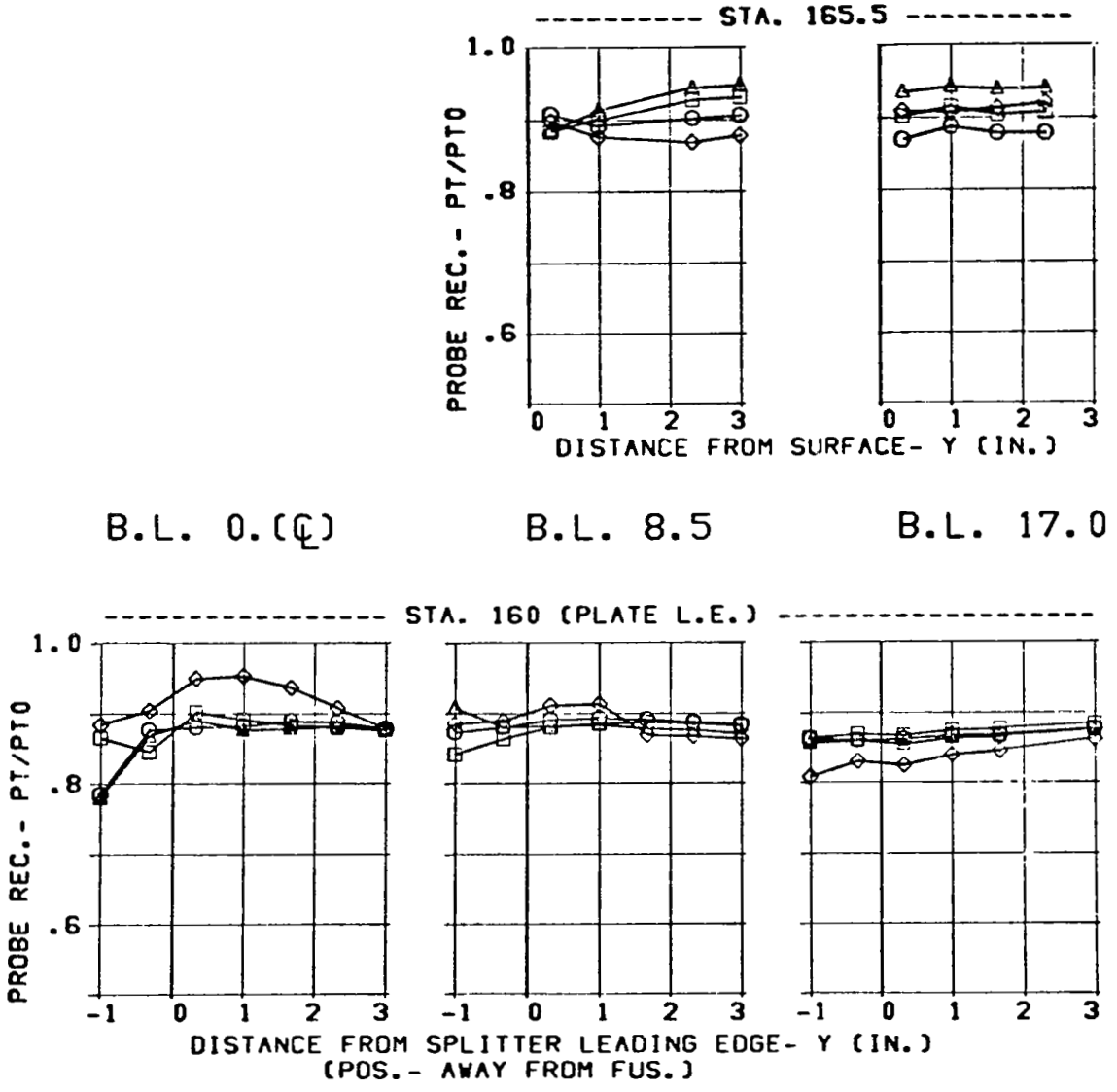

Figure 95 Splitter-Plate Boundary Layer Total Pressure Profiles

CONFIGURATION	CONDITION	SYM.	BETA (DEG)
SPLITTER ONLY	MACH = 1.57	O	4.
3.65 IN. DIV. HT.	ALPHA= 1.	◇	2.
NOSE BOOM ON		□	0.
FUS. RAKES OFF		△	-5.
		◇	-10.

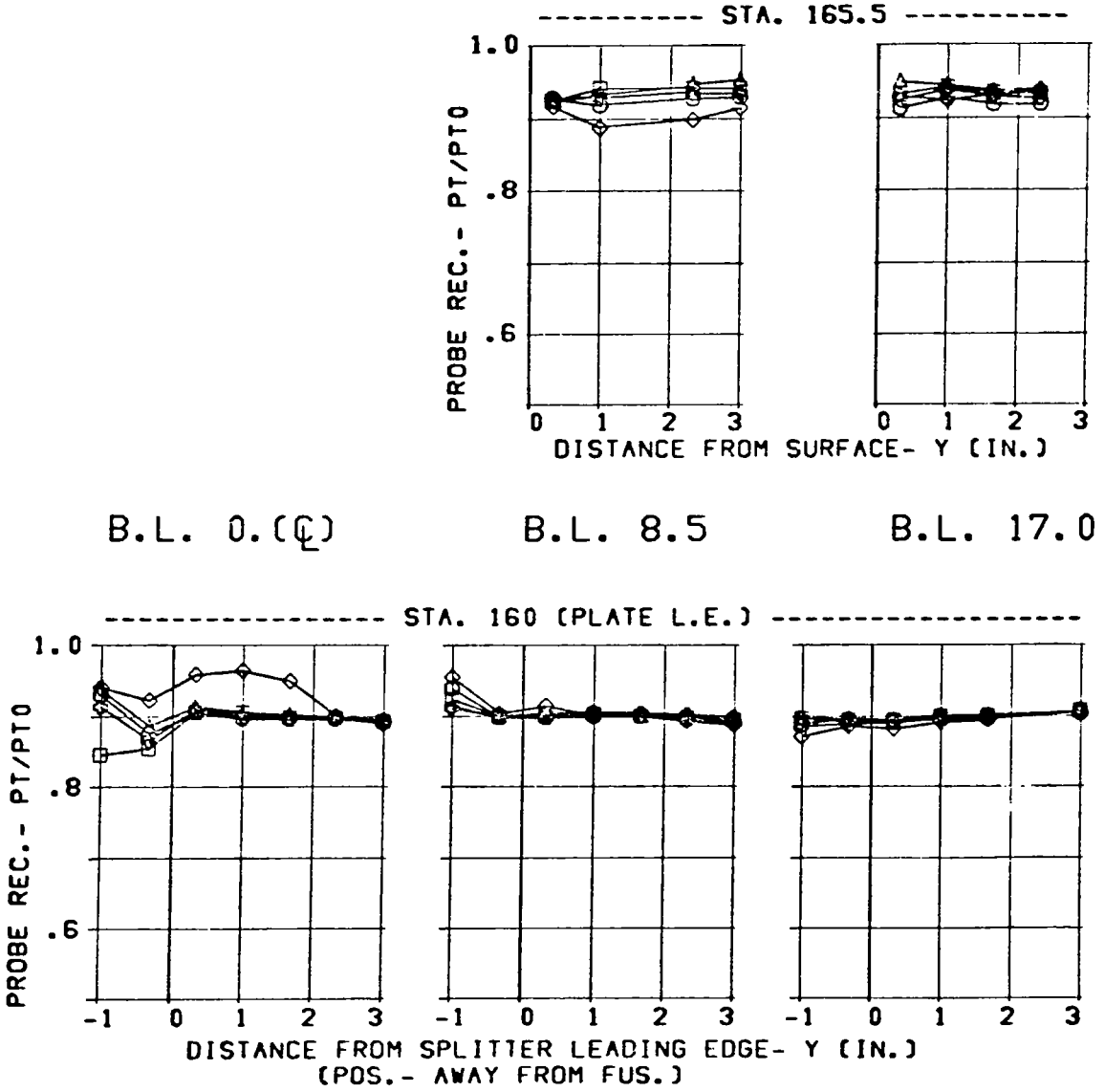

Figure 96 Splitter-Plate Boundary Layer Total Pressure Profiles

CONFIGURATION	CONDITION	SYM.	BETA (DEG)
SPLITTER ONLY	MACH = 1.57	○	5.
3.65 IN. DIV. HT.	ALPHA= 6.	□	0.
NOSE BOOM ON		△	-5.
FUS. RAKES OFF		◇	-10.

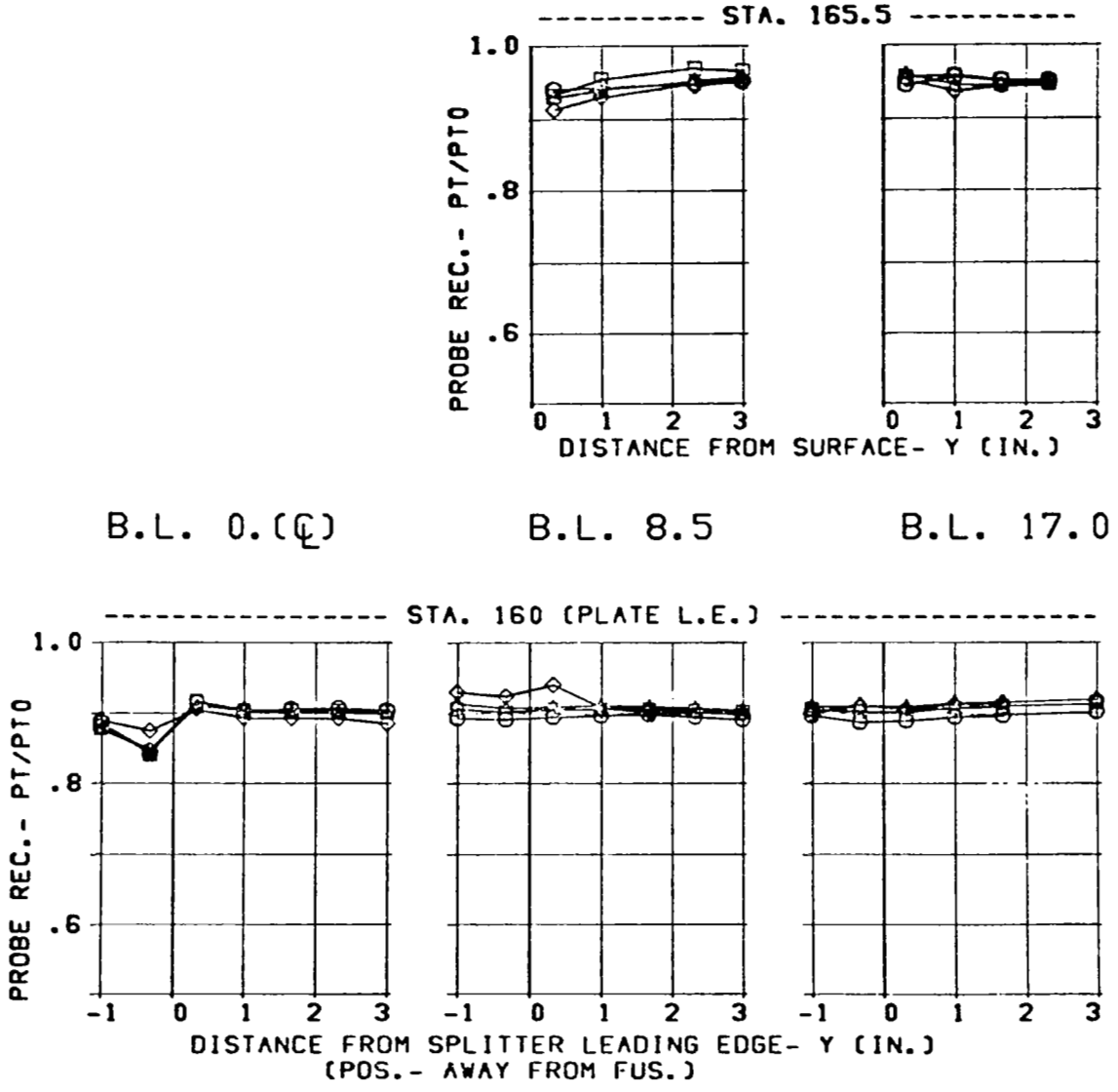

Figure 97 Splitter-Plate Boundary Layer Total Pressure Profiles

CONFIGURATION	CONDITION	SYM.	BETA (DEG)
SPLITTER ONLY	MACH = 1.57	O	5.
3.65 IN. DIV. HT.	ALPHA= 10.	□	0.
NOSE BOOM ON		△	-5.
FUS. RAKES OFF		◇	-10.

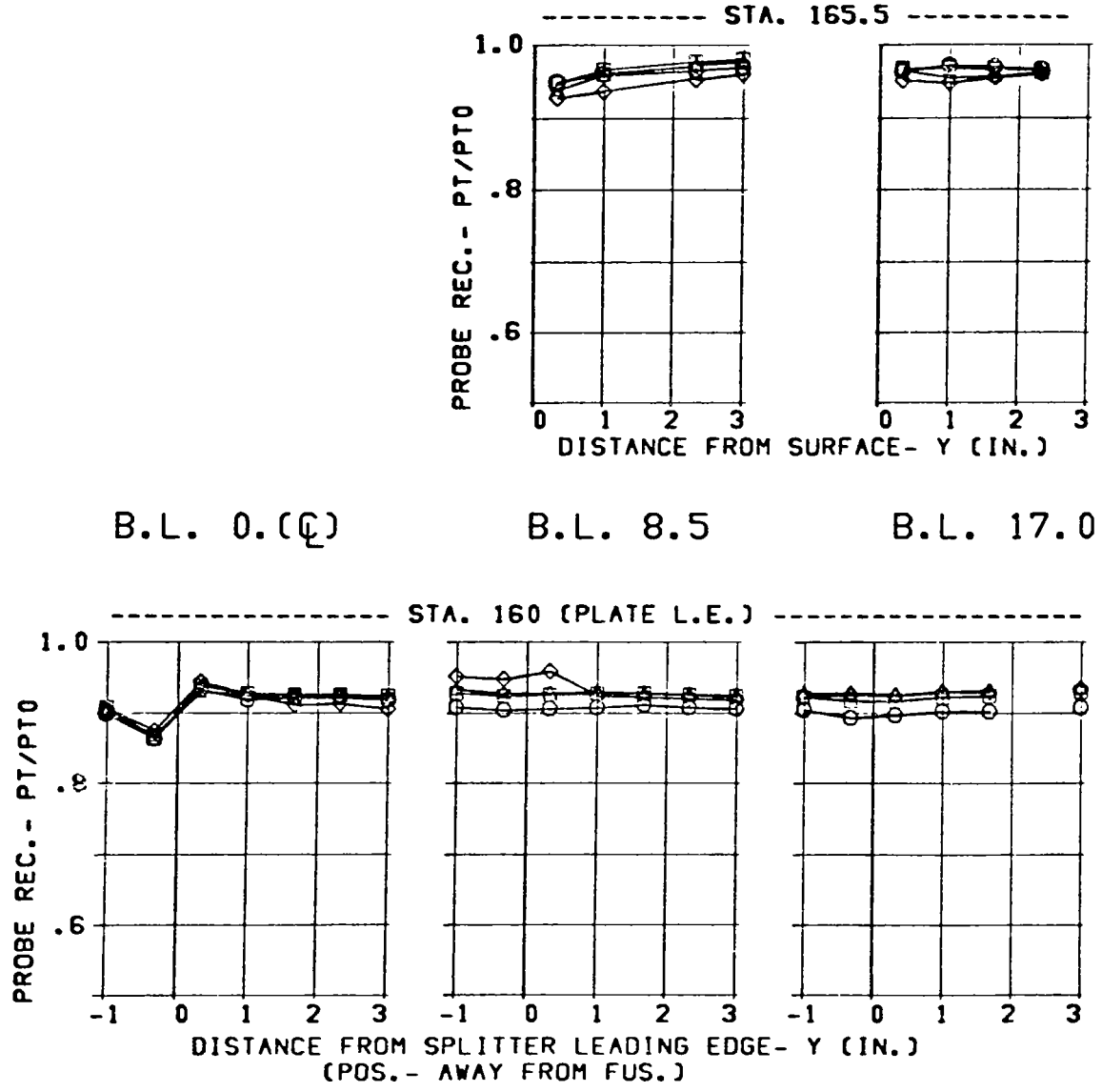

Figure 98 Splitter-Plate Boundary Layer Total Pressure Profiles

CONFIGURATION	CONDITION	SYM.	BETA (DEG)
SPLITTER ONLY	MACH = 1.96	○	5.
3.65 IN. DIV. HT.	ALPHA= -5.	□	0.
NOSE BOOM ON		△	-5.
FUS. RAKES OFF		◇	-10.

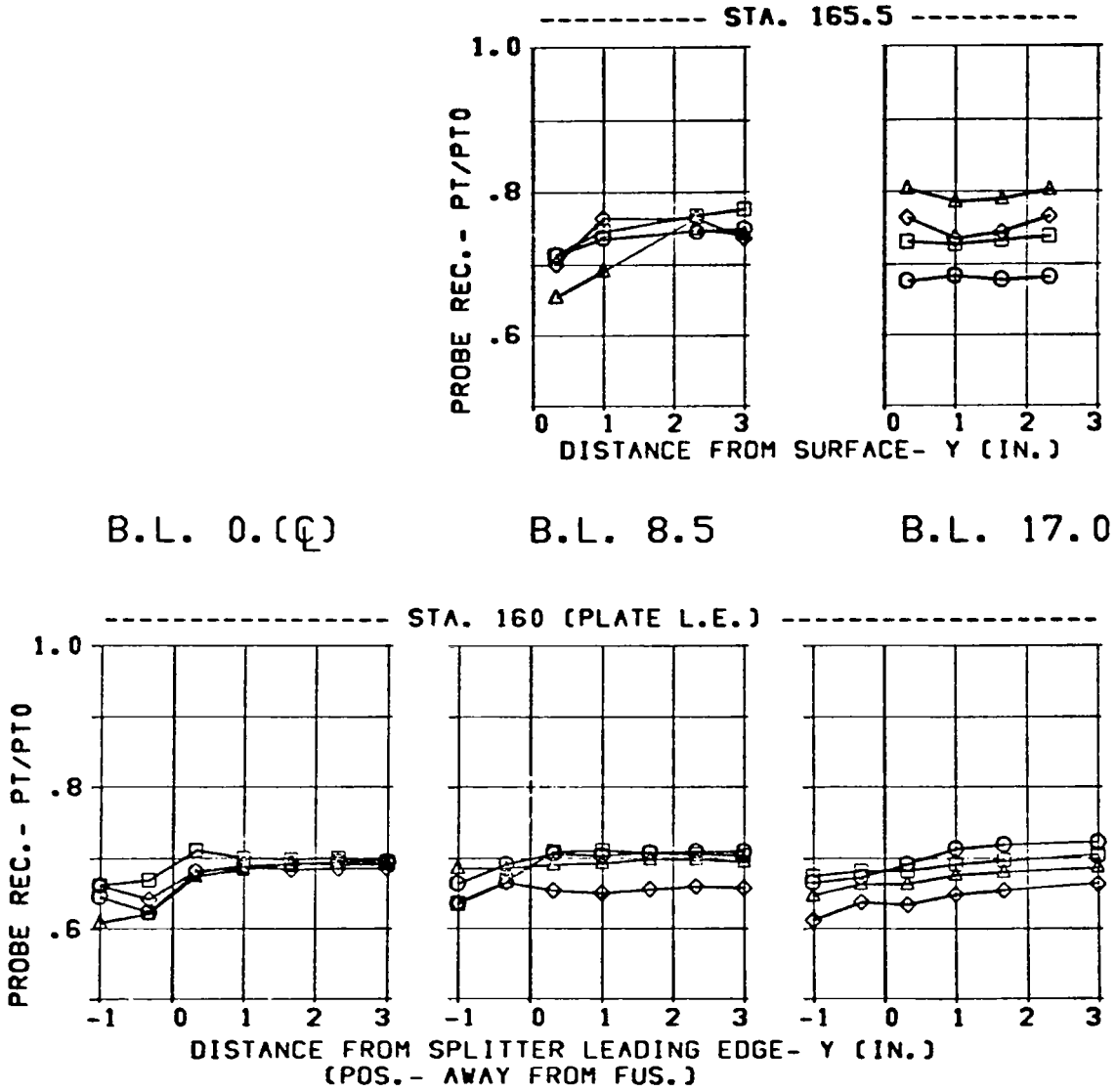

Figure 99 Splitter-Plate Boundary Layer Total Pressure Profiles

CONFIGURATION	CONDITION	SYM.	BETA (DEG)
SPLITTER ONLY	MACH = 1.96	○	5.
3.65 IN. DIV. HT.	ALPHA= 1.	◇	2.
NOSE BOOM ON		□	0.
FUS. RAKES OFF		△	-5.
		◇	-10.

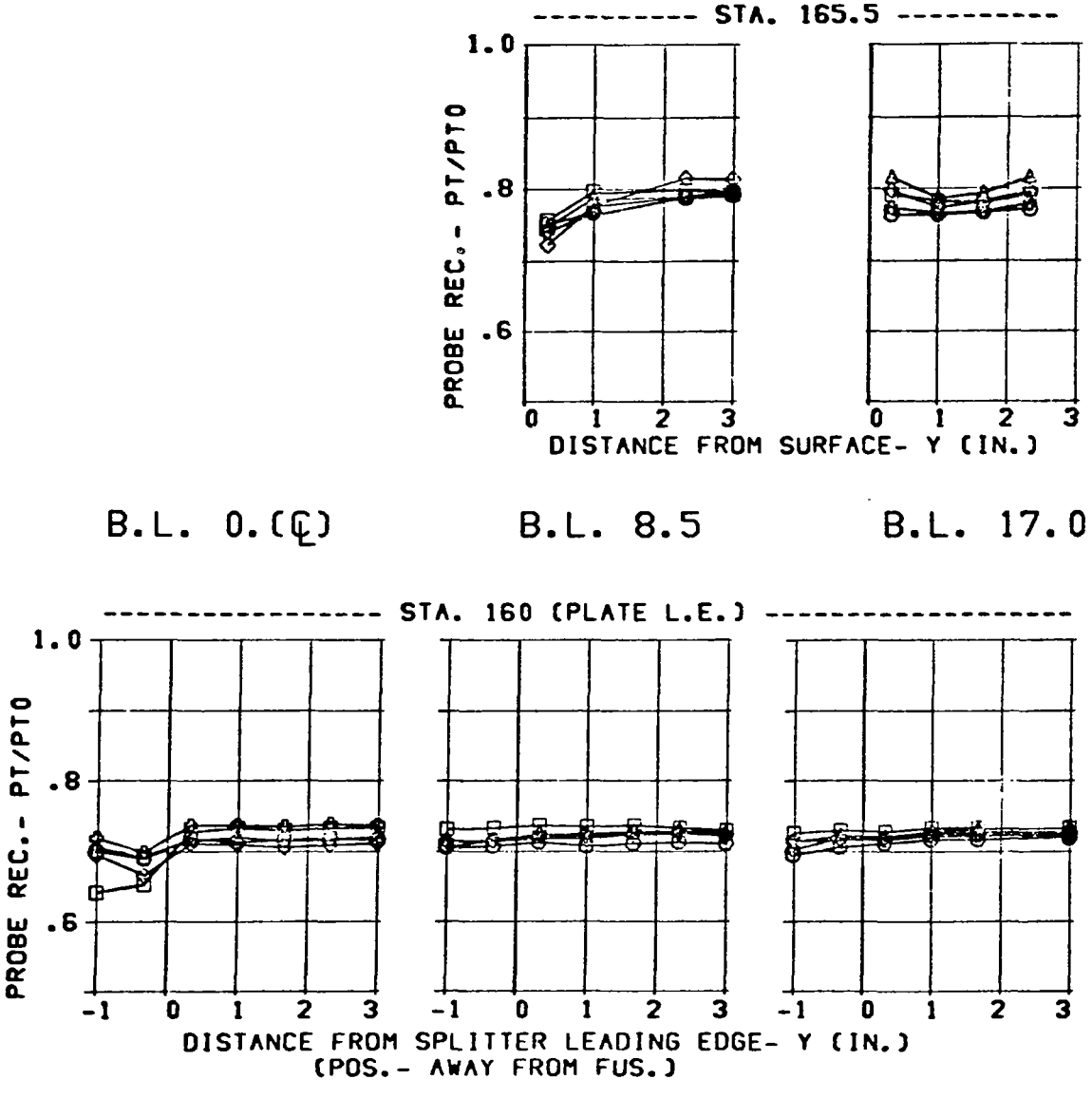

Figure 100 Splitter-Plate Boundary Layer Total Pressure Profiles

CONFIGURATION	CONDITION	SYM.	BETA (DEG)
SPLITTER ONLY	MACH = 1.96	○	5.
3.65 IN. DIV. HT.	ALPHA= 6.	□	0.
NOSE BOOM ON		△	-5.
FUS. RAKES OFF		◇	-10.

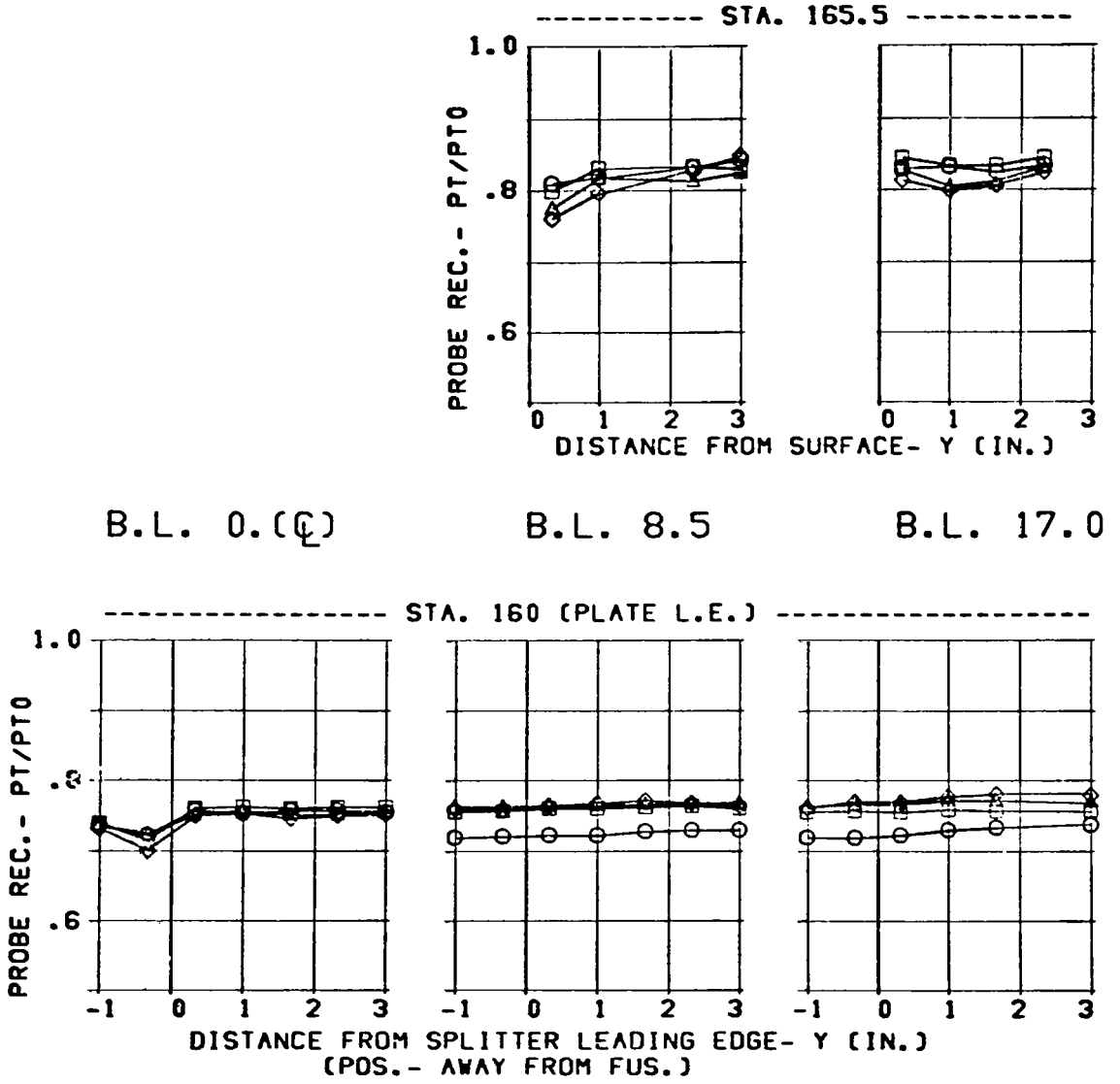

Figure 101 Splitter-Plate Boundary Layer Total Pressure Profiles

CONFIGURATION	CONDITION	SYM.	BETA (DEG)
SPLITTER ONLY	MACH = 1.96	○	5.
3.65 IN. DIV. HT.	ALPHA= 10.	□	0.
NOSE BOOM ON		△	-5.
FUS. RAKES OFF		◇	-10.

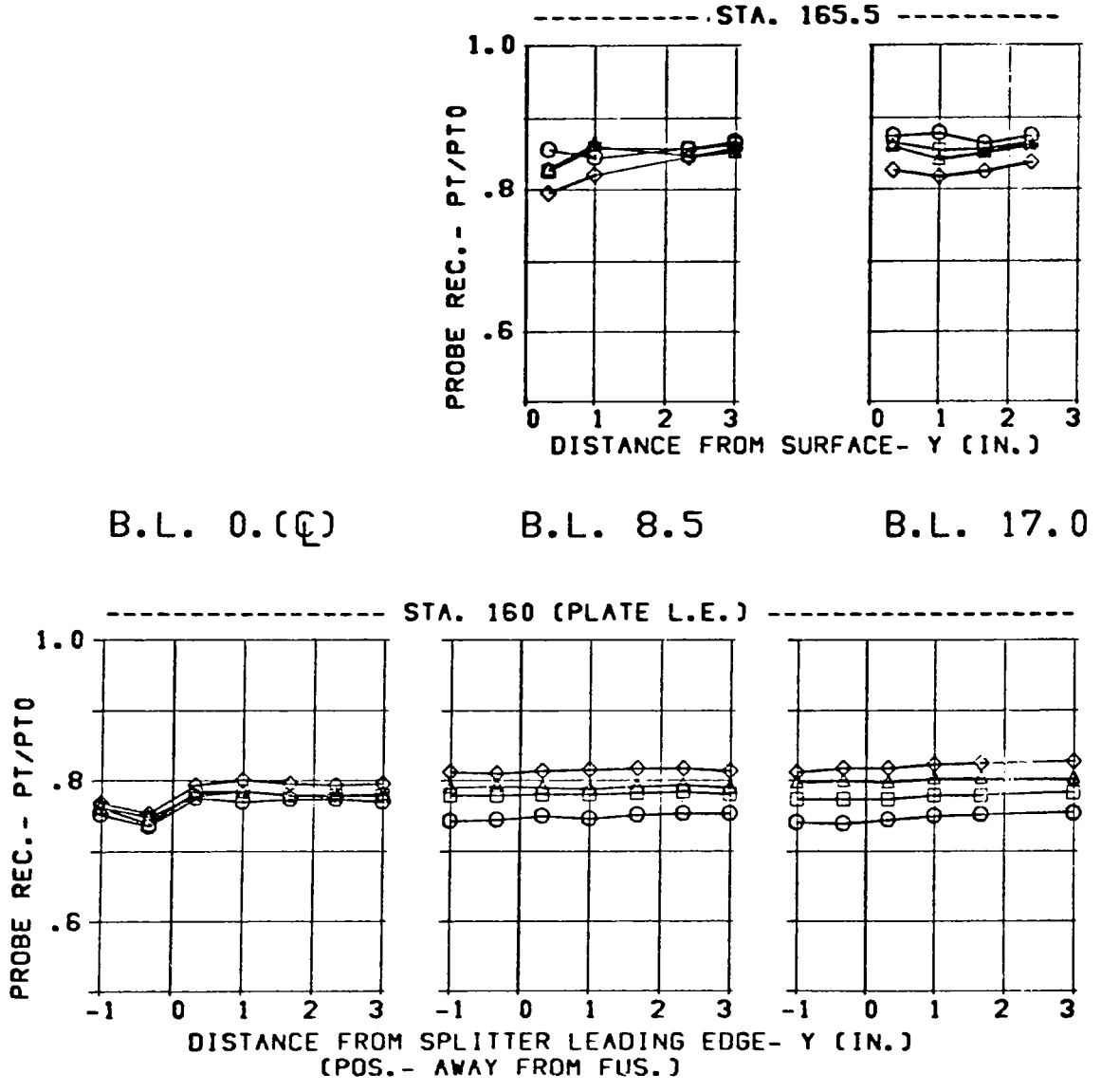

Figure 102 Splitter-Plate Boundary Layer Total Pressure Profiles

CONFIGURATION	CONDITION	SYM.	BETA (DEG)
C13	MACH = .89	□	0.
3.65 IN. DIV. HT.	ALPHA= -9.	△	-5.
NOSE BOOM ON	WC2 = 231.		

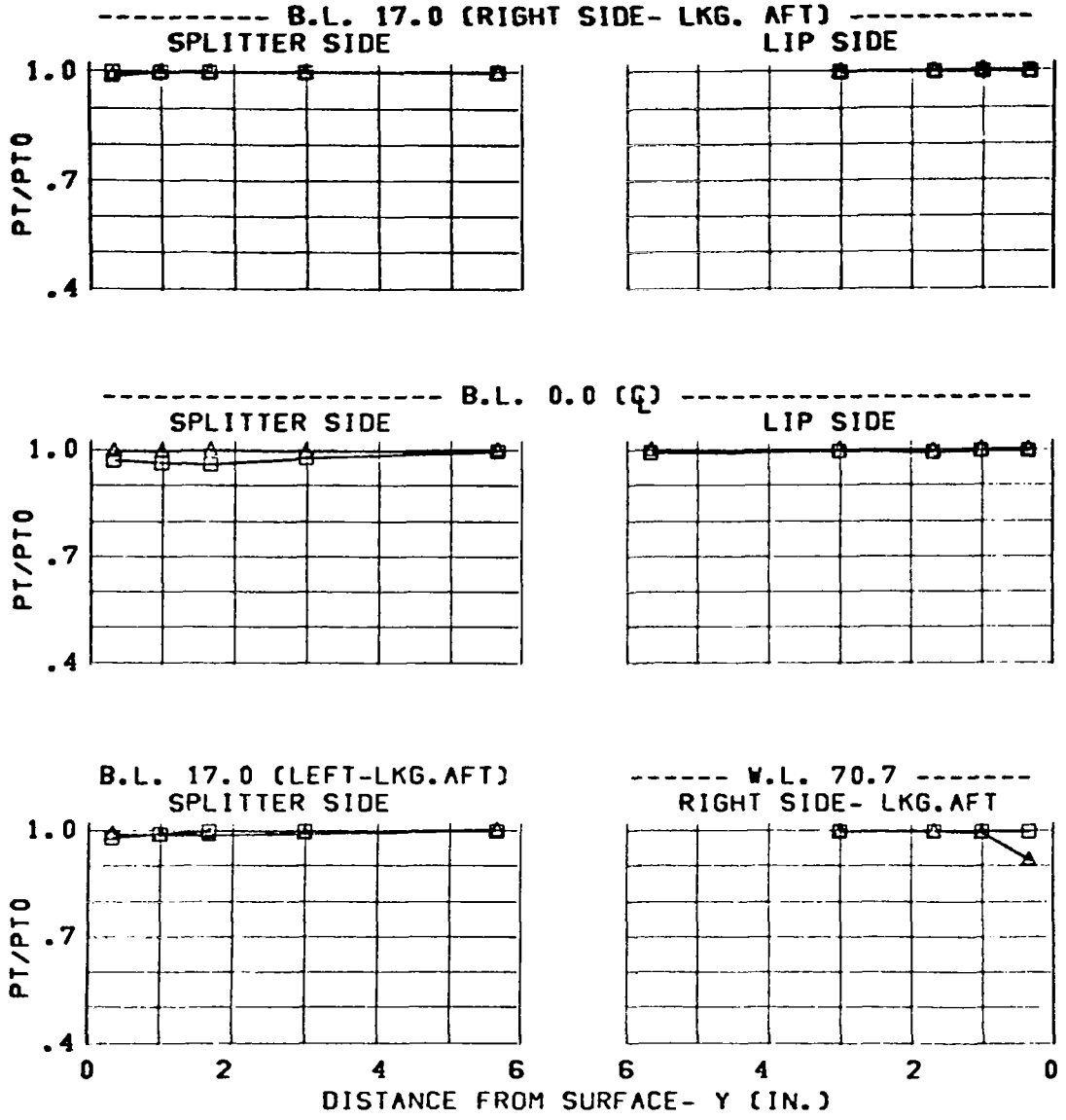

Figure 103 Inlet Configuration C13 Throat Total-Pressure Profiles

CONFIGURATION	CONDITION	SYM.	BETA (DEG)
C13	MACH = .89	□	0.
3.65 IN. DIV. HT.	ALPHA= -5.	△	-5.
NOSE BOOM ON	WC2 = 233.	◇	-10.

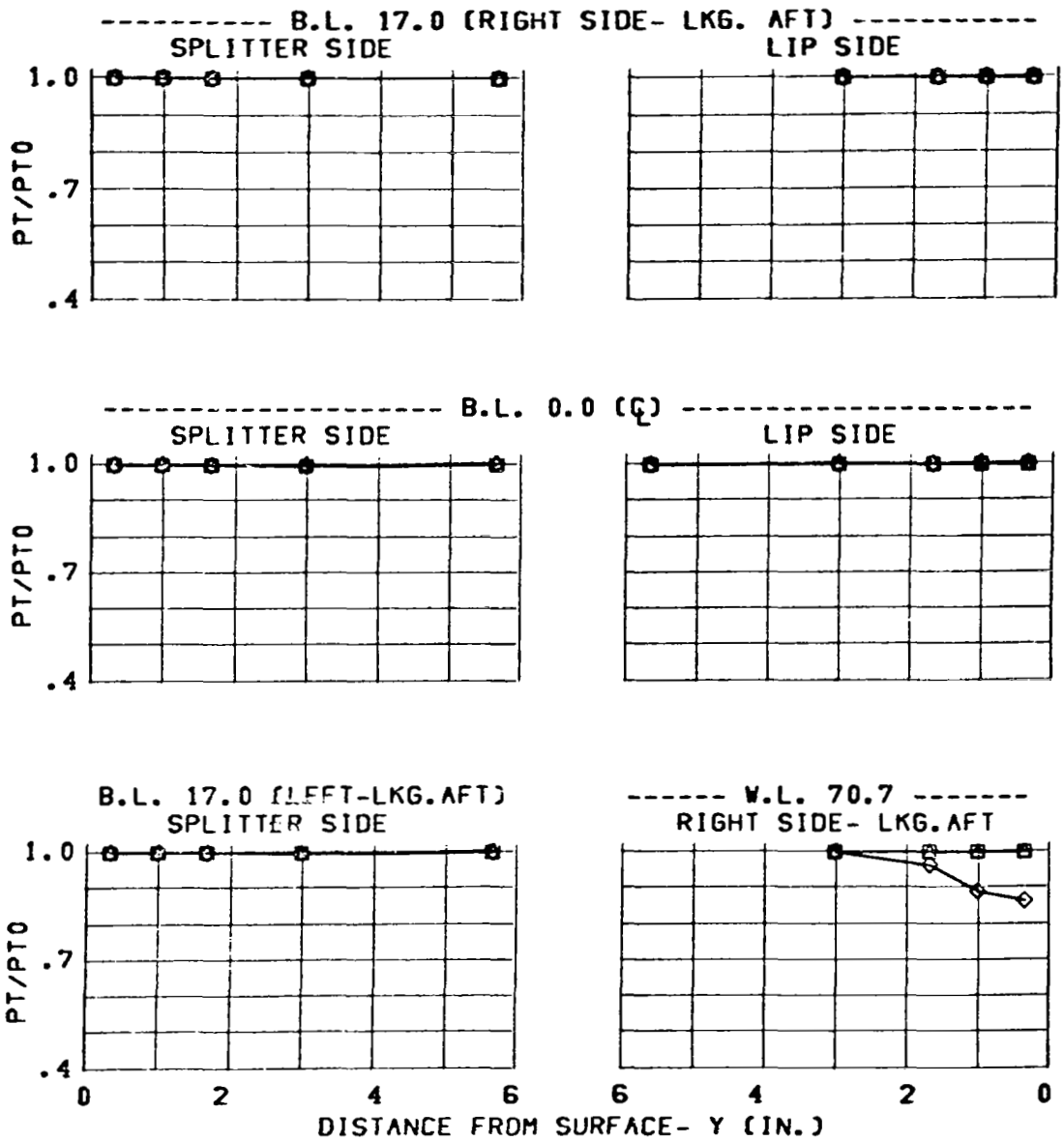

Figure 104 Inlet Configuration C13 Throat Total-Pressure Profiles

CONFIGURATION	CONDITION	SYM.	BETA (DEG)
C13	MACH = .90	□	0.
3.65 IN. DIV. HT.	ALPHA= 1.	△	-5.
NOSE BOOM ON	WC2 = 233.	◇	-10.

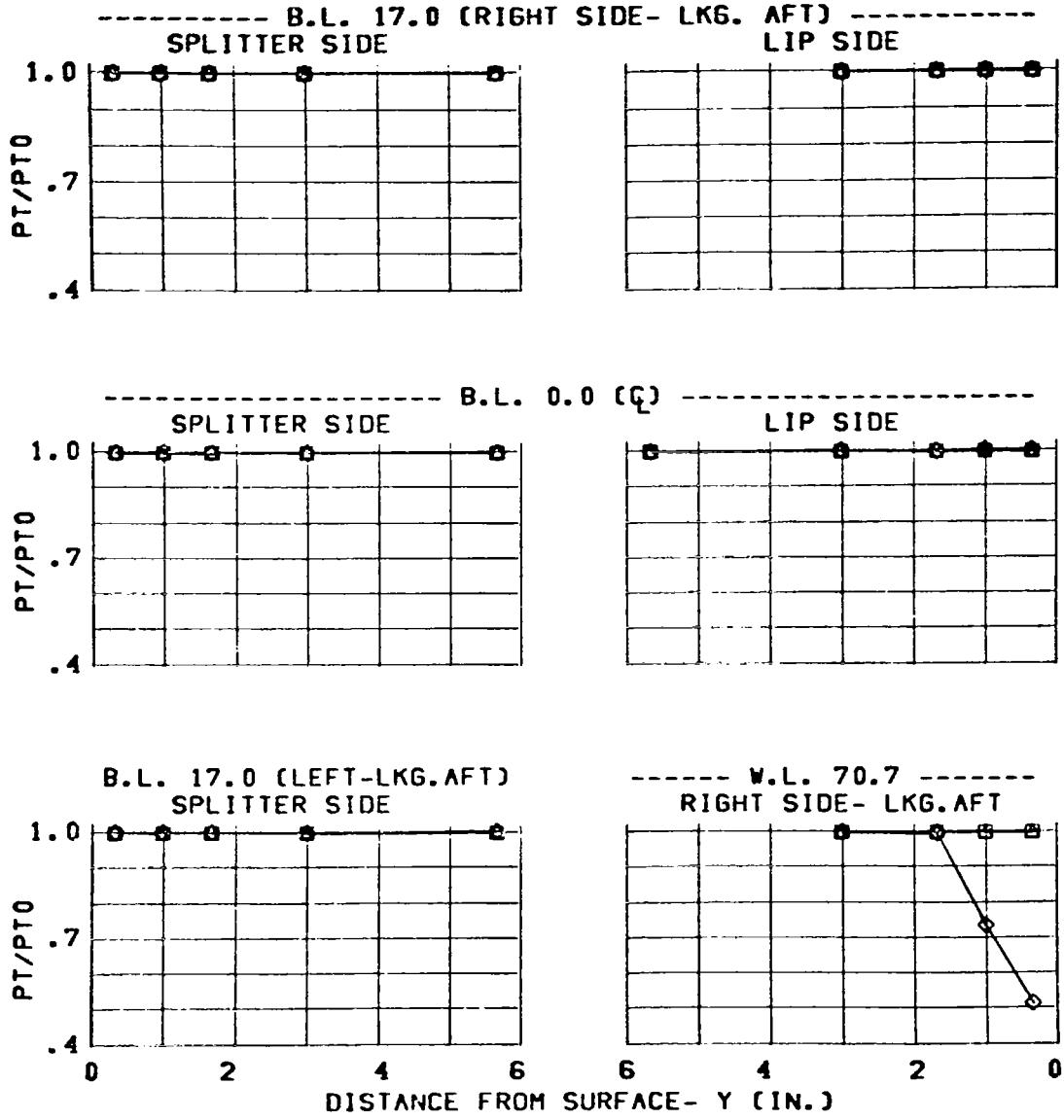

Figure 105 Inlet Configuration C13 Throat Total-Pressure Profiles

CONFIGURATION	CONDITION	SYM.	BETA (DEG)
C13	MACH = .89	□	0.
3.65 IN. DIV. HT.	ALPHA= 20.	△	-5.
NOSE BOOM ON	WC2 = 233.	◇	-10.

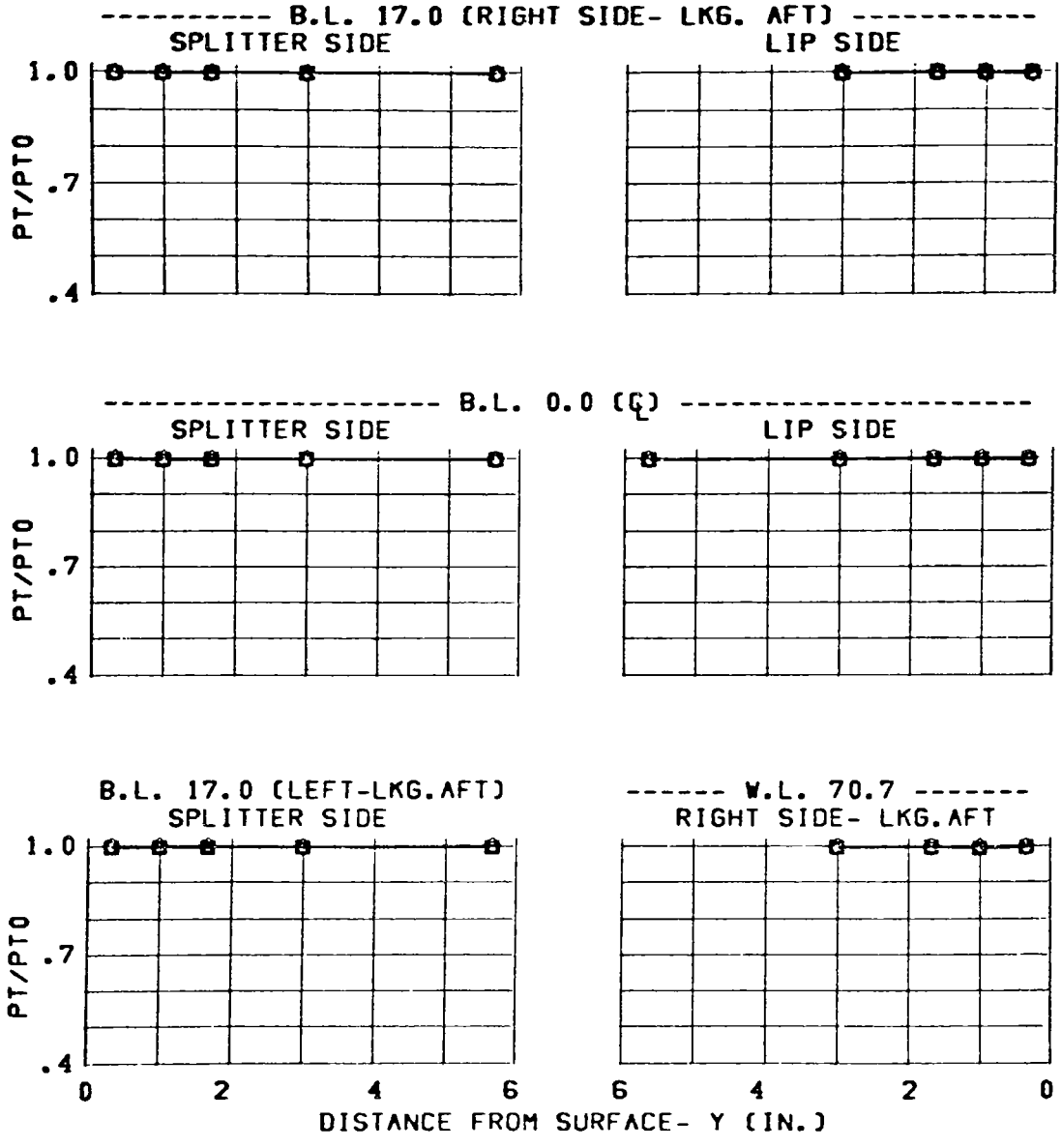

Figure 106 Inlet Configuration C13 Throat Total-Pressure Profiles

CONFIGURATION	CONDITION	SYM.	BETA (DEG)
C13	MACH = 1.57	□	0.
3.65 IN. DIV. HT.	ALPHA= -5.	△	-5.
NOSE BOOM ON	WC2 = 218.	◇	-10.

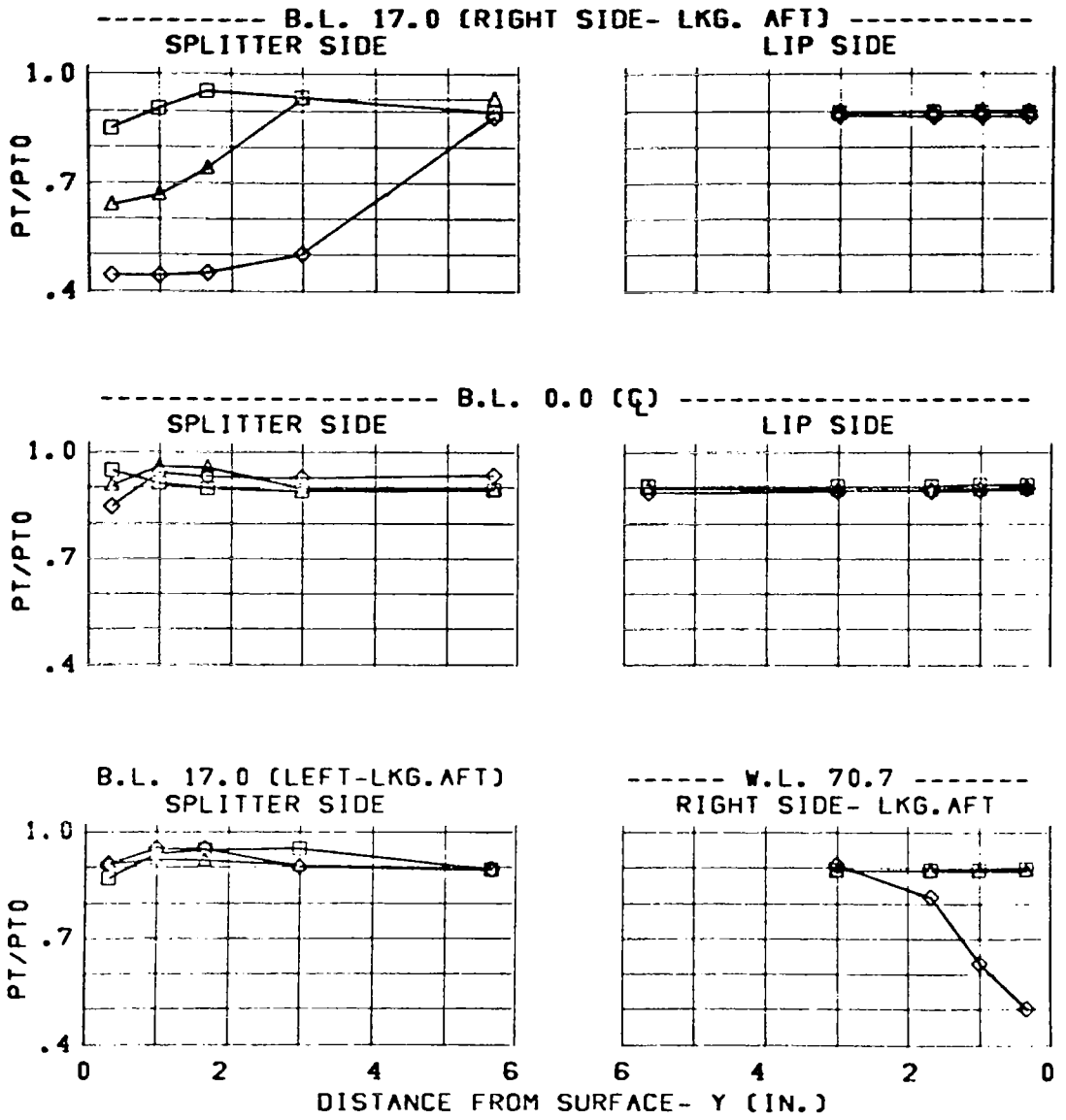

Figure 107 Inlet Configuration C13 Throat Total-Pressure Profiles

CONFIGURATION	CONDITION	SYM.	BETA (DEG)
C13	MACH = 1.57	□	0.
3.65 IN. DIV. HT.	ALPHA= 1.	△	-5.
NOSE BOOM ON	WC2 = 217.	◇	-10.

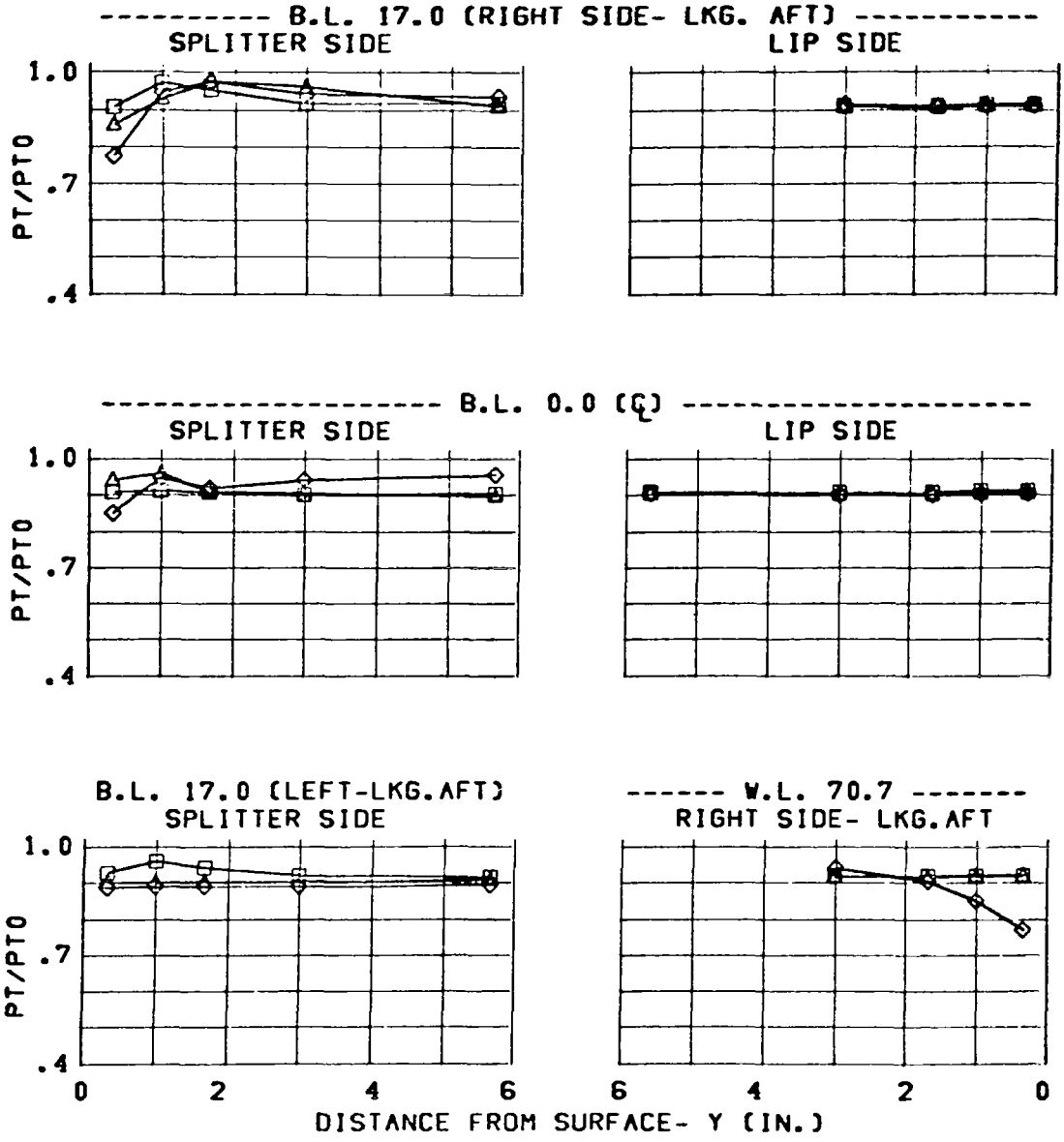

Figure 108 Inlet Configuration C13 Throat Total-Pressure Profiles

CONFIGURATION	CONDITION	SYM.	BETA (DEG)
C13	MACH = 1.57	□	0.
3.65 IN. DIV. HT.	ALPHA= 6.	△	-5.
NOSE BOOM ON	WC2 = 217.	◇	-10.

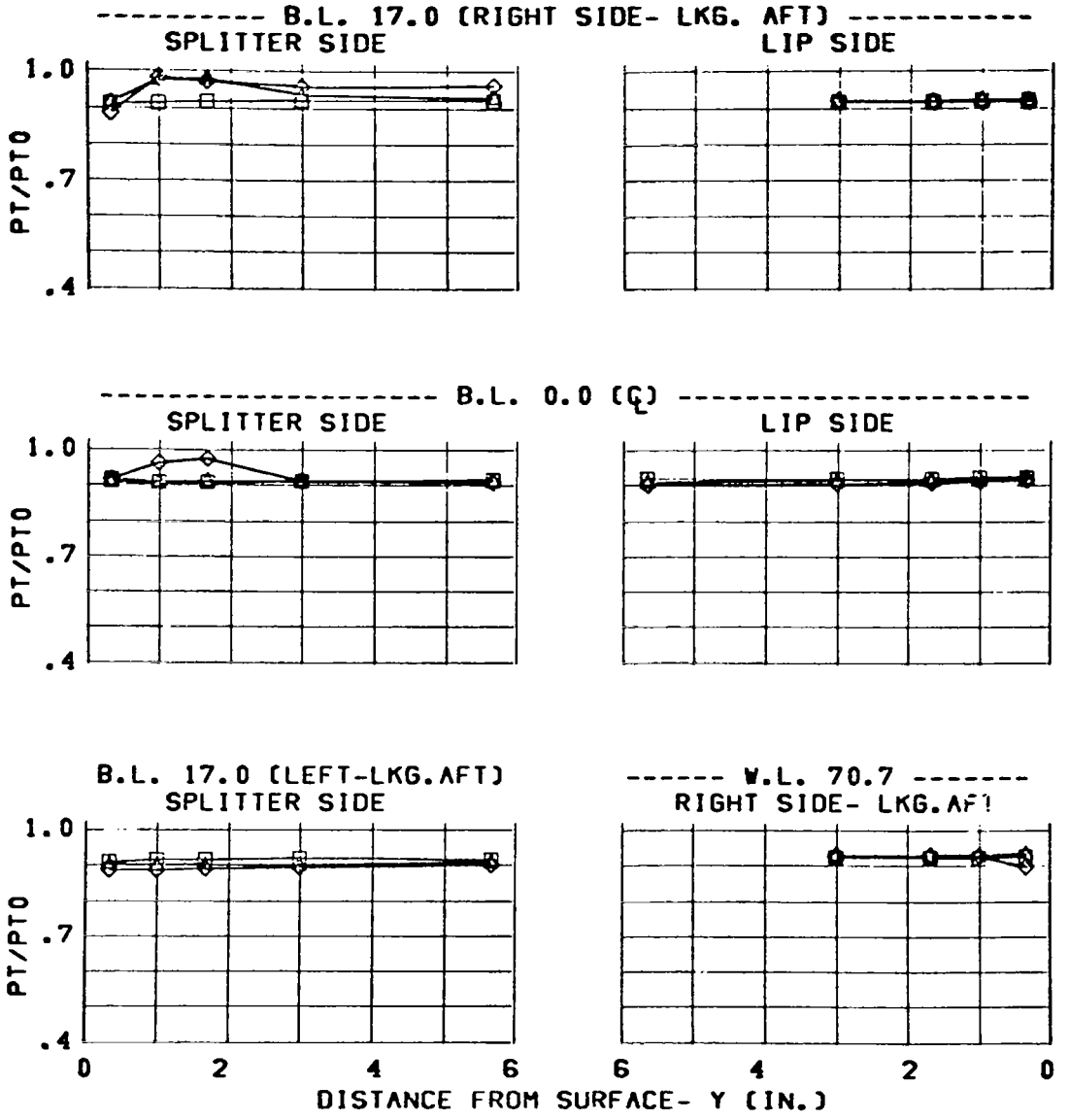

Figure 109 Inlet Configuration C13 Throat Total-Pressure Profiles

CONFIGURATION	CONDITION	SYM.	BETA (DEG)
C13	MACH = 1.57	□	0.
3.65 IN. DIV. HT.	ALPHA= 10.	△	-5.
NOSE BOOM ON	WC2 = 217.	◇	-10.

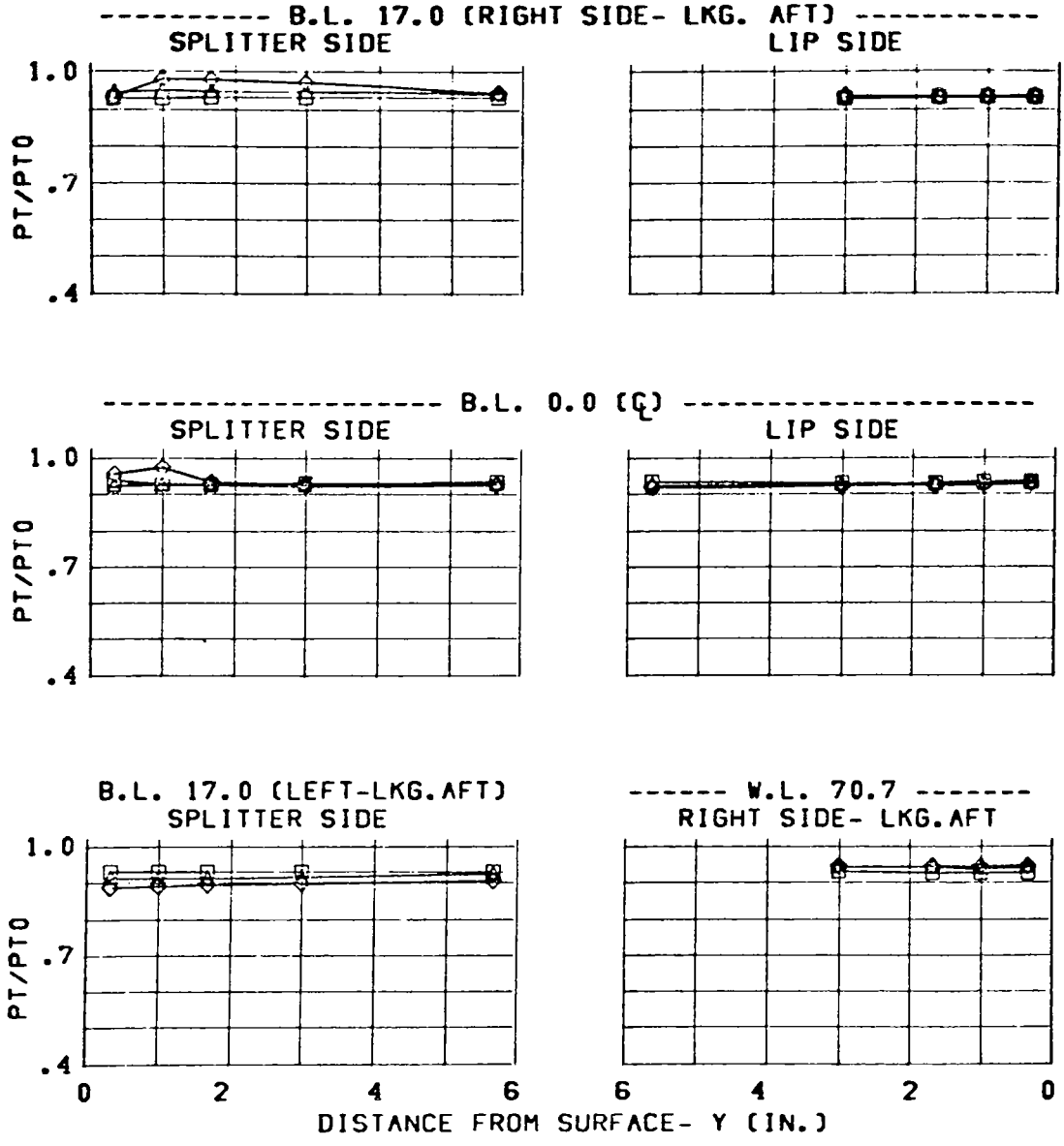

Figure 110 Inlet Configuration C13 Throat Total-Pressure Profiles

CONFIGURATION	CONDITION	SYM.	BETA (DEG)
C13	MACH = 1.56	□	0.
3.65 IN. DIV. HT.	ALPHA= 20.	△	-5.
NOSE BOOM ON	WC2 = 217.	◇	-10.

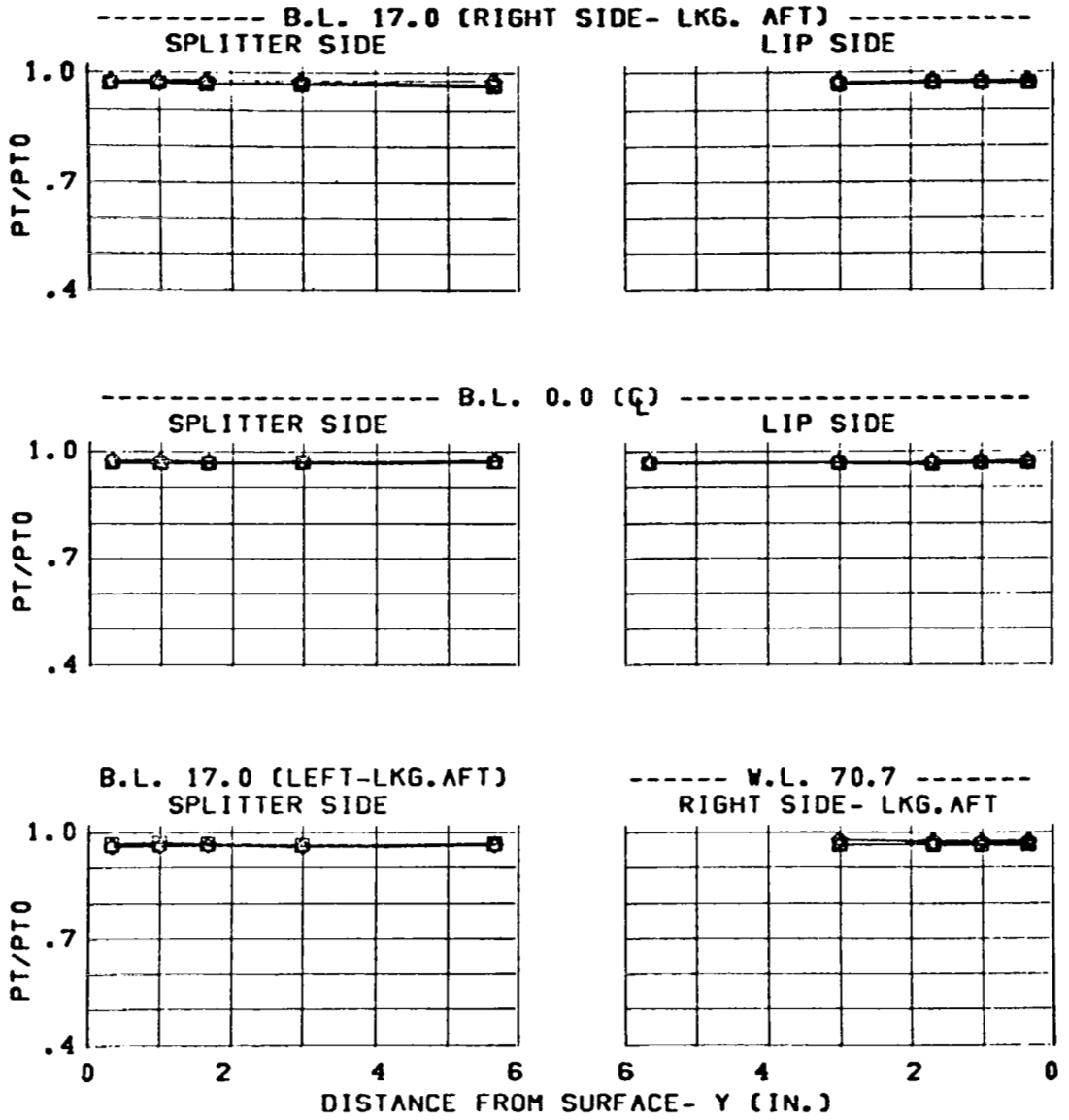

Figure 111 Inlet Configuration C13 Throat Total-Pressure Profiles

CONFIGURATION	CONDITION	SYM.	BETA (DEG)
C13	MACH = 1.96	□	0.
3.65 IN. DIV. HT.	ALPHA= -5.	△	-5.
NOSE BOOM ON	WC2 = 185.		

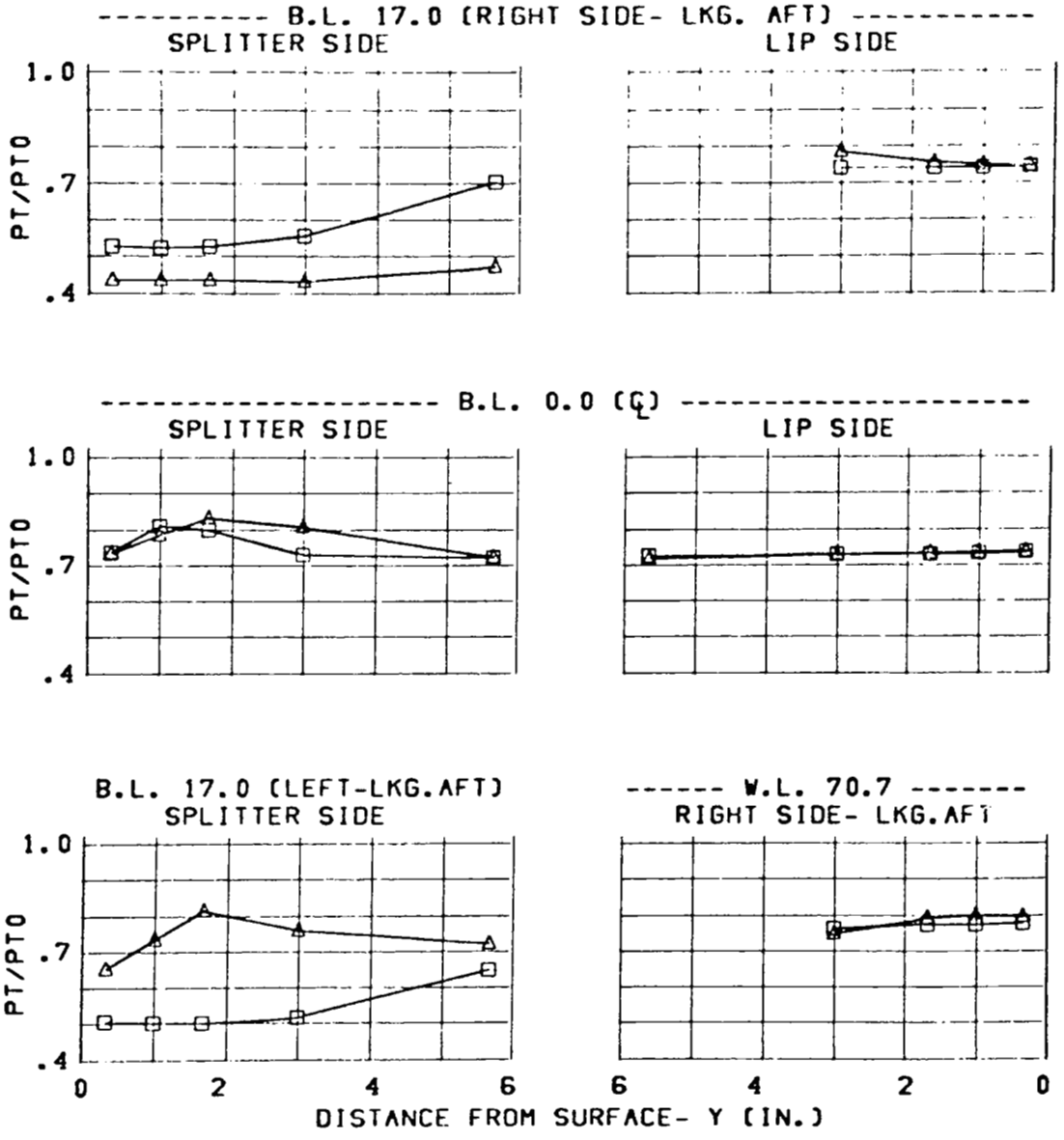

Figure 112 Inlet Configuration C13 Throat Total-Pressure Profiles

CONFIGURATION	CONDITION	SYM.	BETA (DEG)
C13	MACH = 1.96	□	0.
3.65 IN. DIV. HT.	ALPHA= 1.	△	-5.
NOSE BOOM ON	WC2 = 184.	◇	-10.

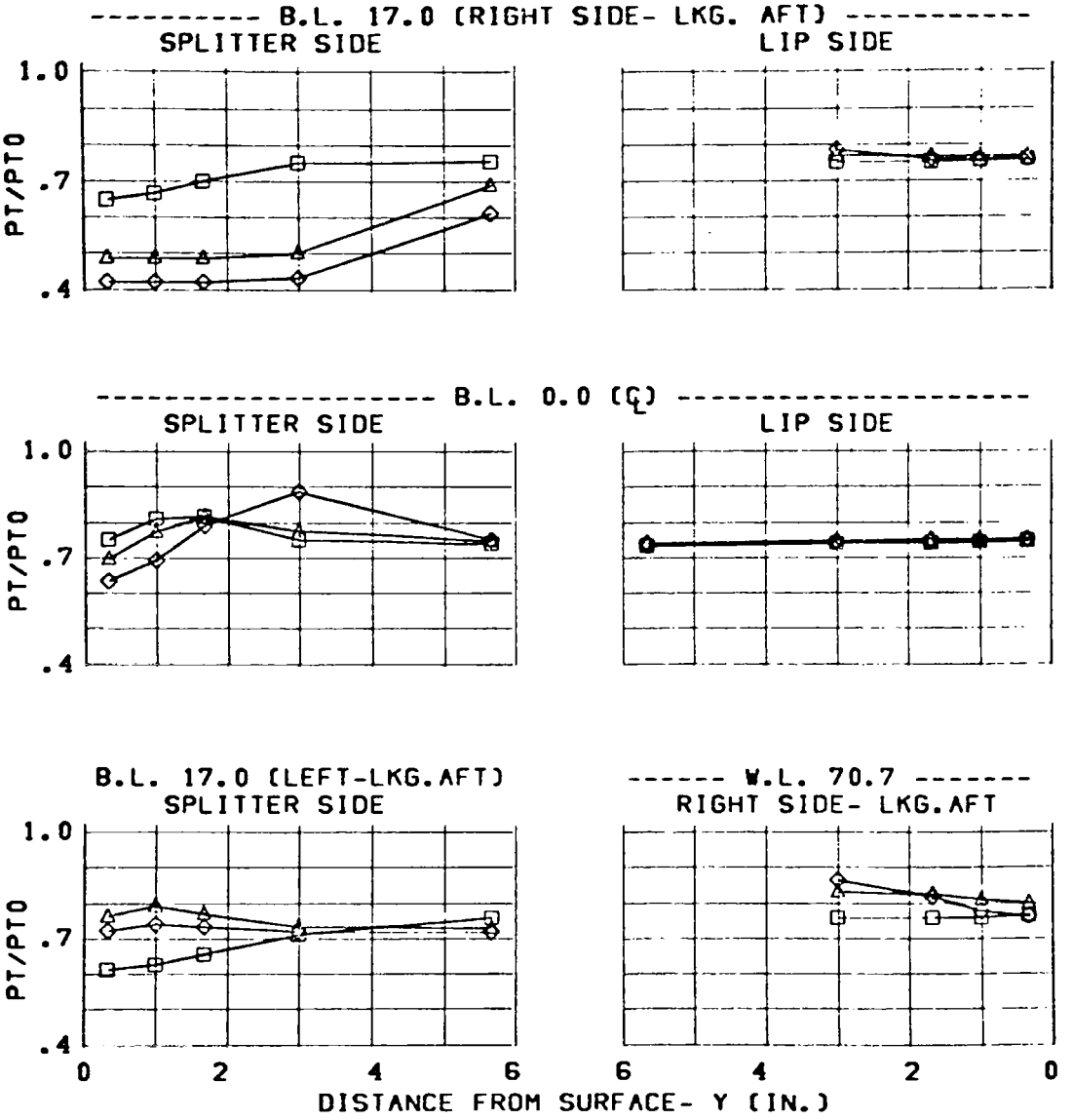

Figure 113 Inlet Configuration C13 Throat Total-Pressure Profiles

CONFIGURATION	CONDITION	SYM.	BETA (DEG)
C13	MACH = 1.96	□	0.
3.65 IN. DIV. HT.	ALPHA= 6.	△	-5.
NOSE BOOM ON	WC2 = 184.	◇	-10.

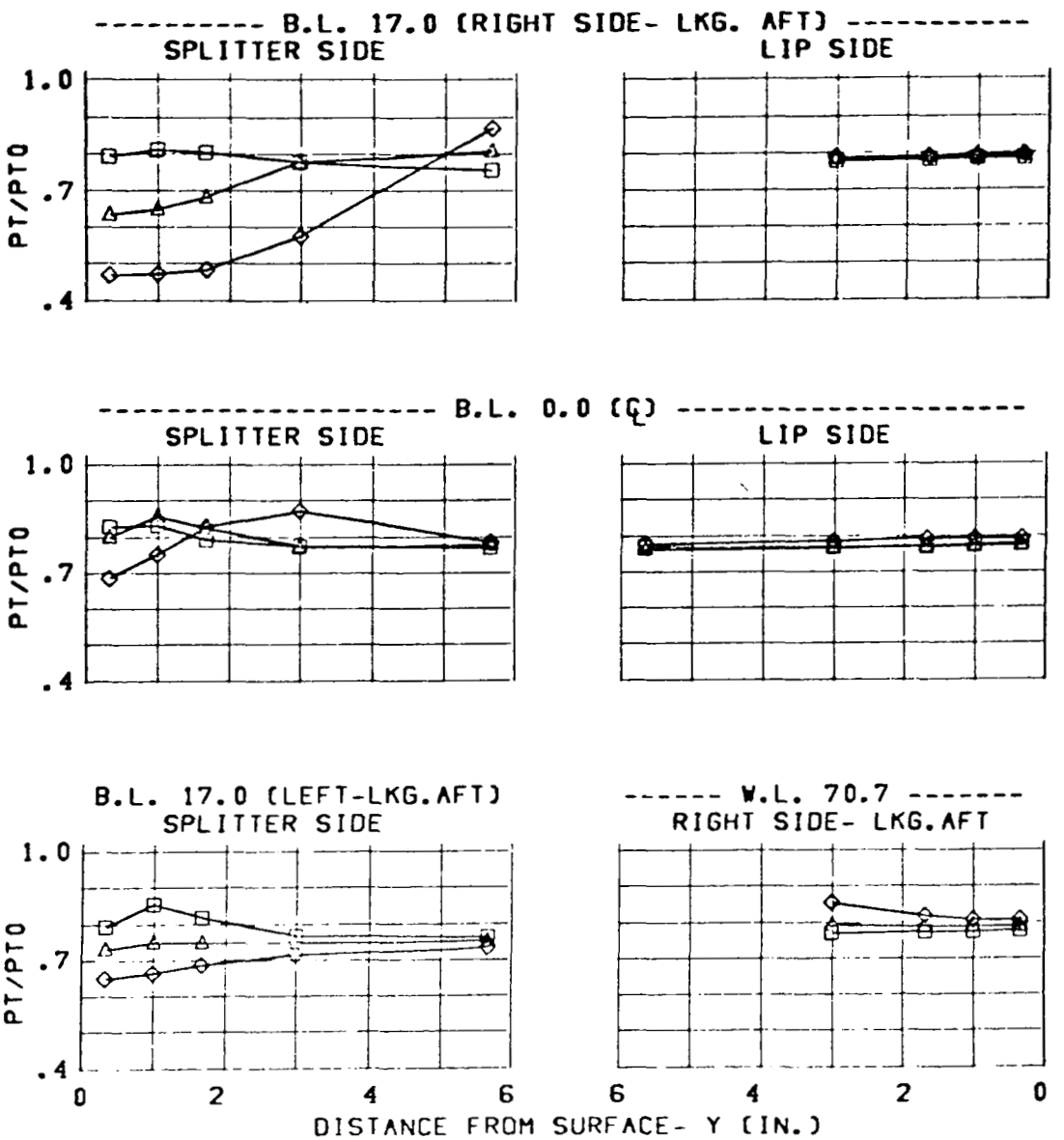

Figure 114 Inlet Configuration C13 Throat Total-Pressure Profiles

CONFIGURATION	CONDITION	SYM.	WC2(LBS/SEC)
C13	MACH = 1.96	○	197.
3.65 IN. DIV. HT.	ALPHA= -5.	□	184.
NOSE BOOM ON	BETA = 0.	△	172.
		◇	155.
		×	141.

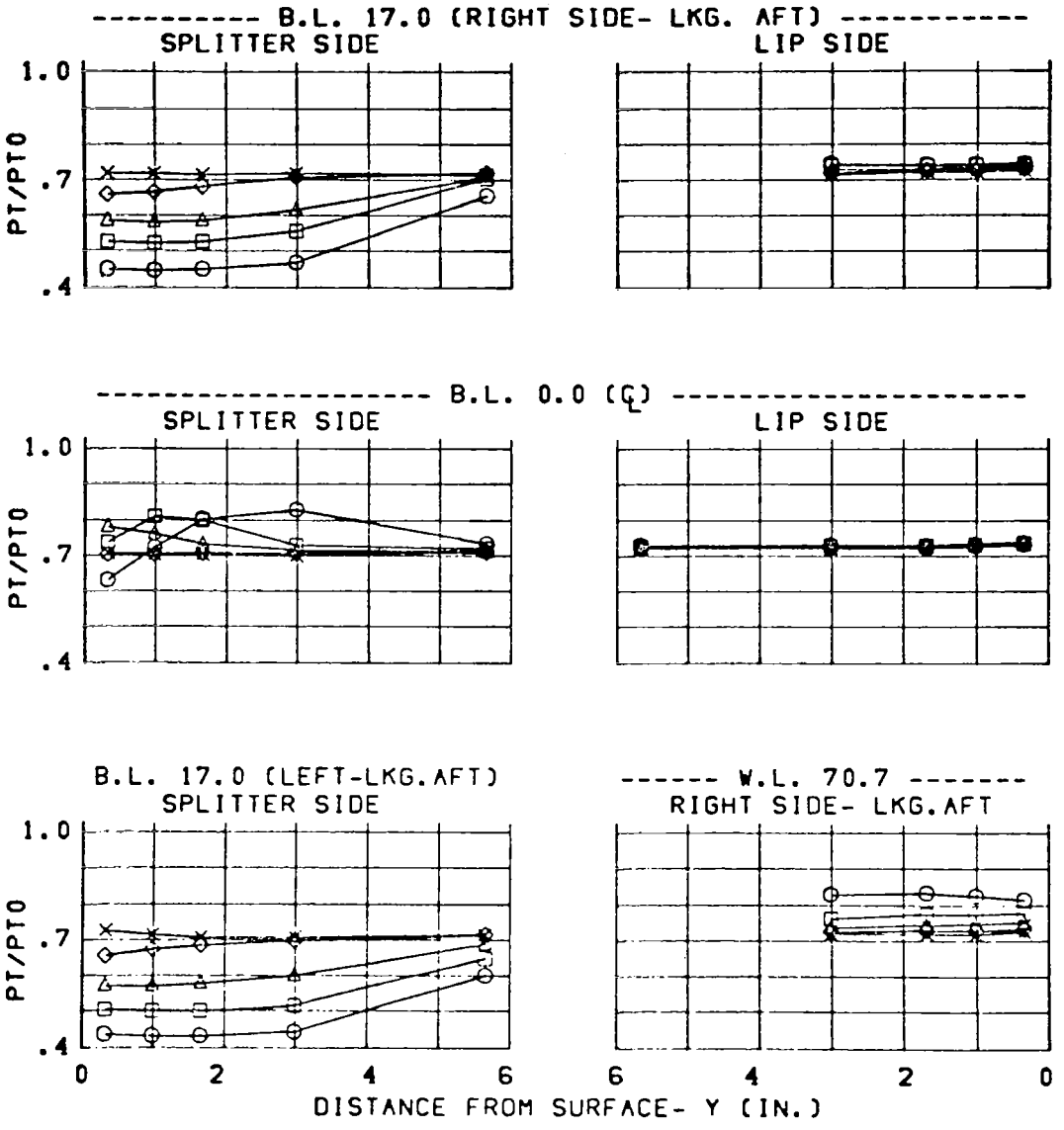

Figure 115 Inlet Configuration C13 Throat Total-Pressure Profiles

CONFIGURATION	CONDITION	SYM.	WC2(LBS/SEC)
C13	MACH = 1.96	○	196.
3.65 IN. DIV. HT.	ALPHA= 1.	□	184.
NOSE BOOM ON	BETA = 0.	△	172.
		◇	155.
		×	141.

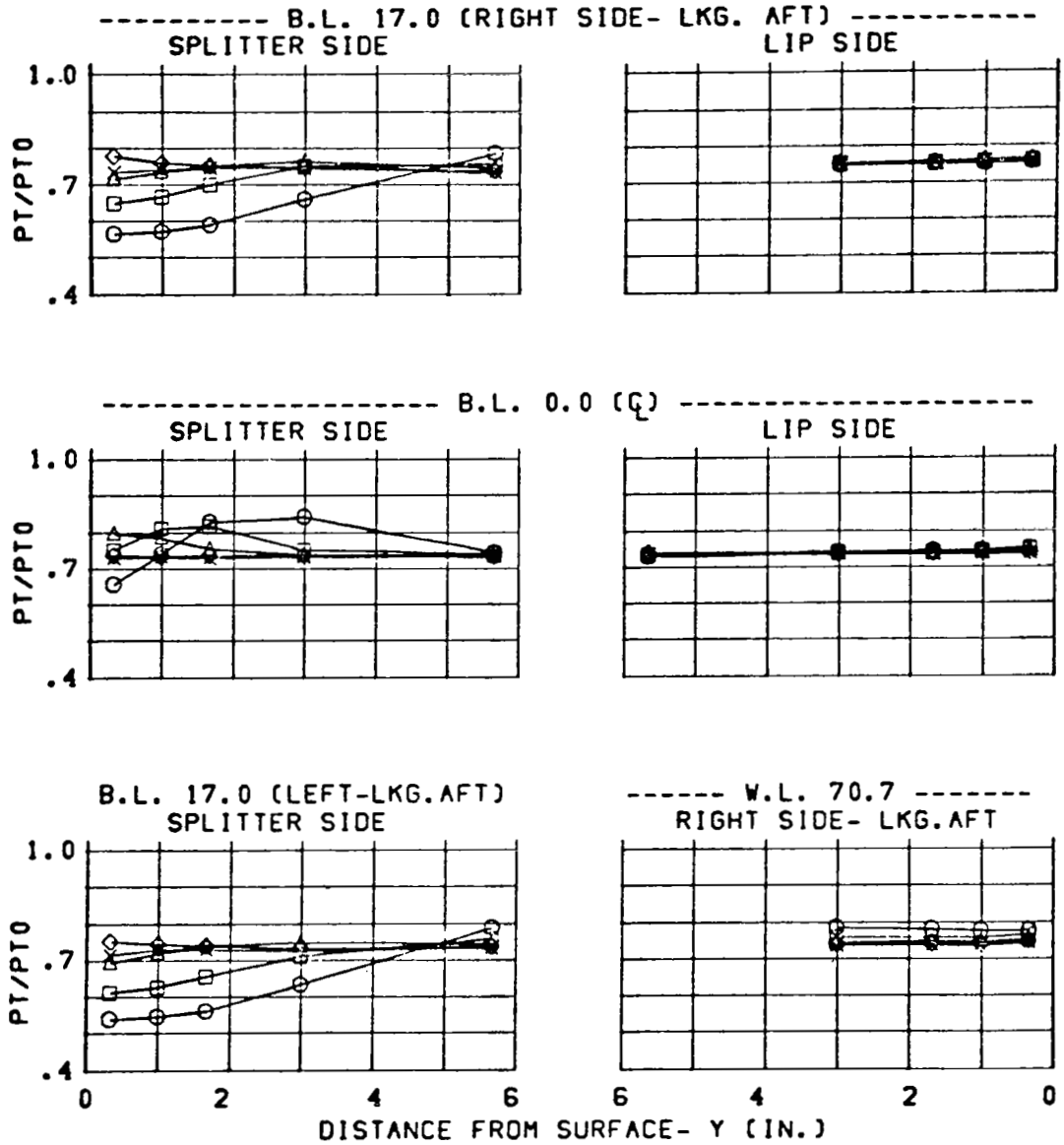

Figure 116 Inlet Configuration C13 Throat Total-Pressure Profiles

CONFIGURATION	CONDITION	SYM.	WC2(LBS/SEC)
C13	MACH = 1.96	○	197.
3.65 IN. DIV. HT.	ALPHA= 6.	□	184.
NOSE BOOM ON	BETA = 0.	△	172.
		◇	155.
		×	141.

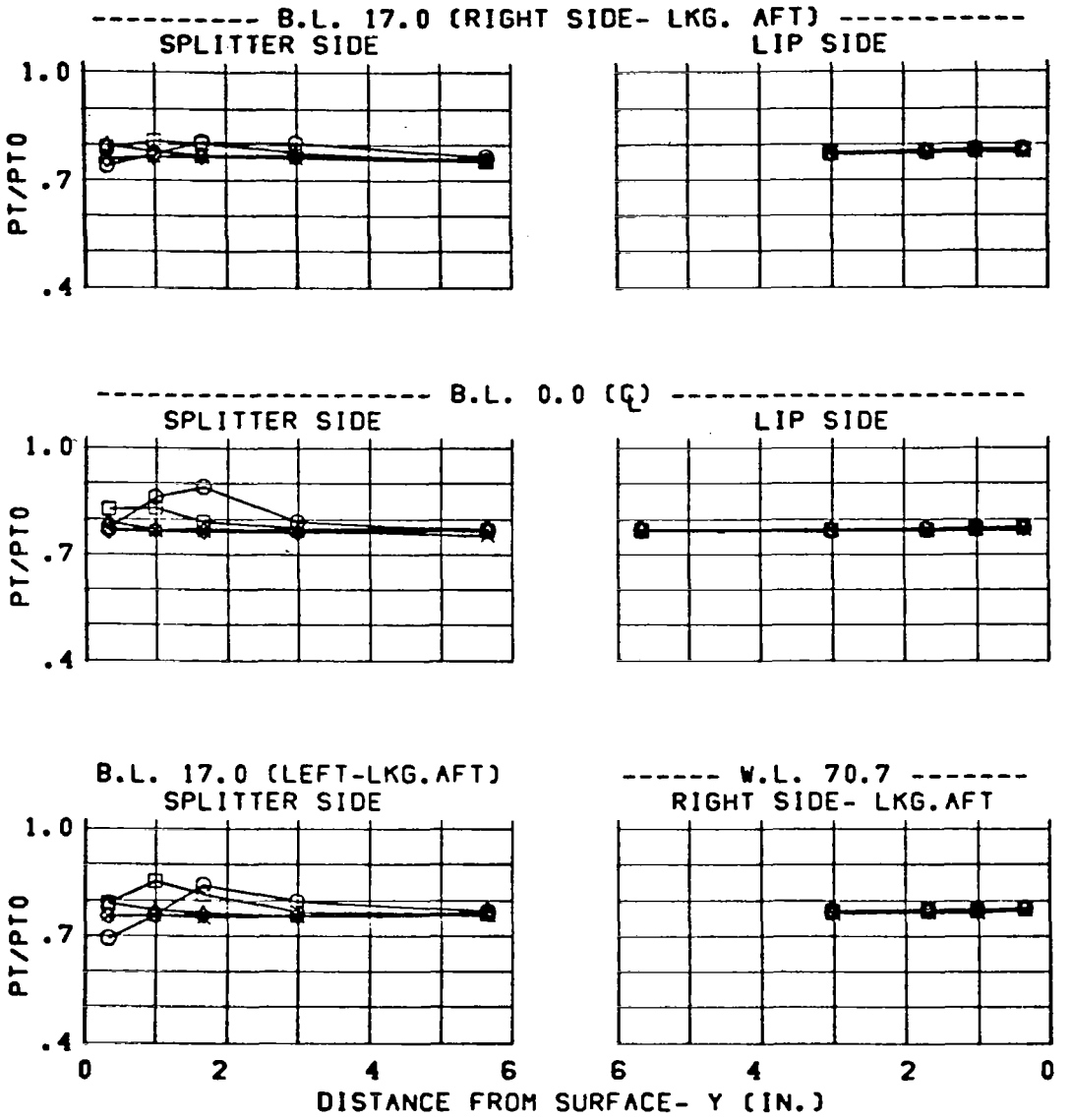

Figure 117 Inlet Configuration C13 Throat Total-Pressure Profiles

CONFIGURATION	CONDITION	SYM.	WC2(LBS/SEC)
C13	MACH = 1.96	○	197.
3.65 IN. DIV. HT.	ALPHA= -5.	□	185.
NOSE BOOM ON	BETA = -5.	△	172.
		◇	155.
		×	141.

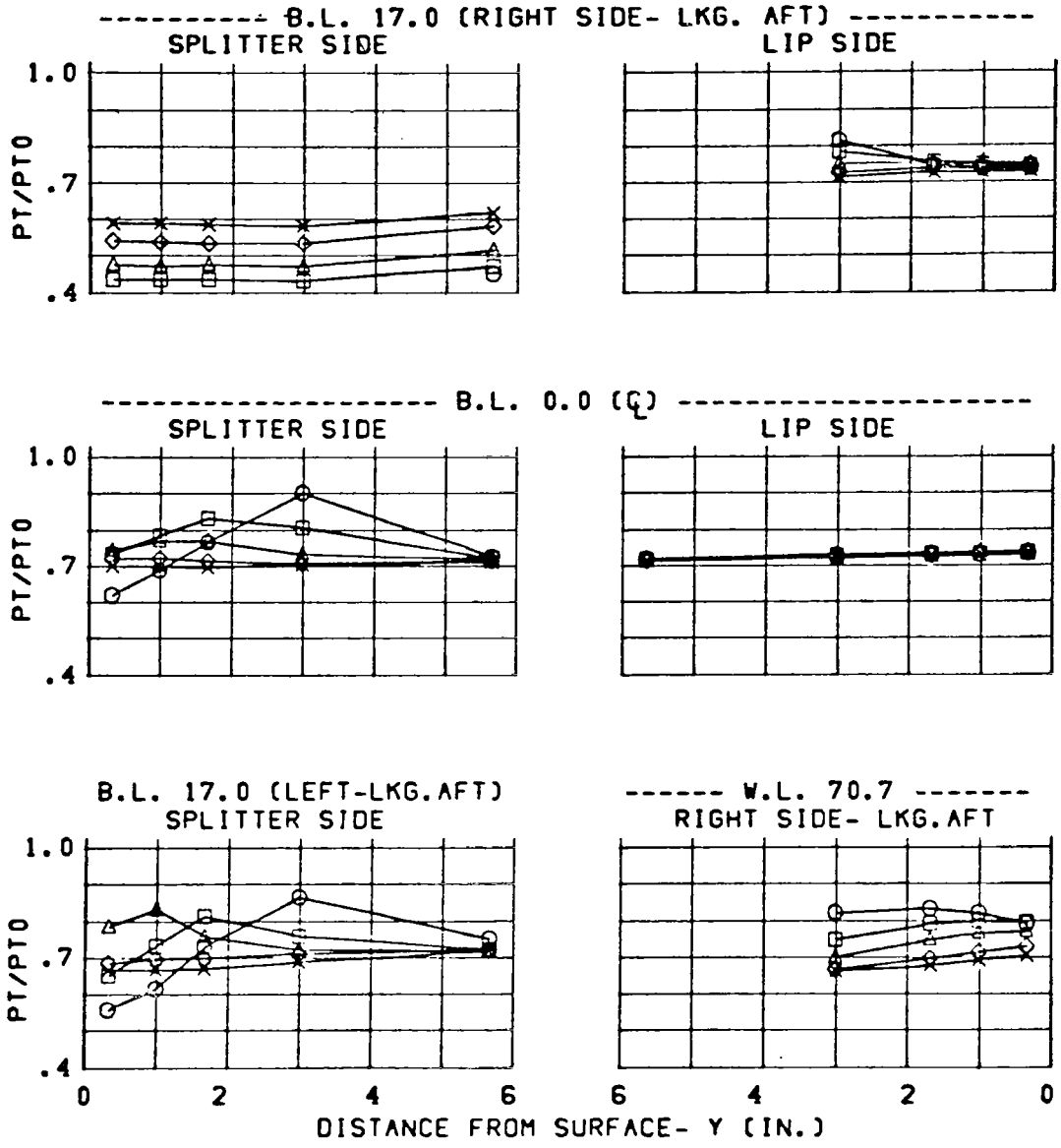

Figure 118 Inlet Configuration C13 Throat Total-Pressure Profiles

CONFIGURATION	CONDITION	SYM.	WC2(LBS/SEC)
C13	MACH = 1.96	○	197.
3.65 IN. DIV. HT.	ALPHA= 1.	□	184.
NOSE BOOM ON	BETA = -5.	△	172.
		◇	155.
		×	141.

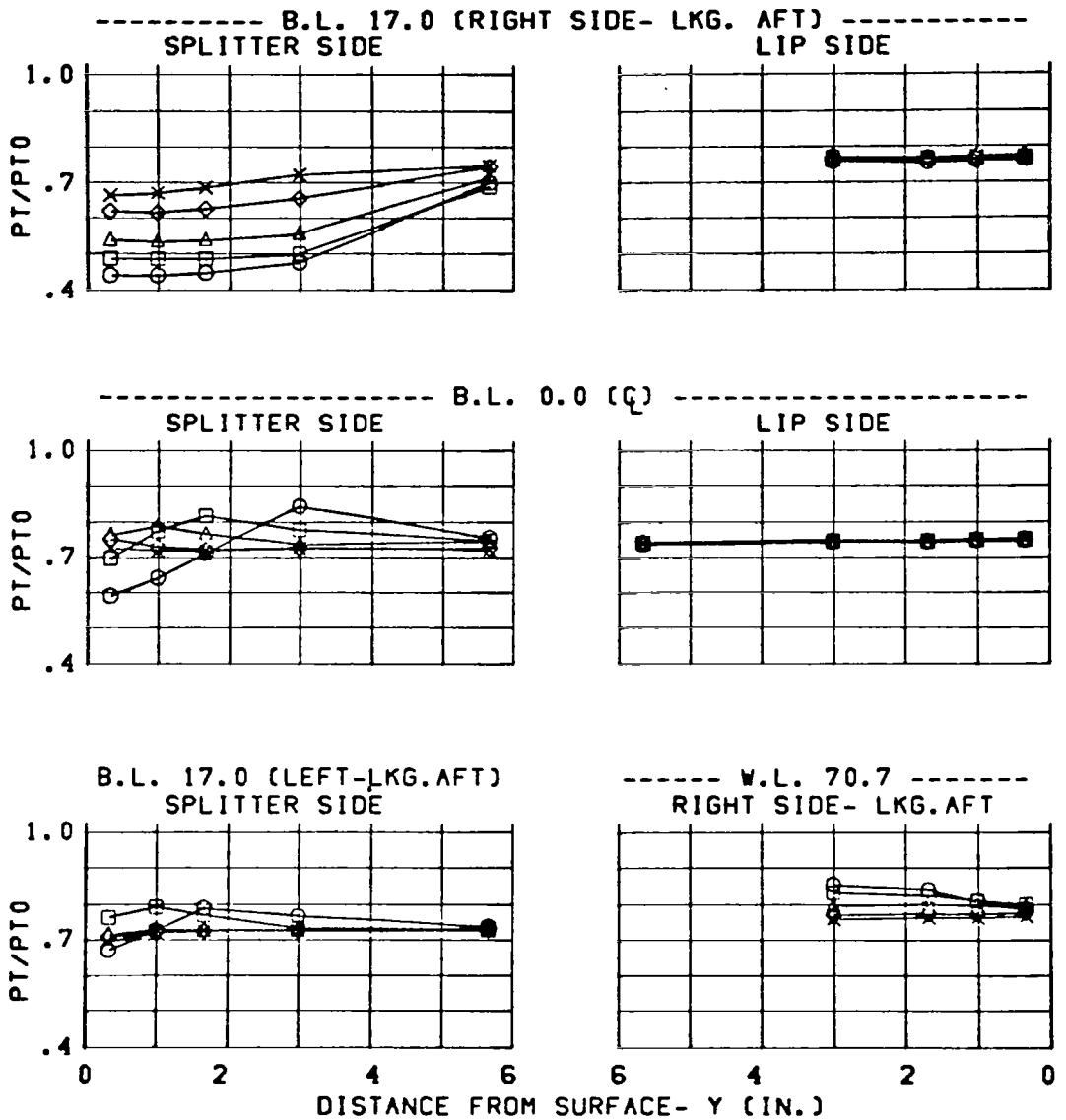

Figure 119 Inlet Configuration C13 Throat Total-Pressure Profiles

CONFIGURATION	CONDITION	SYM.	WC2(LBS/SEC)
C13	MACH = 1.96	○	197.
3.65 IN. DIV. HT.	ALPHA= 6.	□	184.
NOSE BOOM ON	BETA = -5.	△	172.
		◇	155.
		×	141.

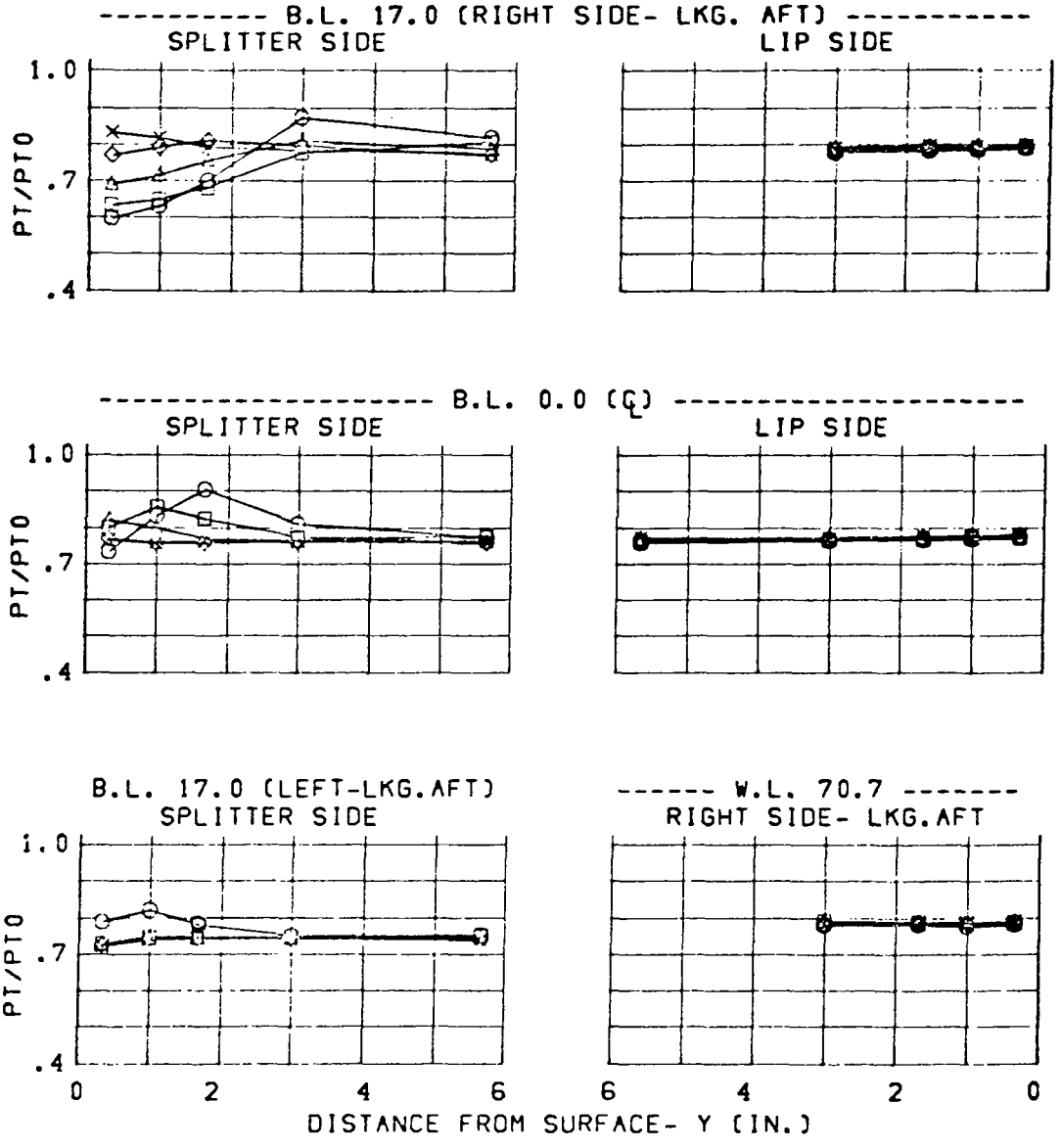

Figure 120 Inlet Configuration C13 Throat Total-Pressure Profiles

CONFIGURATION	CONDITION	SYM.	WC2(LBS/SEC)
C13	MACH = 1.96	○	197.
3.65 IN. DIV. HT.	ALPHA= 1.	□	184.
NOSE BOOM ON	BETA = -10.	△	172.
		◇	155.
		×	141.

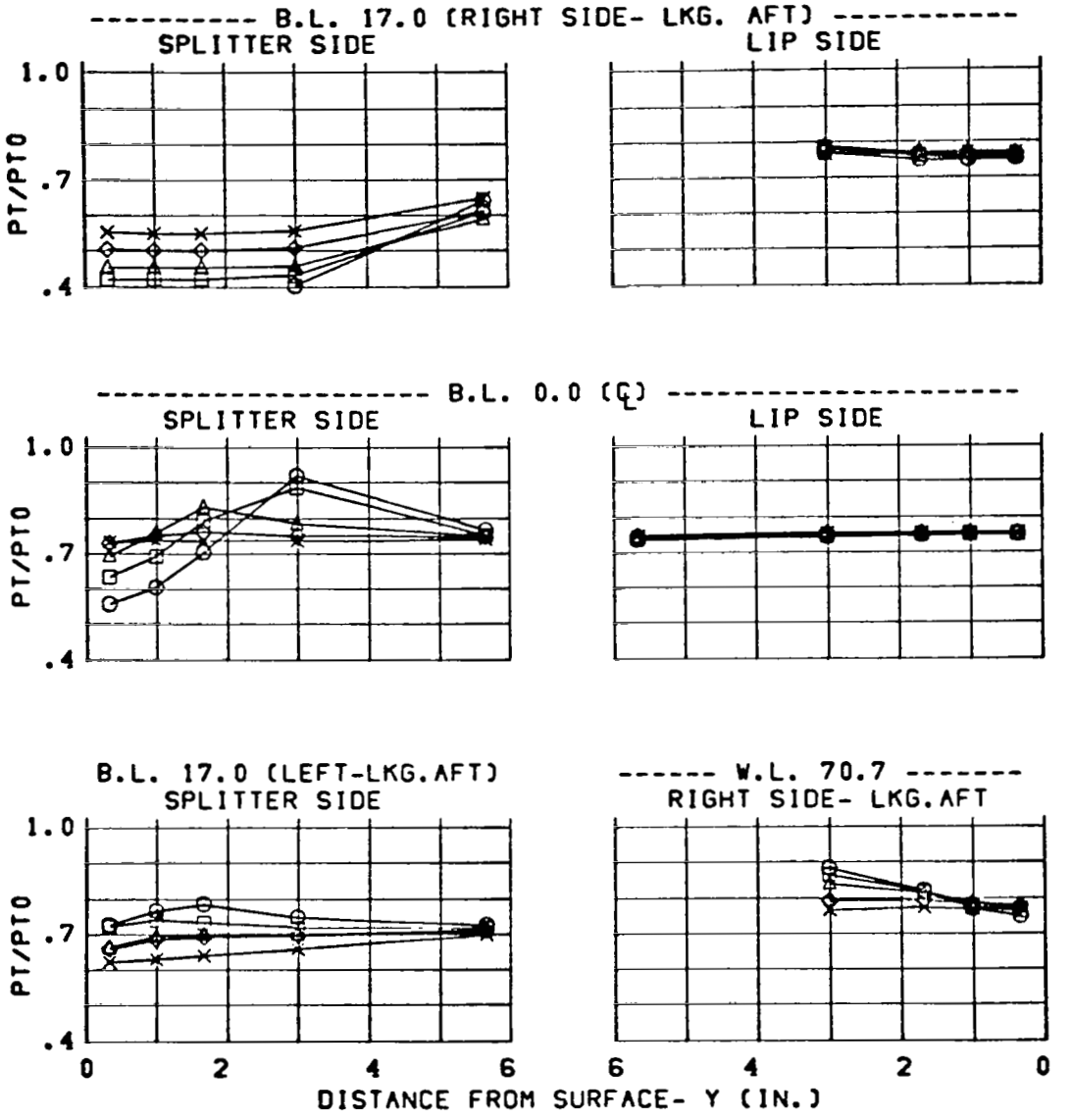

Figure 121 Inlet Configuration C13 Throat Total-Pressure Profiles

CONFIGURATION	CONDITION	SYM.	WC2(LBS/SEC)
C13	MACH = 1.95	○	197.
3.65 IN. DIV. HT.	ALPHA= 6.	□	184.
NOSE BOOM ON	BETA = -10.	△	172.
		◇	155.
		×	141.

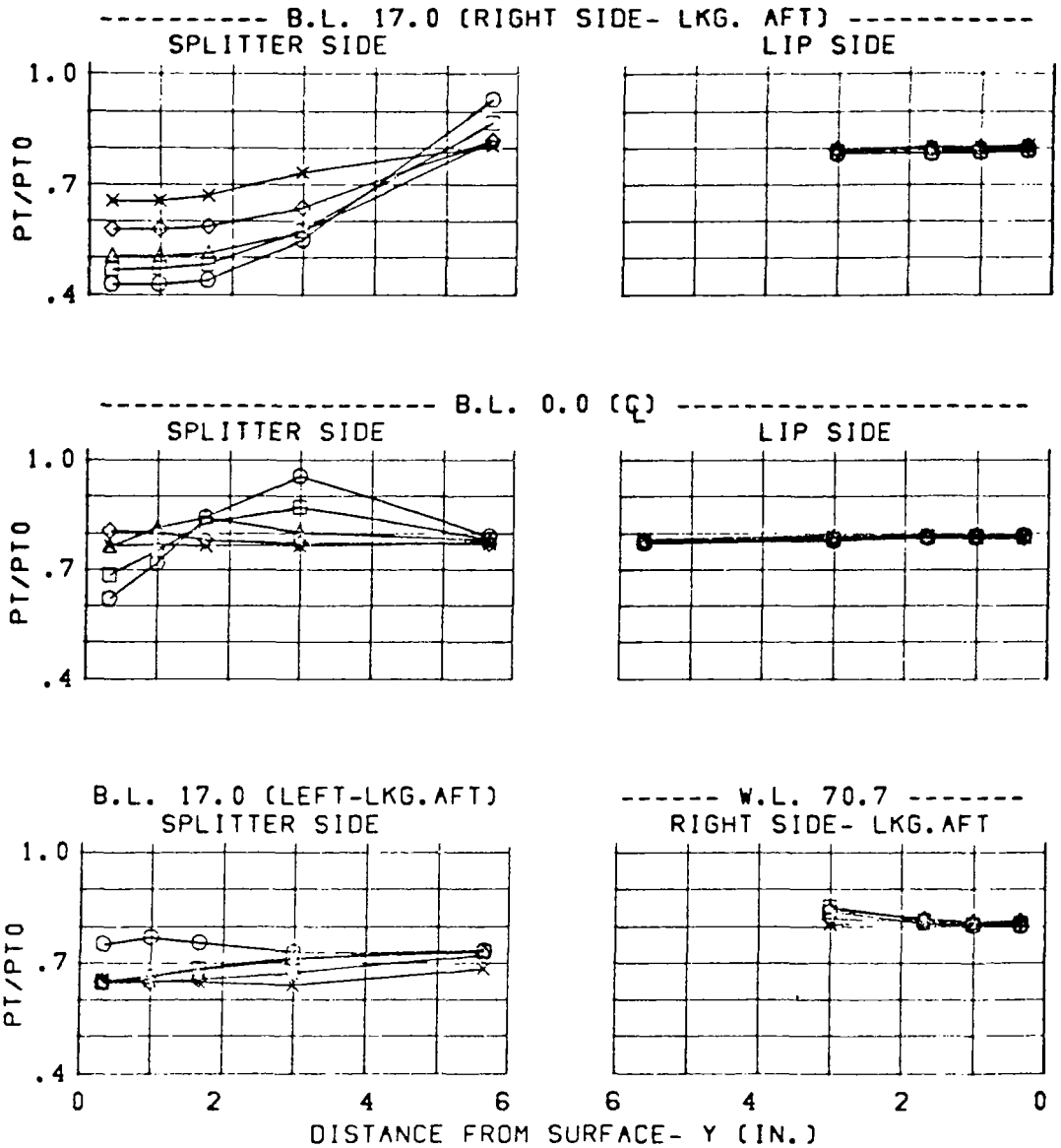

Figure 122 Inlet Configuration C13 Throat Total-Pressure Profiles

CONFIGURATION	CONDITION	SYM.	WC2(LBS/SEC)
C13	MACH = .91	○	249.
3.65 IN. DIV. HT.	ALPHA= -9.	□	234.
NOSE BOOM ON	BETA = 0.	△	209.
DIV. STRUTS OUT		◇	185.
		×	160.

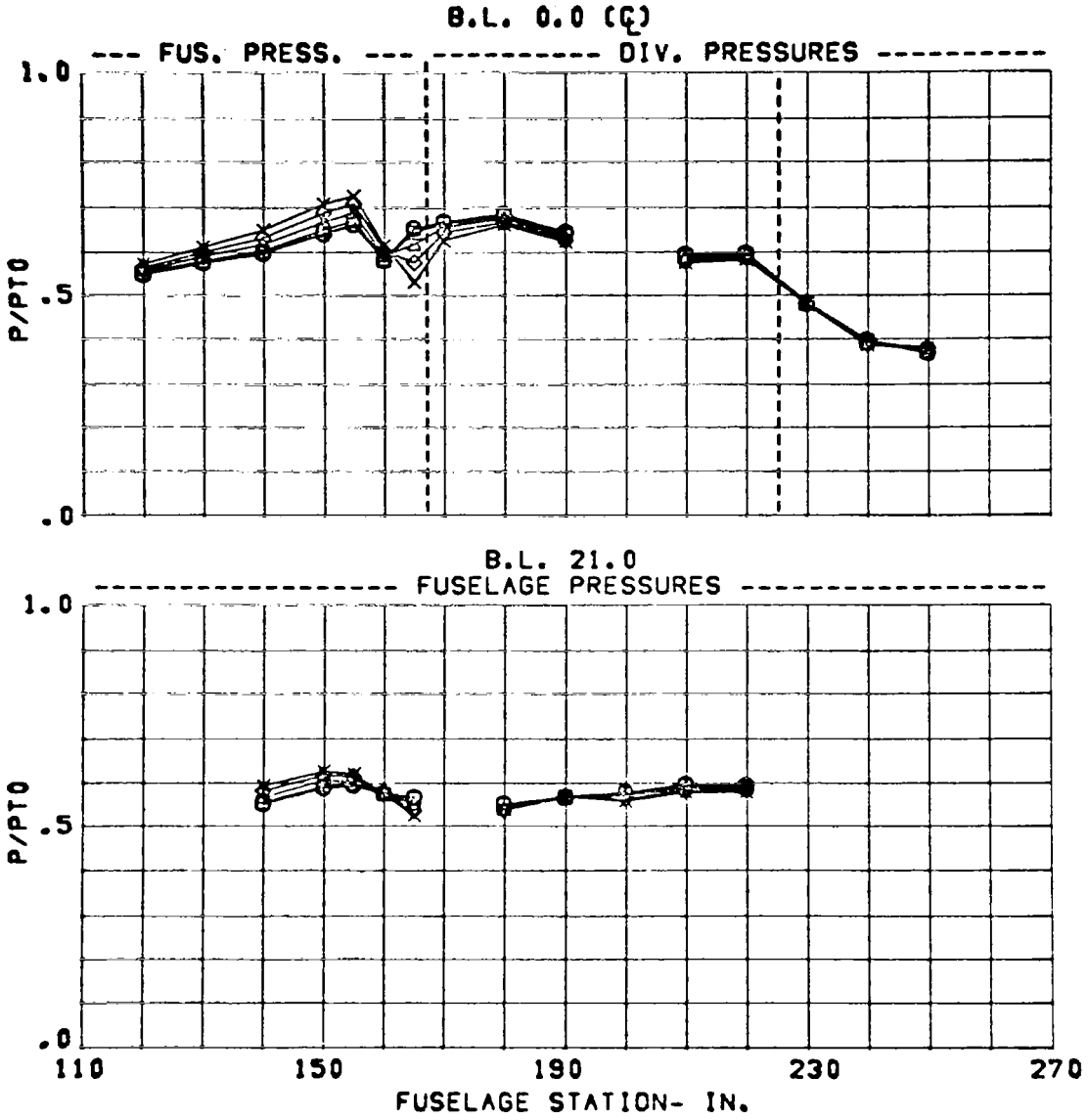

Figure 123 Fuselage and Diverter Static Pressures, Configuration C13

CONFIGURATION	CONDITION	SYM.	WC2(LBS/SEC)
C13	MACH = .91	O	248.
3.65 IN. DIV. HT.	ALPHA= 1.	□	233.
NOSE BOOM ON	BETA = 0.	△	209.
DIV. STRUTS OUT		◇	185.
		×	159.

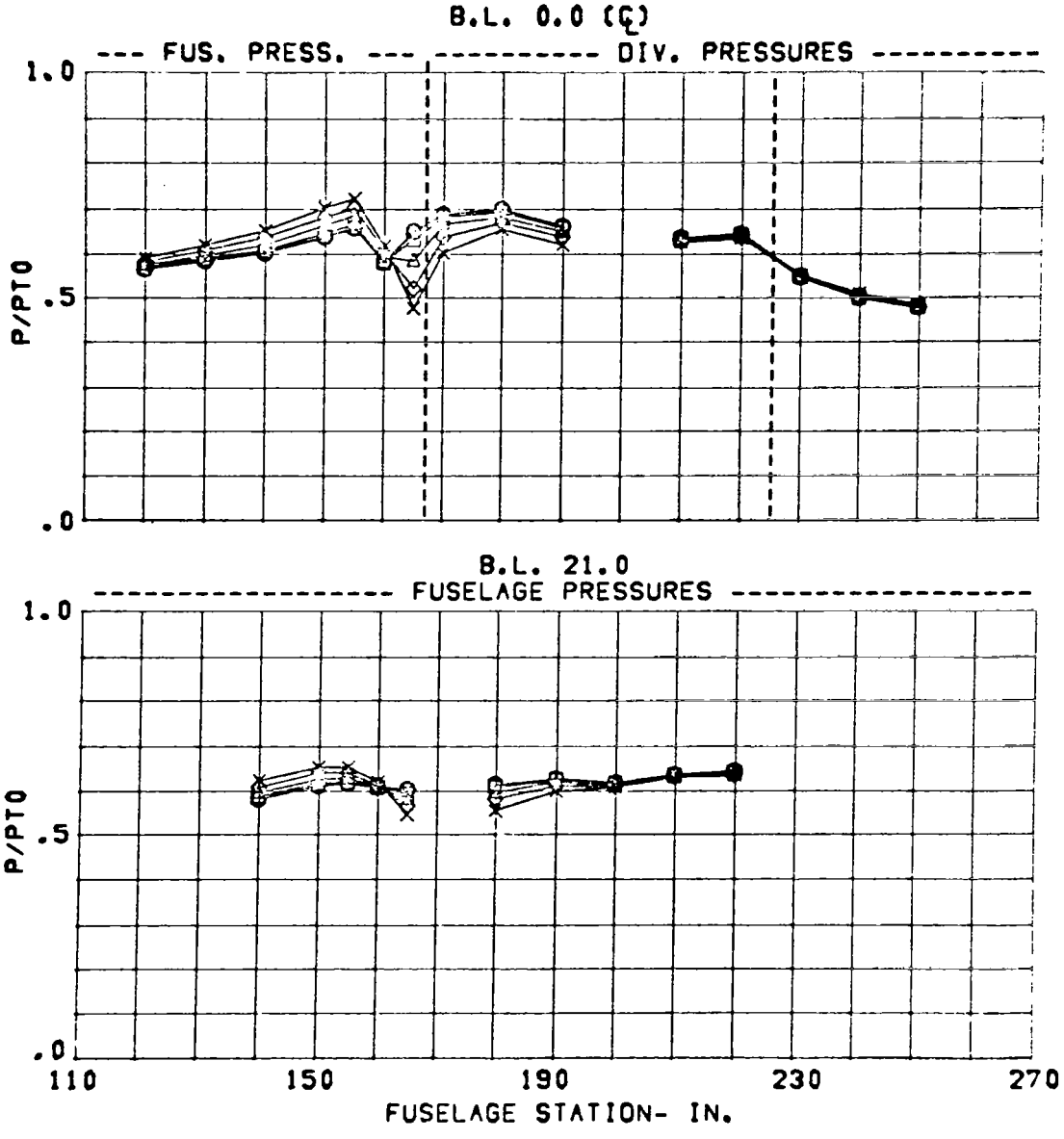

Figure 124 Fuselage and Diverter Static Pressures, Configuration C13

CONFIGURATION	CONDITION	SYM.	WC2(LBS/SEC)
C13	MACH = .91	O	247.
3.65 IN. DIV. HT.	ALPHA= 30.	□	231.
NOSE BOOM ON	BETA = -0.	△	208.
DIV. STRUTS OUT		◇	184.
		×	158.

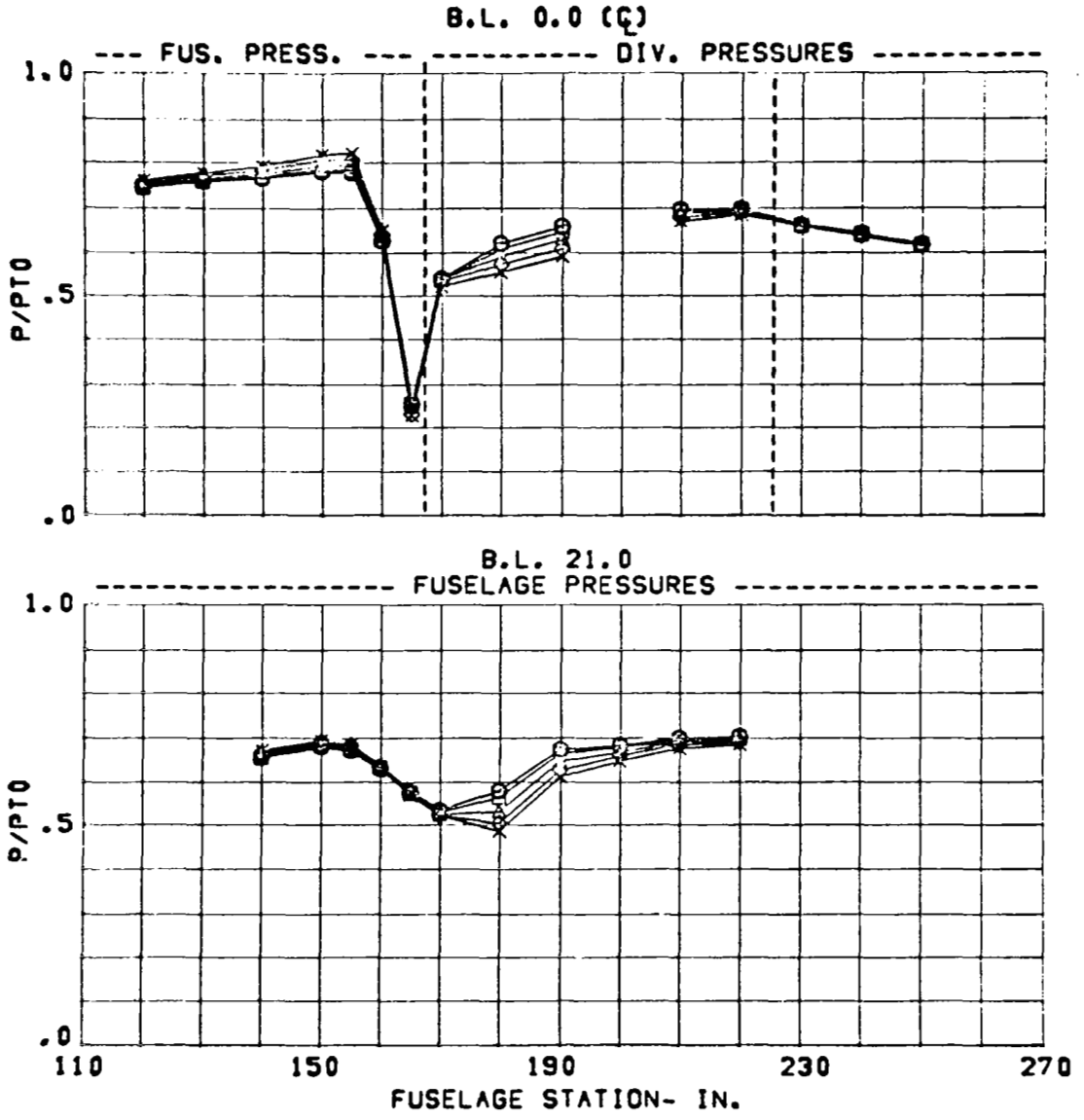

Figure 125 Fuselage and Diverter Static Pressures, Configuration C13

CONFIGURATION	CONDITION	SYM.	WC2(LBS/SEC)
C13	MACH = 1.21	O	246.
3.65 IN. DIV. HT.	ALPHA= -9.	□	231.
NOSE BOOM ON	BETA = 0.	△	209.
DIV. STRUTS OUT		◇	185.
		×	159.

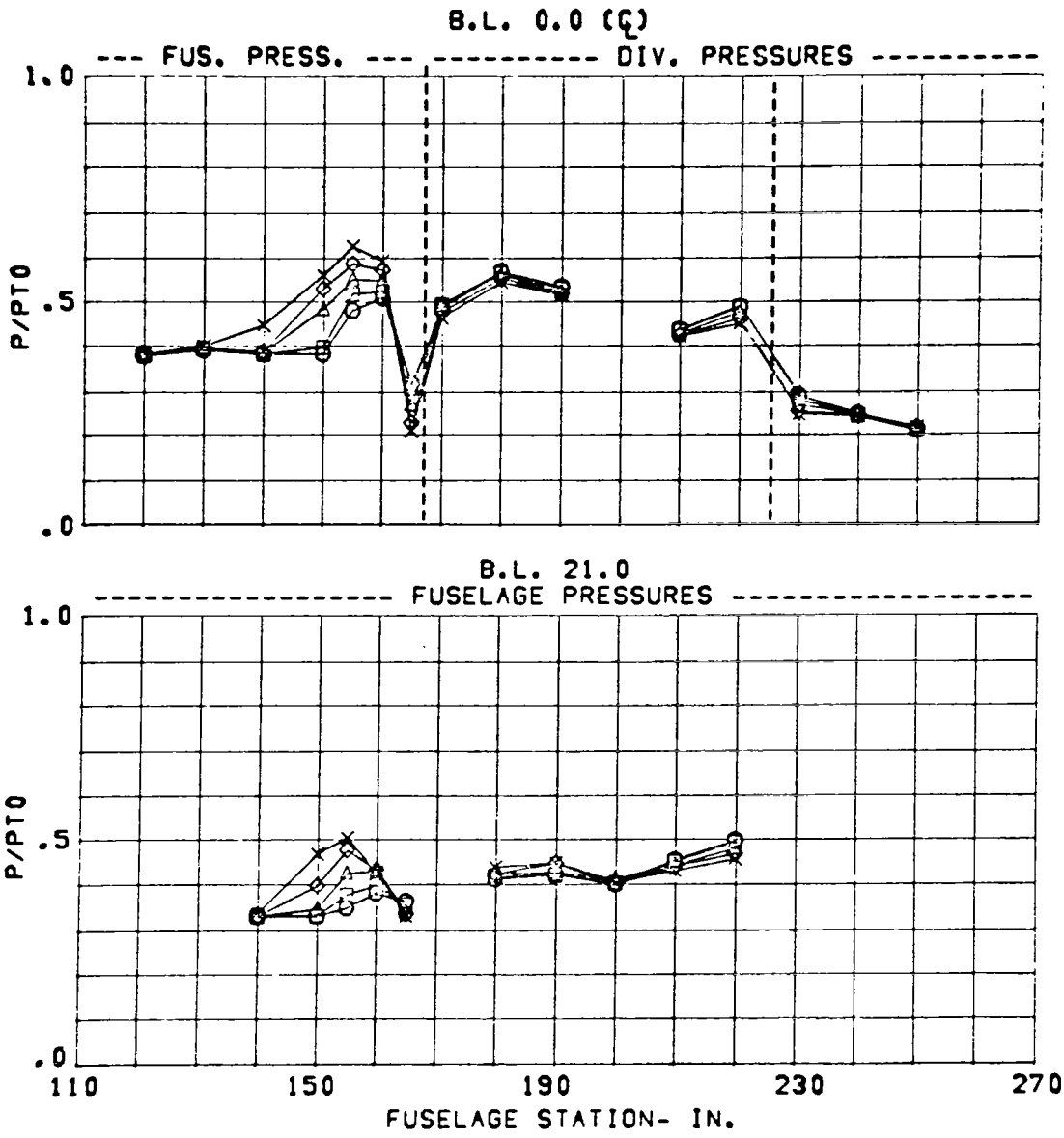

Figure 126 Fuselage and Diverter Static Pressures, Configuration C13

CONFIGURATION	CONDITION	SYM.	WC2(LBS/SEC)
C13	MACH = 1.21	○	245.
3.65 IN. DIV. HT.	ALPHA= 1.	□	232.
NOSE BOOM ON	BETA = 0.	△	208.
DIV. STRUTS OUT		◇	185.
		×	159.

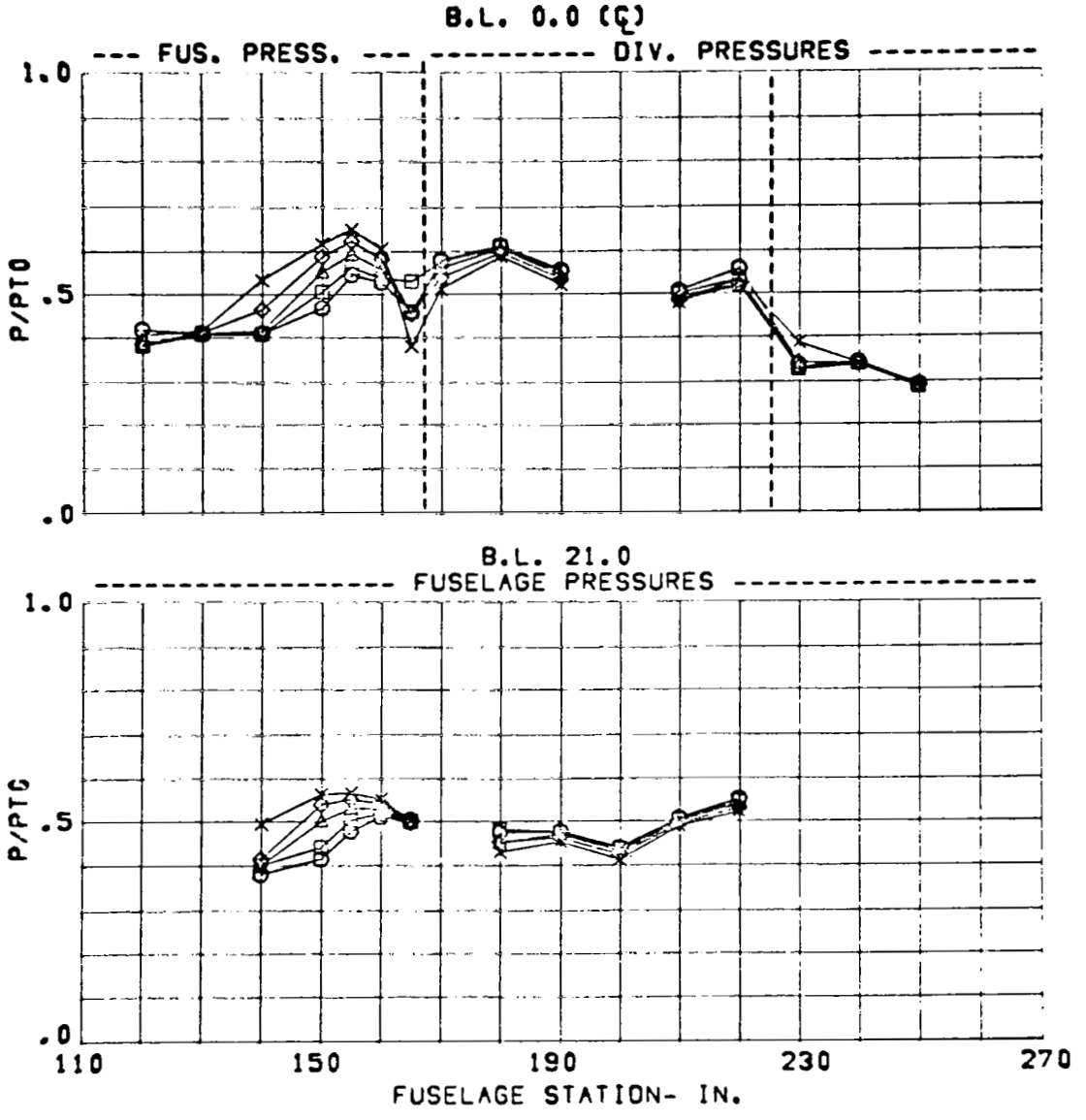

Figure 127 Fuselage and Diverter Static Pressures, Configuration C13

CONFIGURATION	CONDITION	SYM.	WC2(LBS/SEC)
C13	MACH = 1.22	○	246.
3.65 IN. DIV. HT.	ALPHA= 15.	□	232.
NOSE BOOM ON	BETA = 0.	△	209.
DIV. STRUTS OUT		◇	185.
		×	159.

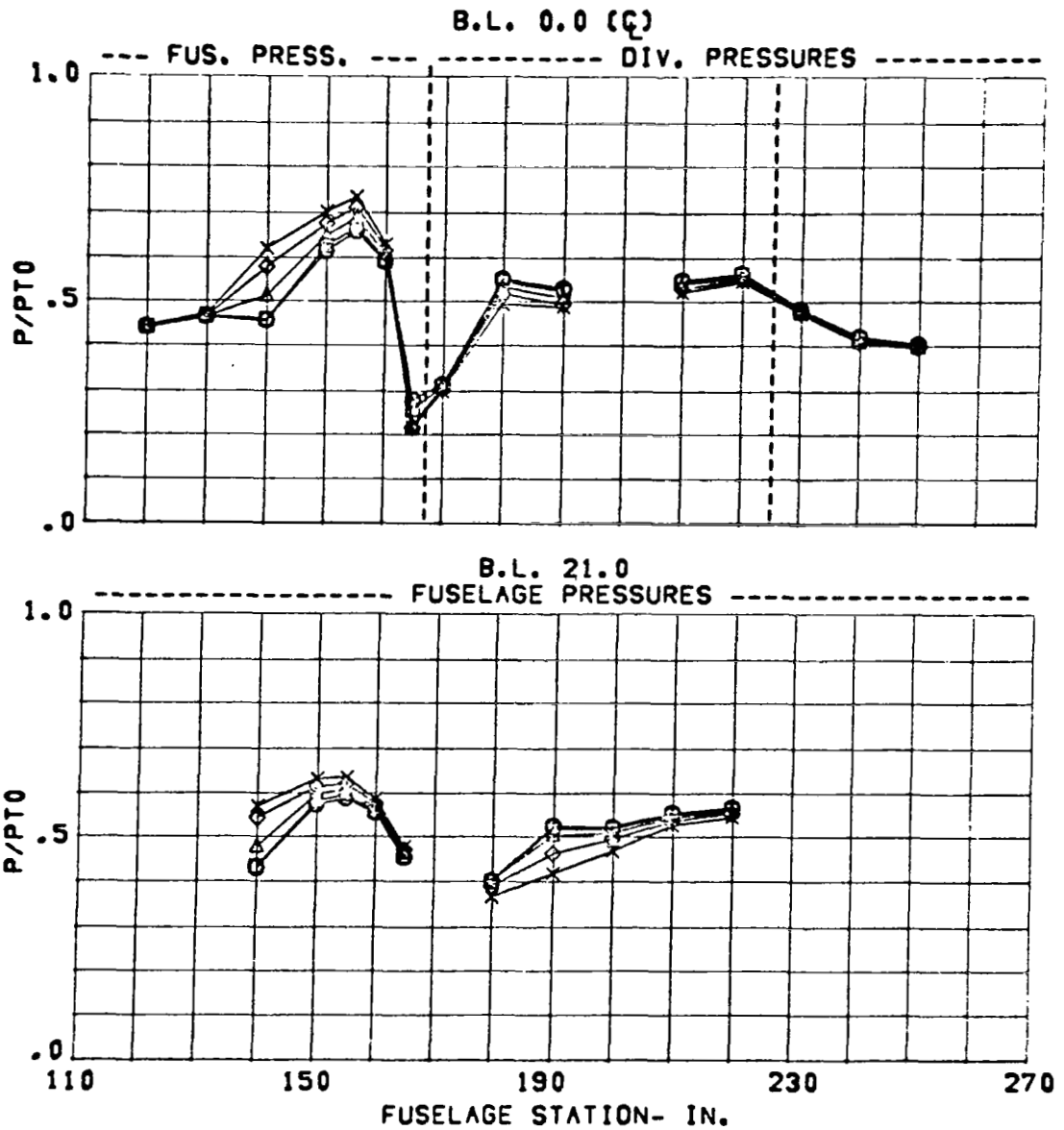

Figure 128 Fuselage and Diverter Static Pressures, Configuration C13

CONFIGURATION	CONDITION	SYM.	WC2(LBS/SEC)
C13	MACH = 1.22	O	245.
3.65 IN. DIV. HT.	ALPHA= 30.	□	232.
NOSE BOOM ON	BETA = -1.	△	209.
DIV. STRUTS OUT		◇	184.
		×	159.

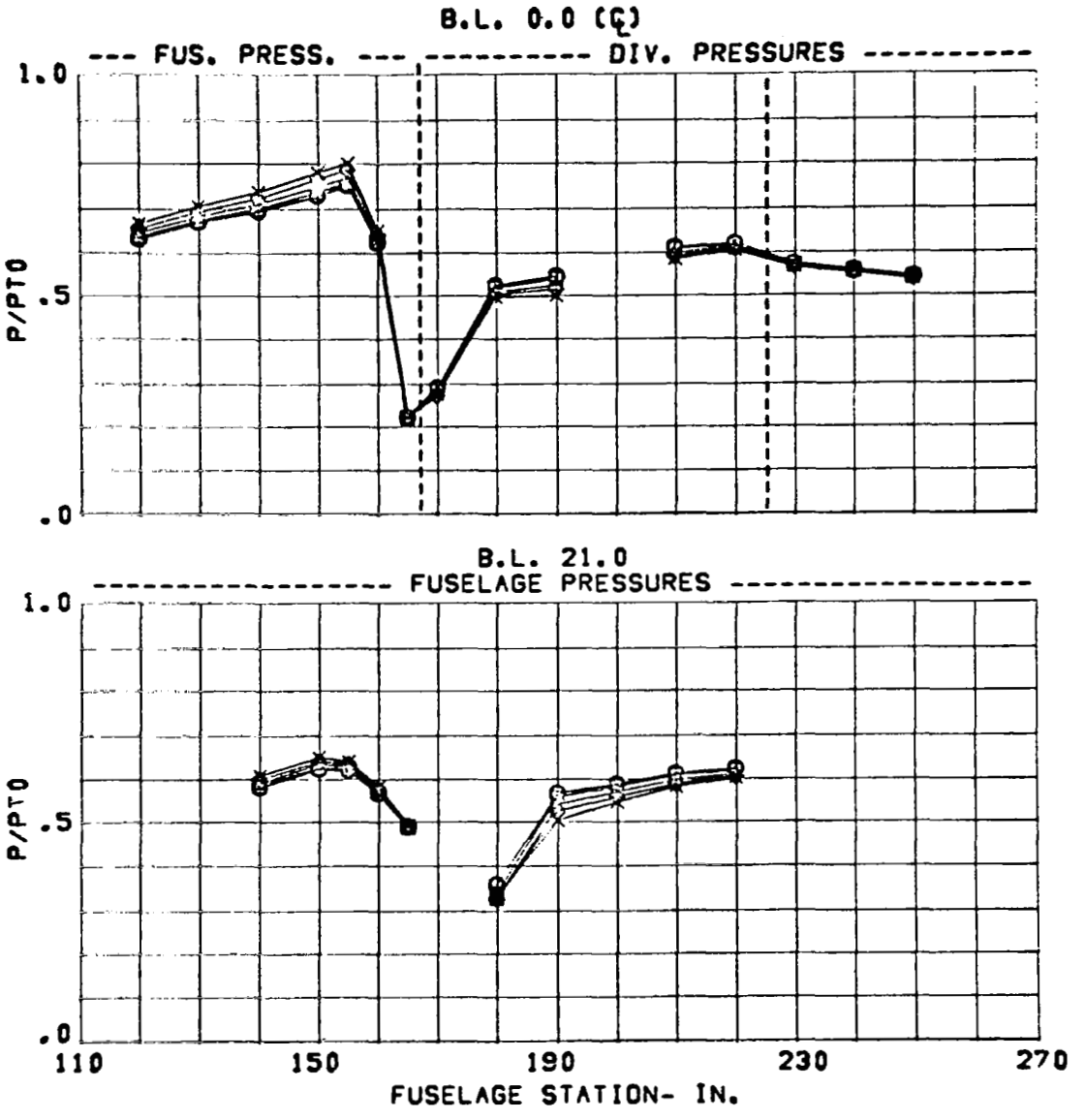

Figure 129 Fuselage and Diverter Static Pressures, Configuration C13

CONFIGURATION	CONDITION	SYM.	WC2(LBS/SEC)
C13	MACH = 1.37	O	244.
3.65 IN. DIV. HT.	ALPHA= -5.	□	228.
NOSE BOOM ON	BETA = 0.	△	207.
DIV. STRUTS OUT		◇	185.
		×	159.

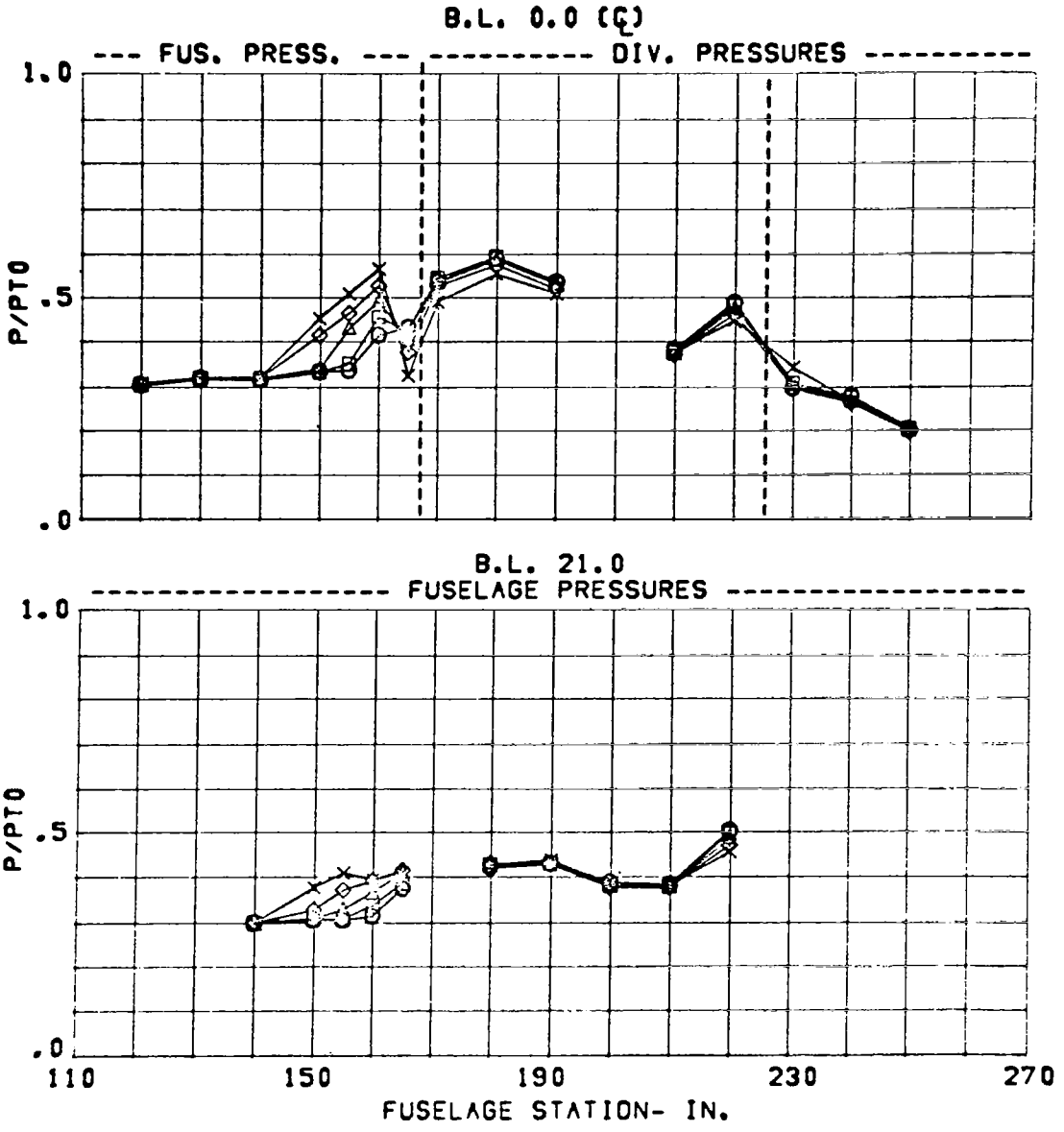

Figure 130 Fuselage and Diverter Static Pressures, Configuration C13

CONFIGURATION	CONDITION	SYM.	WC2(LBS/SEC)
C13	MACH = 1.39	○	244.
3.65 IN. DIV. HT.	ALPHA= 1.	□	228.
NOSE BOOM ON	BETA = 0.	△	207.
DIV. STRUTS OUT		◇	185.
		×	159.

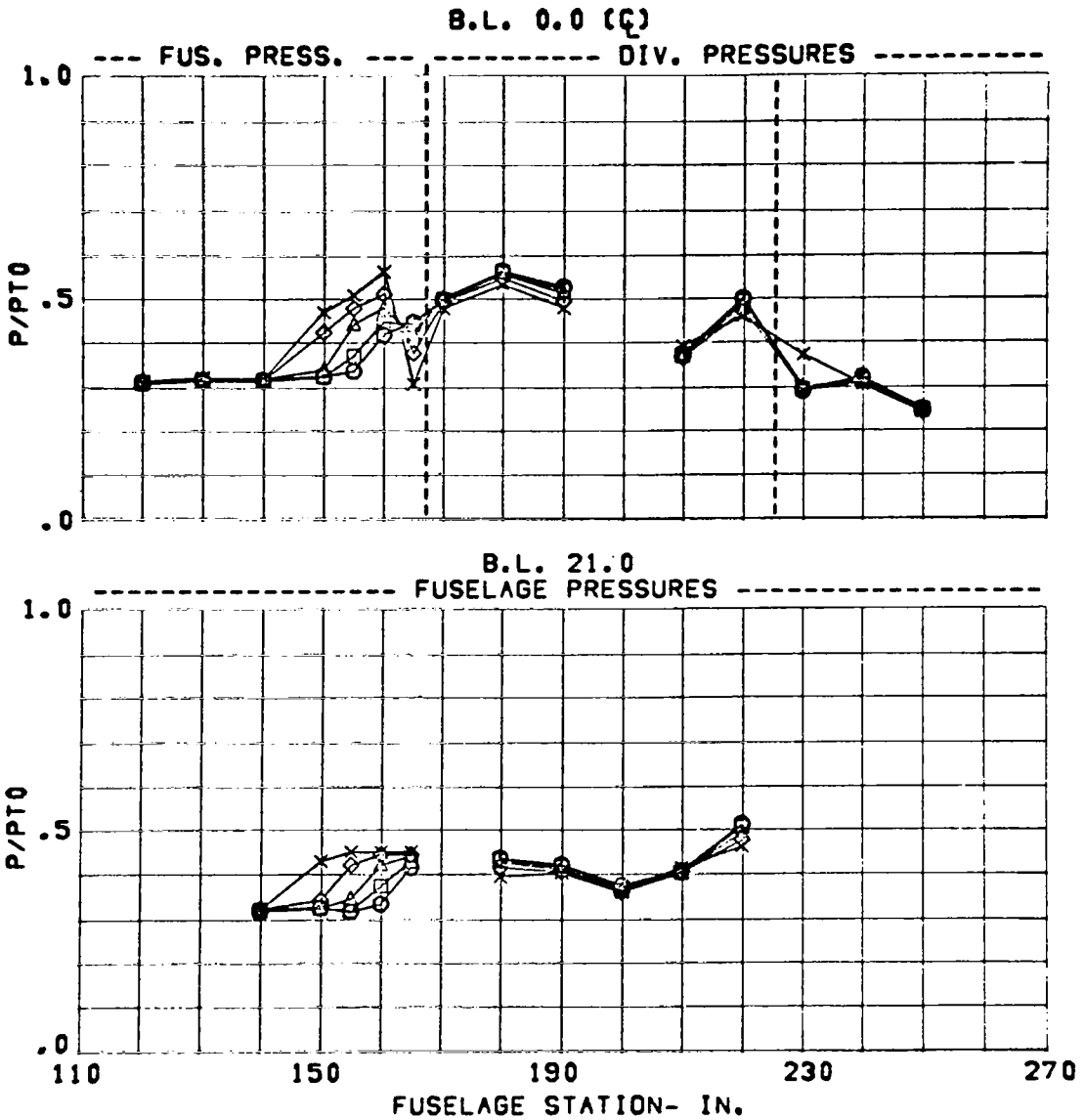

Figure 131 Fuselage and Diverter Static Pressures, Configuration C13

CONFIGURATION	CONDITION	SYM.	WC2(LBS/SEC)
C13	MACH = 1.38	○	244.
3.65 IN. DIV. HT.	ALPHA= 15.	□	228.
NOSE BOOM ON	BETA = 0.	△	207.
DIV. STRUTS OUT		◇	185.
		×	159.

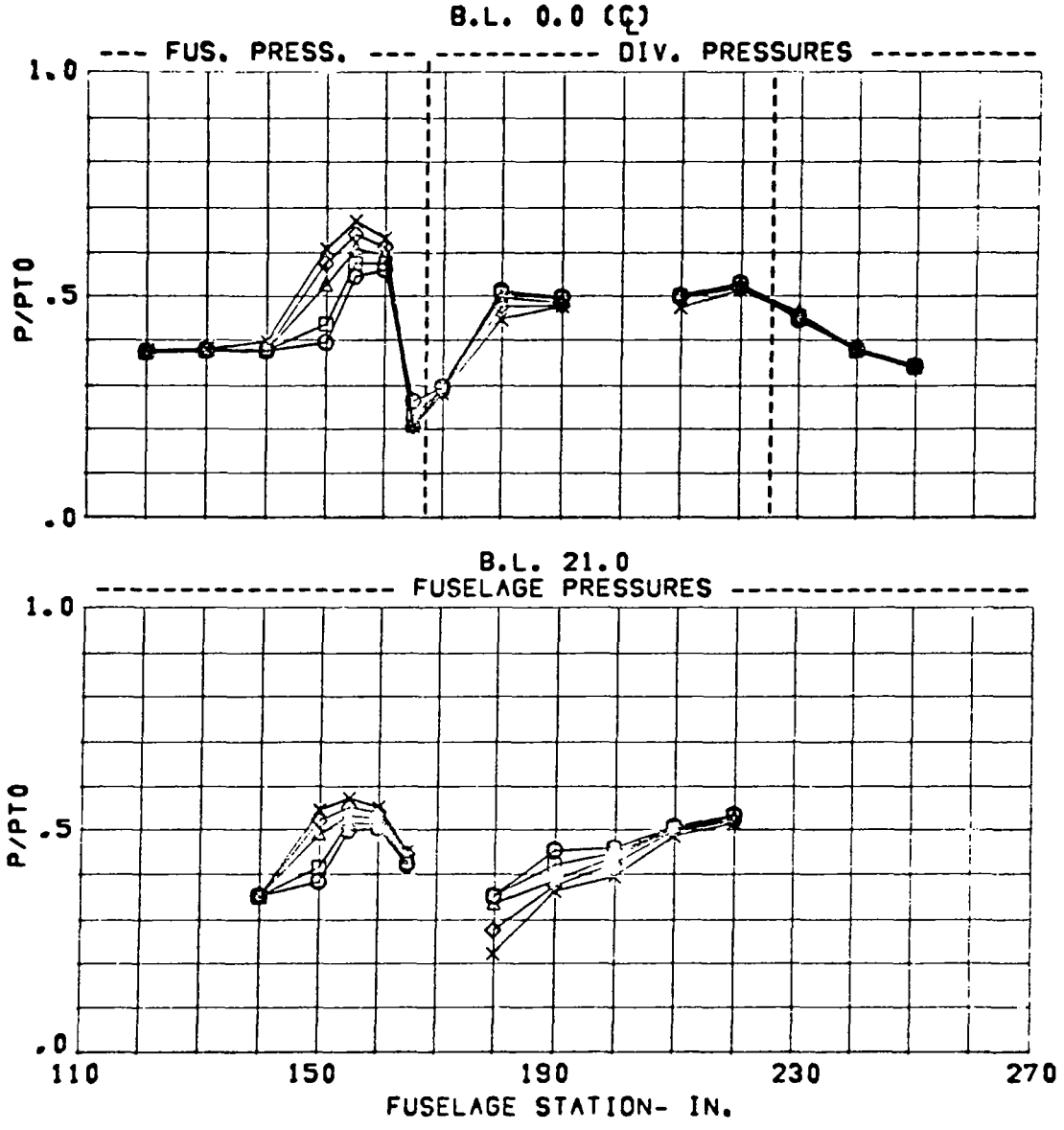

Figure 132 Fuselage and Diverter Static Pressures, Configuration C13

CONFIGURATION	CONDITION	SYM.	WC2(LBS/SEC)
C13	MACH = 1.36	O	245.
3.65 IN. DIV. HT.	ALPHA= 25.	□	228.
NOSE BOOM ON	BETA = 0.	△	207.
DIV. STRUTS OUT		◇	185.
		×	159.

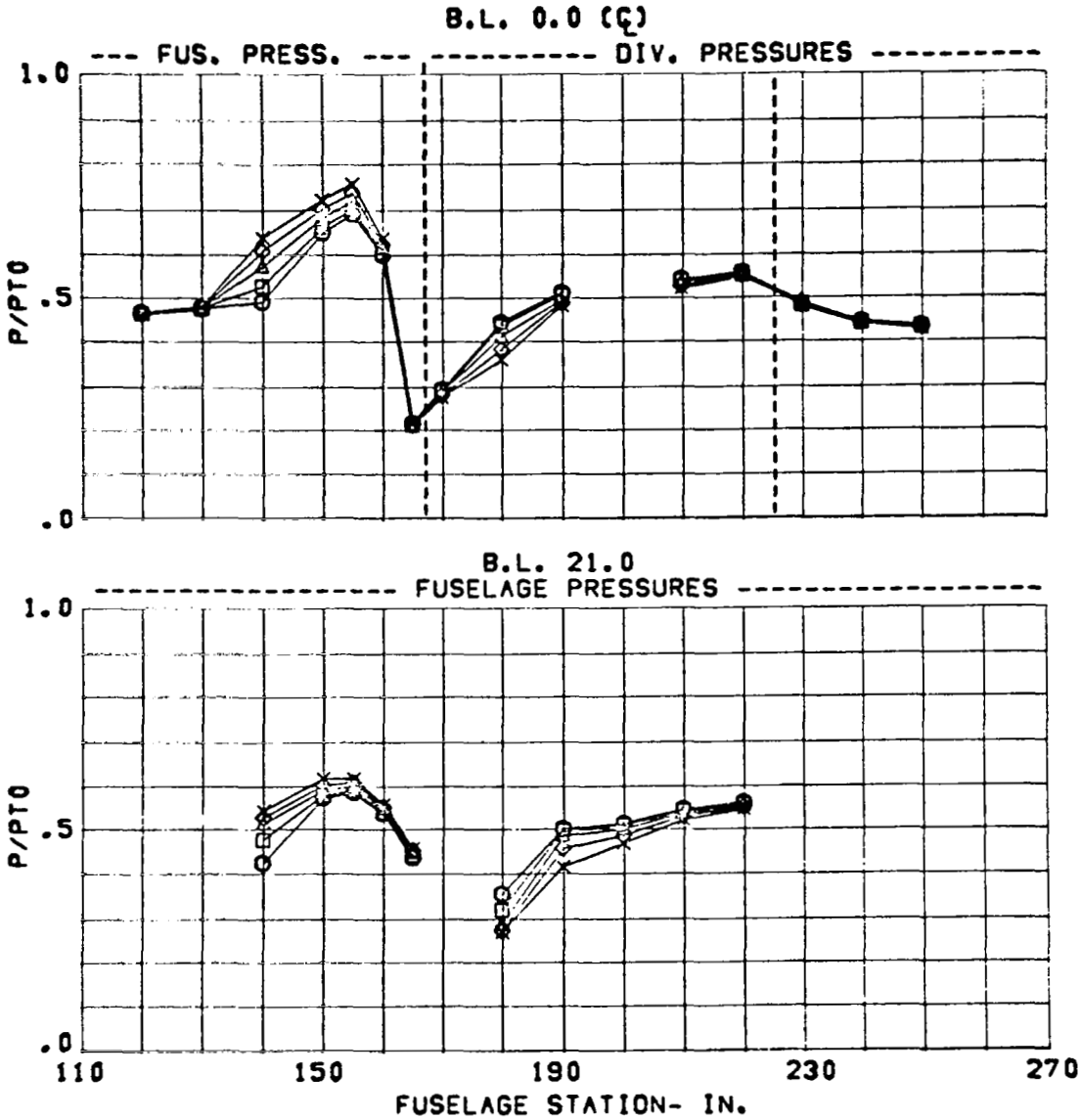

Figure 133 Fuselage and Diverter Static Pressures, Configuration C13

CONFIGURATION	CONDITION	SYM.	WC2(LBS/SEC)
C13	MACH = 1.58	○	232.
3.65 IN. DIV. HT.	ALPHA= -5.	□	217.
NOSE BOOM ON	BETA = 0.	△	199.
DIV. STRUTS OUT		◇	179.
		×	159.

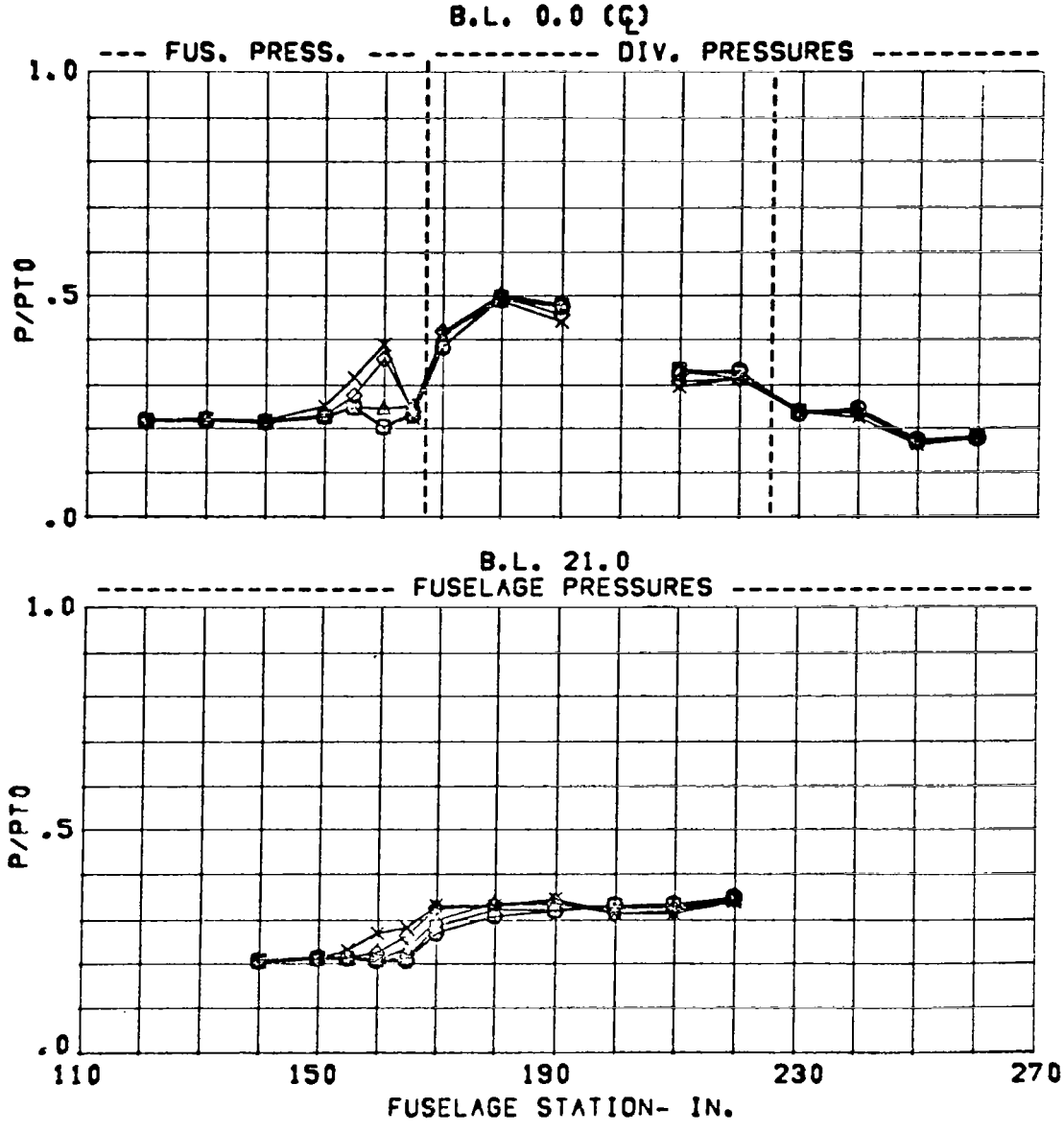

Figure 134 Fuselage and Diverter Static Pressures, Configuration C13

CONFIGURATION	CONDITION	SYM.	WC2(LBS/SEC)
C13	MACH = 1.58	○	232.
3.65 IN. DIV. HT.	ALPHA= 1.	□	217.
NOSE BOOM ON	BETA = 0.	△	199.
DIV. STRUTS OUT		◇	179.
		×	159.

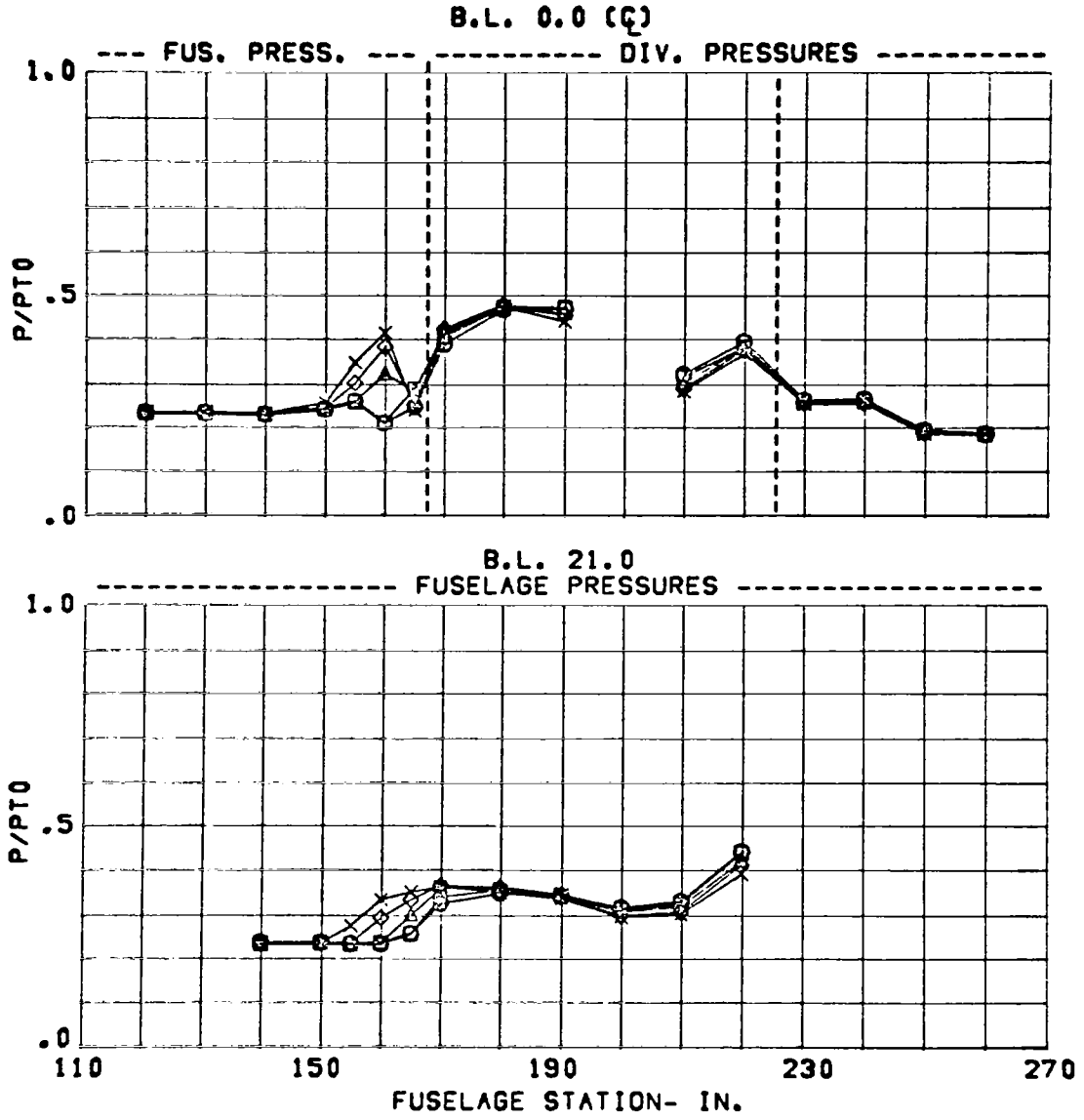

Figure 135 Fuselage and Diverter Static Pressures, Configuration C13

CONFIGURATION	CONDITION	SYM.	WC2(LBS/SEC)
C13	MACH = 1.58	○	233.
3.65 IN. DIV. HT.	ALPHA= 6.	□	218.
NOSE BOOM ON	BETA = 0.	△	199.
DIV. STRUTS OUT		◇	179.
		×	160.

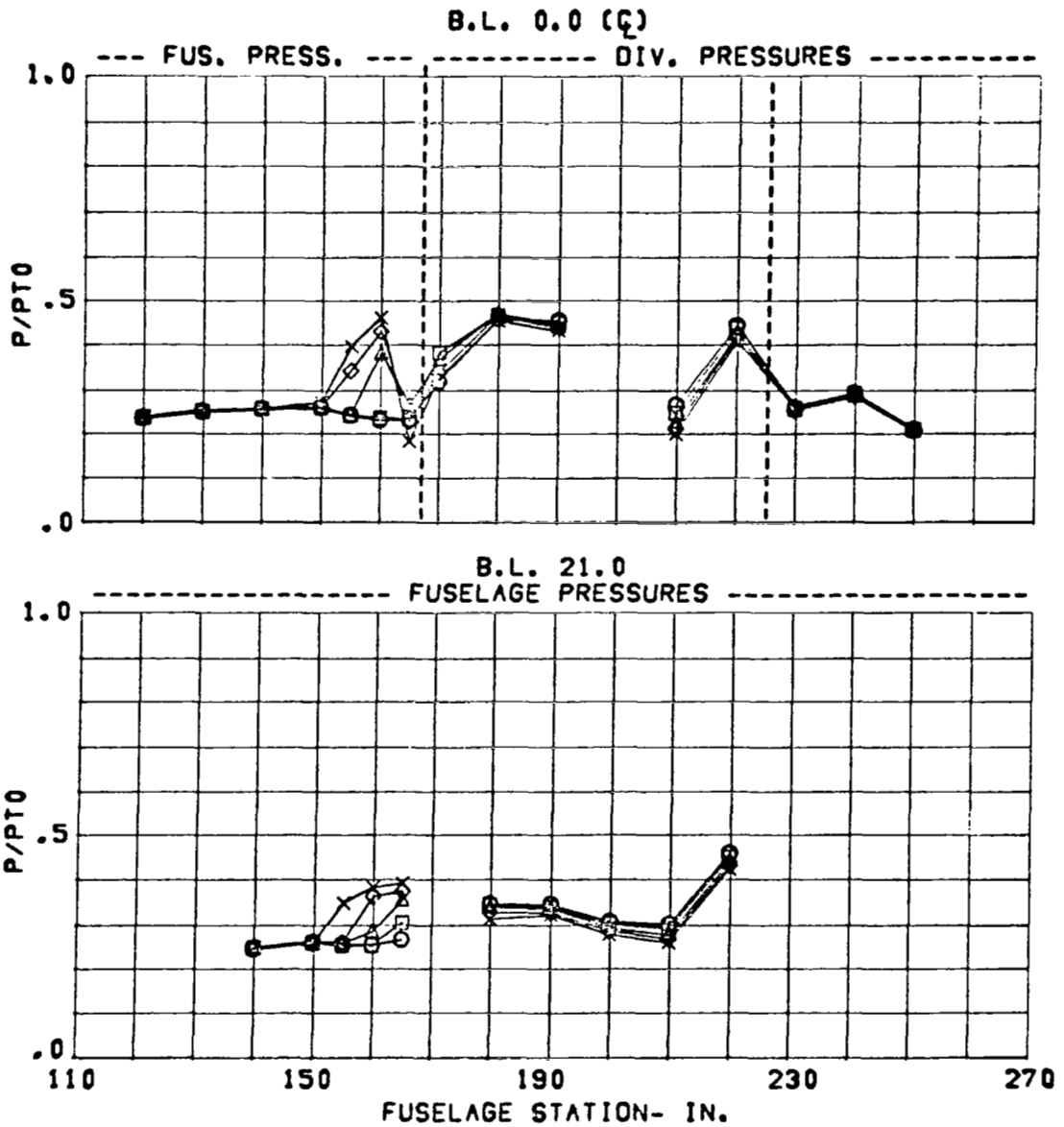

Figure 136 Fuselage and Diverter Static Pressures, Configuration C13

CONFIGURATION	CONDITION	SYM.	WC2(LBS/SEC)
C13	MACH = 1.58	O	233.
3.65 IN. DIV. HT.	ALPHA= 20.	□	218.
NOSE BOOM ON	BETA = 0.	△	199.
DIV. STRUTS OUT		◇	179.
		×	160.

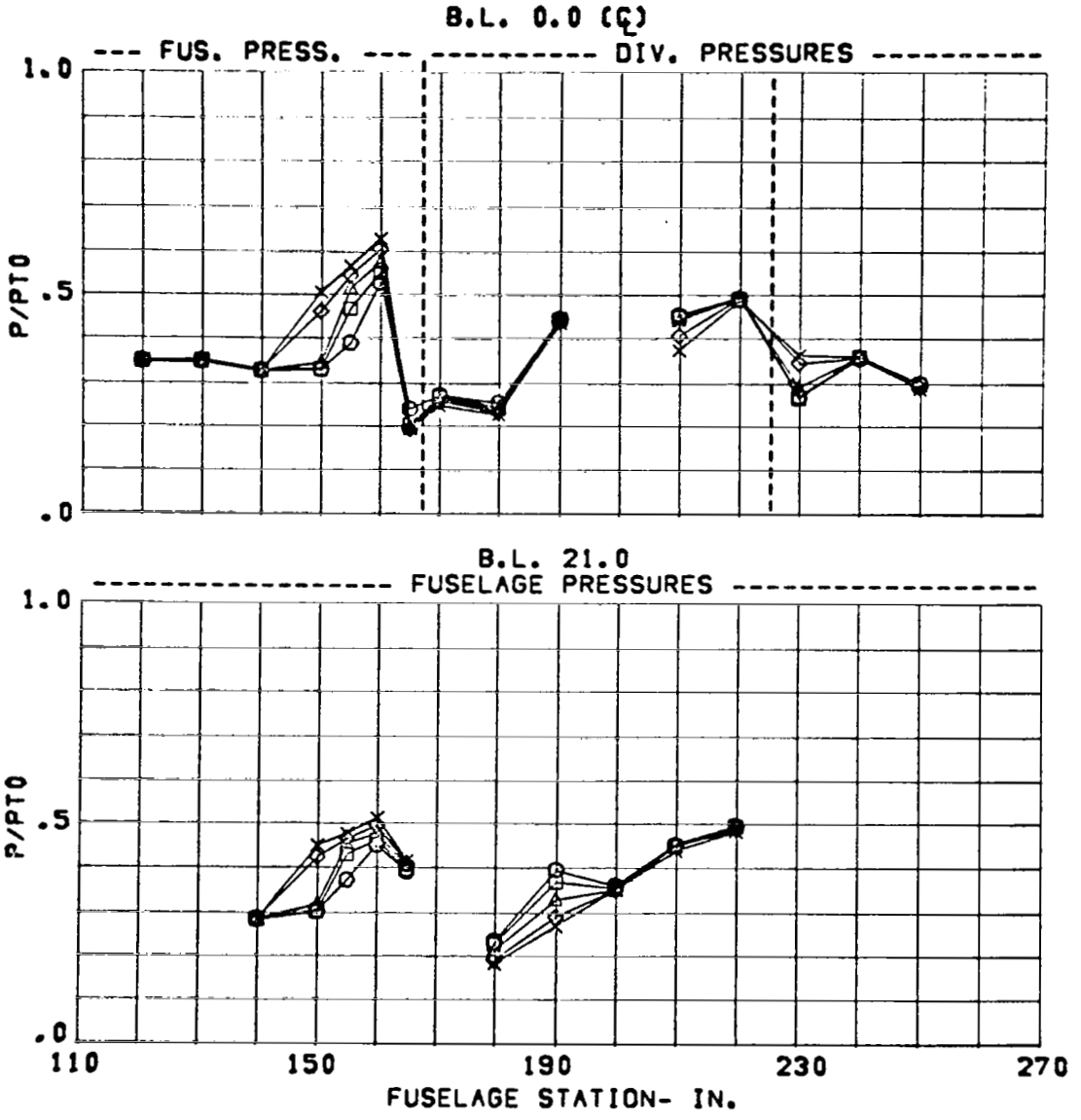

Figure 137 Fuselage and Diverter Static Pressures, Configuration C13

CONFIGURATION	CONDITION	SYM.	WC2(LBS/SEC)
C13	MACH = 1.78	O	214.
3.65 IN. DIV. HT.	ALPHA= -5.	□	200.
NOSE BOOM ON	BETA = 0.	△	185.
DIV. STRUTS OUT		◇	169.
		×	150.

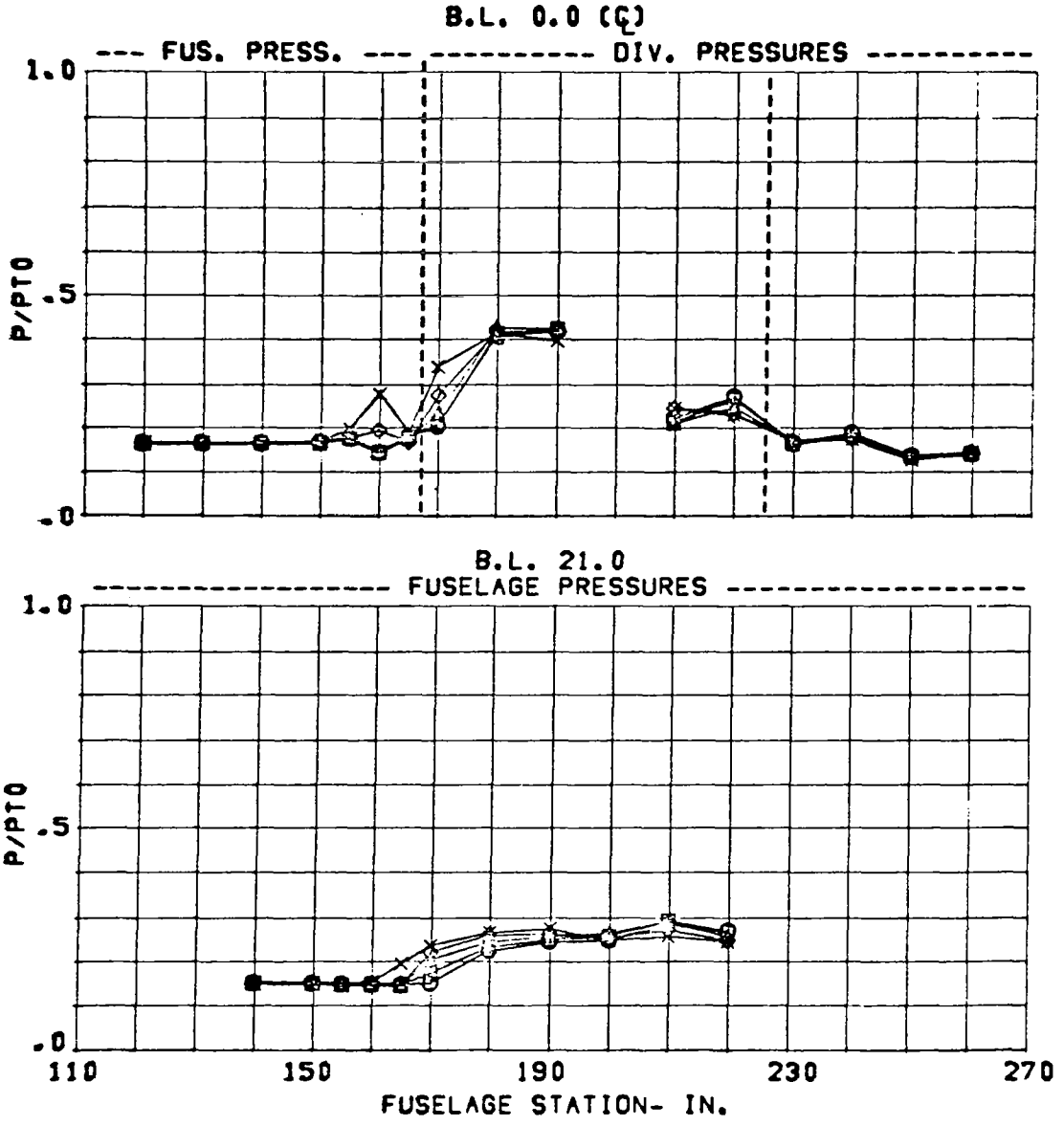

Figure 138 Fuselage and Diverter Static Pressures, Configuration C13

CONFIGURATION	CONDITION	SYM.	WC2(LBS/SEC)
C13	MACH = 1.78	○	214.
3.65 IN. DIV. HT.	ALPHA= 1.	□	199.
NOSE BOOM ON	BETA = 0.	△	185.
DIV. STRUTS OUT		◇	169.
		×	149.

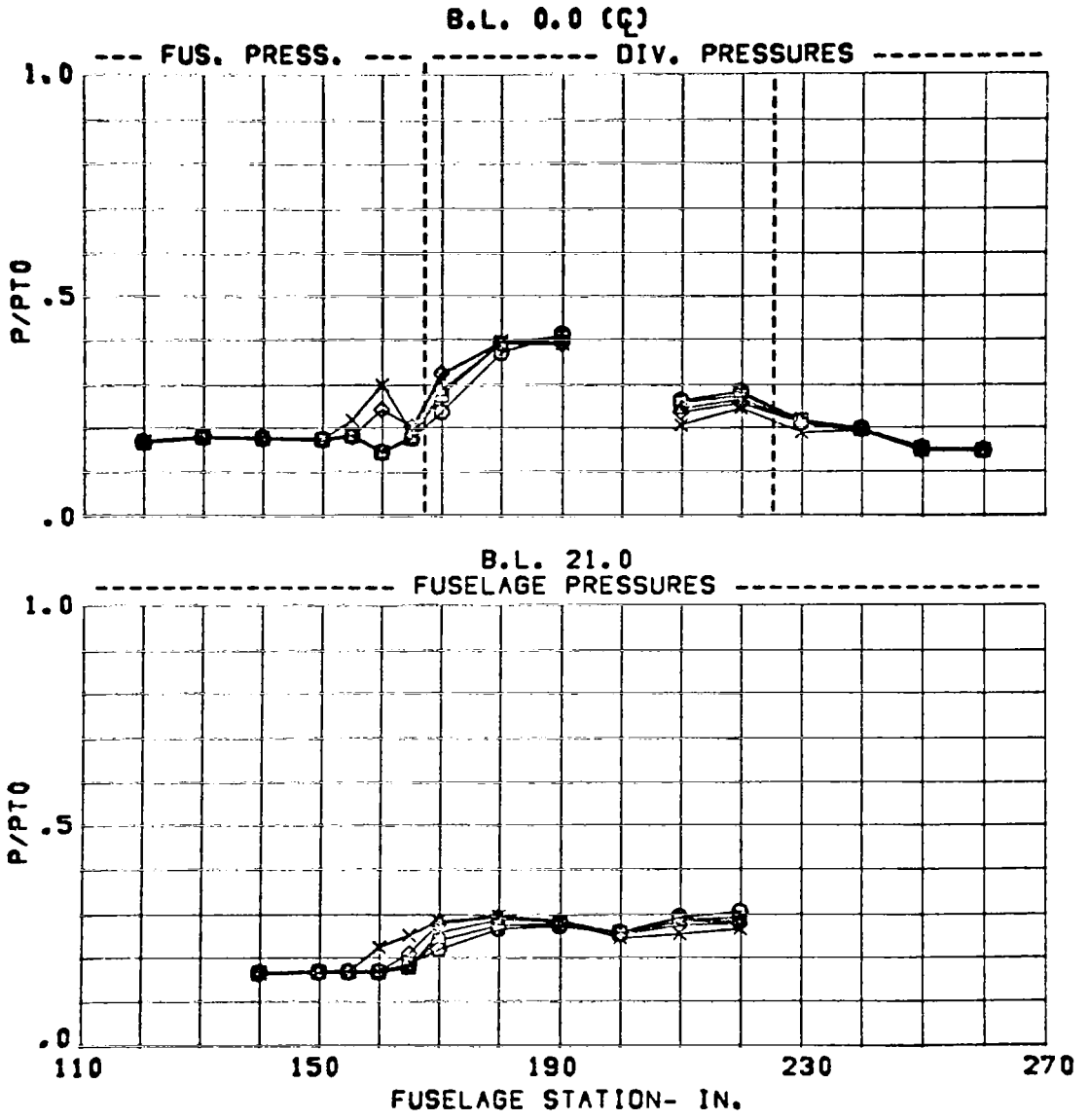

Figure 139 Fuselage and Diverter Static Pressures, Configuration C13

CONFIGURATION	CONDITION	SYM.	WC2(LBS/SEC)
C13	MACH = 1.78	O	214.
3.65 IN. DIV. HT.	ALPHA= 6.	□	200.
NOSE BOOM ON	BETA = 0.	△	185.
DIV. STRUTS OUT		◇	169.
		×	149.

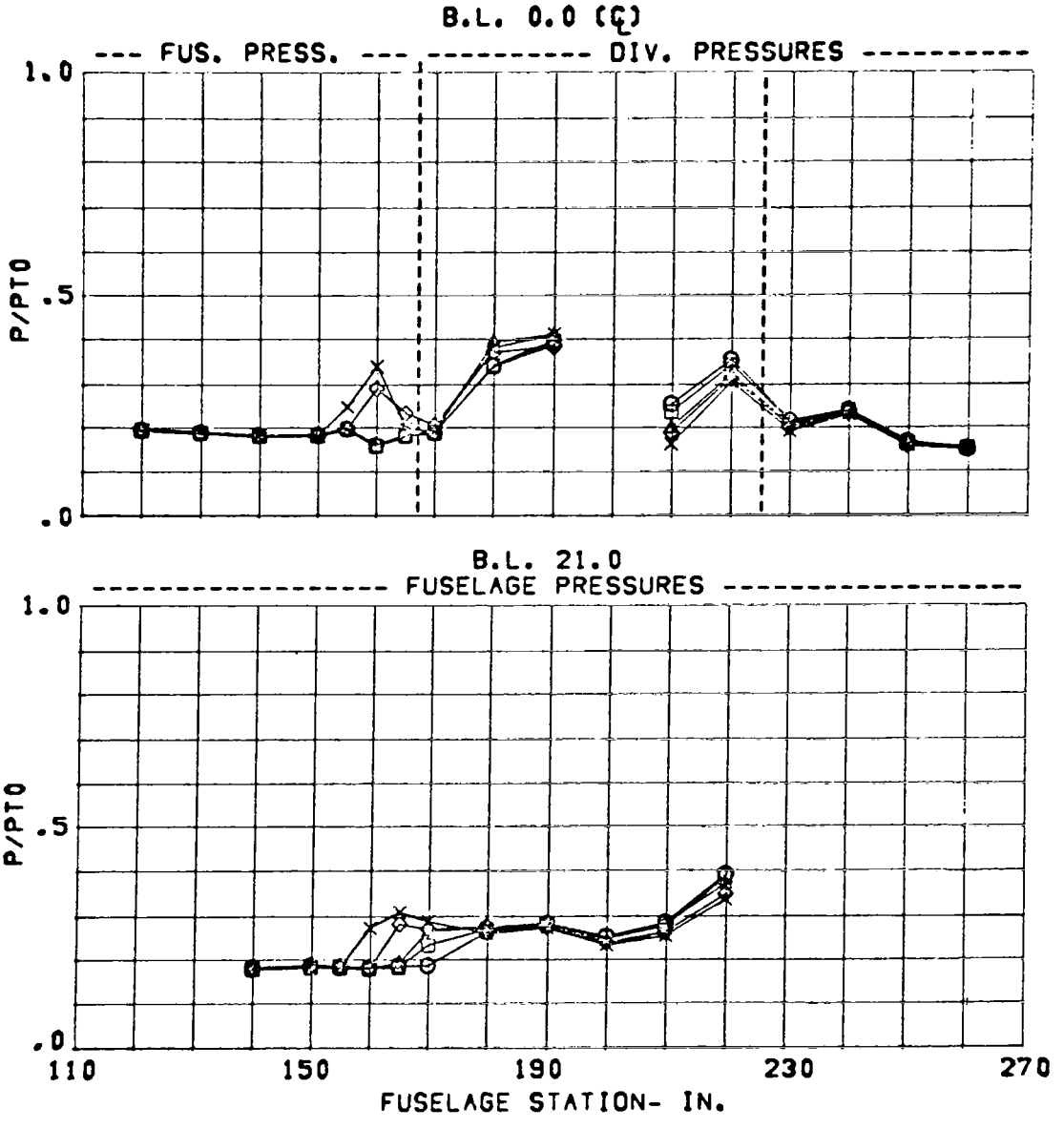

Figure 140 Fuselage and Diverter Static Pressures, Configuration C13

CONFIGURATION	CONDITION	SYM.	WC2(LBS/SEC)
C13	MACH = 1.78	O	215.
3.65 IN. DIV. HT.	ALPHA= 20.	□	200.
NOSE BOOM ON	BETA = 0.	△	185.
DIV. STRUTS OUT		◇	169.
		×	150.

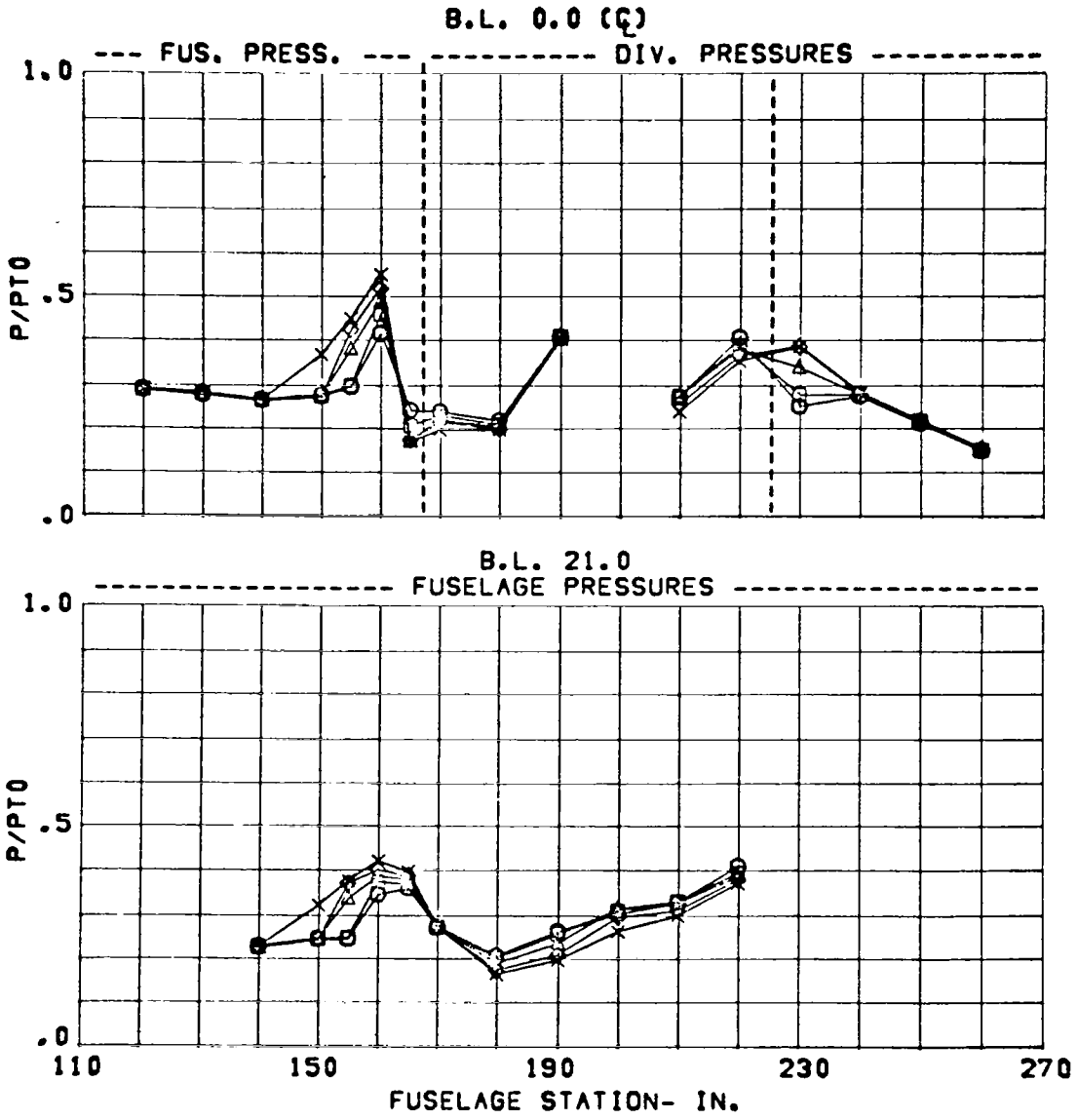

Figure 141 Fuselage and Diverter Static Pressures, Configuration C13

CONFIGURATION	CONDITION	SYM.	WC2(LBS/SEC)
C13	MACH = 1.97	O	197.
3.65 IN. DIV. HT.	ALPHA= -5.	□	184.
NOSE BOOM ON	BETA = 0.	△	172.
DIV. STRUTS OUT		◇	155.
		×	140.

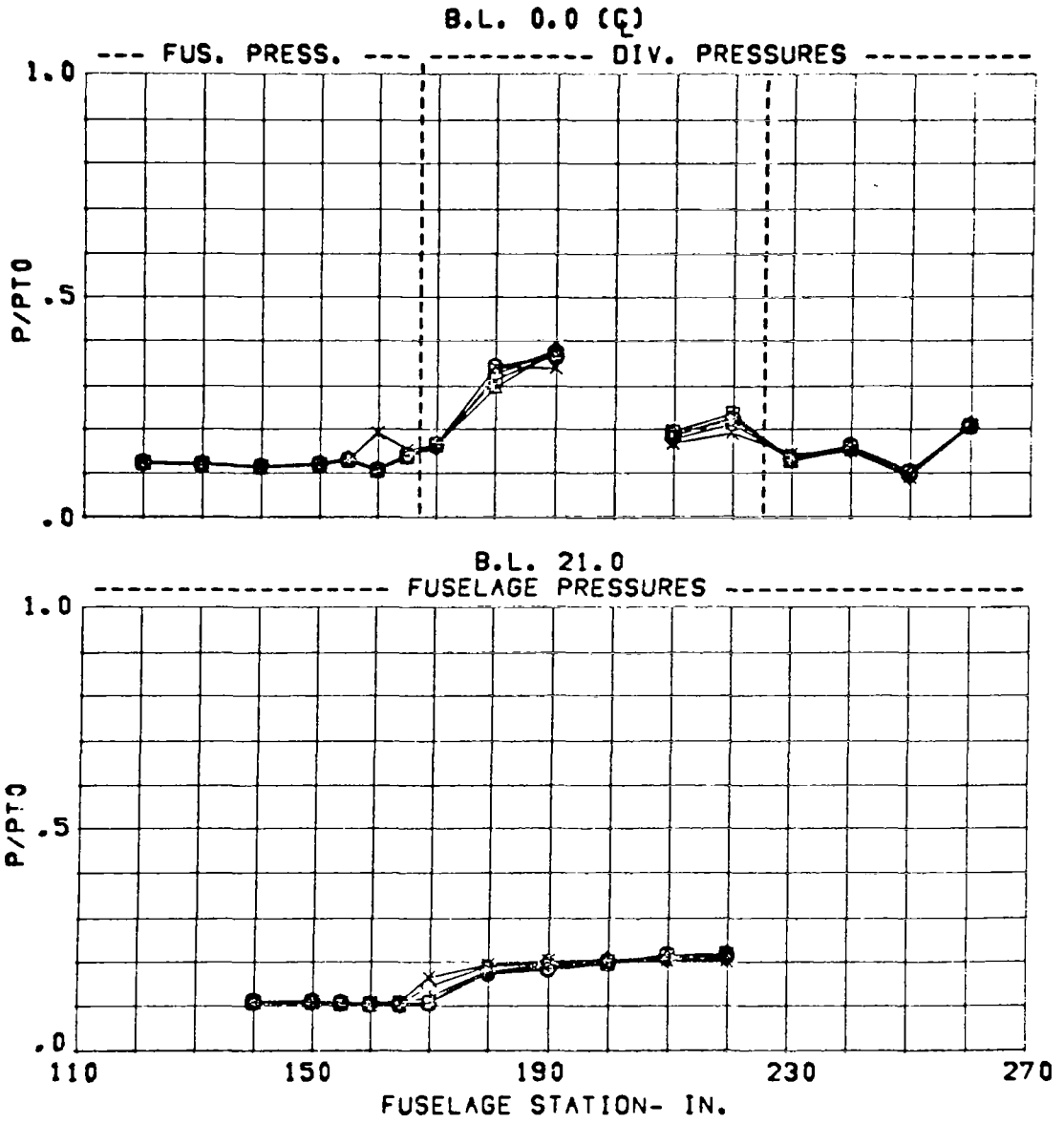

Figure 142 Fuselage and Diverter Static Pressures, Configuration C13

CONFIGURATION	CONDITION	SYM.	WC2(LBS/SEC)
C13	MACH = 1.97	○	197.
3.65 IN. DIV. HT.	ALPHA= 1.	□	183.
NOSE BOOM ON	BETA = 0.	△	172.
DIV. STRUTS OUT		◇	155.
		×	140.

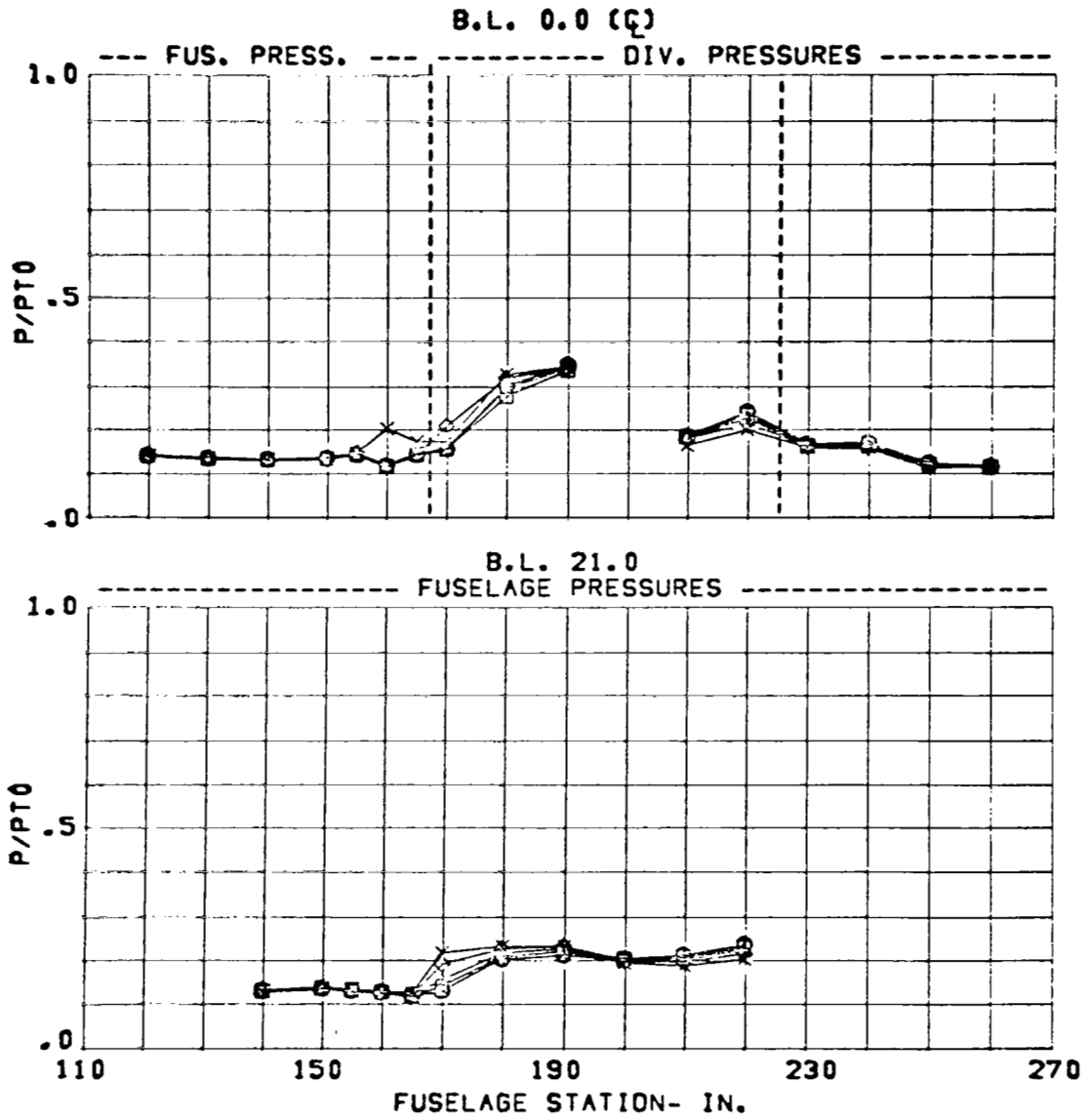

Figure 143 Fuselage and Diverter Static Pressures, Configuration C13

CONFIGURATION	CONDITION	SYM.	WC2(LBS/SEC)
C13	MACH = 1.97	○	197.
3.65 IN. DIV. HT.	ALPHA= 6.	□	183.
NOSE BOOM ON	BETA = 0.	△	172.
DIV. STRUTS OUT		◇	155.
		×	140.

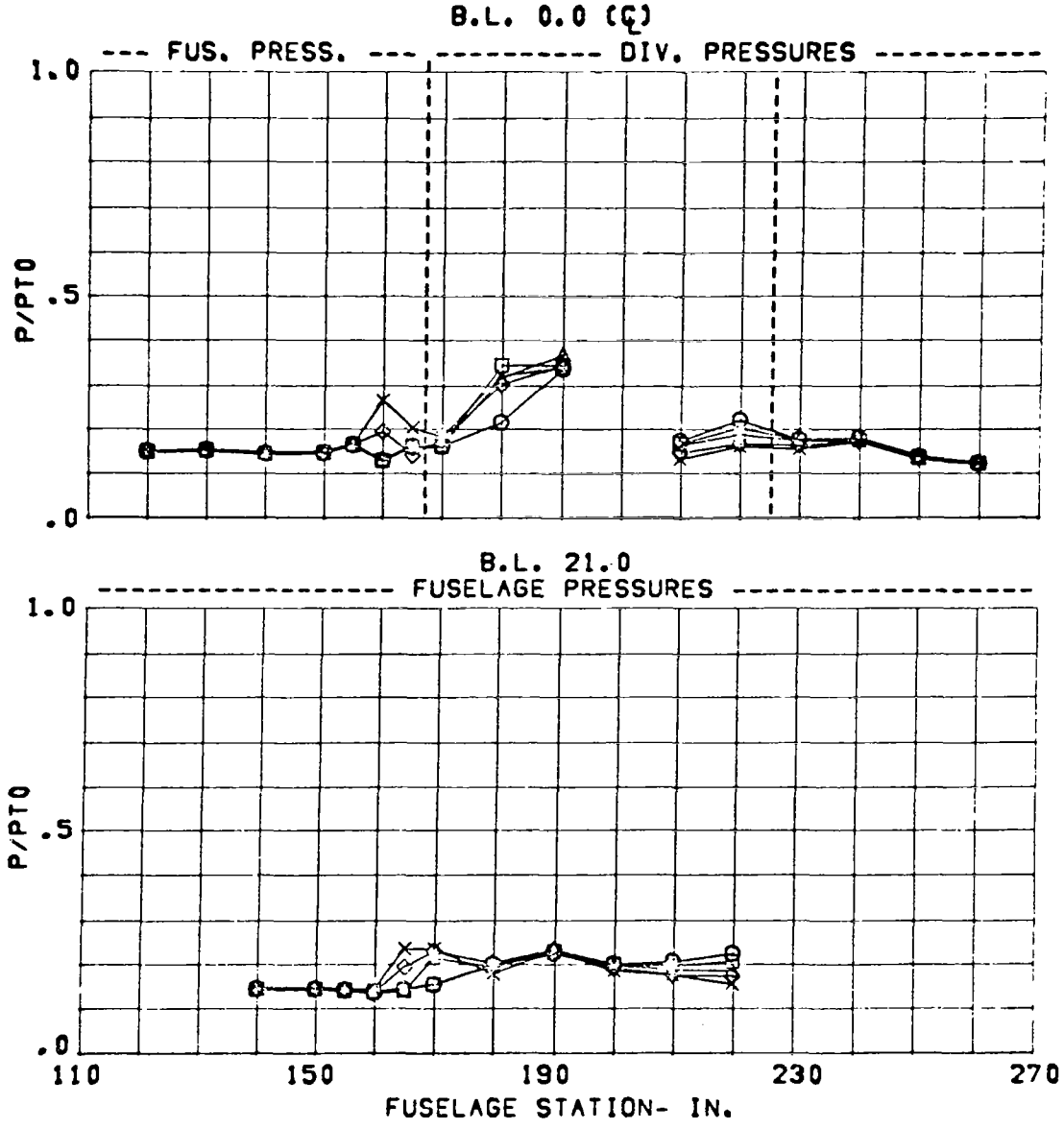

Figure 144 Fuselage and Diverter Static Pressures, Configuration C13

CONFIGURATION	CONDITION	SYM.	WC2(LBS/SEC)
C13	MACH = 1.96	O	197.
3.65 IN. DIV. HT.	ALPHA= 20.	□	183.
NOSE BOOM ON	BETA = 0.	△	172.
DIV. STRUTS OUT		◇	155.
		×	140.

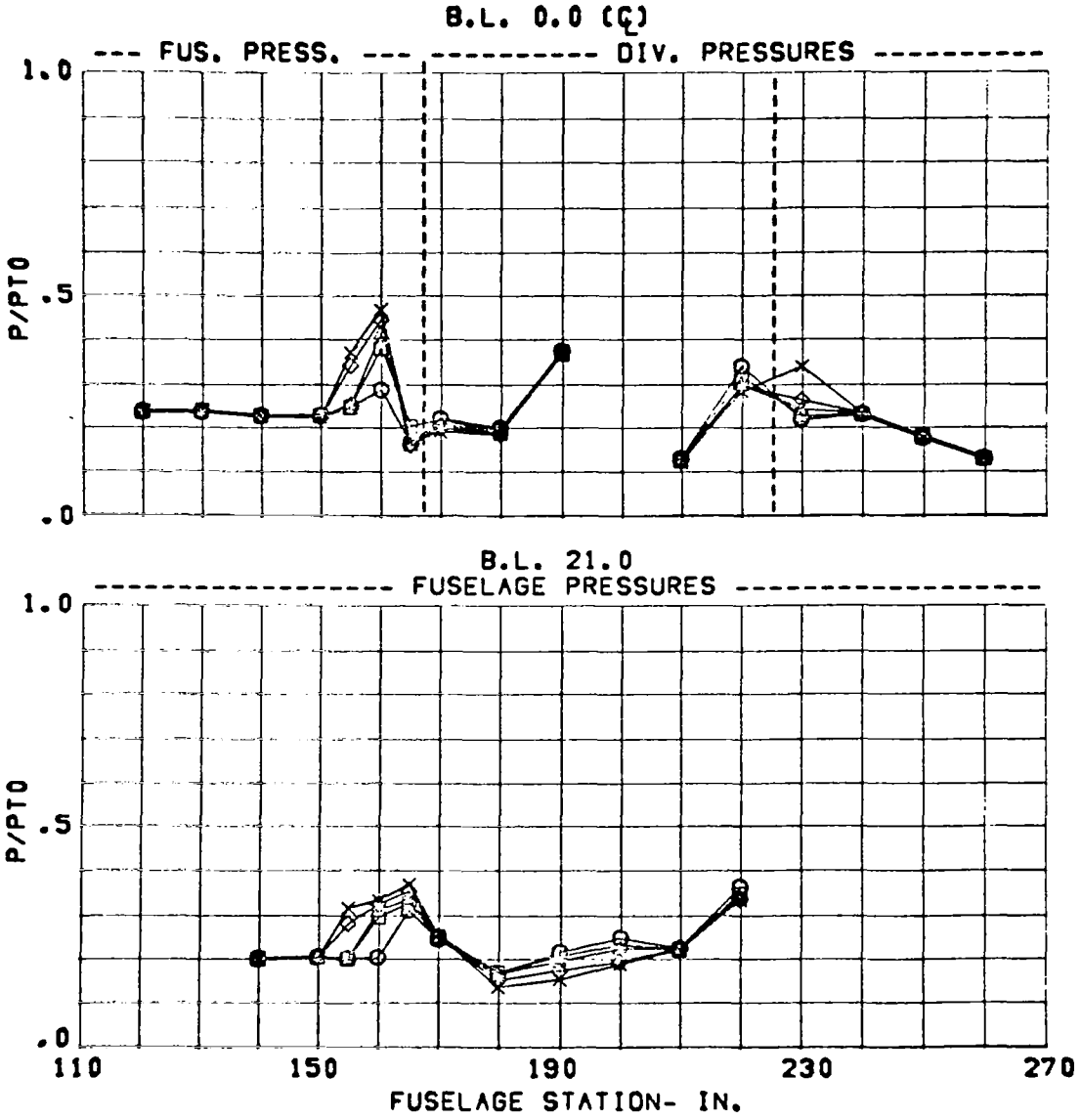

Figure 145 Fuselage and Diverter Static Pressures, Configuration C13

CONFIGURATION	CONDITION	SYM.	WC2(LBS/SEC)
C13	MACH = .61	□	218.
3.65 IN. DIV.	ALPHA= -9.	△	201.
NOSE BOOM ON	BETA = 0.	◇	178.
DIV. STRUTS OUT		×	158.

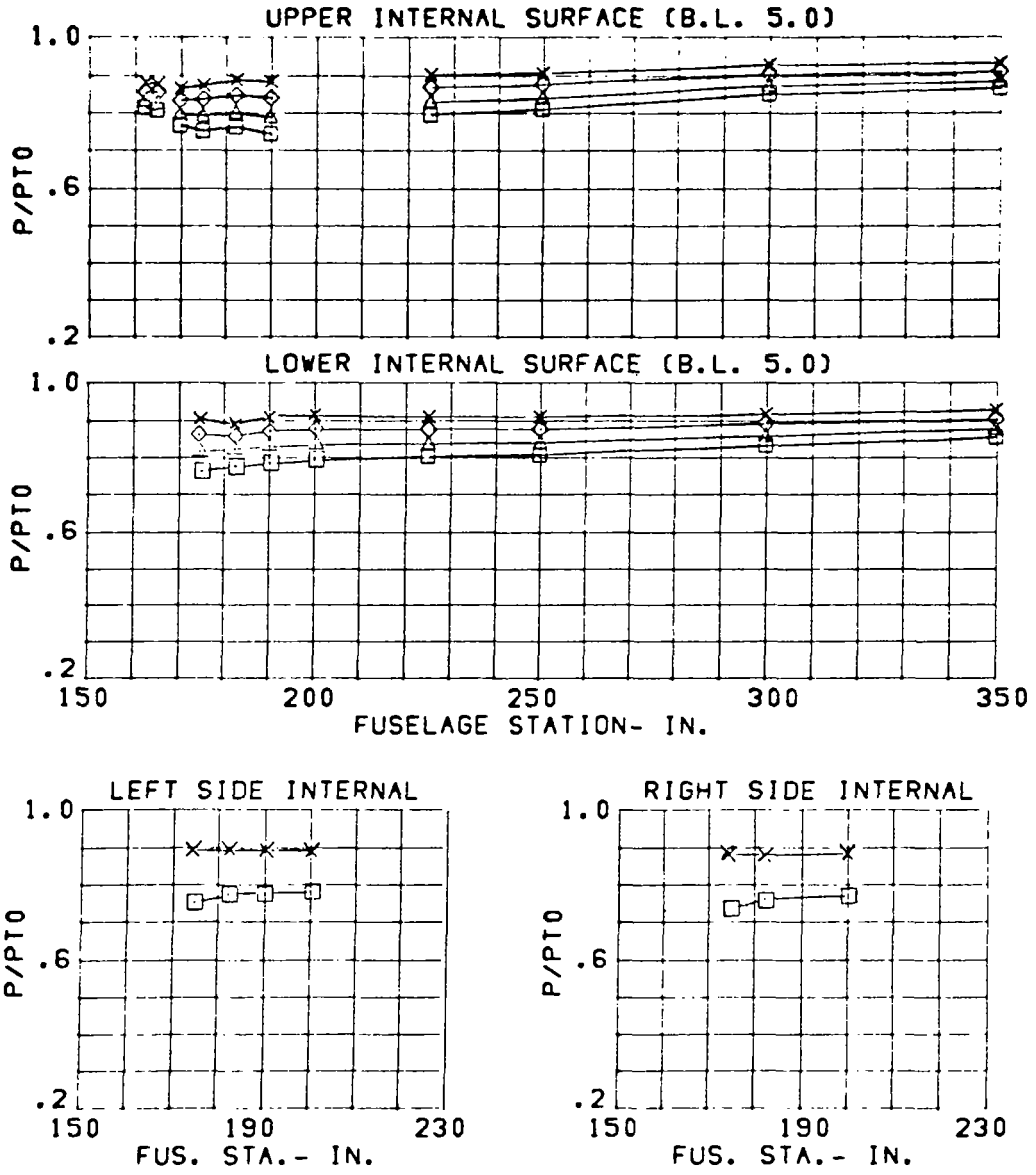

Figure 146 Cowl and Duct Static Pressures, Configuration C13

CONFIGURATION	CONDITION	SYM.	WC2(LBS/SEC)
C13	MACH = .60	□	217.
3.65 IN. DIV.	ALPHA= 1.	△	199.
NOSE BOOM ON	BETA = 0.	◇	177.
DIV. STRUTS OUT		×	157.

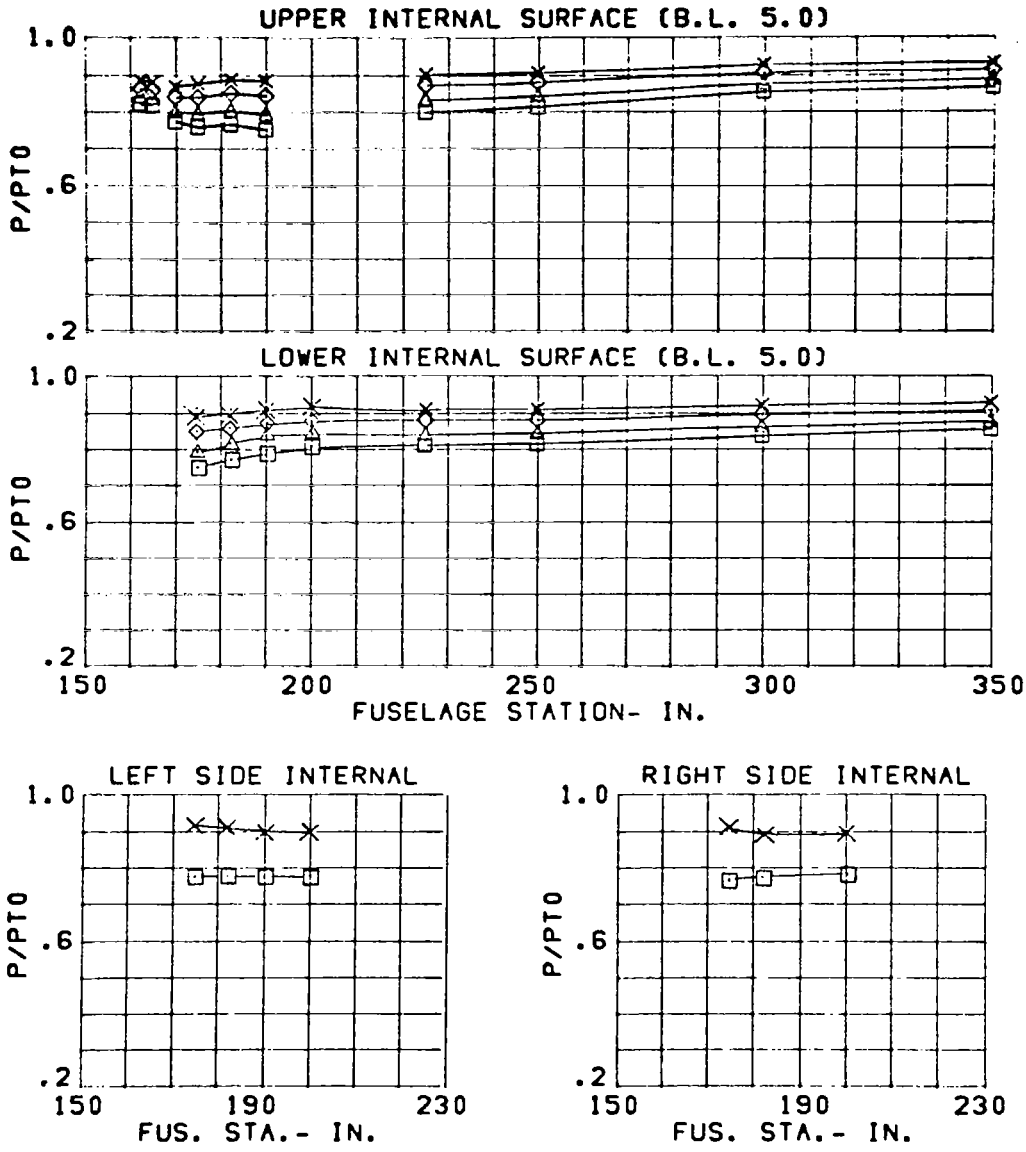

Figure 147 Cowl and Duct Static Pressures, Configuration C13

CONFIGURATION	CONDITION	SYM.	WC2(LBS/SEC)
C13	MACH = .60	□	219.
3.65 IN. DIV.	ALPHA= 20.	△	201.
NOSE BOOM ON	BETA = 0.	◇	179.
DIV. STRUTS OUT		×	158.

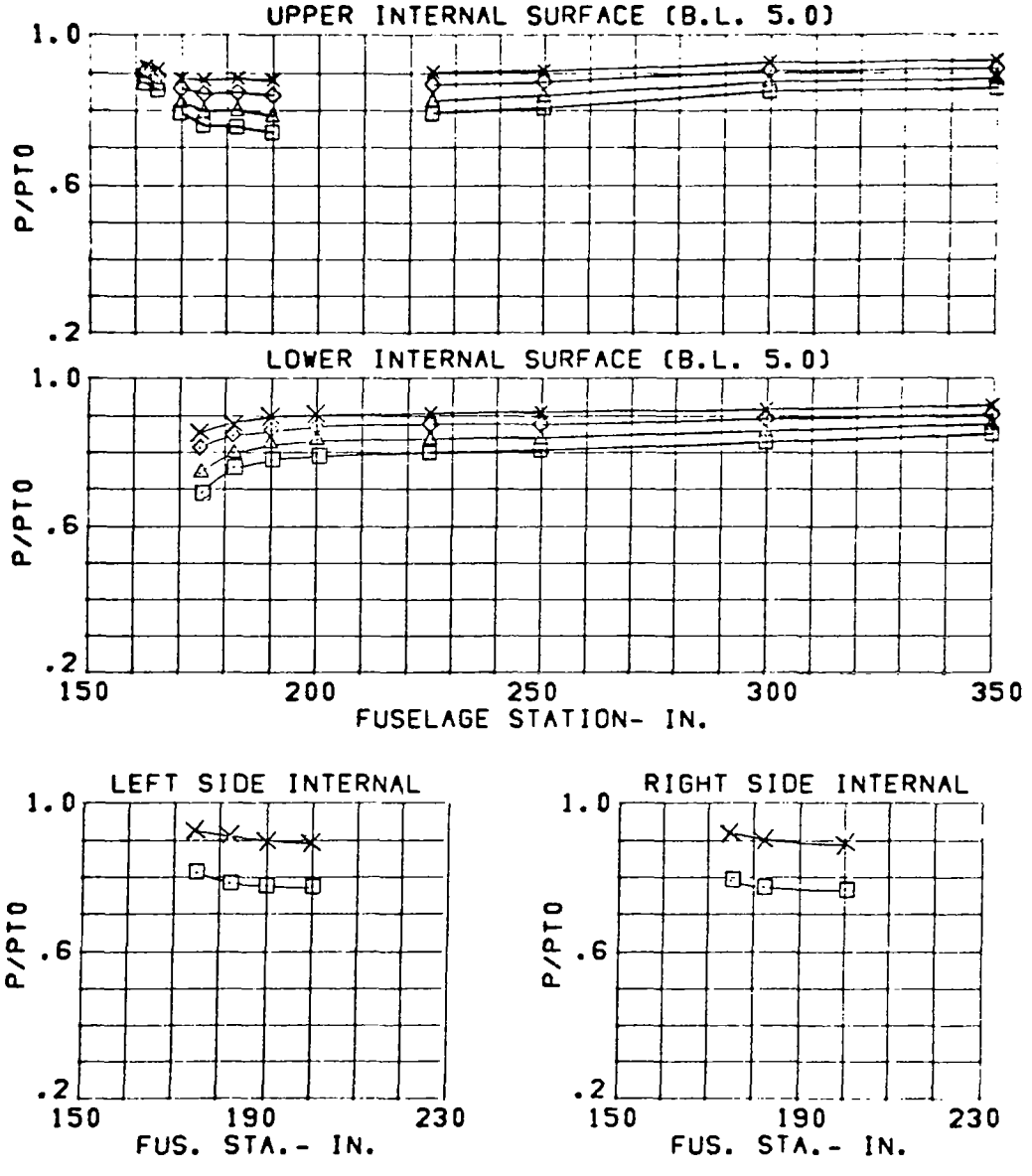

Figure 148 Cowl and Duct Static Pressures, Configuration C13

CONFIGURATION	CONDITION	SYM.	WC2(LBS/SEC)
C13	MACH = .60	□	215.
3.65 IN. DIV.	ALPHA= 30.	△	196.
NOSE BOOM ON	BETA = -0.	◇	176.
DIV. STRUTS OUT		×	155.

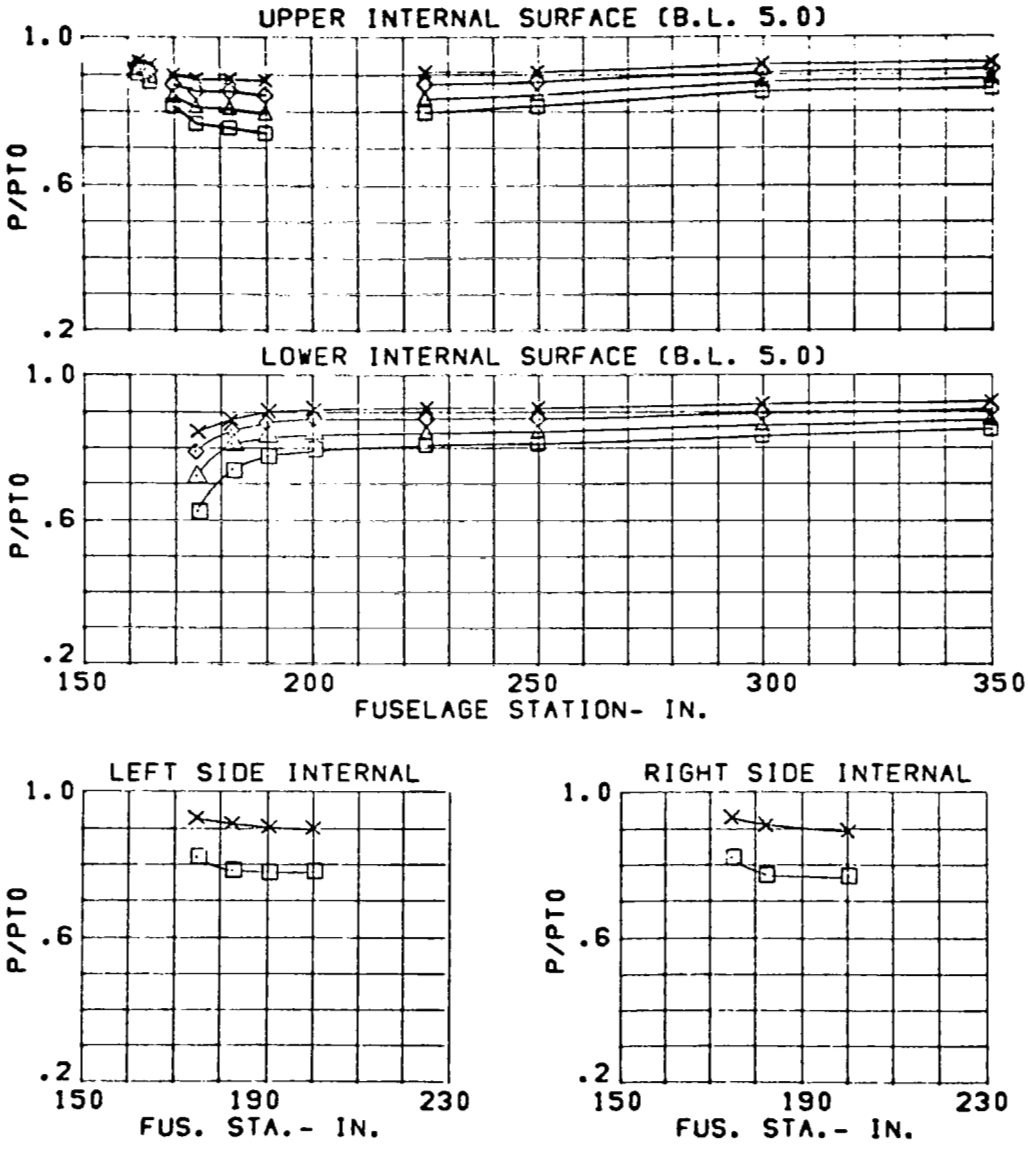

Figure 149 Cowl and Duct Static Pressures, Configuration C13

CONFIGURATION	CONDITION	SYM.	WC2(LBS/SEC)
C13	MACH = .60	□	211.
3.65 IN. DIV.	ALPHA= 40.	△	191.
NOSE BOOM ON	BETA = -0.	◇	172.
DIV. STRUTS OUT		×	153.

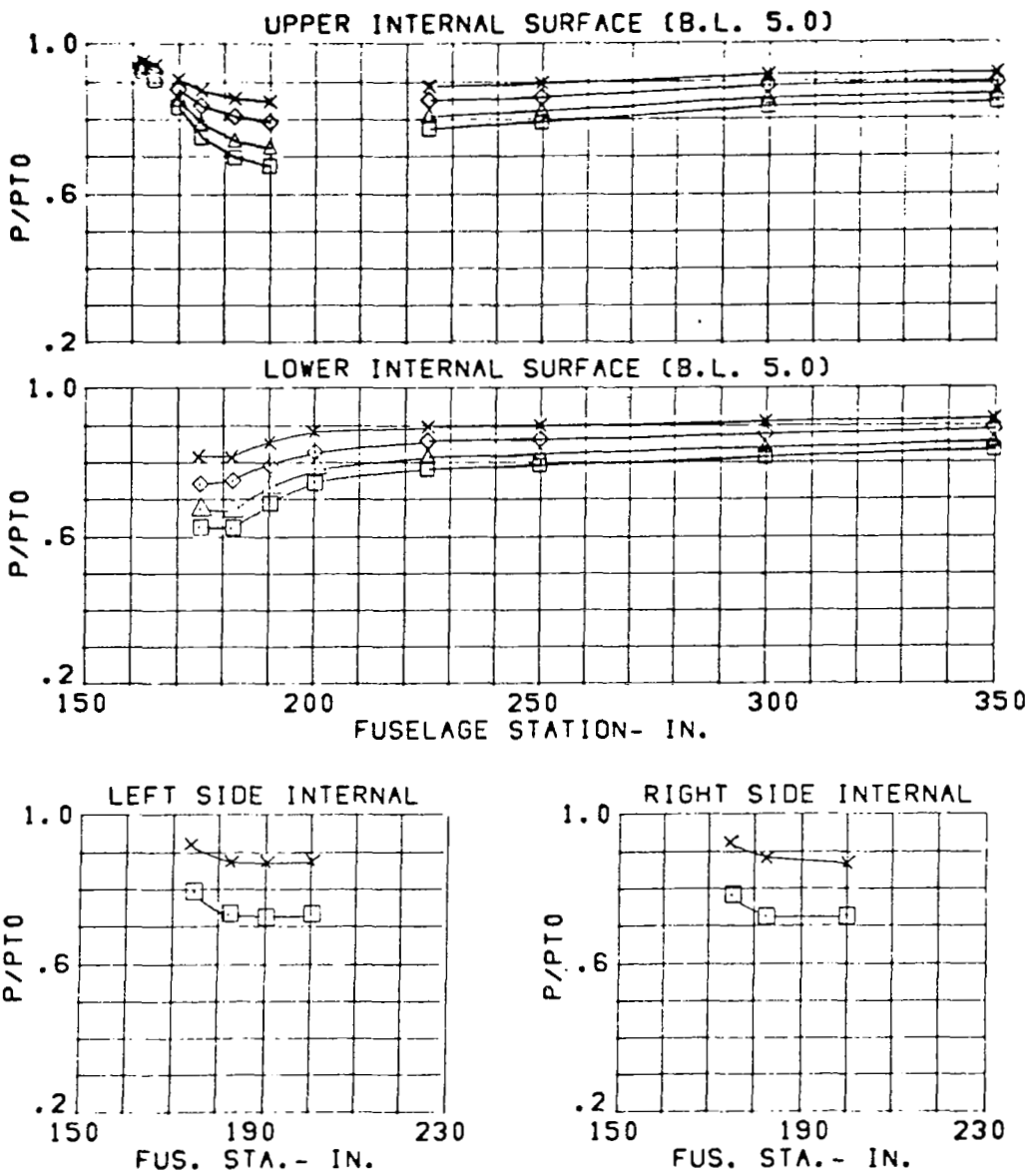

Figure 150 Cowl and Duct Static Pressures, Configuration C13

CONFIGURATION	CONDITION	SYM.	WC2(LBS/SEC)
C13	MACH = .91	○	249.
3.65 IN. DIV.	ALPHA= -9.	□	234.
NOSE BOOM ON	BETA = 0.	△	209.
DIV. STRUTS OUT		◇	185.
		×	160.

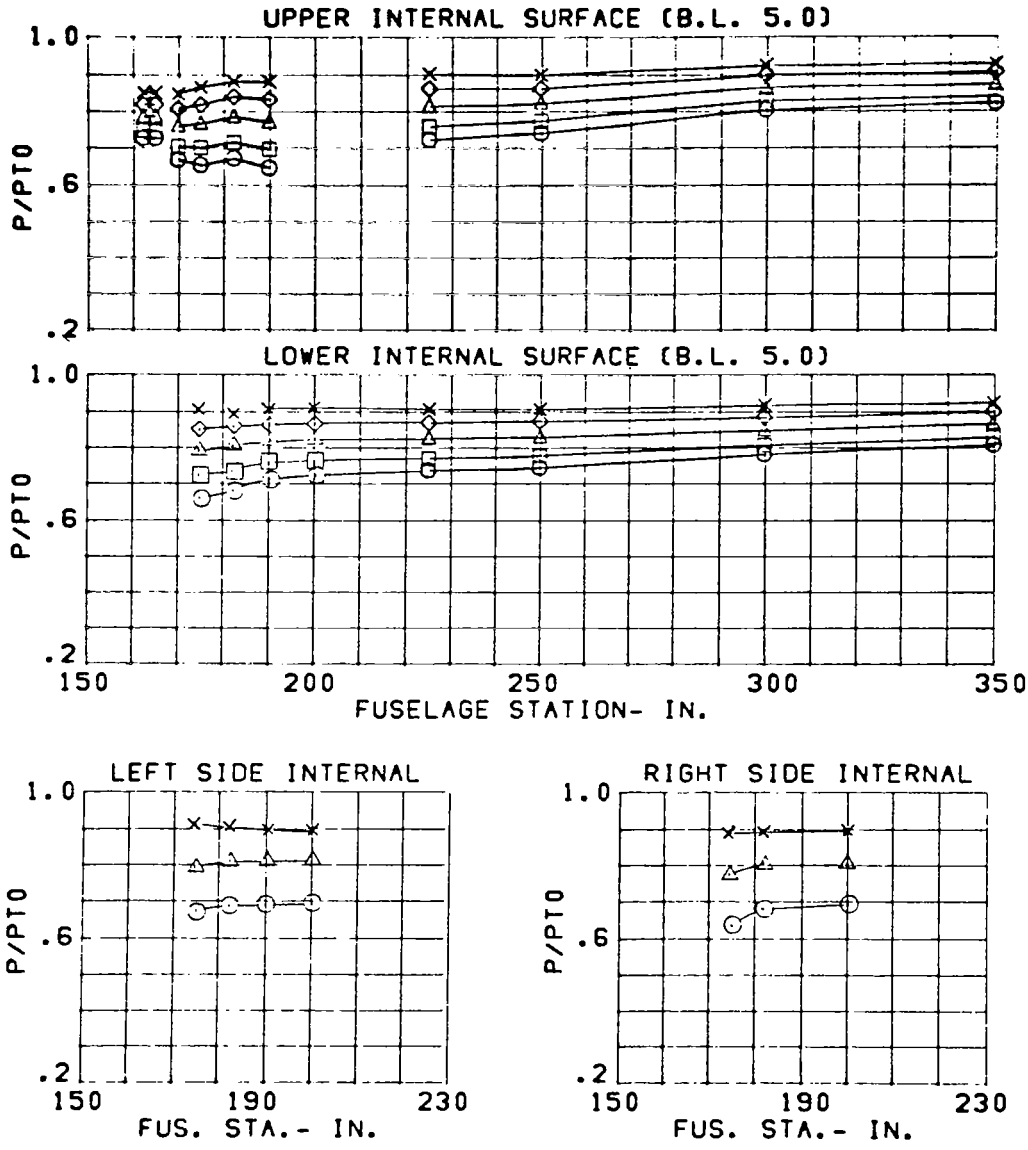

Figure 151 Cowl and Duct Static Pressures, Configuration C13

CONFIGURATION	CONDITION	SYM.	WC2(LBS/SEC)
C13	MACH = .91	○	248.
3.65 IN. DIV.	ALPHA= 1.	□	233.
NOSE BOOM ON	BETA = 0.	△	209.
DIV. STRUTS OUT		◇	185.
		×	159.

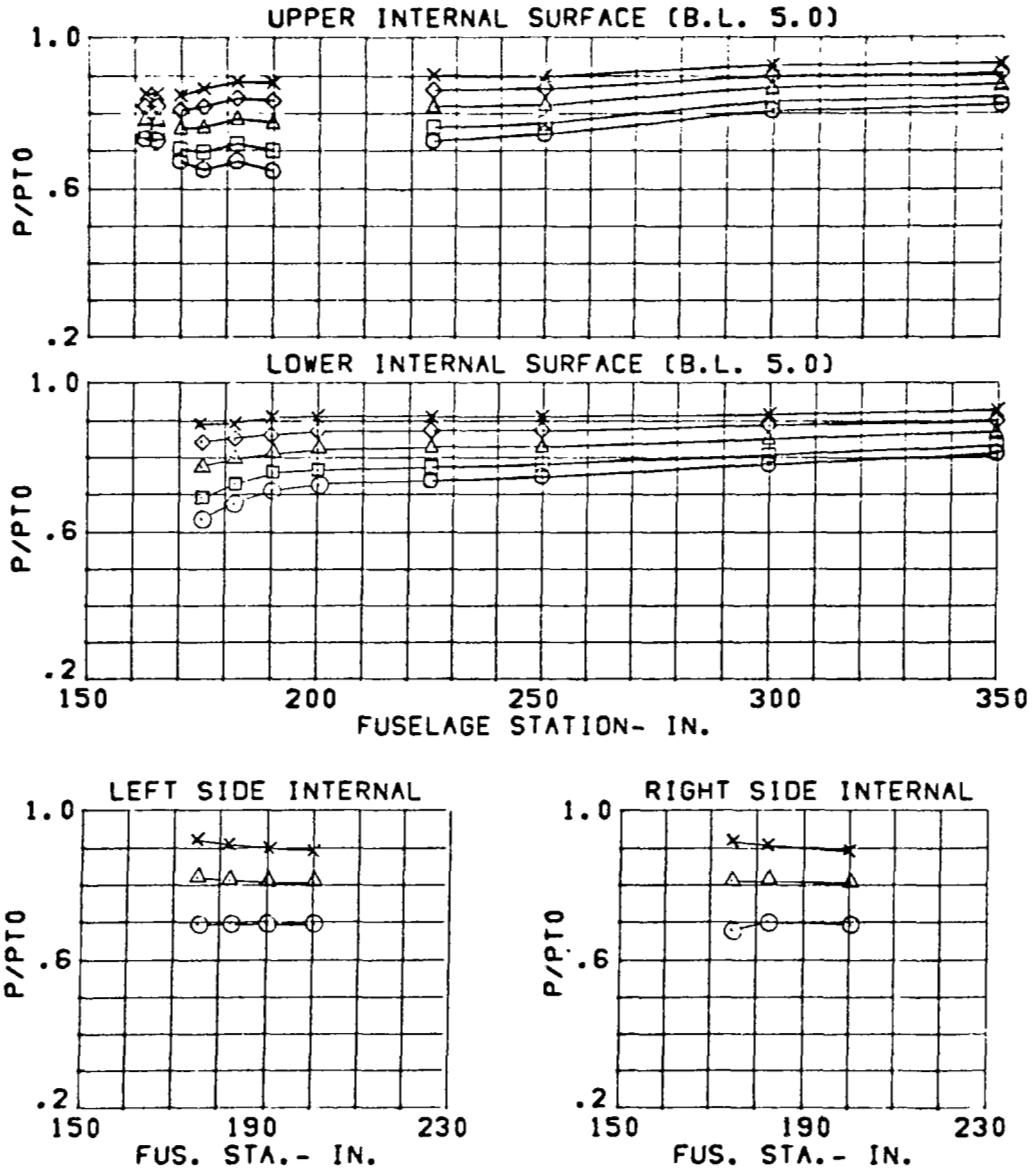

Figure 152 Cowl and Duct Static Pressures, Configuration C13

CONFIGURATION	CONDITION	SYM.	WC2(LBS/SEC)
C13	MACH = .89	○	249.
3.65 IN. DIV.	ALPHA= 20.	□	233.
NOSE BOOM ON	BETA = -3.	△	209.
DIV. STRUTS OUT		◇	185.
		×	159.

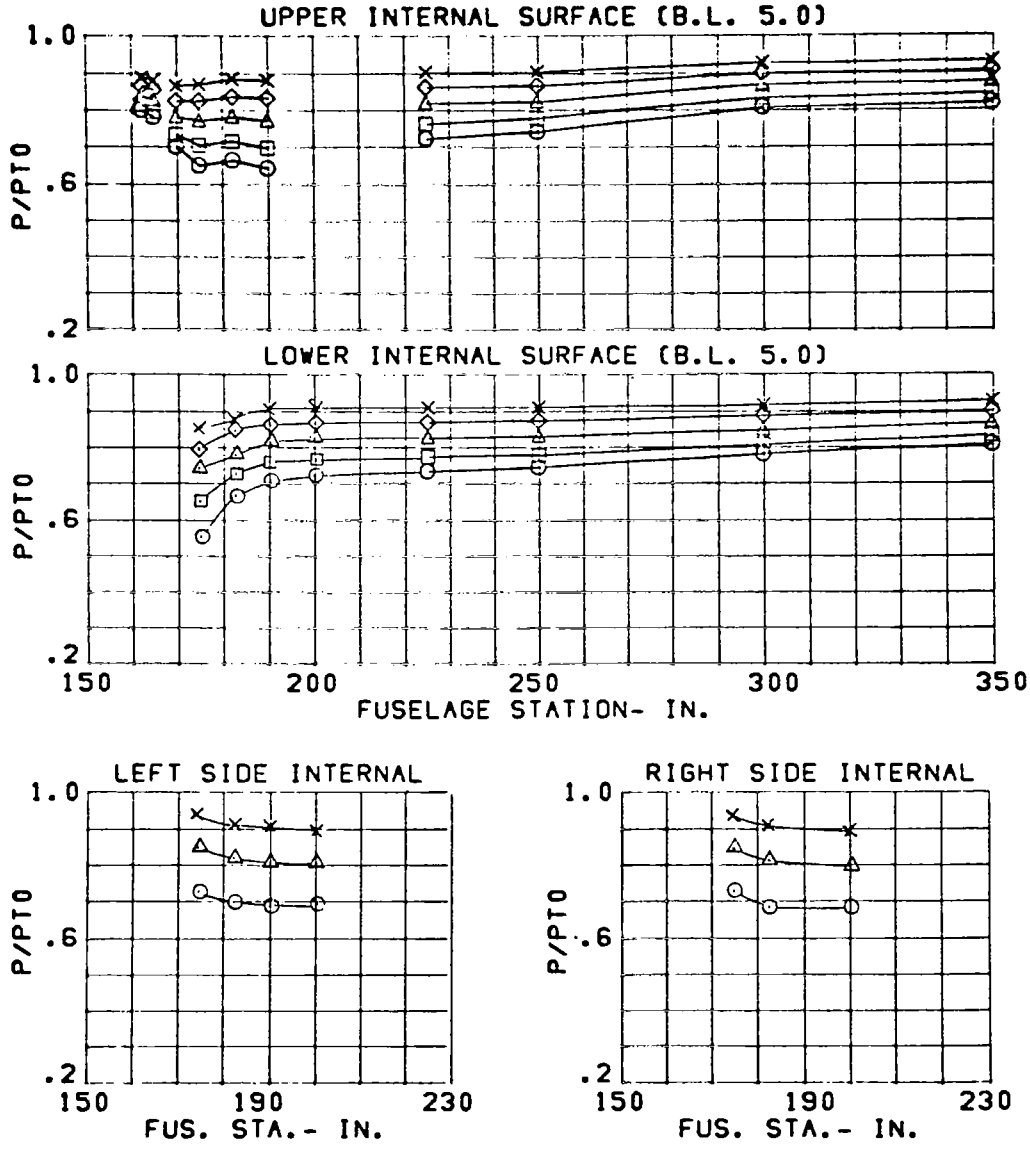

Figure 153 Cowl and Duct Static Pressures, Configuration C13

CONFIGURATION	CONDITION	SYM.	WC2(LBS/SEC)
C13	MACH = .91	○	247.
3.65 IN. DIV.	ALPHA= 30.	□	231.
NOSE BOOM ON	BETA = -0.	△	208.
DIV. STRUTS OUT		◇	184.
		×	158.

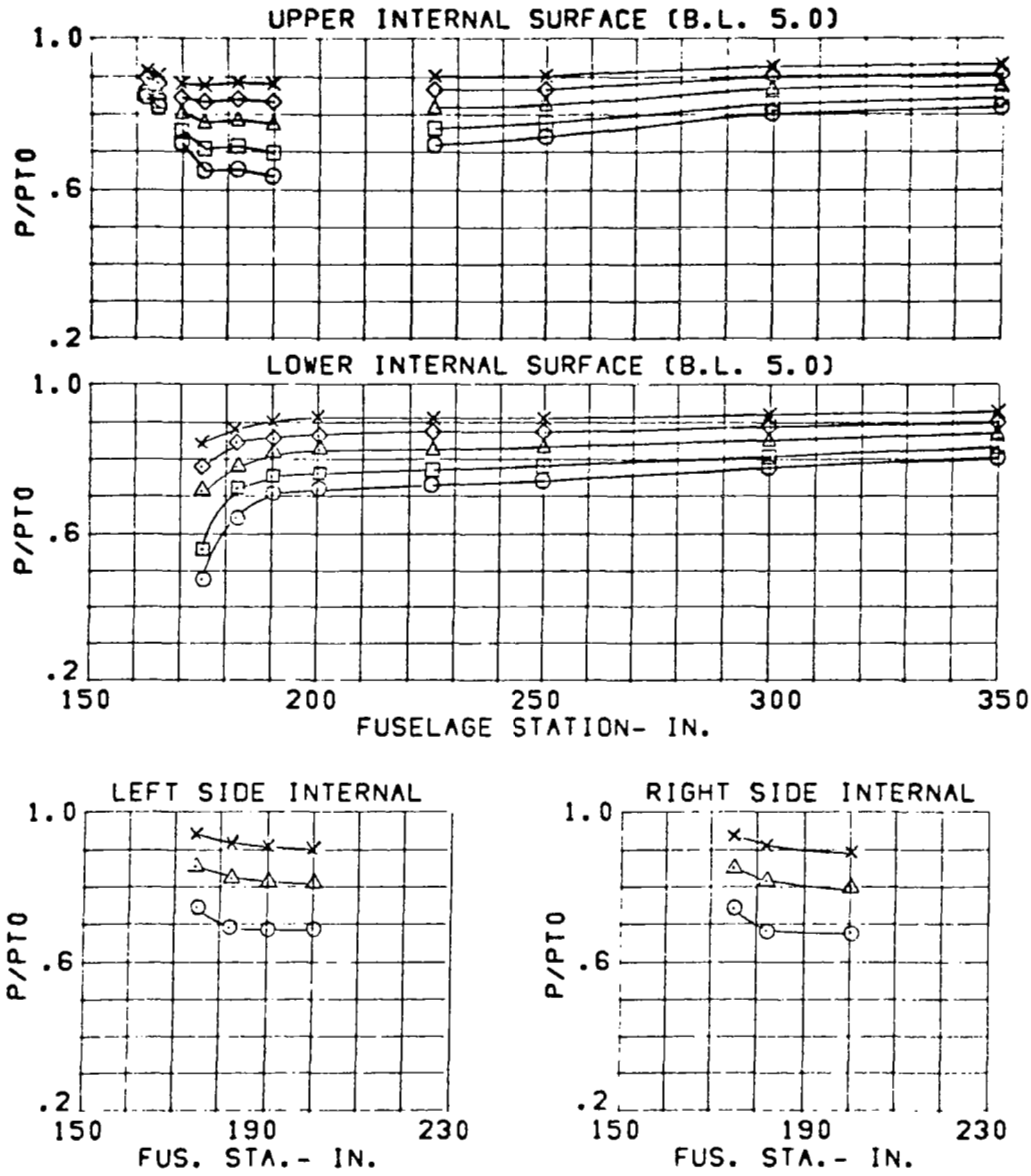

Figure 154 Cowl and Duct Static Pressures, Configuration C13

CONFIGURATION	CONDITION	SYM.	WC2(LBS/SEC)
C13	MACH = .90	○	244.
3.65 IN. DIV.	ALPHA= 40.	□	229.
NOSE BOOM ON	BETA = 0.	△	206.
DIV. STRUTS OUT		◇	183.
		×	157.

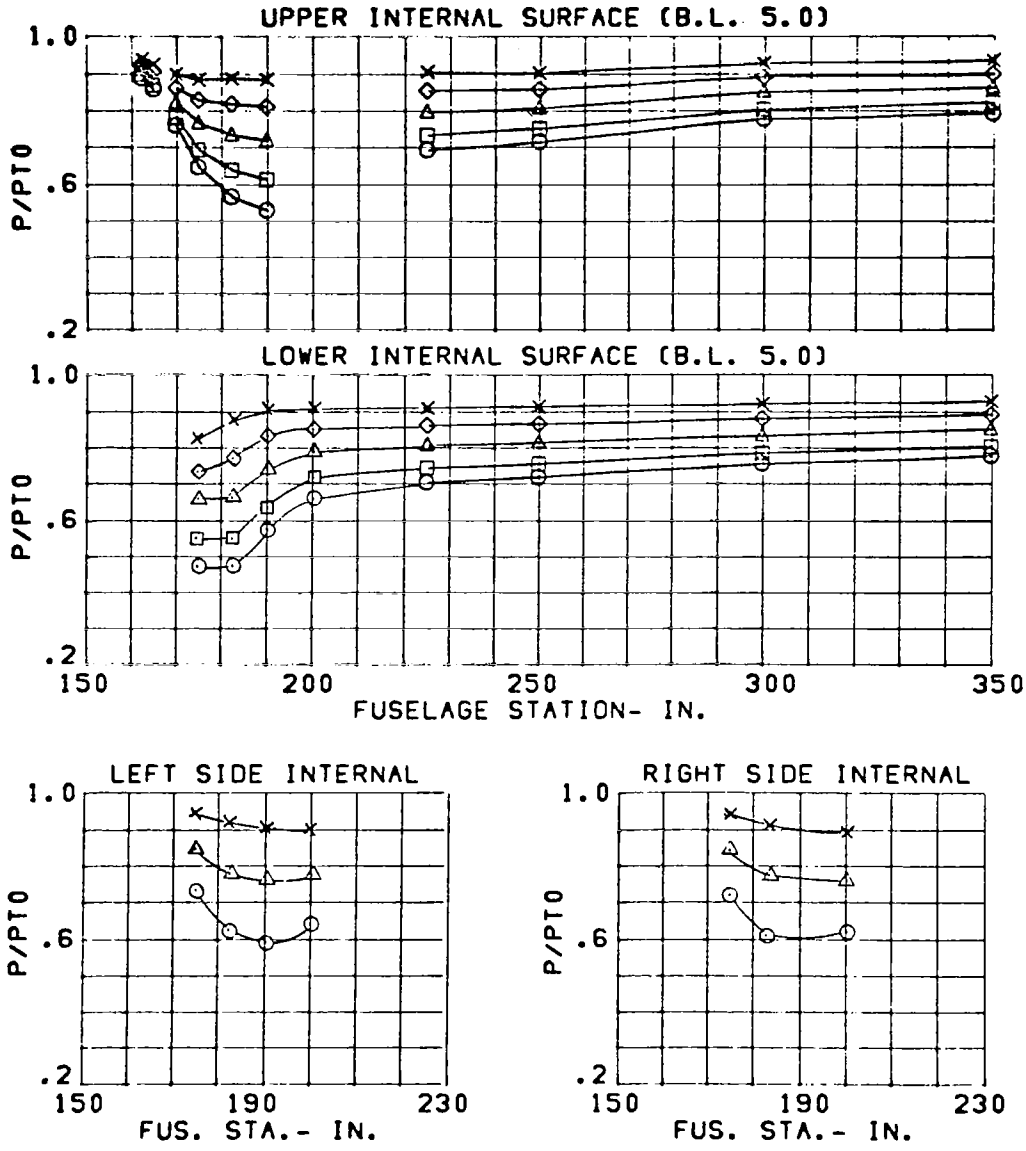

Figure 155 Cowl and Duct Static Pressures, Configuration C13

CONFIGURATION	CONDITION	SYM.	WC2(LBS/SEC)
C13	MACH = 1.21	○	246.
3.65 IN. DIV.	ALPHA= -9.	□	231.
NOSE BOOM ON	BETA = 0.	△	209.
DIV. STRUTS OUT		◇	185.
		×	159.

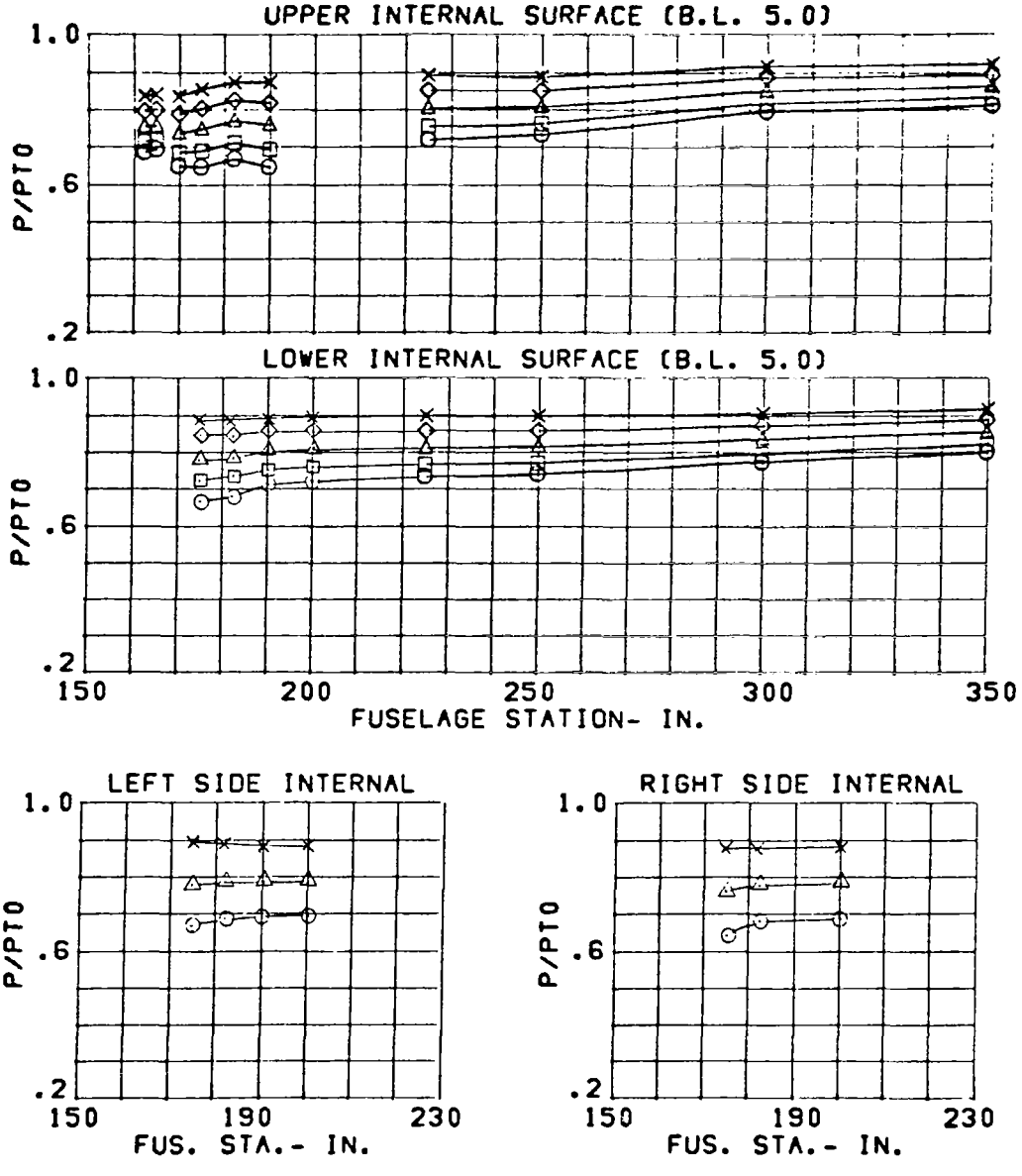

Figure 156 Cowl and Duct Static Pressures, Configuration C13

CONFIGURATION	CONDITION	SYM.	WC2(LBS/SEC)
C13	MACH = 1.21	○	245.
3.65 IN. DIV.	ALPHA= 1.	□	232.
NOSE BOOM ON	BETA = 0.	△	208.
DIV. STRUTS OUT		◇	185.
		×	159.

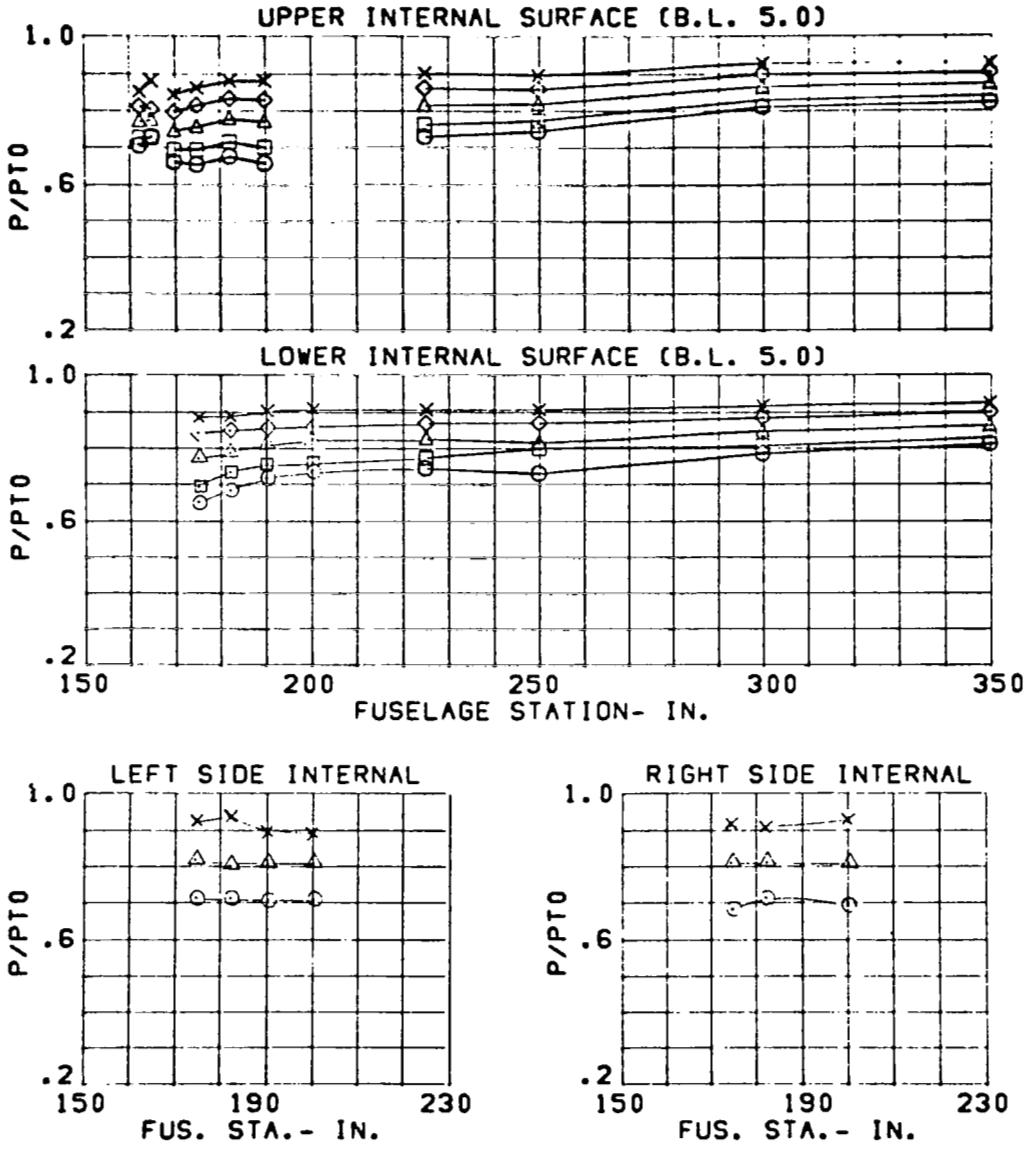

Figure 157 Cowl and Duct Static Pressures, Configuration C13

CONFIGURATION	CONDITION	SYM.	WC2(LBS/SEC)
C13	MACH = 1.22	○	246.
3.65 IN. DIV.	ALPHA= 15.	□	232.
NOSE BOOM ON	BETA = 0.	△	209.
DIV. STRUTS OUT		◇	185.
		×	159.

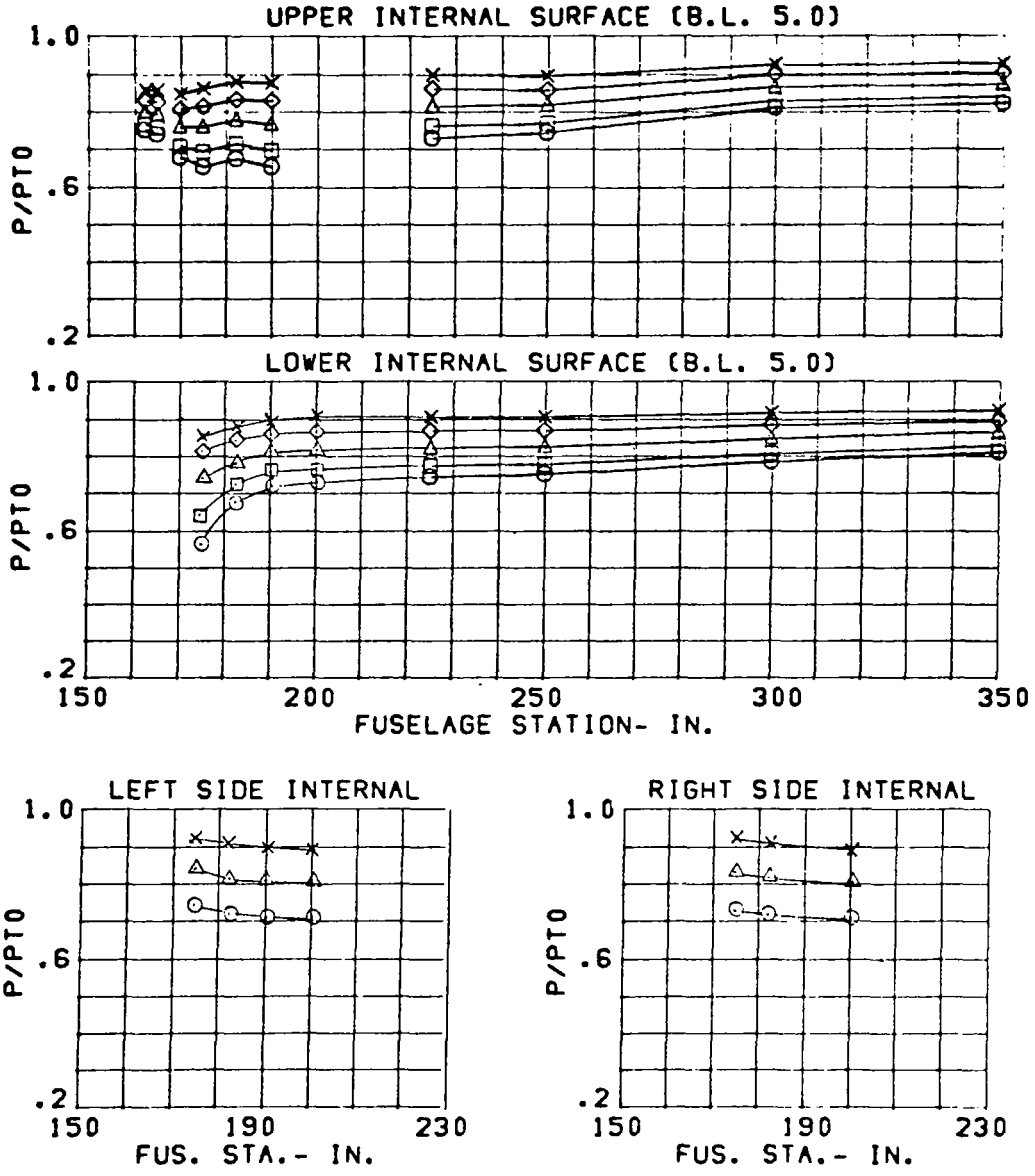

Figure 158 Cowl and Duct Static Pressures, Configuration C13

CONFIGURATION	CONDITION	SYM.	WC2(LBS/SEC)
C13	MACH = 1.22	○	245.
3.65 IN. DIV.	ALPHA= 30.	□	232.
NOSE BOOM ON	BETA = -1.	△	209.
DIV. STRUTS OUT		◇	184.
		×	159.

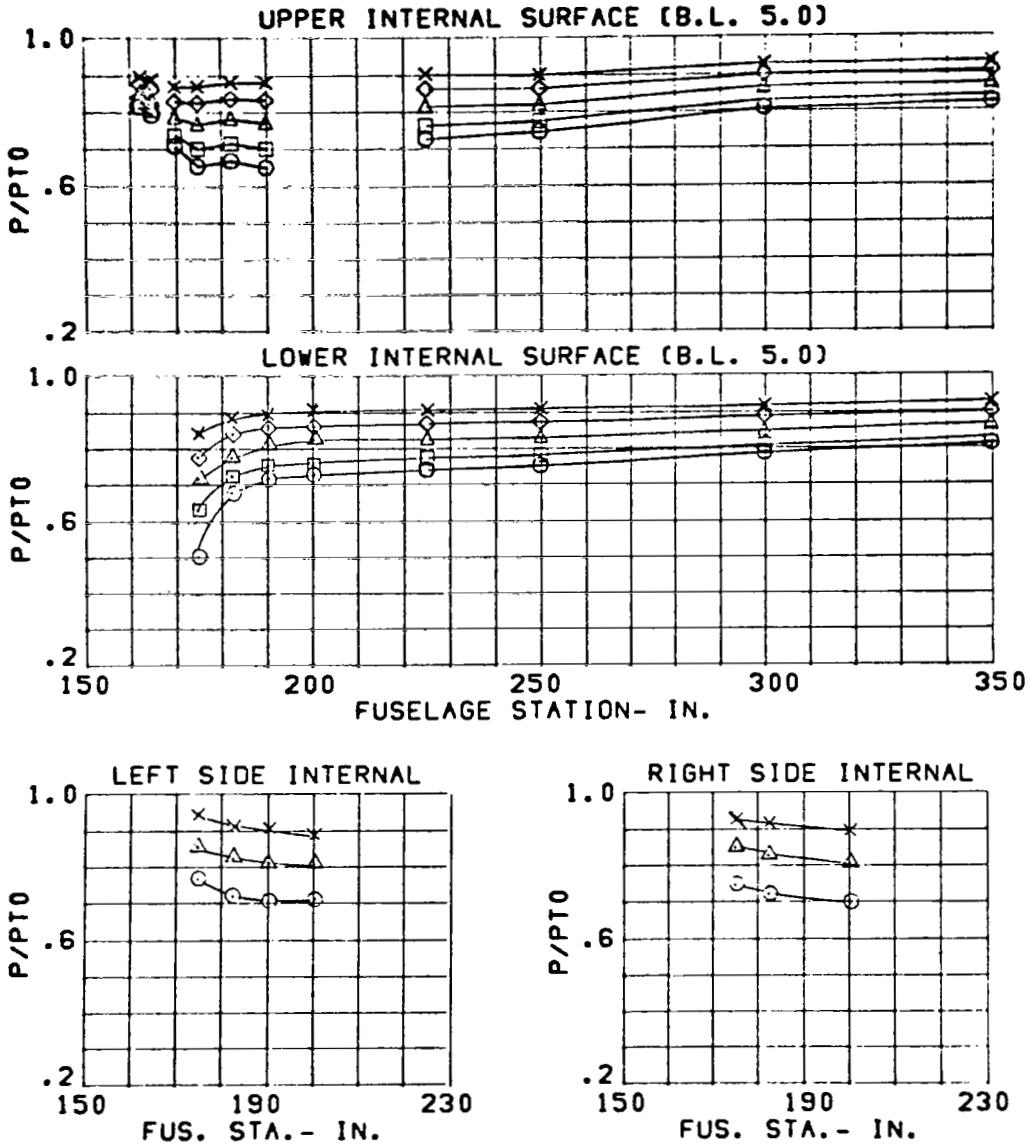

Figure 159 Cowl and Duct Static Pressures, Configuration C13

CONFIGURATION	CONDITION	SYM.	WC2(LBS/SEC)
C13	MACH = 1.37	○	244.
3.65 IN. DIV.	ALPHA= -5.	□	228.
NOSE BOOM ON	BETA = 0.	△	207.
DIV. STRUTS OUT		◇	185.
		×	159.

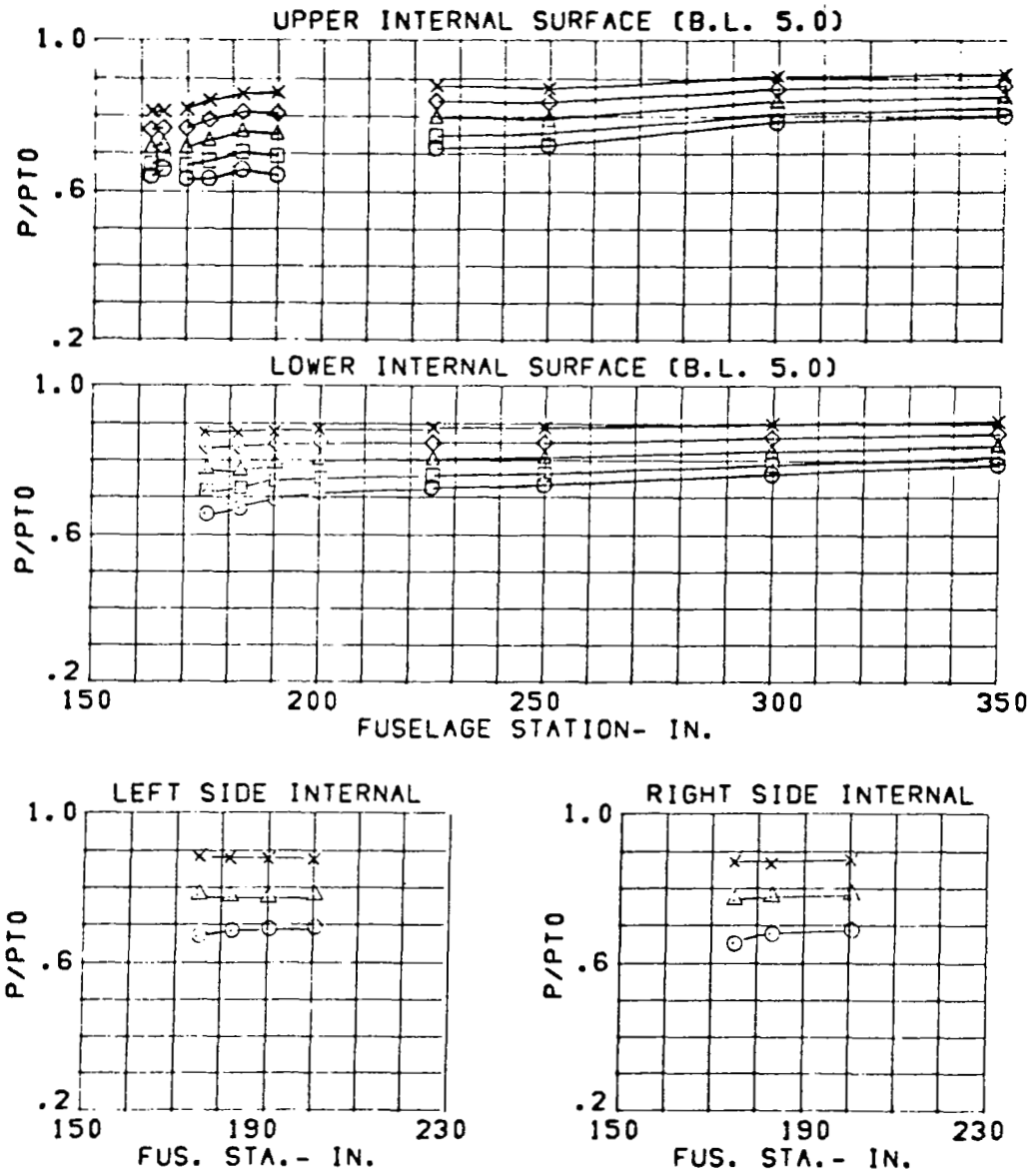

Figure 160 Cowl and Duct Static Pressures, Configuration C13

CONFIGURATION	CONDITION	SYM.	WC2(LBS/SEC)
C13	MACH = 1.39	○	244.
3.65 IN. DIV.	ALPHA= 1.	□	228.
NOSE BOOM ON	BETA = 0.	△	207.
DIV. STRUTS OUT		◇	185.
		×	159.

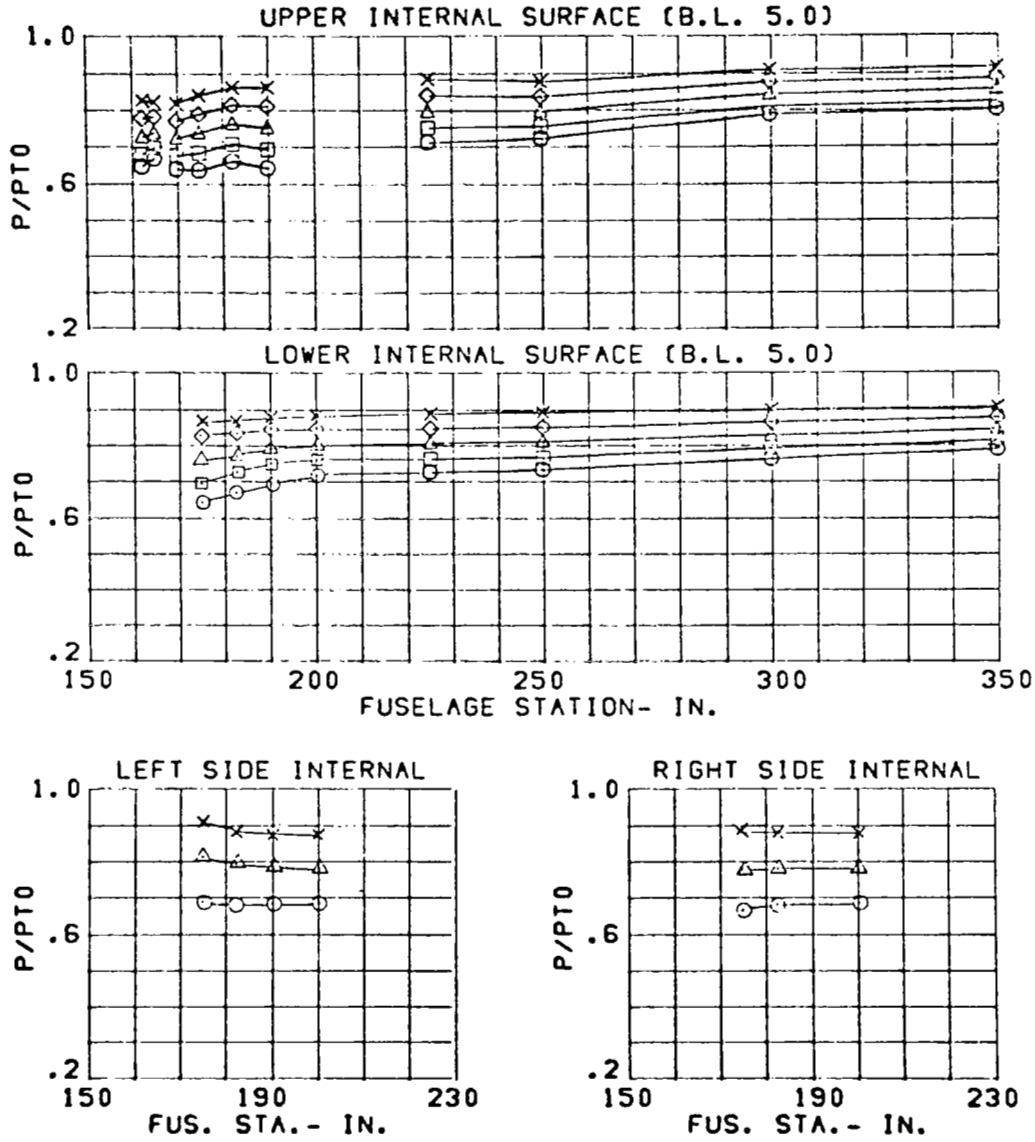

Figure 161 Cowl and Duct Static Pressures, Configuration C13

CONFIGURATION	CONDITION	SYM.	WC2(LBS/SEC)
C13	MACH = 1.38	○	244.
3.65 IN. DIV.	ALPHA= 15.	□	228.
NOSE BOOM ON	BETA = 0.	△	207.
DIV. STRUTS OUT		◇	185.
		×	159.

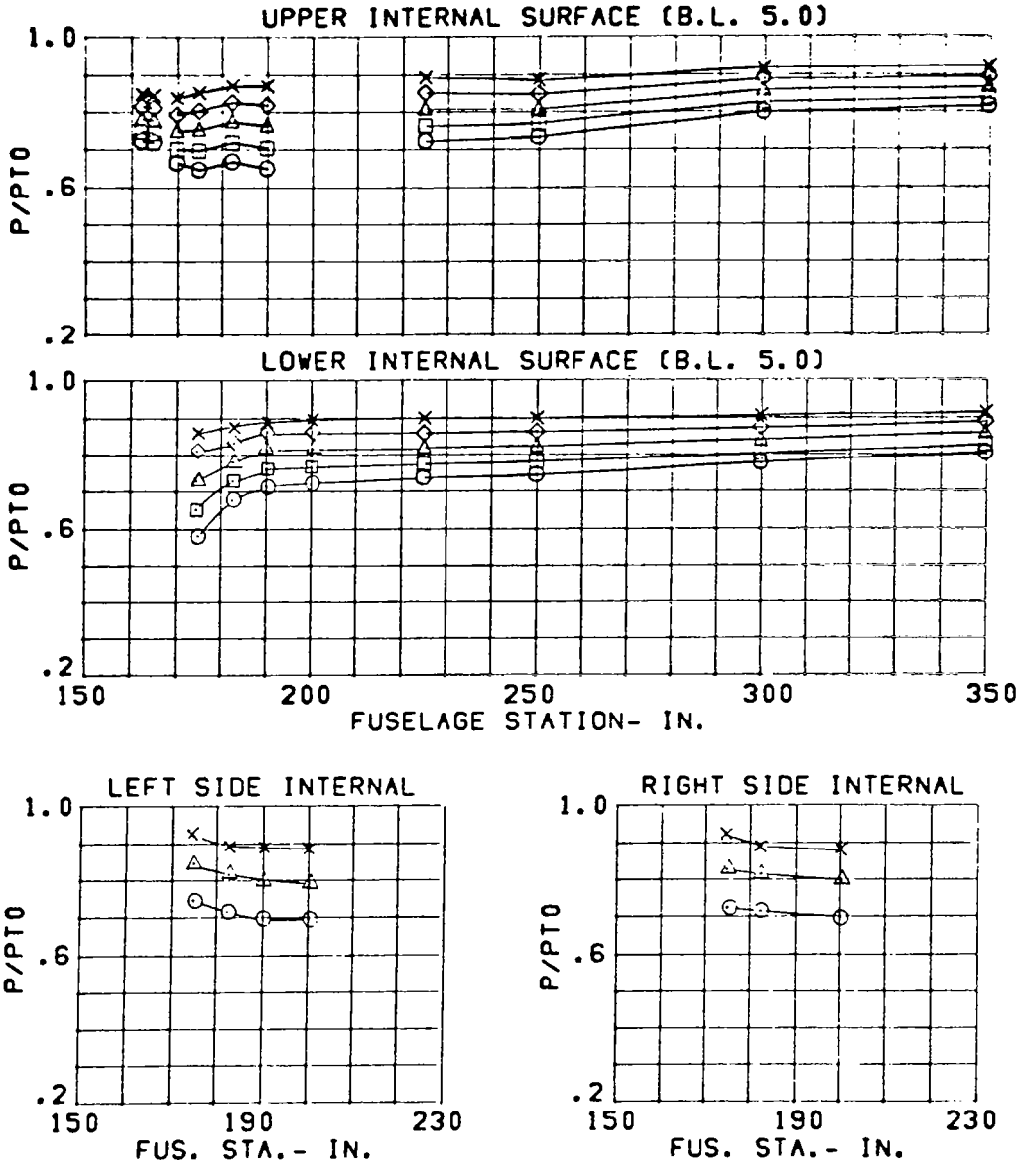

Figure 162 Cowl and Duct Static Pressures, Configuration C13

CONFIGURATION	CONDITION	SYM.	WC2(LBS/SEC)
C13	MACH = 1.36	○	245.
3.65 IN. DIV.	ALPHA= 25.	□	228.
NOSE BOOM ON	BETA = 0.	△	207.
DIV. STRUTS OUT		◇	185.
		×	159.

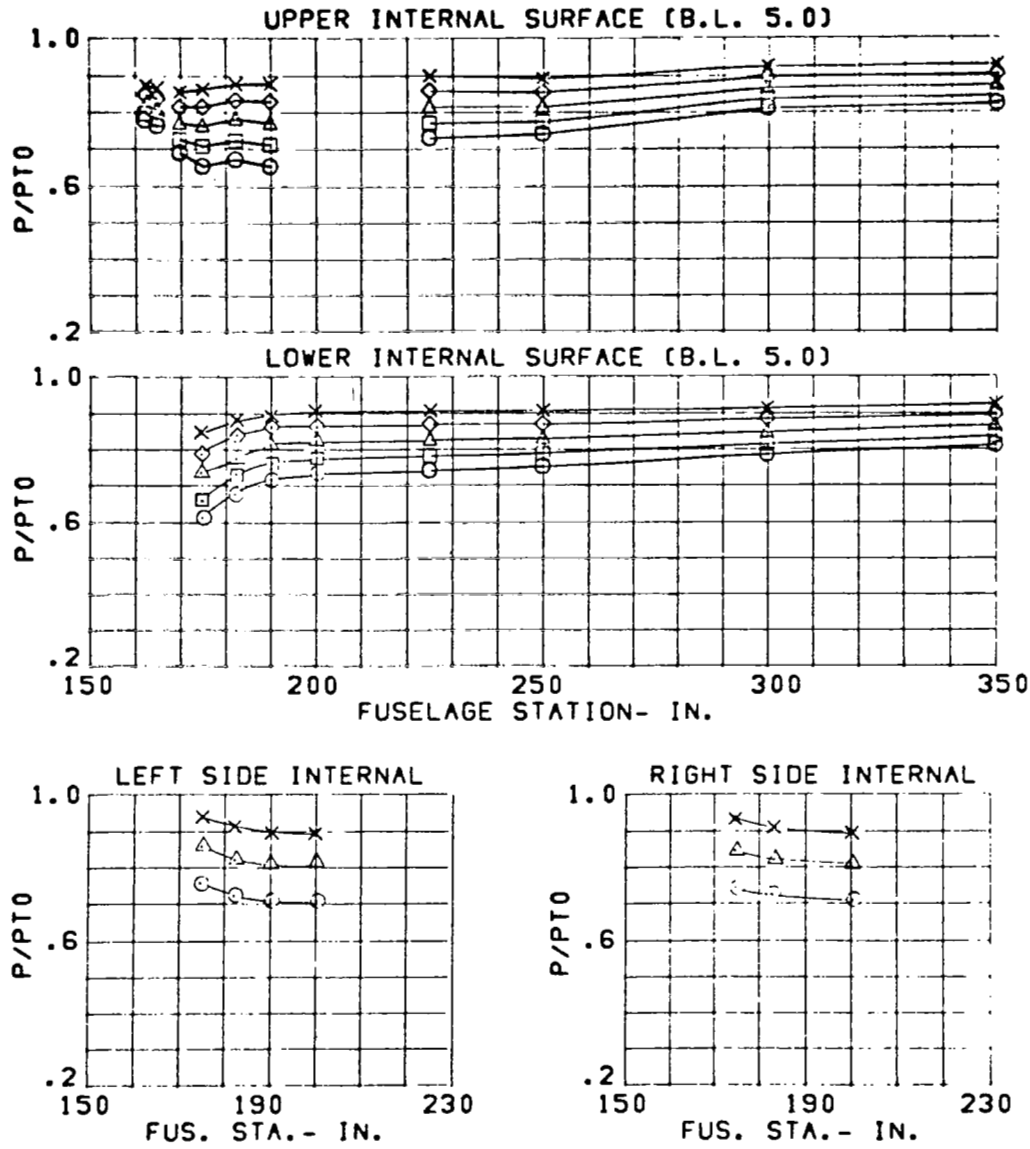

Figure 163 Cowl and Duct Static Pressures, Configuration C13

CONFIGURATION	CONDITION	SYM.	WC2(LBS/SEC)
C13	MACH = 1.58	○	232.
3.65 IN. DIV.	ALPHA= -5.	□	217.
NOSE BOOM ON	BETA = 0.	△	199.
DIV. STRUTS OUT		◇	179.
		×	159.

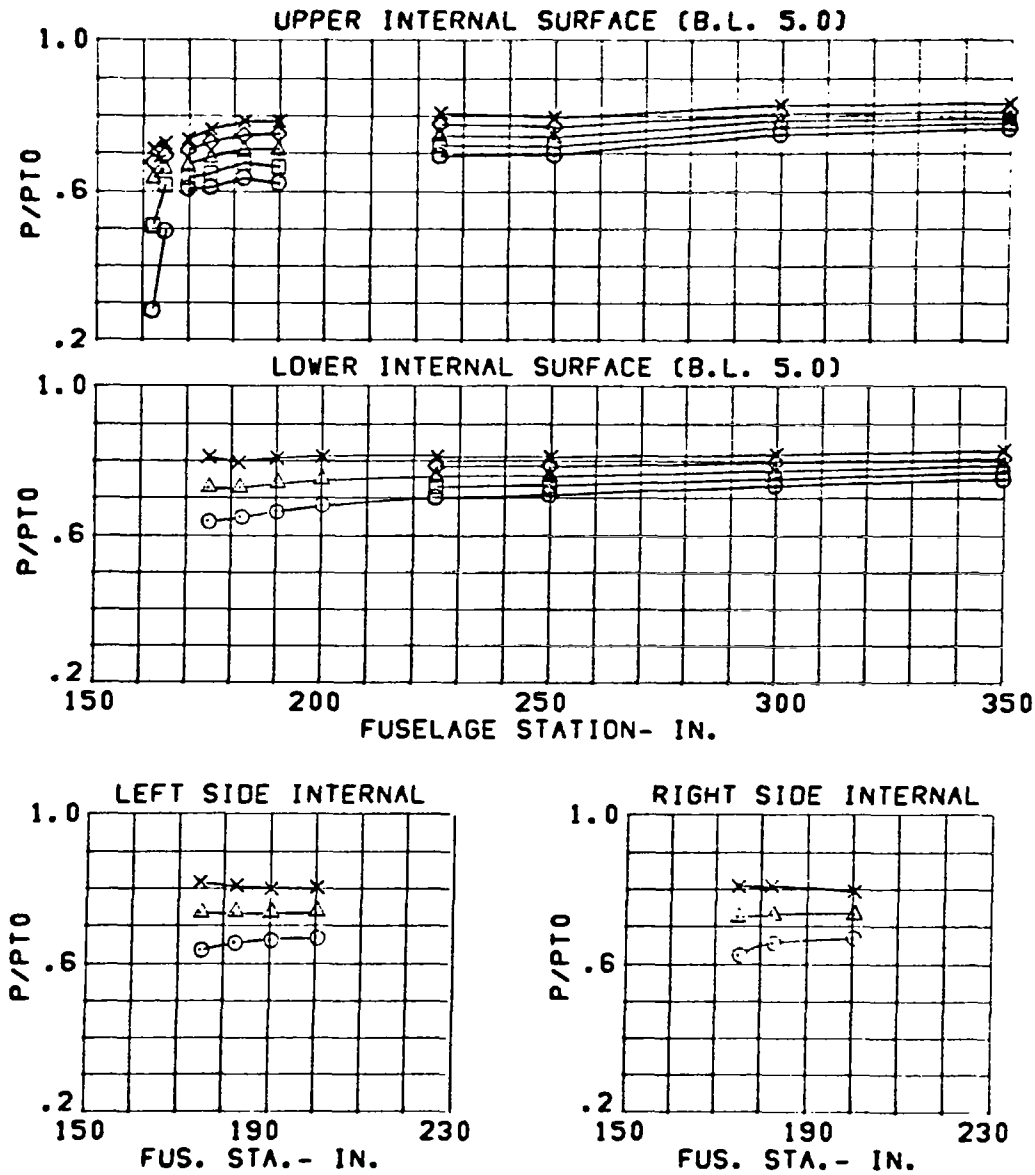

Figure 164 Cowl and Duct Static Pressures, Configuration C13

CONFIGURATION	CONDITION	SYM.	WC2(LBS/SEC)
C13	MACH = 1.58	○	232.
3.65 IN. DIV.	ALPHA= 1.	□	217.
NOSE BOOM ON	BETA = 0.	△	199.
DIV. STRUTS OUT		◇	179.
		×	159.

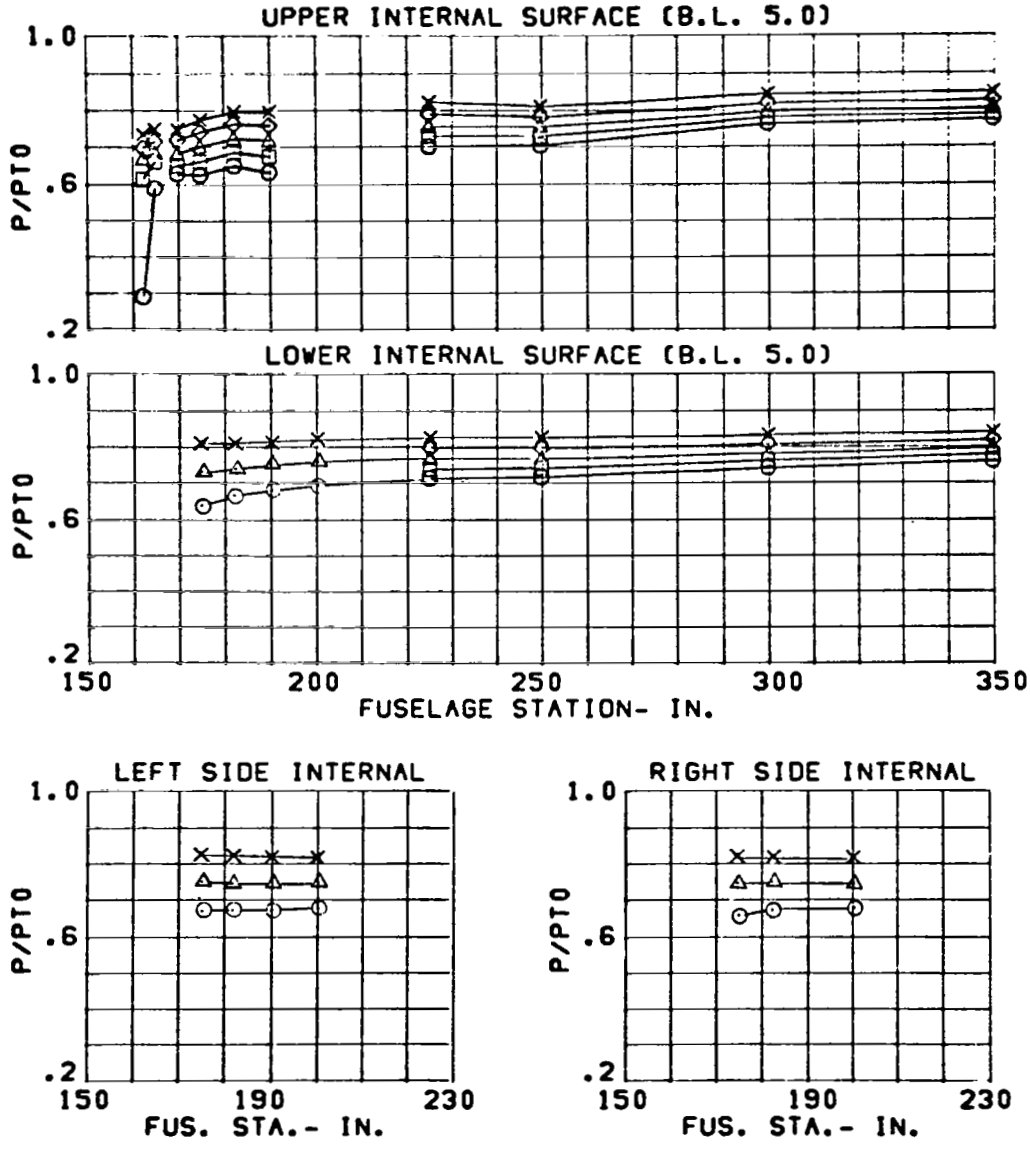

Figure 165 Cowl and Duct Static Pressures, Configuration C13

CONFIGURATION	CONDITION	SYM.	WC2(LBS/SEC)
C13	MACH = 1.58	○	233.
3.65 IN. DIV.	ALPHA= 6.	□	218.
NOSE BOOM ON	BETA = 0.	△	199.
DIV. STRUTS OUT		◇	179.
		×	160.

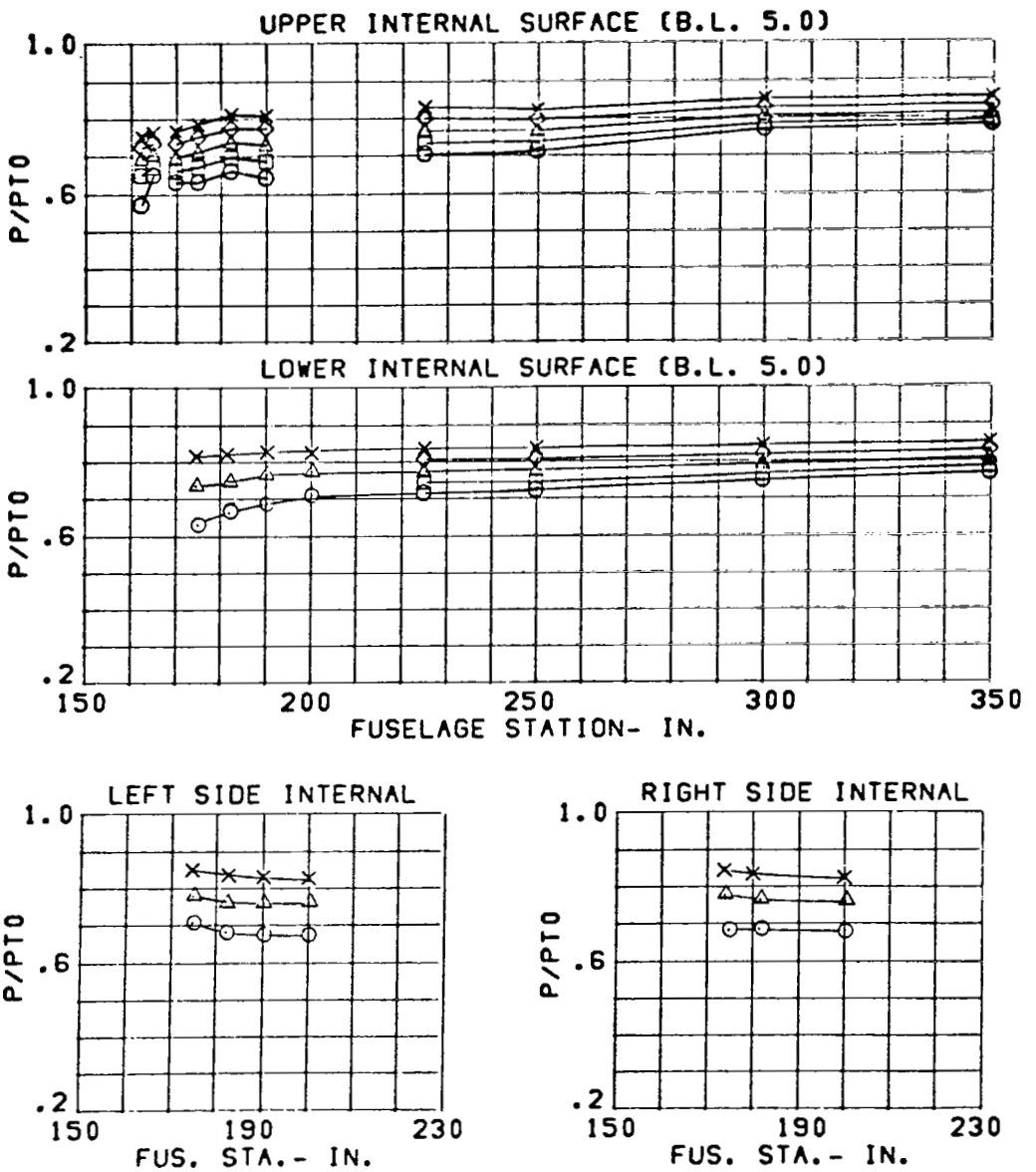

Figure 166 Cowl and Duct Static Pressures, Configuration C13

CONFIGURATION	CONDITION	SYM.	WC2(LBS/SEC)
C13	MACH = 1.58	O	233.
3.65 IN. DIV.	ALPHA= 20.	□	218.
NOSE BOOM ON	BETA = 0.	△	199.
DIV. STRUTS OUT		◇	179.
		×	160.

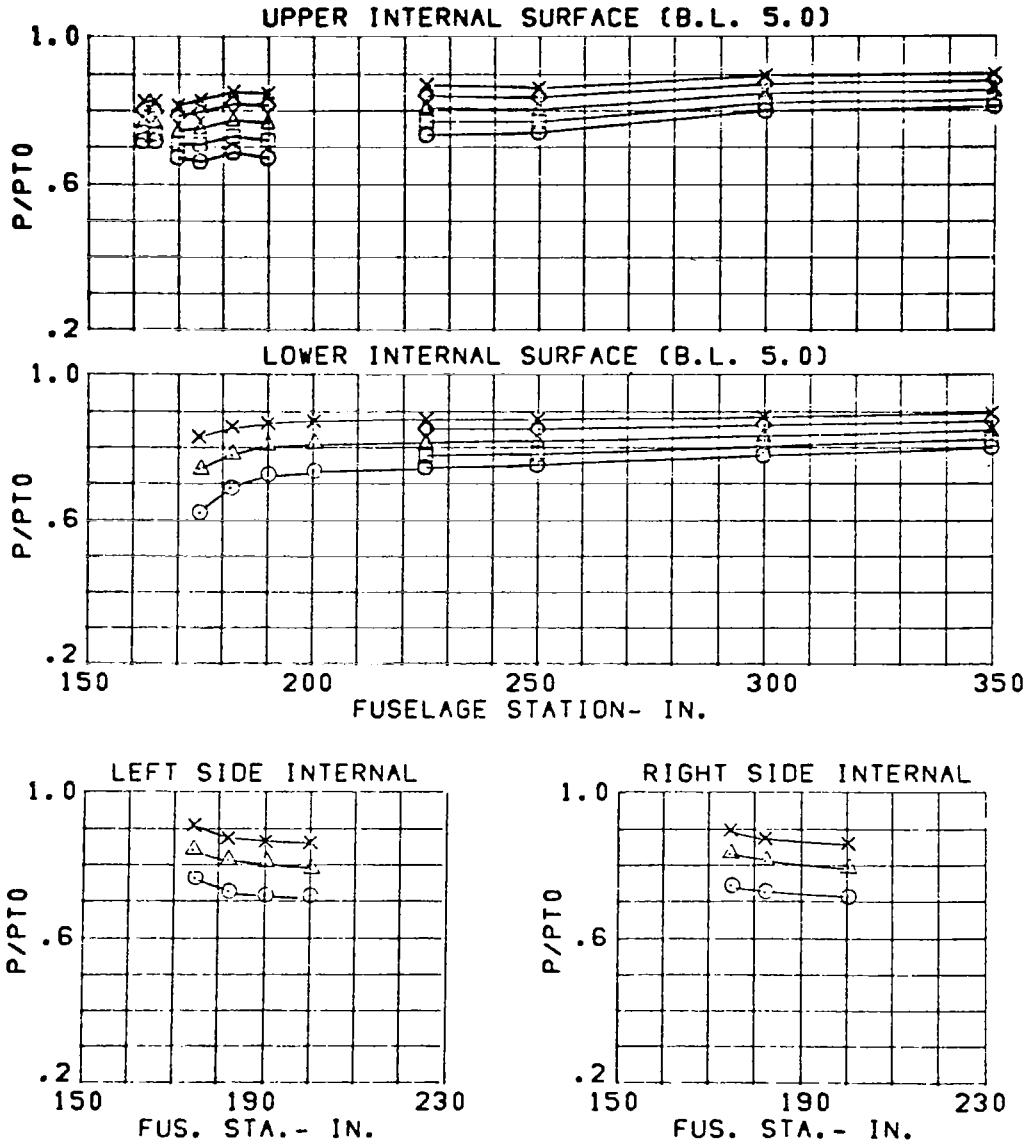

Figure 167 Cowl and Duct Static Pressures, Configuration C13

CONFIGURATION	CONDITION	SYM.	WC2(LBS/SEC)
C13	MACH = 1.78	○	214.
3.65 IN. DIV.	ALPHA= -5.	□	200.
NOSE BOOM ON	BETA = 0.	△	185.
DIV. STRUTS OUT		◇	169.
		×	150.

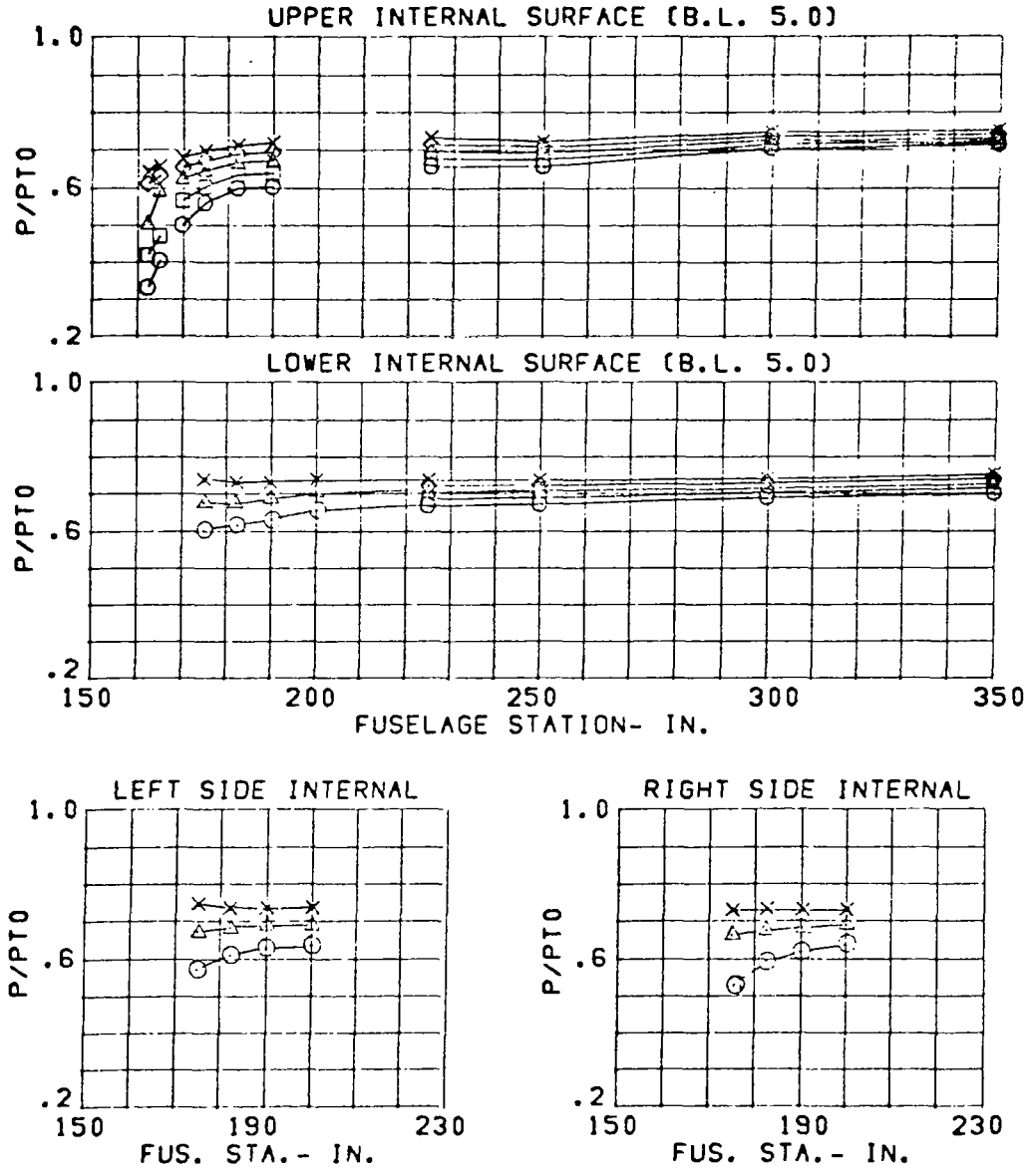

Figure 168 Cowl and Duct Static Pressures, Configuration C13

CONFIGURATION	CONDITION	SYM.	WC2(LBS/SEC)
C13	MACH = 1.78	○	214.
3.65 IN. DIV.	ALPHA= 1.	□	199.
NOSE BOOM ON	BETA = 0.	△	185.
DIV. STRUTS OUT		◇	169.
		×	149.

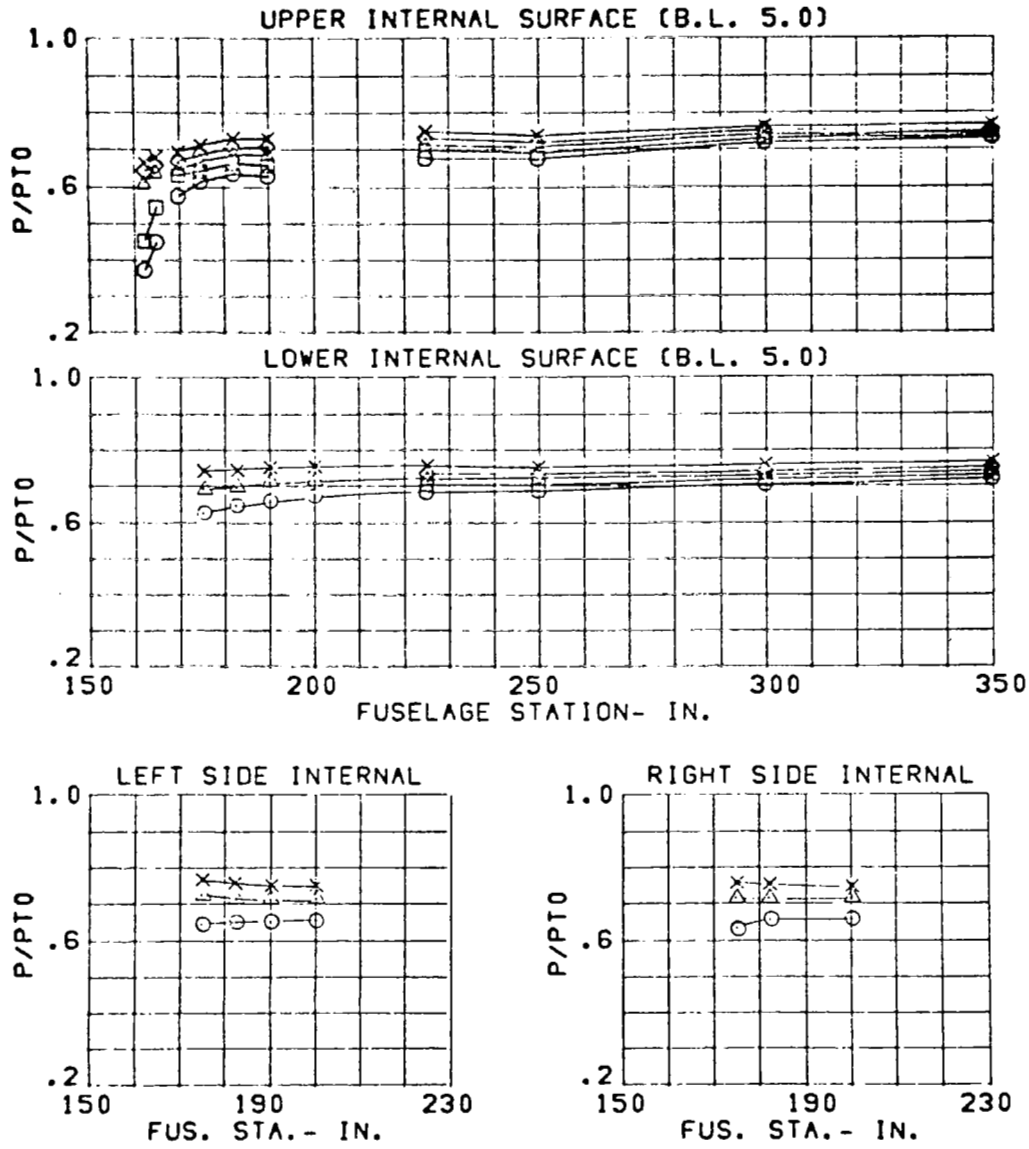

Figure 169 Cowl and Duct Static Pressures, Configuration C13

CONFIGURATION	CONDITION	SYM.	WC2(LBS/SEC)
C13	MACH = 1.78	○	214.
3.65 IN. DIV.	ALPHA= 6.	□	200.
NOSE BOOM ON	BETA = 0.	△	185.
DIV. STRUTS OUT		◇	169.
		×	149.

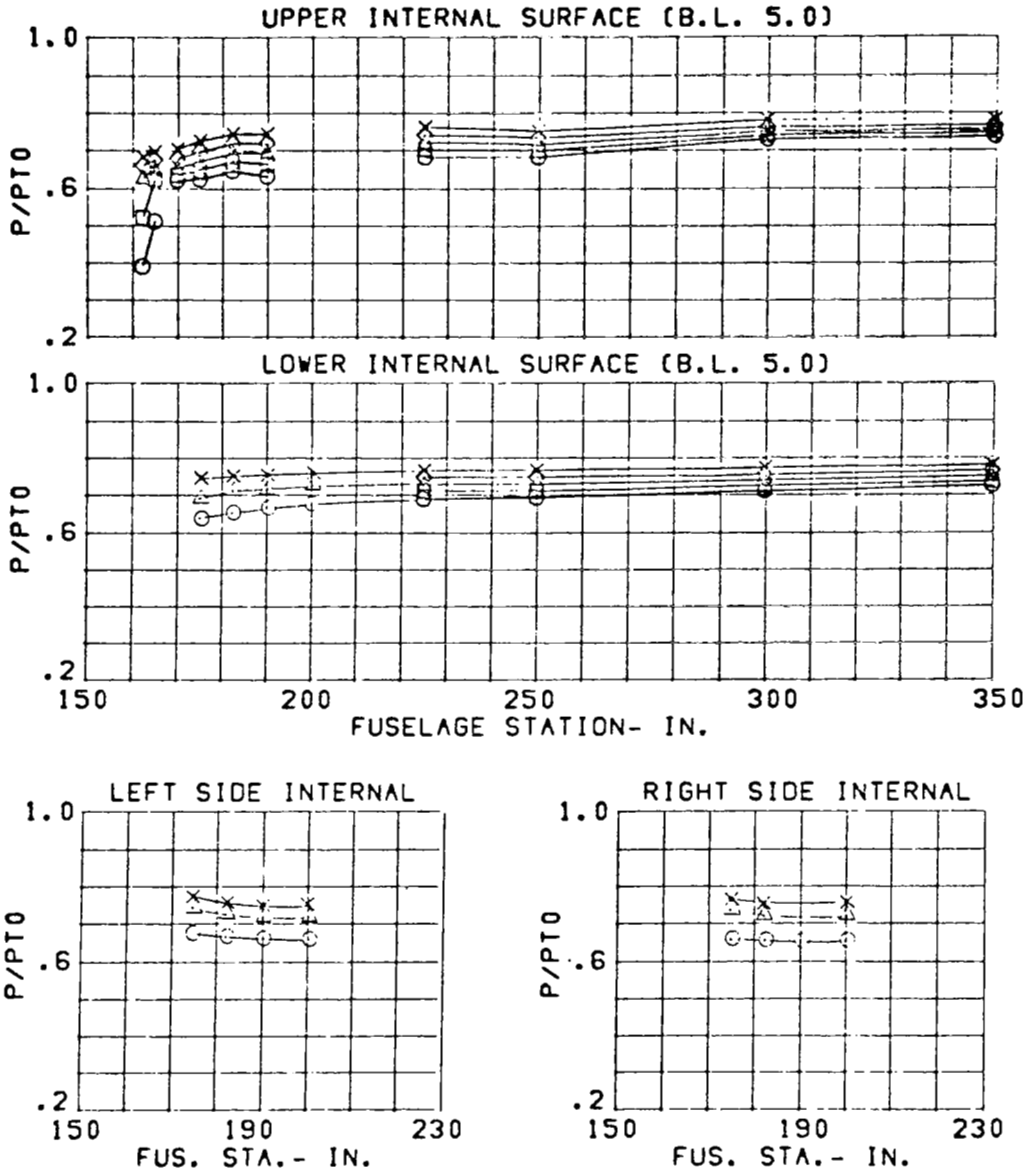

Figure 170 Cowl and Duct Static Pressures, Configuration C13

CONFIGURATION	CONDITION	SYM.	WC2(LBS/SEC)
C13	MACH = 1.78	○	215.
3.65 IN. DIV.	ALPHA= 20.	□	200.
NOSE BOOM ON	BETA = 0.	△	185.
DIV. STRUTS OUT		◇	169.
		×	150.

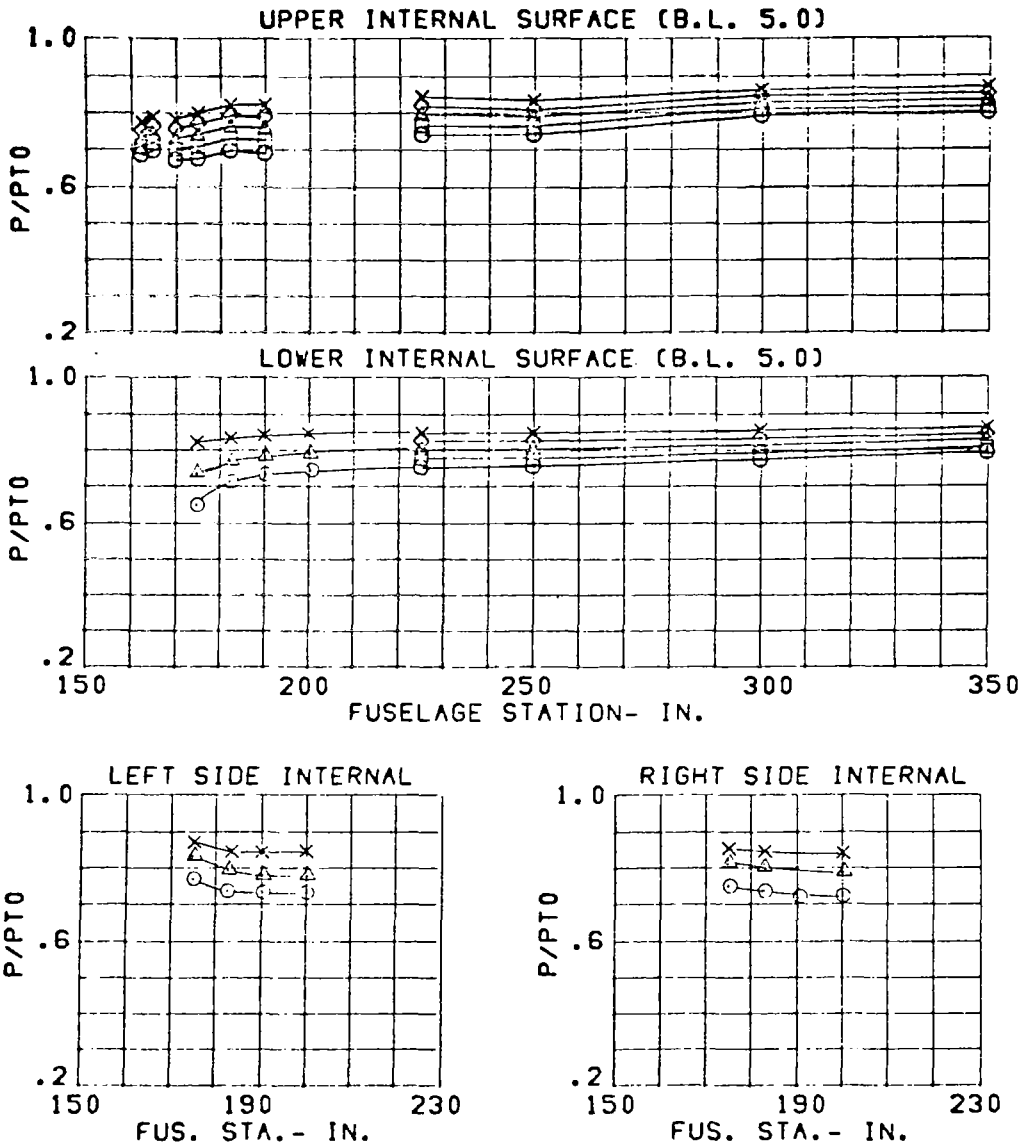

Figure 171 Cowl and Duct Static Pressures, Configuration C13

CONFIGURATION	CONDITION	SYM.	WC2(LBS/SEC)
C13	MACH = 1.97	○	197.
3.65 IN. DIV.	ALPHA= -5.	□	184.
NOSE BOOM ON	BETA = 0.	△	172.
DIV. STRUTS OUT		◇	155.
		×	140.

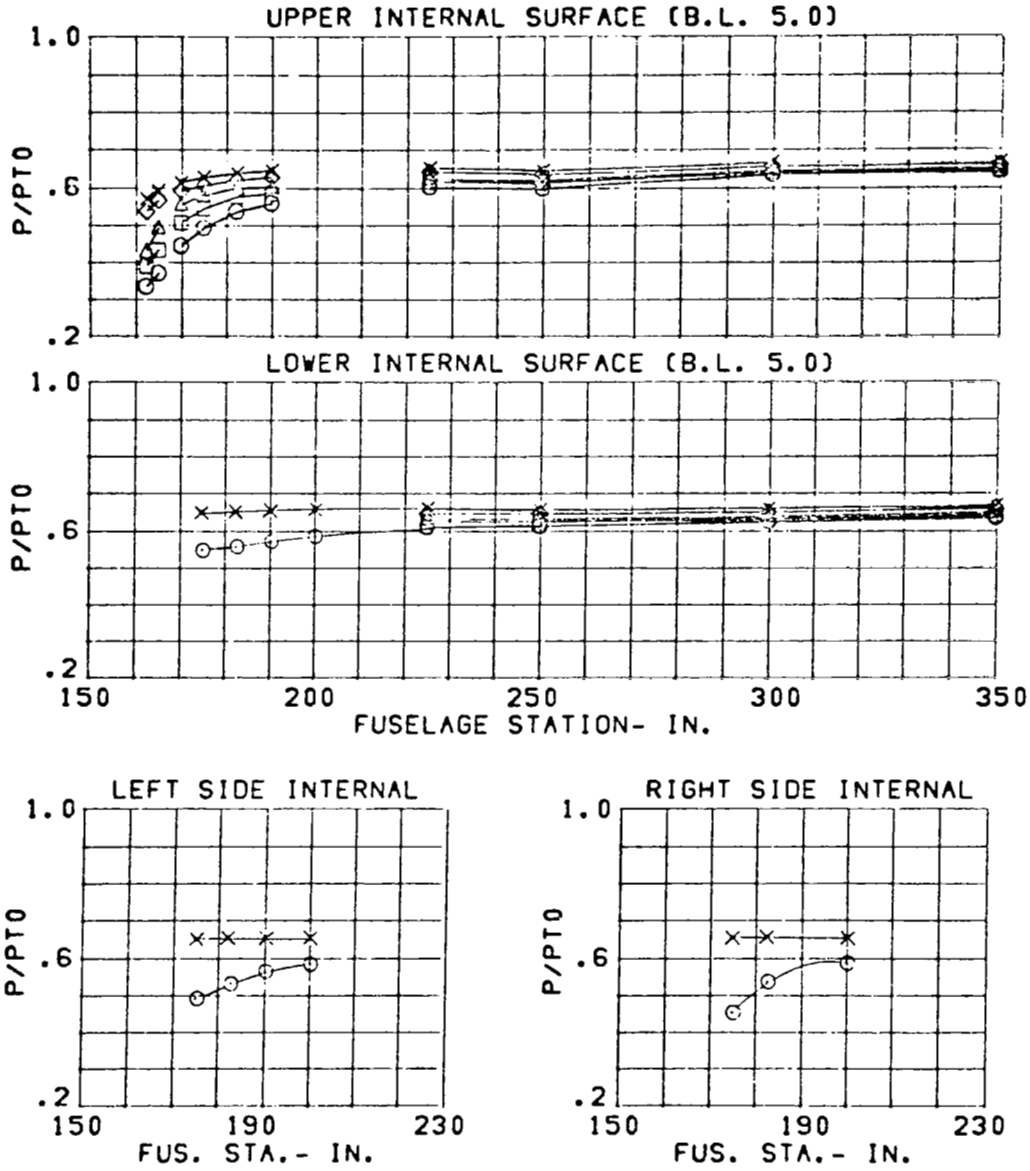

Figure 172 Cowl and Duct Static Pressures, Configuration C13

CONFIGURATION	CONDITION	SYM.	WC2(LBS/SEC)
C13	MACH = 1.97	○	197.
3.65 IN. DIV.	ALPHA= 1.	□	183.
NOSE BOOM ON	BETA = 0.	△	172.
DIV. STRUTS OUT		◇	155.
		×	140.

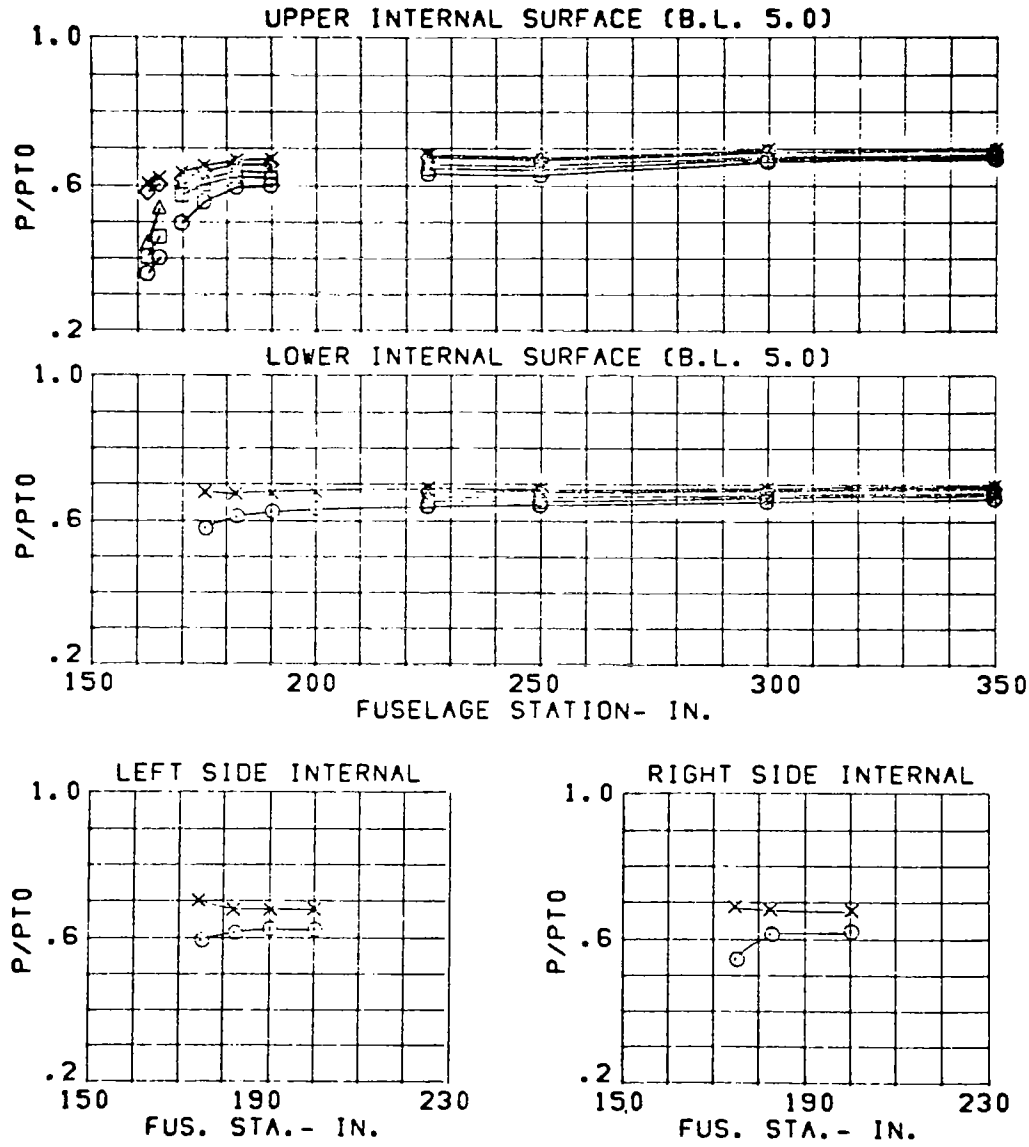

Figure 173 Cowl and Duct Static Pressures, Configuration C13

CONFIGURATION	CONDITION	SYM.	WC2(LBS/SEC)
C13	MACH = 1.97	○	197.
3.65 IN. DIV.	ALPHA= 6.	□	183.
NOSE BOOM ON	BETA = 0.	△	172.
DIV. STRUTS OUT		◇	155.
		×	140.

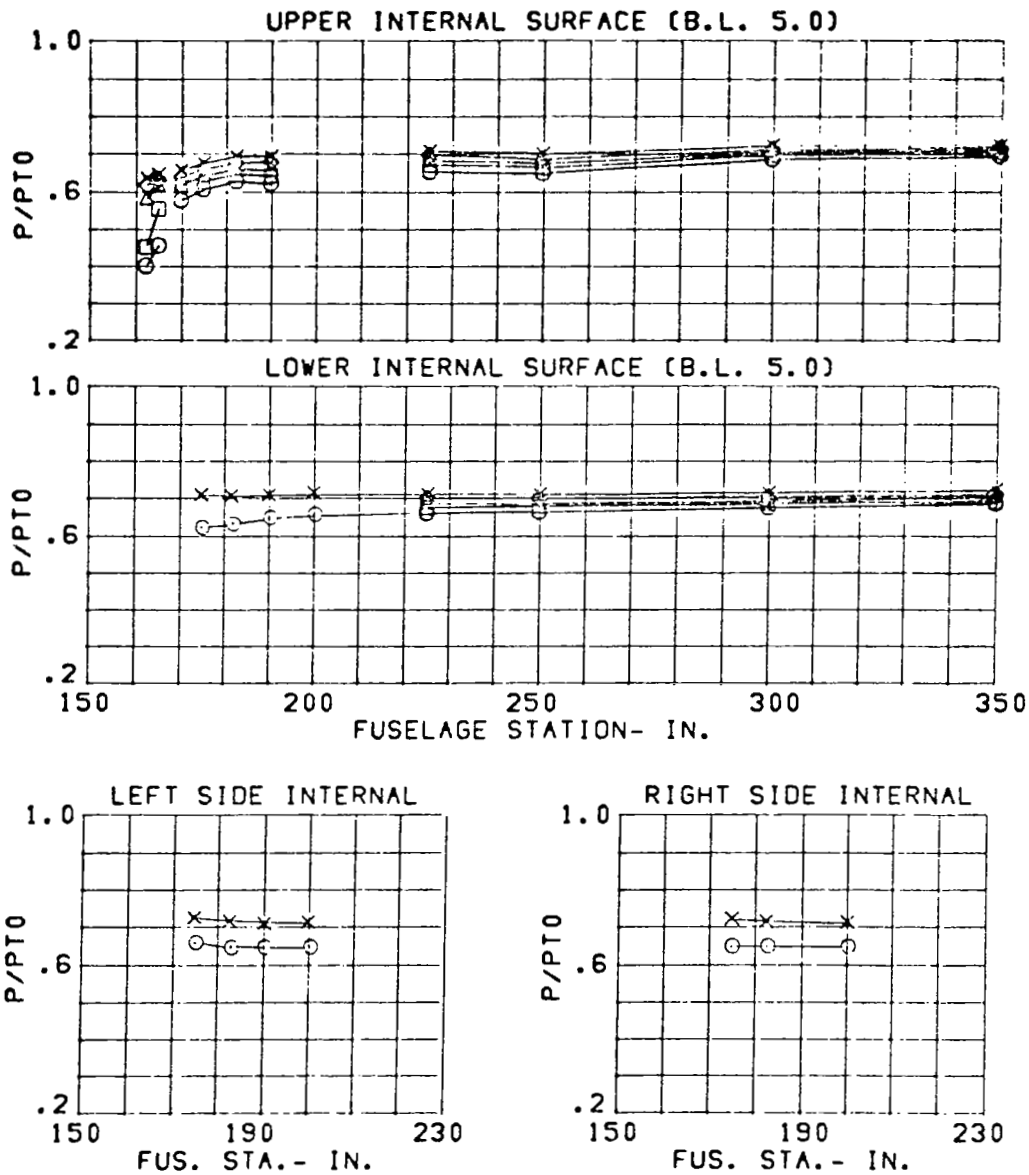

Figure 174 Cowl and Duct Static Pressures, Configuration C13

CONFIGURATION	CONDITION	SYM.	WC2(LBS/SEC)
C13	MACH = 1.96	○	197.
3.65 IN. DIV.	ALPHA= 20.	□	183.
NOSE BOOM ON	BETA = 0.	△	172.
DIV. STRUTS OUT		◇	155.
		×	140.

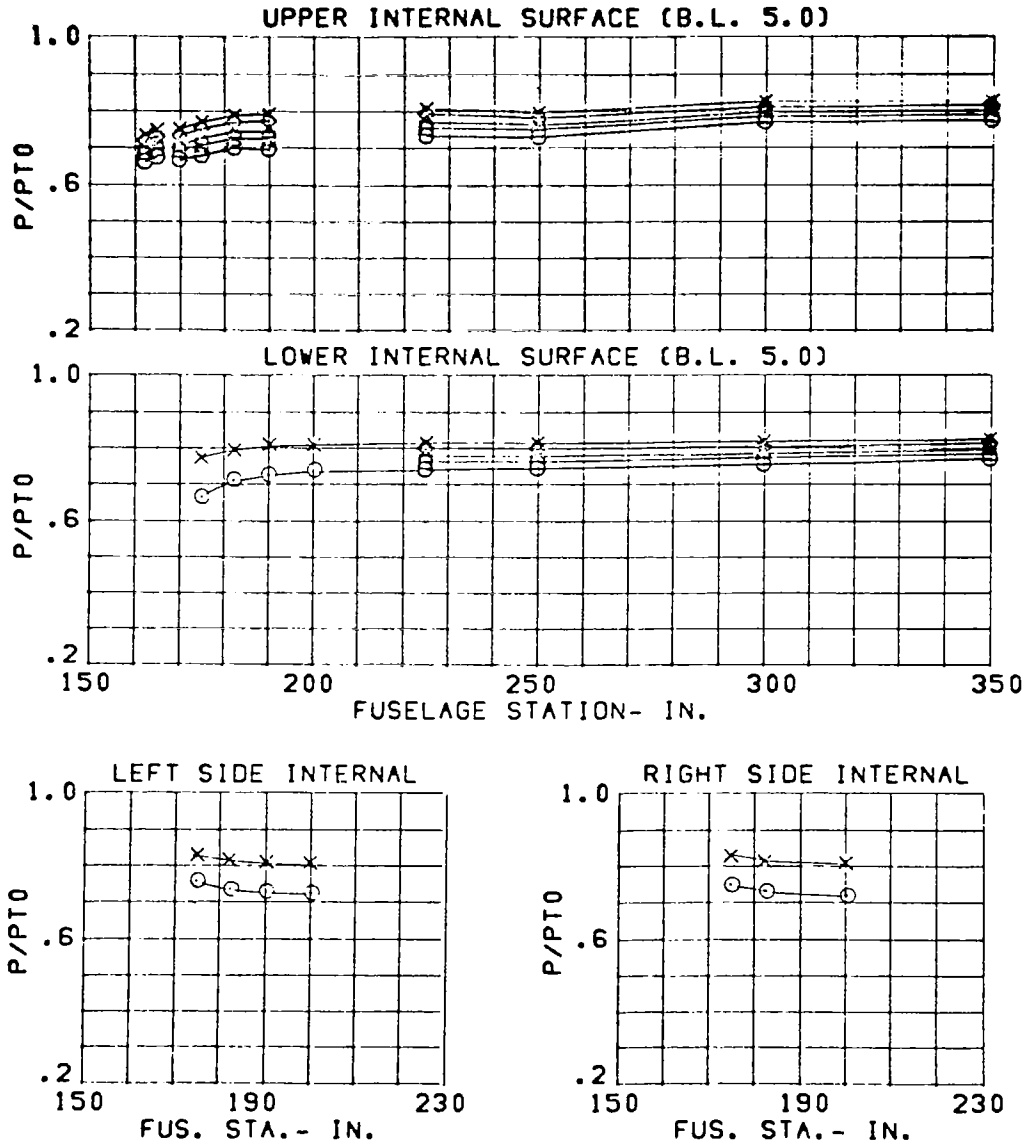

Figure 175 Cowl and Duct Static Pressures, Configuration C13

CONFIG.	DIVERTER HT.	SYM.	MACH	WC2	CONDITION
C13	3.65	○	1.57	217.	ALPHA= -5.
	3.30	□			BETA = 0.

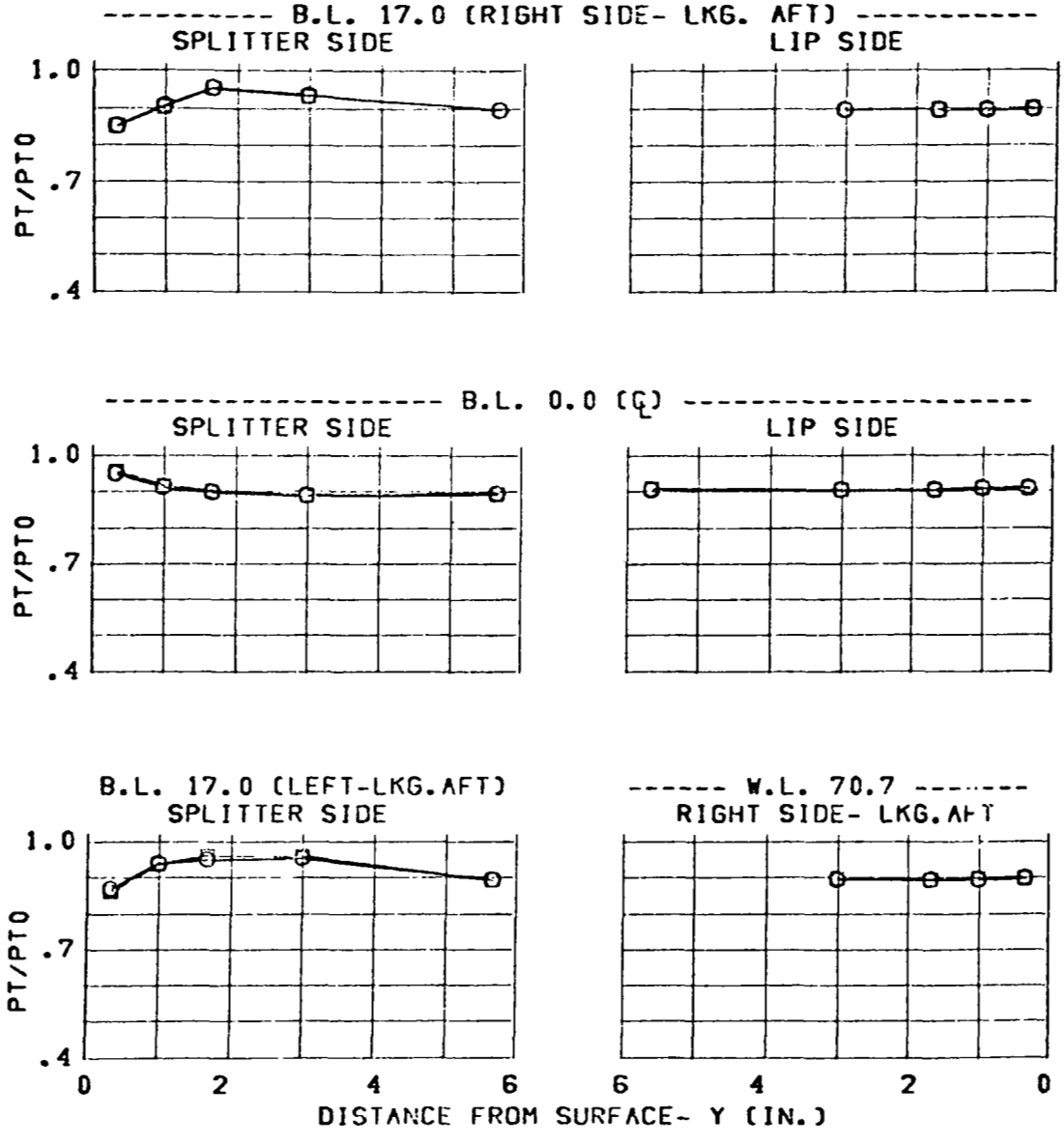

Figure 176 Effect of Diverter Height on Throat-Pressure Profiles, Configuration C13

CONFIG.	DIVERTER HT.	SYM.	MACH	WC2	CONDITION
C13	3.65	O	1.57	217.	ALPHA= 1.
	3.30	□			BETA = 0.

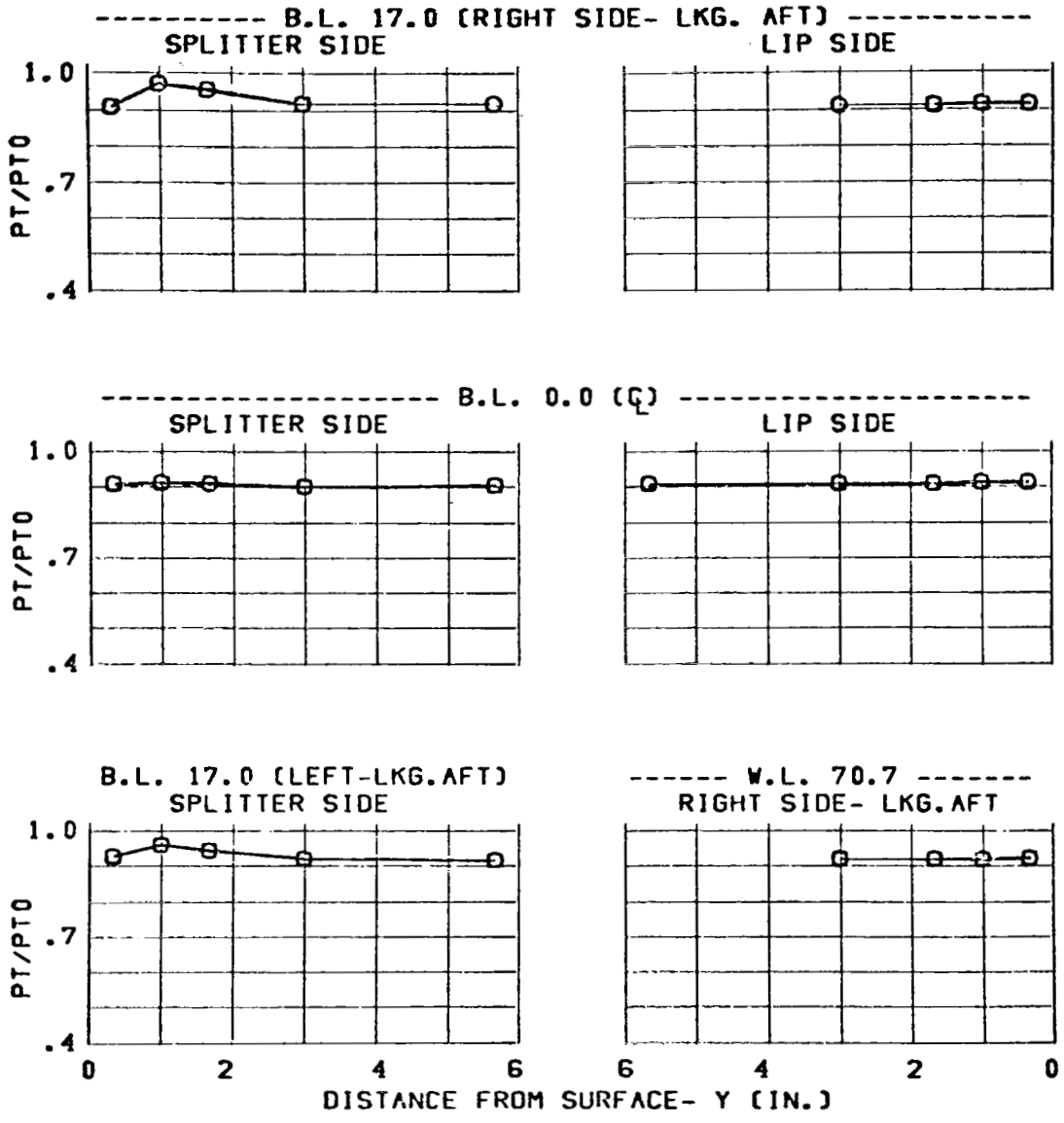

Figure 177 Effect of Diverter Height on Throat-Pressure Profiles, Configuration C13

CONFIG.	DIVERTER HT.	SYM.	MACH	WC2	CONDITION	
C13	3.65	O	1.57	217.	ALPHA=	6.
	3.30	□			BETA =	0.

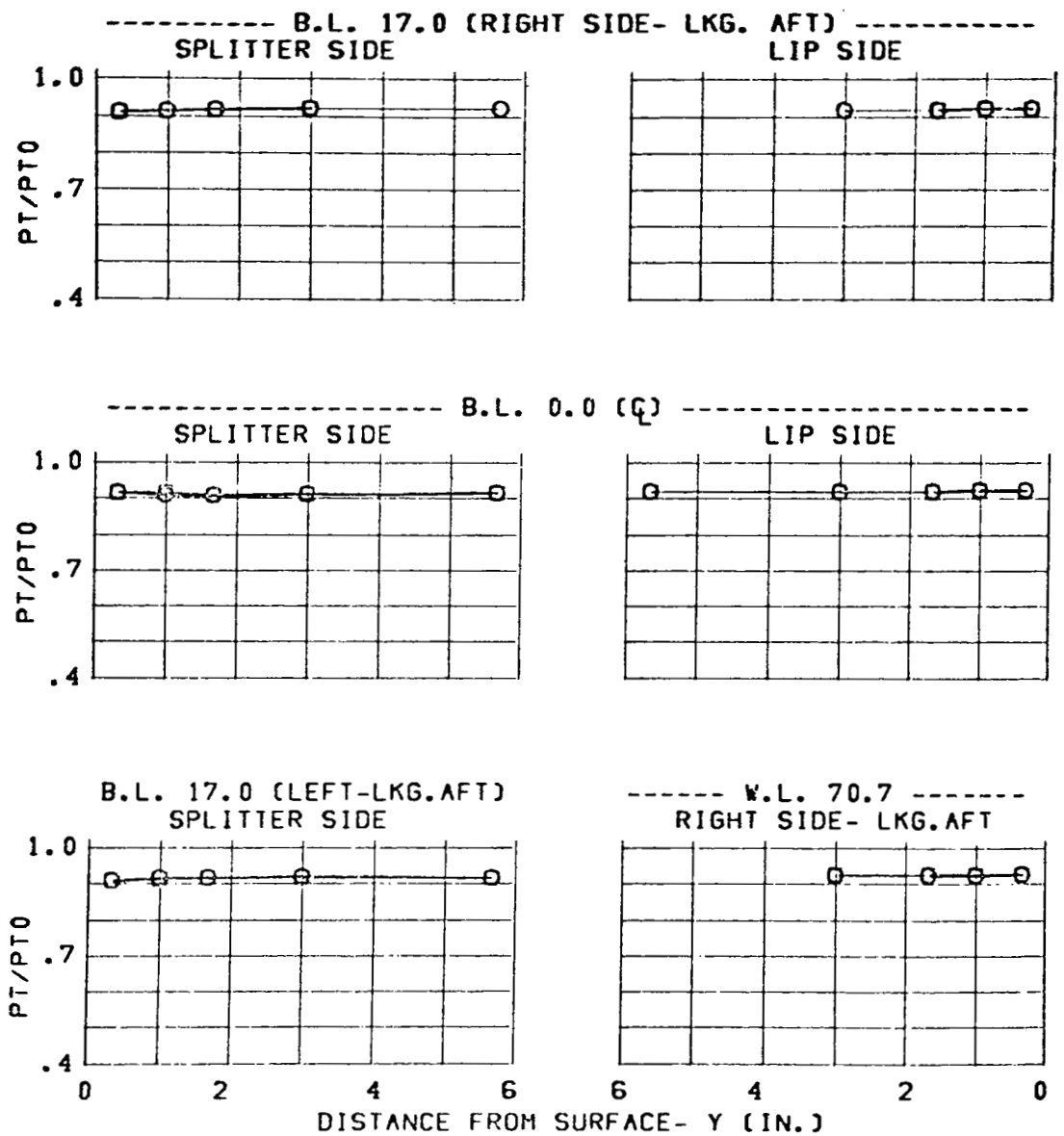

Figure 178 Effect of Diverter Height on Throat-Pressure Profiles, Configuration C13

CONFIG.	DIVERTER HT.	SYM.	MACH	WC2	CONDITION
C13	3.65	O	1.96	184.	ALPHA= -5.
	3.30	□			BETA = 0.

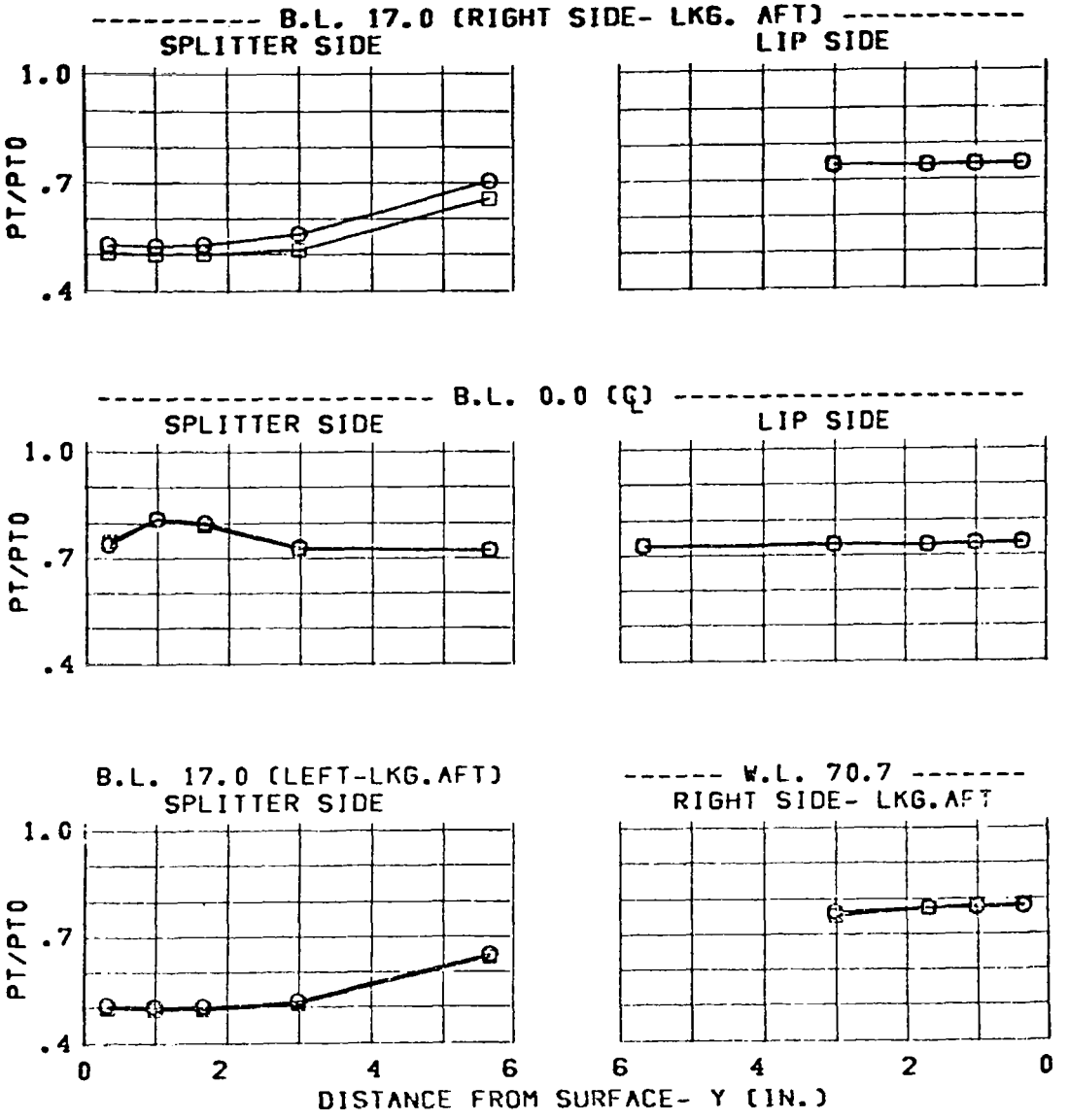

Figure 179 Effect of Diverter Height on Throat-Pressure Profiles, Configuration C13

CONFIG.	DIVERTER HT.	SYM.	MACH	WC2	CONDITION
C13	3.65	O	1.96	184.	ALPHA= 1.
	3.30	□			BETA = 0.

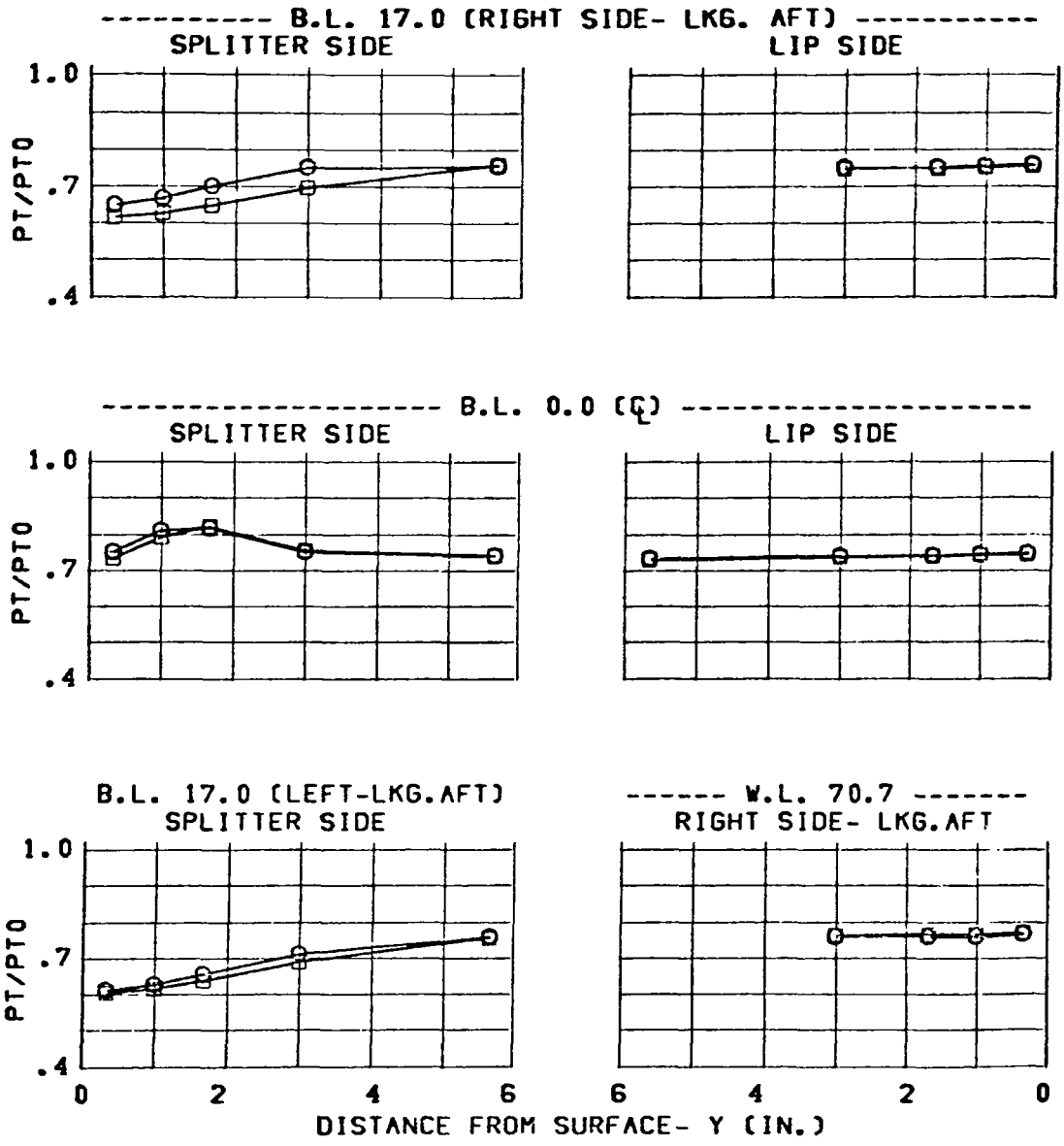

Figure 180 Effect of Diverter Height on Throat-Pressure Profiles, Configuration C13

CONFIG.	DIVERTER HT.	SYM.	MACH	WC2	CONDITION
C13	3.65	O	1.96	184.	ALPHA= 6.
	3.30	□			BETA = 0.

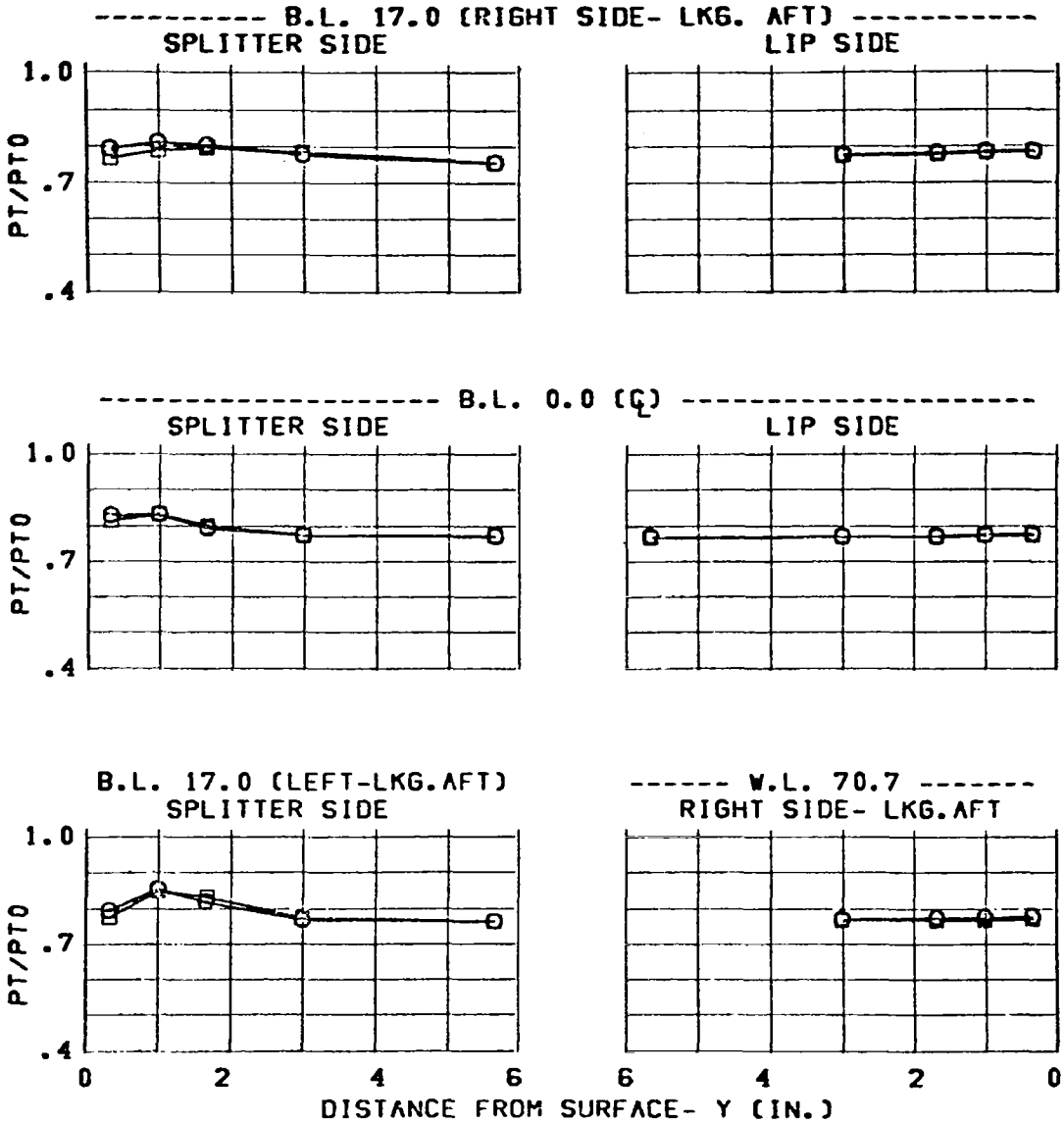

Figure 181 Effect of Diverter Height on Throat-Pressure Profiles, Configuration C13

THROAT RAKES IN

CONFIG.	DIVERTER HT.	SYM.	MACH	CONDITION
C13	3.65	○	1.57	ALPHA= -5.
	3.30	□		BETA = 0.

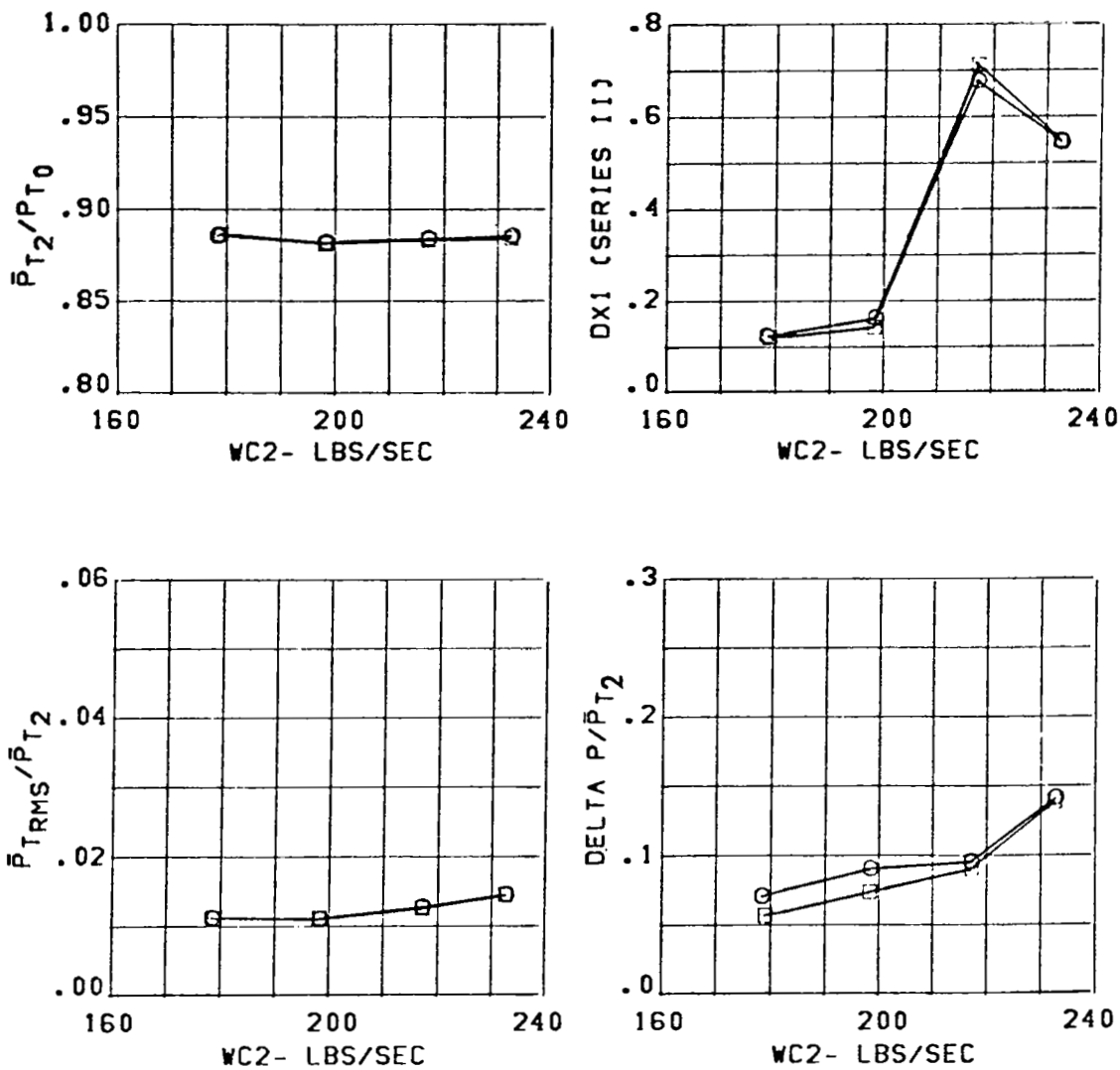

Figure 182 Effect of Diverter Height on Inlet Configuration C13 Performance

THROAT RAKES IN

CONFIG.	DIVERTER HT.	SYM.	MACH	CONDITION
C13	3.65	O	1.56	ALPHA= 1.
	3.30	□		BETA = 0.

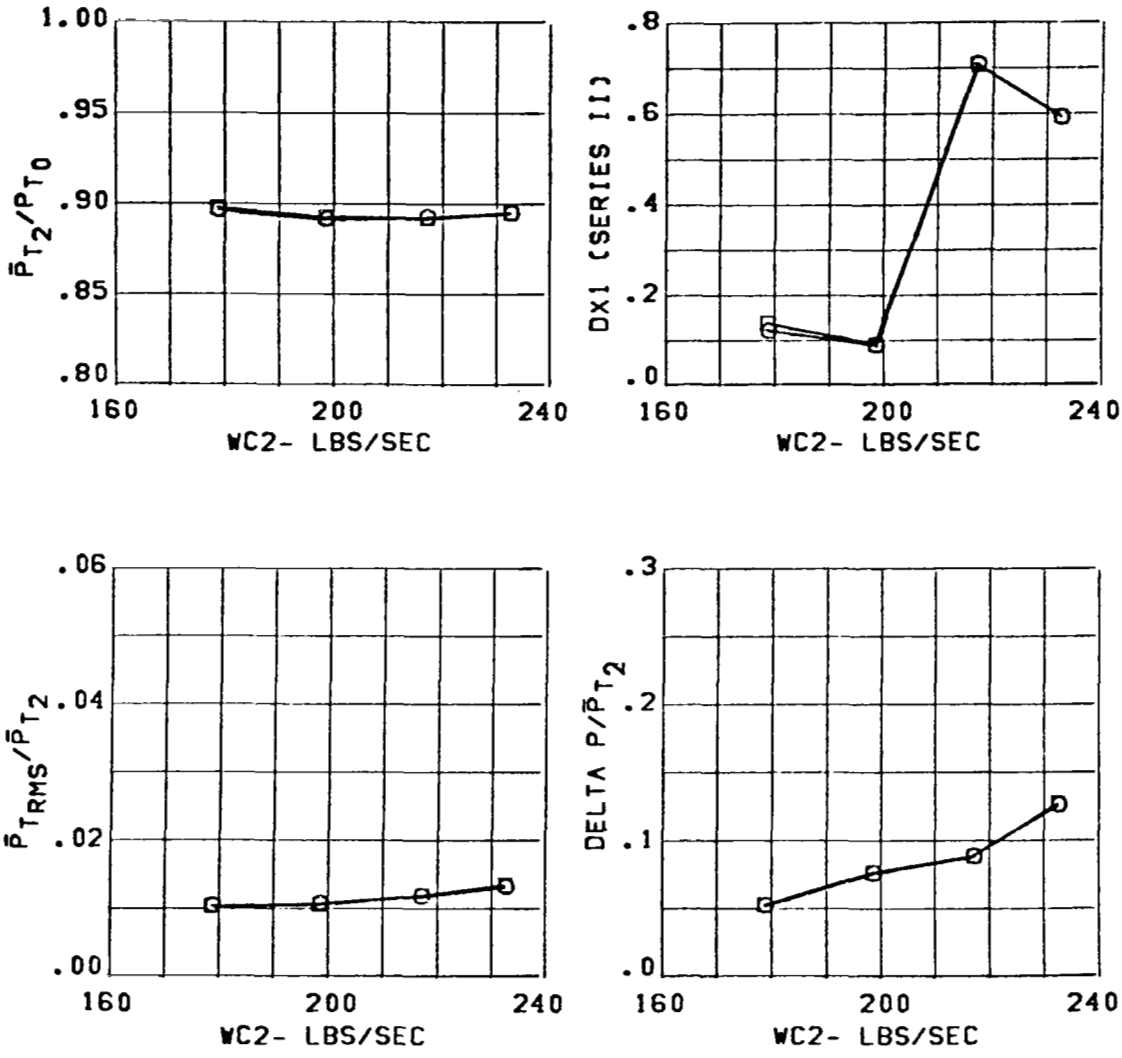

Figure 183 Effect of Diverter Height on Inlet Configuration C13 Performance

THROAT RAKES IN

CONFIG.	DIVERTER HT.	SYM.	MACH	CONDITION
C13	3.65	○	1.56	ALPHA= 6.
	3.30	□		BETA = 0.

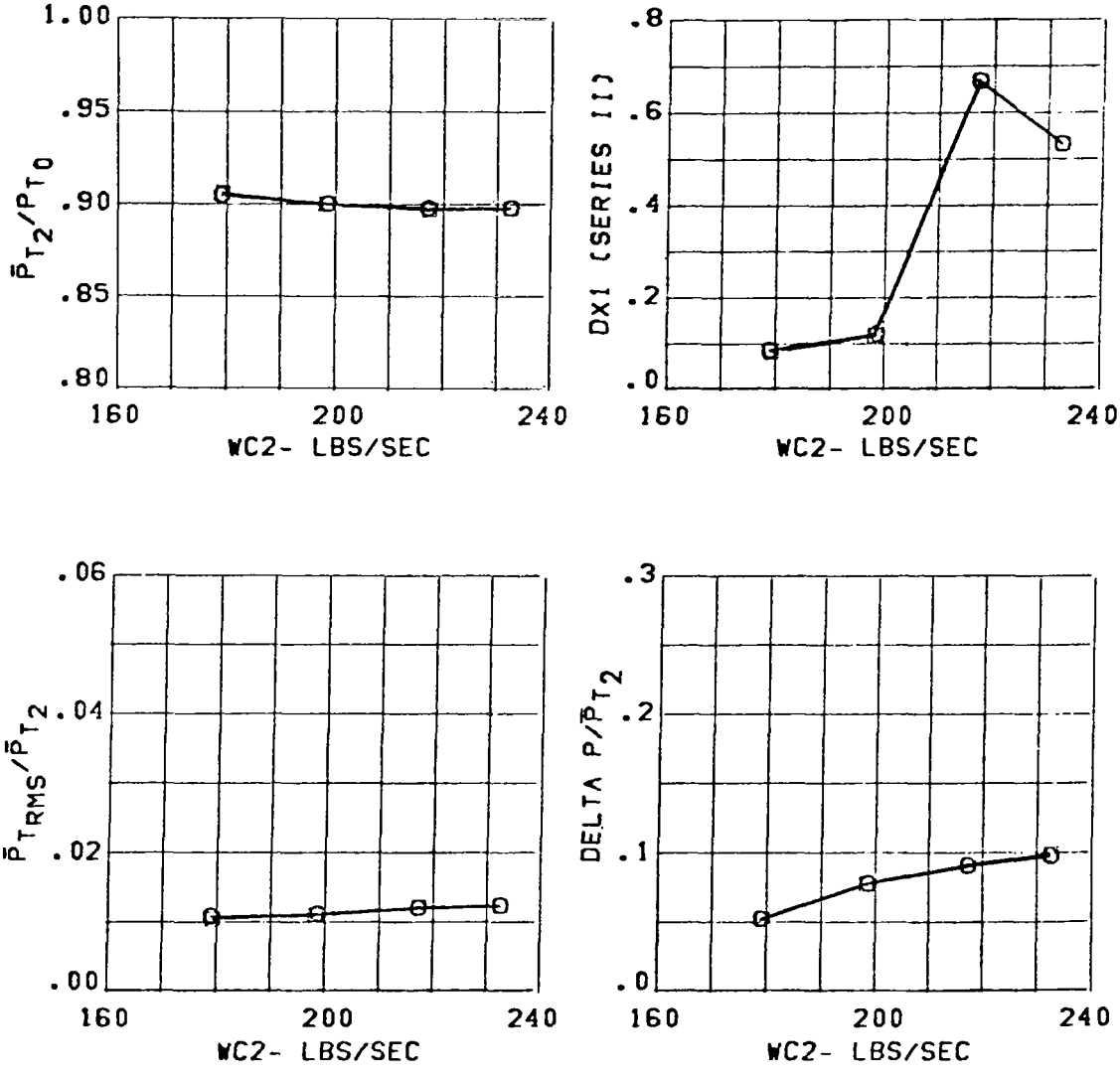

Figure 184 *Effect of Diverter Height on Inlet Configuration C13 Performance*

THROAT RAKES IN

CONFIG.	DIVERTER HT.	SYM.	MACH	CONDITION
C13	3.65	O	1.96	ALPHA= -5.
	3.30	□		BETA = 0.

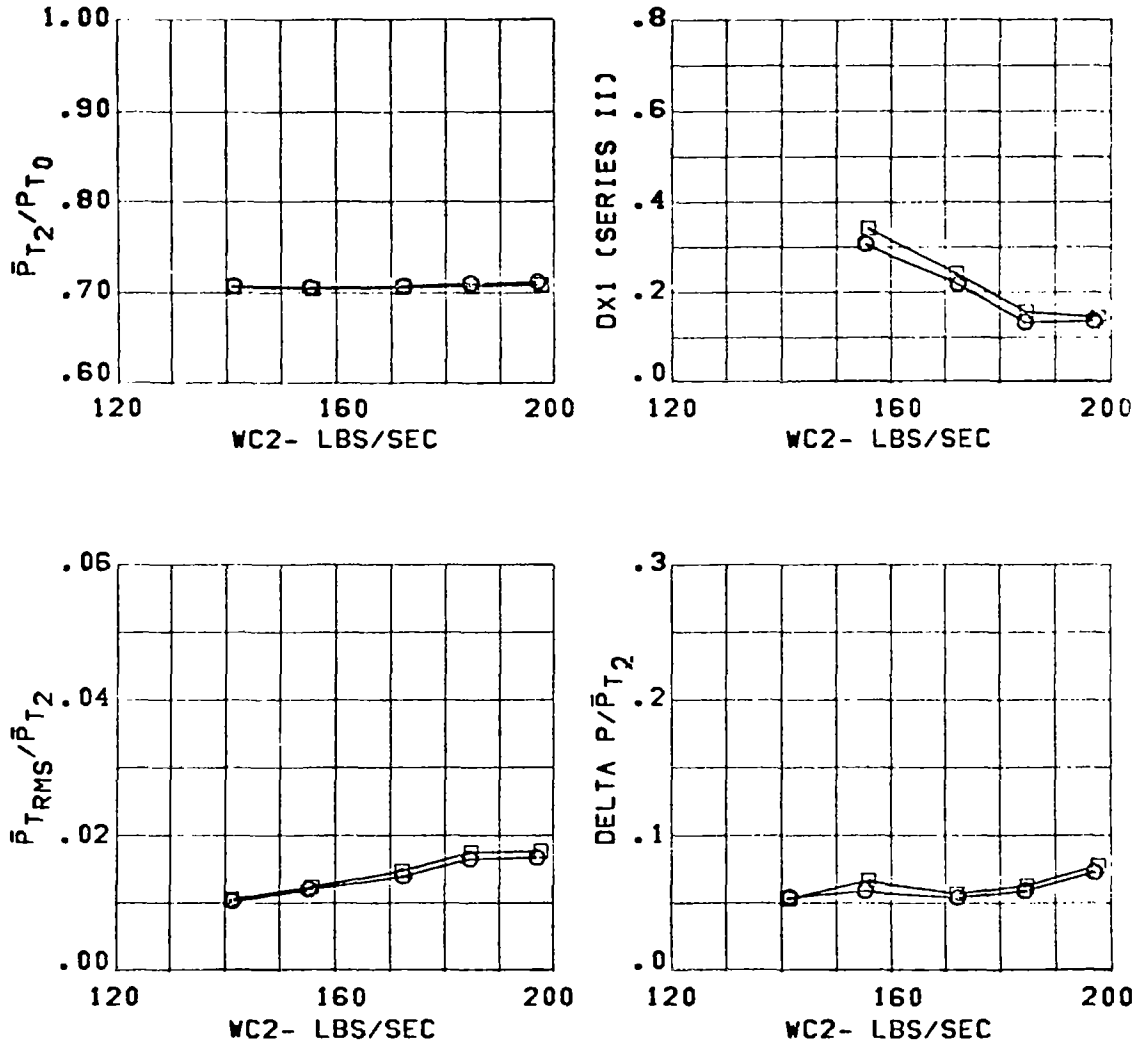

Figure 185 Effect of Diverter Height on Inlet Configuration C13 Performance

THROAT RAKES IN

CONFIG.	DIVERTER HT.	SYM.	MACH	CONDITION
C13	3.65	O	1.96	ALPHA= 1.
	3.30	□		BETA = 0.

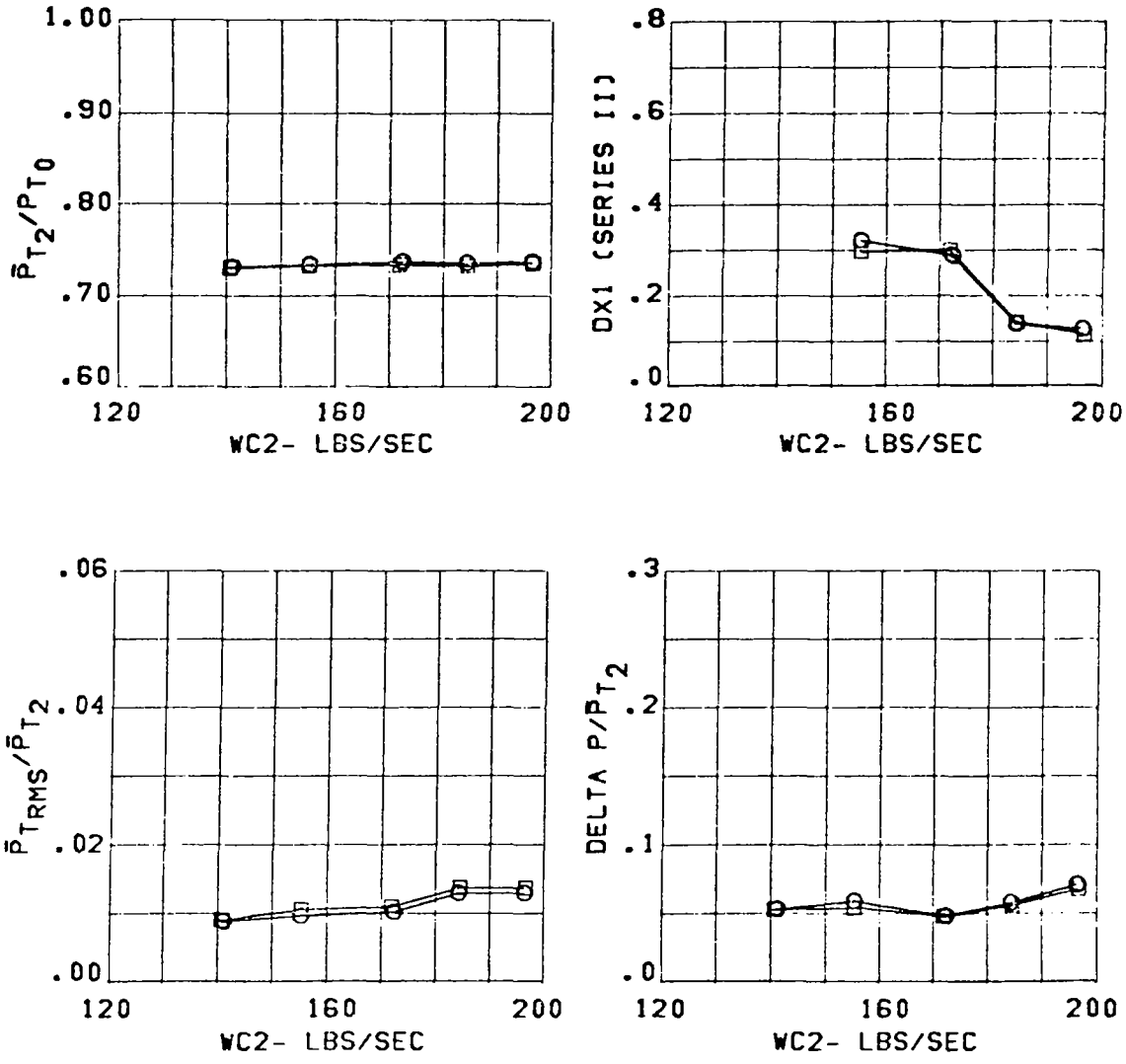

Figure 186 Effect of Diverter Height on Inlet Configuration C13 Performance

THROAT RAKES IN

CONFIG.	DIVERTER HT.	SYM.	MACH	CONDITION
C13	3.65	O	1.96	ALPHA= 6.
	3.30	□		BETA = 0.

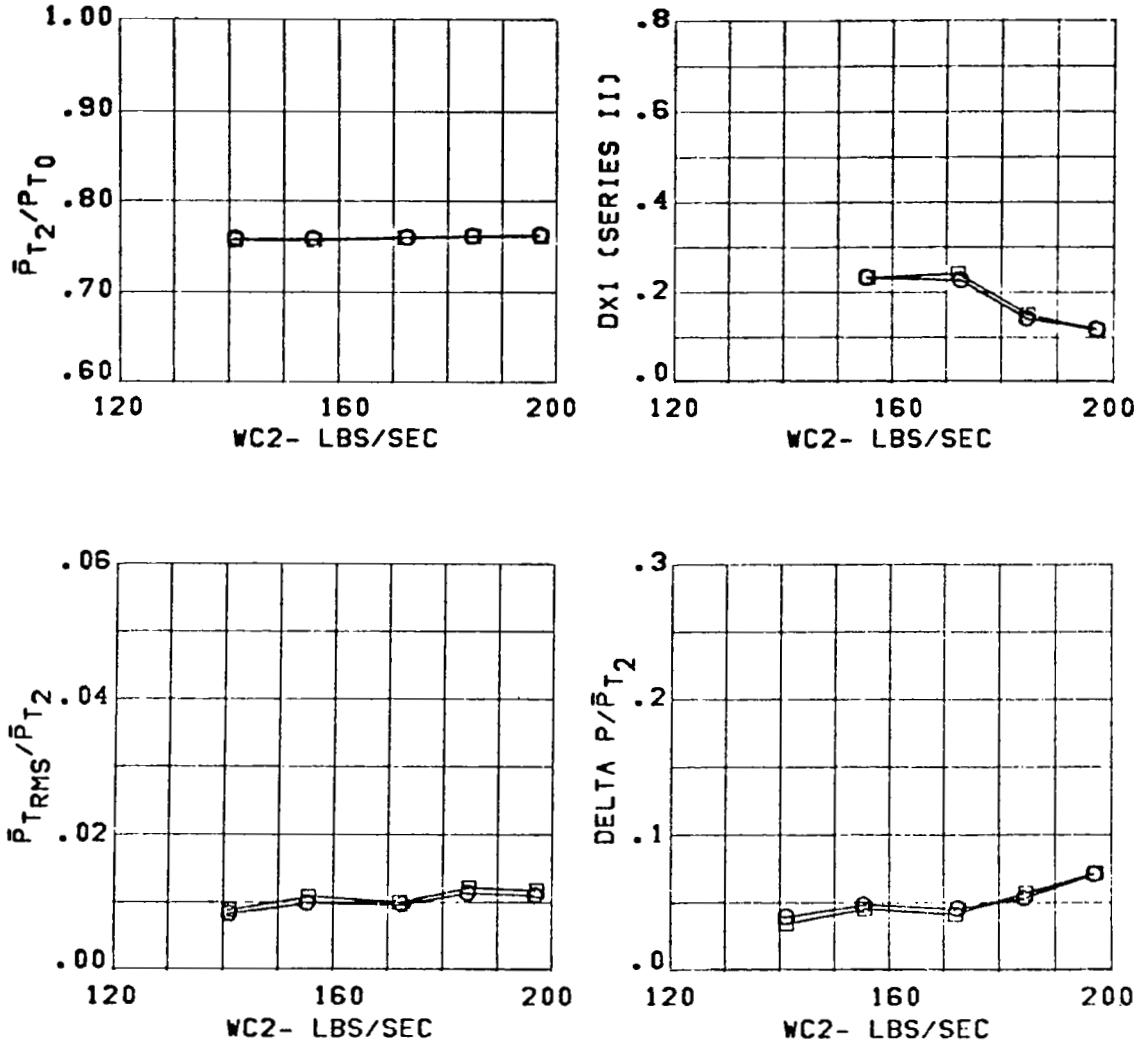

Figure 187 Effect of Diverter Height on Inlet Configuration C13 Performance

CONFIGURATION	CONDITION	SYM.	NOSE BOOM
SPLITTER ONLY	ALPHA= -5.	O	ON
3.65 IN. DIV. HT.	BETA = 0.	□	OFF
	MACH = 1.56		

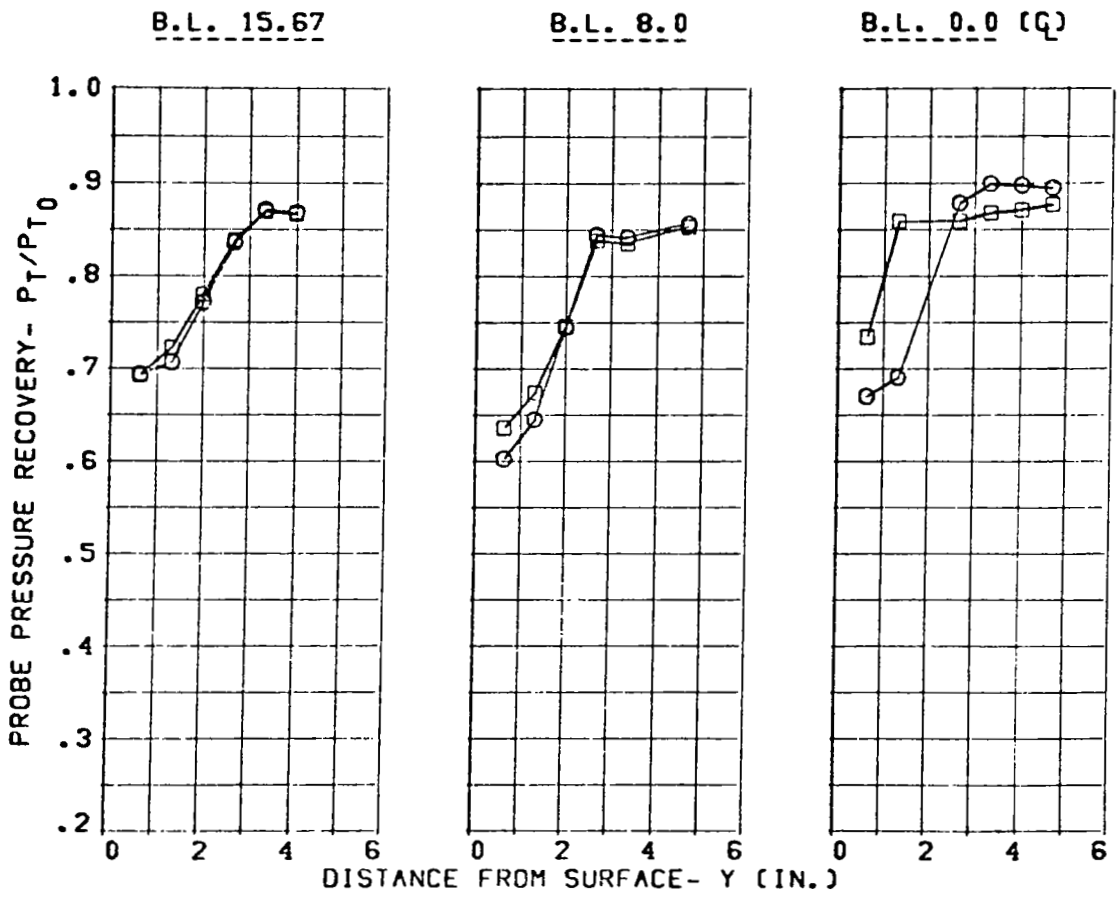

Figure 188 Effect of Nose Boom on Fuselage Boundary-Layer Profiles

CONFIGURATION	CONDITION	SYM.	NOSE BOOM
SPLITTER ONLY	ALPHA= 1.	O	ON
3.65 IN. DIV. HT.	BETA = 0.	□	OFF
	MACH = 1.56		

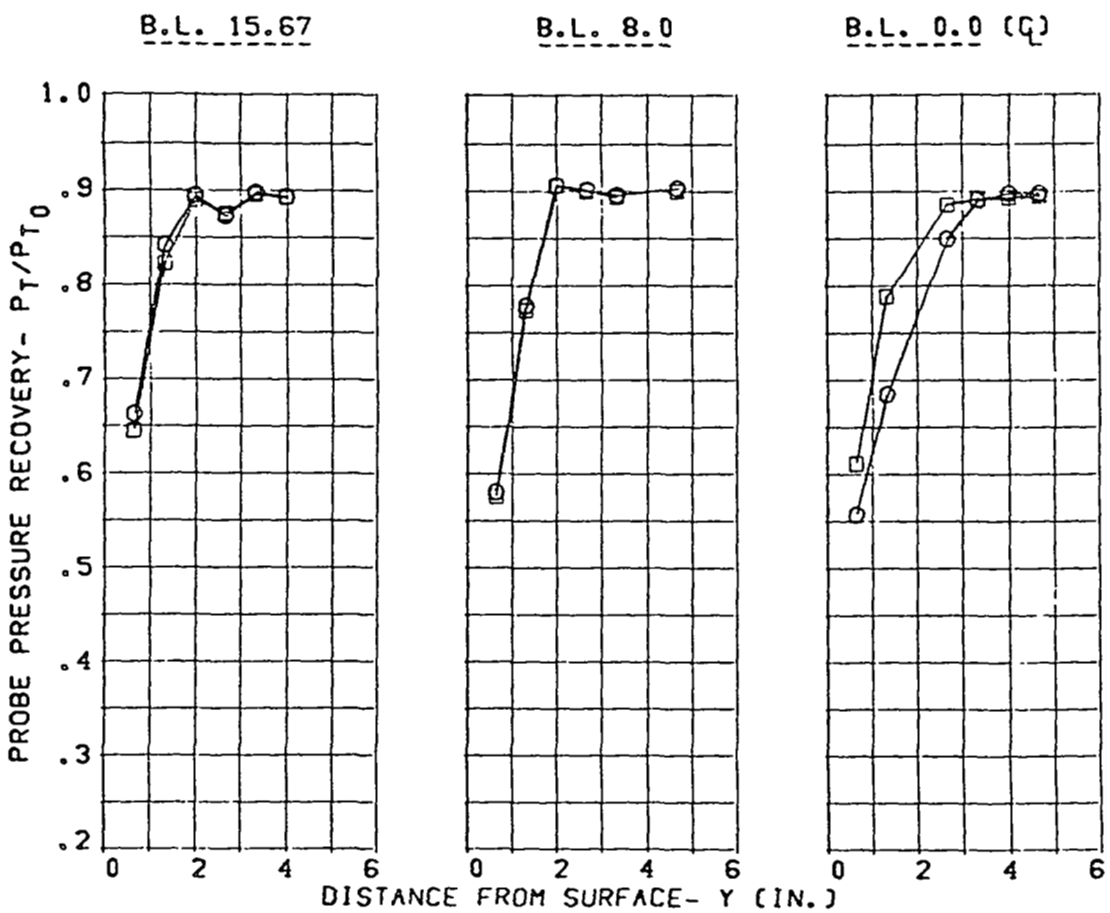

Figure 189 Effect of Nose Boom on Fuselage Boundary-Layer Profiles

CONFIGURATION	CONDITION	SYM.	NOSE BOOM
SPLITTER ONLY	ALPHA= 6.	O	ON
3.65 IN. DIV. HT.	BETA = -0.	□	OFF
	MACH = 1.56		

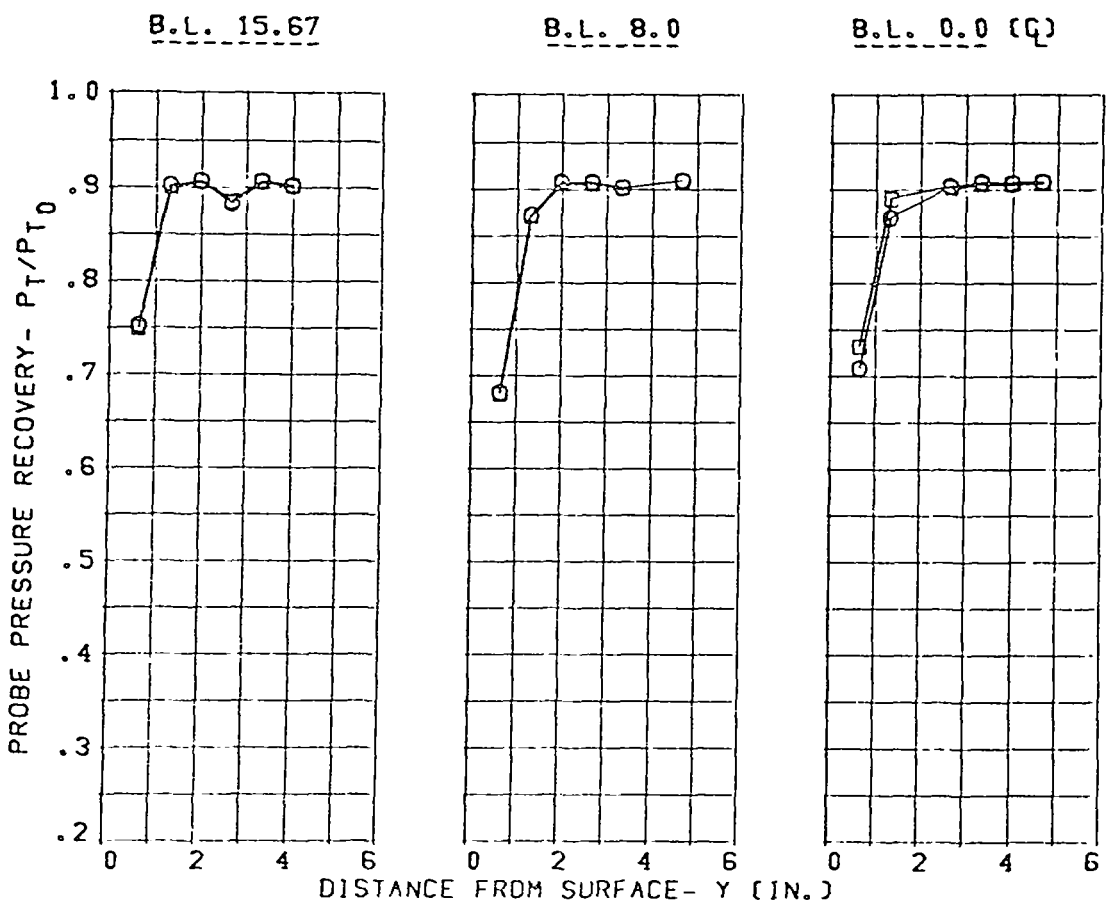

Figure 190 Effect of Nose Boom on Fuselage Boundary-Layer Profiles

CONFIGURATION	CONDITION	SYM.	NOSE BOOM
SPLITTER ONLY	ALPHA= -5.	O	ON
3.65 IN. DIV. HT.	BETA = 0.	□	OFF
	MACH = 1.96		

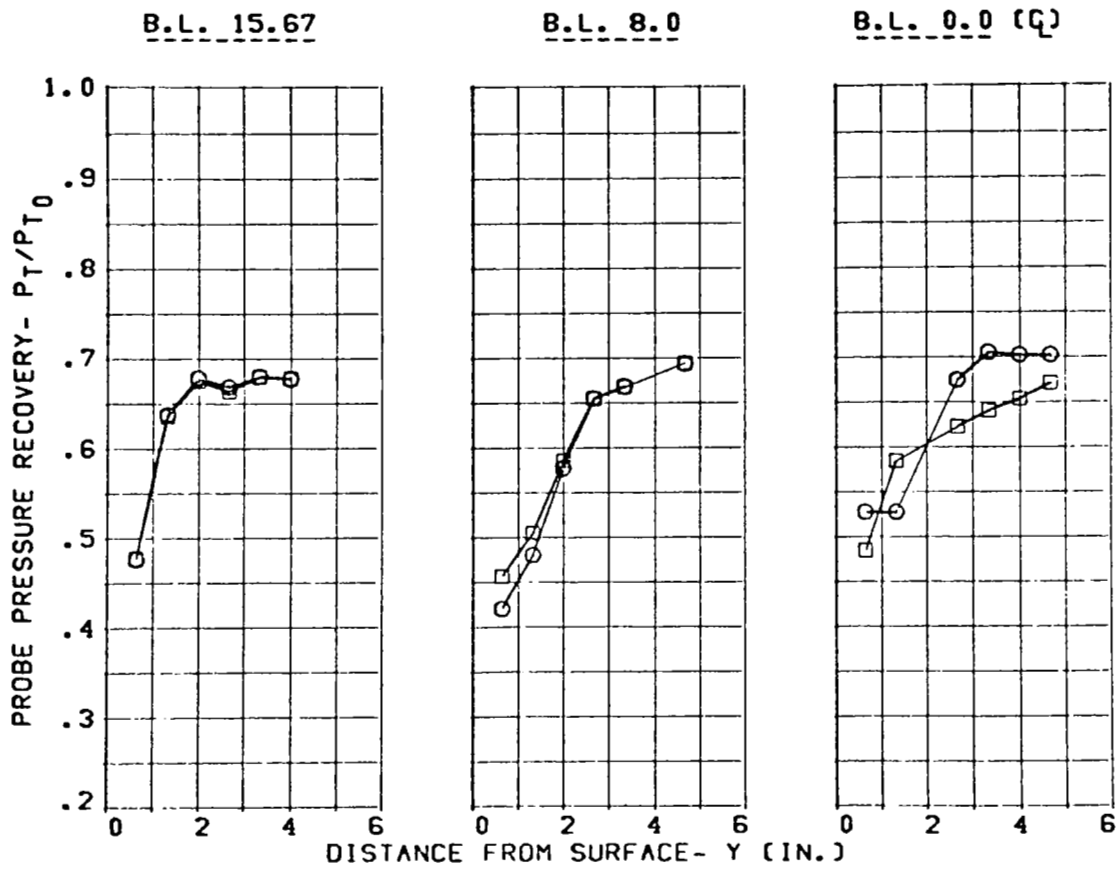

Figure 191 Effect of Nose Boom on Fuselage Boundary-Layer Profiles

CONFIGURATION	CONDITION	SYM.	NOSE BOOM
SPLITTER ONLY 3.65 IN. DIV. HT.	ALPHA= 1. BETA = 0. MACH = 1.96	O □	ON OFF

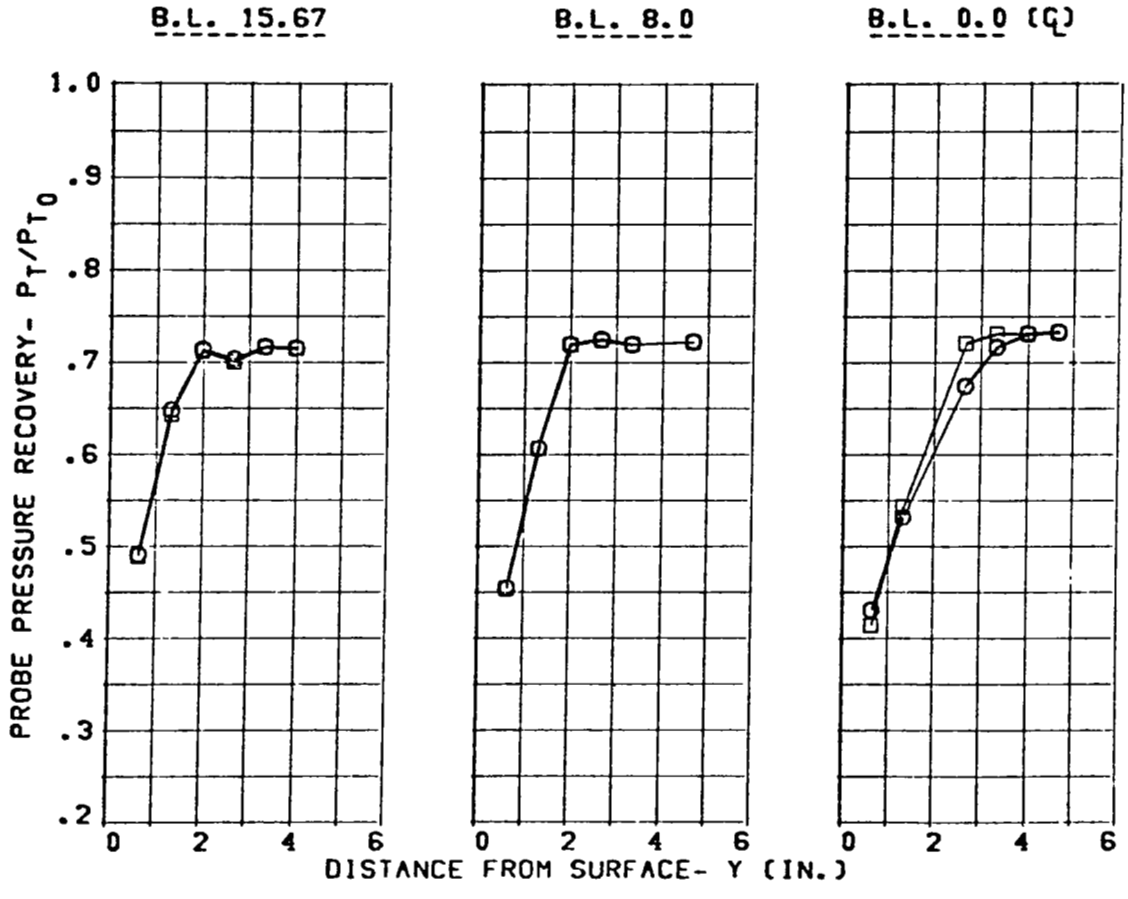

Figure 192 Effect of Nose Boom on Fuselage Boundary-Layer Profiles

CONFIGURATION	CONDITION	SYM.	NOSE BOOM
SPLITTER ONLY 3.65 IN. DIV. HT.	ALPHA= 6. BETA = 0. MACH = 1.96	O □	ON OFF

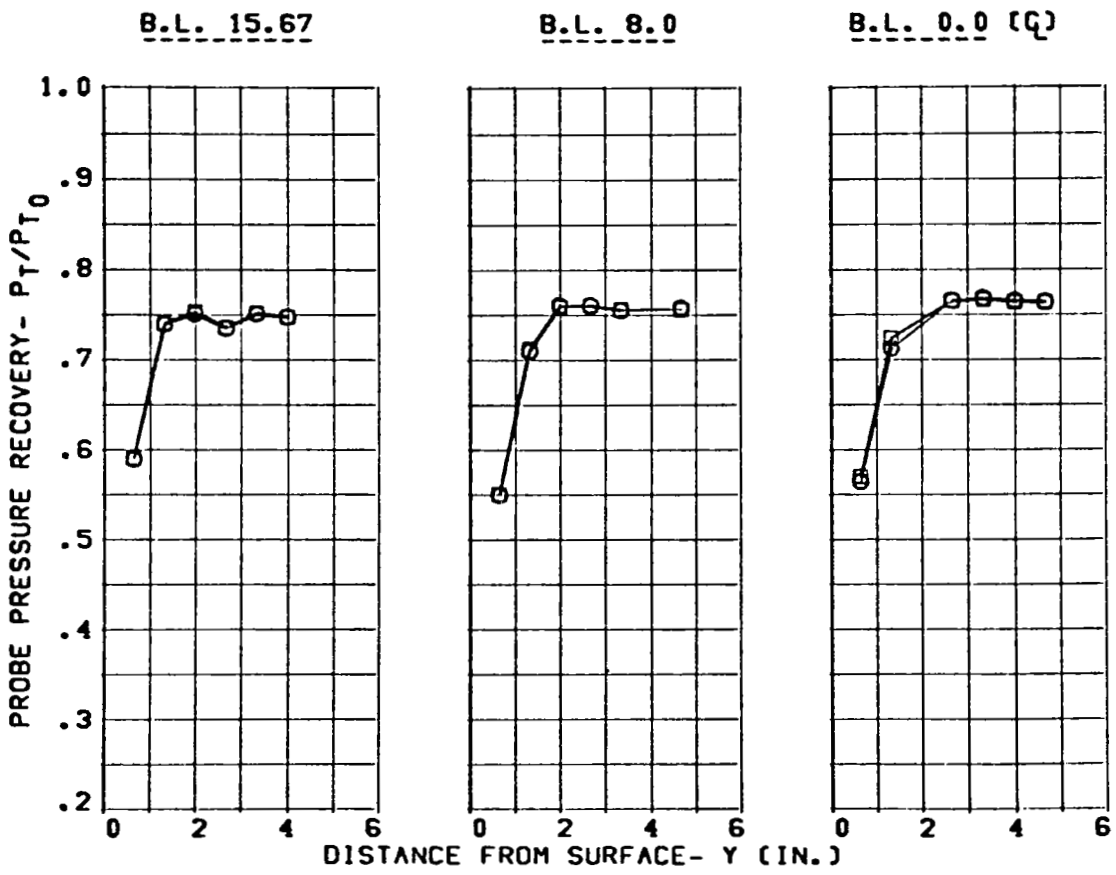

Figure 193 Effect of Nose Boom on Fuselage Boundary-Layer Profiles

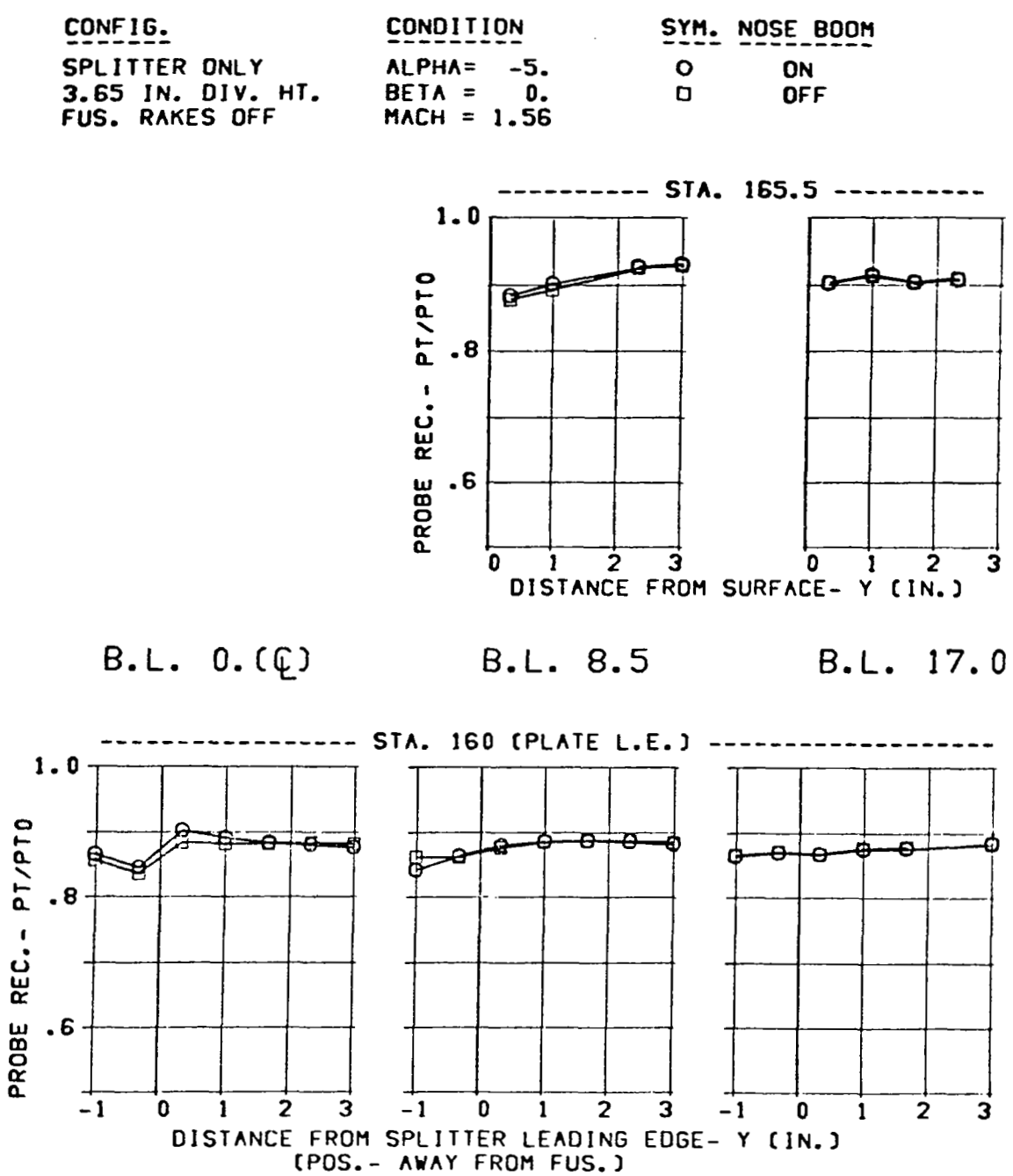

Figure 194 Effect of Nose Boom on Splitter-Plate Boundary-Layer Profiles

CONFIG.	CONDITION	SYM.	NOSE BOOM
SPLITTER ONLY	ALPHA= 1.	O	ON
3.65 IN. DIV. HT.	BETA = 0.	□	OFF
FUS. RAKES OFF	MACH = 1.56		

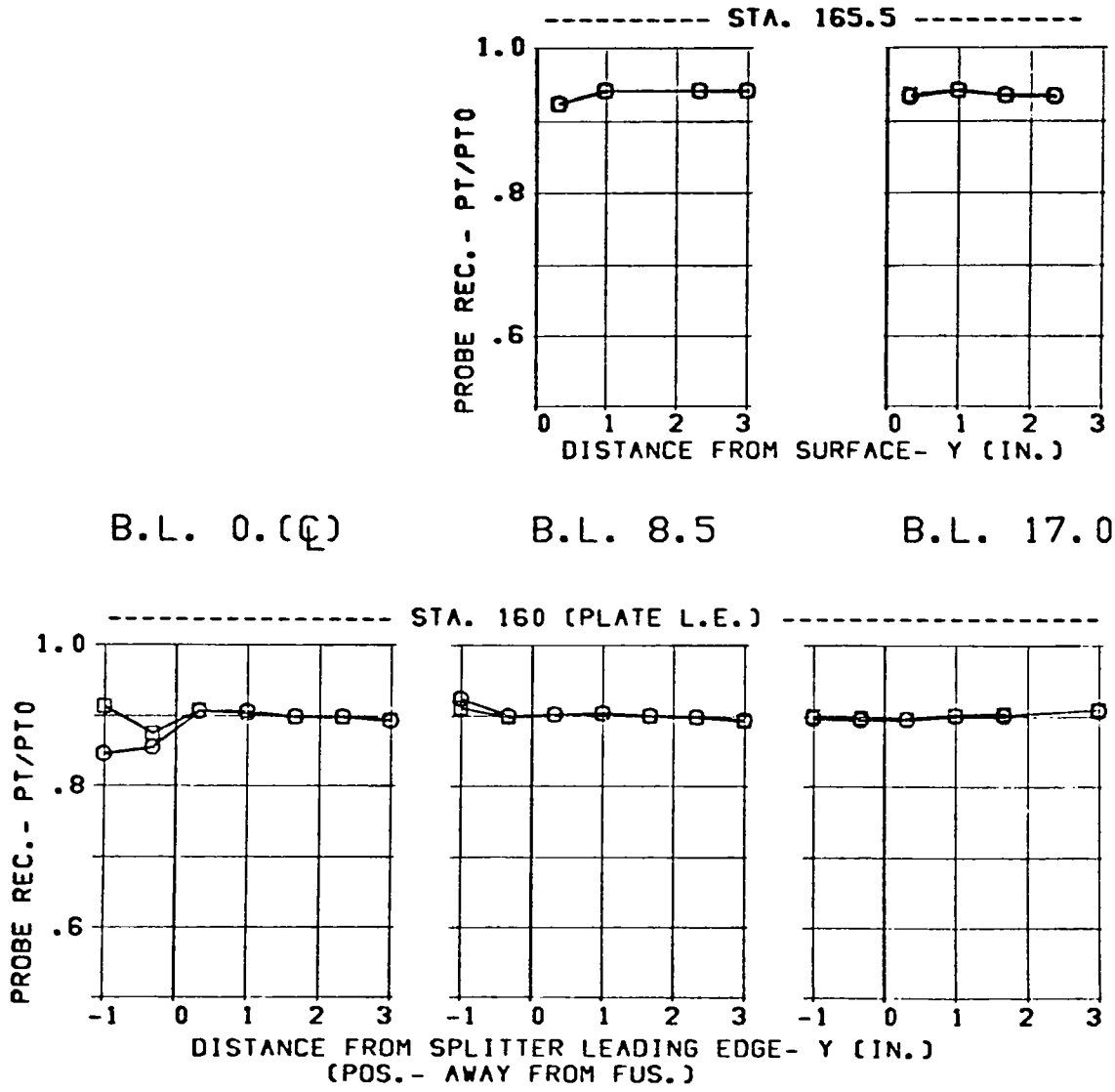

Figure 195 Effect of Nose Boom on Splitter-Plate Boundary-Layer Profiles

CONFIG.	CONDITION	SYM.	NOSE BOOM
SPLITTER ONLY	ALPHA= 6.	O	ON
3.65 IN. DIV. HT.	BETA = 0.	□	OFF
FUS. RAKES OFF	MACH = 1.56		

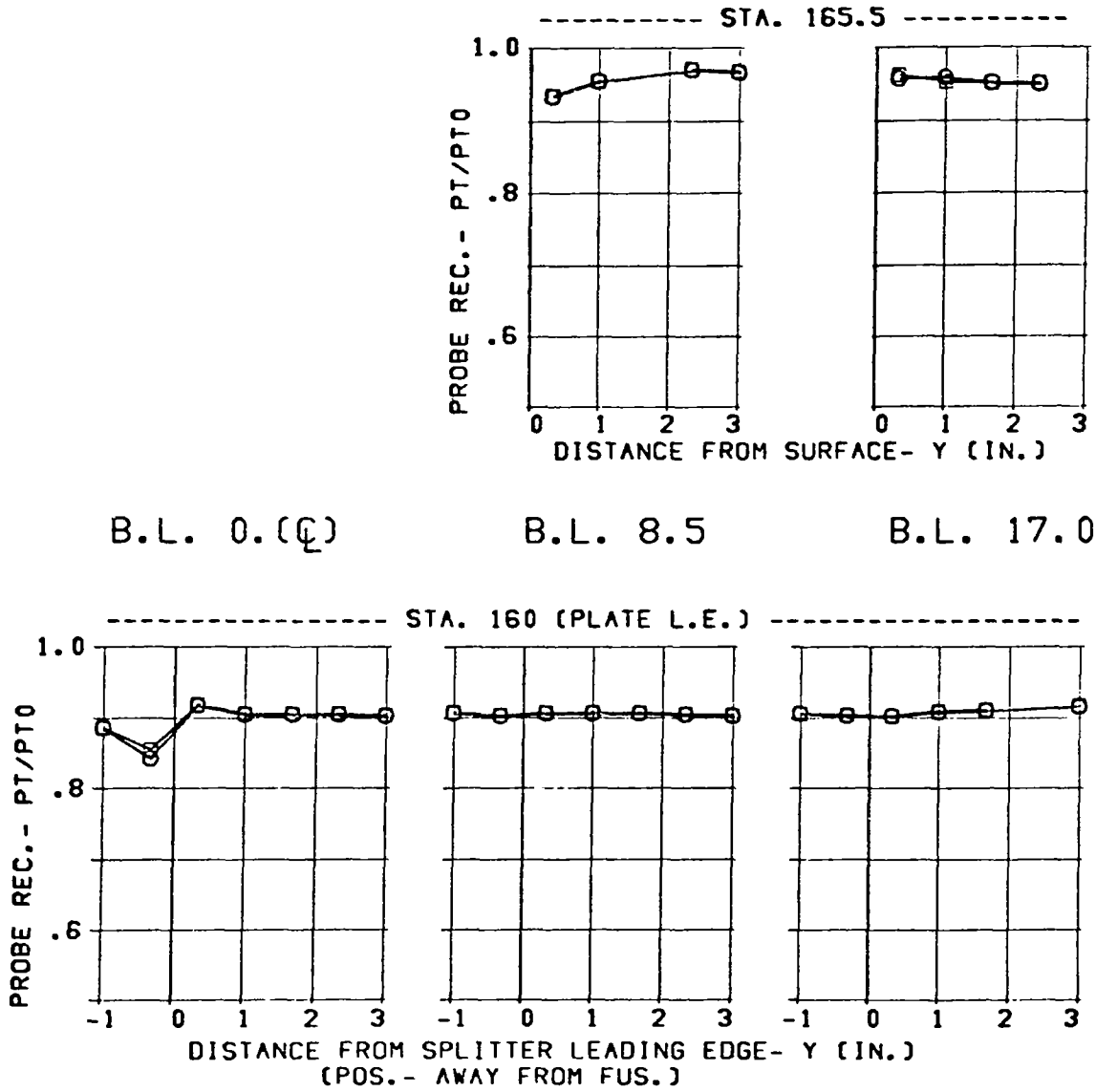

Figure 196 Effect of Nose Boom on Splitter-Plate Boundary-Layer Profiles

CONFIG.	CONDITION	SYM.	NOSE BOOM
SPLITTER ONLY	ALPHA= -5.	O	ON
3.65 IN. DIV. HT.	BETA = 0.	□	OFF
FUS. RAKES OFF	MACH = 1.96		

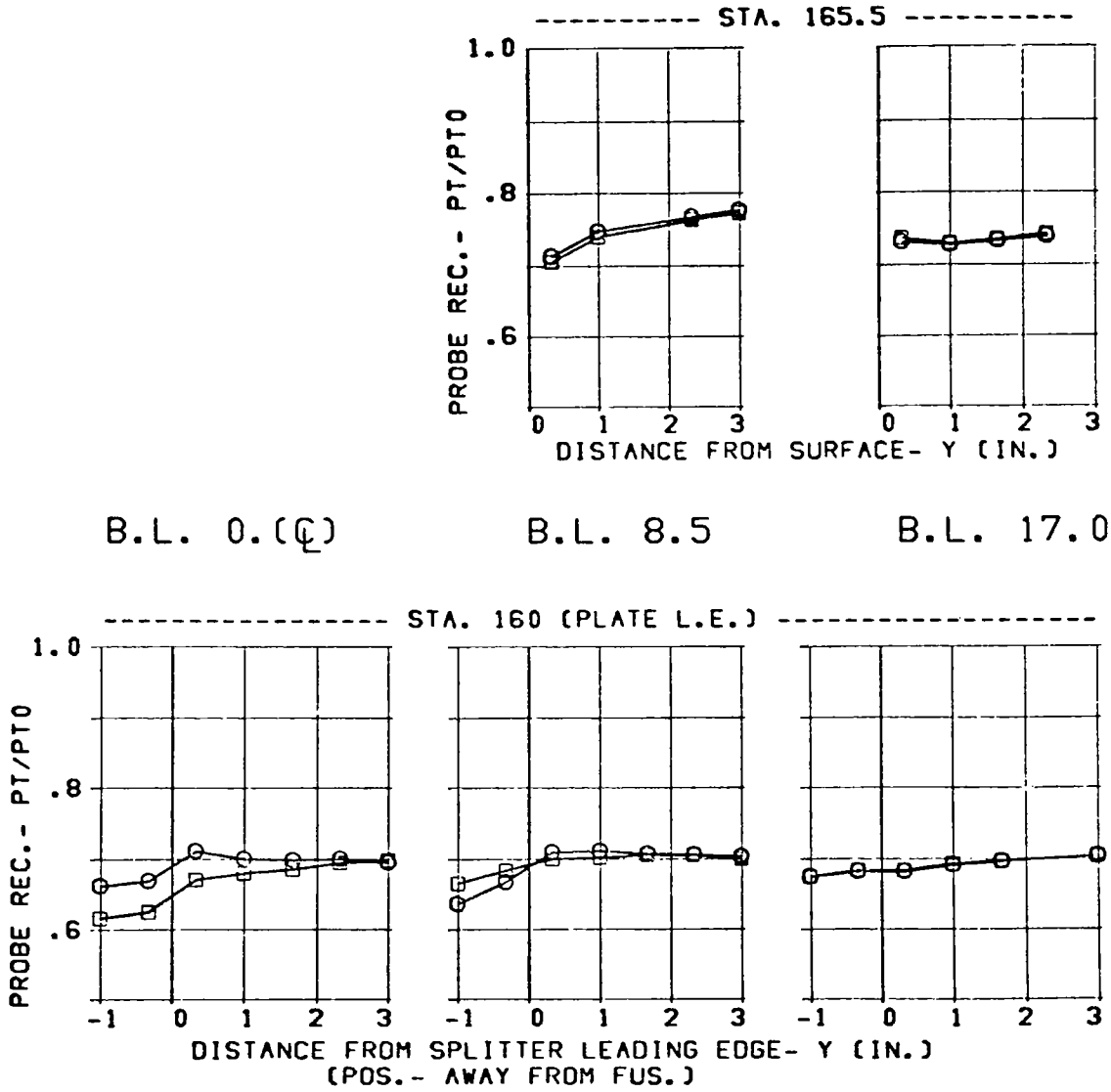

Figure 197 Effect of Nose Boom on Splitter-Plate Boundary-Layer Profiles

CONFIG.	CONDITION	SYM.	NOSE BOOM
SPLITTER ONLY 3.65 IN. DIV. HT. FUS. RAKES OFF	ALPHA= 1. BETA = 0. MACH = 1.96	O □	ON OFF

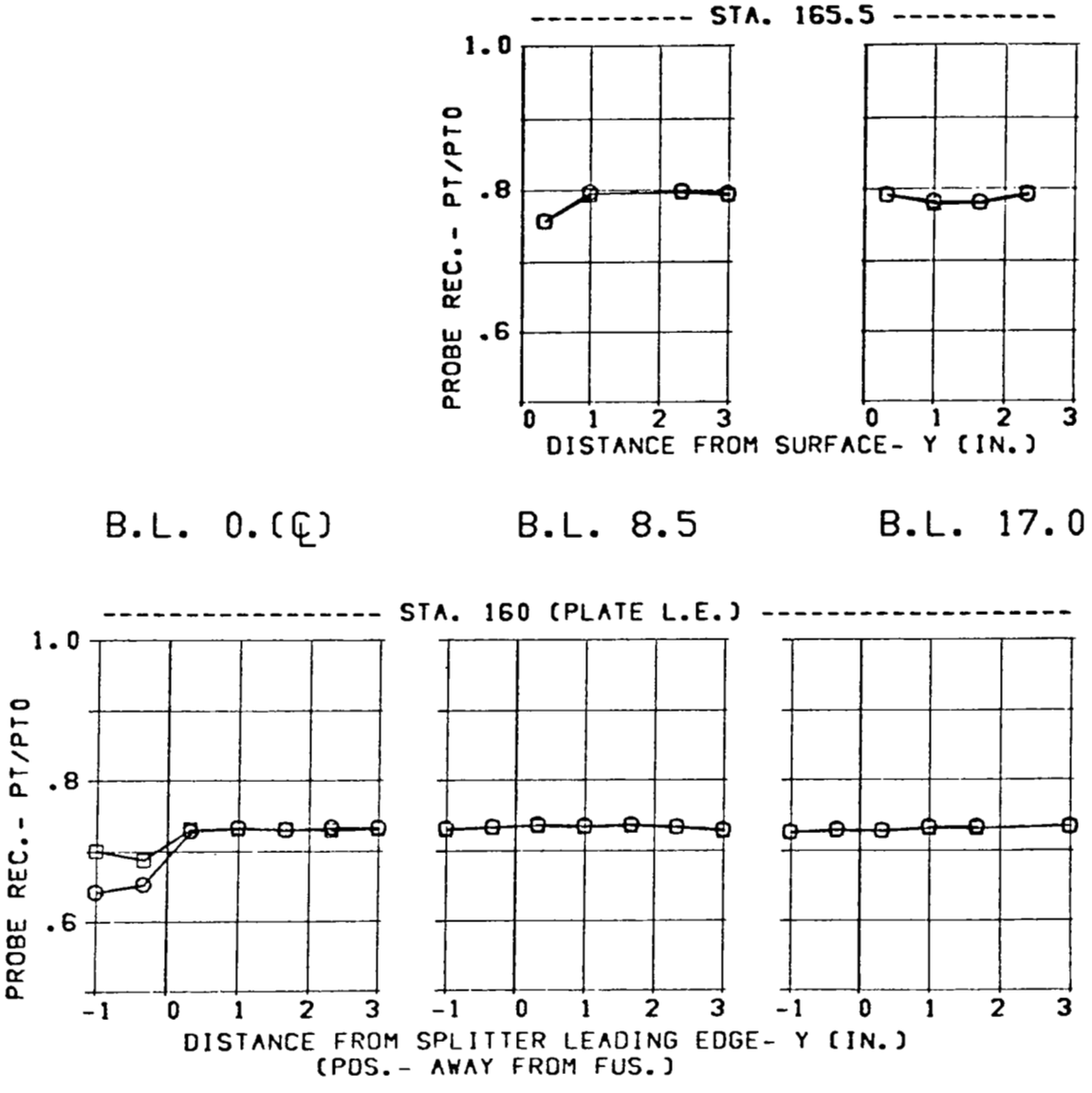

Figure 198 Effect of Nose Boom on Splitter-Plate Boundary-Layer Profiles

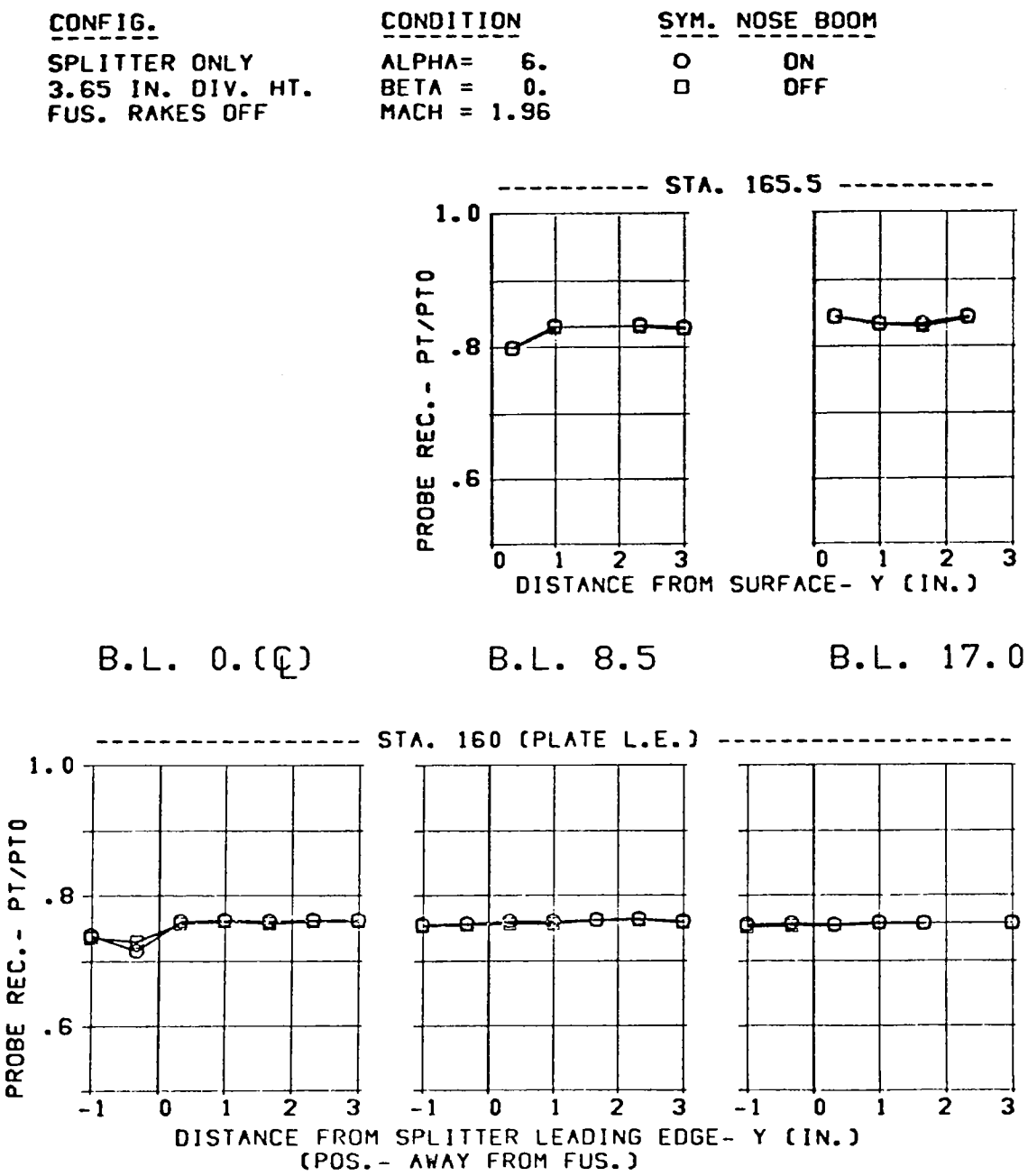

Figure 199 Effect of Nose Boom on Splitter-Plate Boundary-Layer Profiles

CONFIG.	DIV.	MACH	WC2	CONDITION		SYM.	NOSE BOOM
C13	3.65	1.96	184.	ALPHA=	-5.	O	ON
				BETA =	0.	□	OFF

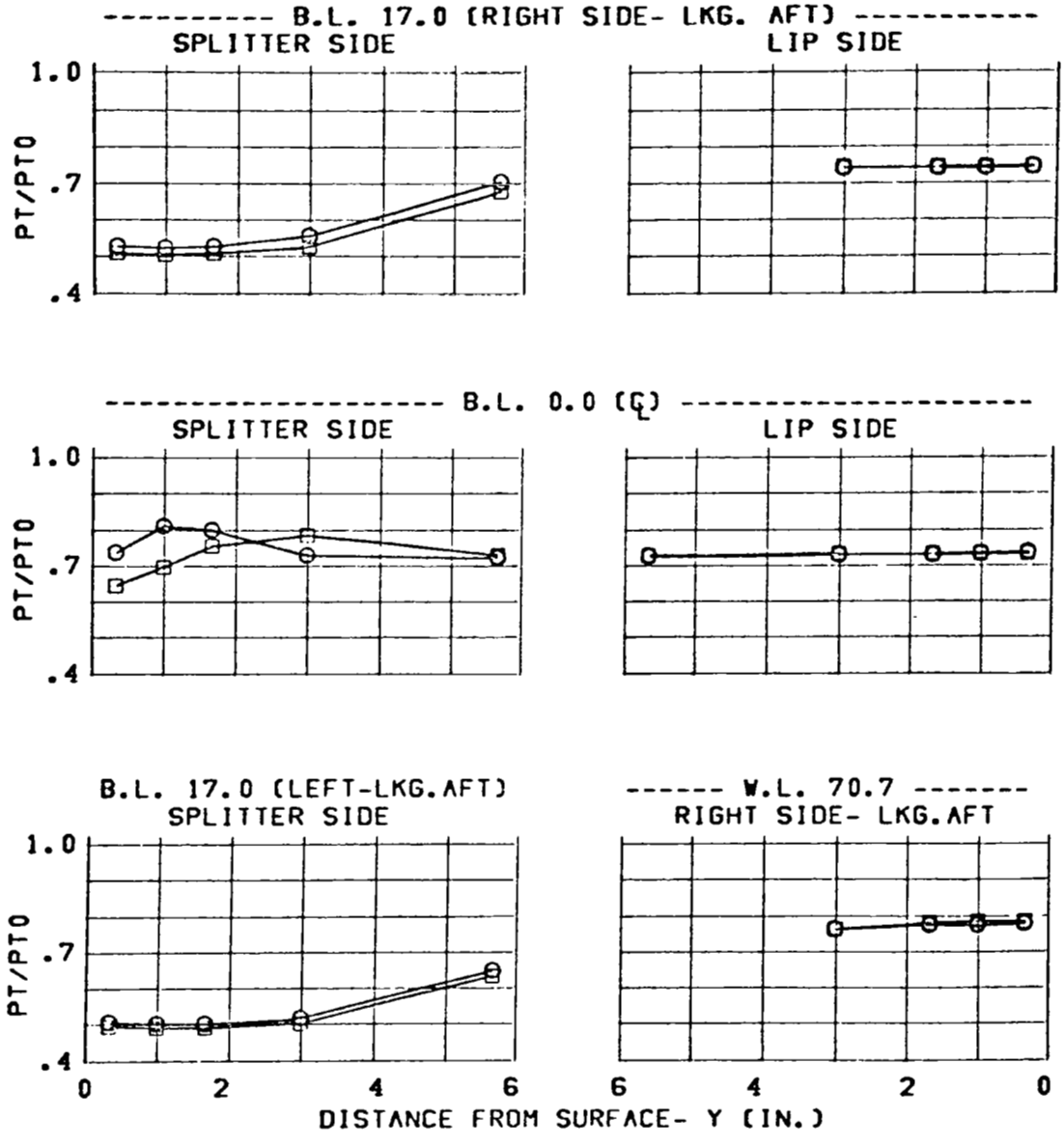

Figure 200 Effect of Nose Boom on Throat-Pressure Profiles

CONFIG.	DIV.	MACH	WC2	CONDITION		SYM.	NOSE BOOM
C13	3.65	1.96	184.	ALPHA=	1.	O	ON
				BETA =	0.	□	OFF

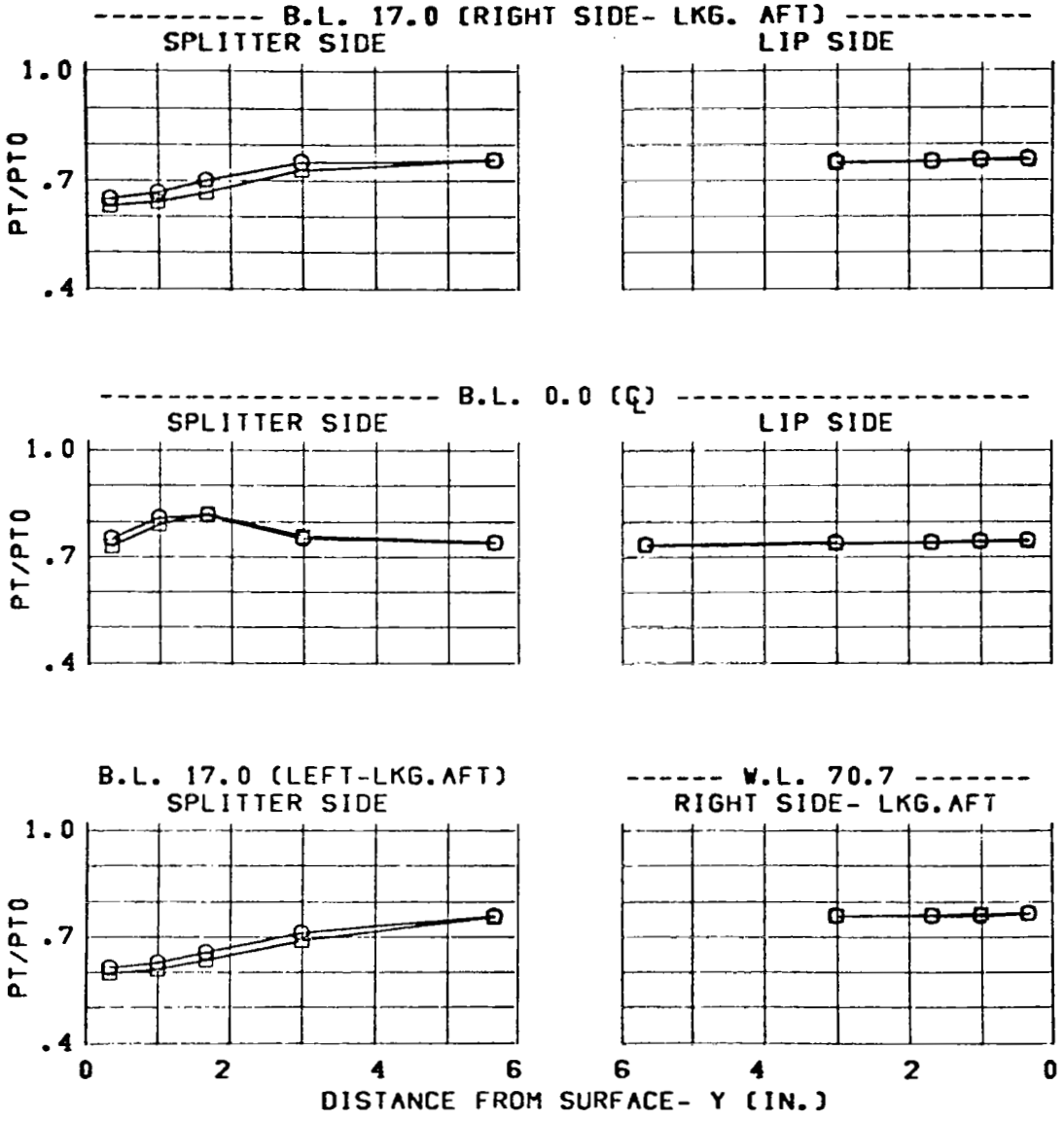

Figure 201 Effect of Nose Boom on Throat-Pressure Profiles

CONFIG.	DIV.	MACH	WC2	CONDITION		SYM.	NOSE BOOM
C13	3.65	1.96	184.	ALPHA=	6.	O	ON
				BETA =	0.	□	OFF

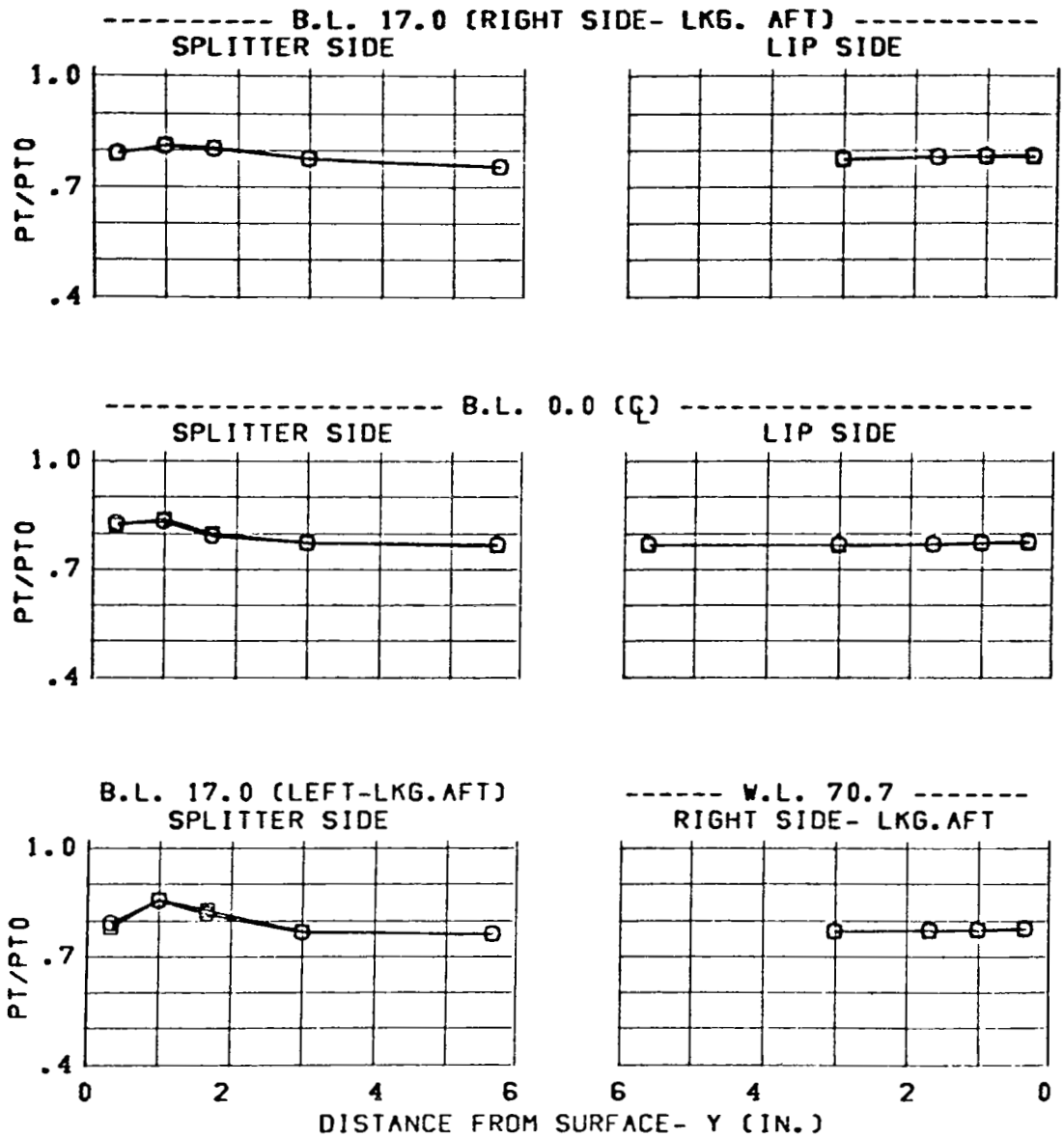

Figure 202 Effect of Nose Boom on Throat-Pressure Profiles

THROAT RAKES IN

CONFIG.	DIV.	MACH	CONDITION		SYM.	NOSE BOOM
C13	3.65	1.96	ALPHA=	-5.	O	ON
			BETA =	0.	□	OFF

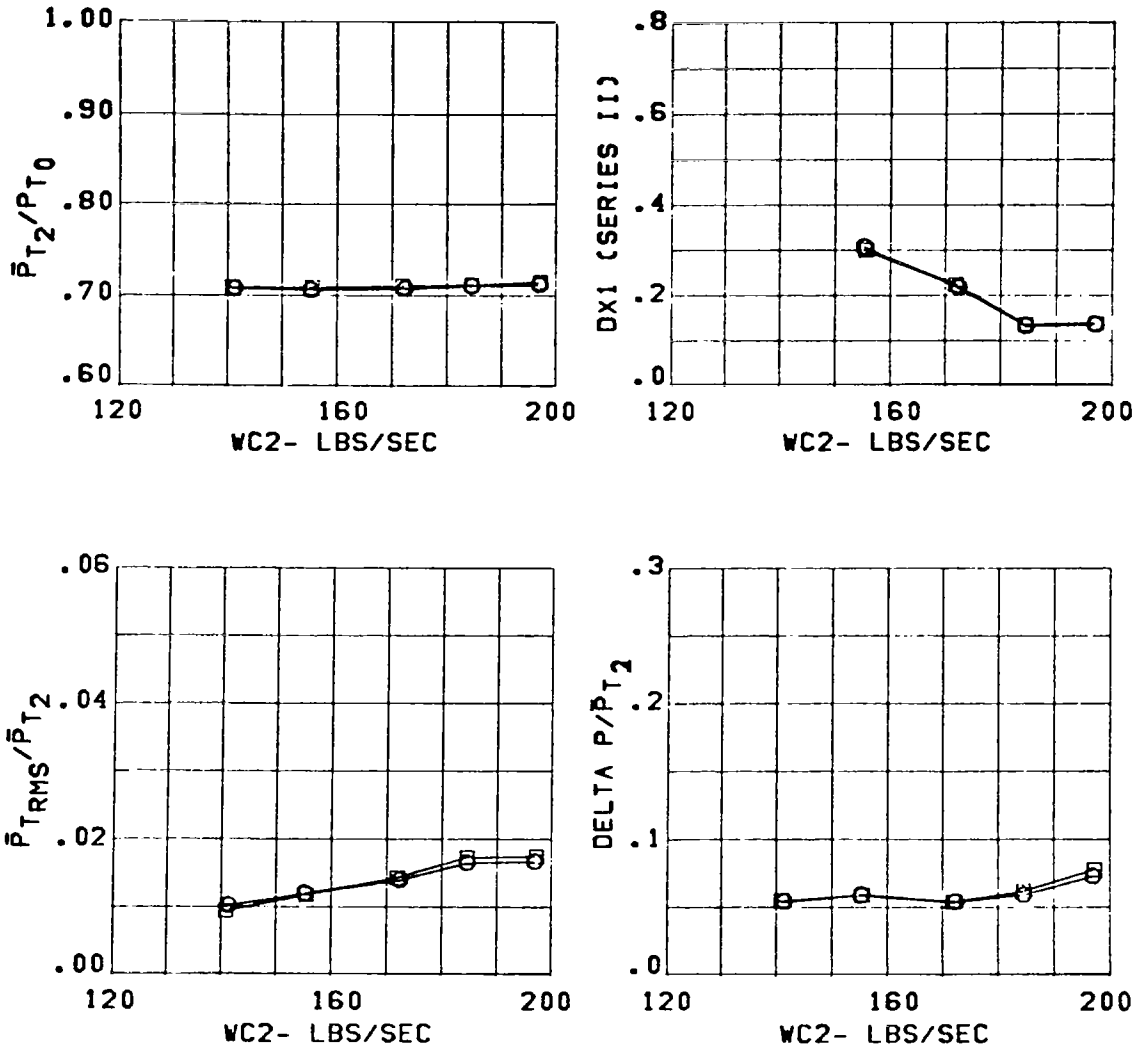

Figure 203 Effect of Nose Boom on C13 Inlet Performance

THROAT RAKES IN

CONFIG.	DIV.	MACH	CONDITION		SYM.	NOSE BOOM
C13	3.65	1.96	ALPHA=	1.	O	ON
			BETA =	0.	□	OFF

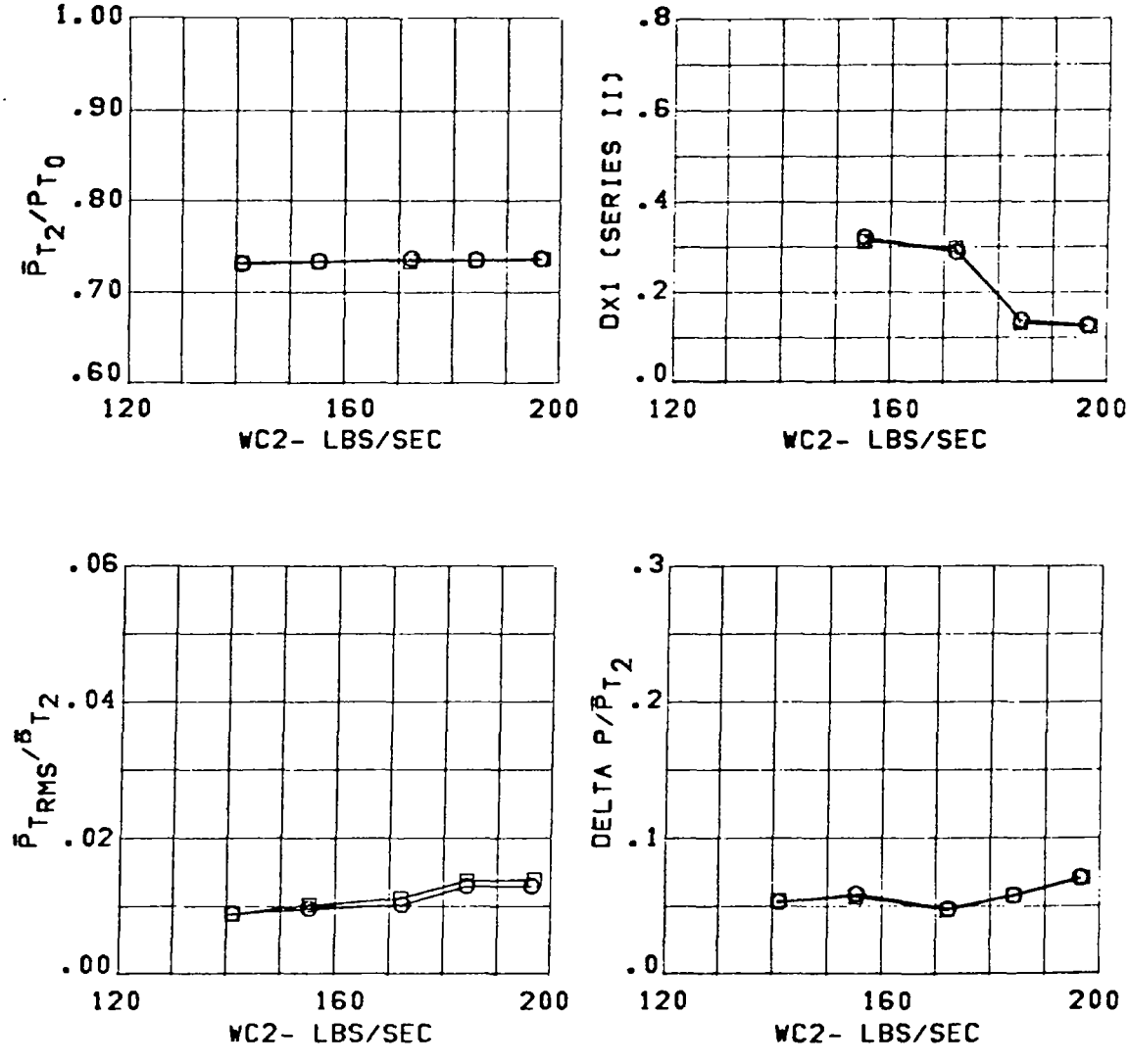

Figure 204 Effect of Nose Boom on C13 Inlet Performance

THROAT RAKES IN

CONFIG.	DIV.	MACH	CONDITION		SYM.	NOSE BOOM
C13	3.65	1.96	ALPHA=	6.	O	ON
			BETA =	0.	□	OFF

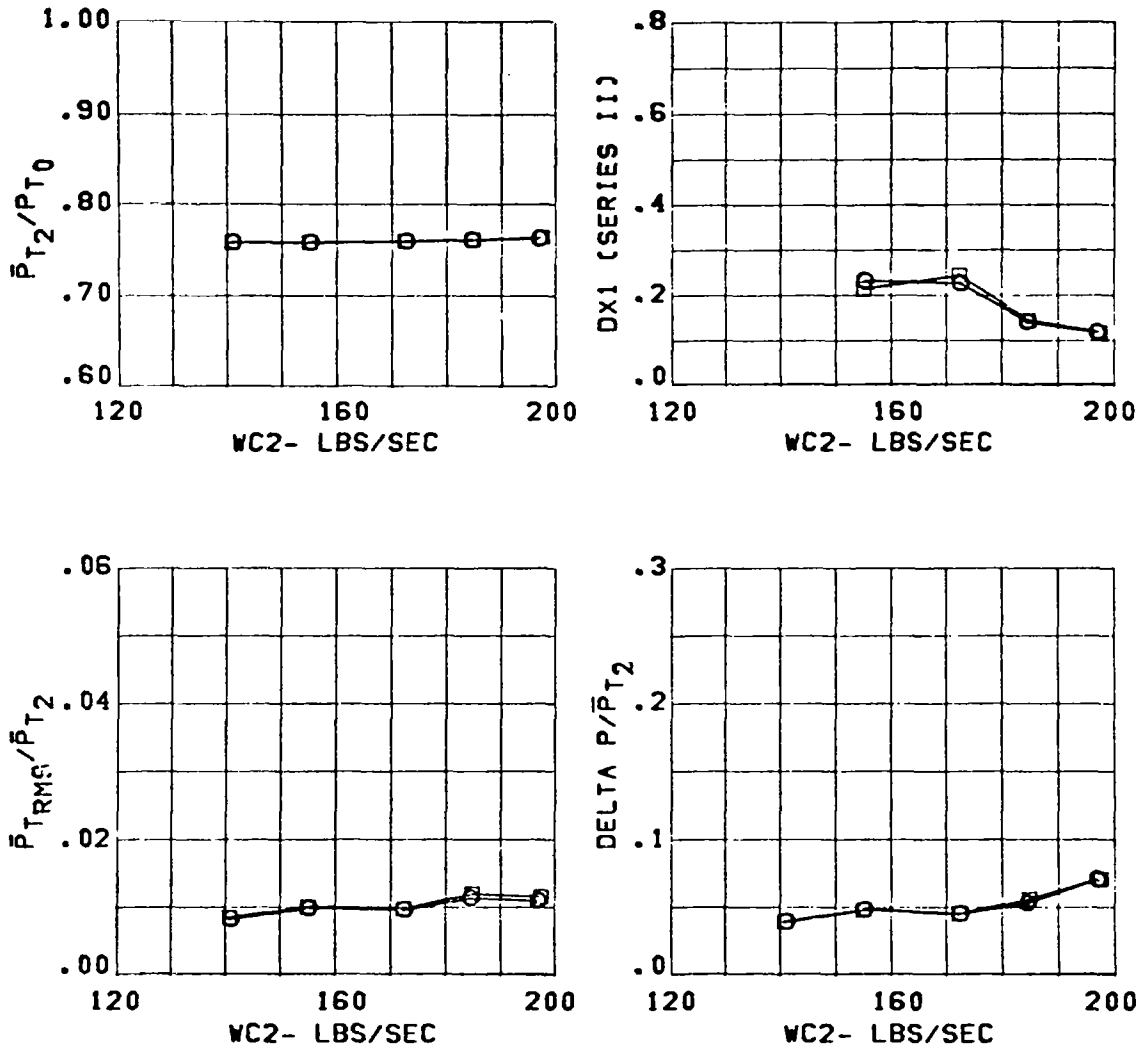

Figure 205 Effect of Nose Boom on C13 Inlet Performance

CONFIGURATION	SYM.	DIV.	MACH	WC2	CONDITION
C13 (5 DEG.BASIC)	○	3.30	1.57	217.	ALPHA= -5.
C13A (5 DEG.SLOTTED)	□				BETA = 0.

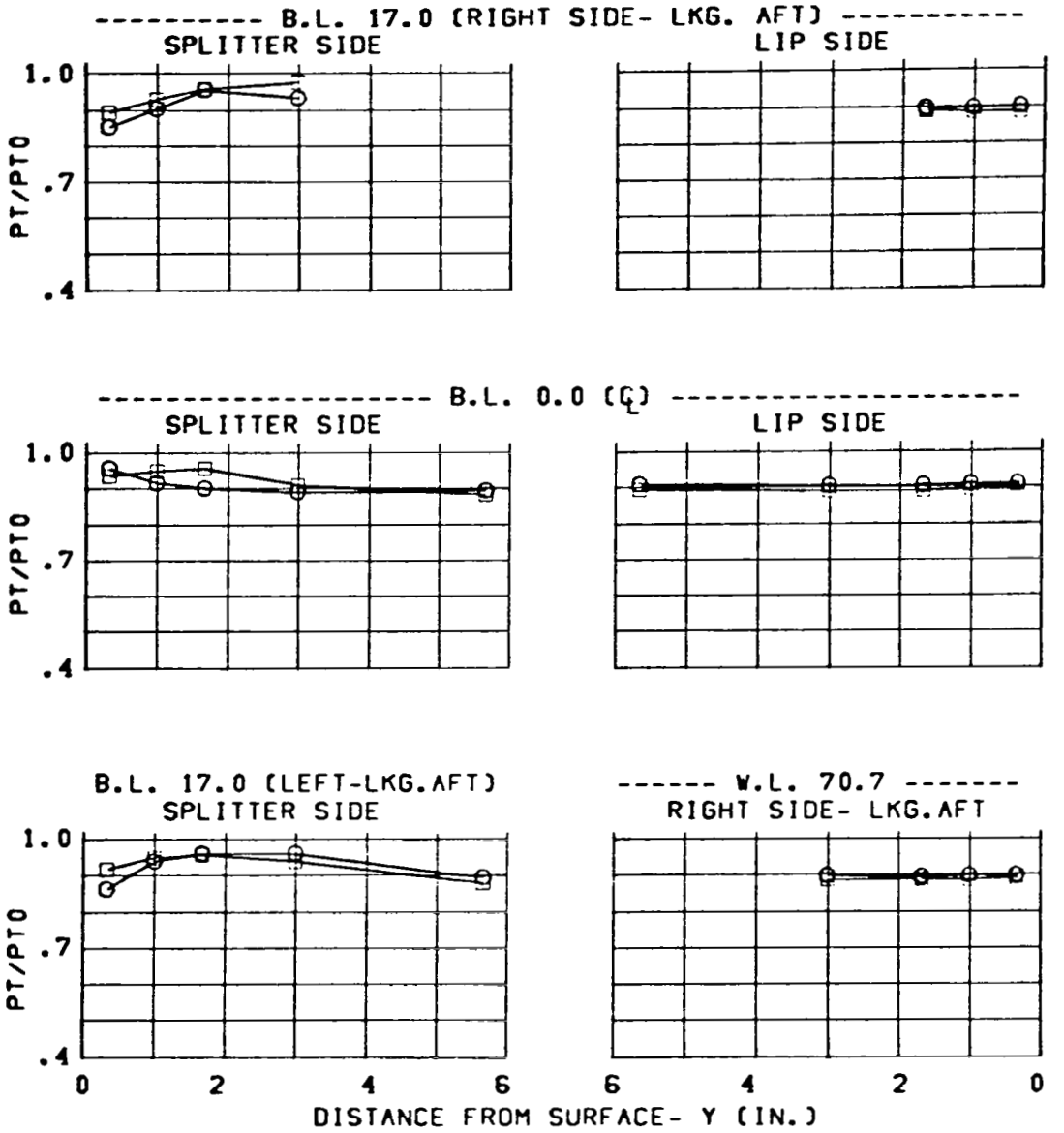

Figure 206 Effect of Slotted Ramp (Configuration C13A) on Throat-Pressure Profiles

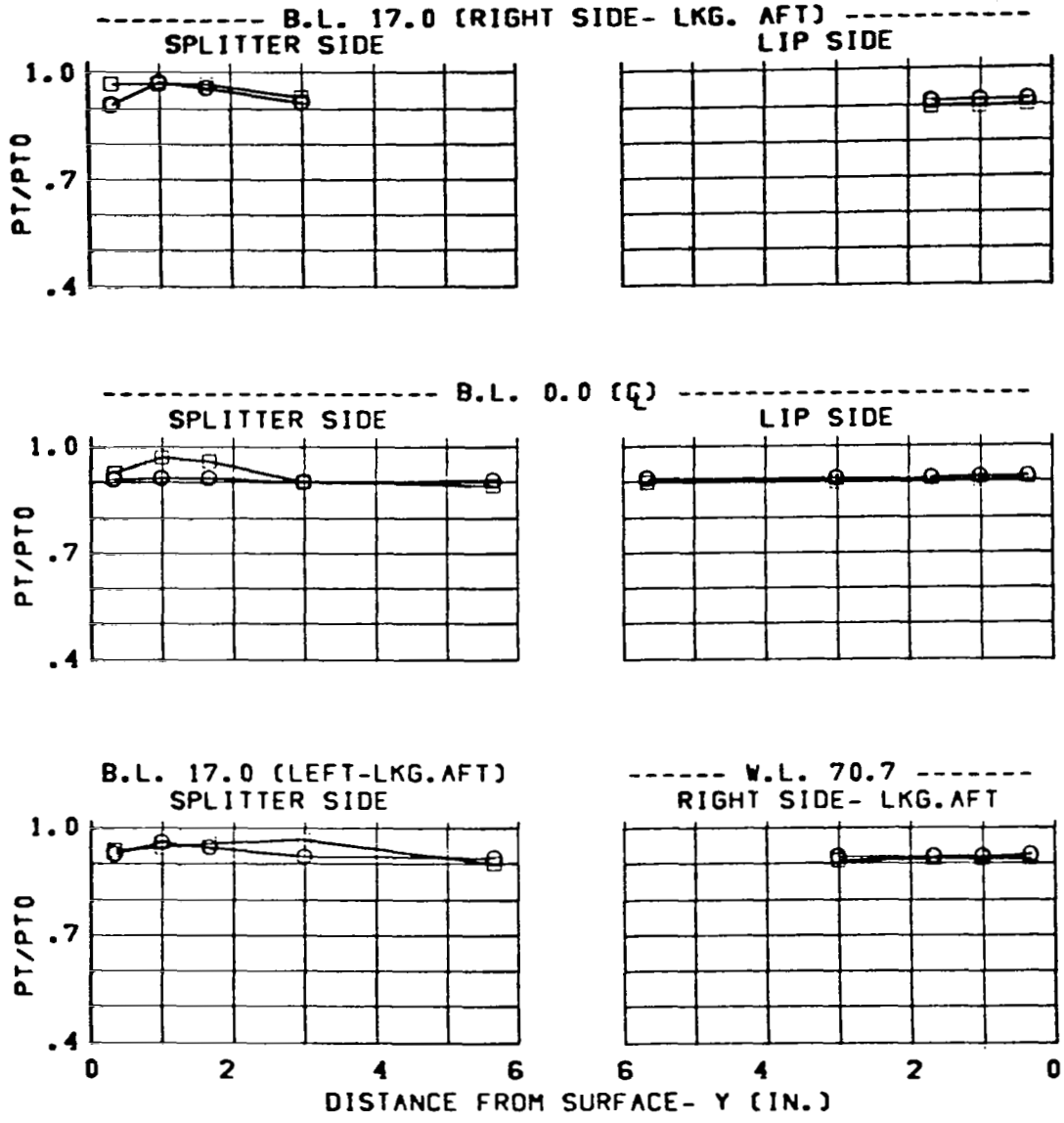

Figure 207 Effect of Slotted Ramp (Configuration C13A) on Throat-Pressure Profiles

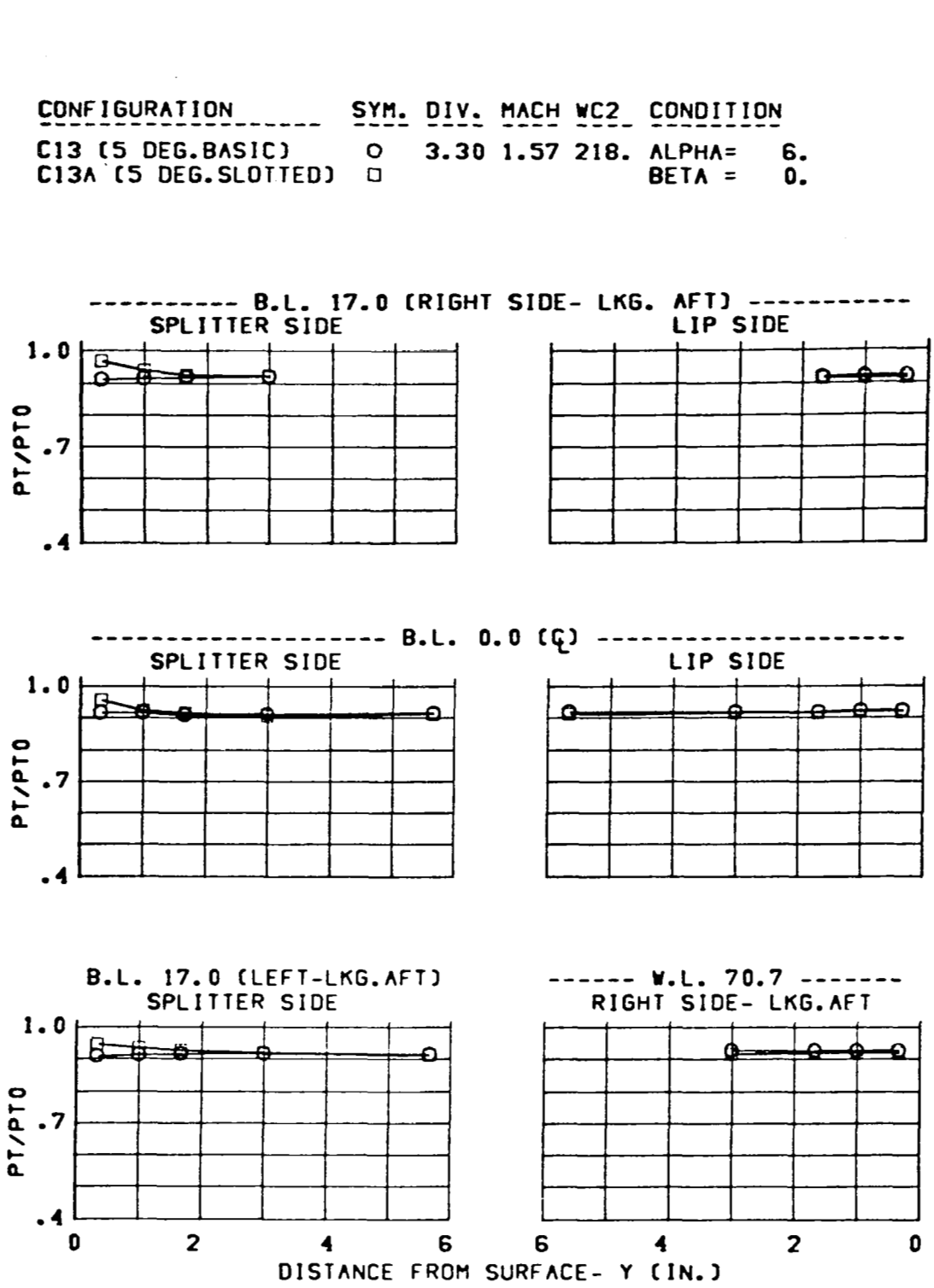

Figure 208 Effect of Slotted Ramp (Configuration C13A) on Throat-Pressure Profiles

CONFIGURATION	SYM.	DIV.	MACH	WC2	CONDITION
C13 (5 DEG.BASIC)	○	3.30	1.96	185.	ALPHA= -5.
C13A (5 DEG.SLOTTED)	□				BETA = 0.

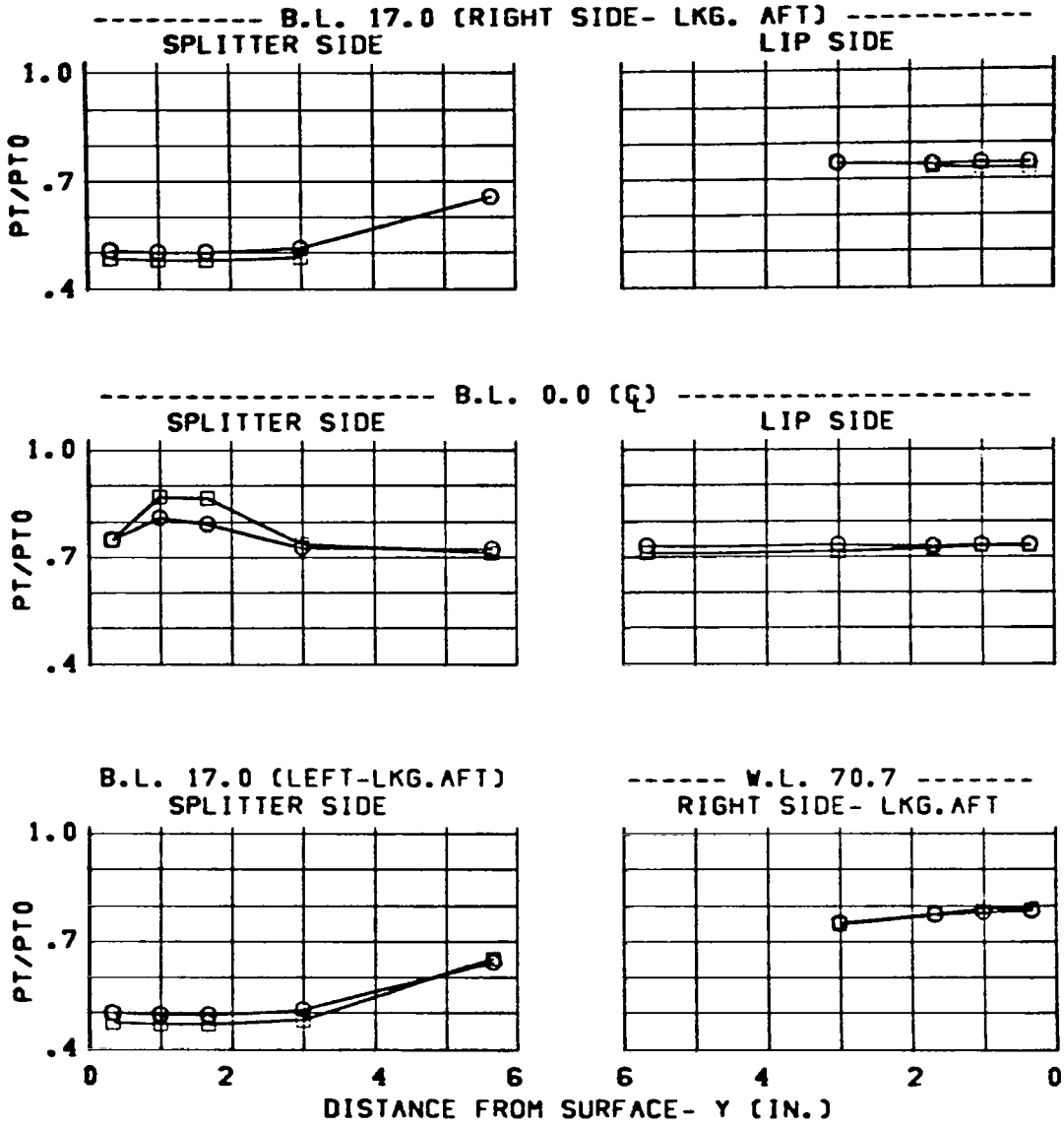

Figure 209 Effect of Slotted Ramp (Configuration C13A) on Throat-Pressure Profiles

CONFIGURATION	SYM.	DIV.	MACH	WC2	CONDITION	
C13 (5 DEG.BASIC)	○	3.30	1.96	184.	ALPHA=	1.
C13A (5 DEG.SLOTTED)	□				BETA =	0.

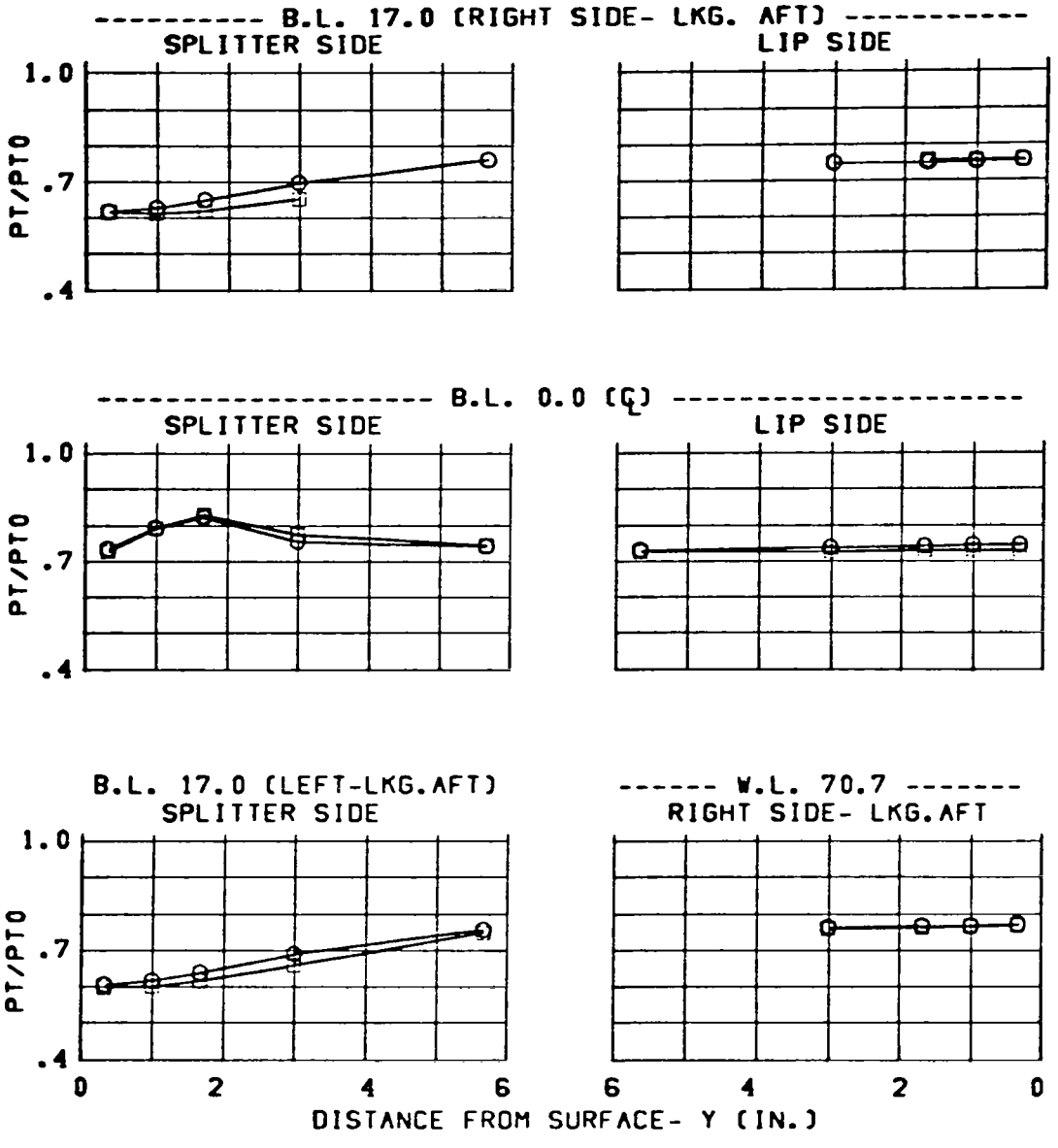

Figure 210 Effect of Slotted Ramp (Configuration C13A) on Throat-Pressure Profiles

CONFIGURATION	SYM.	DIV.	MACH	WC2	CONDITION	
C13 (5 DEG.BASIC)	○	3.30	1.96	185.	ALPHA=	6.
C13A (5 DEG.SLOTTED)	□				BETA =	0.

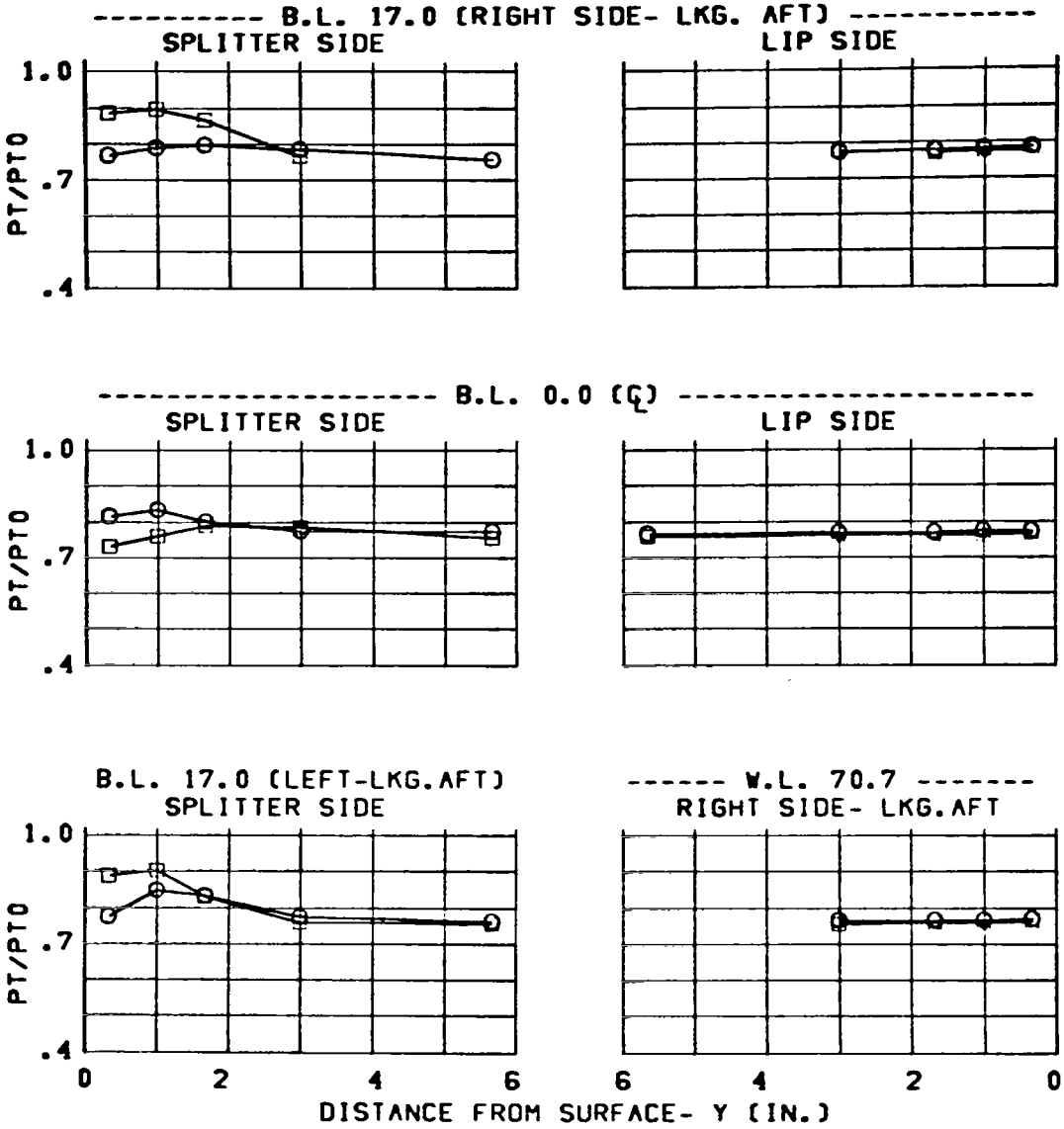

Figure 211 Effect of Slotted Ramp (Configuration C13A) on Throat-Pressure Profiles

CONFIG.	DIV.	MACH	SYM.	THROAT RAKES	CONDITION
C13	3.30	1.57	○	IN	ALPHA= -5.
C13A			□		BETA = 0.

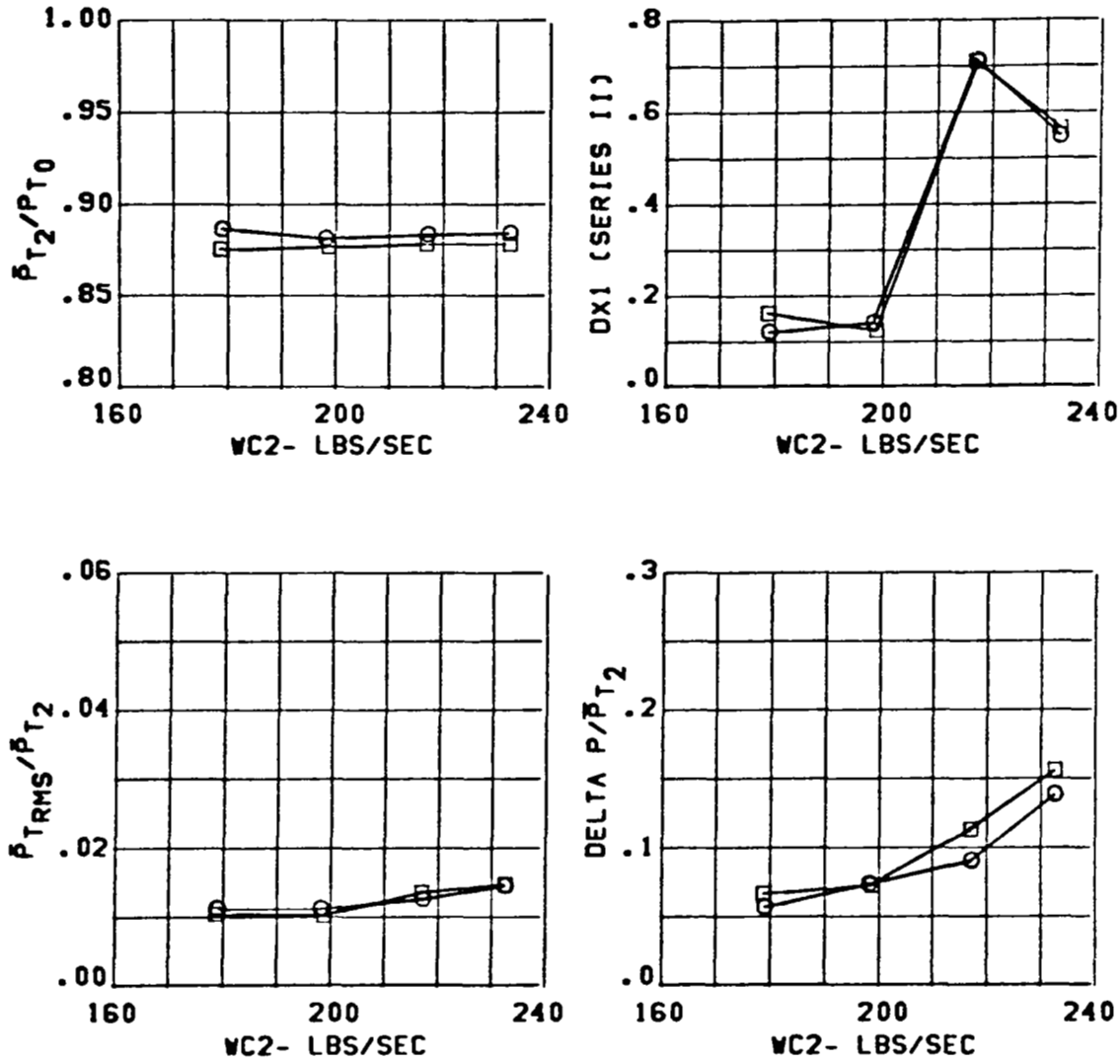

Figure 212 Effect of Slotted Ramp (Configuration C13A) on Inlet Performance

CONFIG.	DIV.	MACH	SYM.	THROAT RAKES	CONDITION
C13	3.30	1.57	○	IN	ALPHA= 1.
C13A			□		BETA = 0.

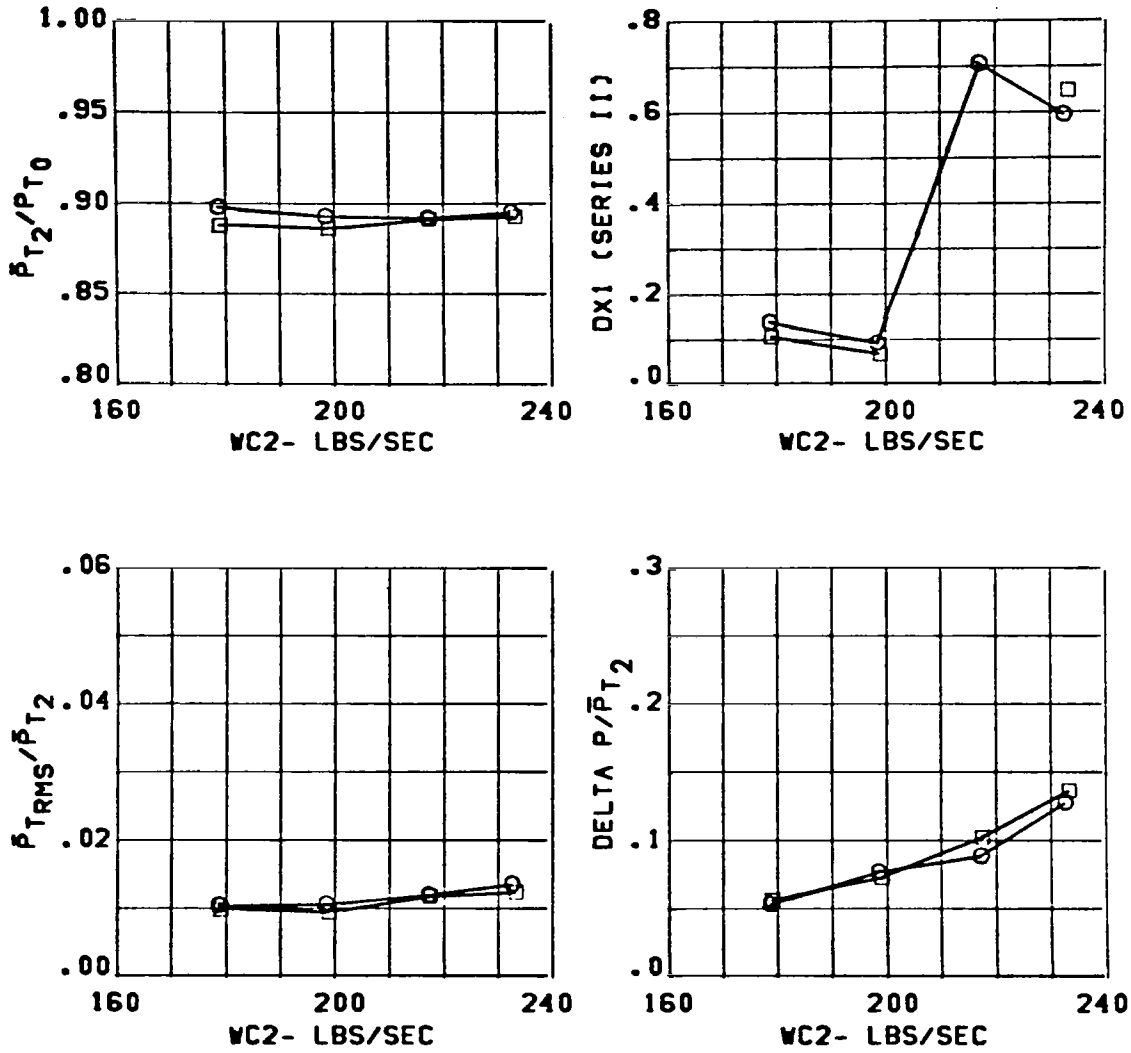

Figure 213 Effect of Slotted Ramp (Configuration C13A) on Inlet Performance

CONFIG.	DIV.	MACH	SYM.	THROAT RAKES	CONDITION
C13	3.30	1.56	O	IN	ALPHA= 6.
C13A			□		BETA = 0.

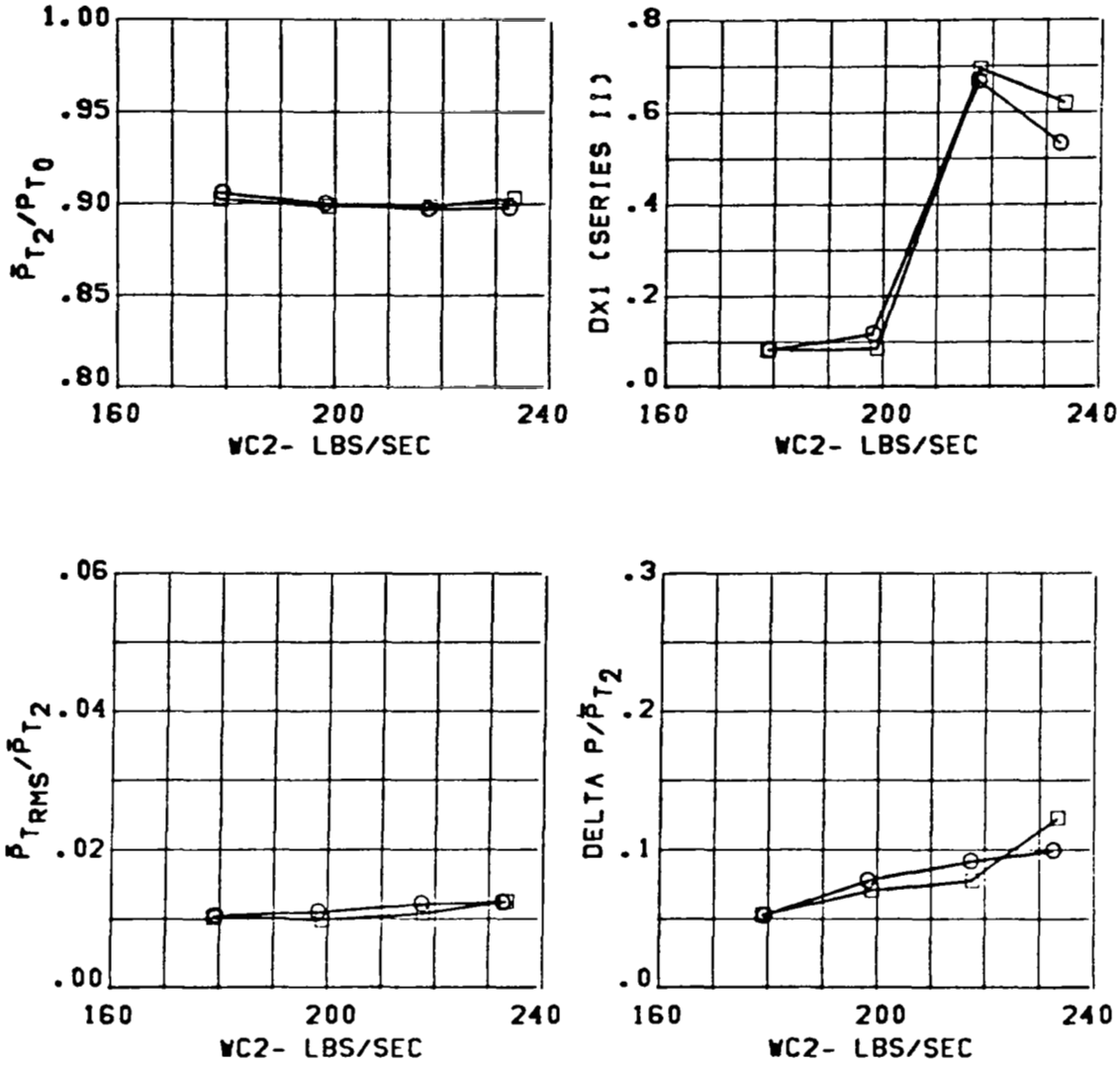

Figure 214 Effect of Slotted Ramp (Configuration C13A) on Inlet Performance

CONFIG.	DIV.	MACH	SYM.	THROAT RAKES	CONDITION
C13	3.30	1.96	○	IN	ALPHA= -5.
C13A			□		BETA = 0.

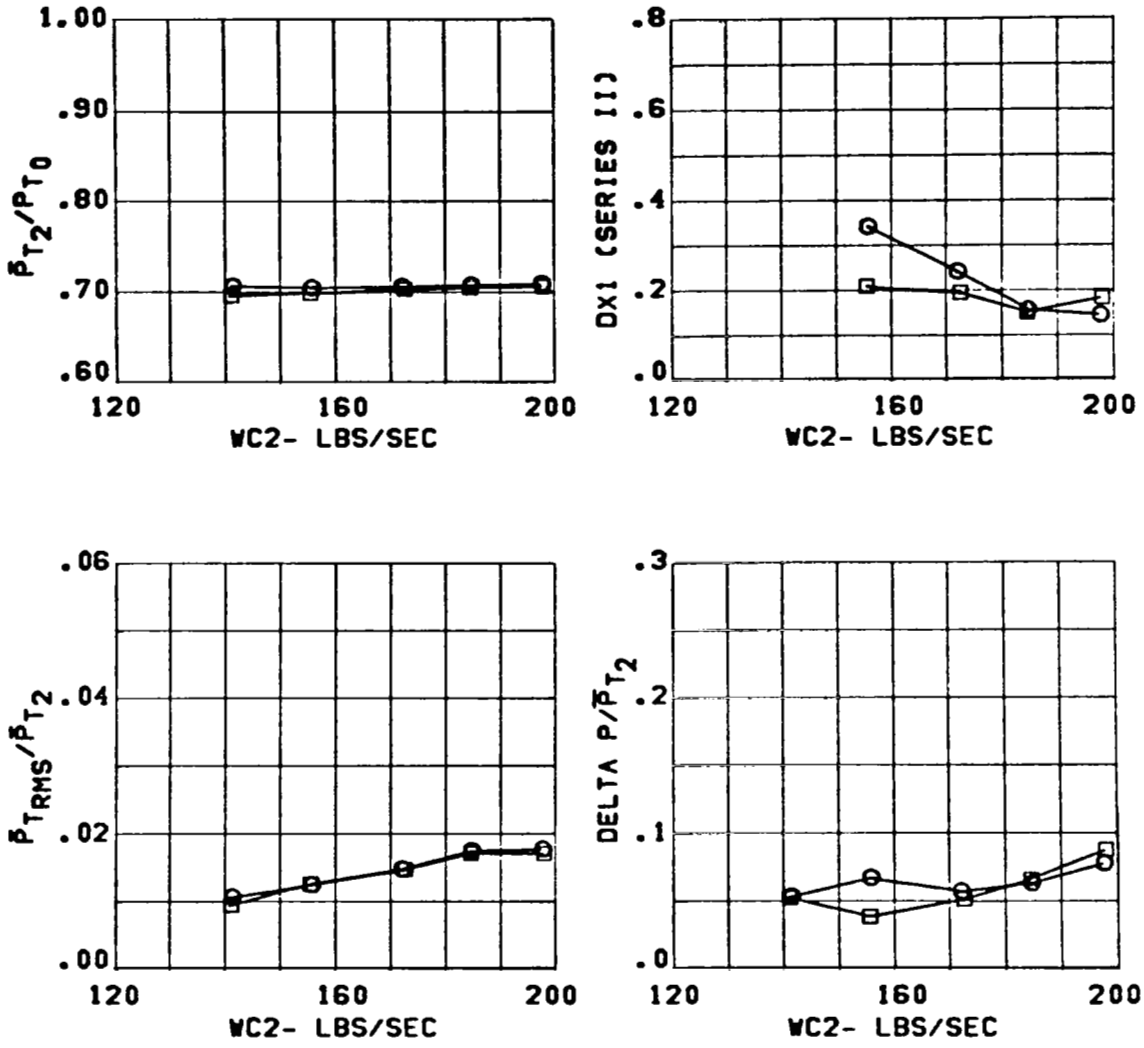

Figure 215 Effect of Slotted Ramp (Configuration C13A) on Inlet Performance

CONFIG.	DIV.	MACH	SYM.	THROAT RAKES	CONDITION	
C13	3.30	1.96	O	IN	ALPHA=	1.
C13A			□		BETA =	0.

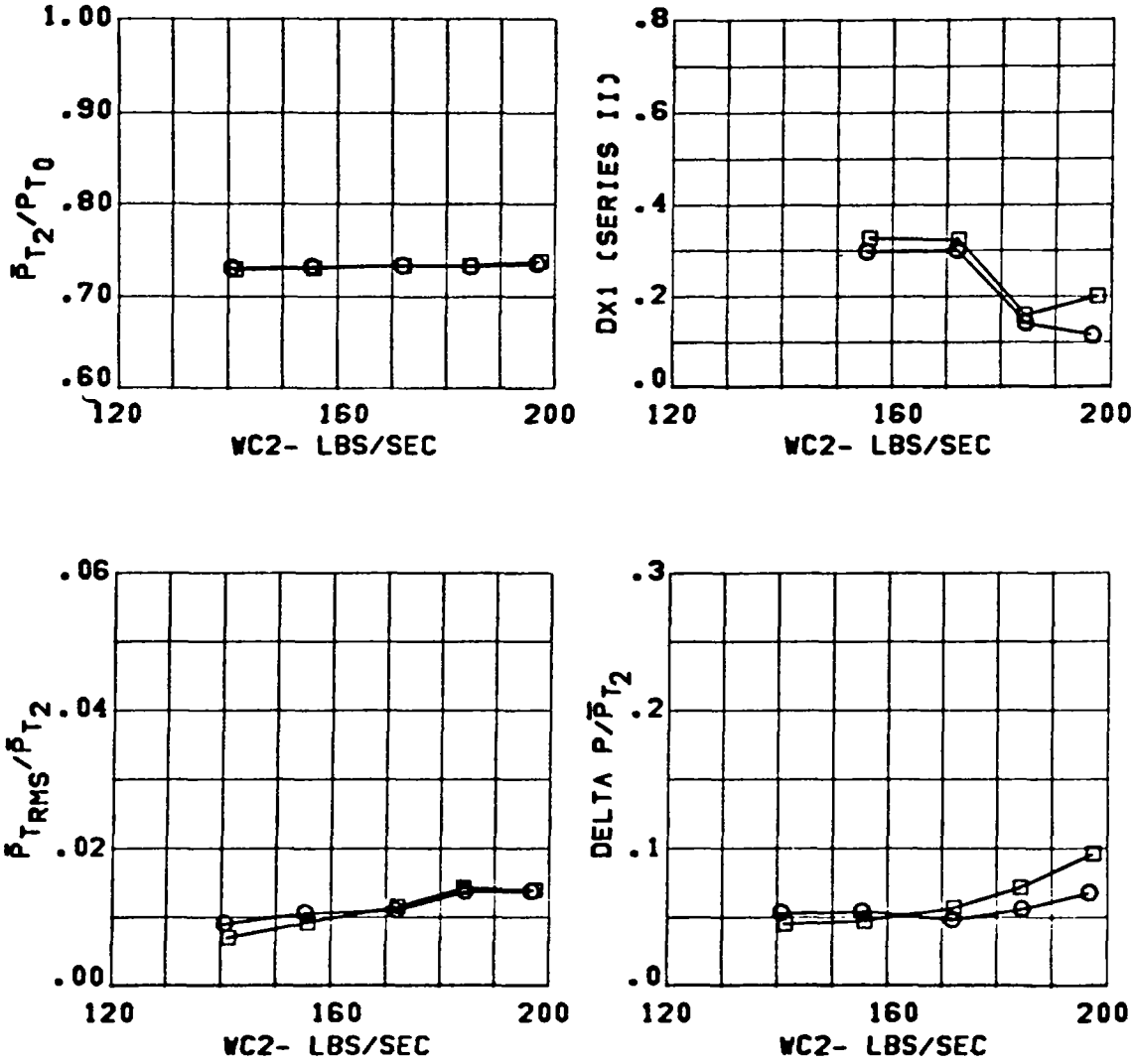

Figure 216 Effect of Slotted Ramp (Configuration C13A) on Inlet Performance

CONFIG.	DIV.	MACH	SYM.	THROAT RAKES	CONDITION
C13	3.30	1.95	O	IN	ALPHA= 6.
C13A			□		BETA = 0.

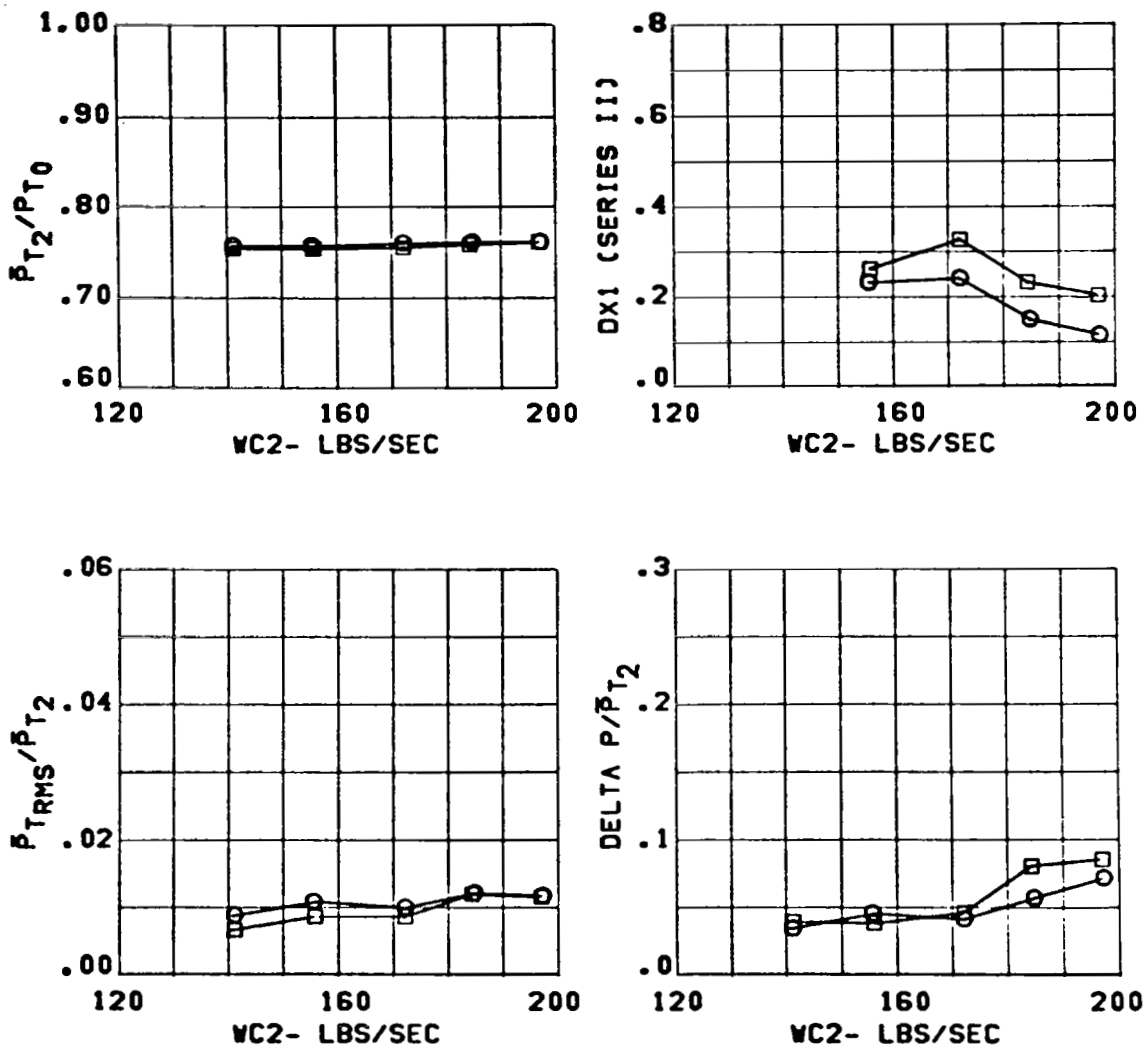

Figure 217 Effect of Slotted Ramp (Configuration C13A) on Inlet Performance

CONFIGURATION	SYM.	DIV.	MACH	WC2	CONDITION
C13 (5 DEG.BASIC)	○	3.65	1.57	217.	ALPHA= -5.
C15A (13 DEG.SOLID)	□				BETA = 0.

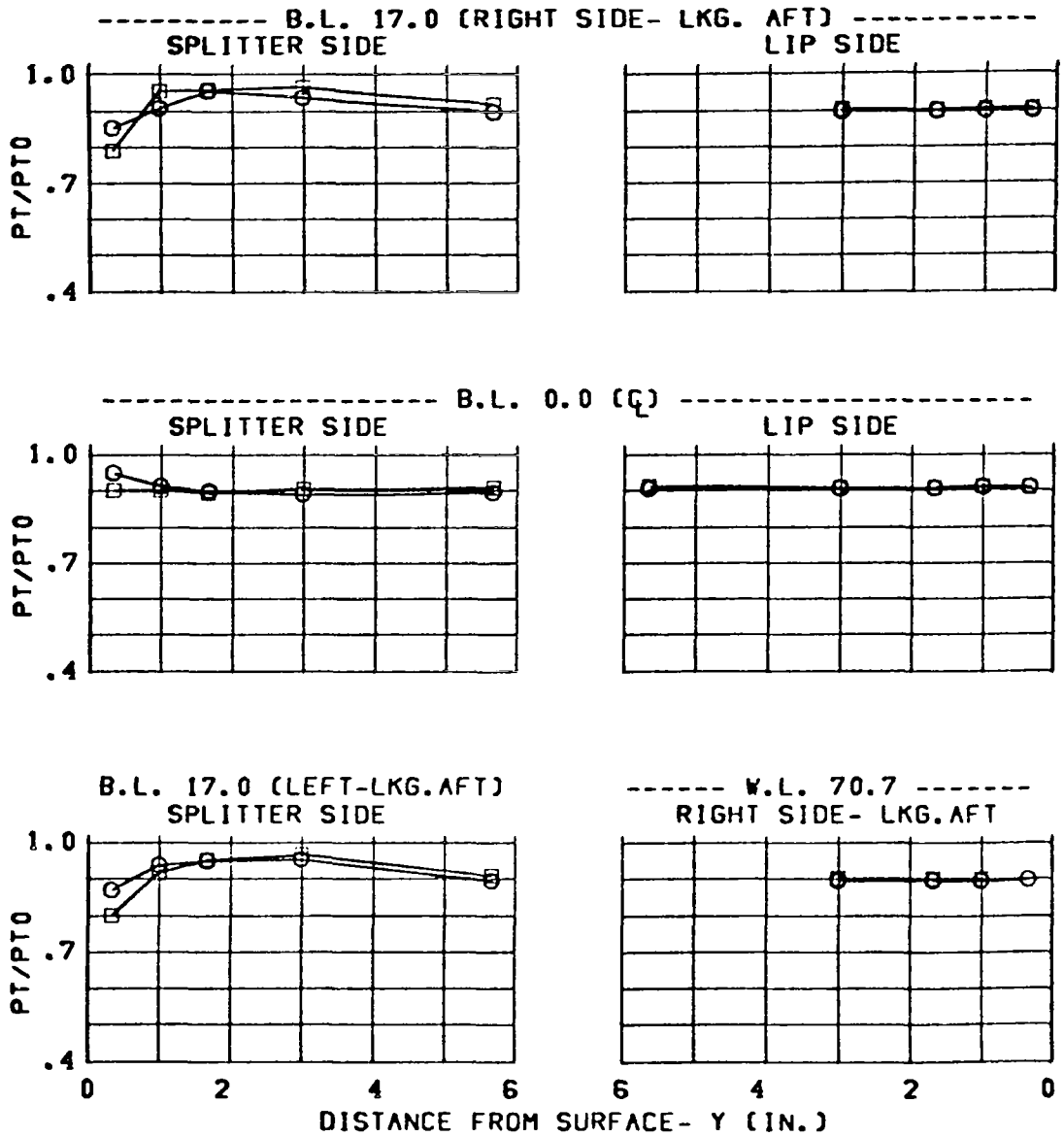

Figure 218 Effect of 13° Ramp (Configuration C15A) on Throat-Pressure Profiles

CONFIGURATION	SYM.	DIV.	MACH	WC2	CONDITION	
C13 (5 DEG.BASIC)	○	3.65	1.57	217.	ALPHA=	1.
C15A (13 DEG.SOLID)	□				BETA =	0.

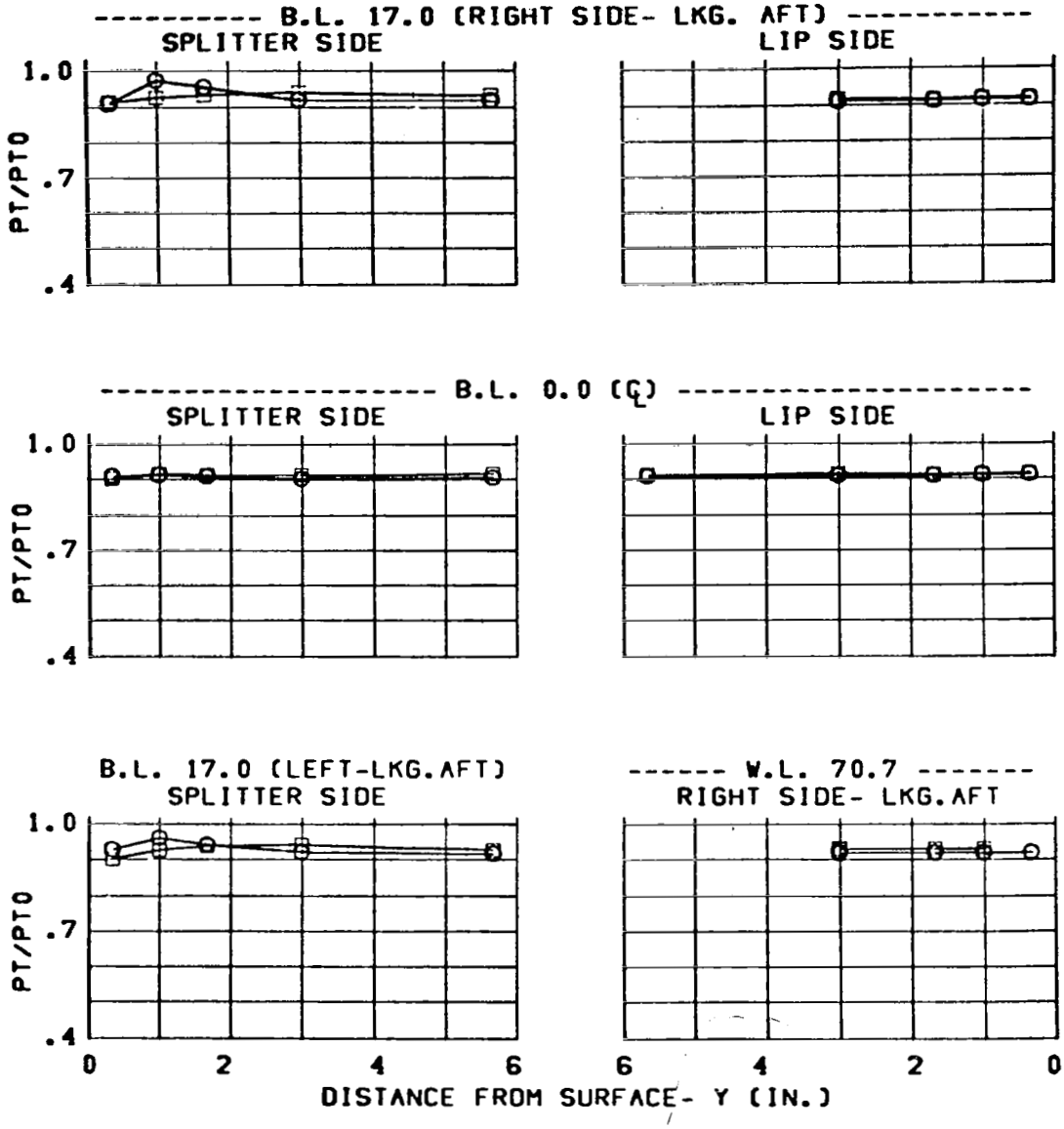

Figure 219 Effect of 13° Ramp (Configuration C15A) on Throat-Pressure Profiles

CONFIGURATION	SYM.	DIV.	MACH	WC2	CONDITION	
C13 (5 DEG.BASIC)	○	3.65	1.57	217.	ALPHA=	6.
C15A (13 DEG.SOLID)	□				BETA =	0.

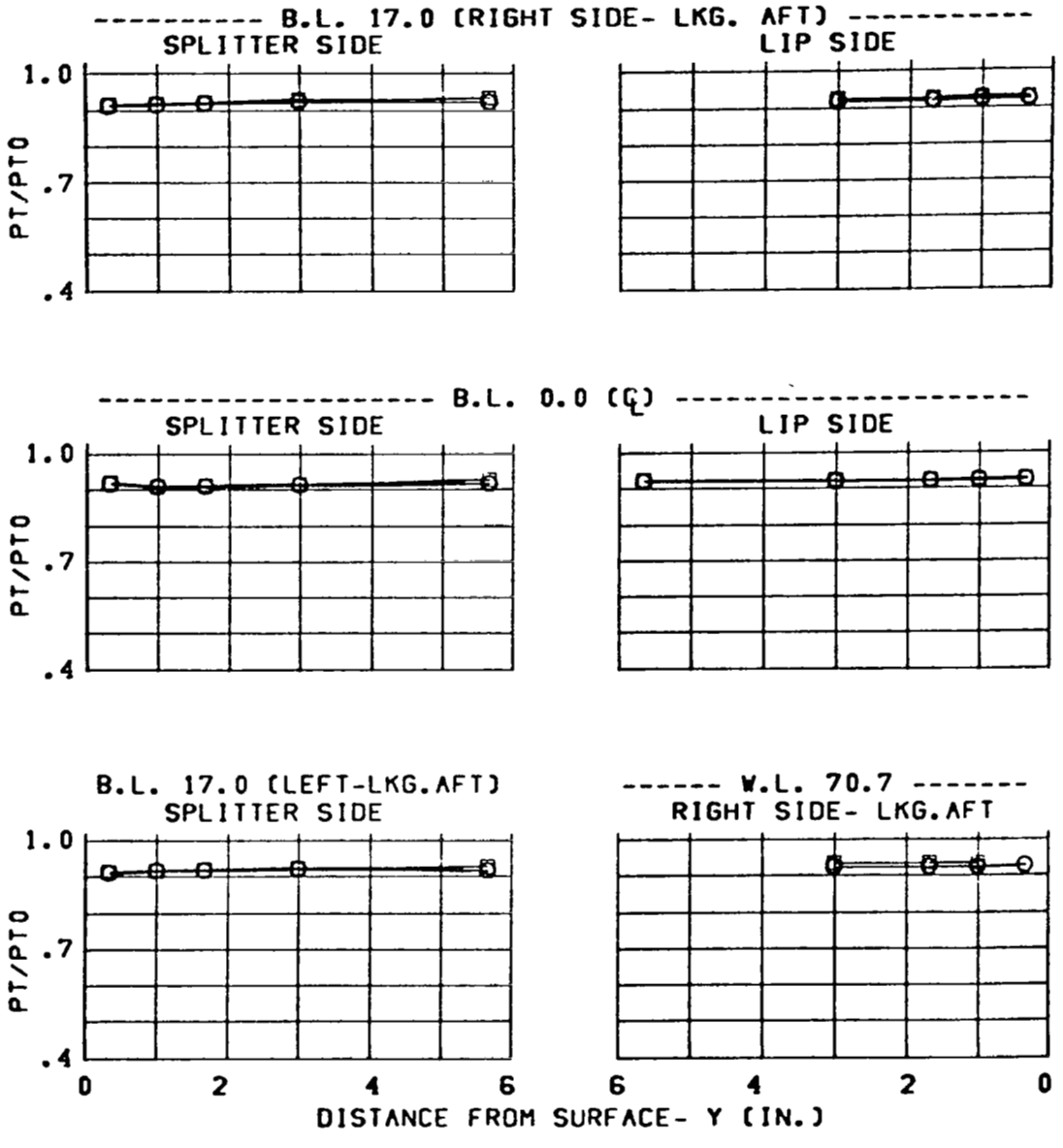

Figure 220 Effect of 13° Ramp (Configuration C15A) on Throat-Pressure Profiles

CONFIGURATION	SYM.	DIV.	MACH	WC2	CONDITION	
C13 (5 DEG.BASIC)	O	3.65	1.96	184.	ALPHA=	-5.
C15A (13 DEG.SOLID)	□				BETA =	0.

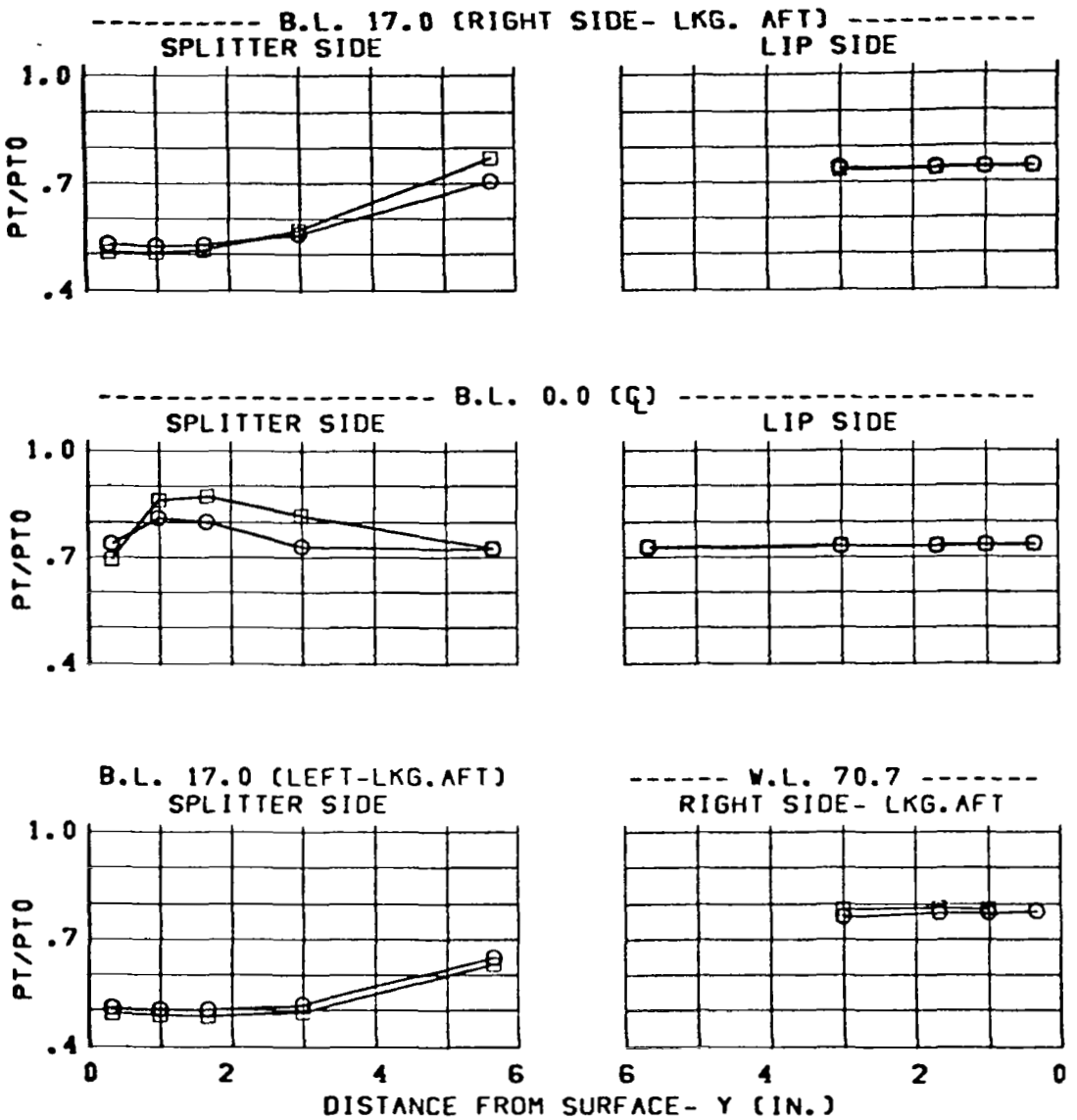

Figure 221 Effect of 13° Ramp (Configuration C15A) on Throat-Pressure Profiles

CONFIGURATION	SYM.	DIV.	MACH	WC2	CONDITION	
C13 (5 DEG.BASIC)	○	3.65	1.96	184.	ALPHA=	1.
C15A (13 DEG.SOLID)	□				BETA =	0.

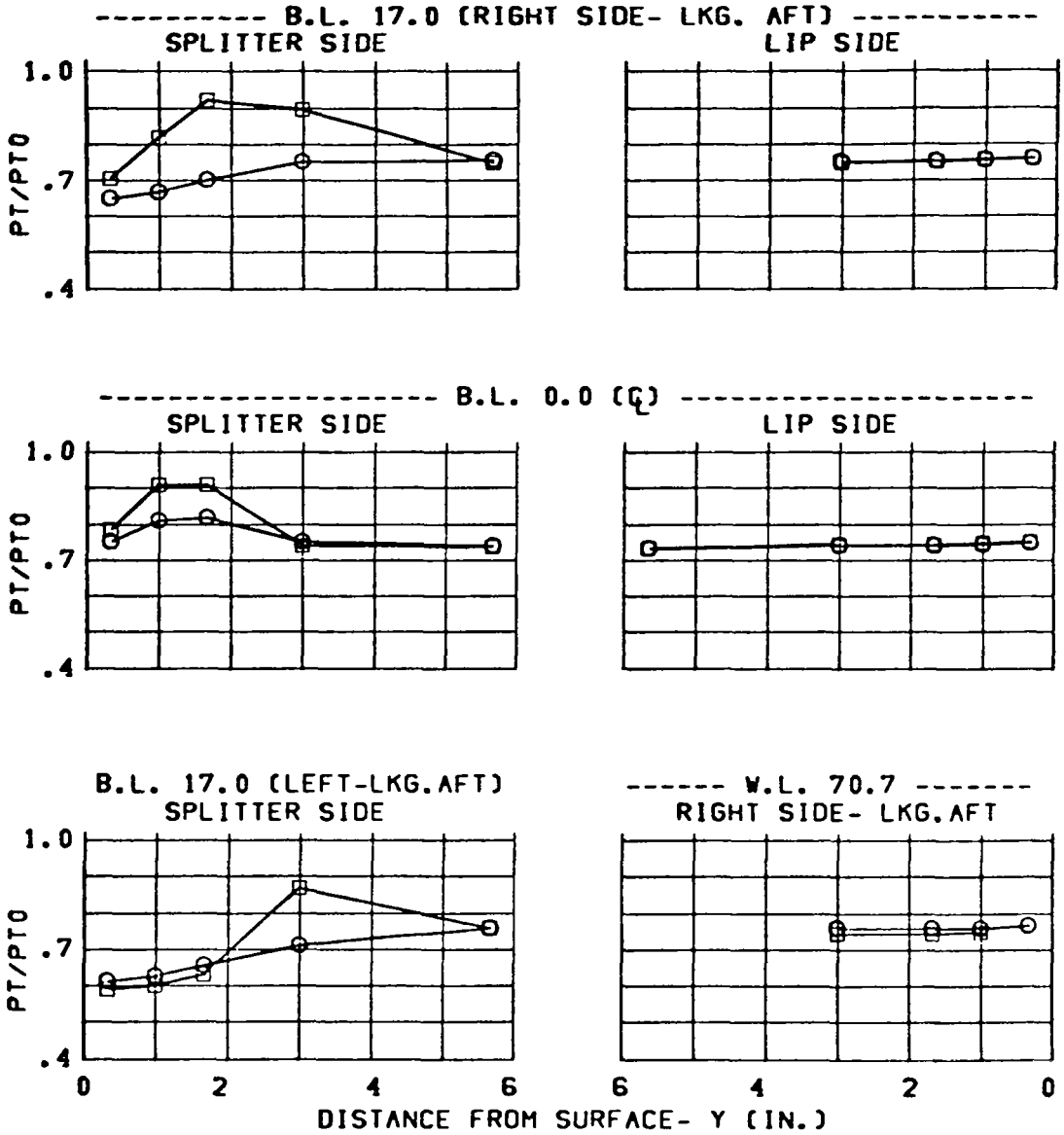

Figure 222 Effect of 13° Ramp (Configuration C15A) on Throat-Pressure Profiles

CONFIGURATION	SYM.	DIV.	MACH	WC2	CONDITION	
C13 (5 DEG.BASIC)	O	3.65	1.96	184.	ALPHA=	6.
C15A (13 DEG.SOLID)	□				BETA =	0.

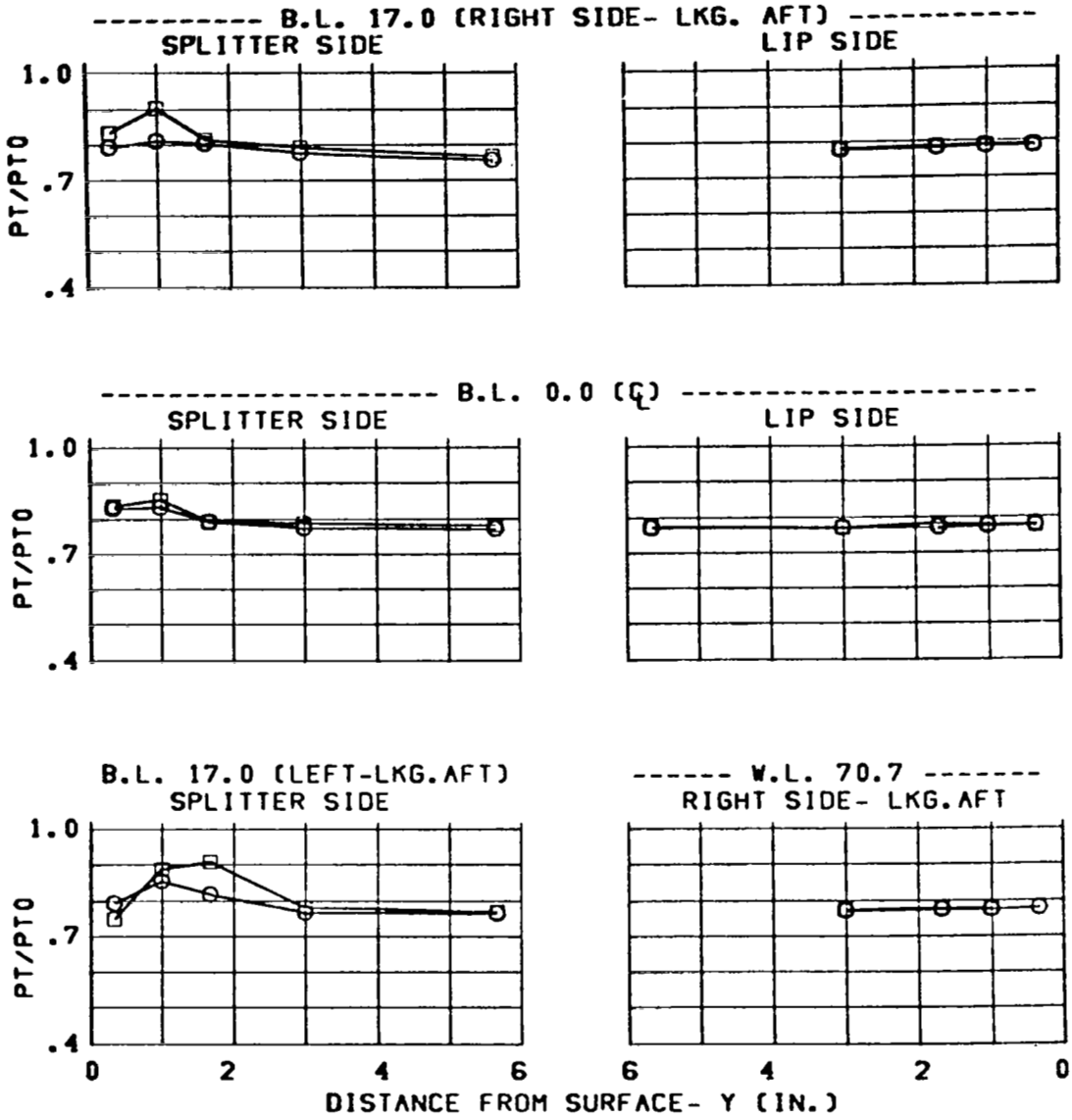

Figure 223 Effect of 13° Ramp (Configuration C15A) on Throat-Pressure Profiles

CONFIG.	DIV.	MACH	SYM.	THROAT RAKES	CONDITION
C13	3.65	1.57	○	IN	ALPHA= -5.
C15A			□		BETA = 0.

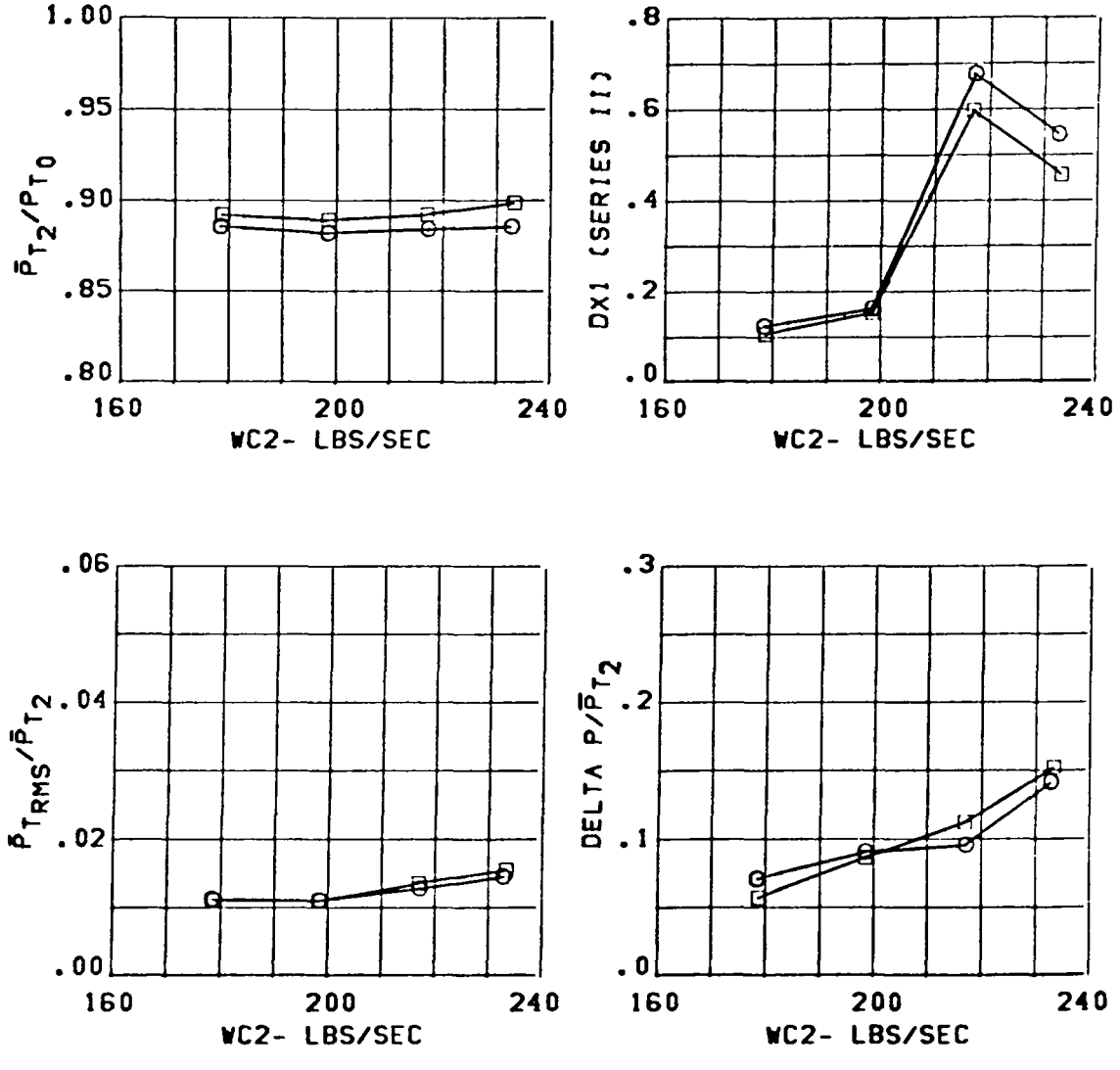

Figure 224 Effect of 13° Ramp (Configuration C15A) on Inlet Performance

CONFIG.	DIV.	MACH	SYM.	THROAT RAKES	CONDITION
C13	3.65	1.56	○	IN	ALPHA= 1.
C15A			□		BETA = 0.

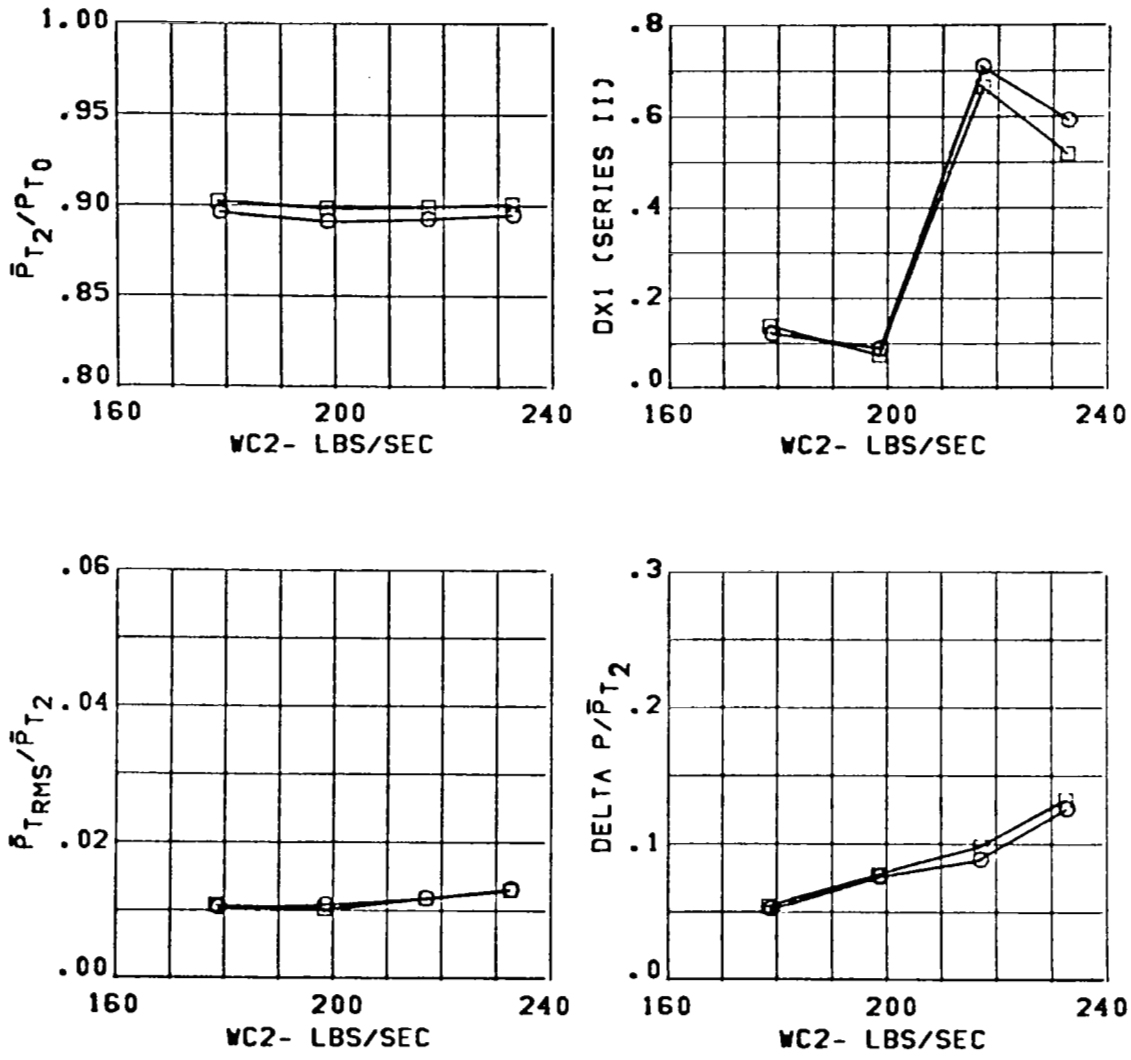

Figure 225 Effect of 13° Ramp (Configuration C15A) on Inlet Performance

CONFIG.	DIV.	MACH	SYM.	THROAT RAKES	CONDITION
C13	3.65	1.56	O	IN	ALPHA= 6.
C15A			□		BETA = 0.

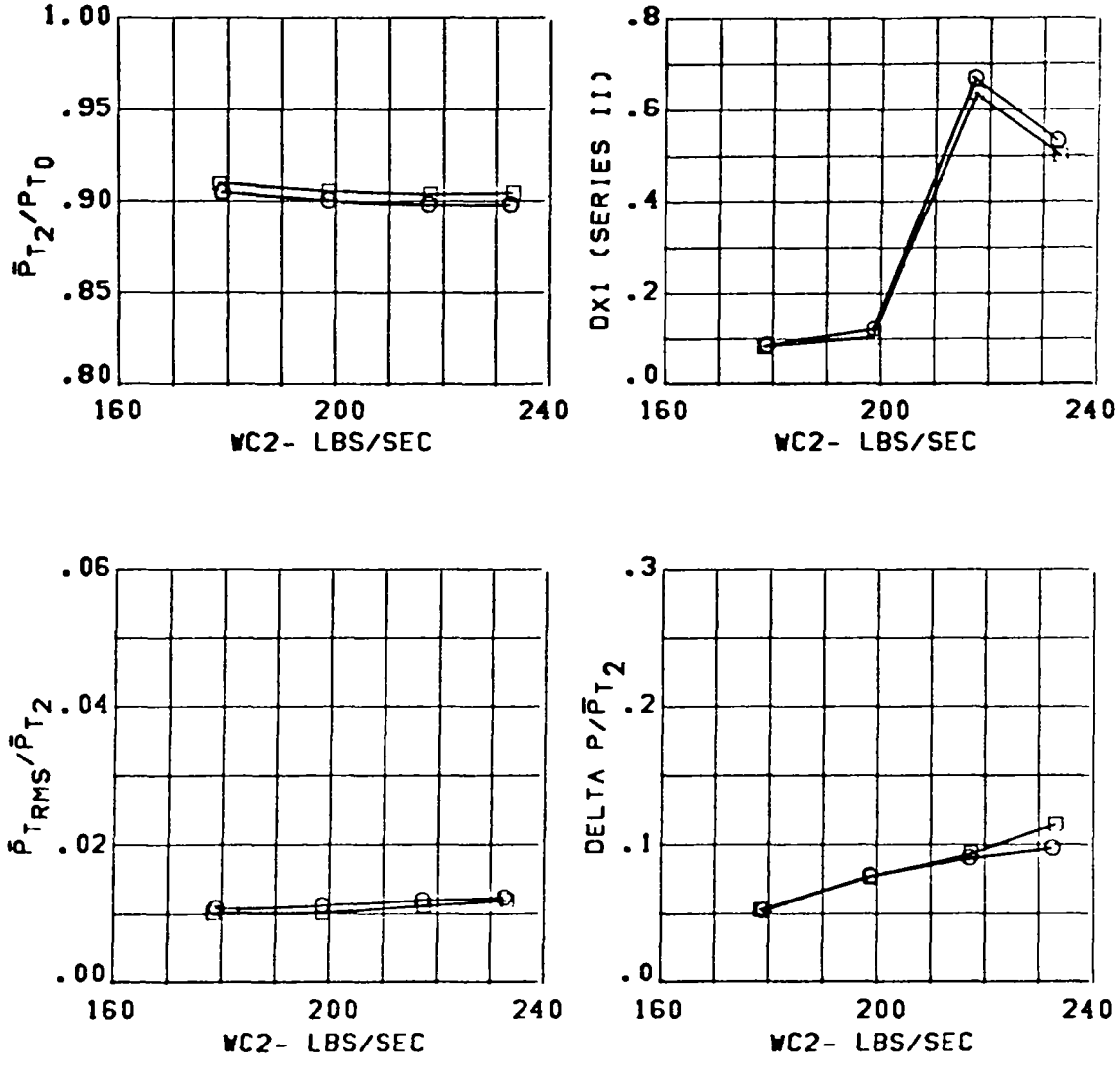

Figure 226 Effect of 13° Ramp (Configuration C15A) on Inlet Performance

CONFIG.	DIV.	MACH	SYM.	THROAT RAKES	CONDITION
C13	3.65	1.96	O	IN	ALPHA= -5.
C15A			□		BETA = 0.

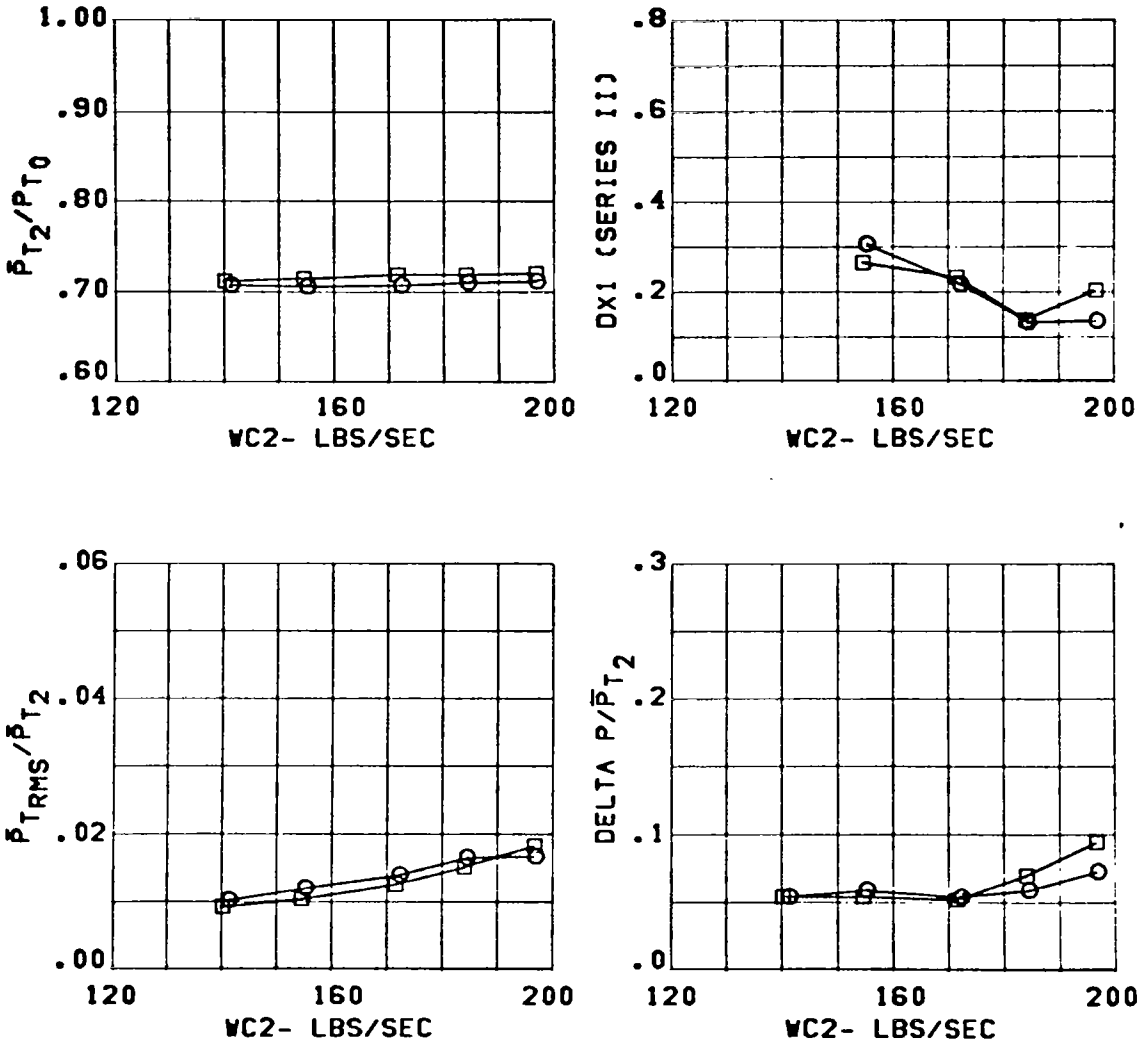

Figure 227 Effect of 13° Ramp (Configuration C15A) on Inlet Performance

CONFIG.	DIV.	MACH	SYM.	THROAT RAKES	CONDITION
C13	3.65	1.96	O	IN	ALPHA= 1.
C15A			□		BETA = 0.

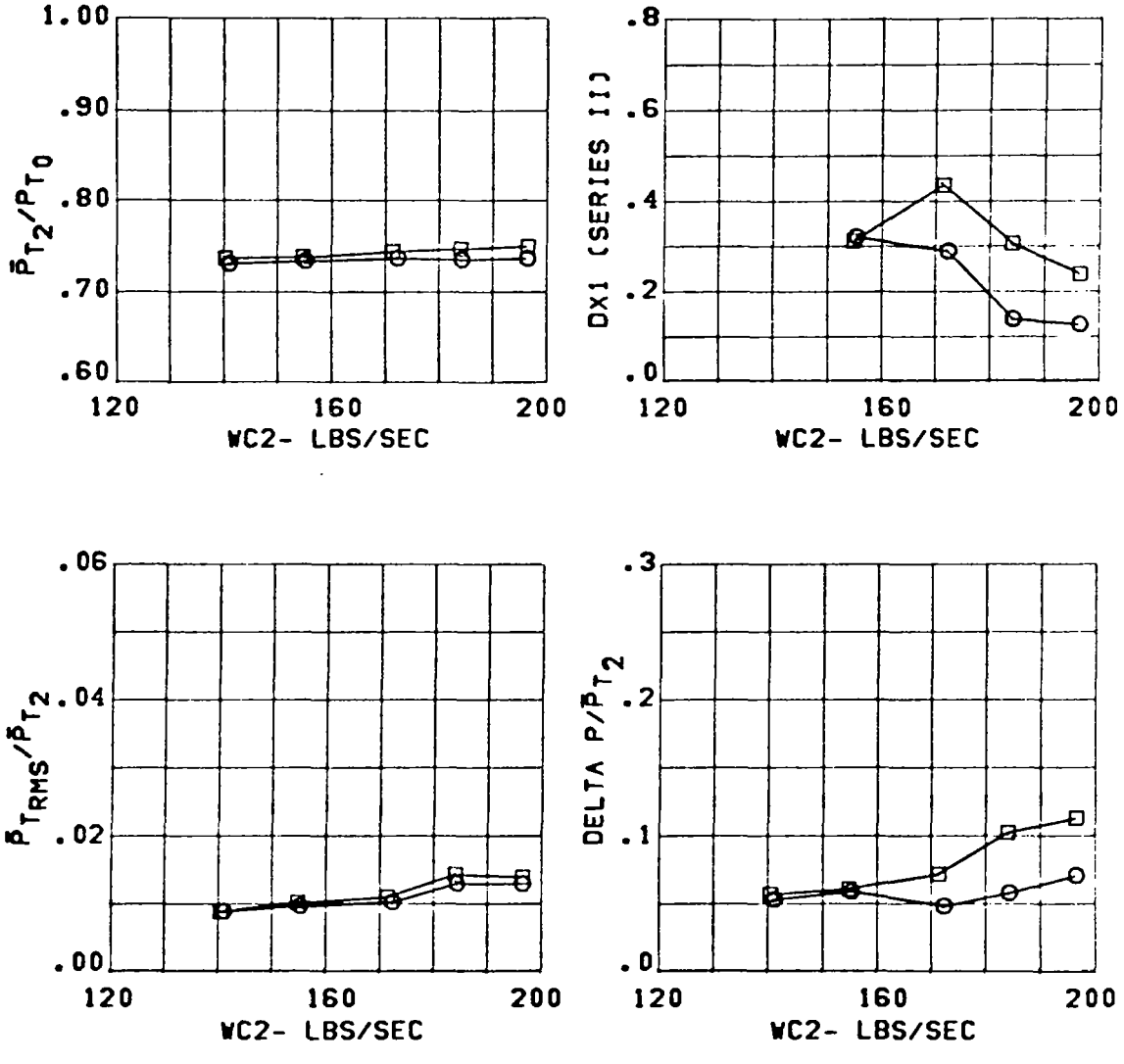

Figure 228 Effect of 13° Ramp (Configuration C15A) on Inlet Performance

CONFIG.	DIV.	MACH	SYM.	THROAT RAKES	CONDITION
C13	3.65	1.96	O	IN	ALPHA= 6.
C15A			□		BETA = 0.

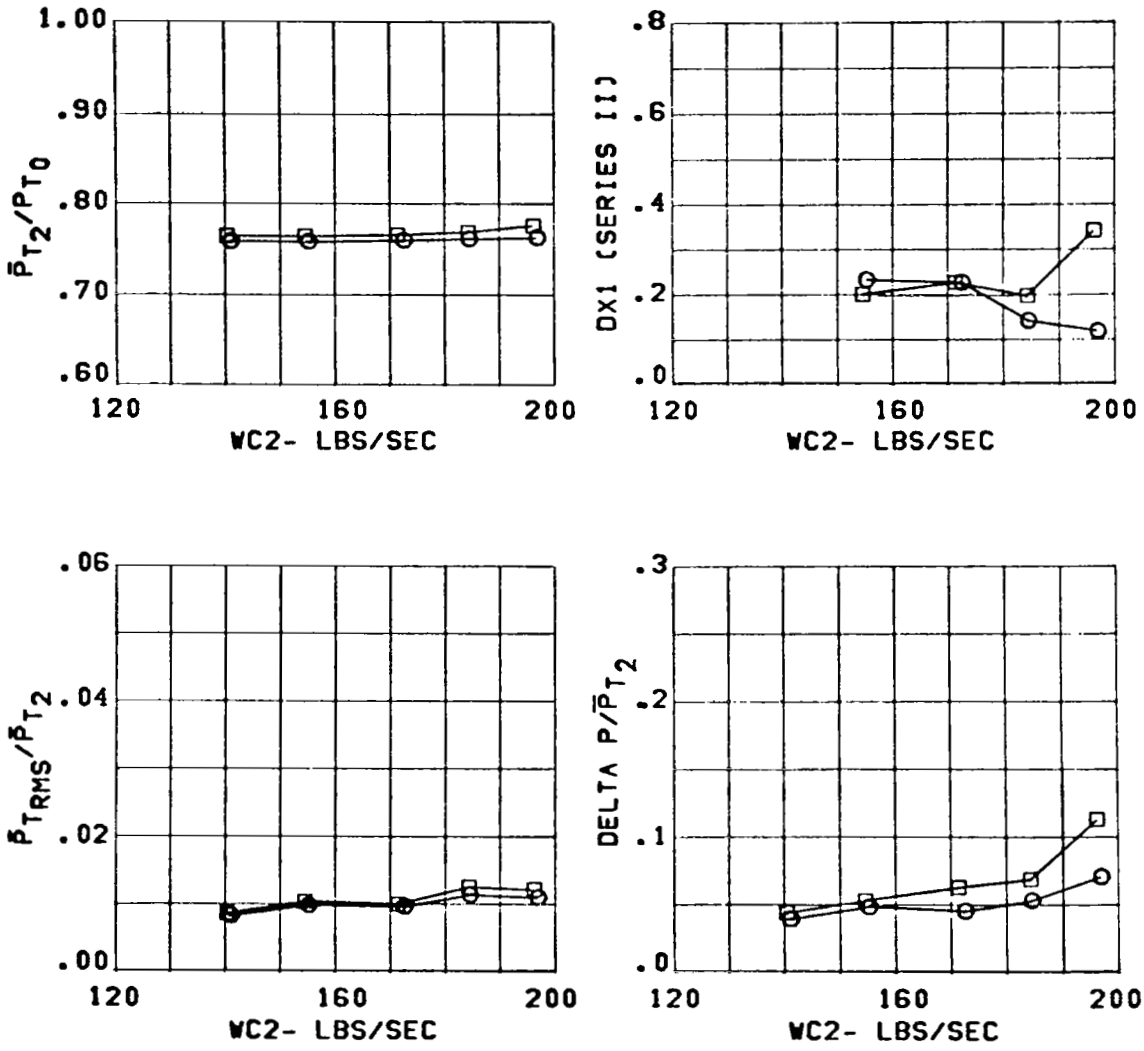

Figure 229 Effect of 13° Ramp (Configuration C15A) on Inlet Performance

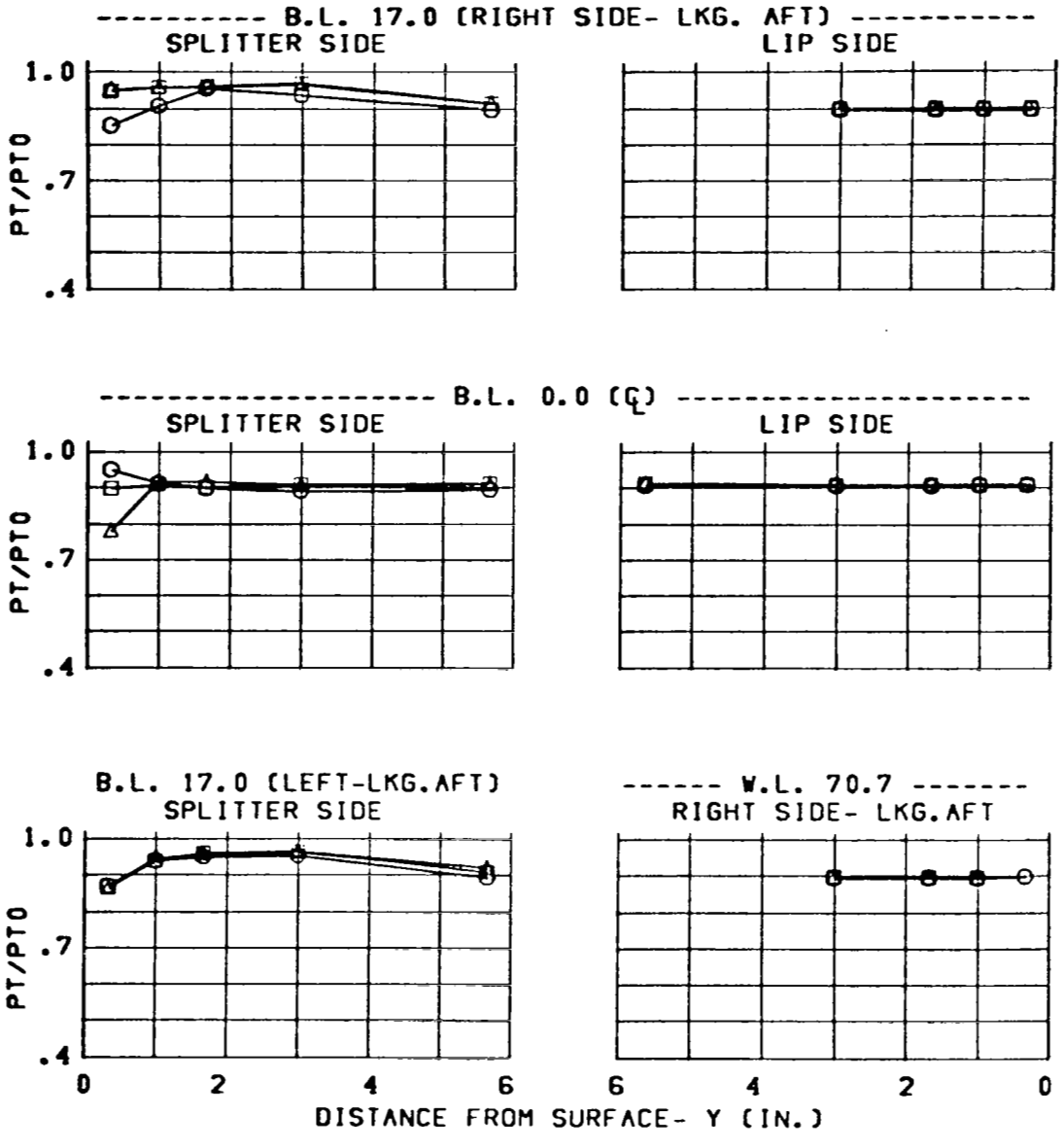

Figure 230 Effect of 13° Porous-Bleed Ramp (Configuration C15) on Throat-Pressure Profiles

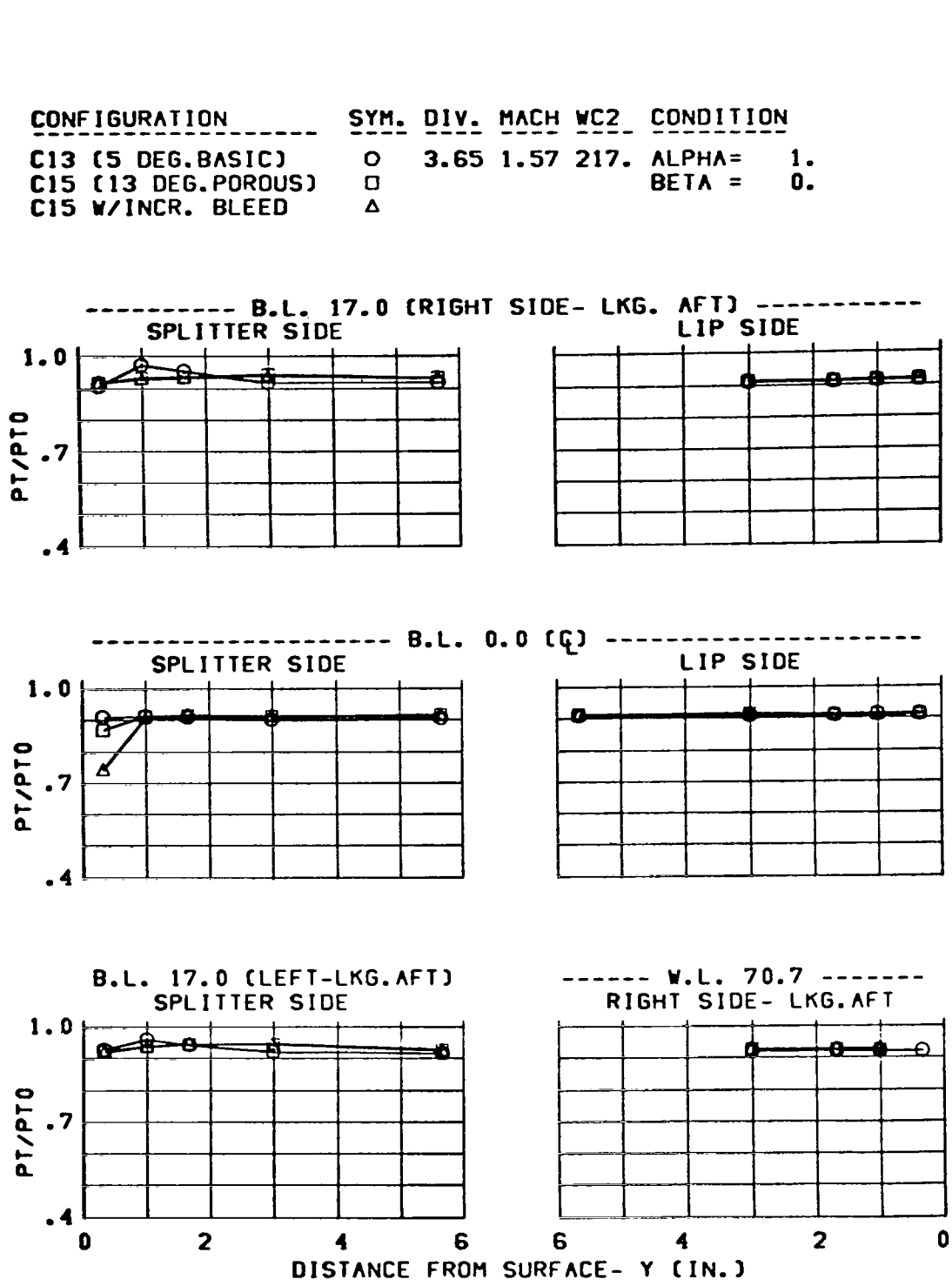

Figure 231 Effect of 13° Porous-Bleed Ramp (Configuration C15) on Throat-Pressure Profiles

CONFIGURATION	SYM.	DIV.	MACH	WC2	CONDITION	
C13 (5 DEG.BASIC)	O	3.65	1.57	217.	ALPHA=	6.
C15 (13 DEG.POROUS)	□				BETA =	0.
C15 W/INCR. BLEED	Δ					

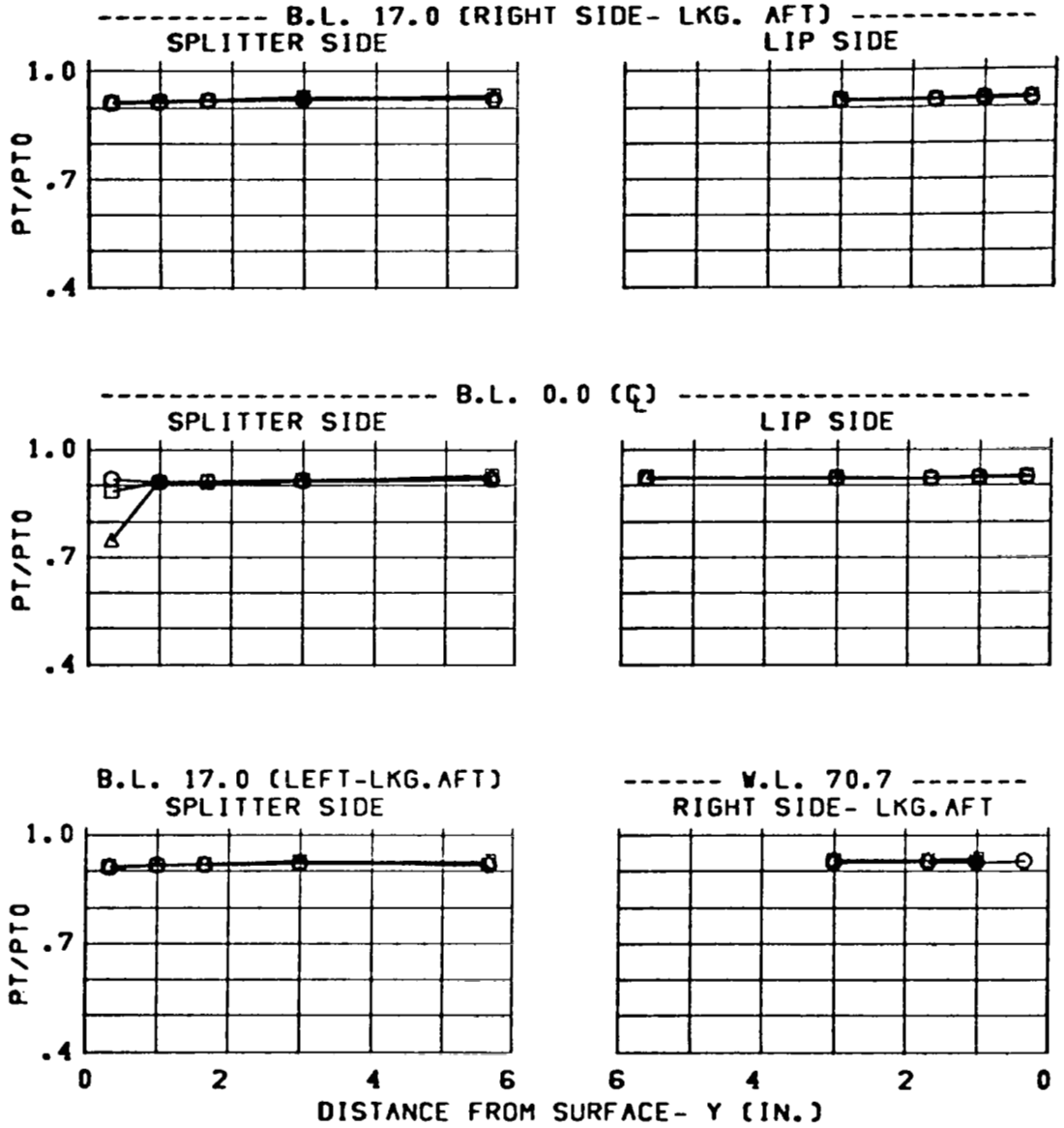

Figure 232 Effect of 13° Porous-Bleed Ramp (Configuration C15) on Throat-Pressure Profiles

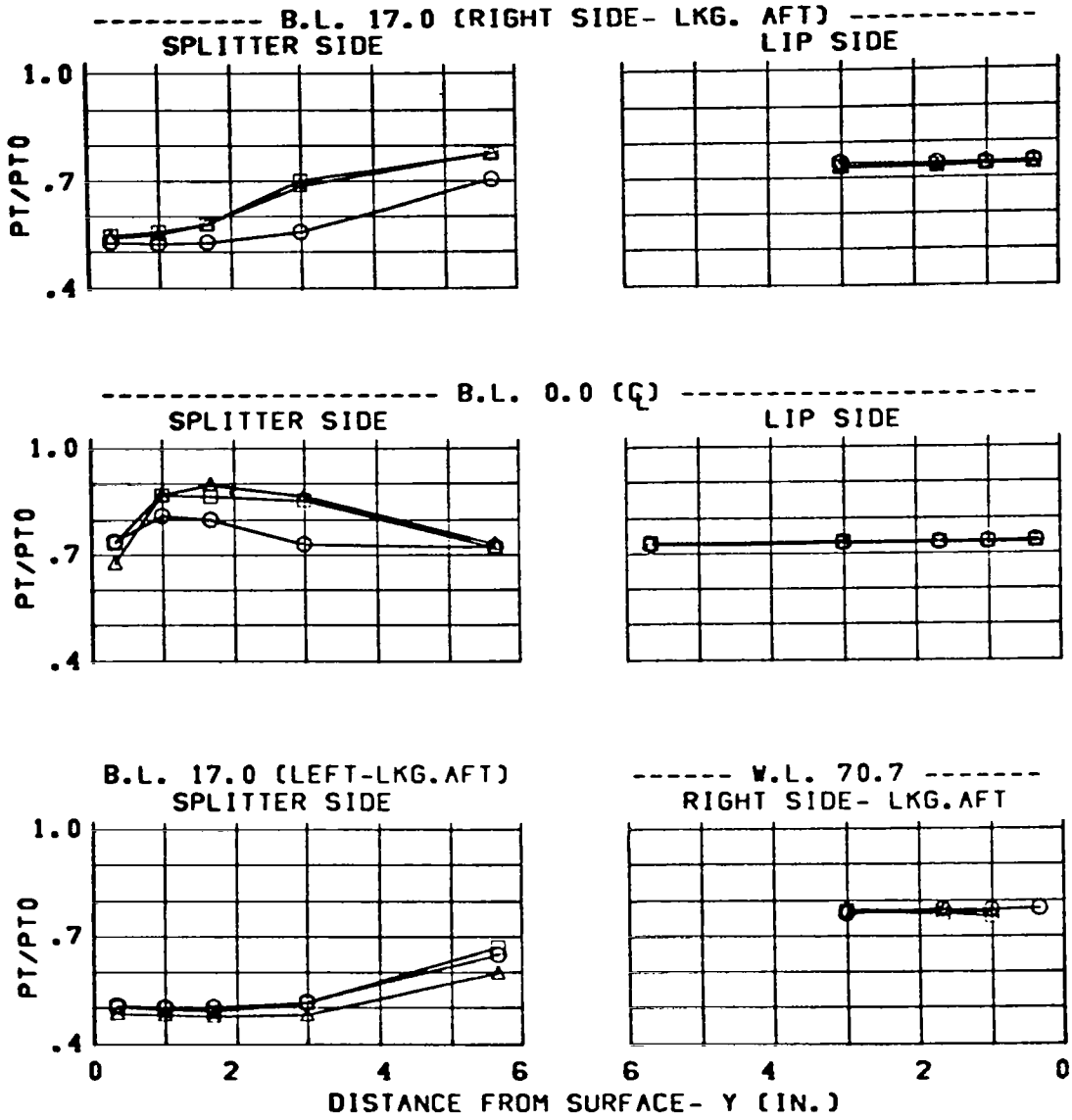

Figure 233 Effect of 13° Porous-Bleed Ramp (Configuration C15) on Throat-Pressure Profiles

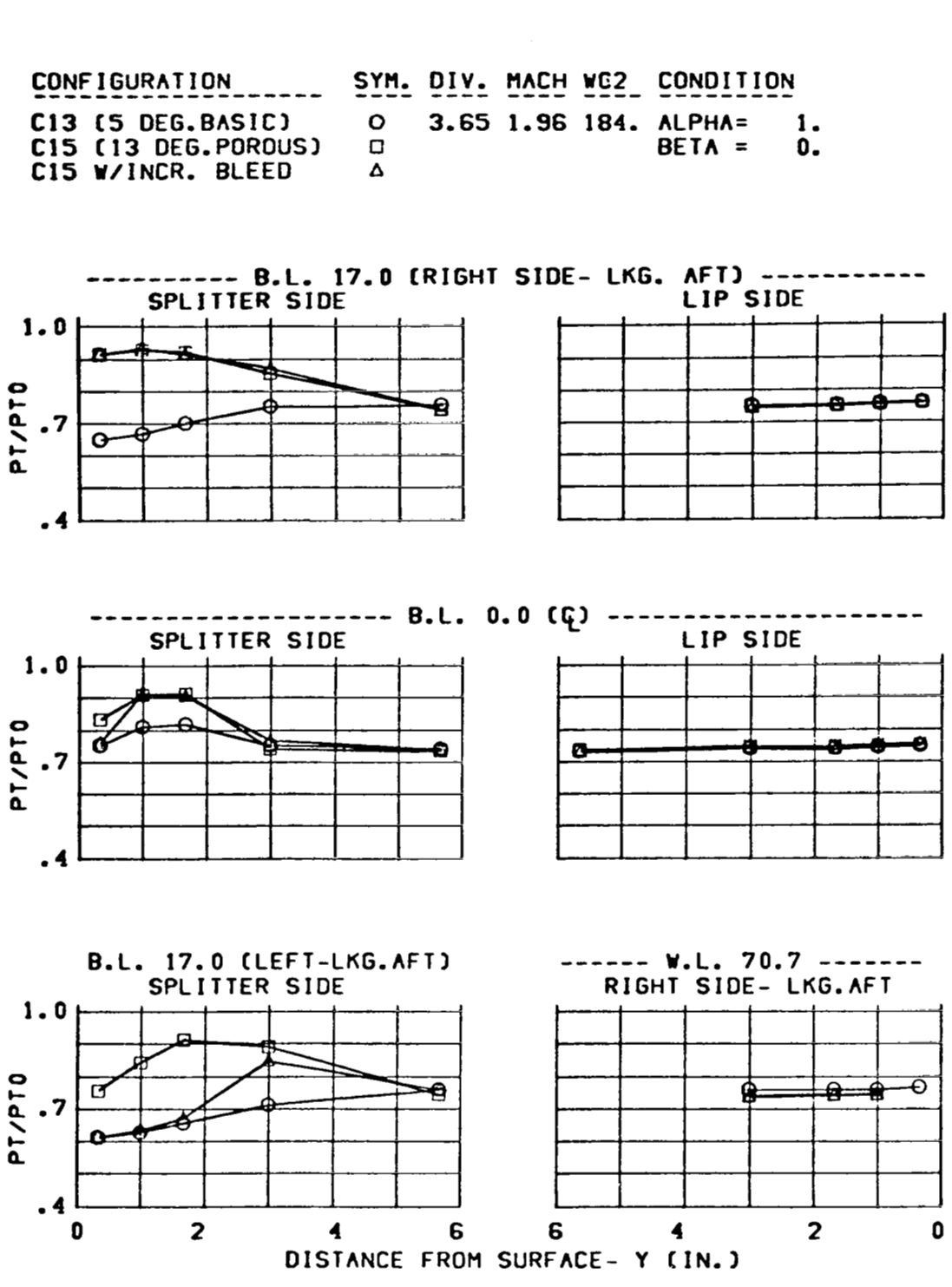

Figure 234 Effect of 13° Porous-Bleed Ramp (Configuration C15) on Throat-Pressure Profiles

CONFIGURATION	SYM.	DIV.	MACH	WC2	CONDITION	
C13 (5 DEG.BASIC)	O	3.65	1.96	184.	ALPHA=	6.
C15 (13 DEG.POROUS)	□				BETA =	0.
C15 W/INCR. BLEED	△					

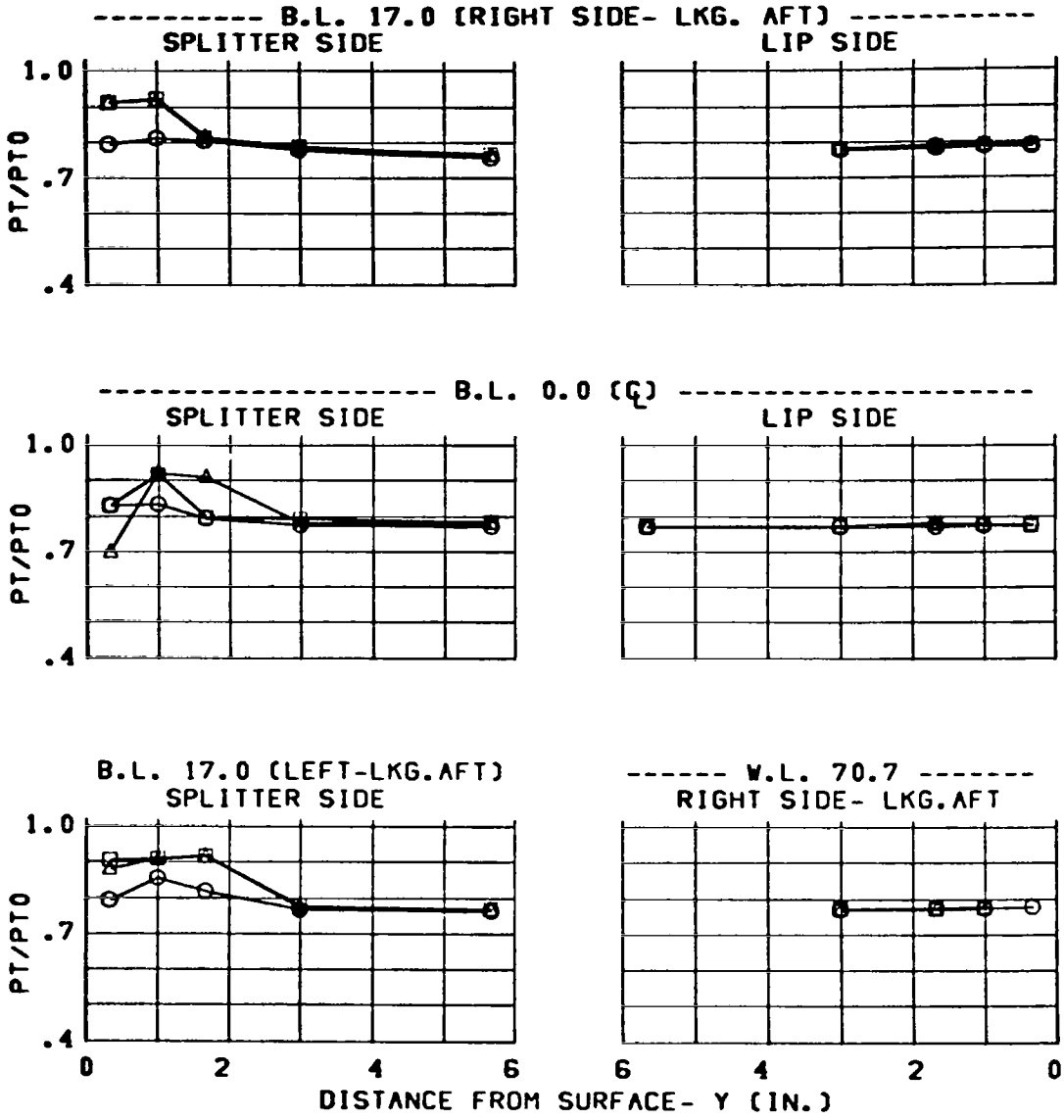

Figure 235 Effect of 13° Porous-Bleed Ramp (Configuration C15) on Throat-Pressure Profiles

CONFIG.	DIV.	MACH	SYM.	THROAT RAKES	CONDITION
C13	3.65	1.57	○	IN	ALPHA= -5.
C15			□		BETA = -0.
C15 W/INCR.BLD.			△		

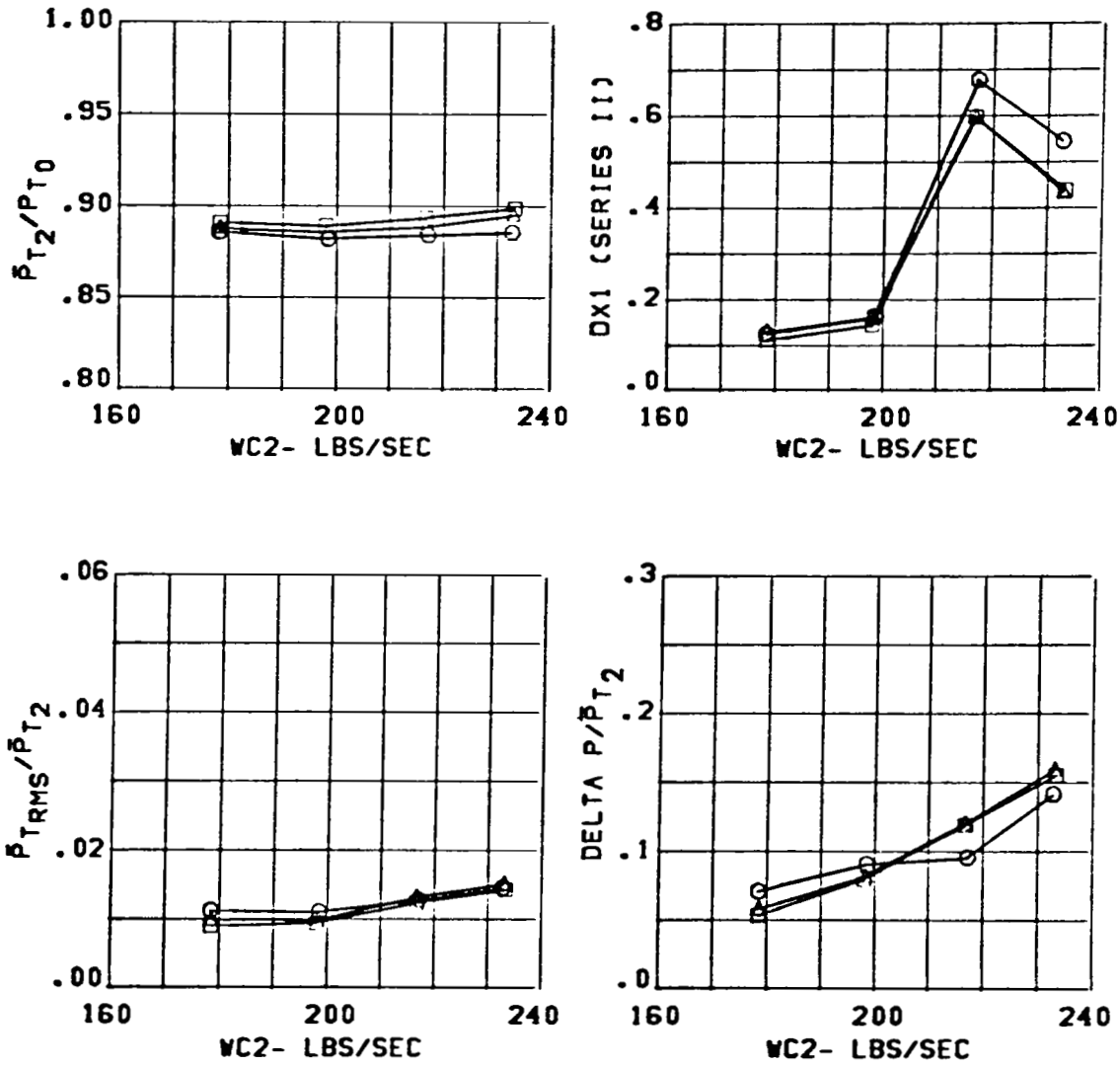

Figure 236 Effect of 13° Porous-Bleed Ramp (Configuration C15) on Throat-Pressure Profiles

CONFIG.	DIV.	MACH	SYM.	THROAT RAKES	CONDITION	
C13	3.65	1.56	O	IN	ALPHA=	1.
C15			□		BETA =	0.
C15 W/INCR.BLD.			Δ			

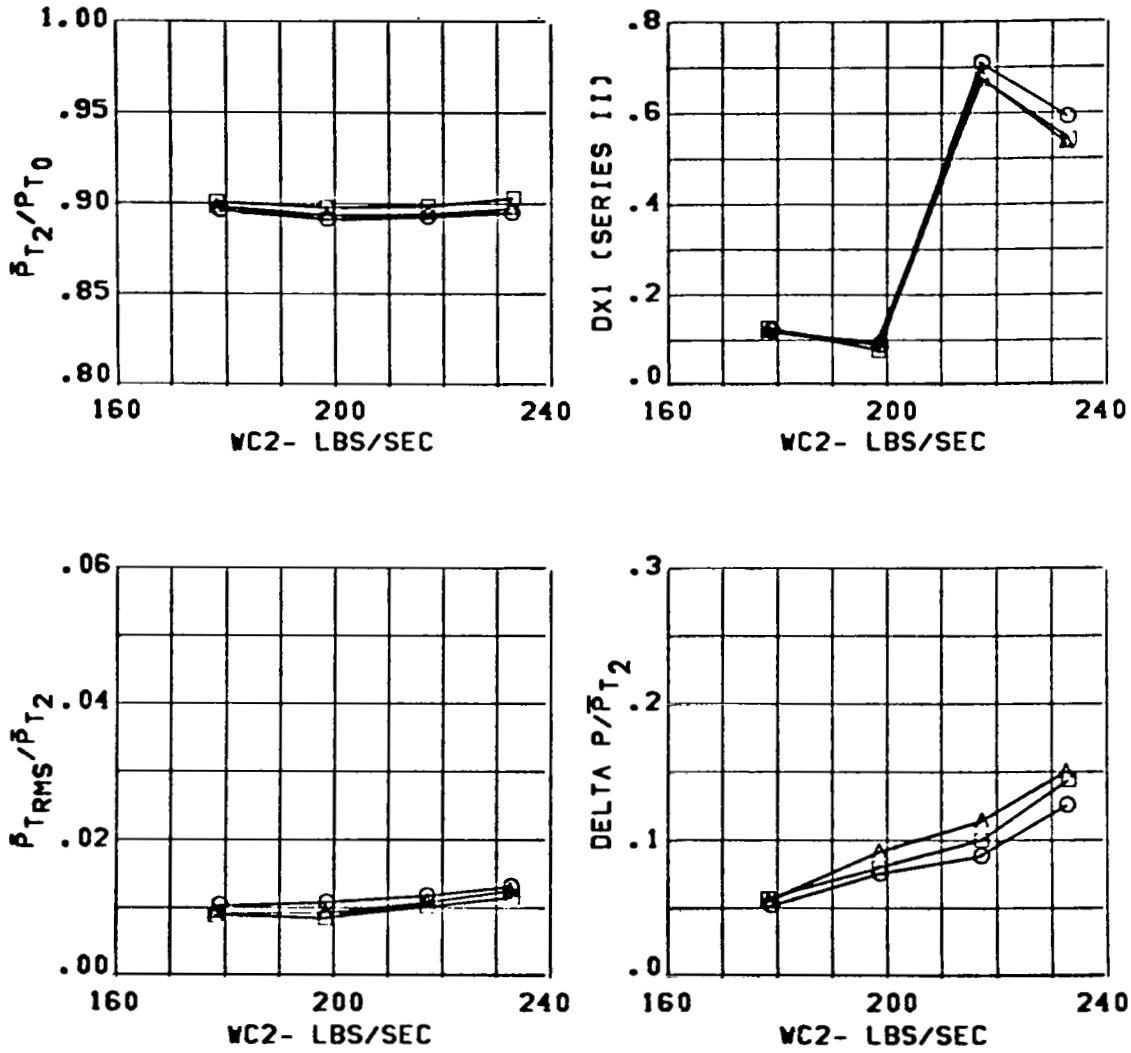

Figure 237 Effect of 13° Porous-Bleed Ramp (Configuration C15) on Throat-Pressure Profiles

CONFIG.	DIV.	MACH	SYM.	THROAT RAKES	CONDITION
C13	3.65	1.56	O	IN	ALPHA= 6.
C15			□		BETA = 0.
C15 W/INCR.BLD.			Δ		

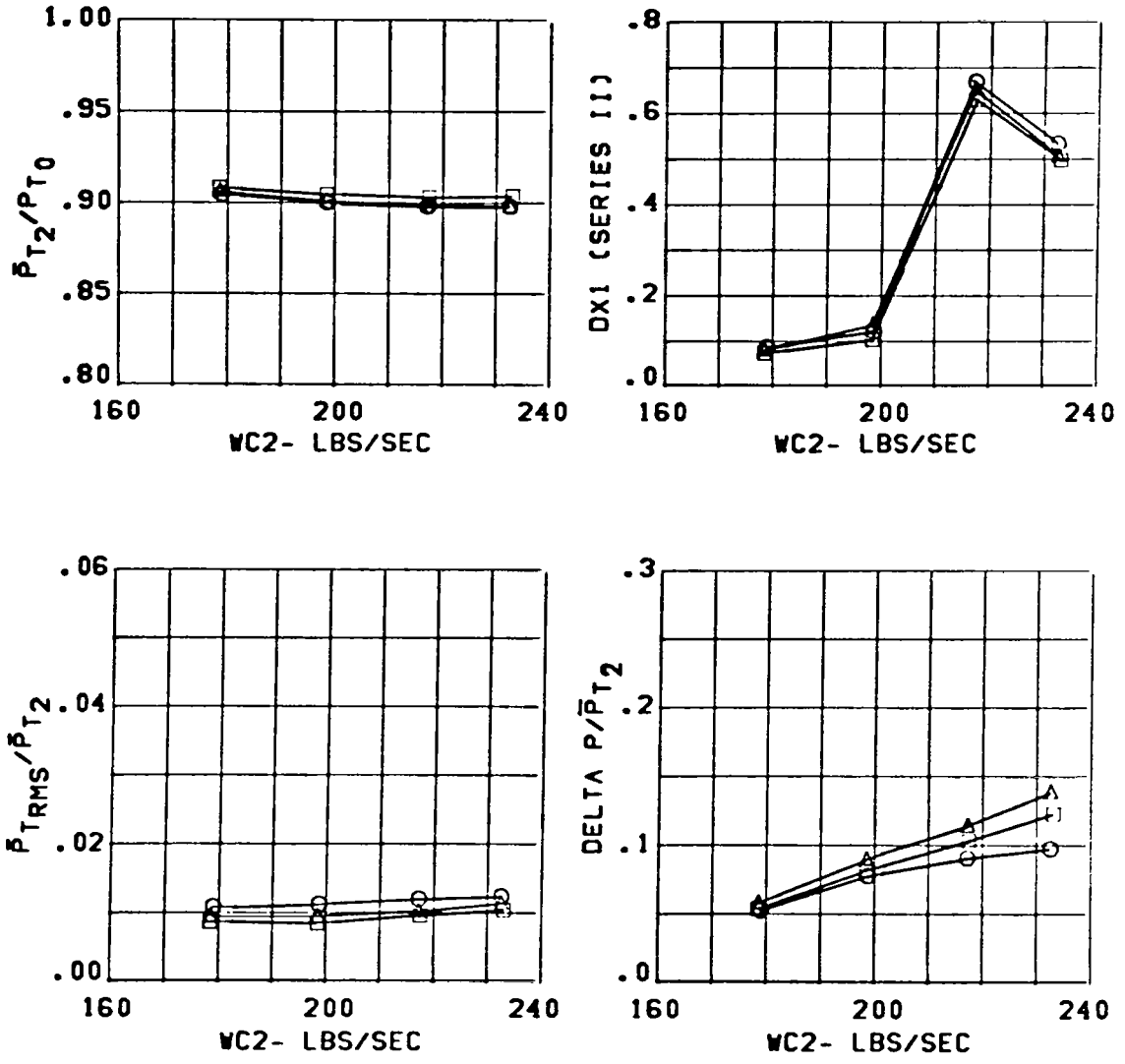

Figure 238 Effect of 13° Porous-Bleed Ramp (Configuration C15) on Throat-Pressure Profiles

CONFIG.	DIV.	MACH	SYM.	THROAT RAKES	CONDITION
C13	3.65	1.96	○	IN	ALPHA= -5.
C15			□		BETA = 0.
C15 W/INCR.BLD.			◇		

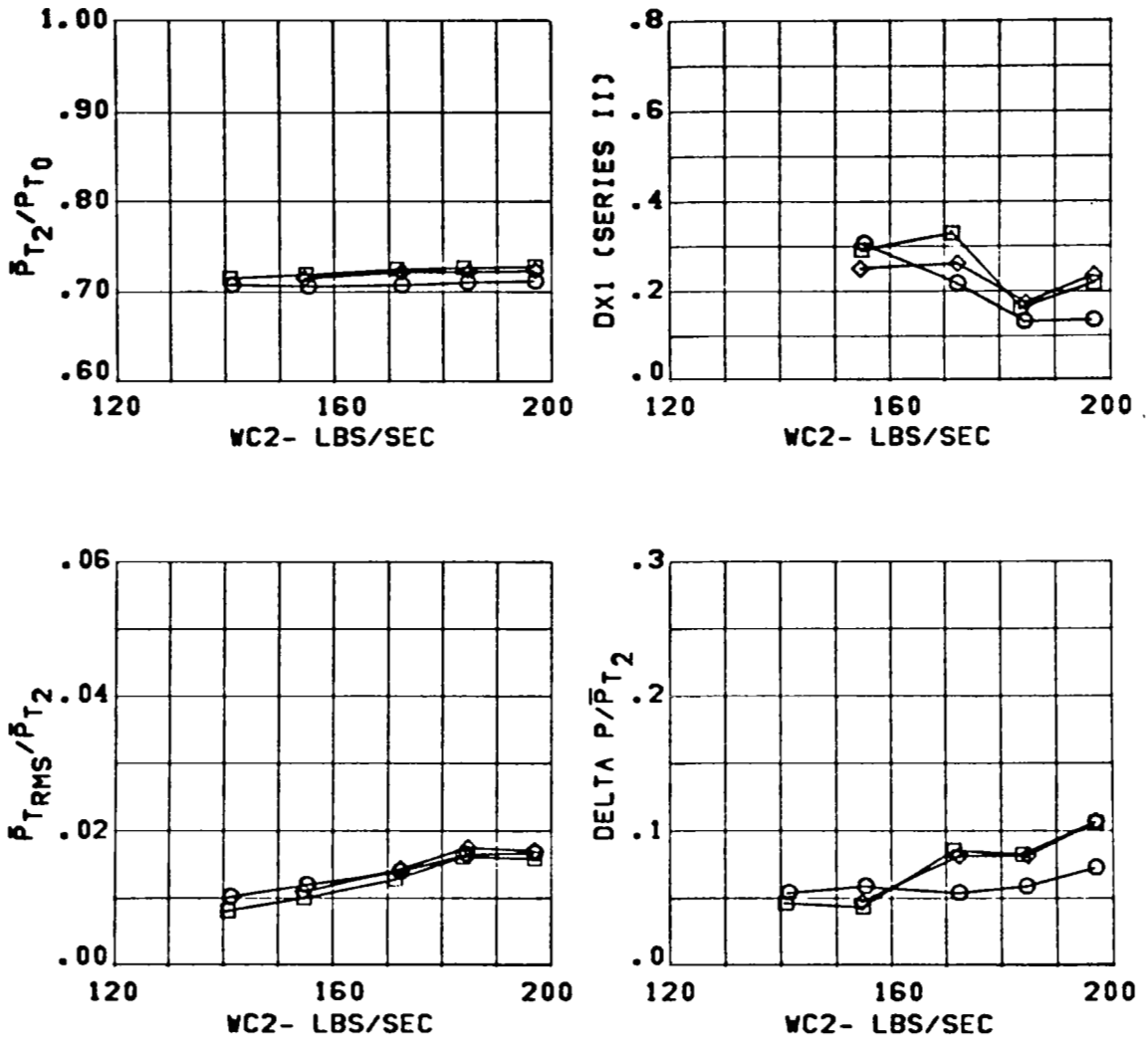

Figure 239 Effect of 13° Porous-Bleed Ramp (Configuration C15) on Throat-Pressure Profiles

CONFIG.	DIV.	MACH	SYM.	THROAT RAKES	CONDITION
C13	3.65	1.96	○	IN	ALPHA= 1.
C15			□		BETA = 0.
C15 W/INCR.BLD.			◇		

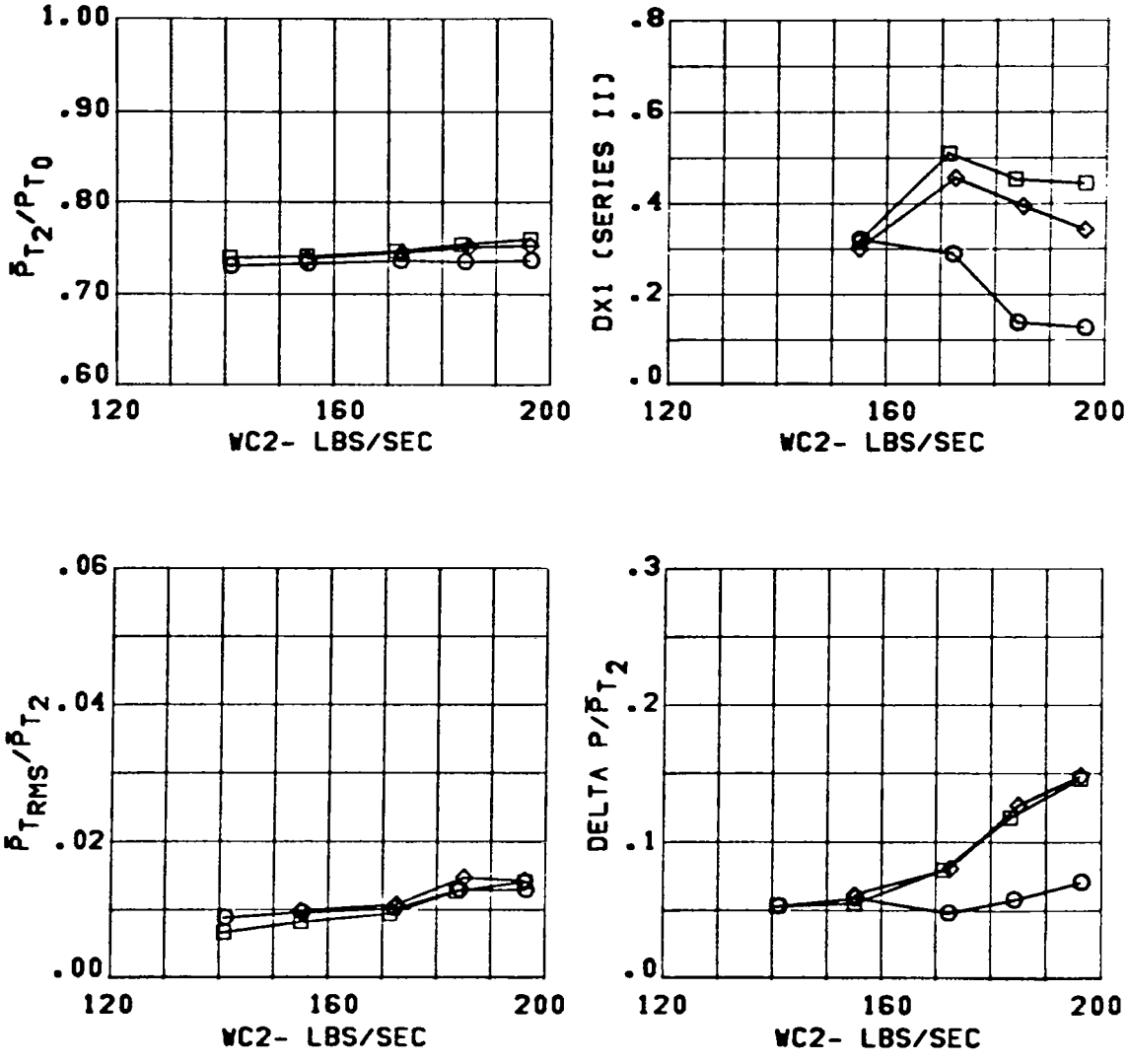

Figure 240 Effect of 13° Porous-Bleed Ramp (Configuration C15) on Throat-Pressure Profiles

CONFIG.	DIV.	MACH	SYM.	THROAT RAKES	CONDITION
C13	3.65	1.96	○	IN	ALPHA= 6.
C15			□		BETA = 0.
C15 W/INCR.BLD.			◇		

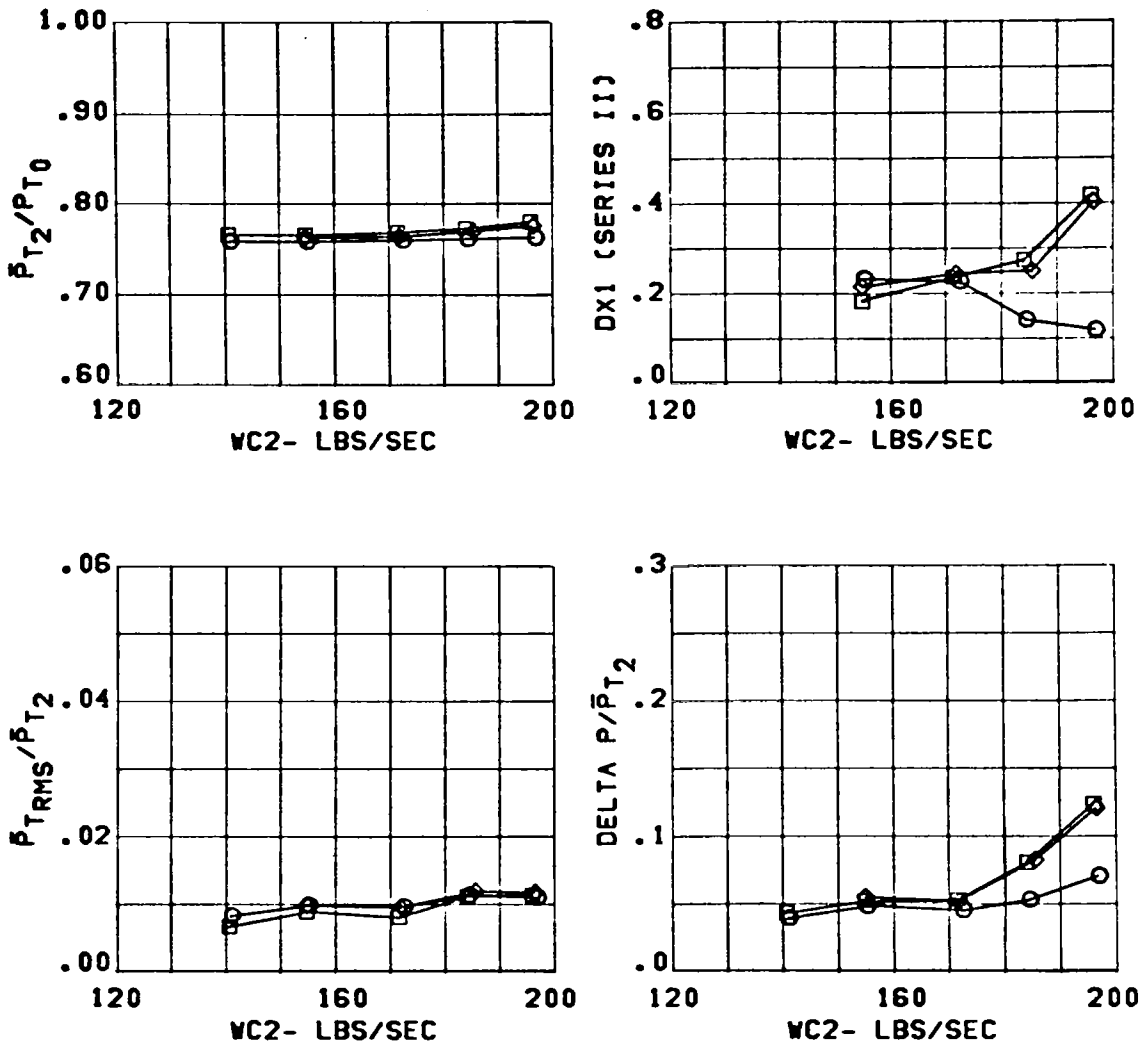

Figure 241 Effect of 13° Porous-Bleed Ramp (Configuration C15) on Throat-Pressure Profiles

CONFIGURATION	SYM.	DIV.	MACH	WC2	CONDITION
C13 (5 DEG.BASIC)	O	3.65	1.57	217.	ALPHA= -5.
C14 (5 DEG.TRIMMED)	□				BETA = 0.

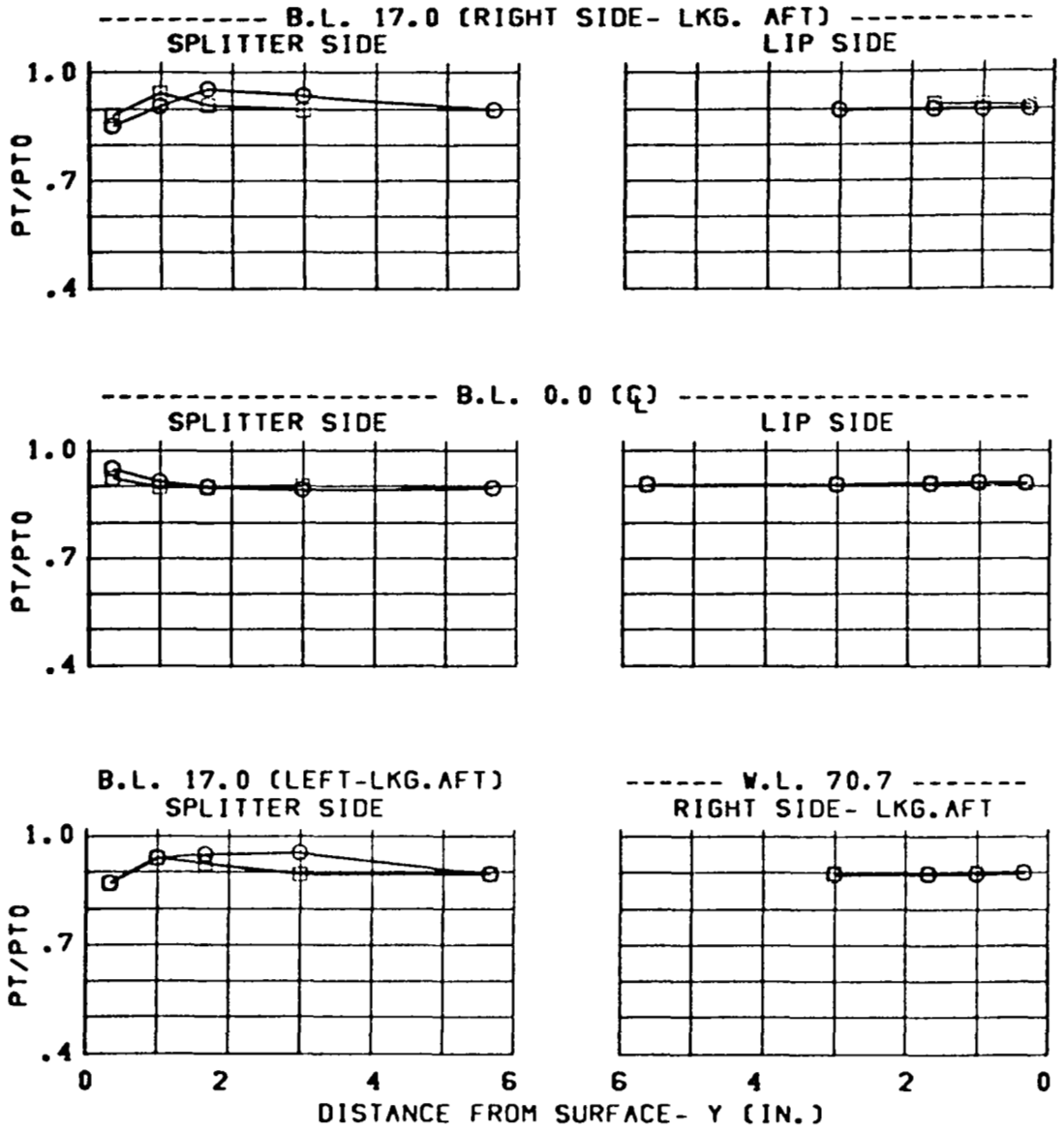

Figure 242 Effect of Trimmed Splitter Plate on Throat-Pressure Profiles

CONFIGURATION	SYM.	DIV.	MACH	WC2	CONDITION	
C13 (5 DEG.BASIC)	○	3.65	1.57	217.	ALPHA=	1.
C14 (5 DEG.TRIMMED)	□				BETA =	0.

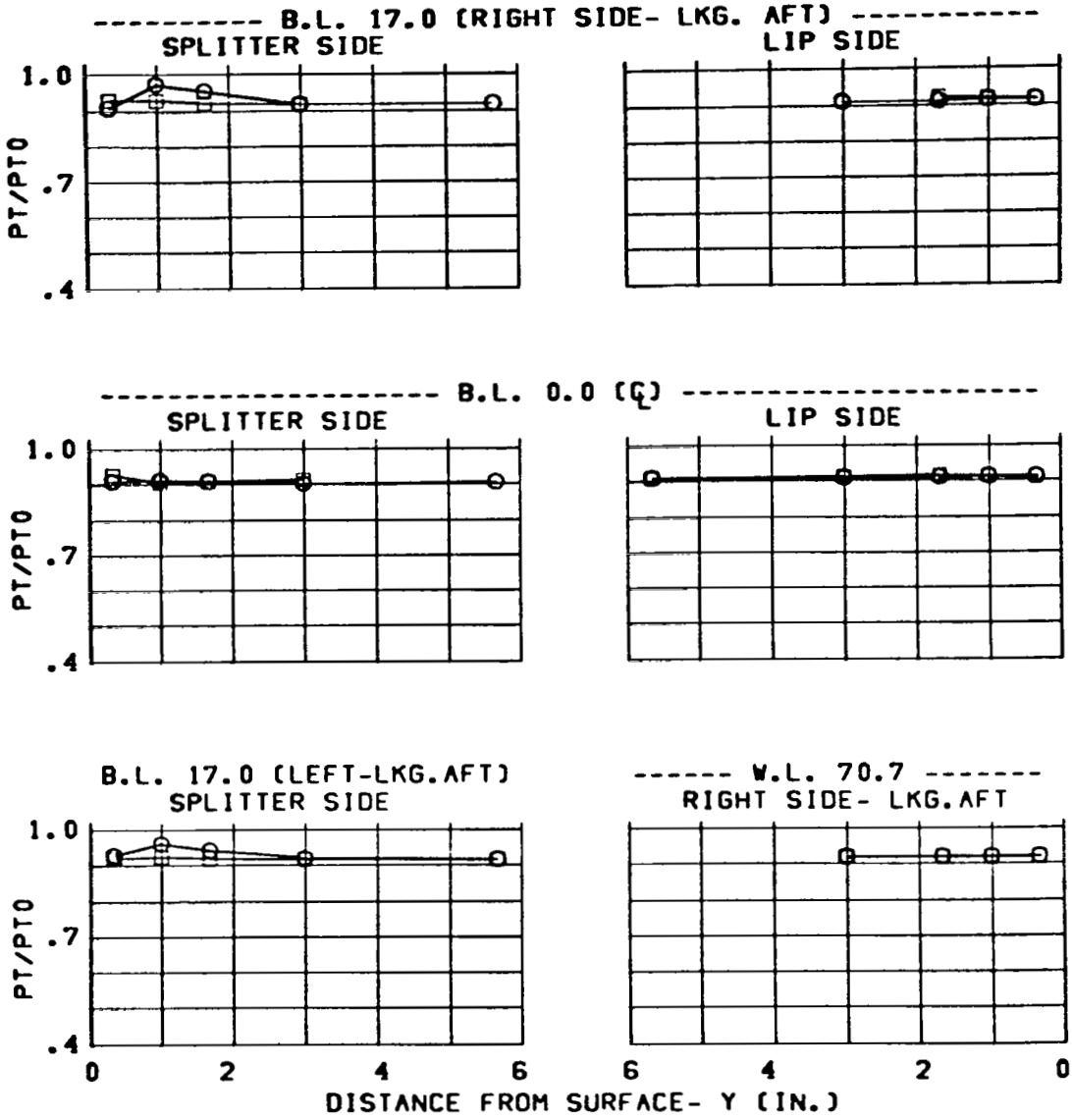

Figure 243 Effect of Trimmed Splitter Plate on Throat-Pressure Profiles

CONFIGURATION	SYM.	DIV.	MACH	WC2	CONDITION	
C13 (5 DEG.BASIC)	○	3.65	1.57	217.	ALPHA=	6.
C14 (5 DEG.TRIMMED)	□				BETA =	0.

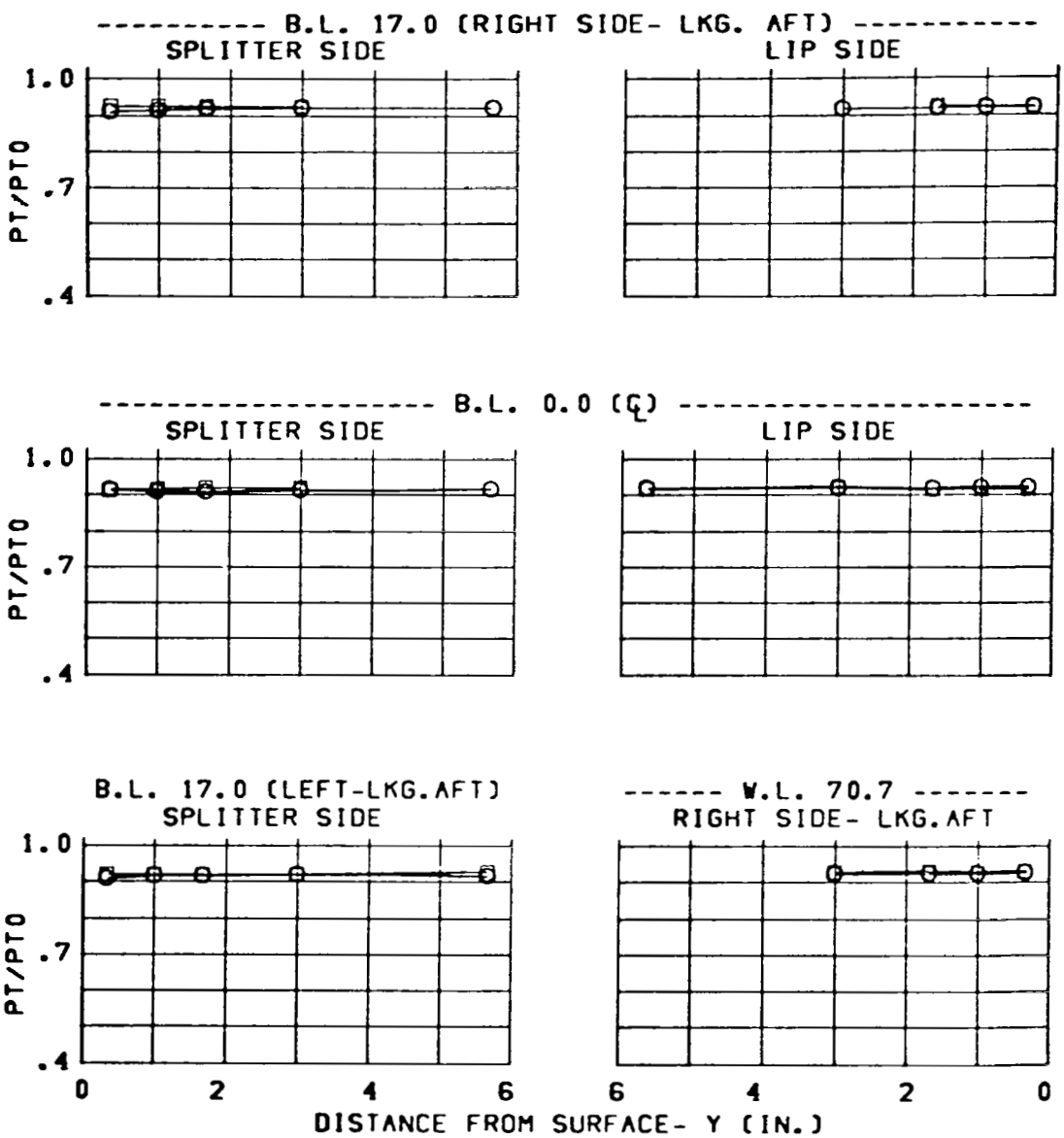

Figure 244 Effect of Trimmed Splitter Plate on Throat-Pressure Profiles

CONFIGURATION	SYM.	DIV.	MACH	WC2	CONDITION
C13 (5 DEG.BASIC)	○	3.65	1.96	184.	ALPHA= -5.
C14 (5 DEG.TRIMMED)	□				BETA = 0.

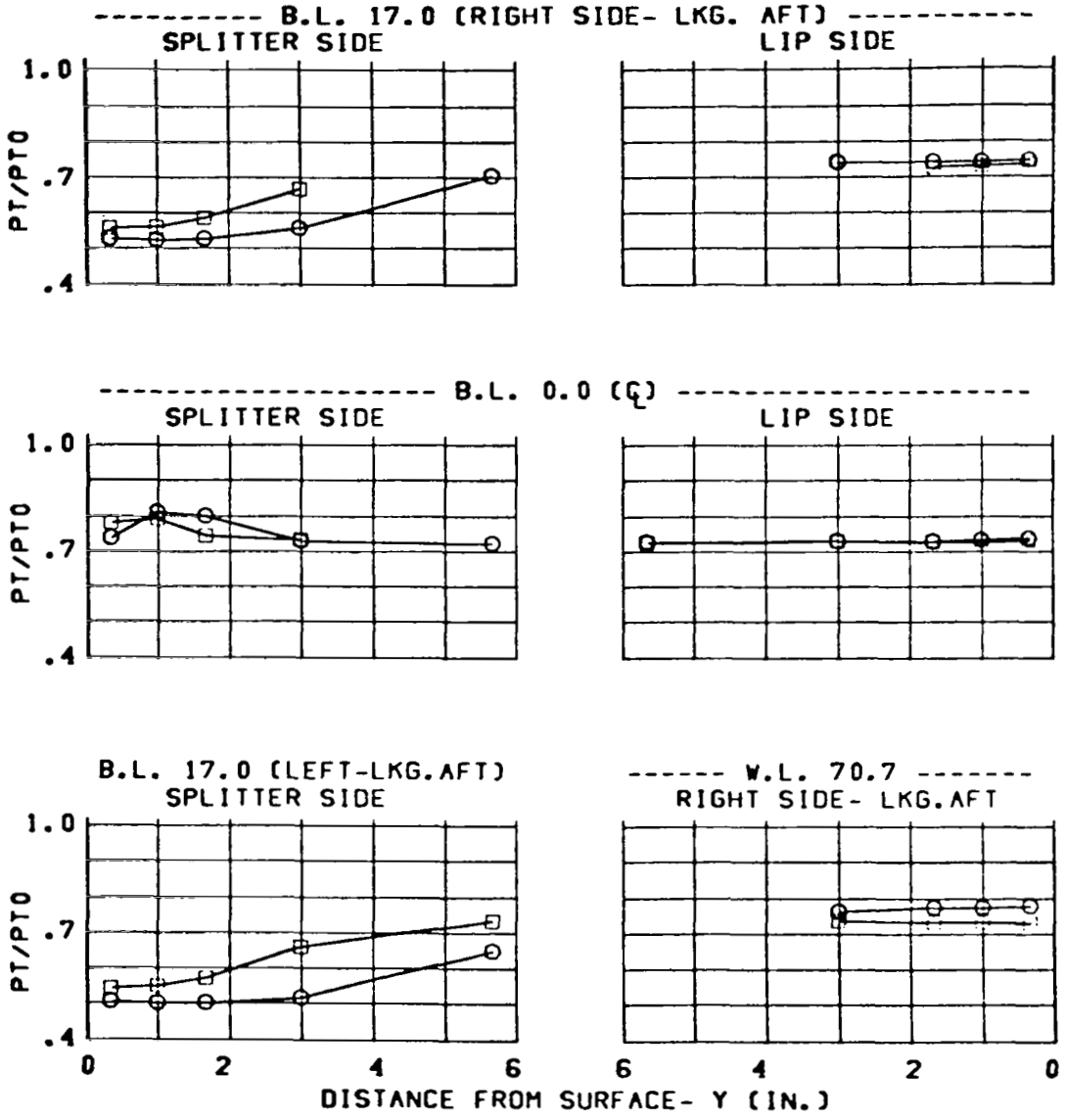

Figure 245 Effect of Trimmed Splitter Plate on Throat-Pressure Profiles

CONFIGURATION	SYM.	DIV.	MACH	WC2	CONDITION	
C13 (5 DEG.BASIC)	O	3.65	1.96	184.	ALPHA=	1.
C14 (5 DEG.TRIMMED)	□				BETA =	0.

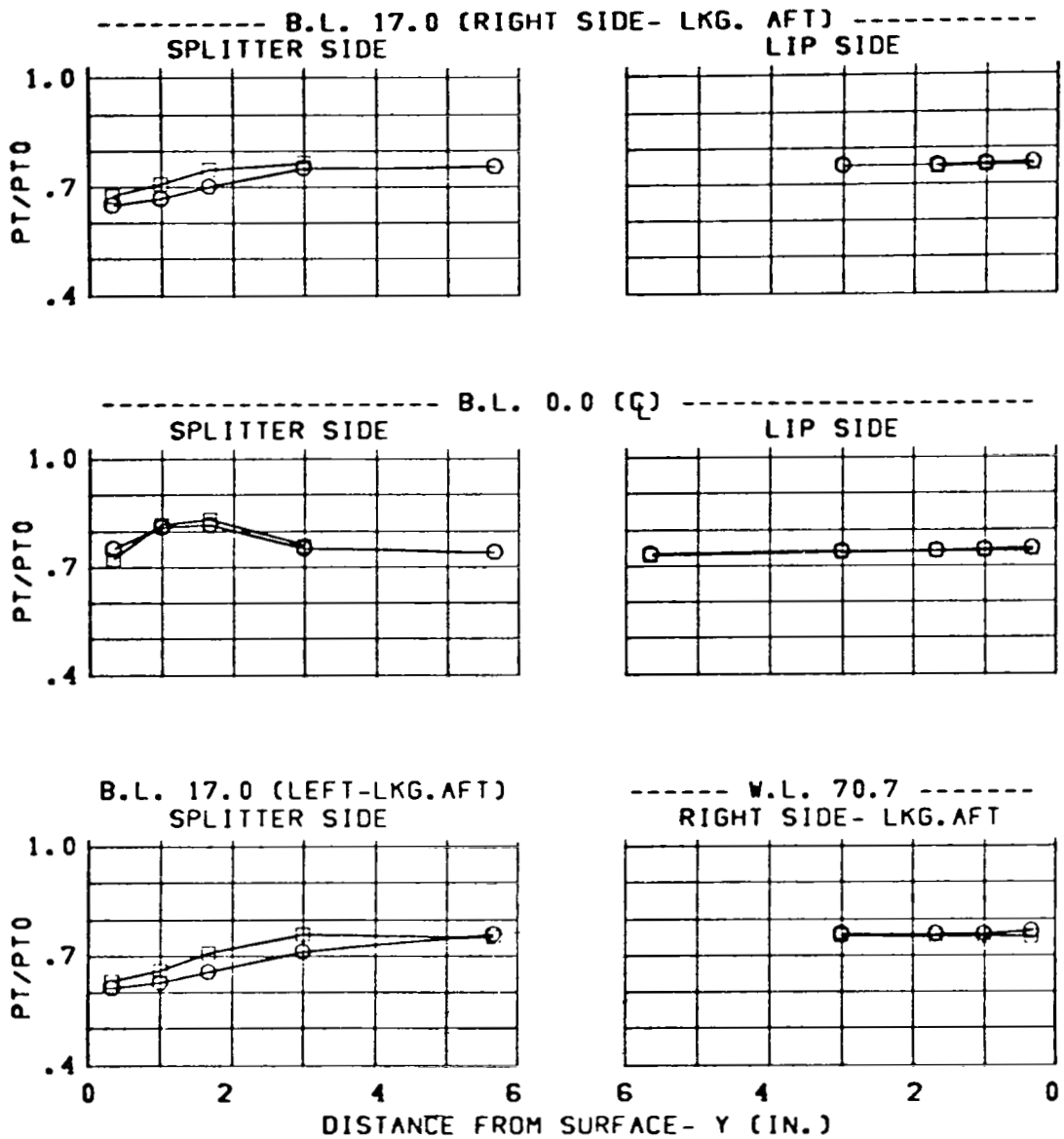

Figure 246 Effect of Trimmed Splitter Plate on Throat-Pressure Profiles

CONFIGURATION	SYM.	DIV.	MACH	WC2	CONDITION	
C13 (5 DEG.BASIC)	○	3.65	1.96	184.	ALPHA=	6.
C14 (5 DEG.TRIMMED)	□				BETA =	0.

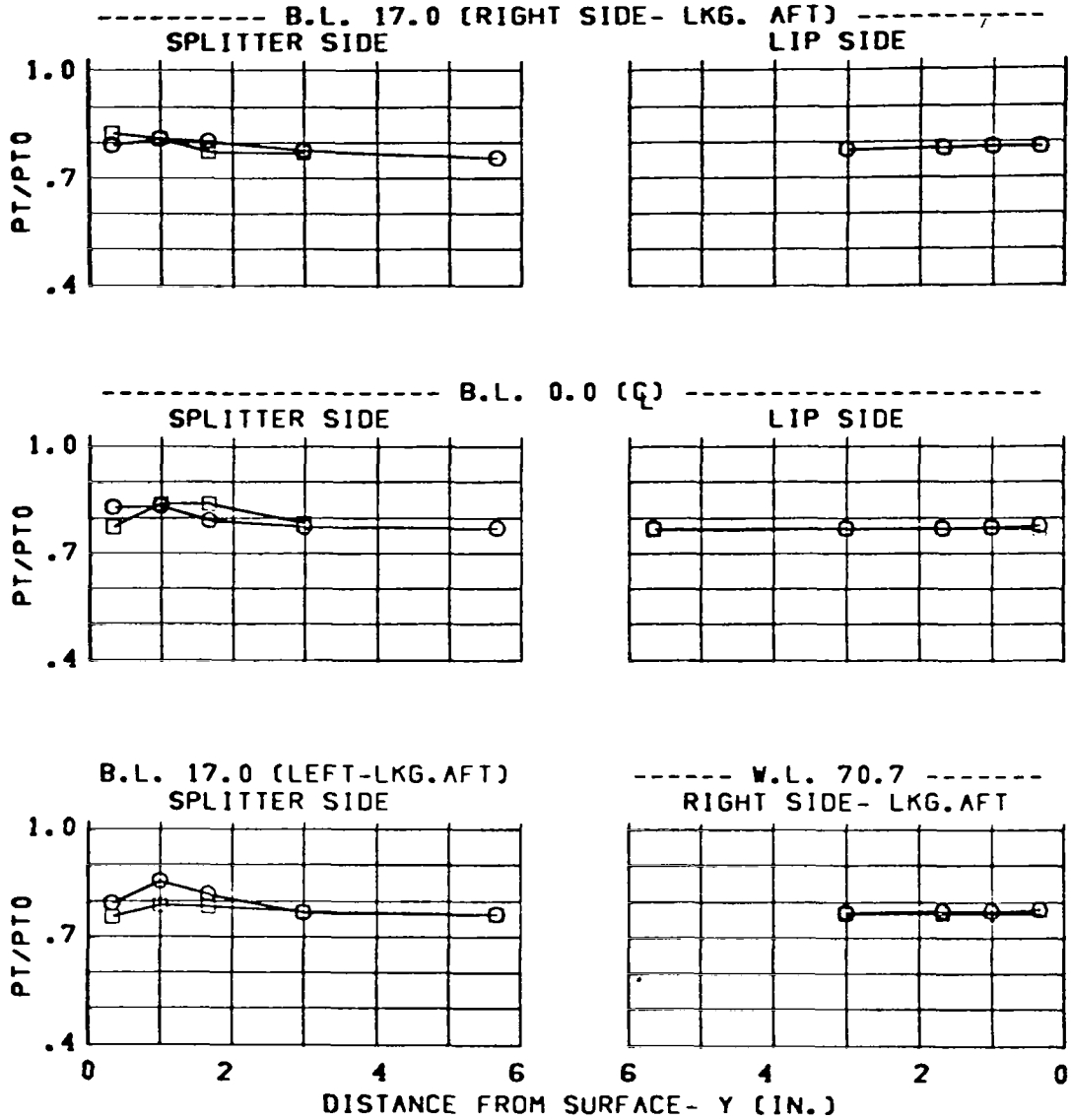

Figure 247 Effect of Trimmed Splitter Plate on Throat-Pressure Profiles

CONFIG.	DIV.	MACH	SYM.	THROAT RAKES	CONDITION
C13	3.65	1.57	O	IN	ALPHA= -5.
C14			□		BETA = 0.

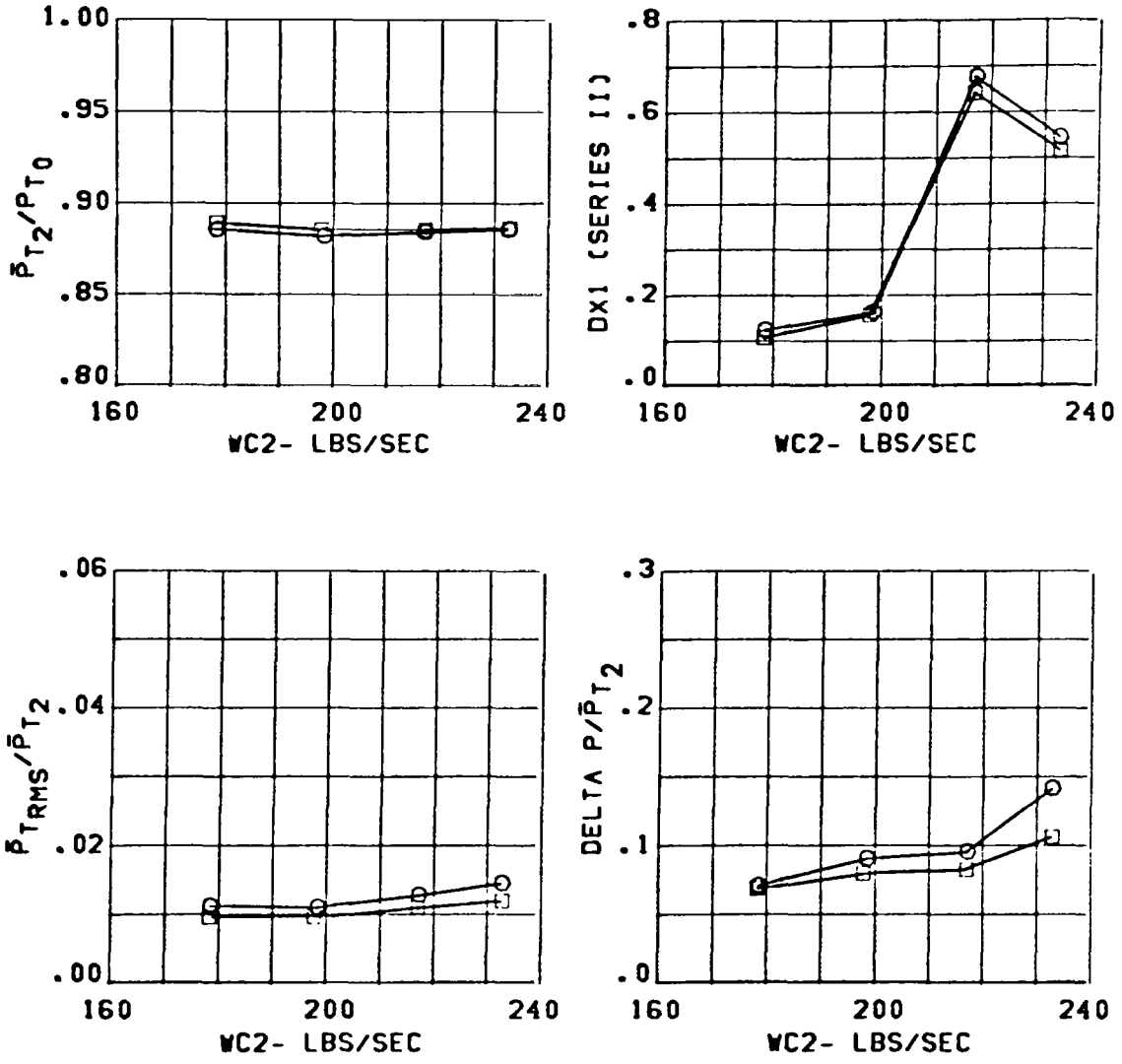

Figure 248 Effect of Trimmed Splitter Plate on Inlet Performance

CONFIG.	DIV.	MACH	SYM.	THROAT RAKES	CONDITION
C13	3.65	1.56	○	IN	ALPHA= 1.
C14			□		BETA = 0.

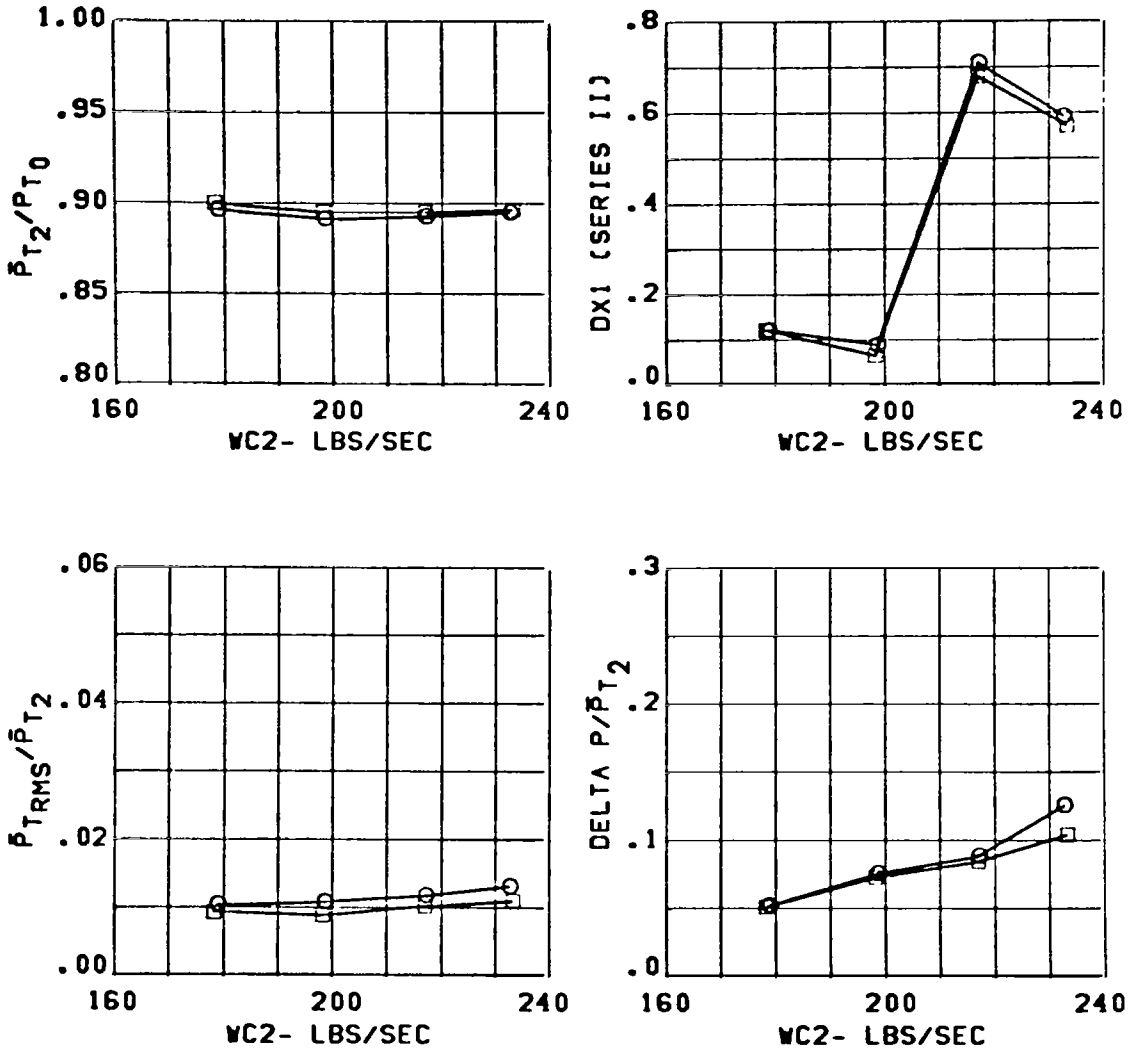

Figure 249 Effect of Trimmed Splitter Plate on Inlet Performance

CONFIG.	DIV.	MACH	SYM.	THROAT RAKES	CONDITION
C13	3.65	1.56	O	IN	ALPHA= 6.
C14			□		BETA = 0.

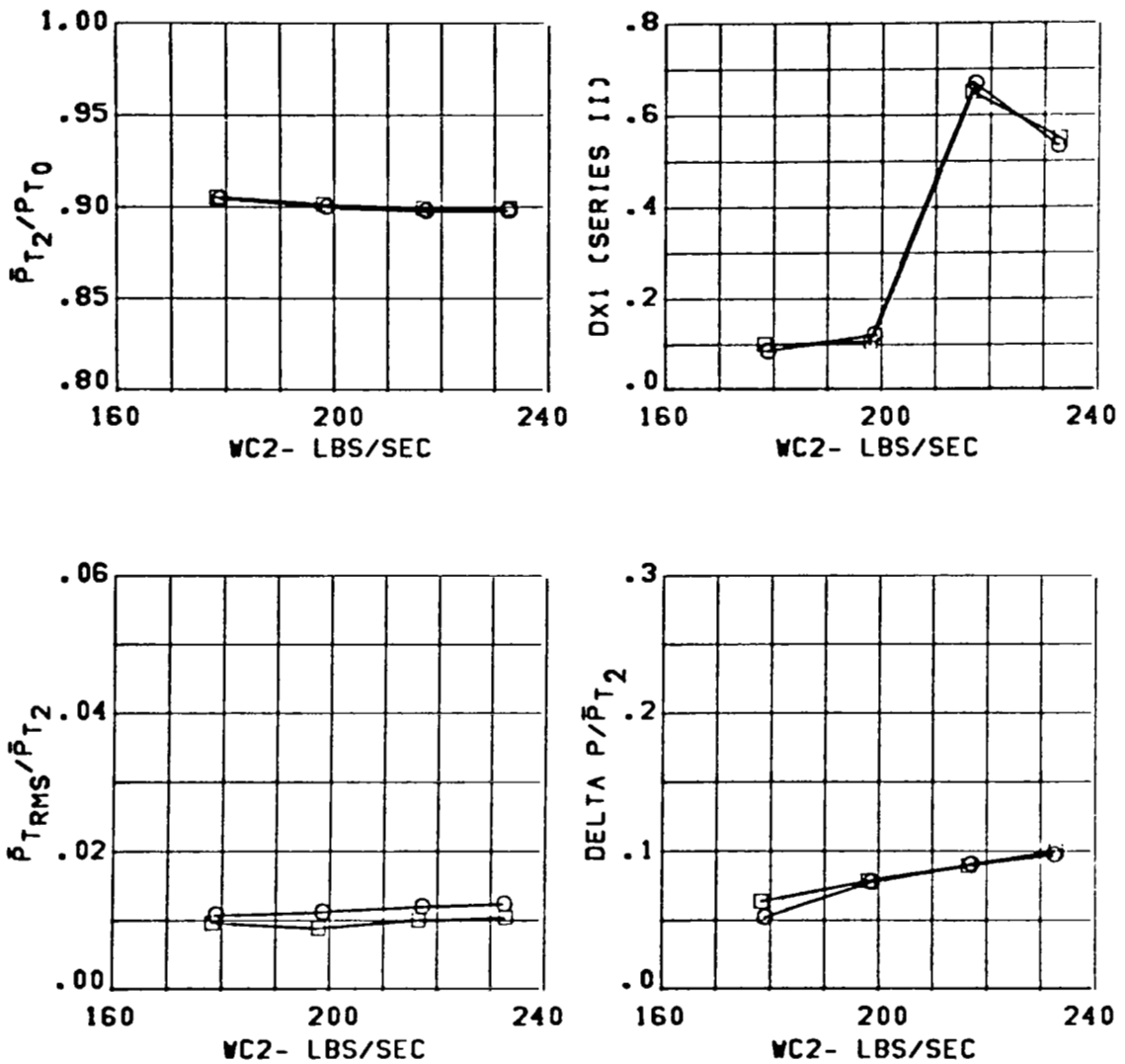

Figure 250 Effect of Trimmed Splitter Plate on Inlet Performance

CONFIG.	DIV.	MACH	SYM.	THROAT RAKES	CONDITION
C13	3.65	1.96	O	IN	ALPHA= -5.
C14			□		BETA = 0.

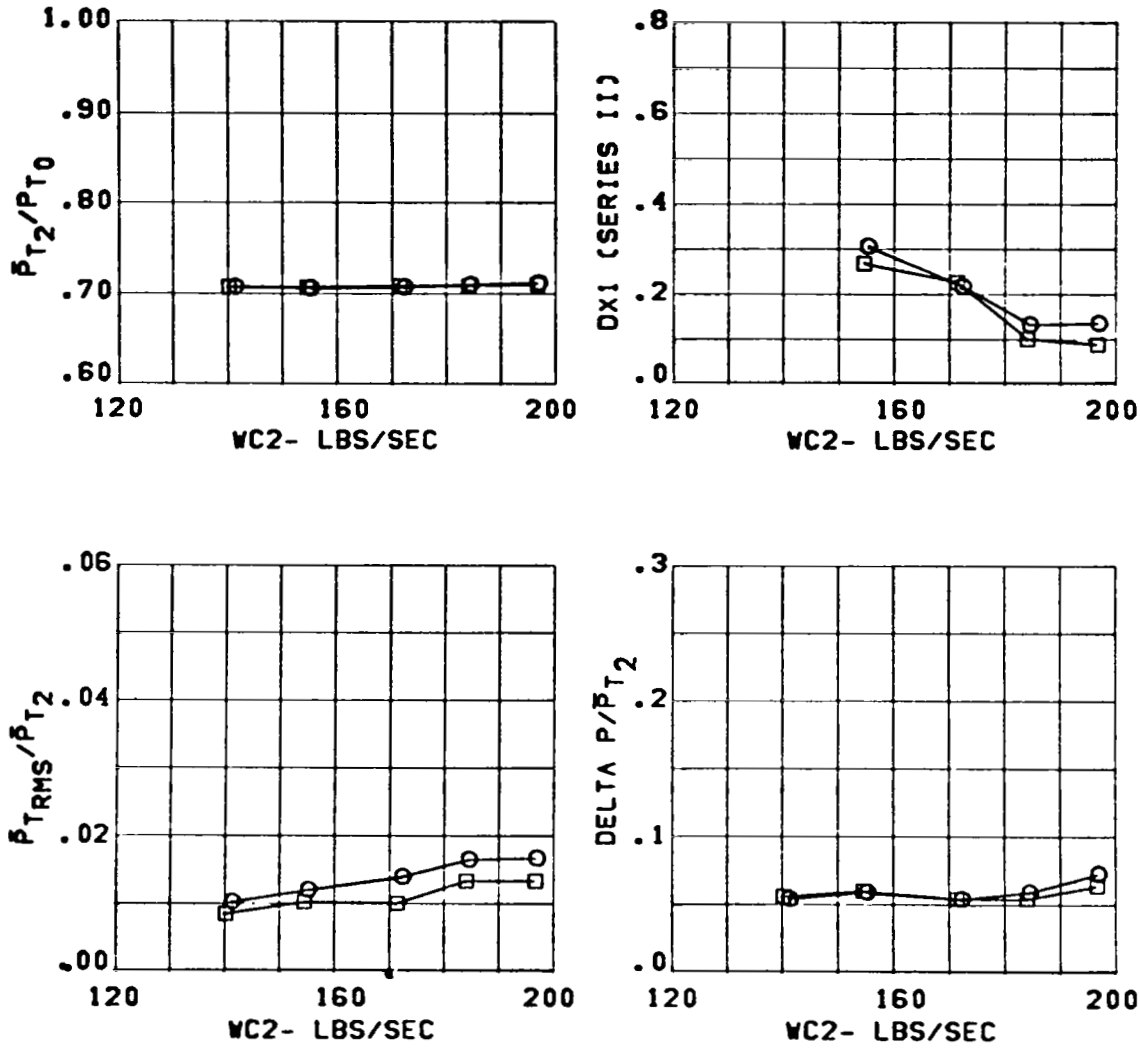

Figure 251 Effect of Trimmed Splitter Plate on Inlet Performance

CONFIG.	DIV.	MACH	SYM.	THROAT RAKES	CONDITION	
C13	3.65	1.96	O	IN	ALPHA=	1.
C14			□		BETA =	0.

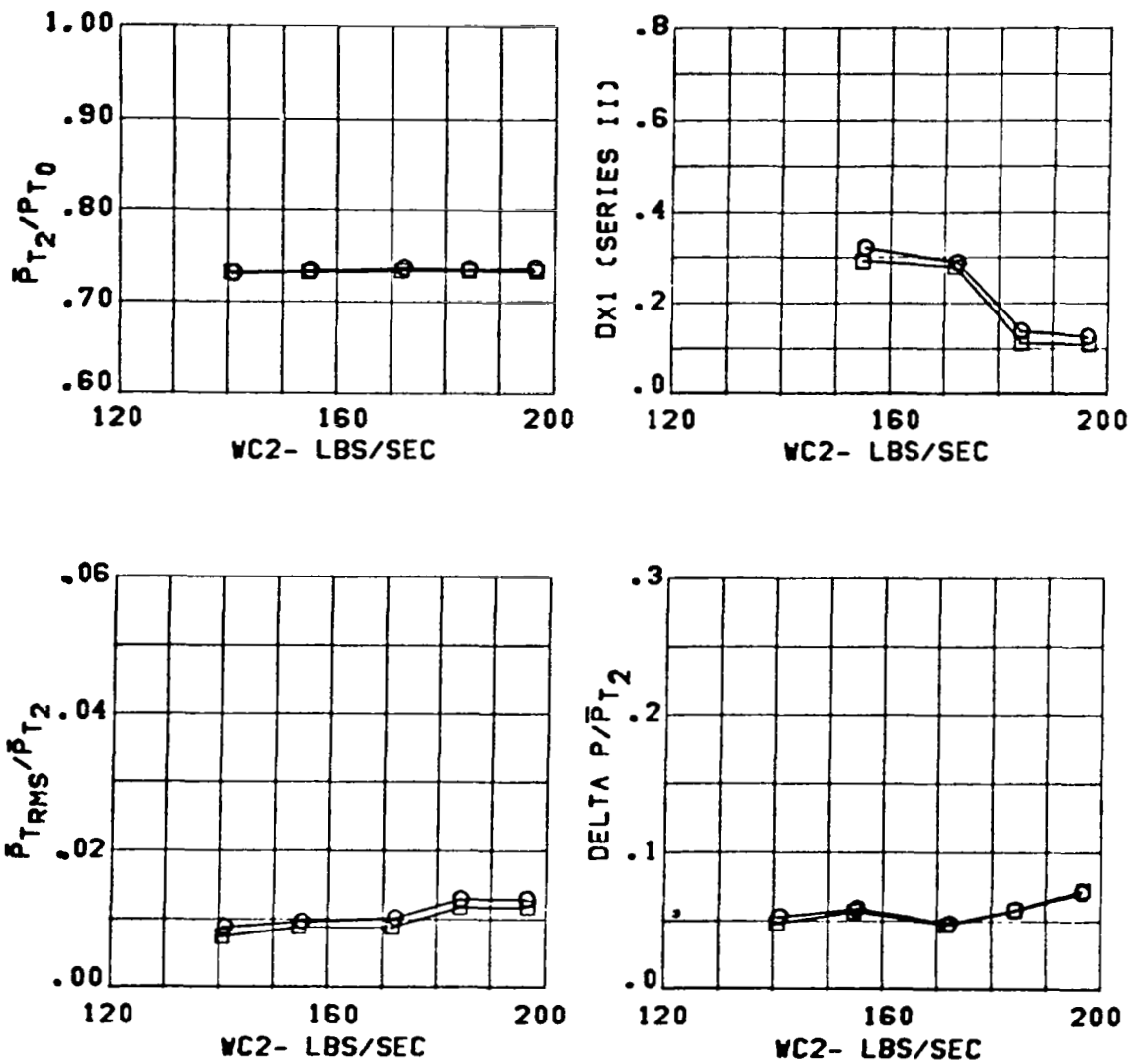

Figure 252 Effect of Trimmed Splitter Plate on Inlet Performance

CONFIG.	DIV.	MACH	SYM.	THROAT RAKES	CONDITION
C13	3.65	1.96	O	IN	ALPHA= 6.
C14			□		BETA = 0.

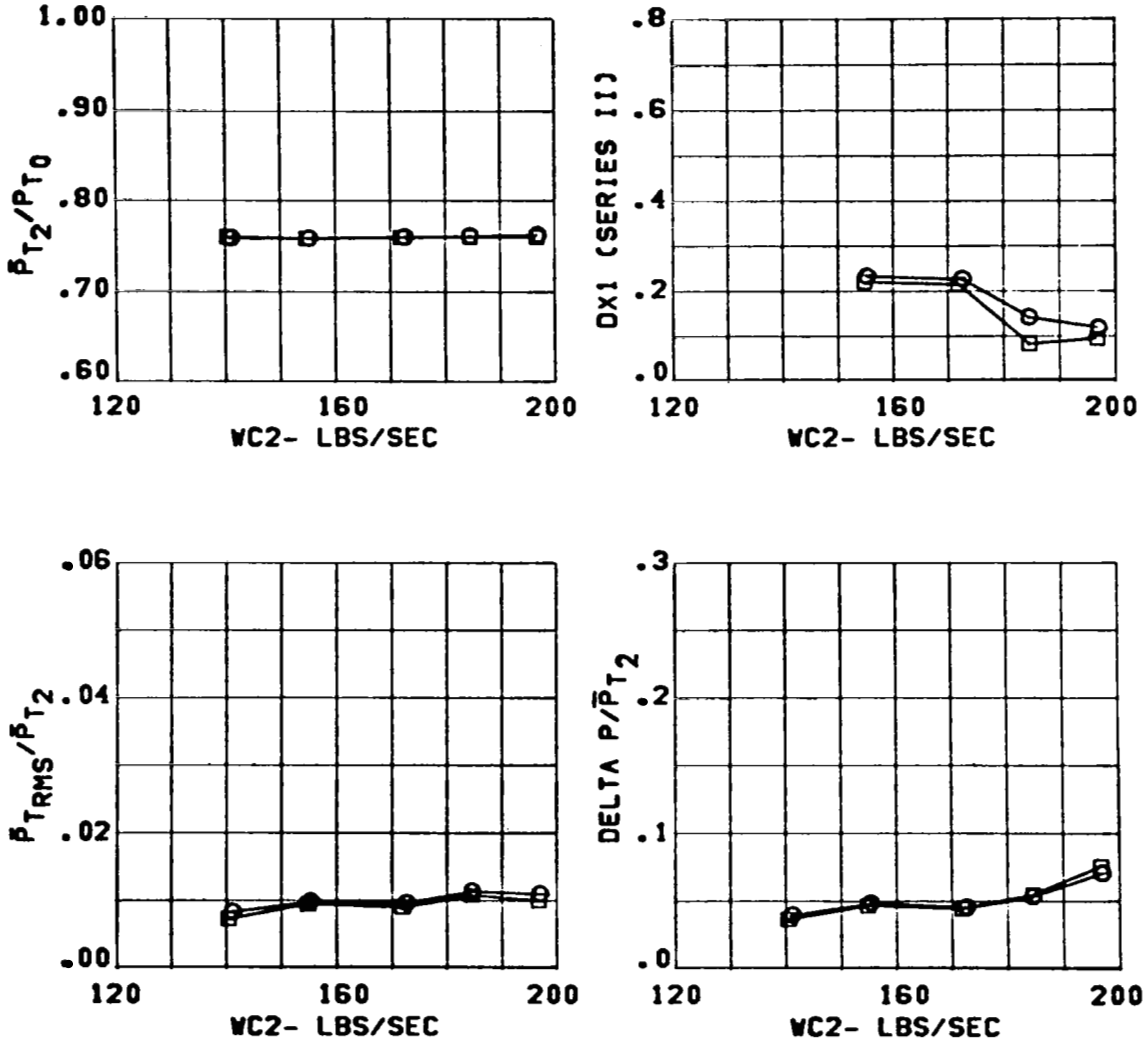

Figure 253 Effect of Trimmed Splitter Plate on Inlet Performance

CONFIGURATION	STRUTS	SYM.	MACH	WC2	CONDITION	
C13	OUT	○	.91	233.	ALPHA=	1.
3.65 IN. DIV.	IN	□			BETA =	0.

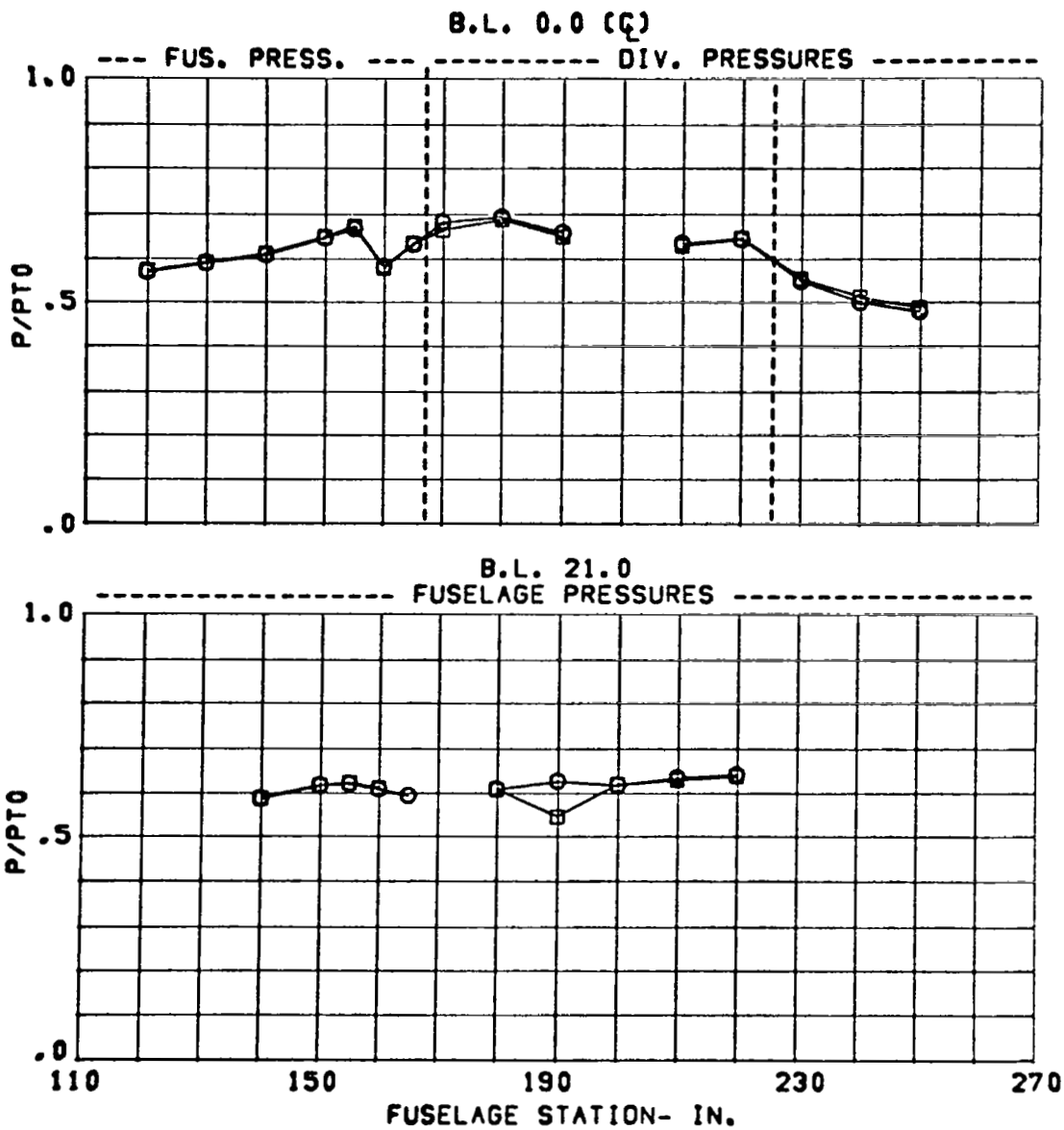

Figure 254 Effect of Diverter Struts on Fuselage and Diverter Static Pressures

CONFIGURATION	STRUTS	SYM.	MACH	WC2	CONDITION
C13	OUT	○	1.58	217.	ALPHA= 1.
3.65 IN. DIV.	IN	□			BETA = 0.

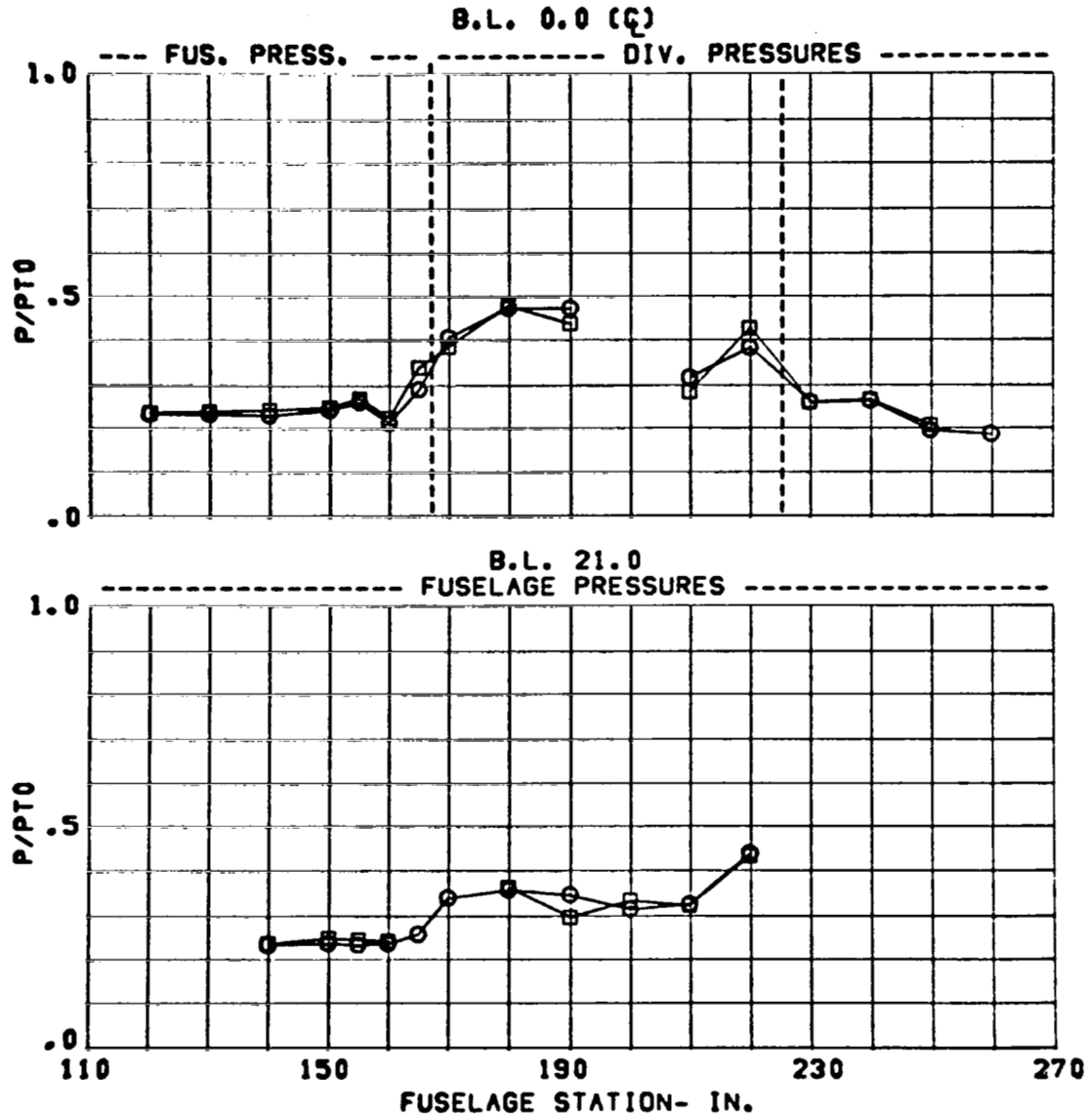

Figure 255 Effect of Diverter Struts on Fuselage and Diverter Static Pressures

CONFIGURATION	STRUTS	SYM.	MACH	WC2	CONDITION	
C13	OUT	○	1.97	183.	ALPHA=	1.
3.65 IN. DIV.	IN	□			BETA =	0.

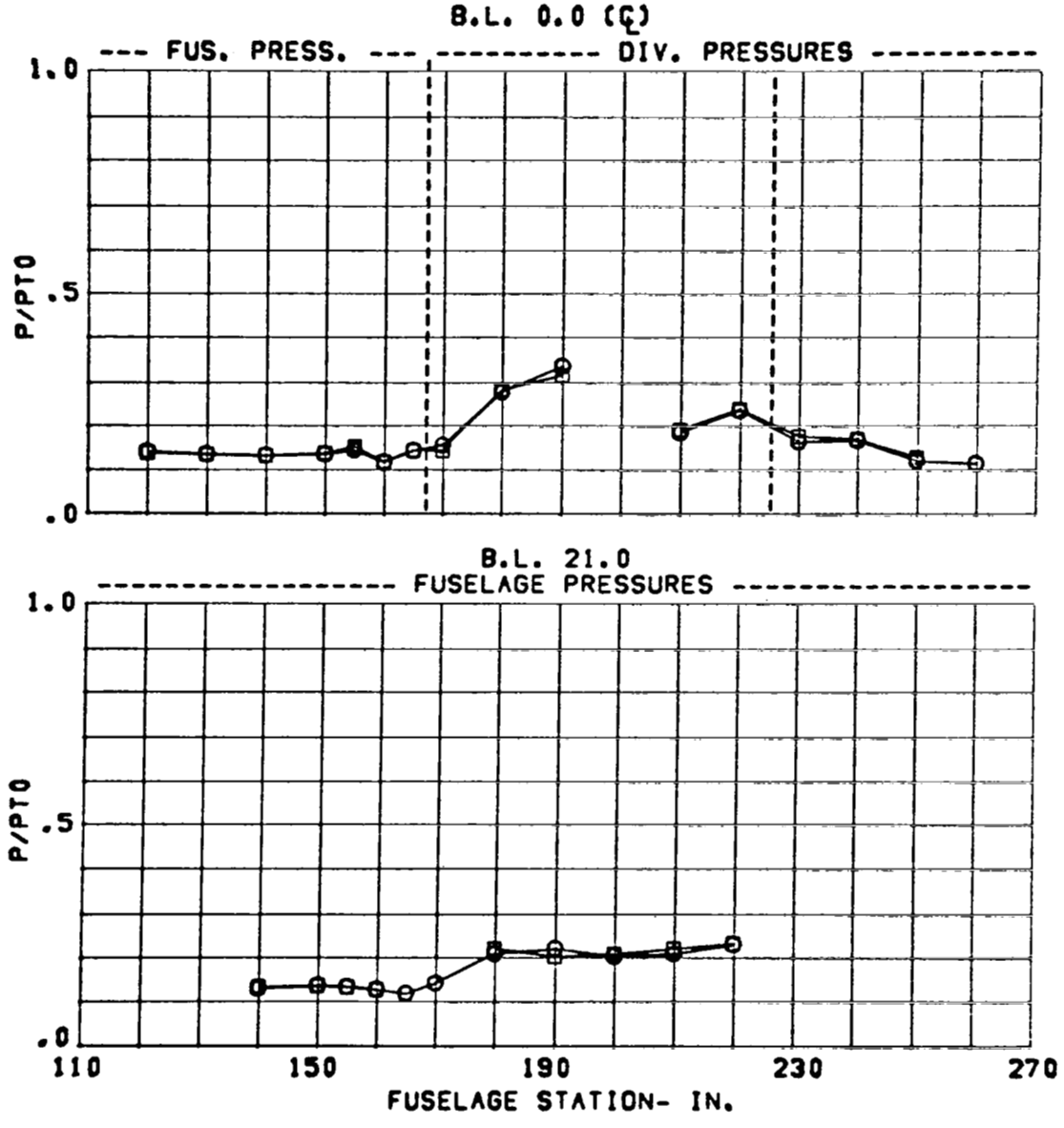

Figure 256 Effect of Diverter Struts on Fuselage and Diverter Static Pressures

CONFIGURATION	SYM.	STRUTS	MACH	CONDITION
C13/3.65 IN. DIV.	O	OUT	.91	ALPHA= 1.
V.G.S OUT	□	IN		BETA = 0.

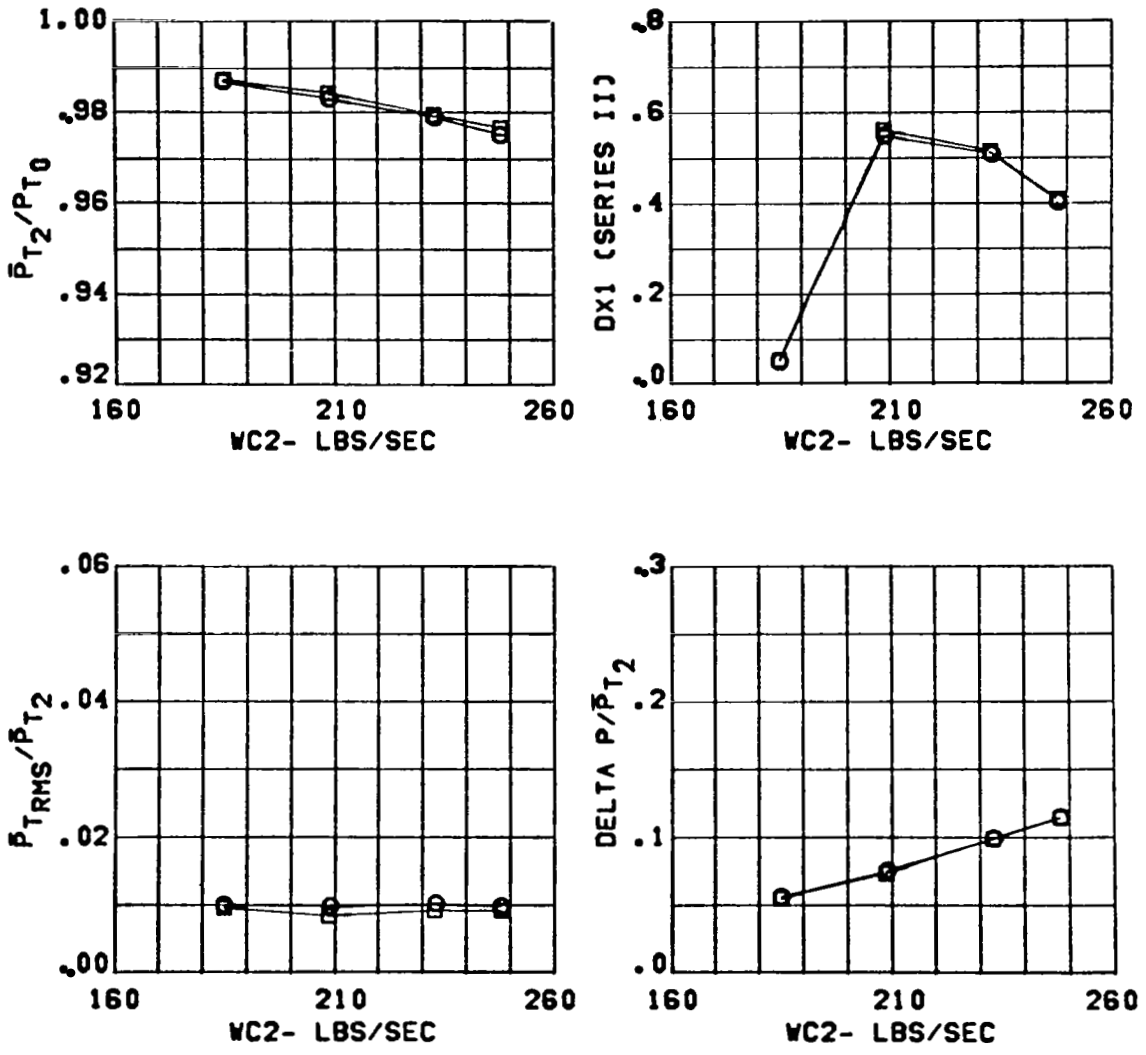

Figure 257 Effect of Diverter Struts on Inlet Performance

CONFIGURATION	SYM.	STRUTS	MACH	CONDITION
C13/3.65 IN. DIV.	O	OUT	1.58	ALPHA= 1.
V.G.S OUT	□	IN		BETA = 0.

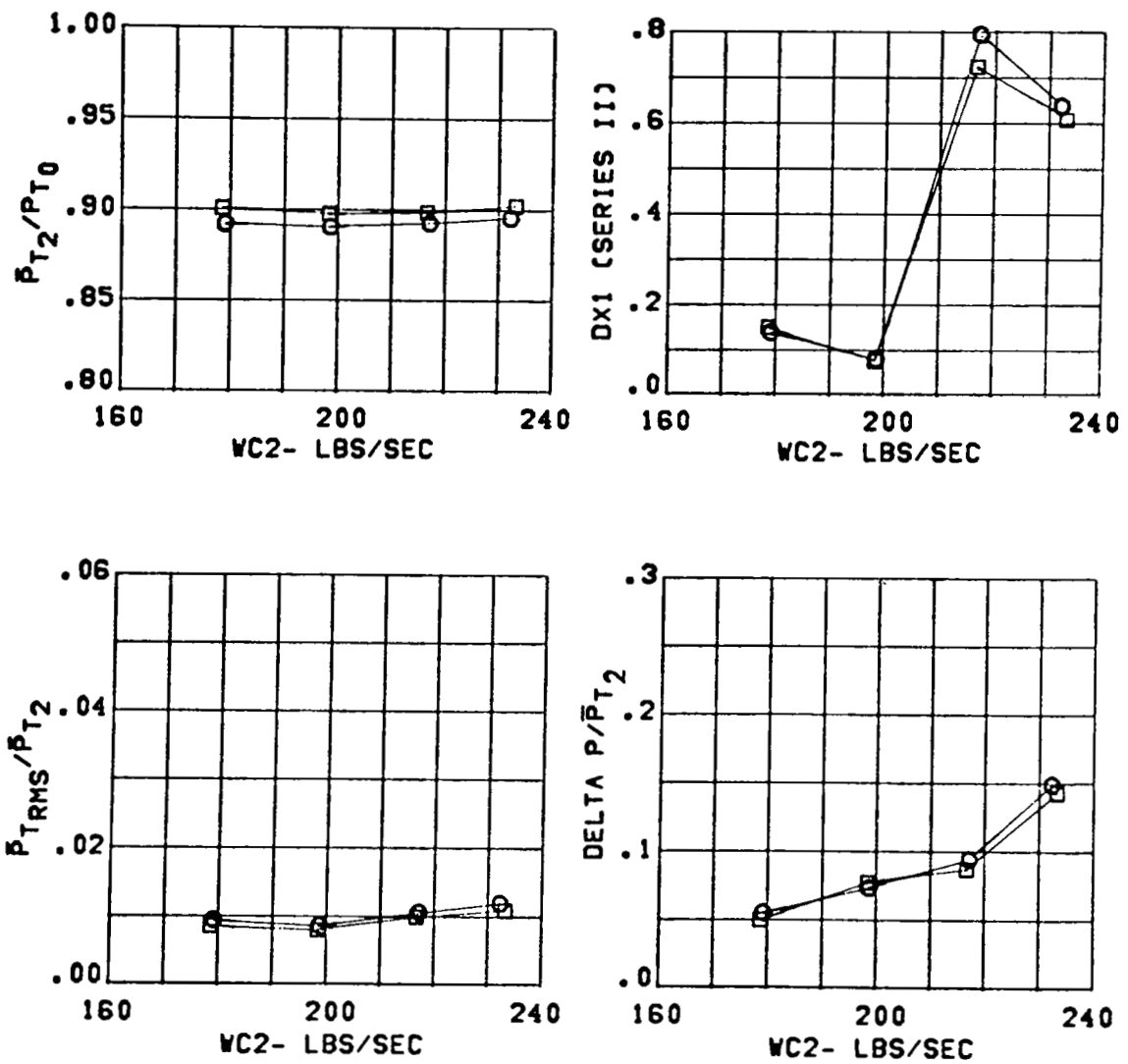

Figure 258 Effect of Diverter Struts on Inlet Performance

CONFIGURATION	SYM.	STRUTS	MACH	CONDITION
C13/3.65 IN. DIV.	O	OUT	1.97	ALPHA= 1.
V.G.S OUT	□	IN		BETA = 0.

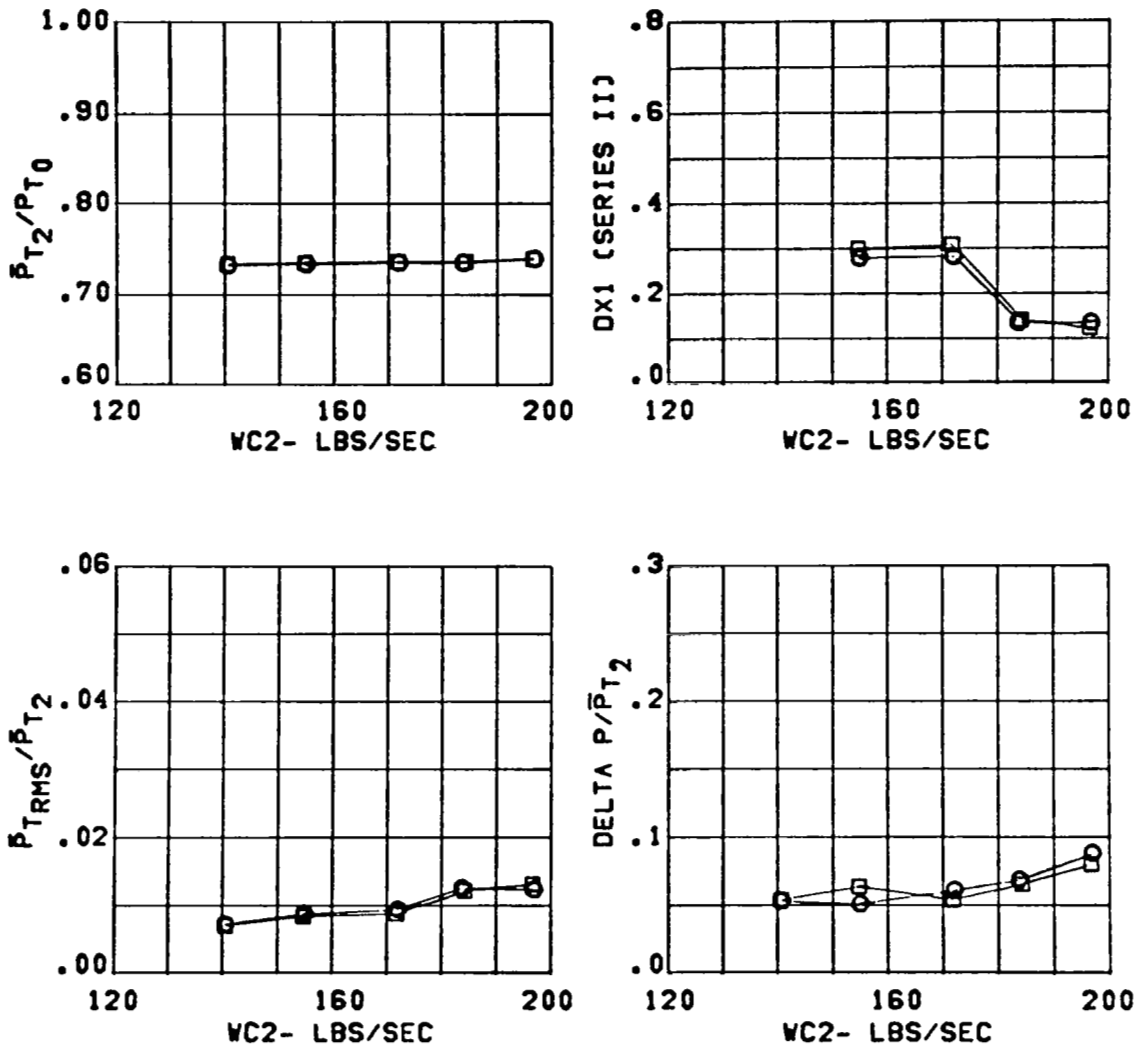

Figure 259 Effect of Diverter Struts on Inlet Performance

CONFIGURATION	SYM.	V.G.S	MACH	CONDITION
C13/3.65 IN. DIV.	O	OUT	.90	ALPHA= -9.
DIV. STRUTS IN	□	IN		BETA = 0.

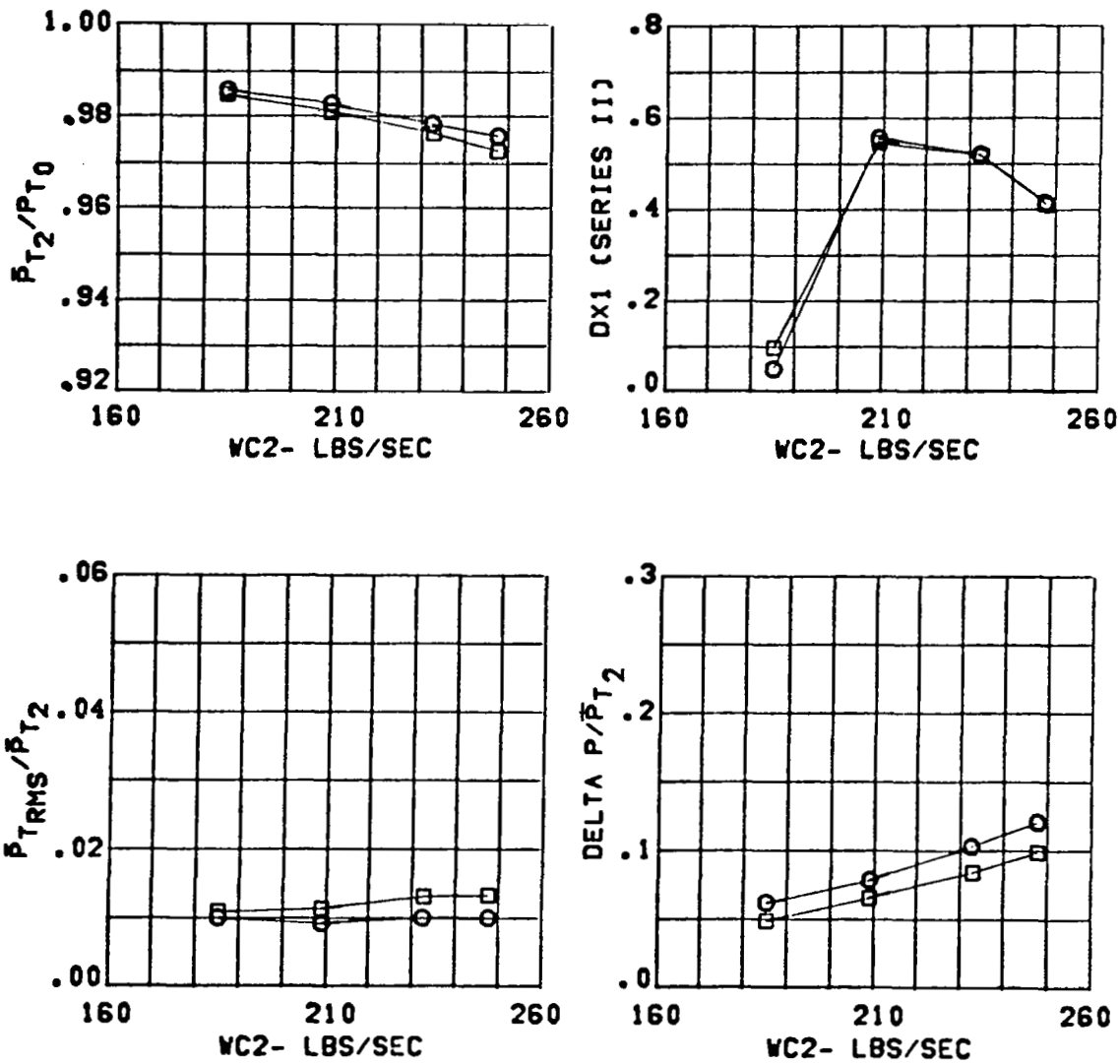

Figure 260 Effect of Vortex Generators on Inlet Performance

CONFIGURATION	SYM.	V.G.S	MACH	CONDITION
C13/3.65 IN. DIV.	O	OUT	.91	ALPHA= 1.
DIV. STRUTS IN	□	IN		BETA = 0.

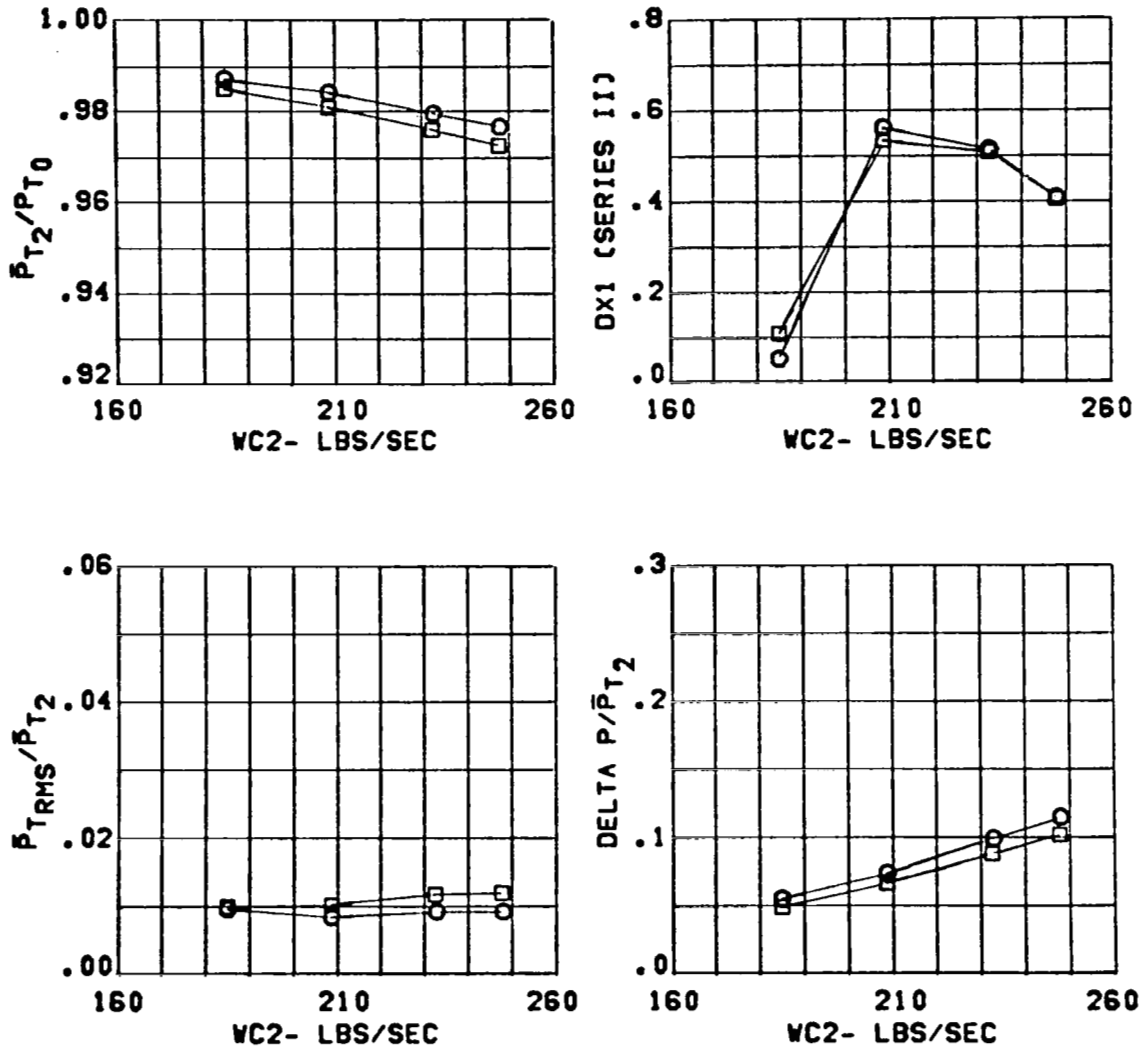

Figure 261 Effect of Vortex Generators on Inlet Performance

CONFIGURATION	SYM.	V.G.S	MACH	CONDITION
C13/3.65 IN. DIV.	O	OUT	.90	ALPHA= 30.
DIV. STRUTS IN	□	IN		BETA = 0.

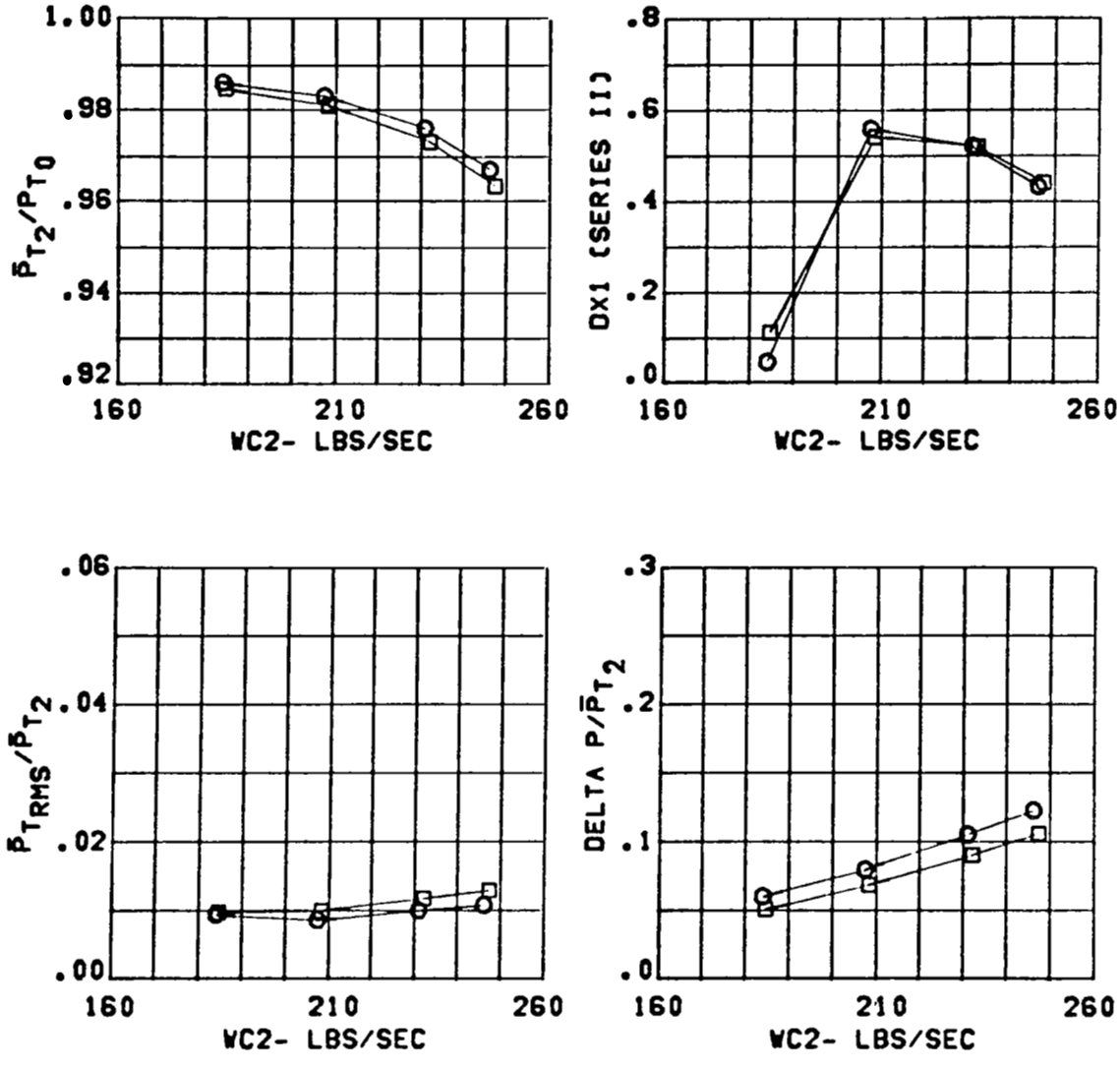

Figure 262 Effect of Vortex Generators on Inlet Performance

CONFIGURATION	SYM.	V.G.S	MACH	CONDITION
C13/3.65 IN. DIV.	O	OUT	.89	ALPHA= 40.
DIV. STRUTS IN	□	IN		BETA = 0.

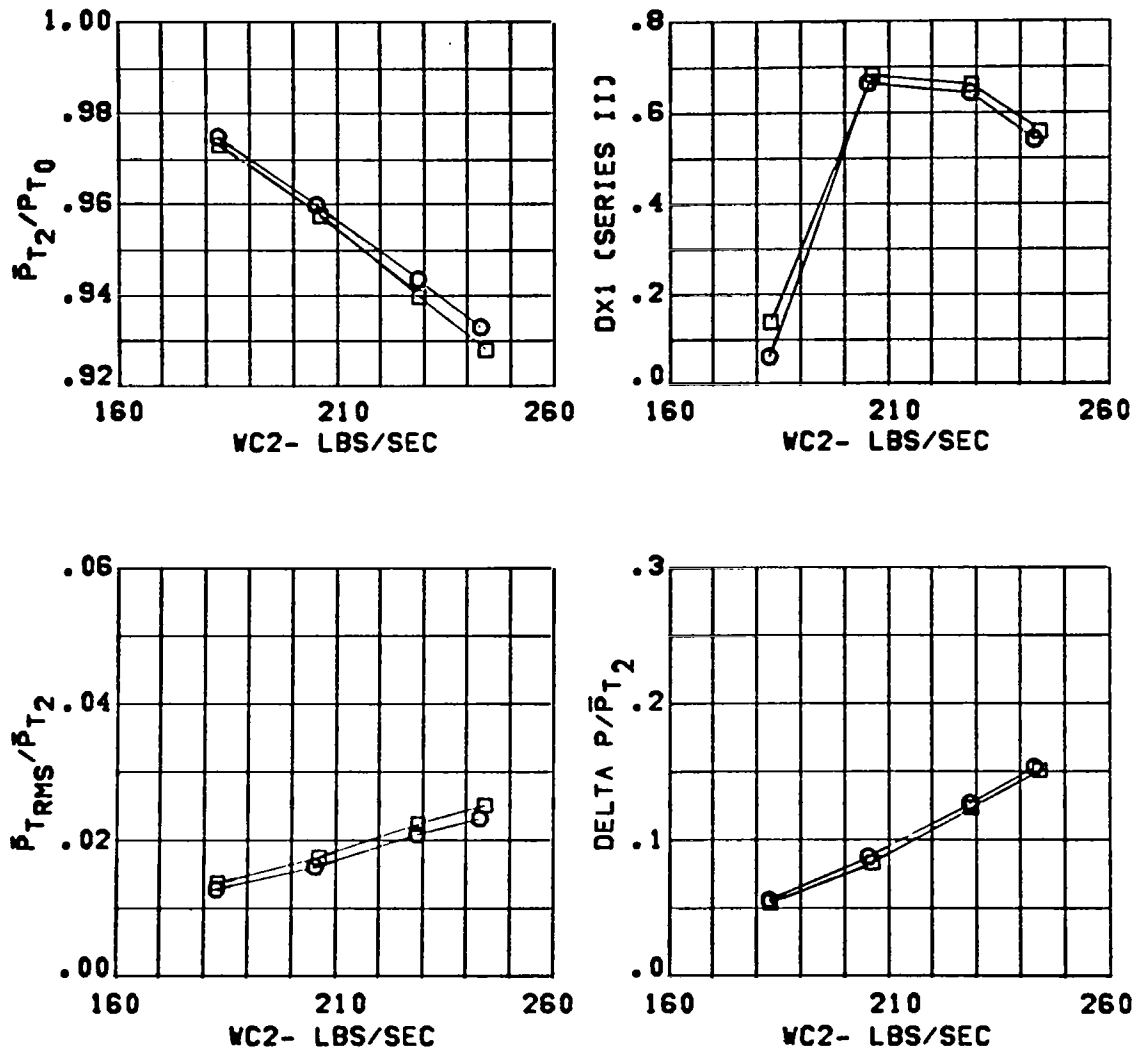

Figure 263 Effect of Vortex Generators on Inlet Performance

CONFIGURATION	SYM.	V.G.S	MACH	CONDITION
C13/3.65 IN. DIV.	O	OUT	.90	ALPHA= 1.
DIV. STRUTS IN	□	IN		BETA = -10.

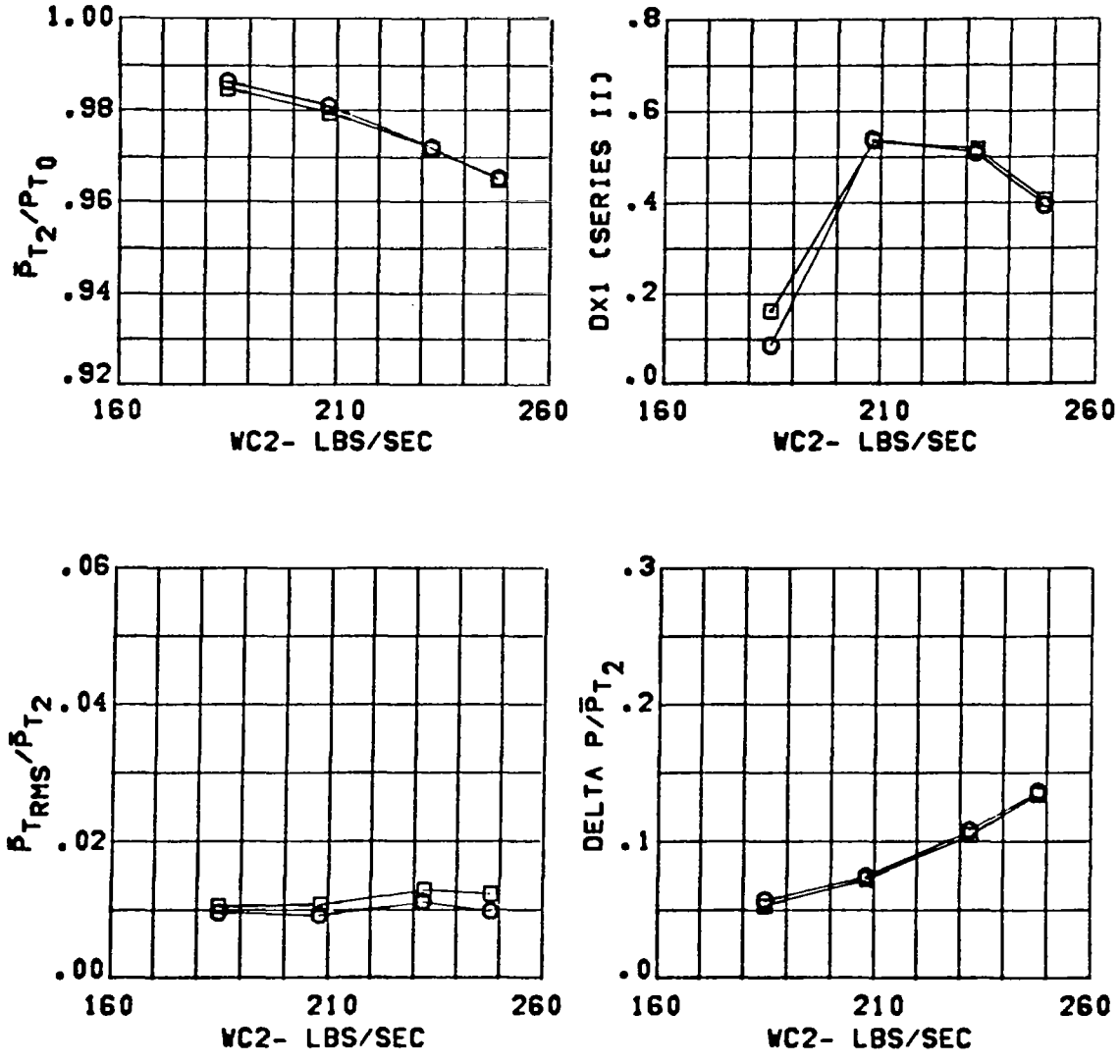

Figure 264 Effect of Vortex Generators on Inlet Performance

CONFIGURATION	SYM.	V.G.S	MACH	CONDITION
C13/3.65 IN. DIV.	○	OUT	.90	ALPHA= 30.
DIV. STRUTS IN	□	IN		BETA = -10.

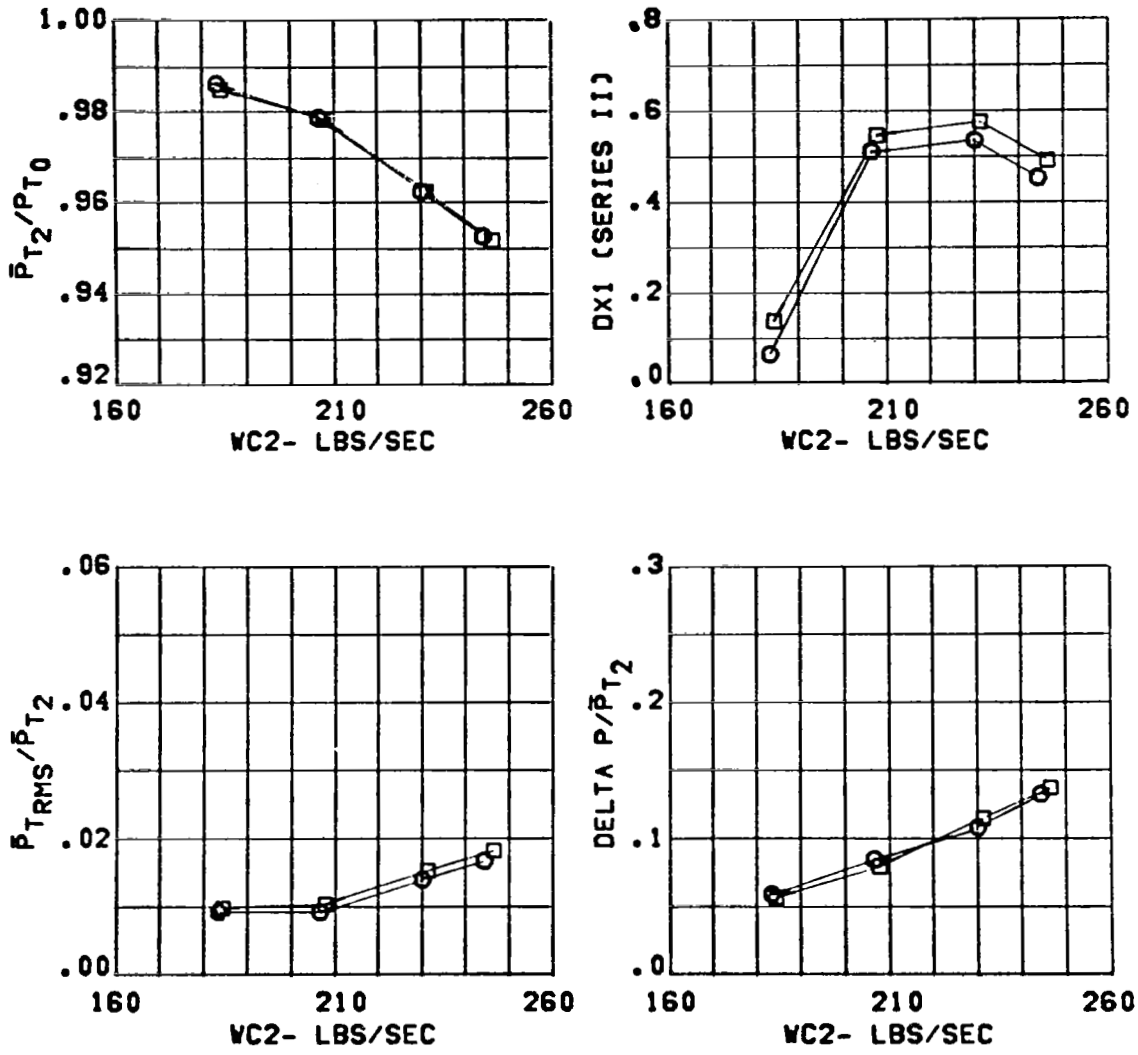

Figure 265 Effect of Vortex Generators on Inlet Performance

CONFIGURATION	SYM.	V.G.S	MACH	CONDITION
C13/3.65 IN. DIV.	O	OUT	1.56	ALPHA= -5.
DIV. STRUTS IN	□	IN		BETA = 0.

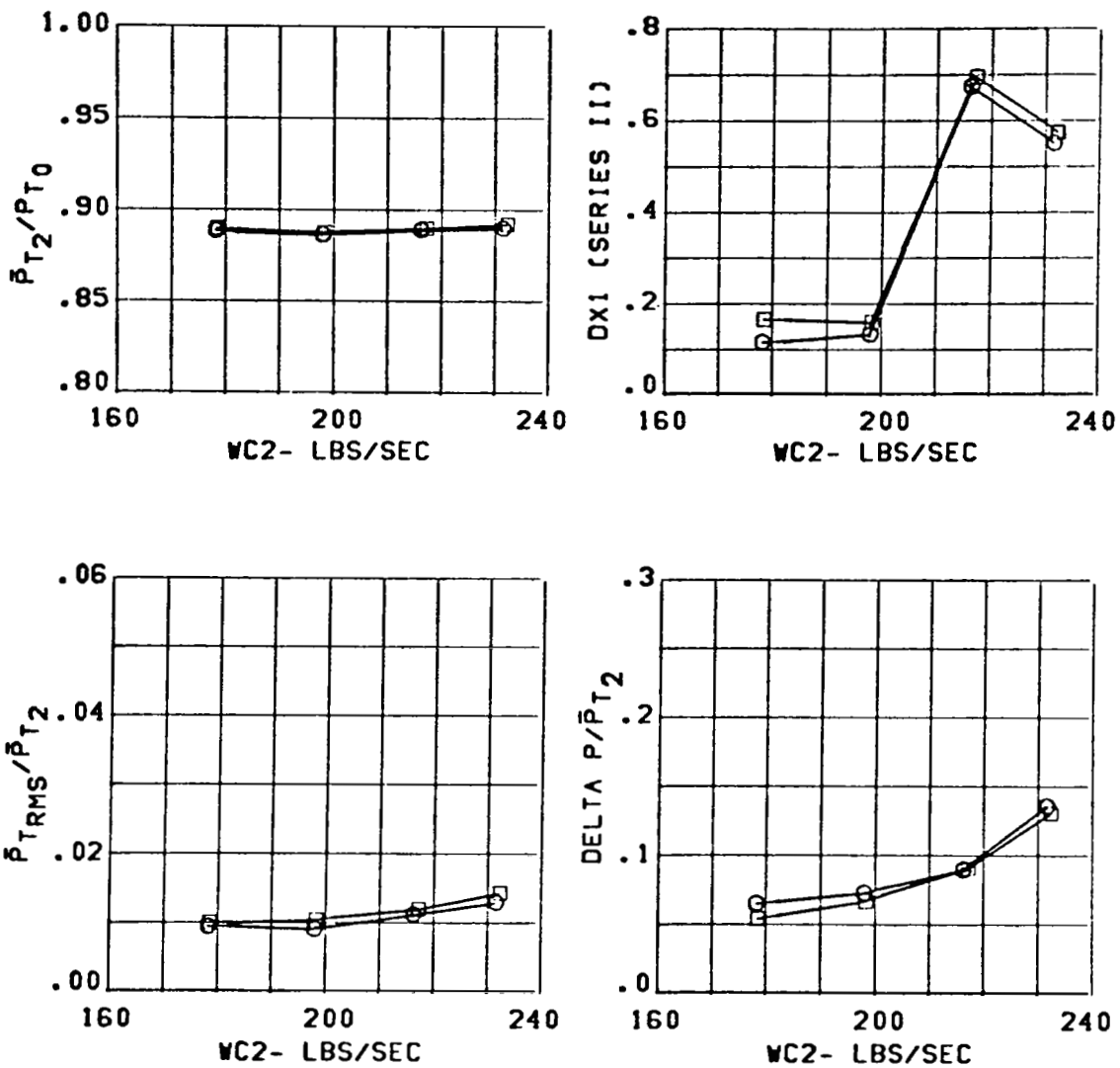

Figure 266 Effect of Vortex Generators on Inlet Performance

CONFIGURATION	SYM.	V.G.S	MACH	CONDITION
C13/3.65 IN. DIV.	O	OUT	1.56	ALPHA= 1.
DIV. STRUTS IN	□	IN		BETA = 0.

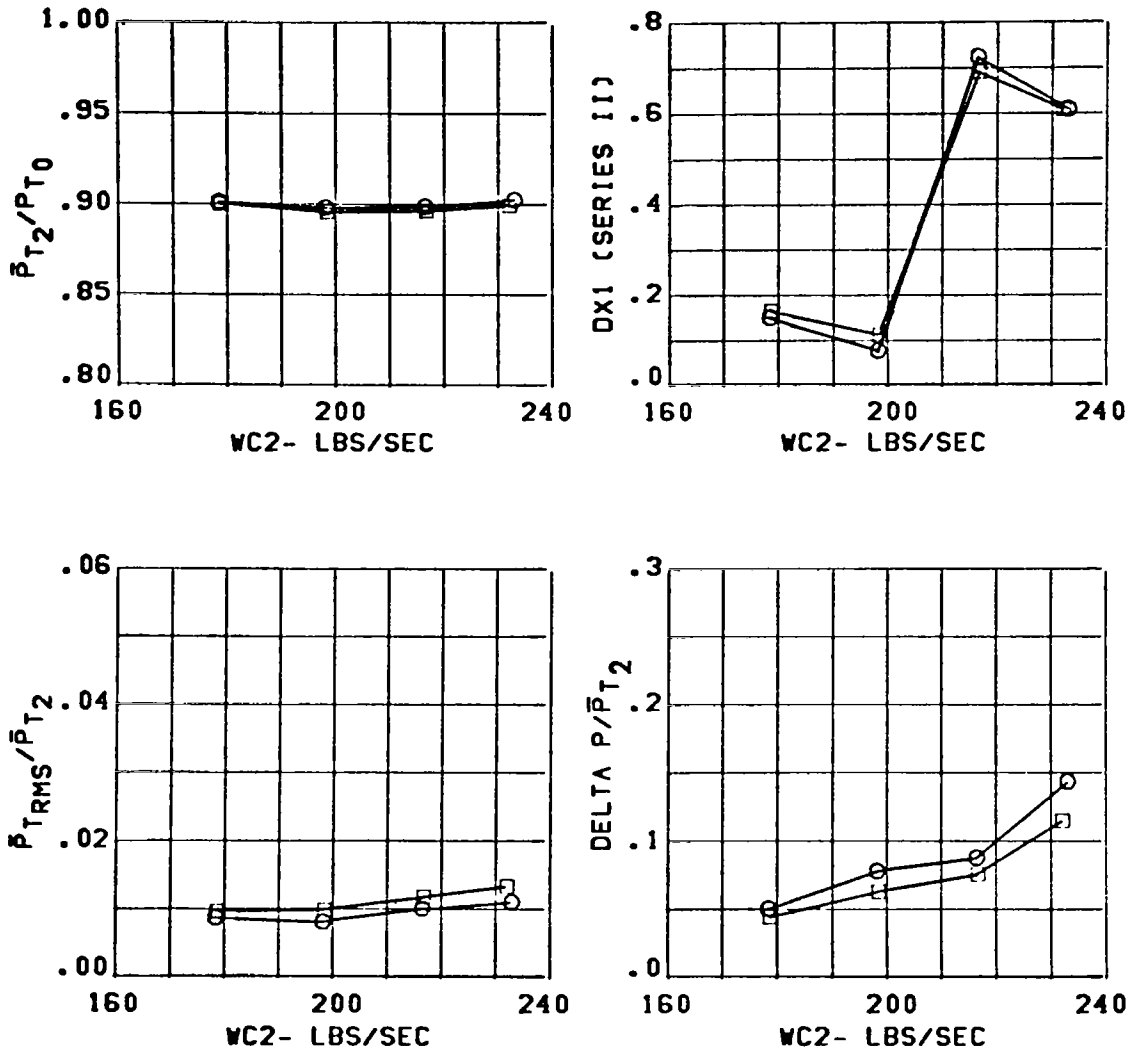

Figure 267 Effect of Vortex Generators on Inlet Performance

CONFIGURATION	SYM.	V.G.S	MACH	CONDITION
C13/3.65 IN. DIV.	○	OUT	1.56	ALPHA= 20.
DIV. STRUTS IN	□	IN		BETA = 0.

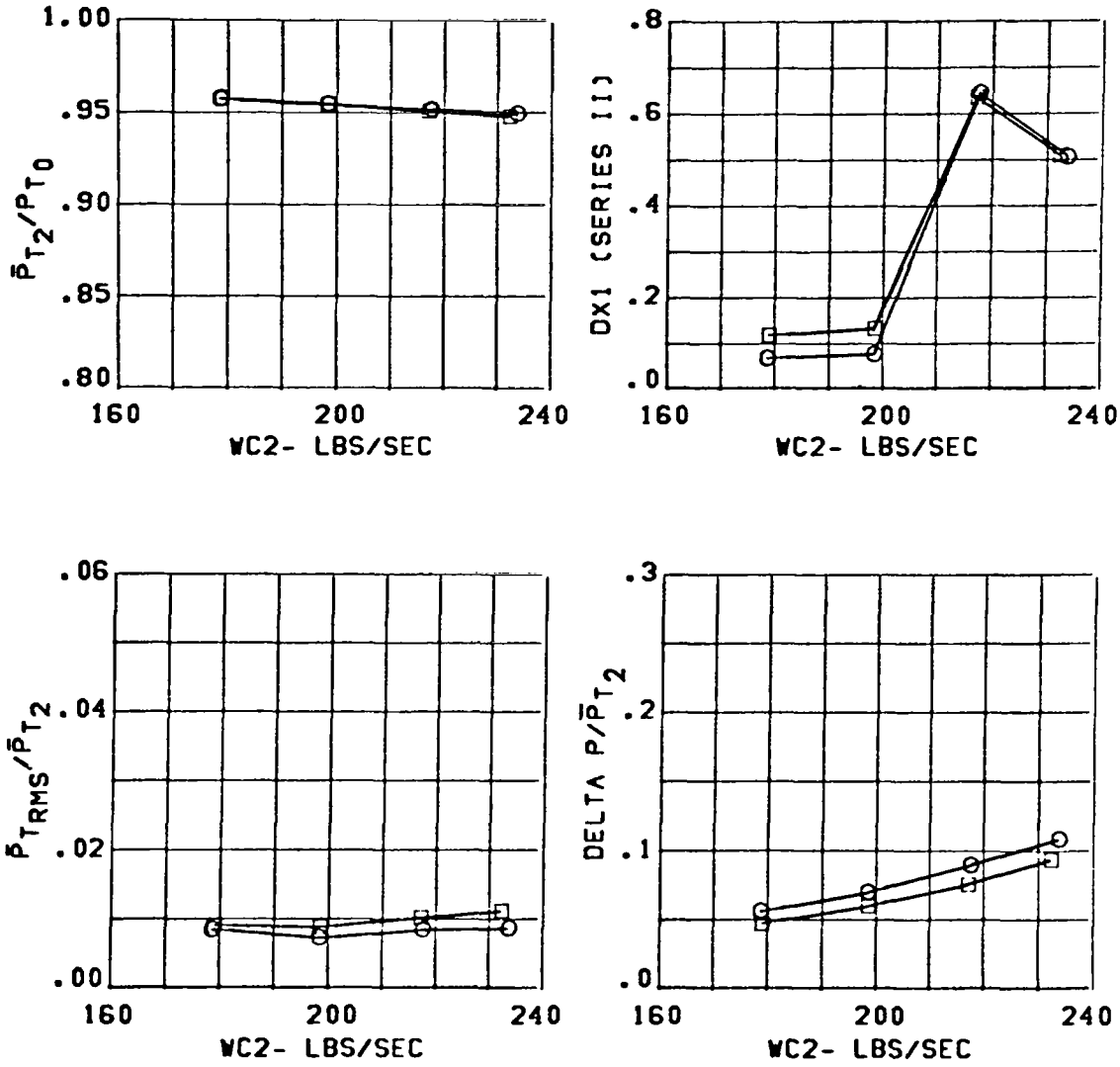

Figure 268 Effect of Vortex Generators on Inlet Performance

CONFIGURATION	SYM.	V.G.S	MACH	CONDITION
C13/3.65 IN. DIV.	○	OUT	1.56	ALPHA= -5.
DIV. STRUTS IN	□	IN		BETA = -10.

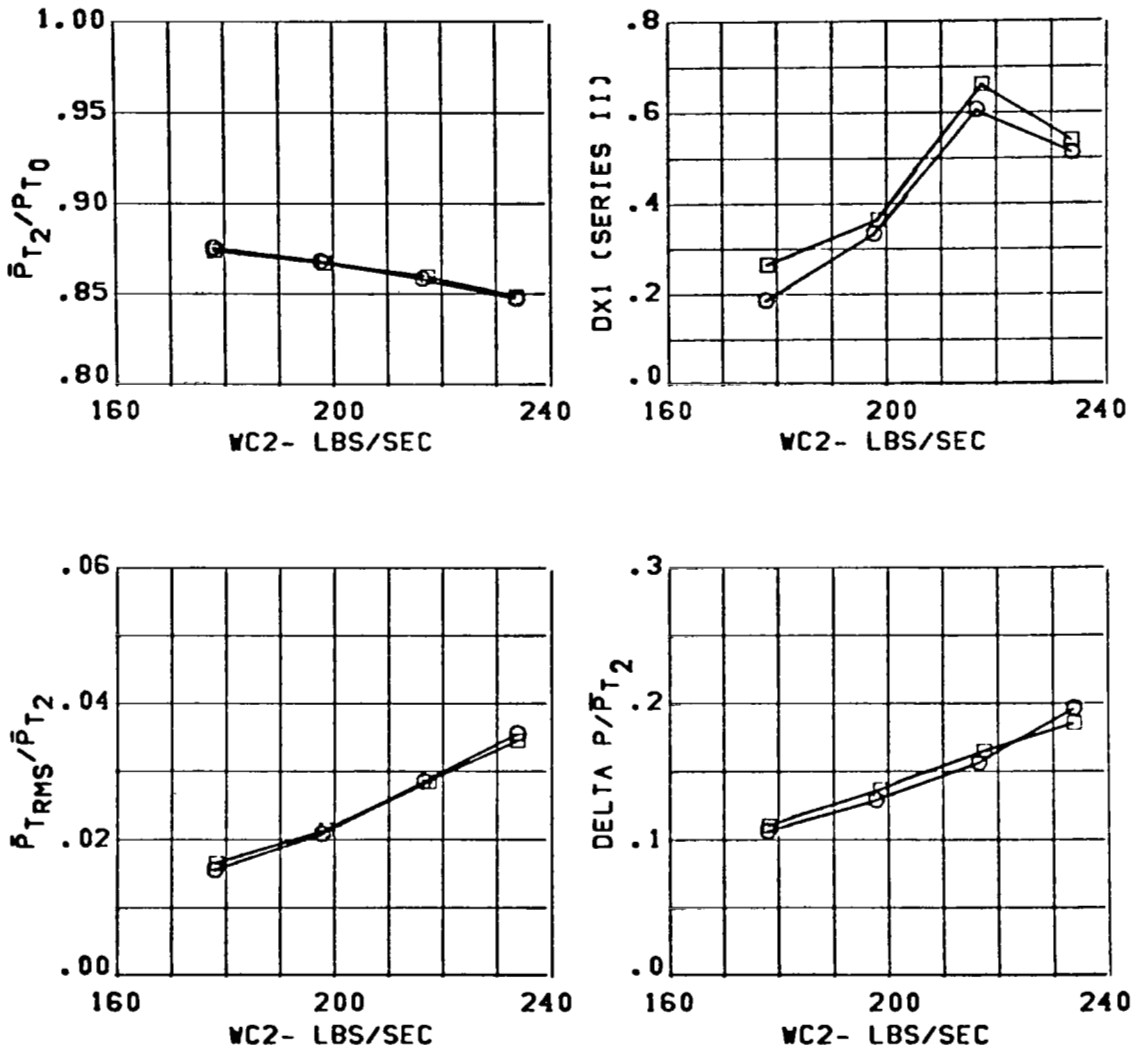

Figure 269 Effect of Vortex Generators on Inlet Performance

CONFIGURATION	SYM.	V.G.S	MACH	CONDITION
C13/3.65 IN. DIV.	○	OUT	1.56	ALPHA= 1.
DIV. STRUTS IN	□	IN		BETA = -10.

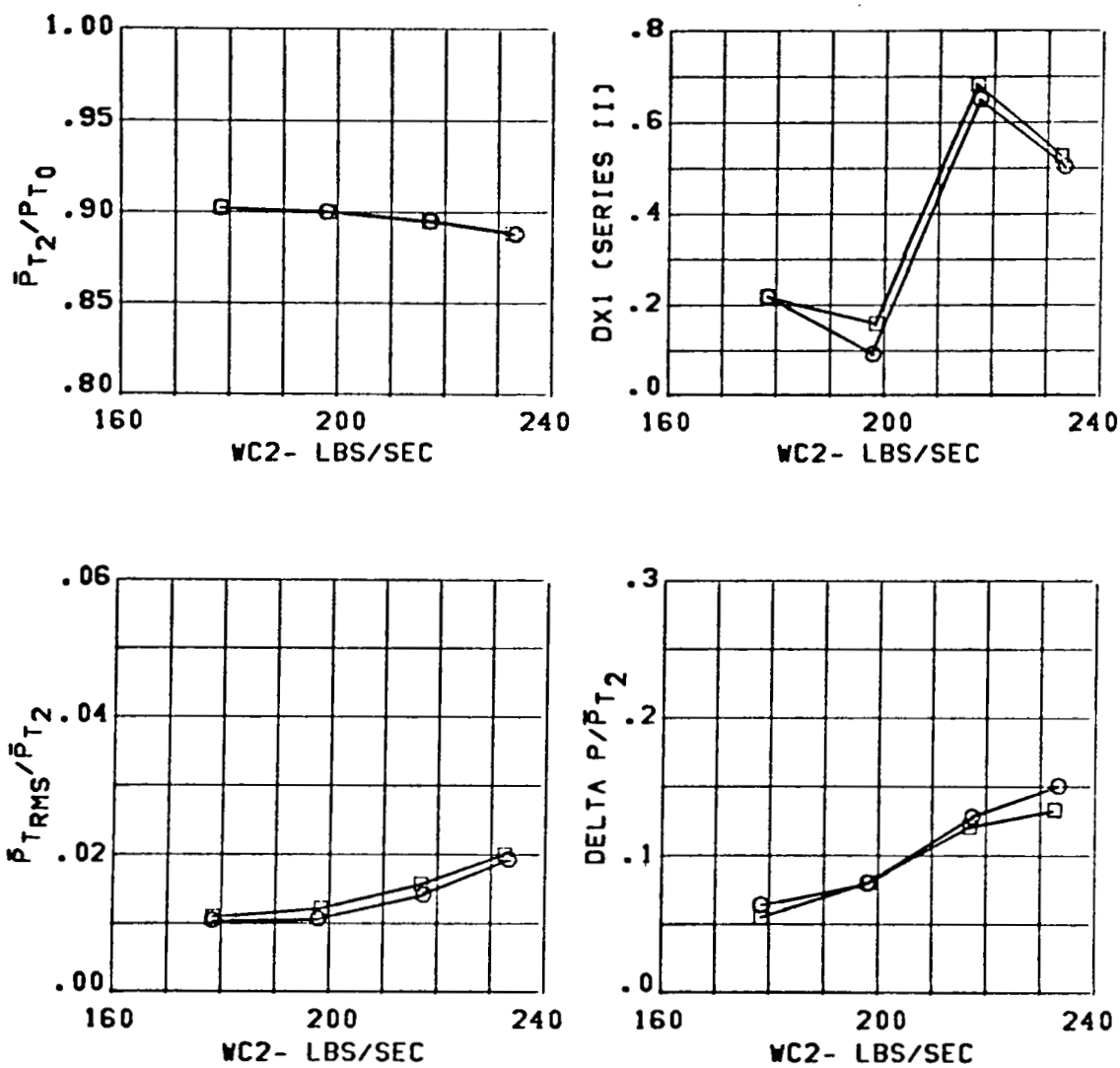

Figure 270 Effect of Vortex Generators on Inlet Performance

CONFIGURATION	SYM.	V.G.S	MACH	CONDITION
C13/3.65 IN. DIV.	O	OUT	1.56	ALPHA= 20.
DIV. STRUTS IN	□	IN		BETA = -10.

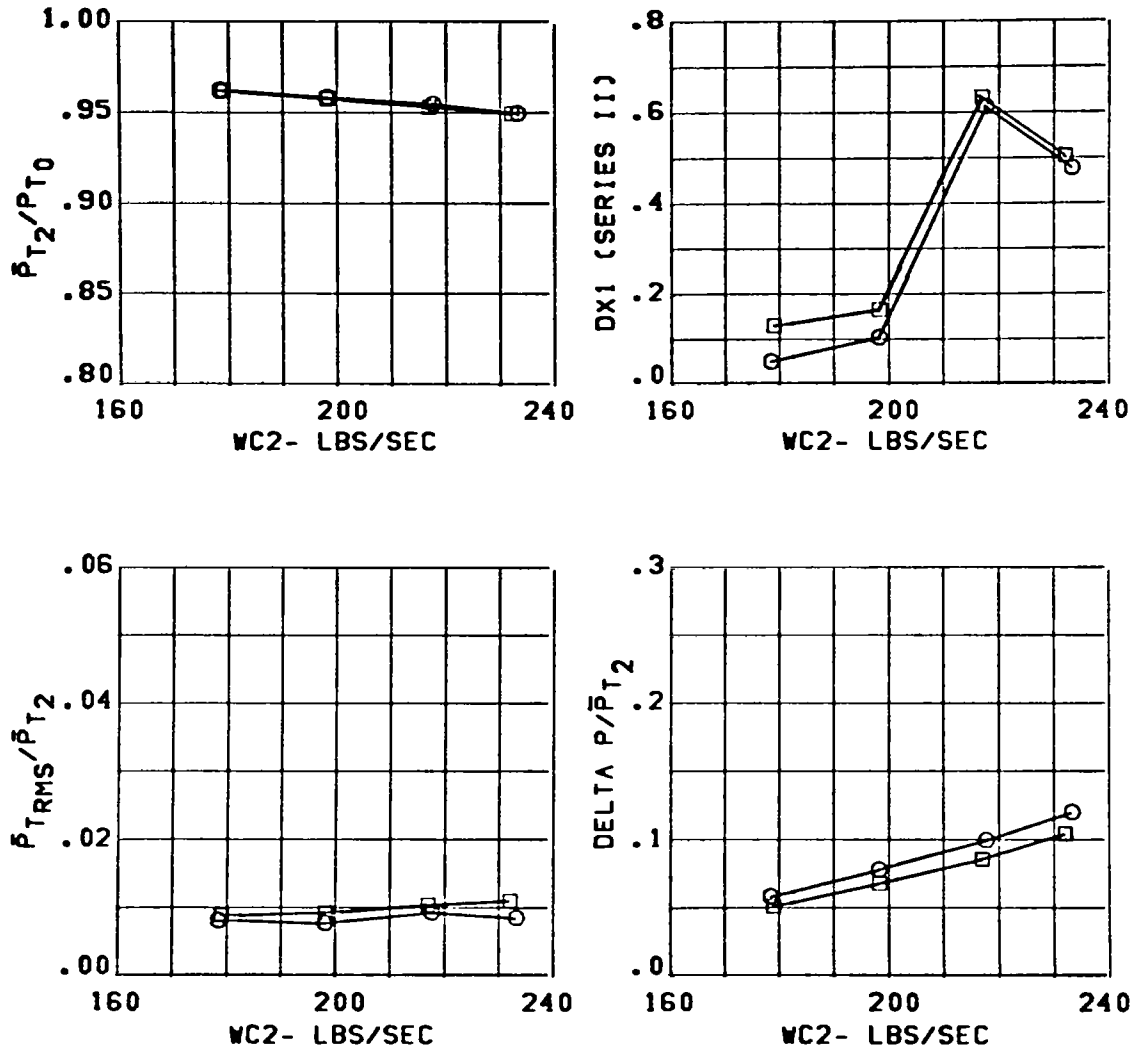

Figure 271 Effect of Vortex Generators on Inlet Performance

CONFIGURATION	SYM.	V.G.S	MACH	CONDITION
C13/3.65 IN. DIV.	O	OUT	1.96	ALPHA= -5.
DIV. STRUTS IN	□	IN		BETA = 0.

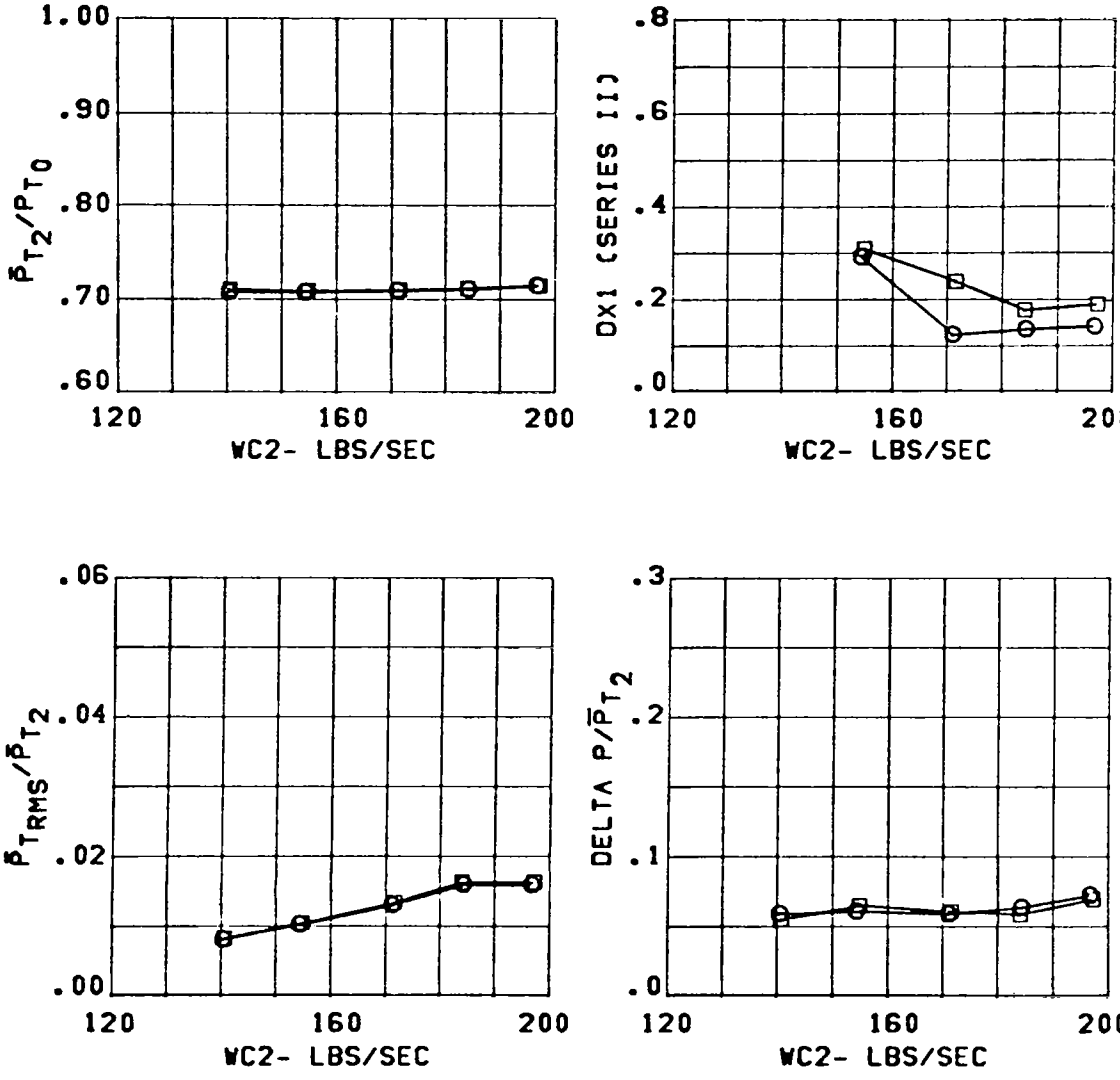

Figure 272 Effect of Vortex Generators on Inlet Performance

CONFIGURATION	SYM.	V.G.S	MACH	CONDITION
C13/3.65 IN. DIV.	O	OUT	1.96	ALPHA= 1.
DIV. STRUTS IN	□	IN		BETA = 0.

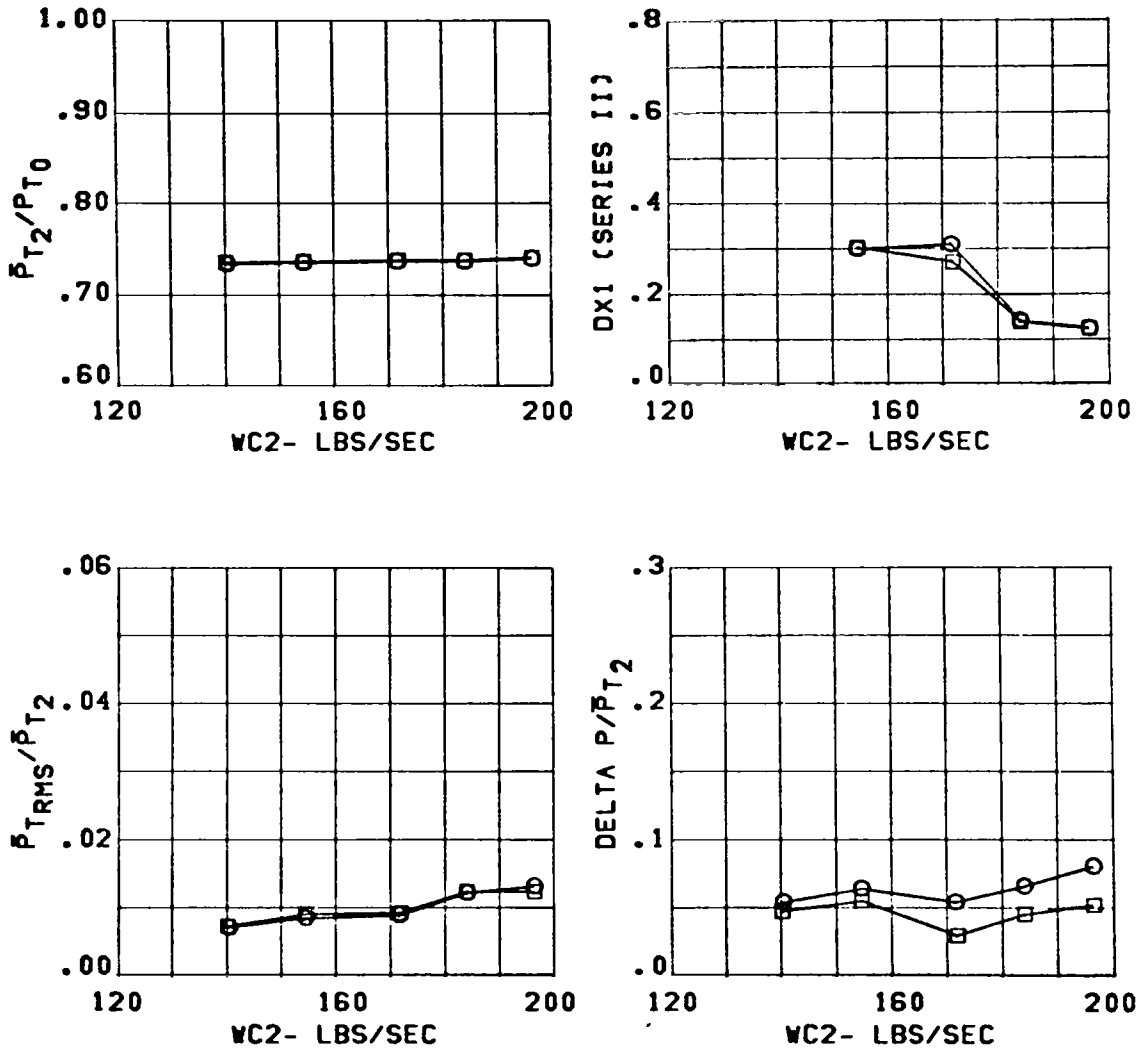

Figure 273 Effect of Vortex Generators on Inlet Performance

CONFIGURATION	SYM.	V.G.S	MACH	CONDITION
C13/3.65 IN. DIV.	O	OUT	1.95	ALPHA= 20.
DIV. STRUTS IN	□	IN		BETA = 0.

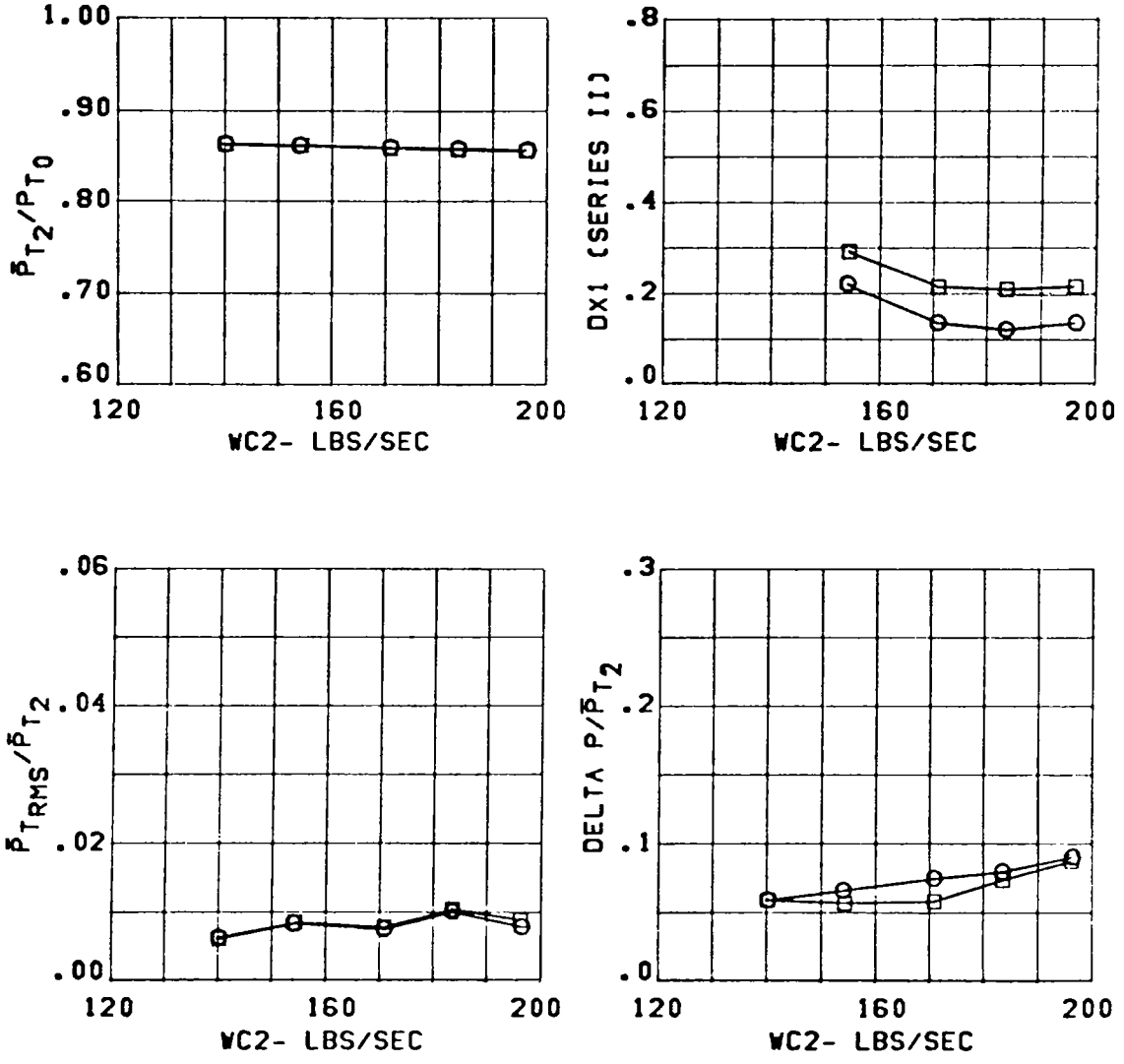

Figure 274 Effect of Vortex Generators on Inlet Performance

CONFIGURATION	SYM.	V.G.S	MACH	CONDITION
C13/3.65 IN. DIV.	O	OUT	1.96	ALPHA= 1.
DIV. STRUTS IN	□	IN		BETA = -10.

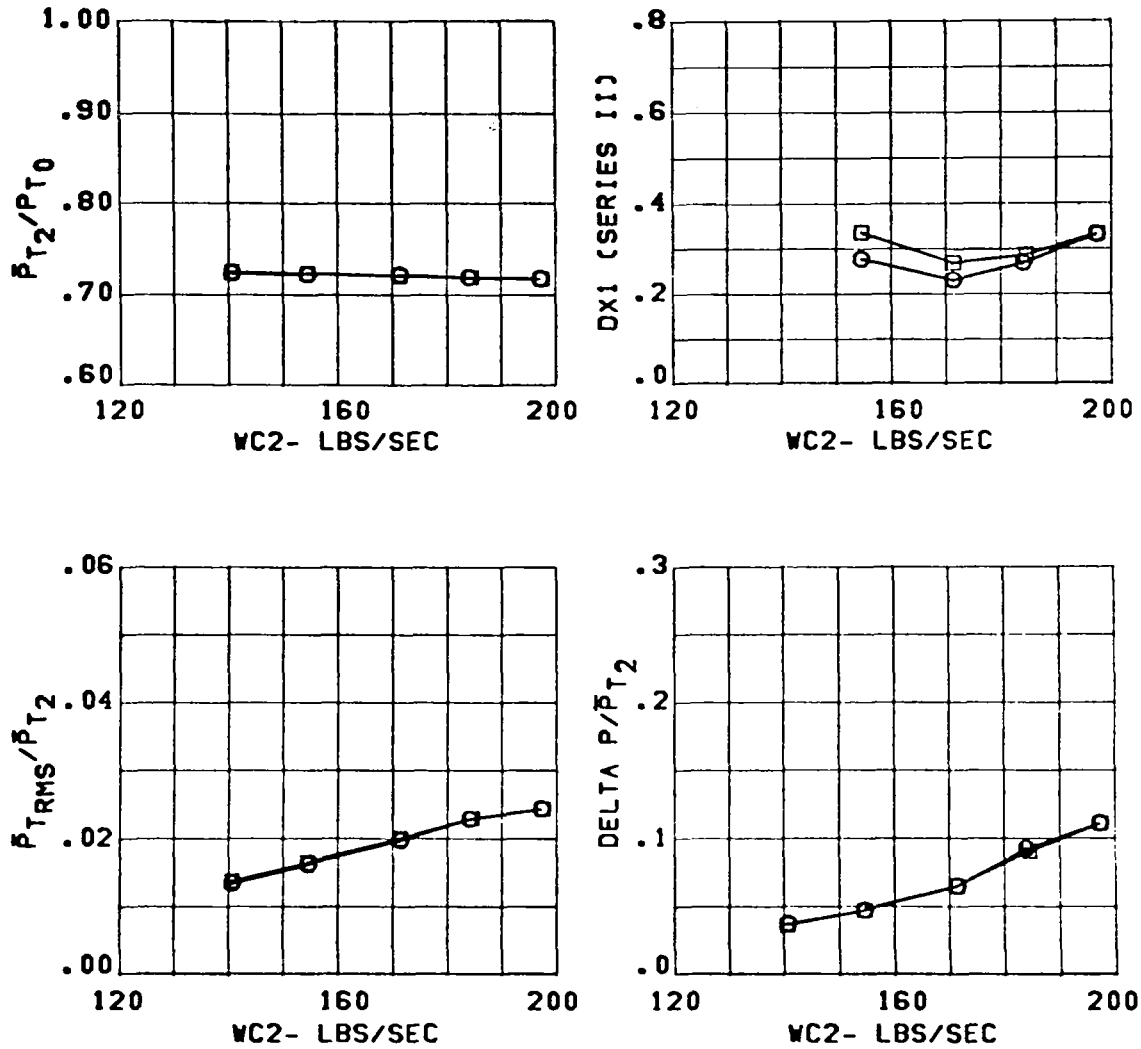

Figure 275 Effect of Vortex Generators on Inlet Performance

CONFIGURATION	SYM.	V.G.S	MACH	CONDITION
C13/3.65 IN. DIV.	O	OUT	1.96	ALPHA= 20.
DIV. STRUTS IN	□	IN		BETA = -10.

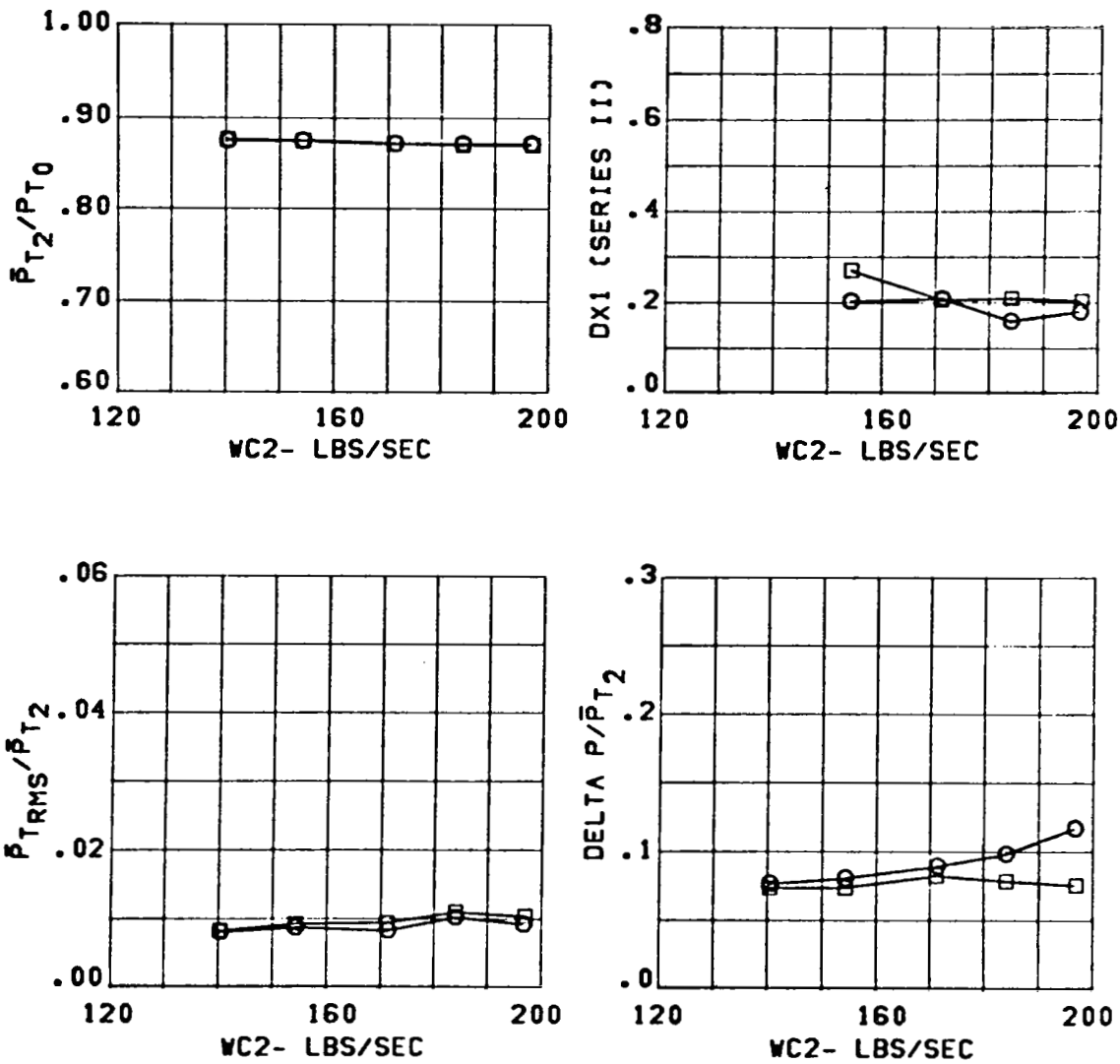

Figure 276 Effect of Vortex Generators on Inlet Performance

CONFIGURATION	SYM.	THROAT RAKES	MACH	CONDITION
C13/3.65 IN. DIV.	○	OUT	.90	ALPHA= -9.
	□	IN		BETA = 0.

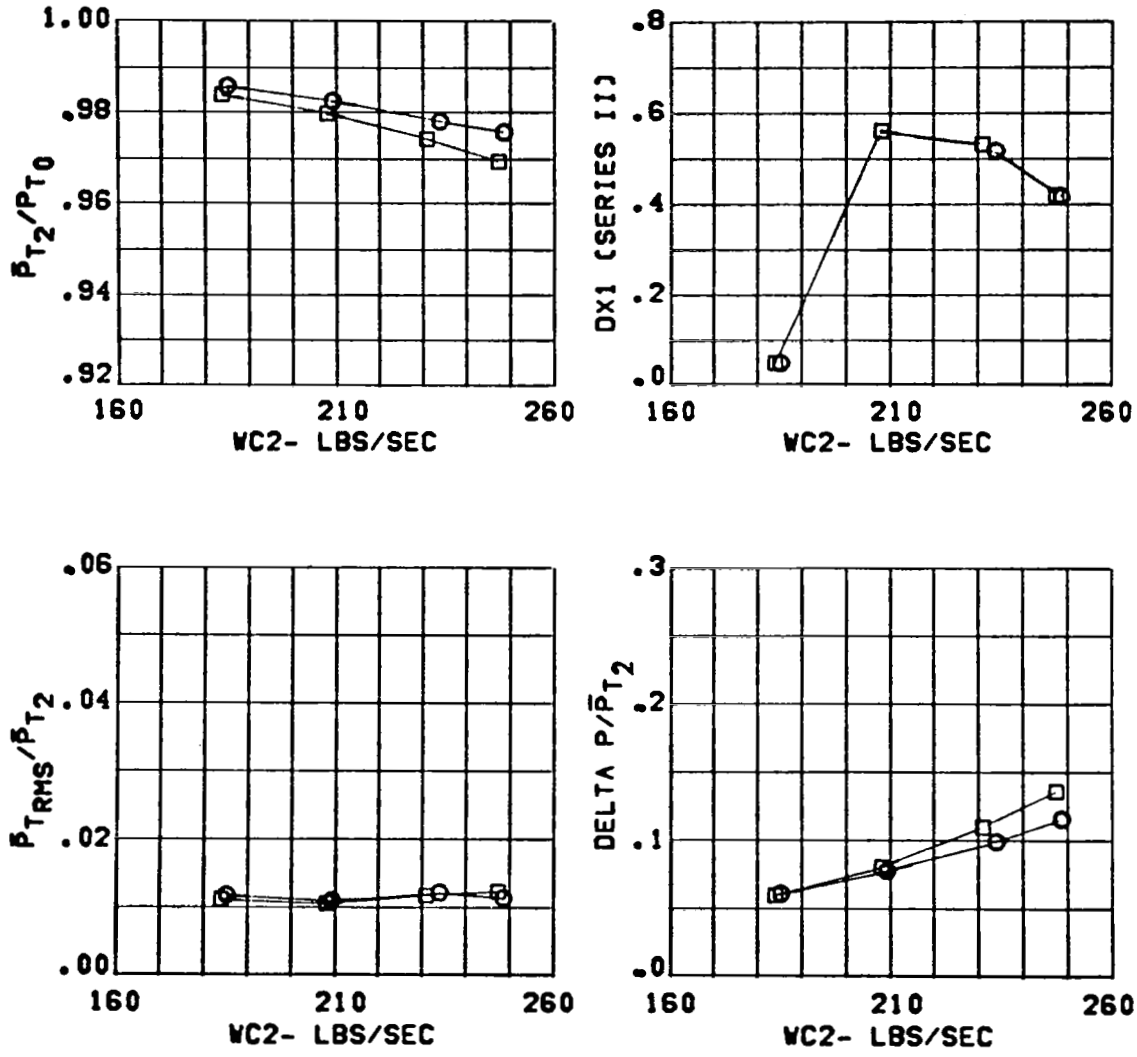

Figure 277 Effect of Throat Rakes on Inlet Performance

CONFIGURATION	SYM.	THROAT RAKES	MACH	CONDITION
C13/3.65 IN. DIV.	○	OUT	.91	ALPHA= 1.
	□	IN		BETA = 0.

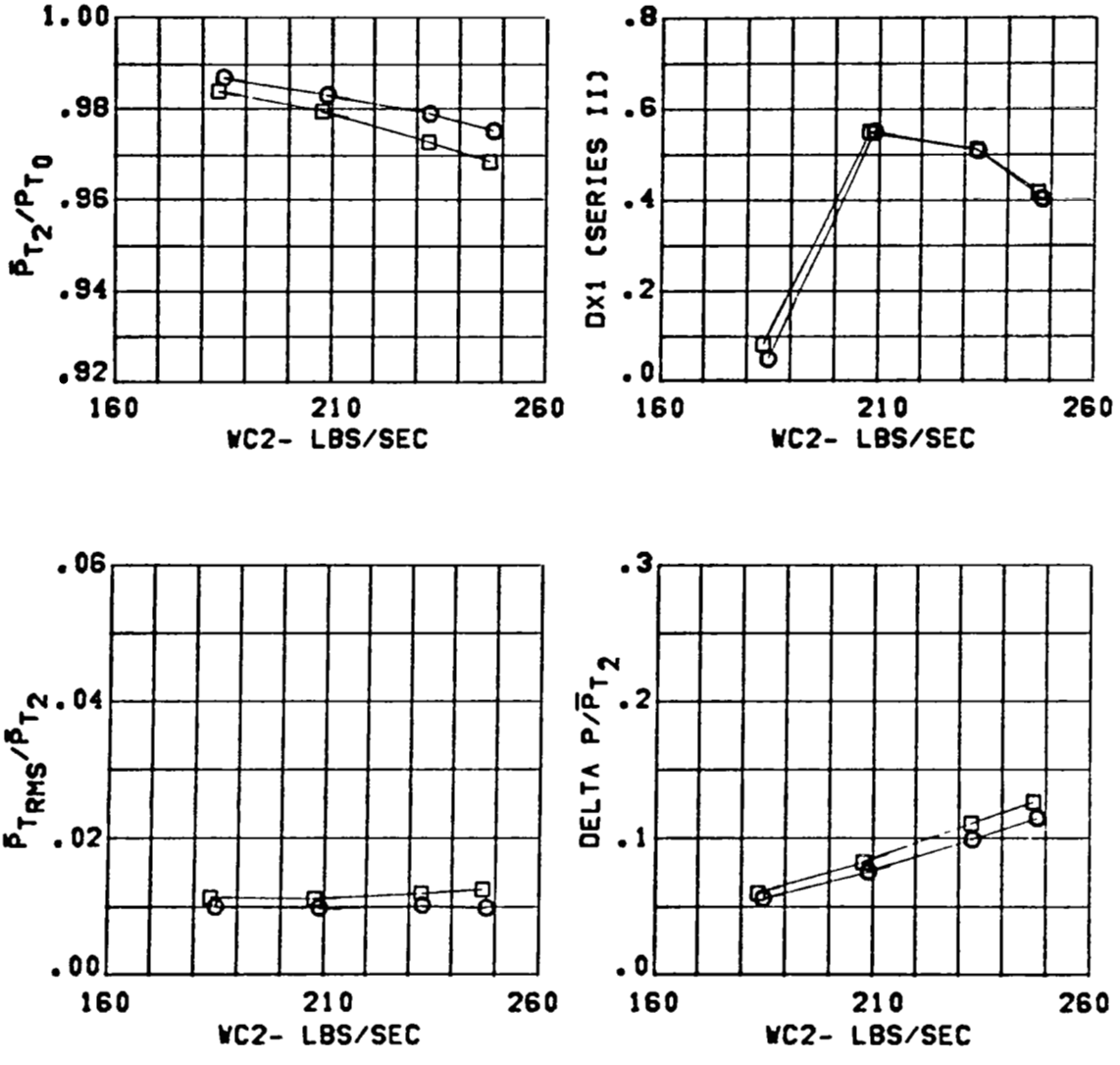

Figure 278 Effect of Throat Rakes on Inlet Performance

CONFIGURATION	SYM.	THROAT RAKES	MACH	CONDITION
C13/3.65 IN. DIV.	○	OUT	.89	ALPHA= 20.
	□	IN		BETA = 0.

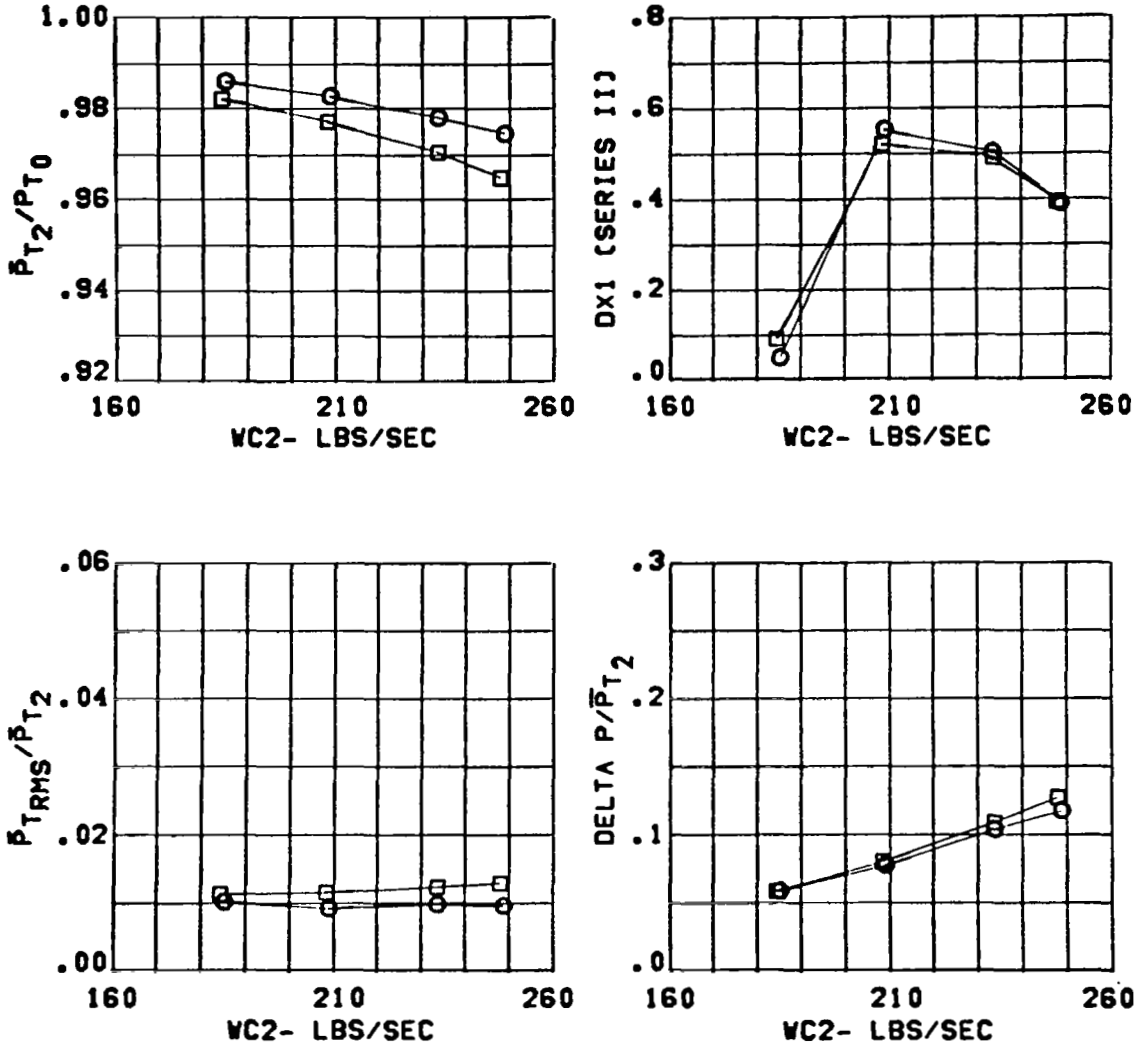

Figure 279 Effect of Throat Rakes on Inlet Performance

CONFIGURATION	SYM.	THROAT RAKES	MACH	CONDITION
C13/3.65 IN. DIV.	○	OUT	1.58	ALPHA= -5.
	□	IN		BETA = 0.

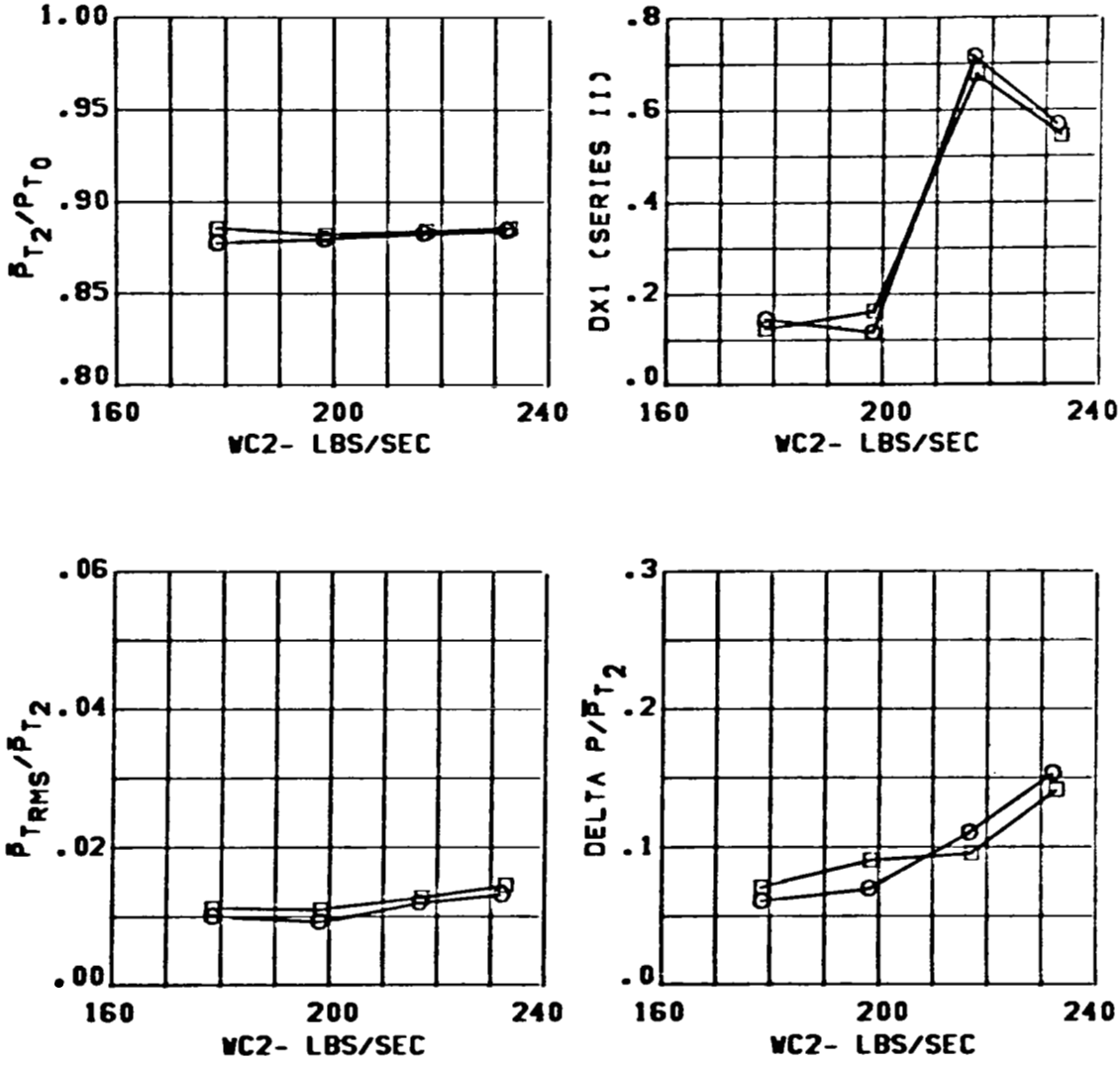

Figure 280 Effect of Throat Rakes on Inlet Performance

CONFIGURATION	SYM.	THROAT RAKES	MACH	CONDITION
C13/3.65 IN. DIV.	O	OUT	1.58	ALPHA= 1.
	□	IN		BETA = 0.

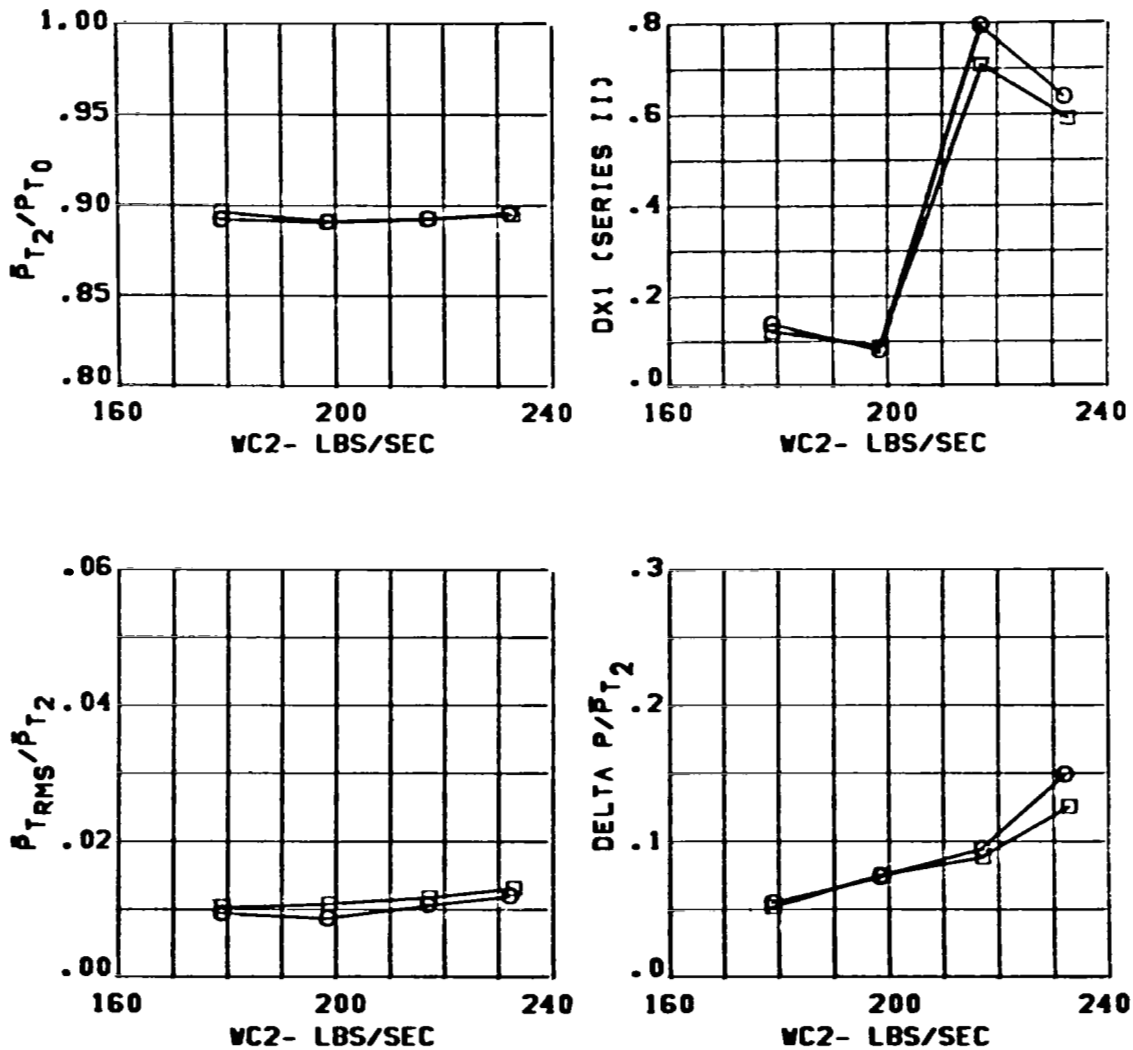

Figure 281 Effect of Throat Rakes on Inlet Performance

CONFIGURATION	SYM.	THROAT RAKES	MACH	CONDITION
C13/3.65 IN. DIV.	O	OUT	1.58	ALPHA= 20.
	□	IN		BETA = 0.

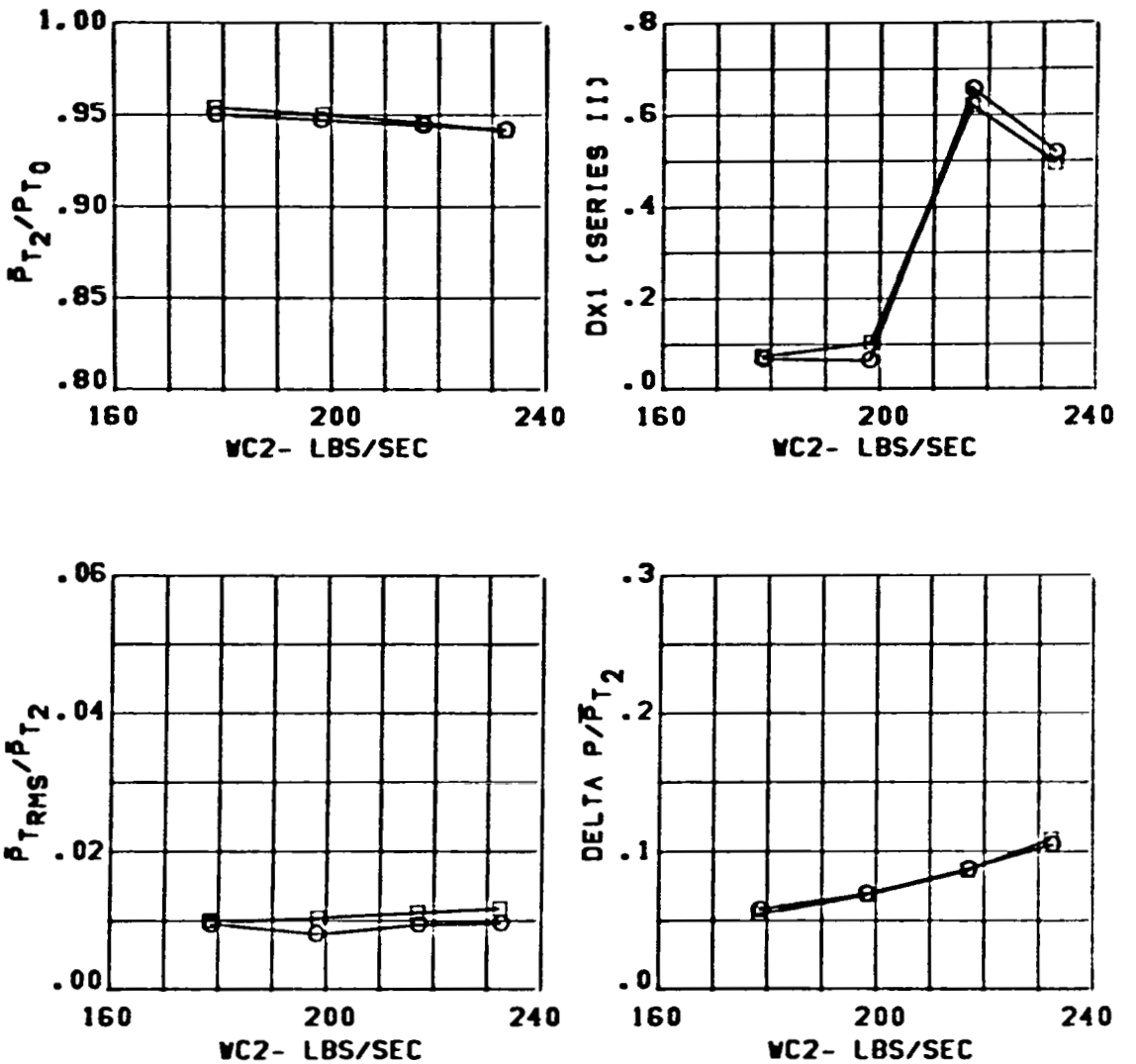

Figure 282 Effect of Throat Rakes on Inlet Performance

CONFIGURATION	SYM.	THROAT RAKES	MACH	CONDITION
C13/3.65 IN. DIV.	O	OUT	1.97	ALPHA= -5.
	□	IN		BETA = 0.

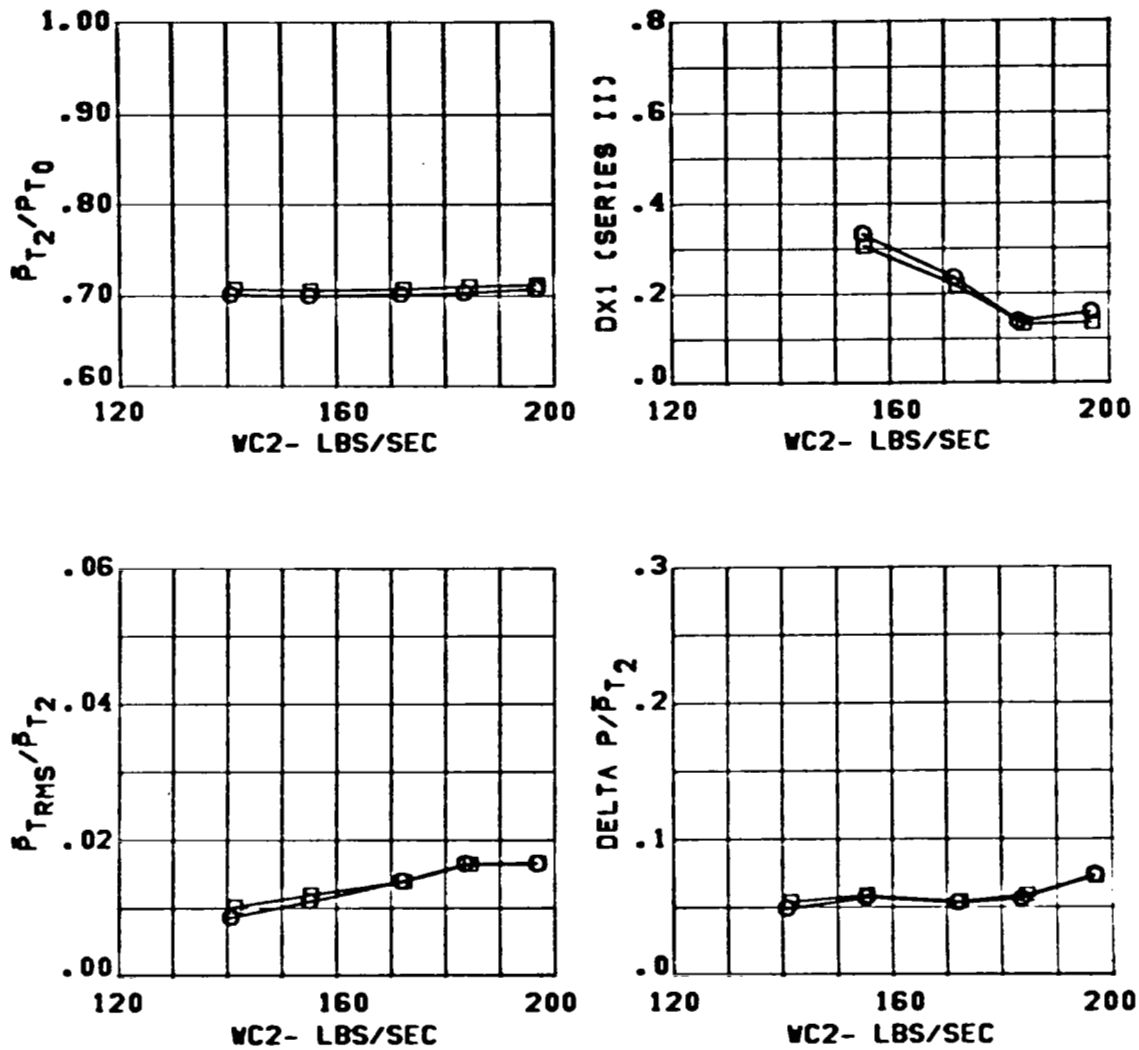

Figure 283 Effect of Throat Rakes on Inlet Performance

CONFIGURATION	SYM.	THROAT RAKES	MACH	CONDITION
C13/3.65 IN. DIV.	O	OUT	1.97	ALPHA= 1.
	□	IN		BETA = 0.

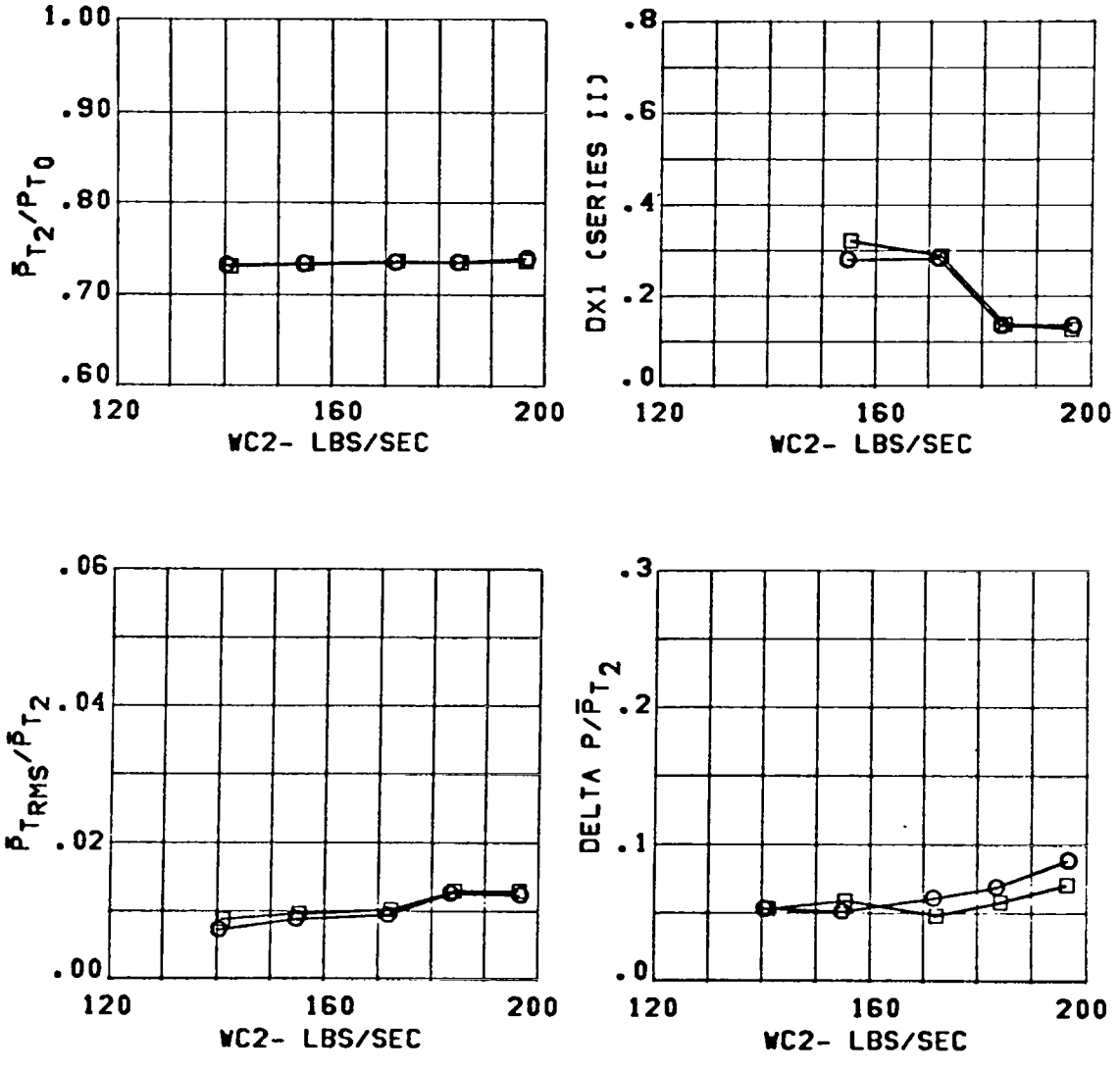

Figure 284 Effect of Throat Rakes on Inlet Performance

APPENDIX A

TEST PROGRAM

0.15-SCALE YF-16 INLET MODEL

NASA-LeRC-013 NOVEMBER-DECEMBER 1972

RUN	CONFIGURATION	DIV. HT.	MACH	$\alpha \sim$ DEG.	$\beta \sim$ DEG.	W_{C_2}
1	Splitter only Fuselage Rakes Nose Boom	3.65	2.0 2.0 1.6 1.6 .9	-5,6 1 -5,6 1 -10,-5,1,6	0,±5,-10 0,±5,-10,2 0,±5,-10 0,±5,-10,2 0,±5,-10,-15	- - - - -
2	Splitter Only Fuselage Rakes No Nose Boom	3.65	2.0,1.6	-5,1,6	0,±5	-
3	Splitter Only No Fuselage Rakes Nose Boom	3.65	2.0,1.6 2.0,1.6 .9	-5,1,6,10 1 -10,-5,1,6	0,±5,-10 2 0,±5,-10,-15	- - -
4	Splitter Only No Fuselage Rakes No Nose Boom	3.65	2.0,1.6	-5,1,6	0,±5	-
5	C_{13}, Nose Boom Throat Rakes	3.3	2.0 2.0	-5,1,6 20	0,-5,10 0	A* 185
6	C_{13} Nose Boom Throat Rakes	3.65	2.0 1.6 .9	-5 1,6 6 -5,1,6,20,10 -10,-5,1,20	0,-5 0,-5,-10 -10 0,-5,-10 0,-5,-10	A A 198 C F
7	C_{13} No Nose Boom Throat Rakes	3.65	2.0 .9	-5,1,6 30,40	0,-5 0,-5,-10	A F
8	C_{13} Nose Boom Throat Rakes	3.3	2.0 1.6 .9	20 -5,1,6,10,20 -10,-5,1,20, 30,40	0,-5,-10 0,-5,-10 0,-5,-10	A C F

***See airflow schedule at end of program.**

APPENDIX A

TEST PROGRAM (Continued)

RUN	CONFIGURATION	DIV. HT.	MACH	$\alpha \sim$ DEG.	$\beta \sim$ DEG.	W_{C_2}
9	$C13_A$	3.3	2.0	-5,10	0,-5	A
	Nose Boom			1,6,20	0,-5,-10	A
	Throat Rakes		1.6	-5,10	0,-5	C
				1,6,20	0,-5,-10	C
			.9	-5,1,20,30	0	F
10	C13	3.65	2.0	-5	0,-5	A^+
	Nose Boom			-5	-10	198
	No Throat Rakes			1,6,10,20	0,-5,-10	A^+
			1.8	-5,1,6,10,20	0,-5,-10	B^+
			1.6	-5,1	0,-5,-10	C^+
11				1	0,-10	C^+
				6,10,20	0,-5,-10	C^+
				-5	0,-5,-10	218
				1	-5,-10	218
			1.4	-5,1,6,15,25	0,-5,-10	D^+
			1.2	-10,-5,1,6, 15,30	0,-5,-10	E^+
			.9	-10,-5,1	0,-5,-10	F^+
12	C13	3.65	.9	6,10,20,30,40	0,-5,-10	F^+
	Nose Boom					
	No Throat Rakes		.6	1	0	F
				-10,-5,1,6,10, 20,30,40	0,-5,-10	G^+
				-10,-5,1,20,30	-15	G^+
			.9	35	0,-5,-10	234
			2.0	1	0	A
13	C15	3.65	2.0	-5,10	0,-5	A
	Nose Boom			1,6	0,-5,-10	A
	Throat Rakes			20	0	A
14	C14	3.65	2.0	-5,1,6,10,20	0,-5,-10	A
	Nose Boom		1.6	-5,1,6,10,20	0,-5,-10	C
	Throat Rakes					
15	C13	3.65	2.0	-5,1,20	0,-5,-10	A
	Nose Boom					
	No Throat Rakes		1.6	-5,1,20	0,-5,-10	C
	Splitter Struts		.9	-10,1,30	0,-5,-10,-15	F
				-5	-15	F
				35,37,40	0	F
				35	-5,-10	F

NOTE: When + appears in the W_{C_2} column, the buzz limit was determined in addition to the airflow schedule shown.

APPENDIX A

TEST PROGRAM (Continued)

RUN	CONFIGURATION	DIV. HT.	MACH	$\alpha\sim$ DEG.	$\beta\sim$ DEG.	W_{C_2}
16	C_{13}	3.65	2.0	-5	0	A
	Nose Boom		2.0	1,6,20	0,-5,-10	A
	No Throat Rakes					
	Splitter Struts		1.6	-5,1,6,20	0,-5,-10	C
	Vortex Generators		.9	-10,-5,1,6,20, 30,40	0,-5	F
			.9	-5,1,20,30	-10	F
			.4	-10,-5,30,40	0	-
			.4	1,6,10,20	0,-5,-10	-
17	C15	3.65	2.0	-5,10	0,-5	A
	Nose Boom			1,6,20	0,-5,-10	A
	Throat Rakes					
	Splitter Struts		1.6	-5,10	0,-5	C
				1,6,20	0,-5,-10	C
	C15A	3.65	2.0	-5,10	0,-5	A
	Nose Boom			1,6,20	0,-5,-10	A
	Throat Rakes					
	Splitter Struts		1.6	-5,10	0,-5	C
				1,6,20	0,-5,-10	C
18	C15	3.65	.9	-10,-5,1,10,20, 30,40	0,-10	F^+
	Nose Boom					
	Throat Rakes		2.0	-5,1,6,10,20	0,-5	+
	Splitter Struts		1.6	-5,1,6,10,20	0,-5	+
			1.4	-5,1,6,15,25	0,-10	D^+
			1.2	-5,1,6,15,30	0,-10	E^+
19	C15	3.65	2.0	-5,1,6	0,-5	A
	Nose Boom					
	Throat Rakes		1.6	-5,1,6	0,-5	C
	Splitter Struts					
	.3 in. more Bleed					
	C15	3.65	2.0	-5,1,6	0,-5	A
	Nose Boom					
	No Throat Rakes		1.6	-5,1,6	0,-5	C
	Splitter Struts					
	.3 in. More Bleed		.9	-10,-5,1,30,40	0,-10	F

NOTE: When + appears in the W_{C_2} column, the buzz limit was determined in addition to the airflow schedule shown.

APPENDIX A

TEST PROGRAM (Concluded)

	AIRFLOW SCHEDULES	
Mach No.	Schedule	Corrected Airflow W_{C_2} or $W\sqrt{\theta_2}/\delta_2$
2.0 (1.96)	A	198, 185, 172, 156, 140
1.8 (1.78)	B	215, 201, 186, 169, 150
1.6 (1.58)	C	234, 218, 200, 180, 160
1.4 (1.38)	D	245, 229, 208, 185, 160
1.2	E	248, 232, 210, 186, 160
0.9	F	250, 234, 210, 186, 160
0.6	G	214, 200, 180, 160

APPENDIX B

CALCULATION METHOD FOR PRATT & WHITNEY DISTORTION PARAMETER DX1

The principal steady-state distortion index for evaluation of engine/inlet compatibility for the Pratt and Whitney F100 engine is the parameter DX1. This parameter is the ratio of the fan distortion factor K_{a_2} to the nominal limiting value of K_{a_2} for stall-free engine operation; i.e.,

$$DX1 = \frac{K_{a_2}}{K_{a_2)_{LIM}}}$$

K_{a_2} is the engine fan distortion factor and consists of both radial, K_{ra_2}, and circumferential, K_θ, distortion. In equation form

$$K_{a_2} = K_\theta + BK_{ra_2},$$

where B is a factor which permits the fan circumferential and fan radial distortion to be considered on a common basis. Other notation is defined at the end of this Appendix.

The calculation procedure for each of the distortion factors (K_θ, K_{ra_2}, and K_{a_2}) is described below. The steady-state data used in these calculations are obtained with 40 (8 rakes/5 rings) compressor-face total-pressure probes located on centroids of equal area as shown in Figure B-1.

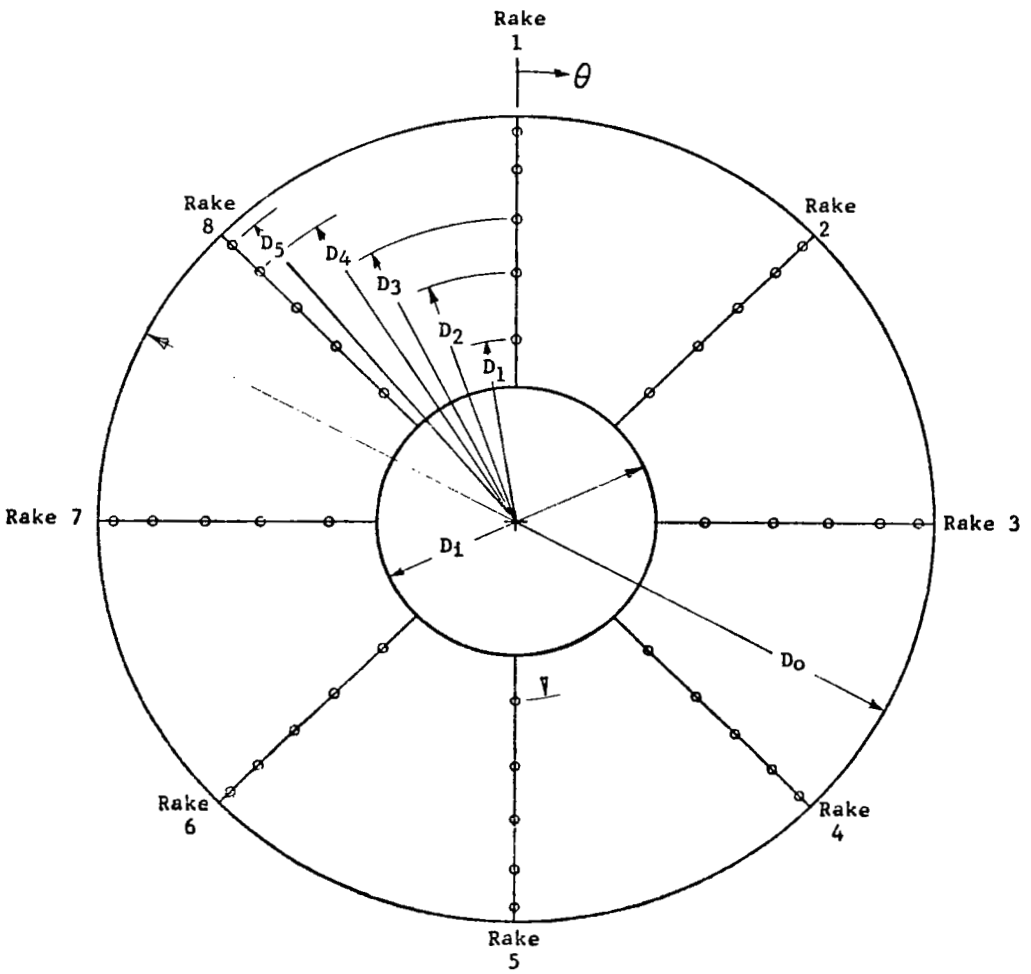

Figure B-1 Computation Plane Nomenclature

The nomenclature given in Figure B-1 is used in the following description.

Fan Circumferential Distortion Factor, K_θ

The P&WA engine specification requires the evaluation of the first ten Fourier coefficients for calculating circumferential distortion. However, for this test the following rapid procedure was used which evaluates only the first three Fourier coefficients.

1. For each test point the 40 compressor-face pressures are obtained. Starting with Ring 1, form the products (P_{t2}/P_{t_o}) cos θ and (P_{t2}/P_{t_o}) sin θ for each probe in the ring. θ is the rake angle measured from Rake 1. Note that θ is always an integer multiple of 45^o.
2. Use the products of Step 1 to obtain the Fourier coefficients a_1 and b_1:

$$\frac{a_1}{P_{to}} = 1/4 \sum_{I=1}^{8} \left(\frac{P_{t2}}{P_{to}}\right)_I \cos \theta_I$$

$$\frac{b_1}{P_{to}} = 1/4 \sum_{I=1}^{8} \left(\frac{P_{t2}}{P_{to}}\right)_I \sin \theta_I$$

where I is the rake designation.

3. Then

$$\frac{A1}{P_{to}} = \left[\left(\frac{a_1}{P_{to}}\right)^2 + \left(\frac{b_1}{P_{to}}\right)^2\right]^{\frac{1}{2}}$$

4. Repeat Steps 1 and 2 substituting Nθ (i.e., 2θ and 3θ) for θ to obtain a_2, b_2 and a_3, b_3. Then compute A_N/P_{to} as done in Step 3 (where previously, N = 1). Divide the quantity A_N/P_{to} by N^2 to yield $A_N/N^2/P_{to}$. The largest value of A_N/N^2P_{to} for the ring is designated $A_N/N^2P_{to})_{MAX}$ and retained.
5. Repeat Steps 1 through 4 for each ring.
6. For each ring, form the product $A_N/N^2P_{to})_{MAX}$ 1/D and sum over all rings to obtain

$$\sum_{J=1}^{5} \left[\frac{A_N}{N^2P_{to}}\right)_{MAX}\Bigg]_J \frac{1}{D_J}$$

where J is the ring designation and D_J is the radial distance to each ring as indicated in Figure B-1.

7. Obtain the sum of $1/D_J$ to obtain

$$\sum_{J=1}^{5} \frac{1}{D_J}$$

8. Obtain the average pressure for each ring

$$\overline{P}_{t2_r}/P_{to})_J = 1/8 \sum_{I=1}^{8} (P_{t_2}/P_{to})_{I,J}$$

and the average pressure for the compressor-face

$$\overline{P}_{t2}/P_{to} = 1/5 \sum_{J=1}^{5} (\overline{P}_{t2_r}/P_{to})_J$$

9. Calculate the percent corrected airflow and obtain $Q/\overline{P}_{t2}$:

$$\%W_{c_2} = W_{c2}\left(\frac{100}{217}\right)$$

$$Q/\overline{P}_{t_2} = f(\%\ W_{c_2}) \quad \text{(P\&WA correlation)}$$

10. Calculate K_θ using the results of Steps 6 through 9:

$$K_\theta = \frac{\sum_{J=1}^{5}\left[\frac{AN}{N^2P_{to}}\right)_{MAX}\Bigg]_J \frac{1}{D_J}}{\left(\frac{\overline{P}_{t2}}{P_{to}}\right)\left(\frac{Q}{\overline{P}_{t2}}\right)\sum_{J=1}^{5}\frac{1}{D_J}}$$

Fan Radial Distortion Factor, K_{ra_2}

11. Normalize each ring average pressure by the compressor face average to establish the radial profile.

$$\left.\frac{\overline{P}_{t2_r}}{\overline{P}_{t2}}\right)_J = \left.\frac{\overline{P}_{t2_r}}{\overline{P}_{t_o}}\right)_J \div \frac{\overline{P}_{t_2}}{P_{t_o}}$$

12. Enter P&WA correlation data with $\%W_{c_2}$ to obtain the base-radial-profile, $P_{t2r}/P_{t2})_{BASE\ J}$, for each ring.

13. For each ring, compute

$$\left| \left.\frac{\overline{P}_{t2_r}}{\overline{P}_{t2}}\right)_J - \left.\frac{\overline{P}_{t2_r}}{\overline{P}_{t2}}\right)_{BASE\ J} \right| \frac{1}{\left.\overline{P}_{t2_r}/\overline{P}_{t2}\right)_{BASE\ J}} \frac{1}{D_J}$$

14. Then compute K_{ra_2},

$$K_{ra_2} = \frac{\sum_{J=1}^{5} \left| \left.\frac{\overline{P}_{t2_r}}{\overline{P}_{t2}}\right)_J - \left.\frac{\overline{P}_{t2_r}}{\overline{P}_{t2}}\right)_{BASE\ J} \right| \frac{1}{\left.\overline{P}_{t2_r}/\overline{P}_{t2}\right)_{BASE\ J}} \frac{1}{D_J}}{\left(Q/\overline{P}_{t_2}\right) \sum_{J=1}^{5} \frac{1}{D_J}}$$

15. Enter P&WA correlation of $B = f(\%W_{c_2})$ with $\%W_{c_2}$ to obtain B and compute K_{a_2}.

$$K_{a_2} = K_\theta + BK_{ra_2}$$

16. Normalize K_{a_2} from Step 15 by $K_{a_2})_{LIM}$ to obtain DX1:

$$DX1 = \frac{K_{a_2}}{K_{a_2})_{LIM}}$$

$K_{a_2})_{LIM}$ is obtained from a P&WA correlation as a function of $\%W_{c_2}$, and represents a first-order approximation to the maximum value of K_{a_2} for stall-free engine operation. The limiting value of DX1 presented in this report is less than 1.0 because it is based on steady-state rather than instantaneous peak values of K_{a_2} and because no turbulence effects (P_{TRMS}) are included. The ultimate determination of whether a test condition represents stall-free operation of the engine/inlet combination is determined from a stability audit performed by Pratt and Whitney Aircraft.

APPENDIX B (Concluded)

NOTATION FOR DISTORTION PARAMETER CALCULATION

a_N, b_N	Fourier coefficients
B	B-factor in K_{a2} calculation
D	Diameters at the computation plane
DX1	Normalized K_{a2}
I, J	Rake and ring designation, respectively
K_{a2}, K_{ra2}, K_θ	P&WA distortion factors
$K_{a2})_{LIM}$	Screening limit for K_{a2}
N	Order of Fourier coefficients
P&WA	Pratt and Whitney Aircraft
P_{t_2}	Pressure from a specific (I, J) rake tube
$\overline{P}_{t_2}$	Average of the P_{t_2} values
$\overline{P}_{t_{2r}}$	Average of the eight P_{t_2} values in a given ring, J
$\overline{P}_{t_{2r_{BASE}}}$	Base-radial-profile for a given ring, J
Q	Dynamic pressure at the compressor face
θ	Angle of a rake measured from rake 1
θ^-	Greatest circumferential extent where $P_{t_2} \leq \overline{P}_{t_{2r}}$

REFERENCES

1. Garner, J. E.; and Strong, J. T.: Data Analysis Report of 0.15-Scale Lightweight Fighter Inlet Test. General Dynamics Convair Aerospace Division Report No. MR-P-330, 18 February 1972.

2. Leamer, P. C.: F33657-72-C-072 LWF Prototype Program, Data Analysis Report for Model 401A 0.15-Scale Inlet Test. General Dynamics Convair Aerospace Division Report No. MR-P-340, 2 October 1972.

3. Garner, J. E.; and Leamer, P. C.: YF-16/F100-PW-100 Inlet-Engine Compatibility Analysis. General Dynamics Convair Aerospace Division Report No. MR-P-364, 30 June 1973.

4. Swallow, R. J.; and Aiello, R. A.: NASA Lewis 8- by 6-Foot Supersonic Wind Tunnel. NASA TMX-71542, 1974.

5. Crosthwait, E. L., et al: Preliminary Design Methodology for Air-Induction Systems. SEG-TR-67-1, 1967.

1. Report No.	2. Government Accession No.	3. Recipient's Catalog No.
NASA CR-3049		

4. Title and Subtitle	5. Report Date
EXPERIMENTAL INVESTIGATION OF A 0.15-SCALE MODEL OF AN UNDERFUSELAGE NORMAL-SHOCK INLET	October 1978
	6. Performing Organization Code
7. Author(s)	8. Performing Organization Report No.
P. C. Leamer and I. G. Kennon	
	10. Work Unit No.
9. Performing Organization Name and Address	
General Dynamics Fort Worth Division P. O. Box 748 Fort Worth, Texas 76101	11. Contract or Grant No. NAS3-21139
	13. Type of Report and Period Covered
12. Sponsoring Agency Name and Address	Contractor Report
National Aeronautics and Space Administration Washington, D. C. 20546	14. Sponsoring Agency Code

15. Supplementary Notes

Final report. Project Manager, Bobby W. Sanders, Wind Tunnel and Flight Division, NASA Lewis Research Center, Cleveland, Ohio 44135.

16. Abstract

A 0.15-scale model of an underfuselage inlet designed for a single-engine fighter airplane was tested during 1972 at the NASA Lewis Research Center by General Dynamics' Fort Worth Division. The inlet is a fixed-geometry, normal-shock configuration designed to operate at flight speeds up to Mach 2.0. Performance data for the basic inlet and several configuration variations are presented as a function of angle of attack, angle of sideslip, and airflow in the 0.6 to 2.0 Mach number range. The configuration variations include boundary-layer diverter height, cowl and splitter-plate modifications, and inlet bleed system variations. Flow-field characteristics at the simulated engine face, at the inlet throat, at the splitter-plate leading edge, and forward of the inlet are presented. The pressure recovery of the inlet is approximately equal to the product of theoretical normal-shock and duct pressure recoveries at cruise angle of attack. Very good performance at high angle of attack was obtained. Pressure distortion and turbulence at the engine face are low, and the inlet remains stable at all engine airflows over the flight maneuver envelope of the aircraft for which the inlet was designed.

17. Key Words (Suggested by Author(s))	18. Distribution Statement
Air induction systems; Air inlets; Air intakes; Engine inlets; Inlet flow; Inlets; Intake systems; Pressure recovery; Supersonic inlets	Unclassified - unlimited STAR Category 02

19. Security Classif. (of this report)	20. Security Classif. (of this page)	21. No. of Pages	22. Price*
Unclassified	Unclassified	330	A15

* For sale by the National Technical Information Service, Springfield, Virginia 22161

NASA-Langley, 1978